T | Theoretical Division

at Los Alamos National Laboratory

RESEARCH HIGHLIGHTS 2006

A Supplement to the Division Annual Self-Assessment

Issued April 2006

Division Leader
Alan R. Bishop

Deputy Division Leader
Paul J. Dotson

Publication Designer
Sharon Mikkelson

Editor
Denise Sessions

Printing Coordinator
Guadalupe D. Archuleta

We gratefully acknowledge the authors who contributed to this publication.

Address mail to
Los Alamos National Laboratory
Theoretical Division Office
P.O. Box 1663, Mailstop B210
Los Alamos NM 87545

http://www.lanl.gov/orgs/t/
Tel: 505.667.4401, Fax: 505.665.4055

• Unclassified •

Los Alamos NATIONAL LABORATORY EST. 1943

Preface

The Theoretical Division is an intellectual resource to Los Alamos National Laboratory and the nation, providing creative scientific and technological solutions to challenges in national security and related problems of national and global importance. The Laboratory's national security mission has an enduring need for science and technology beyond today's frontiers. Theoretical Division responds to this need by striving to provide the best science and scientists to current LANL missions, and by pursuing frontier science to ensure excellence in scientific capabilities, creating new scientific directions, and attracting scientific leaders to LANL.

The Theoretical Division's capabilities are central to the Laboratory's Strategic Goals. Working with teams across the Laboratory, we undertake the major multidisciplinary challenge of integrating theory, modeling, simulation, and visualization with experimental and other data to provide cutting-edge, validated tools to interpret and guide experiments and expand predictive capability and uncertainty quantification to complex phenomena and systems. The core Nuclear Weapons Program—the centerpiece of the DOE Weapons Complex—depends critically on the viability of our approach. However, virtually every major initiative at LANL also relies heavily on this integrated capability: threat reduction and homeland security, manufacturing science, biology, nanoscience, quantum information, energy, infrastructure, and so on.

Each year, T-Division staff selects a collection of brief topical reports on their progress, as part of our self-assessment process. This collection is not intended to be complete. Rather it aims to demonstrate, through timely examples, the energy and progress across (and between) many disciplines in the Division in pursuit of our goal to serve the Laboratory and nation by furthering our fundamental understanding of, and predictive capabilities for, complex phenomena.

Alan R. Bishop
Division Leader

Paul J. Dotson
Deputy Division Leader

Contents

Preface

Alan Bishop and Paul Dotson (T-DO)

Part 1: Featured Groups T-1, T-3, T-11, T-12, T-14

T-1
Equation of State and Mechanics of Materials

Equation of State Developments in T-1 5
Nicolas Bock, Leonid Burakovsky, Eric Chisolm, Scott Crockett, Giulia De Lorenzi-Venneri, Denise George, Carl Greeff, J. D. Johnson, Travis Peery, Sven Rudin, and Duane Wallace, T-1

Multiphase Equations of State for the SESAME Database 7
Eric D. Chisolm, Denise C. George, and Carl W. Greeff, T-1

Dynamic Response of HMX Through the β–δ Phase Transition 9
Bradford E. Clements, Eric M. Mas, JeeYeon N. Plohr, Axinte Ionita, T-1; and Francis L. Addessio, T-3

Micromechanics Models for Plastic-Bonded High Explosives: Recent Developments 11
Bradford E. Clements and Eric M. Mas, T-1; and Curt A. Bronkhorst and Todd O. Williams, T-3

Low-Pressure Equation of State of Polymers 13
Bradford E. Clements, T-1

Image Shape Analysis 15
Denise George, T-1

Continuum Models for Multiphase EOS 17
Carl W. Greeff, T-1

Are Lattice Relaxations in Thin Film Nanodevices Driven by Quantum-Size or Interface Proximity Effects? 19
Erik Holmström, Nicolas Bock, John Wills, and Anders M. N. Niklasson, T-1

Two-Scale FEM Approach in the Dynamic Response of a Heterogeneous Material 21
Axinte Ionita, Eric M. Mas, and Bradford E. Clements, T-1

First Principles Calculations of the 3-k Magnetic Structure and 3-k Distortion in UO_2 23
Raquel Lizárraga, T-1; Massimiliano Colarieti-Tosti, IFM, Sweden; Olle Eriksson and Lars Nordström, Uppsala University, Sweden; and John M. Wills, T-1

Studies of the Incommensurate Magnetic Structure of a Heavy Fermion System: $CeRhIn_5$ 25
Raquel Lizárraga, T-1; Massimiliano Colarieti-Tosti, IFM, Sweden; Olle Eriksson and Lars Nordström, Uppsala University, Sweden; and John M. Wills, T-1

Finite Element Method Calculations on Statistically Consistent Microstructures of PBX 9501 27
Eric M. Mas, Bradford E. Clements, and Axinte Ionita, T-1; and Paul D. Peterson, DX-2

Dynamically Driven Phase Transformations in Damaged Composite Materials 29
JeeYeon N. Plohr and Bradford E. Clements, T-1; and Francis L. Addessio, T-3

Calculated Effects of Ga on the Pu Lattice after the δ to α Transformation 31
Sven P. Rudin and John M. Wills, T-1

Phonons from Density Functional Theory for Equations of State 33
Sven P. Rudin, J. D. Johnson, and John M. Wills, T-1

Vibration-Transit Theory for Time Correlation Functions in Liquids: A Model for Transits 35
Giulia De Lorenzi-Venneri and Duane Wallace, T-1

T-3
Fluid Dynamics

Local Deformation Behavior of Metallic Polycrystals 39
Curt A. Bronkhorst and B. L. Hansen, T-3

A Strength Model for Materials with Phase Transformations 41
Eric N. Harstad, Francis L. Addessio, and Q. Ken Zuo, T-3; and Carl W. Greeff, T-1

Permeating Fluid Effects in Cellular Material Systems under Dynamic Loading 43
Mark W. Schraad and Francis H. Harlow, T-3

Instabilities in Cellular Solids and the Role of Dispersity in Geometric Structure 45
Mark W. Schraad, T-3

Stochastic Multiscale Material Modeling 47
Todd O. Williams, T-3

Properties of Metals at Extreme Loading Rates 49
Aleksander Zubelewicz, T-3

A Two-Component Element for Modeling Strain Localization in Materials 51
Q. Ken Zuo and Paul J. Maudlin, T-3

A Rate-Dependent Damage Model for Brittle Materials under Dynamic Loading .. 53
Q. Ken Zuo and Francis L. Addessio, T-3; and John K. Dienes, T-14

An Implicit Algorithm for a Rate-Dependent Brittle Damage Model 55
Q. Ken Zuo, T-3

T-11
Condensed Matter and Statistical Physics

Fourier Transform Inelastic Electron Tunneling Spectroscopy and STM 59
Alexander V. Balatsky and Jian-Xin Zhu, T-11

Oscillating Elastic Defects: Competition and Frustration 61
Julien Barré, T-11/CNLS; Alan R. Bishop, T-DO; Turab Lookman and Avadh Saxena, T-11

Coexistence of Ferroelectricity and Ferromagnetism 63
Cristian D. Batista and James E. Gubernatis, T-11; and Wei-Guo Yin, Brookhaven National Laboratory

Universal Properties of Modulated Antiferromagnetic Systems 65
Cristian D. Batista, Gerardo Ortiz, and Alexander V. Balatsky, T-11

Strong Electron-Phonon Coupling in δ-phase Stabilized Plutonium 67
Matthias J. Graf and Turab Lookman, T-11; John M. Wills and Duane C. Wallace, T-1; and Jason C. Lashley, MST-NHMFL

The Quantum Dynamics of Polaron Formation 69
Li-Chung Ku, University of Texas; and Stuart Trugman, T-11

Defect Induced Nucleation in Cubic to Tetragonal Martensites 71
Turab Lookman and Avadh Saxena, T-11; and Rajeev Ahluwalia, Institute for Materials Research & Engineering, Singapore

Molecular Bridging in Asymmetric Triblock Copolymers 73
Kim Ø. Rasmussen, T-11; Edward M. Kober, T-14; and R.J. Spontak, North Carolina State University

Theory of Forced DNA Unzipping 75
Kim Ø. Rasmussen, T-11; Nikolaos Voulgarakis, CNLS; and Alan R. Bishop, T-DO

Piezoelectric Response of Domains in Ferroelectrics 77
Avadh Saxena and Turab Lookman, T-11; and Rajeev Ahluwalia, Institute for Materials Research & Engineering, Singapore; and W. Cao, Pennsylvania State University

Electron Spin Flow and Transport in Semiconductor Epilayers 79
Darryl L. Smith, T-11; M. Hruška, Lawrence Livermore National Laboratory; Š. Kos, Cambridge University; Avadh Saxena, T-11; and S.A. Crooker, MST-NHMFL

Phase Diagram and Spectroscopy of Fulde-Ferrell-Larkin-Ovchinnikov States of Two-Dimensional d-wave Superconductors 81
Anton B. Vorontsov, Louisiana State University; James A. Sauls, Northwestern University; and Matthias J. Graf, T-11

Single Molecule DNA Sequencing with Inelastic Tunneling Spectroscopy STM ... 83
Jian-Xin Zhu, Kim Ø. Rasmussen, and Stuart A. Trugman, T-11; Alan R. Bishop, T-DO; and Alexander V. Balatsky, T-11

T-12
Theoretical Chemistry and Molecular Physics

Increasing the Length Scale in Temperature Accelerated Dynamics Simulations ... 87
Jacques Amar and Yunsic Shim, University of Toledo; Blas Uberuaga, MST-8; and Arthur F. Voter, T-12

Role of Fluctuations in a Snug-fit Mechanism of KcsA Channel Selectivity 89
D. Asthagiri and Lawrence R. Pratt, T-12; and Michael E. Paulaitis, Ohio State University

Structure and Electronic Excitations in Organometallic Transition Metal Complexes 91
Enrique R. Batista and Richard L. Martin, T-12

A Mechanism for the Mullins Effect 93
David E. Hanson, T-12; and Marilyn Hawley and Robert Houlton, MST-8

Electronic Interactions in Organometallic Actinide Complexes 95
P. Jeffrey Hay, Richard L. Martin, Enrique R. Batista, T-12; and Aurora E. Clark, Washington State University

Simulating the Structure and Properties of Magnesium Methoxide 97
Neil J. Henson, T-12; and Kevin C. Ott, C-SIC

Update on the Aging of PBX 9501 via Free-Radical Oxidation **99**
Joel D. Kress, T-12

Avalanches and Scaling in Plastic Deformation **101**
Richard LeSar, T-12; Marisol Koslowski, Purdue University; and Robb Thomson, T-12

Investigations of Hybrid Density Functional Theory in Condensed Matter **103**
Richard L. Martin, Cristian V. Diaconu, Enrique R. Batista, and P. Jeffrey Hay, T-12

Photoexcited Vibrational Dynamics in Vicinity of Conical Intersections **105**
Andrei Piryatinski and Sergei Tretiak, T-12; Misha Stepanov, T-13; and Vladimir Chernyak, Wayne State University

Noise at the Crossover from Wigner Liquid to Wigner Glass **107**
Charles Reichhardt, T-13; and Cynthia J. Olson Reichhardt, T-12

Do Vortices Entangle? **109**
Cynthia J. Olson Reichhardt, T-12, and Matthew B. Hastings, T-13

Coulomb Explosion Mechanisms for Ion Damage **111**
Cynthia J. Olson Reichhardt, T-12

Time-Dependent Density Functional Theory for Frequency-Dependent Nonlinear Optical Response **113**
Sergei Tretiak, T-12

Real Time Observation of Nonlinear Coherent Phonon Dynamics in Single-Wall Carbon Nanotubes **115**
Sergei Tretiak and Andrei Piryatinski, T-12; CNLS; Avadh Saxena, T-11; Richard L. Martin, T-12; Alan R. Bishop, T-DO; A. Gambetta, C. Manzoni, E. Menna, M. Meneghetti, G. Cerullo, and G. Lanzani, Politecnico di Milano

T-14
Explosives and Organic Materials

The Rayleigh-Taylor Instability via Direct Simulation Monte Carlo **119**
John L. Barber and Kai Kadau, T-14; Timothy C. Germann, X-1; Peter S. Lomdahl, T-14; Brad L. Holian, X-1; and Berni Alder, Lawrence Livermore National Laboratory

Coupling Grain Scale and Bulk Mechanical Response of PBXs via Numerical Simulation **121**
Scott Bardenhagen and Andrew Brydon, T-14

Simulation and Analysis of Real Foam Microstructures **123**
Scott Bardenhagen, Andrew Brydon, and Lucas Wharton, T-14

Influence of Supercoiling on the Disruption of dsDNA **125**
Shirish M. Chitanvis and Paul Welch, T-14

Can Low-Power Electromagnetic Radiation Disrupt Hydrogen Bonds in dsDNA? **127**
Shirish M. Chitanvis, T-14

Probing the Physics of Mix **129**
Shirish M. Chitanvis, T-14

Atomistic Studies of Quasi-Static Compression in α-HMX **131**
Eugenio Jaramillo and Thomas D. Sewell, T-14; and Alejandro Strachan, Purdue University

Inelastic Deformation in Shock Loaded HMX **133**
Eugenio Jaramillo and Thomas D. Sewell, T-14; and Alejandro Strachan, Purdue University

Direct Observation of the alpha-epsilon Transition in Shock-Compressed Iron via Nanosecond X-ray Diffraction **135**
Kai Kadau, T-14; Timothy C. Germann, X-1; Peter S. Lomdahl, T-14; Brad L. Holian, X-1; D.H. Kalantar and J. Hawreliak, Lawrence Livermore National Laboratory; and K. Rosolankova and J.S. Wark, University of Oxford

Multibillion-atom Molecular Dynamics Simulations of Shockwave Phenomena on BlueGene/L **137**
Timothy C. Germann and Brad L. Holian, X-1; and Kai Kadau and Peter S. Lomdahl, T-14

Modeling Strategies for Containing Pandemic Influenza in the U.S. **139**
Kai Kadau, T-14; Timothy C. Germann, X-1; Peter S. Lomdahl, T-14; Norman L. Johnson, CHS; Tim McPherson, D-4; Ira M. Longini, Jr., Emory University; and Catherine A. Macken, T-10

Detonation Wave Profile in PBX 9501 ..... **141**
Ralph Menikoff, T-14

The Effects of Crowding in Dendronized Polymers **143**
Paul M. Welch, T-14; and Cynthia F. Welch, LANSCE-12

Parameterizing Dynamic Field Simulations from Image Analysis **145**
Paul M. Welch and Thomas D. Sewell, T-14; Kim Ø. Rasmussen, T-11; Shirish M. Chitanvis, T-14; and Turab Lookman, T-11

A Tunable Dendritic Molecular Actuator **147**
Paul M. Welch, T-14

Atomistic Simulations of Chemical Reaction in Nanolaminates under Shock Loading **149**
Shijin Zhao, T-14; Timothy C. Germann, X-1; and Alejandro Strachan, Purdue University

Part 2:
Other T-Division Groups
T-3 Nonmaterials, T-4, T-6 T-7, T-8, T-10, T-13, T-15, T-16, T-QC

T-3
Fluid Dynamics (Nonmaterials)

Multiphysics Time Integration and Long Time Integration Error 155
Dana A. Knoll, Vincent A. Mousseau, Rick M. Rauenzahn, Katherine J. Evans, T-3; and Luis Chacón, T-15

Nuclear Reactor Safety.....157
Vincent A. Mousseau, T-3

Multiphase Flow Approach Toward Fluid-Structure Interactions.....159
Xia Ma, Qisu Zou, Duan Z. Zhang, and W. Brian VanderHeyden, T-3; and Nely Padial-Collins, CCS-2

Acoustic Wave Propagation in a Particle-Laden Gas 161
Peter J. O'Rourke, Michael C. Cline, and Manjit S. Sahota, T-3

KIVA-4: An Unstructured Version of KIVA-3V 163
David J. Torres, T-3

Coupled Chemical Climate Modeling.....165
Mathew E. Maltrud, T-3; Scott Elliott, CCS-2; Shaoping Chu, EES-2; P. Jones, T-3; and J. Drake, Oak Ridge National Laboratory

Temporal Accuracy of the Solution of Radiation Hydrodynamics Equations.....167
Rick M. Rauenzahn, Vincent A. Mousseau, and Dana A. Knoll, T-3

T-4
Atomic and Optical Theory

Small Polarons in a Dilute Bose-Einstein Condensate.....171
Fernando M. Cucchietti and Eddy Timmermans, T-4

Spectroscopic Characterization of an Ultrashort Laser Driven Ar Cluster Target ..173
Manolo Sherrill, Joseph Abdallah, Jr., George Csanak, T-4; Evan Dodd, X-1; Yuji Fukuda,

JAERI, Kyoto, Japan; and Anatoly Faenov, VNIIFTRI Moscow, Russia

***Ab-initio* Simulations of the Nonequilibrium Properties of Warm Dense Gold....175**
Stephane Mazevet, T-4; and J. Clérouin, P.M. Anglade, V. Recoules, and G. Zerah, CEA/DAM Île-de-France

Improvements to the Finite-Temperature Average-Atom Model 177
James Colgan, George Csanak, and Lee A. Collins, T-4; Christopher J. Fontes, X-1

Triple Photoionization of Li and Be 179
James Colgan, T-4

Mean-Field Statistical Theory of Finite Quantum Systems with Applications to Hot Dense Plasmas 181
Sergey A. Ponomarenko, George Csanak, David P. Kilcrease, and Manolo Sherrill, T-4

T-6
Theoretical Astrophysics

Oscillating Burning on Accreting Neutron Stars.....186
Alexander Heger, T-6; Andrew Cumming, McGill University; and Stan Woosley, University of California, Santa Cruz

Hydrodynamic Simulations of He-shell Flash Convection.....187
Falk Herwig, T-6; Bernd Freytag, T-6/Michigan State University/Uppsala University; Robert M. Hueckstaedt and Francis X. Timmes, X-2

T-7
Mathematical Modeling and Analysis

A Family of Mimetic Finite Difference Methods on Polygonal and Polyhedral Meshes.....191
Franco Brezzi, Konstantin Lipnikov, and Valeria Simoncini, T-7

New Discretization Methodology on Generalized Polyhedral Meshes 193
Franco Brezzi, Konstantin Lipnikov, and Mikhail Shashkov, T-7

Interface Reconstruction in Multifluid Flow Simulations.....195
Rao Garimella, Vadim Dyadechko, Blair Swartz, and Mikhail Shashkov, T-7

Bloch-Front Turbulence in a Periodically Forced Belousov-Zhabotinsky Reaction.....197
Aric Hagberg, T-7

Rare Events in Turbulence Might Not Be So Rare.....199
Susan Kurien, T-7

Differential Equations in Random Domains 201
Daniel M. Tartakovsky, T-7; and Dongbin Xiu, Purdue University

T-8
Elementary Particles and Field Theory

Inverse-Scattering Theory and the Density Perturbations from Inflation 205
Salman Habib, T-8; Katrin Heitmann, ISR-1; and Gerard Jungman, T-6

T-10
Theoretical biology and Biophysics

Conformational Dependence of Enzyme Function 209
Montiago X. LaBute, Paul W. Fenimore, Chang-Shung Tung, Benjamin H. McMahon, T-10

Nanocomputers Inside Our Bodies: Understanding How the Ribosome Decodes Genetic Information 211
Kevin Y. Sanbonmatsu, T-10

T-13
Complex Systems

Application of Optically Detected Magnetic Resonance in a Nanoprobe to Measurement of Single Electron and Nuclear Spin States 215
Gennady P. Berman, T-13; Alan R. Bishop, T-DO; Boris M. Chernobrod, T-13; Marilyn E. Hawley and Geoffrey W. Brown, MST-8; and Vladimir I. Tsifrinovich, Polytechnic University

Collective Decoherence of the Superpositional Entangled States in Quantum Shor Algorithm 217
Gennady P. Berman and Dmitry I. Kamenev, T-13; and Vladimir I. Tsifrinovich, Polytechnic University

Iterative Algorithm for Finding Frequent Patterns in Transactional Databases 219
Gennady P. Berman, Vyacheslav N. Gorshkov, Edward P. MacKerrow, T-13; and Xidi Wang, Citigroup, Sao Paulo, Brazil

Novel Opto-Nanomechanical Photodetector for Improving the Sensitivity of LIDAR and Local Optical Sensors 221
Gennady P. Berman, T-13; Alan R. Bishop, T-DO; Boris M. Chernobrod, T-13; and Marilyn E. Hawley and Geoffrey W. Brown, MST-8

Quasiclassical Model of Spin Diffusion and Relaxation in a Nonuniform

Magnetic Field 223
Gennady P. Berman, Boris Chernobrod, Vyacheslav N. Gorshkov, T-13; and Vladimir I. Tsifrinovich, Polytechnic University

Sub Shot-Noise Phase Sensitivity with a Bose-Einstein Condensate Mach-Zehnder Interferometer 225
Gennady P. Berman, T-13; Alan R. Bishop, T-DO; Lee A. Collins, T-4; and Luca Pezzé and Augusto Smerzi, T-13

T-15
Plasma Theory

A Nonlinear, Fully Coupled Moving Mesh Adaptive Grid Strategy 229
Luis Chacón and Giovanni Lapenta, T-15

Single Helicity States in Reversed Field Pinches 231
Gian Luca Delzanno, Luis Chacón, and John M. Finn, T-15

Kink Stability with Line Tying 233
Evstati G. Evstatiev, Gian Luca Delzanno, and John M. Finn, T-15

Regression in the Presence of Strongly Correlated Data 235
Christopher S. Jones and John M. Finn, T-15; and Nicolas Hengartner, D-1

NUTHELLA: A Simulation Tool for Generation IV Nuclear Reactors 237
Giovanni Lapenta, T-15

Electrostatic Fields Mediate Micro/Macro Coupling in Plasmas 239
Giovanni Lapenta, T-15; William Daughton, X-1; Thomas Intrator, P-24; and Benoit Lavraud, ISR-1

Virtual Nanoscience Laboratory: A Tool for the Mesoscale Simulation of Nanomaterials 241
Giovanni Lapenta and Gianluca Zuccaro, T-15

PARSEK: A New Integrated Package for Plasma Simulation Based on Particles ... 243
Giovanni Lapenta and Stephano Markidis, T-15

T-16
Nuclear Physics

Symmetry of the Relativistic Quantum Mechanical Harmonic Oscillator and the Antinucleon Spectrum in Nuclei 247
Joseph N. Ginocchio, T-16

Calculation of Neutron Spectra in beta-delayed Neutron-Emission 249
Toshihiko Kawano, Peter Möller, and William B. Wilson, T-16

Determination of Am Fission Barriers from Calculated High-Dimensional Potential-Energy Surfaces 251
Peter Möller, T-16

The Reactions $^{13}C(p,\gamma)\,^{14}N$ and $^{10}B(p,\alpha)\,^{7}Be$ 253
Philip R. Page and Gerald M. Hale, T-16

T-QC
Quantum Computing

Sub-Planck Structures in Phase Space and Heisenberg-Limited Measurements ...257
Diego A. R. Dalvit and Wojciech H. Zurek, T-QC; and Luiz Davidovich and Fabricio Toscano, Federal University, Rio de Janeiro, Brazil

Shock Waves in Ultracold Atomic Gases 259
Bogdan Damski, T-QC

Author Index 261

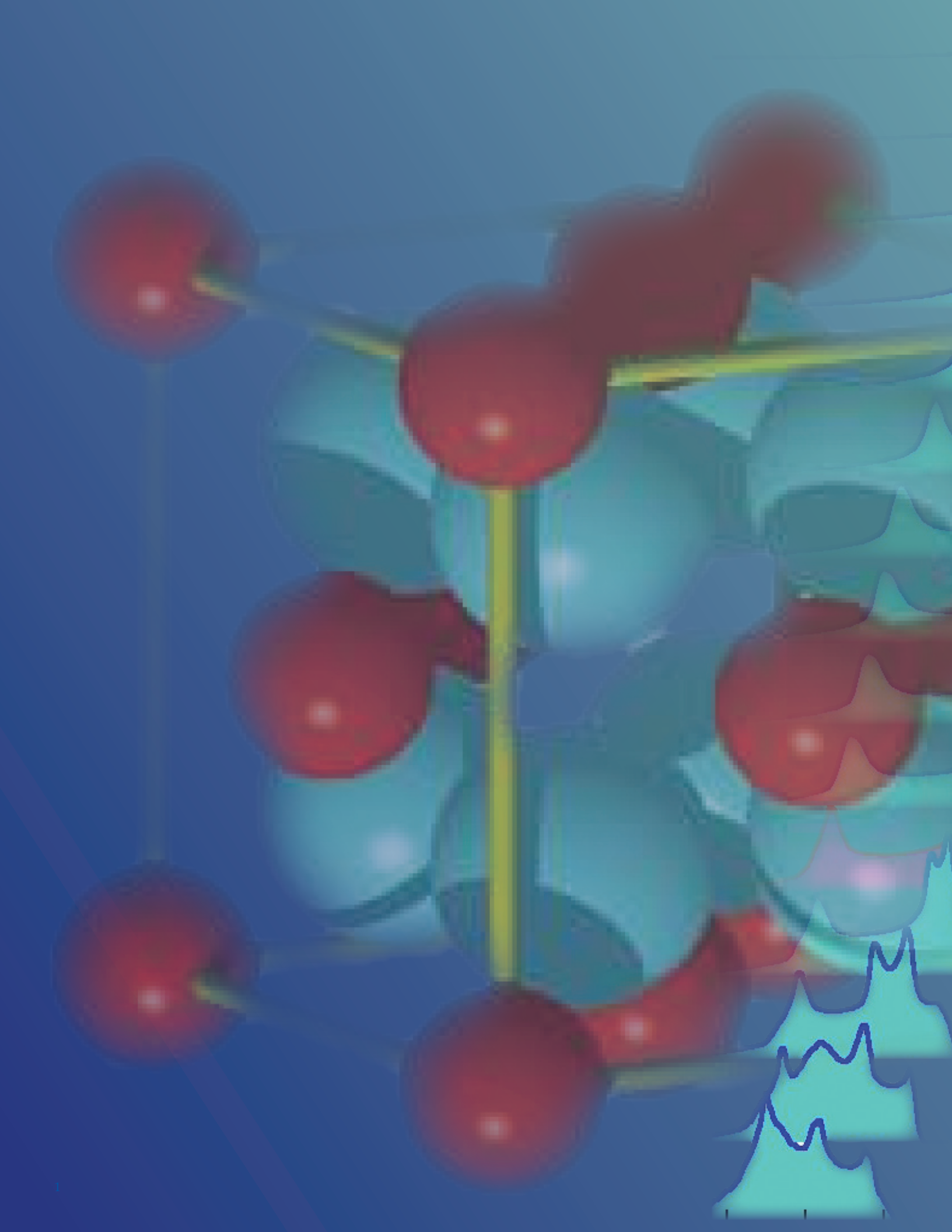

Part 1:

Featured Groups
T-1, T-3, T-11, T-12, T-14

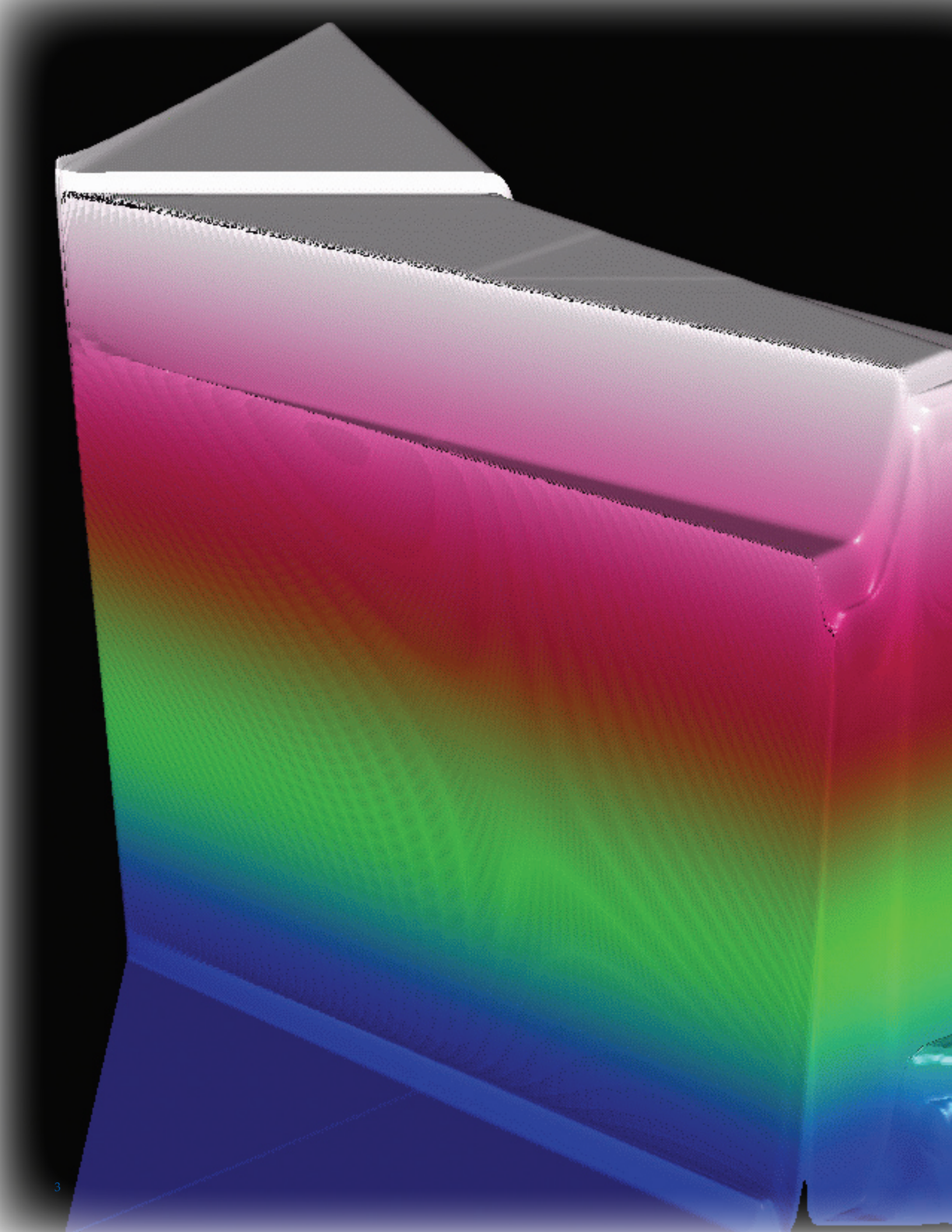

T-1

Equation of State and Mechanics of Materials

Group Leader: John Wills
505.665.2308; jxw@lanl.gov

T-1 Equation of State and Mechanics of Materials studies the thermal and statistical mechanic properties of materials, equation of state, microscopic mesoscopic and continuum-level mechanical behavior of materials, shock physics, hydrodynamic analysis, energetic materials, grain growth phenomena, and advanced techniques using quantitative image analysis for applications in material science and surveillance.

Equation of State Developments in T-1

Nicolas Bock, Leonid Burakovsky, Eric Chisolm, Scott Crockett, Giulia De Lorenzi-Venneri, Tinka Gammel, Denise George, Carl Greeff, J. D. Johnson, Travis Peery, Sven Rudin, and Duane Wallace, T-1

A new unclassified SESAME database was released on June 15, 2005 with five new equations of state (EOS). The update contains four LiH isotopes, one CO_2 modified from an existing EOS, and a material number change for deuterium. A new classified SESAME database was released on June 20, 2005, with two new EOS. Five of the unclassified EOS and one of the classified EOS were produced by T-1; the other classified EOS was produced by Jonathan Boettger, X-1 [1].

A preliminary release of an extension of the PBX 9501 EOS by Sam Shaw, T-14 was given to the user community to test. The extension technique was developed by adapting existing GRIZZLY algorithms.

A new EOS was created for X-4 to meet a special request from a SESAME user. This EOS played a major role in Campaign 4, Major Technical Effort 4.2, Level 2 milestones 1279 and 605 for FY05 and will be officially released next year.

A memo has been written by T-1 and the X-2 Verification & Validation team outlining the SESAME EOS recommended for use in X-2 simulations.

We have continued work on explicit multiphase EOS, in which separate EOS are produced for each phase and the full EOS is constructed by combining the individual phases.

(a) We have incorporated a simple analytic liquid model developed in T-1 into GRIZZLY and OpenSesame. We have validated the model by comparing with analytic work done in T-1 on a two-phase copper EOS [2].

(b) We have produced an EOS for tin that includes the beta and gamma solid phases and the liquid phase and will be included in the next release of the SESAME library [3]. A new treatment of the nuclear contribution, inspired by the Vibration-Transit (V-T) theory of liquid dynamics developed in T-1, was used for the liquid phase, and the phases were combined using an algorithm suggested by a kinetic model used in work on titanium and zirconium. We have also expanded the SESAME format to include new subtables containing the mass fractions of each phase at each grid point, enabling us to map out explicit two-phase regions. The new models and capability to handle the new subtables have been incorporated into OpenSesame.

We are enhancing the reliability of and confidence in the EOS we construct by using not only experimental data and modeling but also density functional theory (DFT) calculations. For example, we are close to completing an improved EOS for beryllium based on extensive calculations that provide a better cold curve and thermal contributions (from calculated phonons). Good agreement between our results and diamond anvil cell data published this year support our new EOS. Similar work on pressure standards (copper, gold, platinum, and tantalum) is providing validation for this approach as well as significant improvements in the accuracy of the EOS of these important materials.

Progress has been made in the development of the V-T theory of liquid dynamics. A new model has been developed to incorporate the effect of transits on the dynamic structure factor $S(q,\omega)$, measured in x-ray and neutron scattering experiments [4]. We consider two distinct contributions to the inelastic scattering due to the two types of motion: independent harmonic vibrations in random valleys and instantaneous transits between valleys. The first contribution, due to vibrational motion, can be exactly calculated from

the random valley Hamiltonian. The second contribution, due to transits, is the object of the model and enters as a correction. By using the model we reproduce, to very high accuracy, S(q,w) for liquid sodium, both from molecular dynamics simulations and from recent x-ray inelastic scattering data. Further work to understand the microscopic nature of transits is underway.

Density Functional Theory calculations (GGA+U) of fcc Pu indicate that as the Hubbard on-site Coulomb repulsion U increases, the fcc Pu system goes through a sharp phase transition. Accompanying this transition are sharp drops of the bulk modulus and large values and even negative values of pressure derivatives of the bulk modulus. These effects are consistent with current experimental observations.

Ab initio DFT calculations of the melting of Sn and Na have been performed. The results will be compared with available experimental data and recent constant-energy simulations of superheating of solids to assess the viability of bounding the melting points theoretically (or determining the error bars) of more complex materials at high pressures.

J. D. Johnson and George Baker, T-11, have extended their work on high-temperature expansions of energy to other thermodynamic quantities, such as pressure and entropy [5].

We have continued to develop and evolve the production and maintenance EOS software as the need arises. For example, we have incorporated some more validation checks in the code EOSlibtools. With the help of Jonathan Boettger, X-7, we have also added the capability for machine-independent reading and writing of binary files to accommodate platform-dependent Endian issues. The Ses2d code has also been ported to run on all Unix and Linux platforms.

We have improved the capabilities of the EOS production code OpenSesame in the following ways.

(a) We have replaced the previous command set with a restructured, streamlined set.
(b) We have implemented both the two-phase capability from GRIZZLY and a new multiphase capability.
(c) We have expanded the plotting capabilities by adding a surface plot option (which creates a GMV file) and the ability to plot phase boundaries.
(d) We have standardized the set of units used in inputs to match the units of the SESAME library.
(e) We have expanded the interpolation option to allow any combination of density, temperature, energy, or pressure as long as one of the two supplied variables is either density or temperature.
(f) We have added additional models for the creation of melt and shear tables.
(g) We continue to use version control to maintain a history of source modifications and have updated the documentation and test suite.

The code has also been supplied to several Los Alamos users.

For more information contact Eric Chisolm at echisolm@lanl.gov.

[1] S.D. Crockett, "SESAME Database Release (U)," Los Alamos National Laboratory memorandum t1-2005-06-15-sdc (U), to T-all and X-all (June 15, 2005).
[2] S.D. Crockett, et al., "Testing a liquid EOS model against copper data," to appear in *Shock Compression of Condensed Matter--2005*, M. D. Furnish, Ed. (American Institute of Physics, Melville, New York, 2006).
[3] C.W. Greeff, et al., "SESAME 2161: An explicit multiphase equation of state for tin," Los Alamos National Laboratory report LA-UR-05-9414 (December 2005).
[4] G. De Lorenzi-Venneri and D.C. Wallace, *J. Chem. Phys.* **123**, 244513 (2005).
[5] G.A. Baker, Jr. and J.D. Johnson, *Physica A* **359**, 345 (2006)

Multiphase Equations of State for the SESAME Database

Eric D. Chisolm, Denise C. George, and Carl W. Greeff, T-1

The great majority of the equations of state (EOS) prepared for the SESAME database until now have not treated the effects of phase transitions except for melting, and then only phenomenologically. We are now developing the techniques necessary to produce for the database a genuine multiphase EOS, in which the thermodynamic properties of the phases are computed individually and the equilibrium phase boundaries are determined by matching Gibbs free energies. We are producing a multiphase EOS for tin as a test case. The large range of compressions and temperatures covered by a typical SESAME EOS ($0 < \rho/\rho_o < 10^4$ and $0 < T < 10^4$ eV) presents special challenges for such calculations.

The tin EOS contains the beta and gamma solid phases and the liquid phase. The alpha phase is excluded because the beta phase is slow to transform to alpha, rendering beta metastable except for very long-lived processes. To produce this EOS, we first constructed the individual phases, which involved introducing new models into OpenSesame, our new EOS production code. In particular, we needed a model for the ionic contribution in the liquid phase; for this, we used the ionic treatment developed by Chisolm and Wallace in T-1 [1], using at low temperatures the vibration-transit (V-T) theory of liquid dynamics developed recently in our group (see [2] for a review), and interpolating smoothly to an ideal-gas-like expression at very high temperatures. We also incorporated a new treatment of the liquid cold curve due to V-T theory.

To combine the EOS for the different phases and construct the equilibrium phase diagram, we used a treatment inspired by the infinite-time limit of a kinetic model used by Greeff et al. in their work on titanium and zirconium [3]. This method allows the treatment of an arbitrary number of phases without restrictions on the topology of the phase diagram. A difficulty we encountered at this point is the spurious re-emergence of a phase far from where its free energy was calibrated. Our algorithm allows us to restrict a phase to within a window in the $\rho - T$ plane to avoid this problem.

An important application of multiphase EOS is to allow for phase-dependent strength models in continuum mechanical simulations. To facilitate this, we are extending the SESAME data format to include phase information. In addition to tabulating the pressure and internal energy as functions of density and temperature, we also tabulate the mass fractions of the phases. This completely specifies phase information in mixed and pure phase regions.

The Hugoniot predicted by this EOS is shown in Fig. 1 with experimental data. The beta-gamma phase transition

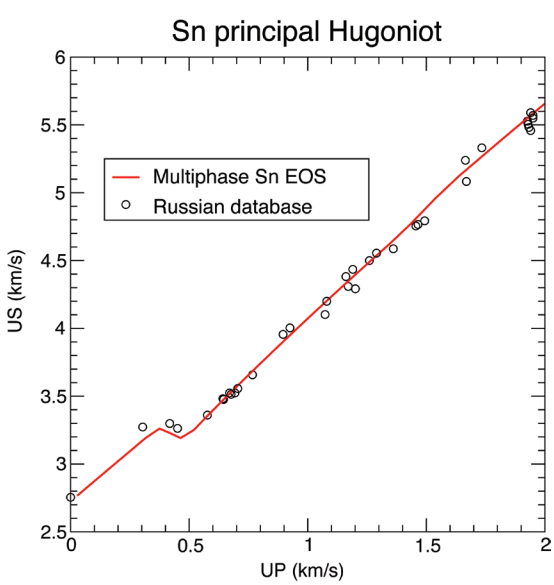

Fig. 1.
The principal Hugoniot of tin predicted by our multiphase EOS compared with experimental data from the Russian shock physics database. Notice that the EOS reproduces the effects of the beta-gamma phase transition as indicated by the data.

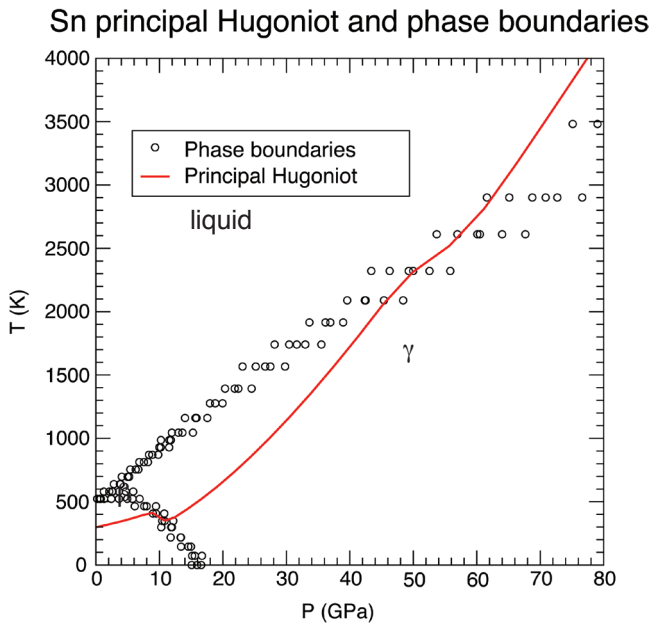

Fig. 2. ***The principal Hugoniot of tin in pressure-temperature space, passing through all three phases. The effects of the phase transitions on the Hugoniot are clearly seen. Circles indicate the SESAME grid points nearest the phase boundaries.***

is clearly visible in both the data and the EOS. The Hugoniot is shown over a larger range in Fig. 2, covering all three phases. The EOS is computed on a density-temperature grid, and grid points near the phase boundaries are indicated by circles.

We will continue to develop the code OpenSesame to address the new issues presented by this new EOS format, and we will also explore the challenge of extrapolating free energies well beyond the stability regions of the relevant phases, both of which will become even more important as we construct EOS for materials with more and more complicated phases.

For more information contact Eric Chisolm at echisolm@lanl.gov.

[1] E.D. Chisolm and D.C. Wallace, "Extending the CCW EOS II: Extending the Nuclear Contribution to High Temperatures," Los Alamos National Laboratory report LA-UR-04-3948 (June 2004).
[2] E.D. Chisolm and D.C. Wallace, "Dynamics of Monatomic Liquids," *J. Phys. Condens. Matter* **13**, R739 (2001).
[3] C.W. Greeff, et al., "Modeling Dynamic Phase Transitions in Ti and Zr," in *Shock Compression of Condensed Matter-2003,* M.D. Furnish, Y.M. Gupta, and J.W. Forbes, Eds. (Melville, NY: American Institute of Physics, 2004).

Dynamic Response of HMX Through the β–δ Phase Transition

Bradford E. Clements, Eric M. Mas, JeeYeon N. Plohr, Axinte Ionita, T-1; and Francis L. Addessio, T-3

The β–δ phase transformation in the explosive HMX has been postulated to be an important first step in the molecular decomposition of the HMX molecule [1]. The transition is also thought to be an important mechanism for the early stages of reaction. The 6–7% volume increase that occurs in the transition causes crack growth in granular HMX with an associated temperature rise [2]. Upon dynamic loading, these cracks are responsible for further heating of the HMX grains. In the present work the β–δ phase transformation is studied using a theoretical analysis based on the theory introduced by Andrews [3]. Because there is much interest in the β–δ transition as it occurs in the plastic-bonded explosive PBX-9501, an analysis based on the method of cells (MOC) that has recently been extended to include phase transformations in metal matrix composites [4] has been applied to study the HMX β–δ transformation in this explosive. Here we discuss only the HMX phase transition, however.

Details of the phase transition model are described in [4] but it is important to note that inelastic contributions come from HMX microcrack growth and plasticity [5]. A complete equation of state (EOS) is needed for both the β and δ phases. Sufficient data exists to determine the coefficients for an empirical form for the β and δ phase Gibbs free energies. Figure 1 is a plot of our calculated specific volume as a function of temperature and pressure for β and δ HMX. Also shown in Fig. 1 is the zero pressure specific volume data of Saw [6]. Along with the data of [6], the pressure-volume isotherms of Gump and Peiris [7], the zero-pressure specific heat at constant pressure of Shoemaker et al. [8], and the *ab initio* calculations of Sewell et al. [9] were used to determine the Gibbs free energy. The bend in the β–δ phase boundary (Fig. 2) is attributed to molecular decomposition and included here by making a judicious choice for the δ phase parameters in the Gibbs free energy.

The first set of simulations to be presented is that of dynamically loaded HMX. Loads are applied by specifying the strain rates. HMX is loaded compressively in one direction and tensile loaded in the two orthogonal directions. Figure 3 is a plot of the HMX volumetric strain. Abrupt jumps in the curves occur as the HMX undergoes the β–δ phase transition. Depending on the loading, HMX can undergo the expected volume increase at the transition but also volume decreases (Fig. 3). Thus, depending on the pressure reached, complex behavior can be observed.

It is known that under slow heating (cooling) rates HMX will remain in a metastable β (δ) phase far above (below) the phase boundary. It is less clear if this remains true under dynamic loading. Figure 4 shows several simulations where τ, the characteristic relaxation time that controls the rate at the transition occurs, is varied. From Fig. 4 it is clear that if the transformation rate, under dynamic loading, is sufficiently slow, the transformation will not be completed before the HMX melts (at zero pressure HMX melts at about 550 K) or reacts.

For more information contact Bradford Clements at bclements@lanl.gov.

[1] B.F. Henson, et al., "The β-δ phase transition in the energetic nitramine octahydro-1,3,5,7-tetranitro-1,3,5,7-tetrazocine: Thermodynamics," *J. Chem. Phys.* **117**, 3780, 2002.
[2] R. Karpowicz, and T. Brill, "The β-δ Transformation of HMX: Its Thermal Analysis and Relationship to Propellants," *AIAA Journal* **20**, 1586, 1982.
[3] D.J. Andrews, "Calculation of Mixed Phases in Continuum Mechanics," *J. Comp. Phys*. **7**, 310, 1971.
[4] F.L. Addessio, et al., "A Model for Heterogeneous Materials including Phase Transformations," *J. Appl. Phys*. **97**, 083509 2005.
[5] B.E. Clements, and E.M. Mas, "A Theory of Plastic Bonded Materials with a Bimodal Size Distribution of Filler Particles," *Mod. Sim. Mat. Sci. Eng*. **12**, 407, 2004.
[6] C.K. Saw, "Kinetics of HMX and Phase Transformations: Effects of Grain Size at Elevated Temperature," Proceedings of the 12th Int. Detonation Symposium.
[7] J.C. Gump, S.M. Peiris, "Isothermal Equations of State of beta octahydro-1,3,5,7-tetranitro-1,3,5,7-tetrazocine at High Temperatures", *J. Appl. Phys.* **97**, 053513, 2005.
[8] R.L. Shoemaker, et al., "Thermophysical Properties of Propellants," *High Temp.-High Press*. **17,** 429, 1985.
[9] T. Sewell, et al., "A Molecular Dynamics Simulation Study of Elastic Properties of HMX," *J. Chem. Phys*. **119,** 7417, 2003.

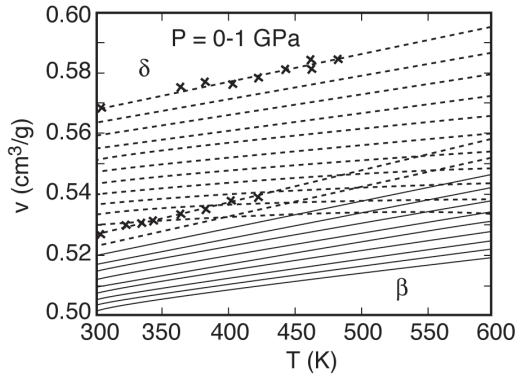

Fig. 1. *Specific volume of β and δ HMX. The points are the ambient pressure data of Saw [6]. The theoretical curves span pressures of 0 to 1 GPa.*

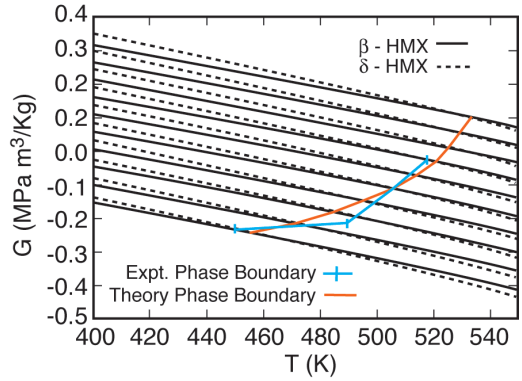

Fig. 2. *Gibbs free energies for β and δ HMX. The curve connecting the three points is an approximation to the experimental P-T phase boundary of [2] which has been overlaid on our phase diagram. The theoretical curves span pressures of 0 to 1 GPa.*

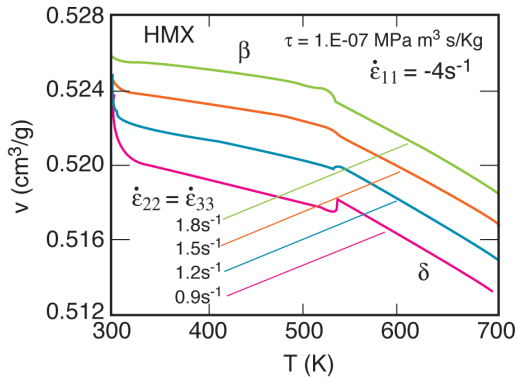

Fig. 3. *Specific volume of HMX as the β–δ phase transition is crossed.*

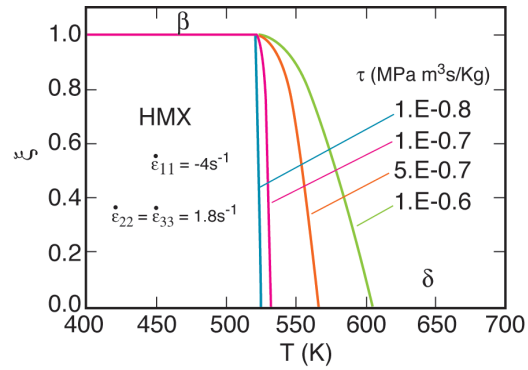

Fig. 4. *Mass fraction for the β phase for different relaxation times.*

Micromechanics Models for Plastic-Bonded High Explosives: Recent Developments

Bradford E. Clements and Eric M. Mas, T-1; and Curt A. Bronkhorst and Todd O. Williams, T-3

A sound theoretical understanding must accompany experimental testing of any explosive material before one can have confidence that it will or will not detonate under a general state of dynamic mechanical loading [1]. A theoretical understanding will help ensure, for example, our ability to safely handle explosives. Our aim is to develop a theory that can aid in our prediction of the mechanical response behavior of an explosive as it is loaded over a wide range of applied stress and temperature states. Because the chemical kinetics depends on the thermal state, which is often coupled to the mechanical state, (the best known example being hot spot generation) the present investigation is also intended to be our first step to address the relationship between loading and chemical reaction in explosives.

There are many advantages to using a micromechanics analysis to model the explosive PBX 9501, and here we enumerate five of them. First, considerable information on the microstructure and thermal-mechanical properties are required for a micromechanics analysis. As a consequence, a micromechanics theory is likely to be more reliable than corresponding theories constructed from less information, for example theories that use only the results from integrated experiments. Second, local stresses and strains are determined in a micromechanics analysis. As will become clear, in our model these local stresses and strains are calculated for the coarse HMX explosive grains, the fine HMX grains, and the plastic binder. Consequently, properties such as localized heating can be calculated independently for these three constituents. Third, material properties can be tailored to the individual constituents. For example, one can develop a theory such that microcrack brittle fracture occurs in the HMX grains while the elastomeric viscoelastic properties are specific to the polymeric binder. Similarly, interfacial debonding between the HMX grains and the binder can be directly incorporated into the theory in an unambiguous way. Fourth, one would like to take advantage of the information gained from experiments done on the constituents. For example, it is expected that the plasticized Estane® binder is responsible for much of the strain rate and temperature dependence observed for PBX 9501. Experiments on the binder have been carried out over a wide range of temperatures and strain rates and this data, which can readily be used in a micromechanics theory, is difficult to use in an integrated continuum theory of the entire explosive. Fifth, having determined the constituent properties and gained confidence in the micromechanics model by comparing its predictions to experiments done on PBX 9501, one can then use our model to explore other volume concentrations of HMX and binder without the need for extensive further experimentation.

We wrote an Advanced Simulation and Computing (ASC) Program milestone report that covers the following topics: A hybrid micromechanics model is proposed for investigating the mechanical behavior of plastic bonded materials having two disparate grain sizes. In this report we discuss our hybrid model (Fig. 1) that uses the first-order Method of Cells (MOC) [2] to treat the coarse HMX grains with a Mori-Tanaka-based analysis used to treat the fine grain-binder mechanical response. The fine grains in this analysis are assumed to be spherical and uniformly distributed in the binder and

have been named the dirty-binder (DB). The formal DB theory is presented in this report. While the hybrid MOC-DB model captures the average thermal-mechanical properties of PBX 9501, it is important to better understand the local fluctuations in the fields caused by the highly irregular microstructure. Direct Numerical Simulations (DNS), described in the report, attempt to model the details of the microstructure by using the finite element method (FEM) where the PBX microstructure is considered at the resolution of the fine grain-dirty binder mixture. Another approach for investigating the accuracy of the MOC-DB model is to allow for microstructural variations in conjunction with the MOC-DB analysis. This work is called statistical element sampling and has been applied to model plate impact. Methods are also described for obtaining FEM grids for the microstructure using various approaches including PBX 9501 micrographs. The HMX β−δ phase transition is modeled using our MOC-DB theory, appropriately generalized to include solid-solid phase transitions. The β−δ phase transformation in the explosive HMX has been postulated to be an important first step in the molecular decomposition of the HMX molecule [3] and is thought to be an important mechanism for the early stages of reaction. Finally, new stochastic micromechanics theories that will allow for much greater predictability are presented in the report.

For more information contact Bradford Clements at bclements@lanl.gov.

[1] P.W. Cooper, *Explosives Engineering* (Wiley-VCH, New York, 1996).
[2] J. Aboudi, "Studies in Applied Mechanics, Vol. 29," *Mechanics of Composite Materials: A Unified Micromechanical Approach* (Elsevier, Amsterdam, 1991).
[3] B.F. Henson, et al., *J. Chem. Phys.* **117**, 3780, 2002.

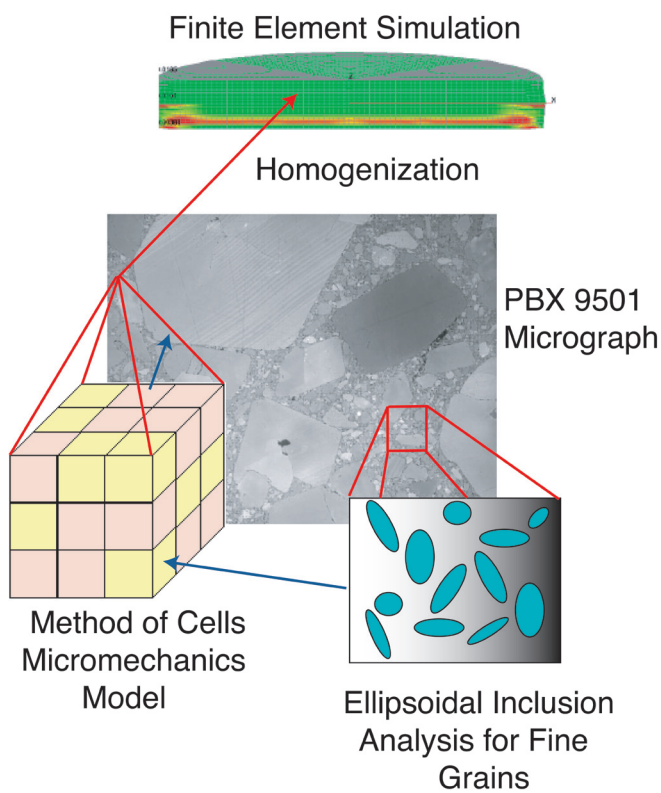

Fig. 1.
The method of cells dirty binder model.

Low-Pressure Equation of State of Polymers

Bradford E. Clements, T-1

The study of the dynamic deformation of polymers requires knowledge of the equation of state (EOS). Because polymers are often used in applications were the loading is either weak shock or nonshock, to model the thermo-mechanical response it is necessary to know the low-pressure EOS. Hugoniot shock data offers a standard means in the shock research community to determine the EOS but unfortunately Hugoniot data below one GPa is typically difficult to obtain with sufficient accuracy to be reliable. The objective here is to show that an alternative low-pressure EOS can be constructed by information that is either already in the published literature or is readily obtained by experiment. In the present work we consider two representative polymers: amorphous polycarbonate (PC) and semi-crystalline polytetrafluoroethylene (PTFE). PTFE is chosen to show that crystalline phases can be handled, at least approximately, by this simple semi-empirical method. The crystalline portion of PTFE, which makes up typically 30-70% of the total volume of the polymer, can exist in four low-pressure phases, three of which will be included in our analysis. Polycarbonate is glassy at room temperature and has a glass transition temperature near 150ºC. The present analysis shows that the glass transition can be included in the EOS. Finally, it is emphasized that the present work uses standard techniques to obtain the Gibbs free energy from which the Hugoniot can be constructed and compared to the low-pressure experimental Hugoniot when it exists.

To construct the EOS the Gibbs free energy is written as the sum of zero-pressure and a pressure-dependent term. The latter term is consistent with the Tait equation for the specific volume [1] and the zero-pressure terms are expressed as a polynomial in temperature plus a logarithmic contribution. For PC we use the specific volume data and analysis of Zoller [2] and the ambient pressure heat capacity data of Cheng and Wunderlich [3]. The coefficients to the logarithmic term and the power series are determined by fitting the heat capacity data, and ambient (approximated as zero) pressure Gibbs free energy of Cheng and Wunderlich [3]. Because heat capacity is discontinuous at the pressure and temperature-dependent glass transition we fit coefficients to the two different regimes ($T<T_g$ and $T<T_g$) of the heat capacity. The pressure-dependent contribution is determined by fitting the theoretical specific volume to the measured specific volume of Zoller [2]. The resulting specific volume and Gibbs free energy for PC are shown in Figs. 1 and 2, respectively. Taking the appropriate derivatives of the Gibbs free energy gets other thermodynamic quantities. For example, Fig. 3 and 4 show the specific at constant pressure and the isothermal bulk modulus. The glass transition is responsible for the pronounced jump occurring in these quantities.

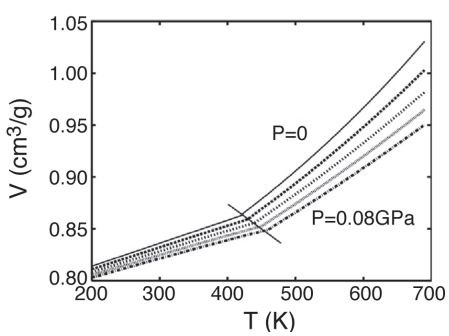

Fig. 1.
Specific volume for PC. The solid line is the glass transition boundary. Pressures correspond to 0.0, 0.2, 0.4, 0.6. and 0.8 GPa.

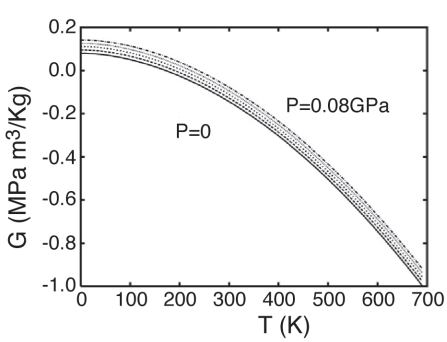

Fig. 2.
Gibbs free energy for PC. Pressures correspond to 0.0, 0.2, 0.4, 0.6. and 0.8 GPa.

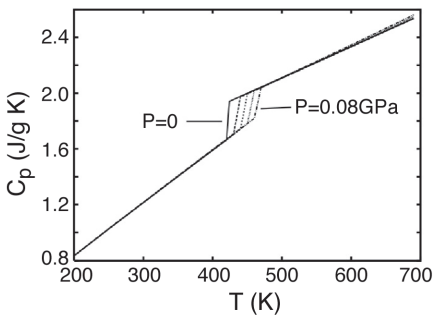

Fig. 3.
Constant pressure heat capacity for PC.

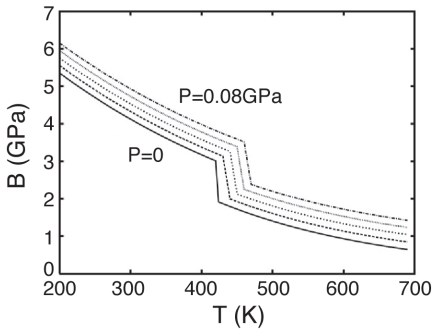

Fig. 4.
Isothermal bulk modlus for PC.

The commonly used phase diagram [4] for PTFE is shown in Fig. 5. The crystalline phases for PTFE exist in 4 low-pressure crystalline structures labeled phase I through IV. Glass transitions, related to the amorphous phase, also occur in PTFE at temperatures outside the range of the phase transitions. Phase IV will be ignored in our work because its properties are intermediate between Phases I and II. We will also ignore the glass transitions. Consequently, the resulting EOS described here will be valid for temperatures between approximately 250 K and 380 K, and pressure below 1 GPa. Using the specific volume data of Weir [5], the heat capacity data of Loufakis and Wunderlich [6], and the phase diagram we have constructed the EOS for PTFE for Phases I, II, and III. Figure 6 shows the Gibbs free energy. The stable thermodynamic state is the one with the lowest Gibbs free energy and the crossing of the free energies determine the solid-solid phase boundaries. The dotted lines in Fig. 6 are our theoretical phase boundaries, as determined by the Gibbs free energy crossings and, when written in terms of pressure and temperature, can be compared favorably with the phase diagram of Fig. 5.

For more information contact Bradford E. Clements at bclements@lanl.gov.

[1] Tait, P. G., *Phys. Chem.* **2**, 1 (1888).
[2] Zoller, P., *J. Poly. Sci.: Part B: Polymer Phys. Eds.* **20** 1453 (1982).
[3] Cheng, S. Z., and Wunderlich, B., *J. Poly. Sci.: Part B: Polymer Phys. Eds.* **24** 1755 (1986).
[4] Beecroft, R. I., and Swenson, C. A., *J. Appl. Phys.* **30** 1793 (1959), (this work omitted Phase IV).
[5] Weir, C. E., *J. of Research. Natl. Bur. Standards* **53** 245 (1954).
[6] Loufakis K., and Wunderlich, B., *Polymer* **26** 1875 (1985).

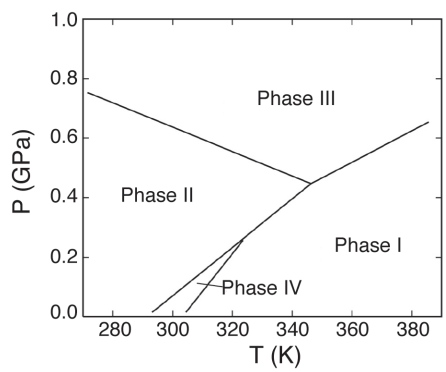

Fig. 5.
PTFE phase diagram.

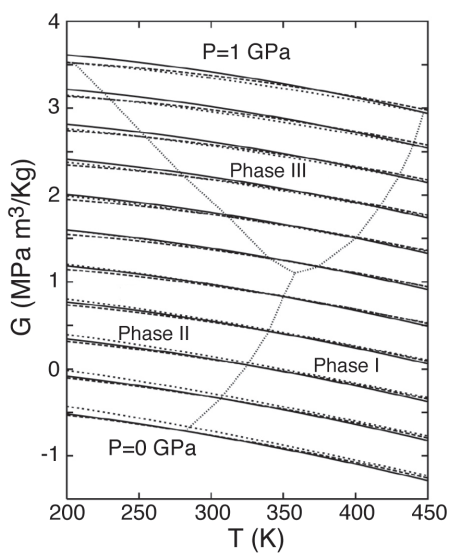

Fig. 6.
Gibbs free energy for PTFE for Phase I, II, and III.

Image Shape Analysis

Denise George, T-1

Image Shape Analysis (ISA) is a software package written in the language C that accepts as input a gray-scale image, extracts objects from the image, and characterizes those objects. This process consists of these steps:

1. A gray-scale range is selected and pixels whose values fall in this range are marked as "active."
2. Connected contours are placed around connected sets of "active" pixels. The interiors of the contours are defined to be objects, and these objects are triangulated using a constrained Delaunay algorithm [1].
3. Statistics are gathered related to the objects' shapes, orientation, and structure.
4. A skeleton is constructed for each object.

Combining the following measured statistics can be used to determine if an object meets the decision criteria:

1. the area of the object,
2. the length of the perimeter of the object,
3. coordinates of the center of mass of the object,
4. the ratio of $\text{radius}_{\text{area}}$ to $\text{radius}_{\text{perimeter}}$ ($2*\pi*\text{sqrt}(\text{area}/\pi)/\text{perimeter}$),
5. the ratio of the area of the junction triangle to the area of the object,
6. the area of the minimum enclosing rectangle (MER),
7. the angle of inclination of the minimum enclosing rectangle from the x-axis,
8. the length and width of the MER, and
9. the aspect ratio (width/length) of the MER.

One application of ISA is to qualify plumes [2]. The ideal plume is a teardrop-shaped object with irregular edges. When triangulated, this type of object will have many interior (junction) triangles, and Measure 5 will be relatively large. Conversely long, thin, straight objects will have few interior triangles, and Measure 5 will be relatively small. These long, thin, straight objects will also be identified by a small aspect ratio of the minimum-enclosing rectangle, Measure 9. The most difficult shapes to characterize are thin and curvy or straight-sided fat rectangles.

For more information contact Denise George at dgeorge@lanl.gov.

[1] B.R. Schlei, "A New Computational Framework for 2D Shape-enclosing Contours," Los Alamos National Laboratory report LA-UR-04-3115 (May 2004).
[2] D.C. George, "Image Shape Analysis for Plume Characterization," Los Alamos National Laboratory report LA-UR-05-7082 (August 2005).

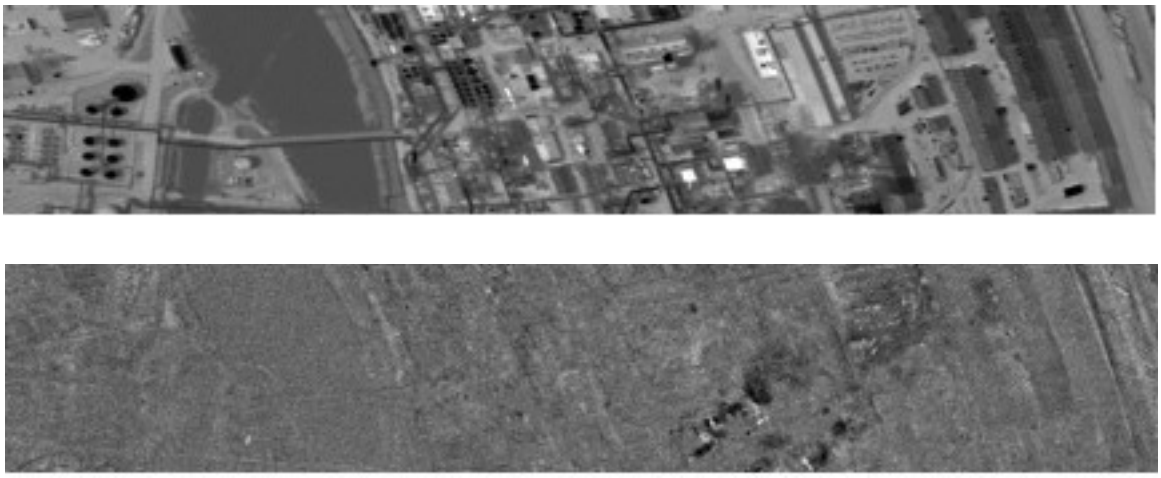

Fig. 1.
Broadband (top) and match filter (bottom) images of the same scene. In the match filter image there are two large plumes originating at the bottom, right of center.

Fig. 2.
ISA identifies these 22 objects when asked to select objects in the match filter image. The gray-scale pixel selection was set to choose both very dark and very light pixels. ISA was told to ignore small objects, those whose perimeters were less than 30 pixels long. The three objects on the far right are not plumes but are structures visible in the broadband image. ISA did not identify any objects in the left half of the image. Combining the two measurements of Triangle Ratio and MER Aspect Ratio, ISA correctly classifies all but three of the objects.

Continuum Models for Multiphase EOS

Carl W. Greeff, T-1

Shock wave and other dynamic compression experiments can reveal a wealth of information about phase transitions, which are often manifested as anomalies in the wave shape [1]. Detailed analysis of time resolved data, as obtained for instance by laser velocity interferometry (VISAR), can give information about transition kinetics on time scales from a few to hundreds of nanoseconds. Because of the complexity of wave propagation in phase transforming media, numerical simulation is an important tool for interpreting such experiments. An important component of such simulations is to model phase transition kinetics in a way that is computationally tractable, and accurately represents the phenomenon.

The standard treatment for dynamic phase transitions in such simulations is to regard each macroscopic region of the sample as containing fractions $\{\lambda\}$ of the various possible phases, with pressure and temperature equilibrium among the coexisting phases. Thermodynamic properties of the individual phases are described by their Helmholtz free energies $F_i(V_i,T)$ [2, 3]. Supplementing the free energies with a kinetic rule for evolving the λ_i in time fully specifies the hydrodynamic equation of state (EOS).

Following the pioneering work of Hayes [4] on transitions in bismuth, a widely used model is

$$\dot{\lambda}_i = \sum_j \alpha_{ij}\left(G_j - G_i\right) \qquad (1)$$

where G is the Gibbs free energy, and the α_{ij} are positive phenomenological rate coefficients. Equation (1) allows for finite transformation rates relaxing toward equilibrium. In spite of its apparent simplicity, Eq. (1) is awkward to apply in practice, because the constraints

$$\sum_i \lambda_i = 1$$

and $0 \le \lambda \le 1$ must be imposed externally. At fixed pressure and temperature, Eq. (1) leads to linear variation of λ_i with time, which is in qualitative disagreement with experimental data.

In considering the origins of these difficulties, it becomes clear that it is natural to describe the rate of transitions from phase i in relation to the amount of material in that phase. The result is that, in place of Eq. (1), one is led to the master equation,

$$\dot{\lambda}_i = \sum_j \lambda_j R_{ji} - \lambda_i R_{ij} \qquad (2)$$

where the rate coefficients R_{ij} are non-negative and describe the fractional transformation rate from phase i to phase j. Equation (2) has the practical advantage that the normalization constraint is naturally preserved. The fractions λ_i asymptotically approach 0 or 1, but never exceed these bounds. The asymptotic approach to complete transformation is in qualitative agreement with experiments [5].

It remains to describe the dependence of the R_{ij} on the thermodynamic state. In contrast to the linear dependence on the Gibbs free energy difference described by Eq. (1), our work on the α–ω transition in Ti and Zr [6] indicates a very nonlinear dependence. It is not known whether this is typical, or special to that transition.

With a simulation capability based on accurate free energies [2, 3] and the model given by Eq. (2), it has been possible to contribute to the design an interpretation of a number of experiments. Figure 1 shows the results of a simulation of an isentropic compression experiment (ICE) on Zr carried out at the Sandia Z-machine. Because of the complicated interaction

of waves with material interfaces in these experiments, their interpretation is not obvious, and simulations play an important role. The large "notch" near the peak of the wave is clearly associated with a second phase transition from ω to bcc, and is well predicted by the simulation, which has no parameters adjusted to this experiment. Figure 2 shows a picture in spacetime of the complex wave interactions when a shock wave induces a phase transition in Sn.

The models used here for the rates R_{ij} are simple and phenomenological. The resulting simulations are useful for interpreting shock wave experiments, but are not predictive regarding effects of temperature or impurities on transformation rates. The combination of more microscopic theories and simulations with experiments such as sample recovery will be needed to develop more predictive models. The framework described here will allow the resulting improved models to be compared with macroscopic experiments.

For more information contact Carl Greeff at greeff@lanl.gov.

[1] G.E. Duval and R.A. Graham, *Rev. Mod. Phys.* **49**, 523 (1977).
[2] J.C. Boettger and D.C. Wallace, *Phys. Rev. B* **55**, 2840 (1997).
[3] C.W. Greeff, *Model. Simul. Mater. Sci. Eng.* **13**, 1015 (2005).
[4] D.B. Hayes, *J. Appl. Phys.* **46**, 3438 (1975).
[5] A.K. Singh, et al., *J. Appl. Phys.* **53**, 1221 (1982).
[6] C.W. Greeff, et al., *Shock Compression of Condensed Matter – 2003*, edited by M.D. Furnish and Y. M. Gupta (AIP Conference Proceedings 706, Melville, NY 2004).

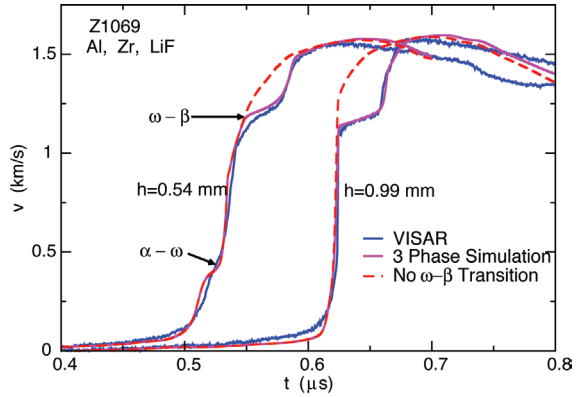

Fig. 1.
Simulations of isentropic compression experiment on Zr (P.A. Rigg, DX-2). The sample was loaded with a smooth magnetic compression wave. Blue curves are experimental VISAR traces. Magenta curve is simulation with 3-phase EOS. Dashed red curve is simulation with second phase transition turned off.

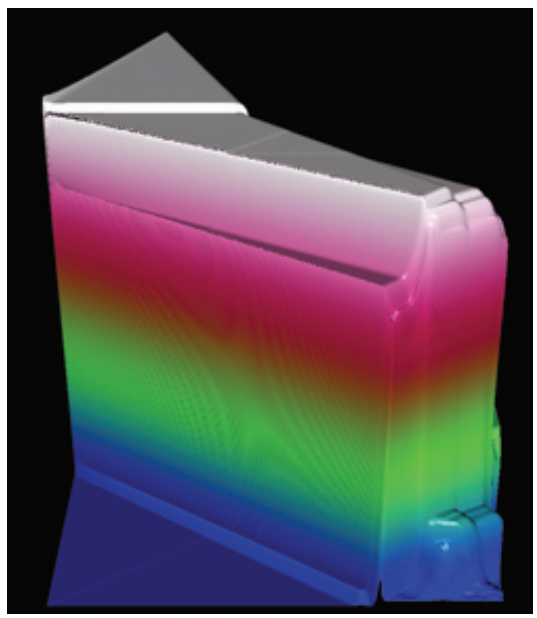

Fig. 2.
Pressure surface in spacetime for Sn sample subject to impact loading. Time advances to the right and space coordinate is out of the page. Viewpoint is from Sn free surface with impactor in the back. The "shelf" in the pink part of the wave is due to the β-bct phase transition.

Are Lattice Relaxations in Thin-Film Nanodevices Driven by Quantum-Size or Interface Proximity Effects?

Erik Holmström, Nicolas Bock, John Wills, and Anders M. N. Niklasson, T-1

The out-of-plane layer relaxations in thin films have been investigated by means of self-consistent density functional theory (DFT). Interface proximity relaxation effects, due to the presence of independent surfaces (or interfaces), have been compared to the relaxation effects driven by quantum-size induced interference between the two interacting surfaces in metallic thin films. We find that the most dominating contribution is due to the interface proximity relaxations and that quantum-size induced effects in fact are small. Our findings give a simple transparent picture of the driving mechanism behind thin film layer relaxations, which can be understood in terms of Fermi surface nesting. Furthermore, the ability to neglect quantum interference makes it possible to estimate thin film relaxations from independent surface or interface relaxation profiles through superposition. Our result provides a limit in the ability to tailor properties due to structural relaxations through size modification of thin film nanodevices.

In the famous gedanken experiment by Democritus a piece of matter is divided into successively smaller and smaller pieces until we finally end up with the individual atoms. Today we may perform a simple extension of this thought experiment. Since individual atoms are very different from the original bulk material, we realize that cutting the material into smaller pieces can be used to alter its properties. This straightforward extension of the Democritus gedanken experiment can be seen as a basis of modern nanoscience, where materials are tailored by a reduction in dimension to have new unique properties not present in the bulk material. This ability is of great scientific interest with numerous technological applications.

From a mathematical point of view the Democritus cutting procedure means that we change the boundary conditions from the periodic Born-von-Karman condition of the crystal, to the boundary condition of the nonperiodic gas phase for the individual atoms. From a physical point of view we have two major effects from reducing the dimension of a material: the presence of a surface or interface, where the relative number of surface atoms to bulk atoms increases when we make a material smaller, and if the material is small enough, the interfaces or the surfaces are close and may interact. These two effects, which we refer to as surface proximity effects and quantum-size (or -interference) effects, respectively, are important for understanding unique properties of materials on the nanoscale.

Recently we have performed a theoretical study of lattice relaxation in thin film nanodevices. The problem is to understand the dominating mechanism behind structural relaxations. Are relaxations due to quantum interference or interface proximity, or do these two effects compete? By analyzing the separate effects on the out-of-plane lattice relaxations of free standing thin metallic films, calculated from *ab initio* theory based on DFT, we find that the influence of quantum-size effects on the out-of-plane lattice relaxation is neglible. This is true even for very thin films of materials where we normally could expect a large electronic effect due to quantum interference. Instead the structural modification is dominated by interface proximity relaxation. This relaxation is driven by the independent interface/surface perturbation, which

can be understood in terms of electronic screening. It is therefore possible to establish a qualitative relationship between structural relaxation in thin film nanodevices and the Fermi surface of the unperturbed bulk material, from which the screening can be estimated. Figure 1 shows the out-of-plane relaxation of a thin film of Rh in comparison with the Fermi surface nesting.

Thus, the ability to neglect quantum-size effects gives us a simple transparent picture of the dominant mechanism behind thin film relaxation, which can be analyzed in terms of nesting properties of the Fermi surface of the unperturbed bulk material. Furthermore, the neglect of interface interference effects makes it possible to superimpose relaxation profiles of independent interface/surface relaxations to estimate the relaxation profile in complex thin film nanodevices. This construction provides a structural limit of the ability to tailor electronic properties of thin fil modifications.

For more information contact Erik Holmström at erikh@lanl.go

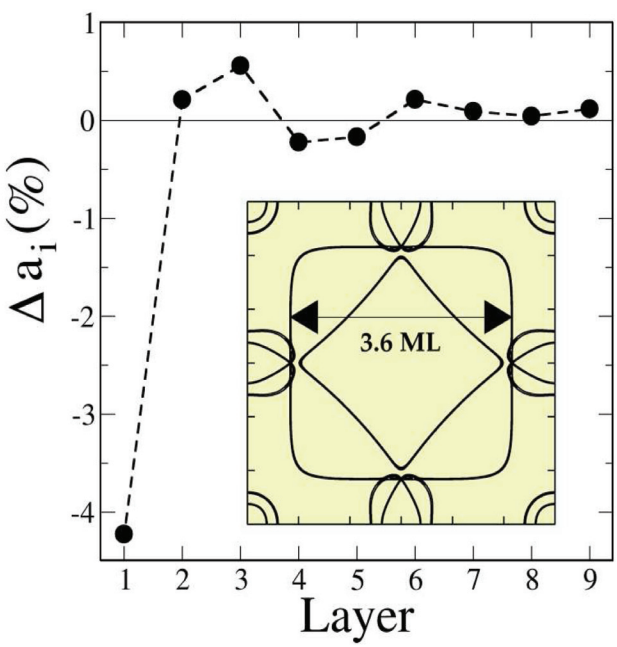

Fig. 1.
The out-of-plane relaxation in the lattice constant a_i for free-standing films of Rh. The periodicity of the relaxation can be estimated from the nesting features of the bulk Fermi surface shown in the inset.

Two-Scale FEM Approach in the Dynamic Response of a Heterogeneous Material

Axinte Ionita, Eric M. Mas, and Bradford E. Clements, T-1

Consider a heterogeneous material composed of grains and binder as shown in Fig. 1 having approximately constant material properties relative to a domain larger than the grains size. In the determination of the dynamic response of such a material, a common approach is to use a homogenized model based on the average values of the material properties relative to the Representative Volume Element (RVE). In the context of the Finite Element Method (FEM) the domain is discretized in elements, each of them having constant averaged material properties and accordingly, one can determine an average response of the material. However if one's interest is in the details below the RVE size, then a fine discretization needs to be used in order to capture the local effects. This can easily lead to a large number of elements and a very small FEM time step, thus leading to a substantial increase in the time necessary for numerical simulations. To overcome these situations we propose a two-scale FEM approach, which can capture the local effects while still keeping a relatively coarse discretization in the dynamic analysis.

For a material having a local structure as shown in Fig. 1 consider a relatively coarse FEM discretization (this will be the 1st scale), similar to what is shown in Fig. 2 (a) for instance. For each element at the 1st scale, consider a second mesh, like in Fig. 2 (b) (this will be the 2nd scale), which captures the local structure. Following [Ref. 1], in order to describe the variation of a magnitude at both levels, one introduces two variables: X to describe the dependency of that magnitude at the 1st scale and y to describe its dependency at the 2nd, scale, relative to the 1st. Thus the velocity and the strain field can be written as

$$v = V(X,t) + \eta\tilde{v}(y), \quad \dot{\varepsilon} = \dot{\varepsilon}(X,t) + \dot{\tilde{\varepsilon}}(y), \qquad (1)$$

where t is the time, V(X,t) and $\dot{\varepsilon}$(X,t) represent the velocity and strain rate at the 1st scale, and $\tilde{v}(y)$ and $\tilde{\varepsilon}(y)$ are the fluctuating velocities and strain rate at the 2nd scale. Introducing two FEM discretizations: a coarse one (a) corresponding to the 1st scale, and a local one (b) corresponding to the 2nd scale, as shown for example in Fig. 2, then

$$v = \Phi(X)V + \eta\phi(y)\tilde{v}, \quad \dot{\varepsilon} = B(X)V + b(y)\tilde{v}, \qquad (2)$$

where $\Phi(X)$ and $\Phi(y)$ are the shape functions corresponding to the meshes at 1st and 2nd scale, and $B(X) = \partial\Phi(X) / \partial(X)$, and $b(y) = \partial\Phi(y) / \partial(y)$.

Using the Principle of Virtual Power [2] written in the average sense at $t + \Delta t$ (Δt being the time step) for each element at the 1st scale, and admitting the conservation of momentum

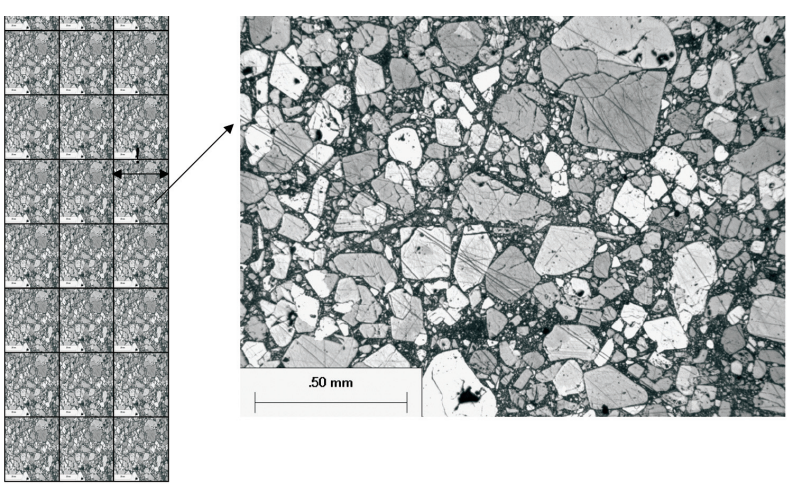

Fig. 1. ***A heterogeneous material exhibiting approximately constant material properties relative to a "window" (RVE) of size "w" (a). The right side (b) shows the "window" structure (picture of a micrograph of PBX 9501).***

while passing from the 1st to the 2nd scale, then for a constitutive law of the form $\sigma = D(\dot{\varepsilon} - \dot{\varepsilon}^{\rho})$ [3], where σ represents an objective stress rate and $\dot{\varepsilon}^{\rho}$ is the inelastic strain rate, one obtains a system having the following structure

$$\begin{bmatrix} < B^T DB > & < B^T Db > \\ < b^T DB > & < b^T Db > \end{bmatrix} \begin{pmatrix} V\Delta t \\ \tilde{v}\Delta t \end{pmatrix} = \begin{pmatrix} F_1(1^{st}) \\ F_2(2^{nd}) \end{pmatrix}. \quad (3)$$

Equation 3 represents the two-scale FEM equations. On the left side one recognizes the well-known finite element stiffness matrix form with the observation that $< B^T DB >$ represents in this case the contribution due to the first scale, $< b^T Db >$ represents the contribution due to the second scale, $< B^T Db >=< (b^T DB)^T >$ and the terms are the coupling terms between the scales. It can be shown that in Eq. 3 the inertial forces appear only at the 1st scale, i.e., in F_1 (1st), and F_2 (2nd) contains terms due to the inelastic strain accumulation at the 2nd scale during the current time step.

In an explicit dynamic FEM code one knows the velocities at the 1st scale $V(X,t + \Delta t)$.

Also on the boundary of the finite element of the 1st scale $\tilde{v}(y) = 0$. Thus the system Eq. 3 can be solved and the fluctuating velocities can be determined. Then the strains can be calculated using Eq. 2, and the stress distributions at the 2nd scale can be obtained by integrating the constitutive law. The feedback to the 1st scale is realized by passing the average values of those stresses, and further use them to calculate the nodal forces at the 1st scale in order to advance to the next time step.

In the above formulation the two-scale FEM approach allows us to capture local effects at the 2nd scale while preserving a relatively coarse discretization at the 1st scale. The use of conservation of momentum while passing between the two scales allows the problem to be to split in two parts. In the first part, the dynamics are solved at the 1st scale while the 2nd scale is used to determine the material response and the fluctuating fields. One may notice that these fields are determined by solving a quasistatic type of problem at each finite element of the 1st scale.

For more information contact Axinte Ionita at ionita@lanl.gov.

[1] P.M. Suquet, "Elements of Homogenization for Inelastic Solid Mechanics", in *Lecture Notes in Physics. Homogenization Techniques for Composite Media,* edited by Sanchez-Palencia, E. and Zaoui A., Springer-Verlag, Vol. 272, pp. 193-278.

[2] T. Belytschko, et al., *Nonlinear Finite Element for Continua and Structures* (J. Wiley & Sons, 2004).

[3] B.E. Cements and E.M. Mas, "A Theory for Plastic-Bonded Materials with Bimodal Size Distribution of Filler Particles," *Modelling Simul. Mater. Sci. Eng.* **12**, 407-421 (2004).

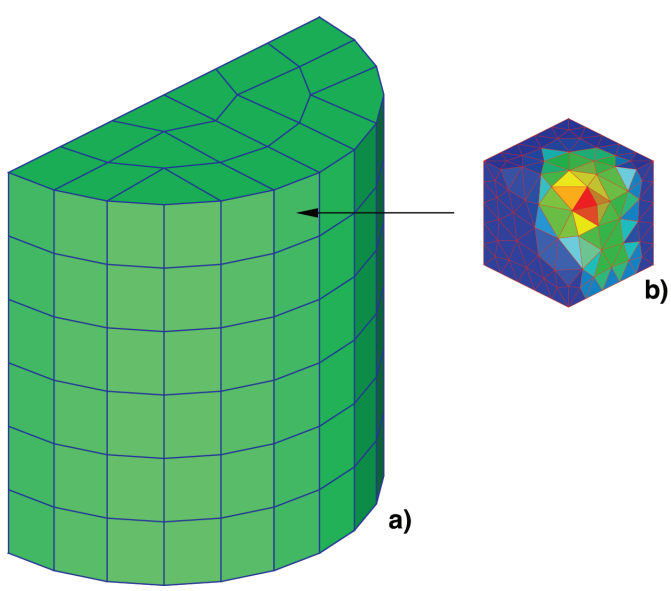

Fig. 2. ***A finite element discretization at 1st scale (a) and 2nd scale (b).***

First Principles Calculations of the 3-k Magnetic Structure and 3-k Distortion in UO_2

Raquel Lizárraga, T-1; Massimiliano Colarieti-Tosti, IFM, Sweden; Olle Eriksson and Lars Nordström, Uppsala University, Sweden; and John M. Wills, T-1

The occurrence of multi-k magnetic structures is often observed in the actinide compounds. These structures may be found in highly symmetric lattices, such as the face-centered cubic (fcc) lattice, in which the star of the wave vector k of the magnetic structure contains several members. If three members of the star are needed to describe the magnetic structure, the magnetic ordering is called 3k. Such is the case in UO_2, which crystallizes in the fcc CaF_2 type structure (see Fig. 1) with a lattice constant of 5.47 Å. UO_2 is a semiconductor with a gap of 2 eV [1,2].

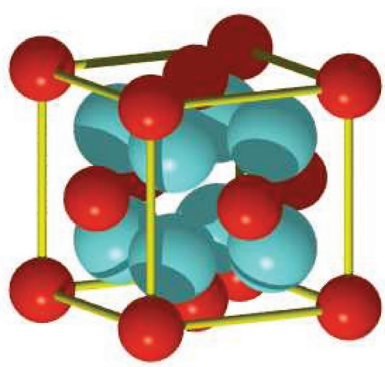

Fig. 1. ***The fluorite crystal structure of UO_2. The uranium ions are represented by the red balls. The oxygen ions are placed at a(1/4,1/4,1/4) and a(3/4,3/4,3/4) respectively and are depicted as blue balls.***

A first order phase transition [3] takes place at 30.8 K from the paramagnetic state towards a transverse type-I antiferromagnetic (AFM) structure with a magnetic moment of 1.74 μ_B[4]. Crystal field calculations [5] in UO_2 predicted that the ground state of the U^{4+} ion is the Γ_5 triplet. Later, Allen [6, 7] developed a microscopic theory of the effect of spin-lattice interaction on the ground state and spin wave excitations in UO_2. In this theory, the competition between the magnetic superexchange and an effective quadrupolar interaction caused by the spin-lattice interaction results in a non-fully polarized spin of the ground state. In particular, this theory successfully explains the order of the phase transition as well as the reduction of the saturation ordered moment from $2\mu_B$, characteristic of the Γ_5 triplet in the absence of quadrupolar interaction, to the observed value.

In order to investigate the oxygen distortion [6] that Allen had predicted to turn up at the phase transition, Faber and Lander [4, 8] performed a neutron diffraction study. They deduced from their data that below the Néel temperature the oxygen ions in UO_2 are indeed shifted from their ideal fluorite positions. However, the observed distortion was not the one suggested by Allen. Similarly, their results indicated that the magnetic structure was the 2k structure contrary to the previously reported AFM (1k structure) [3].

Though the agreement was not perfect, neutron scattering experiments under an external magnetic field [9] found that the 3k magnetic structure fitted their data better than the 2k and the 1k magnetic structures. Recently, an inelastic neutron scattering with polarization analysis [10] explored the evolution of the magnetic response through the phase transition. A scenario arises in which uncorrelated 1k dynamical Jahn-Teller distortions occur above the Néel temperature T_N along the three directions of the <100> star and as T_N is approached a correlation develops between the phases of the corresponding vibrations until, eventually a static 3k distortion is obtained at T_N. First principles calculations [11] investigated different multi-k magnetic structures with their corresponding type of oxygen distortion using LDA+U. They determined that the 1k structure is almost always favored, except when they employed the AMF-DDC ("around mean filed" double counting corrections) implementation

of LDA+U, for values of U greater than 0.35 Ry. Nevertheless, their electric field gradients calculated by assuming a 3k model agreed with experiments, with a somehow larger oxygen displacement.

Our present study is motivated by the partial success of theory to determine the magnetic structure and the associated oxygen distortion in UO_2. We have performed first principles calculations in UO_2 with the full-potential augmented plane-wave with local orbitals [12, 13] (FP-APW+lo) method. One of the challenges in describing correctly the ground state of the actinide compounds is the way the 5f electrons are treated. There is a general consensus that the 5f states are well localized in UO_2. Therefore, we used in our calculations the local spin density approximation (LSDA) as parameterized by von Barth and Hedin [14] together with the self-interaction correction (SIC) [15]. Our method is specially suited to study noncollinear structures, such as the 3k observed in UO_2, since the magnetization density is treated as a vector field, i.e., there is no constraint in the shape nor in the direction of the magnetization. We used in our calculations the experimental lattice constant.

We have investigated the 3k magnetic structure (see Fig. 2) together with the

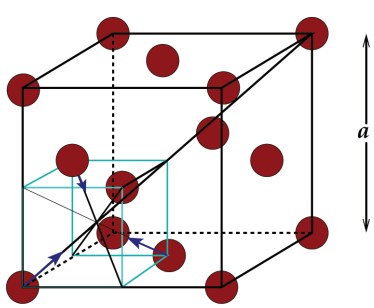

3k oxygen distortion proposed by Burlet et al. [9] and compared with the simple 1k magnetic structure, which is an antiferromagnetic structure suggested by Allen [6, 7].

Table 1 compares the preliminary results of our investigation. The oxygen distortion does not seem to reduce the total energy in either case (the 3k and 1k). The 3k and 1k structures appear to be almost degenerate in energy.

Structure	Energy Difference (mRy)
1k + SOC	0.00
3k transv. 2 + SOC	0.587
3k kmg + SOC	0.640
3k transv. 1 + SOC	0.655
1k + Dist + SOC	1.929
3k transv. 2 + Dist+SOC	3.388
3k transv. 2 + Dist+SOC	3.405

Table 1. ***Energy differences with respect to the energy of the 1k magnetic structure with spin-orbital coupling (SOC).***

For more information contact Raquel Lizárraga at lizarraga@lanl.gov.

[1] J. Schoenes, *J. Appl. Phys.* **49**, 1463 (1978).
[2] J. Schoenes, *Phys. Rev.* **63**, 301 (1980).
[3] B.C. Frazer, et al., *Phys. Rev.* **140**, A1449 (1965).
[4] J. Faber, Jr., et al., *Phys. Rev. Lett.* **35**, 1770 (1975).
[5] H.U. Rahman and W.A. Runciman, J. *Phys. Chem. Solids* **27**, 1833 (1966).
[6] S.J. Allen, Jr., *Phys. Rev.* **166**, 530 (1968).
[7] S.J. Allen, Jr., *Phys. Rev.* **167**, 492 (1968).
[8] J. Faber, Jr. and G. H. Lander, *Phys. Rev. B* **14**, 1151 (1976).
[9] P. Burlet, et al., *J. Less-Common Metals* **121**, 121 (1986).
[10] R. Caciuffo, et al., *Phys. Rev. B* **59**, 13892, (1999).
[11] R. Laskowski, et al., *Phys. Rev. B* **69**, 140408(R), (2004).
[12] E. Sjöstedt, et al., *Solid Commun.* **114**, 15 (2000).
[13] E. Söjstedt and L. Nordström, *Phys. Rev. B* **66**, 014447 (2002).
[14] U. von Barth and L. Hedin, *J. Phys. C* **5**, 1629 (1972).
[15] J.P. Perdew and A. Zunger, *Phys. Rev. B* **23**, 5048 (1981).

Fig. 2. ***The figure displays the 3k magnetic structure (longitudinal). Only the U ions are shown for clarity. The moments point along the (111) direction.***

Studies of the Incommensurate Magnetic Structure of a Heavy Fermion System: $CeRhIn_5$

Raquel Lizárraga, T-1; Massimiliano Colarieti-Tosti, IFM, Sweden; Olle Eriksson and Lars Nordström, Uppsala University, Sweden; and John M. Wills, T-1

$CeRhIn_5$ belongs to the family of heavy fermion (HF) superconductors in which superconductivity (SC) develops out of a normal state where electronic correlations produce a large enhancement of the effective mass of the conduction electrons. $CeRhIn_5$ is an antiferromagnet at ambient pressure with a Néel temperature of 3.8 K and it becomes a superconductor below $T_c = 2.1$ K when pressure is applied (1.65 GPa).

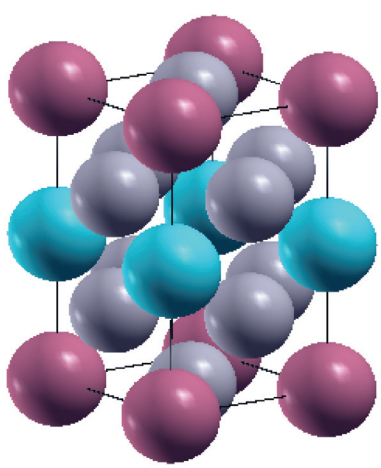

Fig. 1.
The tetragonal crystal structure of $CeRhIn_5$. Ce, Rh, and In ions are represented by purple, cyan, and light grey balls respectively. The lattice parameters are a = 4.65 Å and c = 7.54 Å at 295 K.

This compound crystallizes in the tetragonal $HoCoGa_5$ type of structure displayed in Fig. 1, which is also common to the ambient-pressure superconductors, $CeIrIn_5$, $CeCoIn_5$, and $PuCoGa_5$. This quasi-two-dimensional structure seems to be favorable for heavy fermion SC, in the same way as the $TlCr_2Si_2$-type is often observed in the BCS conventional superconductors as well as in some of HF superconductors. A neutron diffraction study [1] performed on $CeRhIn_5$ revealed an incommensurate magnetic structure with wave vector q = (1/2,1/2,0.297) and a staggered moment of 0.75(2) μ_B per Ce ion [2] at 1.4 K. The nearest-neighbor moments on the tetragonal basal plane align antiferromagnetically. Coexistence of antiferromagnetism (AFM) and SC under pressure (P = 1.75 GPa) in $CeRhIn_5$ has been reported [3]. Recently, neutron diffraction and electrical resistivity studies [4] determined a broader range of pressures (0.9 GPa ≤ P ≥ 1.75 GPa) than previous accounts [3], in which long-range magnetic order and SC exist simultaneously.

Our present investigation has been motivated by the interesting relation between relatively large ordered moments with unconventional SC which in $CeRhIn_5$ appears to be qualitatively different from other Ce-based HF superconductors. We performed noncollinear first principle calculations using the full-potential augmented plane-waves with local orbitals (FP-APW+lo) [5]. This method allows us to study noncollinear magnetic structures like the incommensurate structure that $CeRhIn_5$ has been reported to possesses [1]. The magnetization density is treated, in this method, as a vector field free to vary in magnitude and direction everywhere. We investigated different incommensurate structures described by the wave vector q, the ferromagnetic and the antiferromagnetic arrangement of the magnetic moments at ambient pressure. A study of the magnetic structure under pressure will be presented elsewhere.

The Ce ion possesses one 4f electron in these compounds. We used the LSDA-SIC to describe the localization of the 4f electron. We did not perform calculations with the 4f electron itinerant since previous theoretical studies and our own suggested that the f electron in this compound behaves

localized. This election of the exchange correlation potential gave us consistent results regarding magnetic moments and magnetic structure.

The total energy has been plotted in Fig. 2 as function of the z-component of the wave vector $q = (1/2,1/2,q_z)$. We have investigated the $\overline{\Gamma Z}$ line of the Brillouin zone (BZ) which runs along the z-axis. The ferromagnetic and the antiferromagnetic state are represented by $q_z = 0$ and $q_z = 1/2$ respectively. Our results (Fig. 2) show that there is a q value, that minimizes the total energy. The magnetic structure corresponds then to a spin spiral with a wavevector $q_z \sim 0.2$ which compares very well with the experimental value of 0.29. We are planning to study the evolution of the magnetic structure in $CeRhIn_5$ as pressure is applied, especially in the region where SC is present.

For more information contact Raquel Lizárraga at lizarraga@lanl.gov.

[1] W. Bao, et al., *Phys. Rev. B.* **62**, R14621 (2000).
[2] W. Bao, et al., *Phys. Rev. B.* **67,** 099903 (E) (2003).
[3] T. Mito, et al., *Phys. Rev. Lett.* **90**, 077004 (2003).
[4] A. Llobet, et al., *Phys. Rev. B* **69**, 024403 (2004).
[5] E. Sjöstedt, et al., *Solid Communications* **114**, 15 (2000).

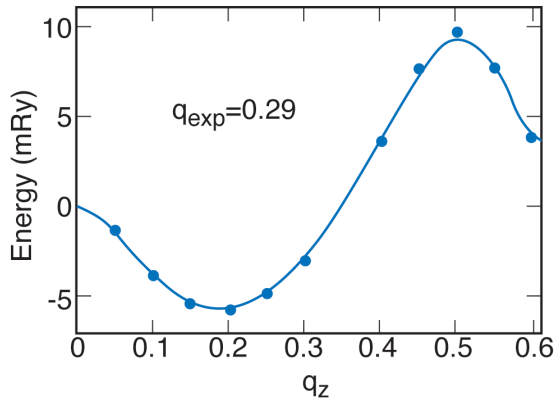

Fig. 2.
The total energy as a function of the z-component of the wave vector.

Finite Element Method Calculations on Statistically Consistent Microstructures of PBX 9501

Eric M. Mas, Bradford E. Clements, and Axinte Ionita, T-1; and Paul D. Peterson, DX-2

We have used data from image analysis to guide us in creating a finite element mesh of PBX 9501. Information about the binder concentration at different length scales taken from micrographs allows us to create a mesh that naturally incorporates inhomogeneities of the microstructure in a manner that is statistically consistent with the observed microstructure. We then apply constitutive models that are consistent with the different binder concentrations and run finite element simulations

Two-dimensional (2-D) micrographs are needed to generate the necessary statistics to use this technique. The images need to be of sufficient magnification to resolve most of the grains but not too magnified as to not include the largest grains.
Figure 1 shows an example of a 50x gray level image of PBX 9501. The image is binarized at a threshold gray level and the percentage of black pixels is found to be 23%. Given the known binder percentage of 9501 we assume that the black pixels are actually 70% HMX crystals too small to resolve with the micrograph.

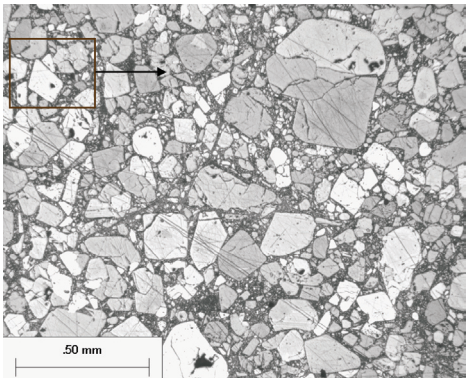

Fig. 1.
A micrograph of PBX 9501.

A complete probability distribution function (PDF) of black pixels can now be determined by successively scanning the image with larger and larger square windows. First 2 pixels by 2 pixels, then 3x3 and so on. The percentage of black pixels in a given window is calculated and the PDF is determined.

To generate a 2-D microstructure we started with a 1024x1024 array of pixels. To be consistent with the image, 23% are black. We now scan the image with a 2x2 pixel window in the same way we did the micrograph. The possible percentages are 0, 25, 50, 75, and 100% black pixels. The probabilities of these percentages are 36, 42, 18, 4, and 0%, respectively, for the randomly generated array, and 65, 7, 9, 10, and 9% for the micrograph. We now calculate the root mean square error (rmse) between the image and generated arrays PDF. Next we randomly switch two pixels, modify the PDF accordingly, and recalculate the rmse. A switch is rejected if the rmse increases. By switching pixels we ensure that the overall ratio of black pixels is preserved. This recipe is followed for 3x3, 2x2, 4x4, 3x3, 2x2 windows and so on until the full PDF is fitted. In Fig. 2 we show the resulting 2-D mesh. We note that the scale is similar to that in Fig. 1. As can be seen in the image we are able to reproduce the various crystal sizes. Also note that the structure is stochastic, so if we started with a different random number seed we would have produced a different but statistically equivalent microstructure.

Creating a 3-D mesh is very similar to creating the 2-D one except instead of a 2-D array we have a 3-D array that we "page through." First we create a 128x128x128 array and randomly populate it. In this case, however, we didn't use the finest scale data. We start with a length scale we can hope to resolve in a simulation, ~ 20 microns or 10 pixels. We now populate

our array with percentages consistent with the micrograph PDF for the 10x10 window. Now, instead of black and white we have gray levels from 0–100 representing the binder percentage for that pixel (element). We now apply our scanning windows for all 128 2-D "pages" of our array. We do this in the three (x, y, and z) directions. This naturally creates 3-D regions that represent individual grains. Note that we are assuming that the composite is isotropic.

Figure 3 illustrates a subset of the 3-D mesh we just described. To use the mesh described here we need a theory that can accommodate different formulations of PBX 9501. Our hybrid Method of Cells / Modified Eshelby-Mori-Tanaka model has this capability [1]. The method hinges on creating a representative volume element of PBX 9501. We use a 2x2x2 RVE with one large subcell representing the large HMX crystals and the other seven subcells use our Modified Eshelby-Mori-Tanaka model [2, 3] or "dirty binder" model to represent small HMX crystals in the polymer matrix. By changing the relative size of the subcells we are able to represent the different binder concentrations in the mesh.

Using the finite element code EPIC [4] to conduct simulations, we applied velocity boundary conditions on the top and bottom nodes in Fig. 3 to approximate a split-Hopkinson pressure bar experiment. The resulting stress strain curve is shown in Fig. 4. Other quantities such as pressure show similar distributions

By incorporating 2-D image analysis data into a 3-D finite element mesh we are able to represent the fluctuations of fields such as stress and pressure. This information may be invaluable when we investigate ignition that is thought to be driven by local fluctuations in pressure and temperature.

For more information contact Eric Mas at mas@lanl.gov.

[1] B.E. Clements and E.M. Mas, *Modeling Simul. Mater. Sci. Eng.* **12**, 407–421, 2004.
[2] B.E. Clements and E.M. Mas, *J. Appl. Phys.* **90**, 5522–5534, 2002.
[3] E.M. Mas, and B.E. Clements, J. *Appl. Phys.* **90**, 5535–5541, 2002.
[4] G.R. Johnson, et al., "User Instructions of the 1997 Version of the APIC Code," Wright Laboratory, Armament Directorate, Eglin Air Force Base report, WL-TR-1997-7037, 1997.

.

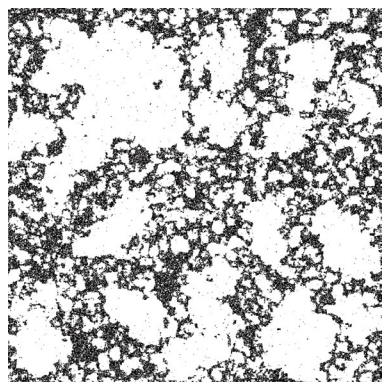

Fig. 2. *The 2-dimensional mesh generated from the statistics taken from the micro-graph. The array is 1024x1024 pixels.*

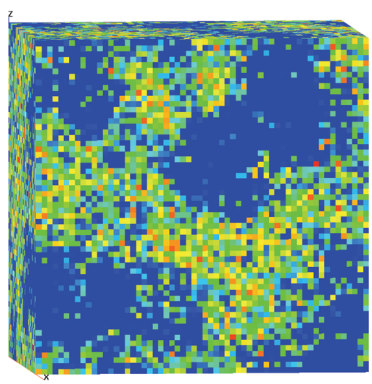

Fig. 3. *A 3-dimesional hex-agonal mesh of PBX 9501. The gray levels indicate different per-centages of binder.*

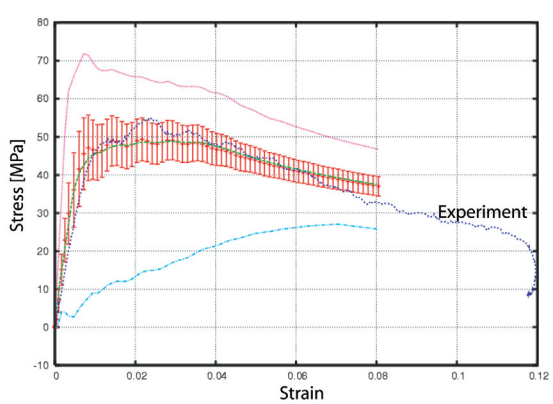

Fig. 4. *Stress-strain curves for PBX 9501. The experimental curve is labeled, the top and bottom curves show the highest and lowest stress in an element at that strain during the simulation, the error bars are one standard deviations above and below the mean and the curve in the middle of those bars is the average stress-strain curve.*

Dynamically Driven Phase Transformations in Damaged Composite Materials

JeeYeon N. Plohr and Bradford E. Clements, T-1; and Francis L. Addessio, T-3

A model developed for composite materials undergoing dynamically driven phase transformations in its constituents [1] has been extended to allow for complex material microstructure, viscoplasticity, and evolution of damage.

In this work, damage is described by interfacial debonding and microcrack growth. Here we have applied the analysis to silicon carbide-titanium (SiC-Ti) unidirectional metal matrix composites. In SiC-Ti composites, Ti is the matrix and SiC is the reinforcement with their volume fractions being 65% and 35%, respectively. This composite has shown potential use in aerodynamics applications due to its excellent properties especially at elevated temperatures. However, the phase transformation of Ti from α(hcp) to ω(hex) phase, viscoplastic flow, cracking in SiC, and debonding at the interface of SiC and Ti complicate its behavior. Understanding these phenomena is important in extending the usage of this material.

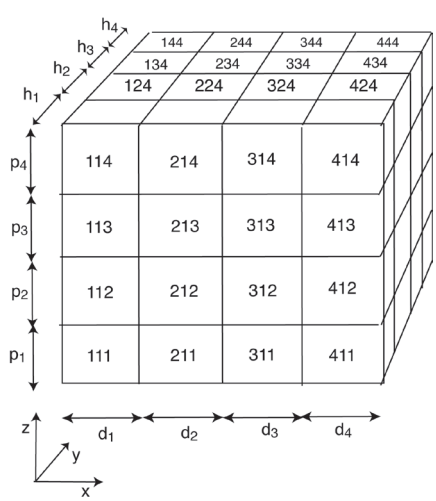

Fig. 1. ***Unit cell of GMC with 4x4x4 subcells: in the simulations discussed, (112), (212), (312), (134), (234), and (334) are SiC.***

First we examined each process independently in order to understand their characteristic behaviors, which appear in a more complicated way when applied simultaneously. In order to accommodate the highly anisotropic behavior of composite materials, we adopted the micromechanical framework, or more specifically, the Generalized Method of Cells (GMC) as our analysis tool. Because micromechanical analysis does not require *a priori* assumption on the behavior of the composites (instead it does the equation of state of each constituents), it is favorable in treating elastoplastic composites or damaged material where anisotropy plays an important role in determining local load and resulting flow (Fig. 1).

With these extensions we have carried out simulations to study the complex interplay between loading rates (Fig. 2), microstructure, viscoplasticity, damage, and the thermomechanical response of the system as it undergoes a solid-solid phase transformations (Figs. 3 and 4). In conclusion, the performance of the SiC/Ti composite is certainly superior to pure Ti, as it can endure higher loading. Because there is not any experimental data available for the regime of the phase transformation, we have performed detailed consistency tests on our analysis.

We hope this work inspires experiments to be performed on this composite. Further refinements of this model include implementing shear deformation, tangential debonding and crack opening. Also other types of phase transformation, (e.g., melting) can be studied by this method.

For more information contact JeeYeon Plohr at jplohr@lanl.gov.

[1] F.L. Addessio, et al., "A Model for Heterogeneous Materials including Phase Transformations," *J. Appl. Phys.* **97**, 083509 (2005).

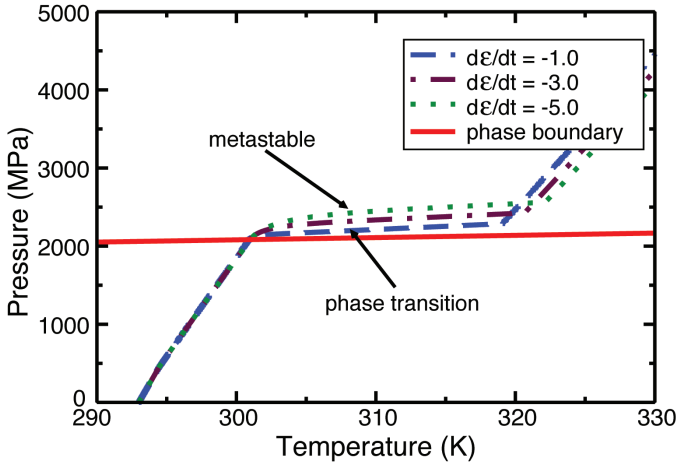

Fig. 2.
The effect of strain rate on phase transformations of Ti; uniaxial strain with $\tau = 3.0\ m^2\ s$.

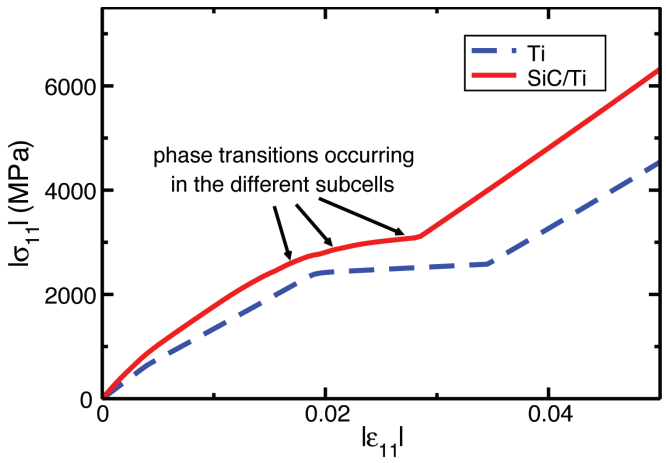

Fig. 3.
The phase transformation in SiC/Ti composite.

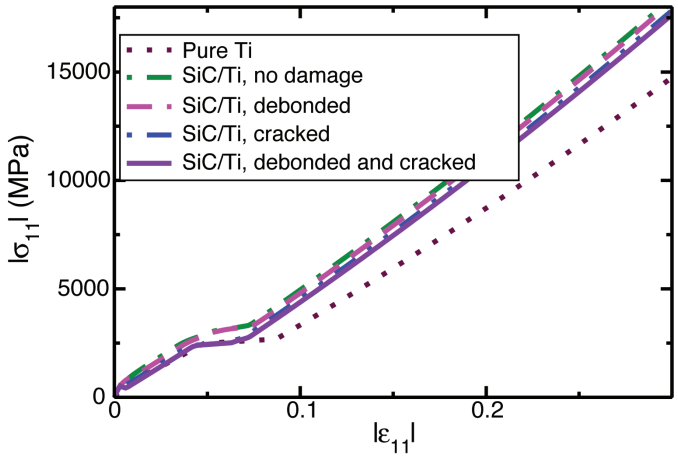

Fig. 4.
SiC/Ti composite with the phase transformations, viscoplasticity, cracking, and debonding.

Calculated Effects of Ga on the Pu Lattice after the δ to α Transformation

Sven P. Rudin and John M. Wills, T-1

The doping of plutonium with gallium atoms stabilizes the technologically important delta structure (face-centered cubic crystal structure) down to room temperature. As the temperature is lowered further, the delta structure transforms into the α-Pu structure with the Ga atoms arranged randomly on the eight symmetrically inequivalent alpha sites. This so-called α′ structure has an expanded volume relative to the (undoped) α-Pu lattice, but with thermal treatment the volume expansion decreases [1].

To further the understanding of these thermal effects we have performed density functional theory (DFT) calculations to investigate the local effects of substitutional Ga doping on the α-Pu structure. In a first step the lattice was held fixed and the total energies compared. A clear correlation emerges between the proximity of Pu atoms around each of the eight sites (Fig. 1) and the energy of the crystal where that site's Pu atom has been replaced by Ga (Fig. 2): the more distant the neighbors, the lower the energy.

This preference for having the Pu atoms farther away from the substitutional Ga atom appears to agree with experiment. Assuming the crystal's volume expands to give the Ga atom the preferred larger distance to its neighbors, the Ga atom will cause a different amount of volume expansion depending on which site it occupies. With thermal treatment the Ga atoms diffuse to energetically more favored sites which allows the volume to reduce its expansion. Further evidence for this appears in the next set of calculations where the lattice positions are allowed to relax (with the volume fixed at the α-Pu equilibrium

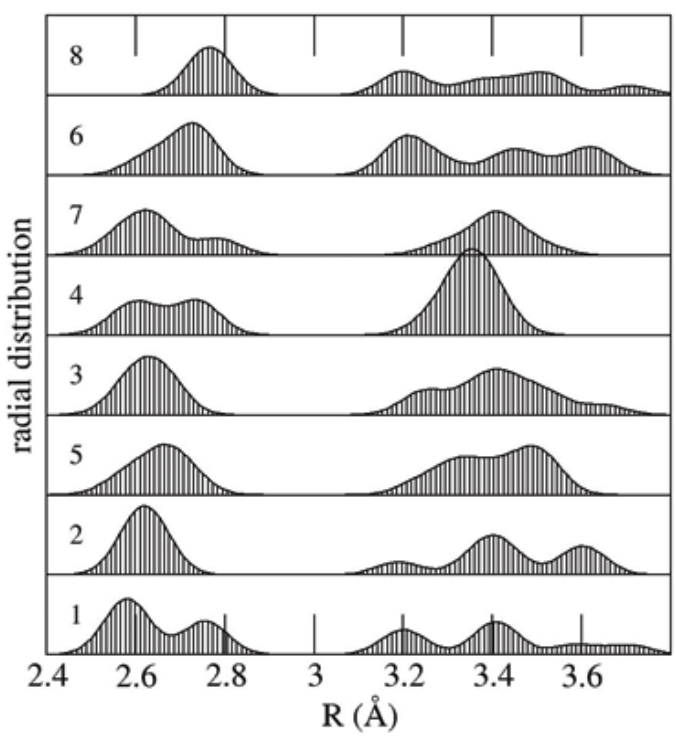

Fig. 1.
Radial distributions of Pu atoms surrounding each of the eight symmetrically unique lattice positions in the α-Pu structure. The distributions are plotted from bottom to top with increasing distance to the nearest neighbors. Each neighbor's position is smeared with a Gaussian for visualization.

volume): the distances between Ga atom and neighboring Pu atoms increases as shown in Fig. 3.

When the volume is allowed to relax in the calculations, the qualitative agreement with experiment remains. The relaxed volume is somewhat smaller than the experimental value for both pure and Ga-doped α-Pu due to the approximation inherent in DFT calculations. Still, the Ga-doped crystal remains expanded relative to pure α-Pu, and the energy remains lower for crystals whose substitutional Ga atoms have the most distant Pu neighbors.

For more information contact Sven Rudin at srudin@lanl.gov.

[1] S. S. Hecker, et al., *Prog. Mat. Sci.* **49**, 429 (2004).

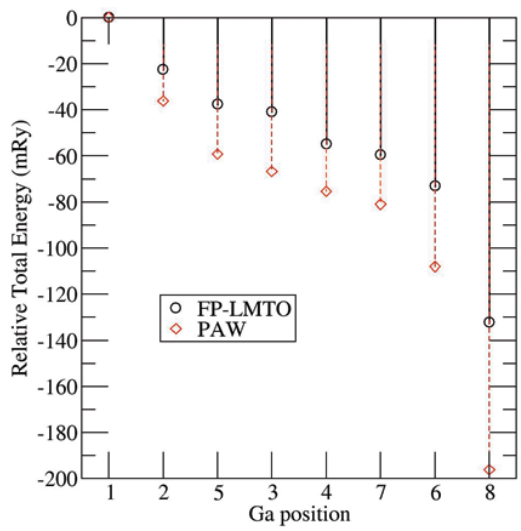

Fig. 2. *Relative energies calculated by substituting Ga for Pu on one of the eight symmetrically unique lattice positions in the α-Pu structure. The energies are relative to the energy of the 16-atom cell with the Pu atom at site 1 substituted by a Ga atom. The main difference between the two FP-LMTO and PAW calculations is the inclusion and exclusion of spin-orbit coupling, respectively.*

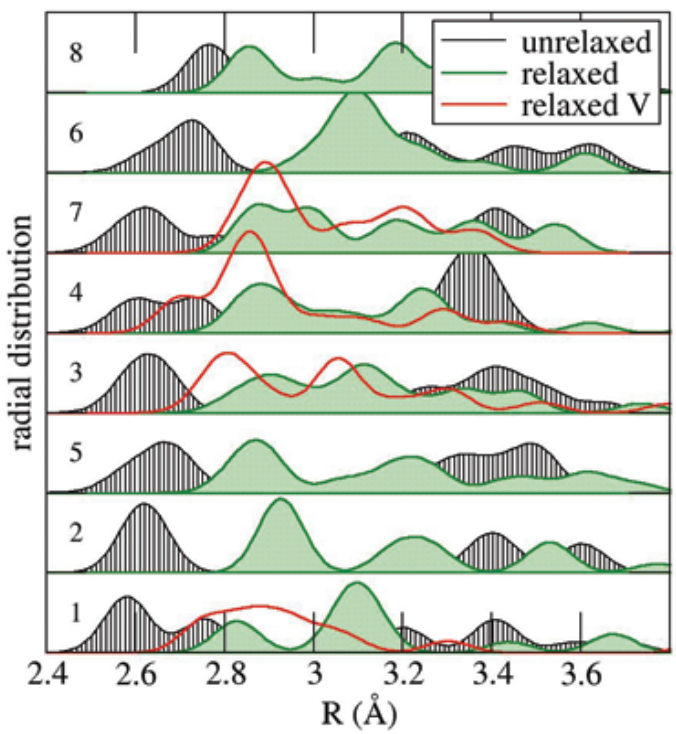

Fig. 3. *Radial distribution of Pu atoms surrounding each of the eight symmetrically unique lattice positions in the unrelaxed α-Pu lattice as well as after Ga substitution and lattice relaxation at fixed volume ("relaxed") and with relaxed volume ("relaxed V"). Relative to the unrelaxed α-Pu lattice, the substitutional Ga atom pushes its neighbors away.*

Phonons from Density Functional Theory for Equations of State

Sven P. Rudin, J. D. Johnson, and John M. Wills, T-1

Phonons cannot be neglected in the construction of a material's equation of state (EOS); they tend to be the main thermal contribution to the free energy. The construction of reliable EOS for the Sesame database from density functional theory (DFT) thus requires the phonons be calculated from DFT. It also requires knowing the reliability of the calculated phonons' accuracy with respect to experiment. We have extensive experience that guides us in knowing the reliability of calculated cold curves; more recent experience sheds light on the reliability of DFT phonon calculations.

For example, the phonon dispersion for hexagonal close-packed (hcp) beryllium shown in Fig. 1 gives an idea of how exact the DFT results can be expected to be. The calculated frequencies agree very well with experiment along the acoustical branches. The differences in the optical phonon frequencies is roughly 10% between results from the two DFT methods used—APW+lo (augmented plane wave plus local orbitals) and PAW (projector-augmented wave). Differences of roughly 10% also appear between either method's results and the experimental data. In our experience this is typical: for most materials DFT calculations and experiment agree very closely on the acoustic mode frequencies and within 10% on the optical mode frequencies.

The details of the phonon dispersion are less important in the construction of a reliable EOS than is the overall phonon density of states (DOS). The phonon DOS determines the contribution to the free energy via weighted frequency integrations of the DOS, i.e., the details of the dispersion are washed out in the process. In practice we calculate the volume-dependent phonon DOS at a sequence of volumes (shown, e.g., in Fig. 2 for tantalum), and from these we evaluate the Helmholtz free energy F(V,T). Interpolating F(V,T) as a function of volume results in the EOS.

The Helmholtz free energy F(V,T) can be transformed into the Gibbs free energy G(P,T). Comparison of the Gibbs free energies G(P,T) of two phases leads to predictions for structural phase transitions, e.g., the hcp to bcc transition for beryllium shown in Fig. 3. At low pressure our calculations predict a phase transition around 400 GPa, in agreement with experiment, where no transformation has been observed up

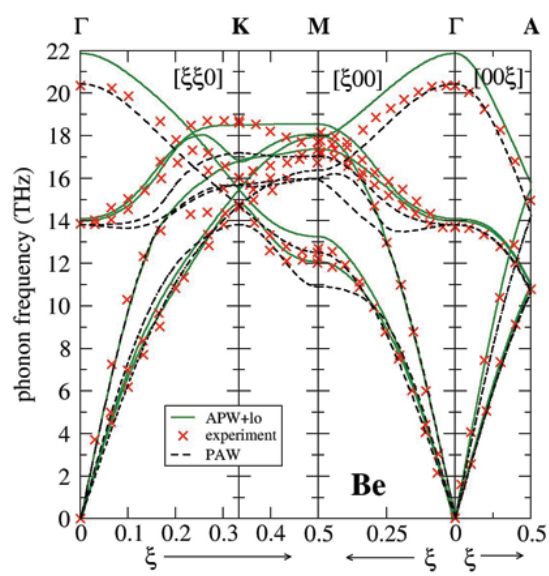

Fig. 1.
Phonon dispersion for beryllium in the hexagonal close-packed structure at the experimental equilibrium geometry. The calculated phonon frequencies agree well with the experimental values, especially for the acoustic branches. The agreement between experiment and theory for the optical branches is within 10%, similar to the agreement between the values calculated with the two DFT methods.

to the maximum pressure achieved to date, 180 GPa. For the low pressure, high temperature transition our results disagree strongly with experiment: the measured ambient pressure transition occurs at a temperature of 1530 K whereas theory predicts the transition to take place near 6000 K. This discrepancy reflects the neglect of strong anharmonicity in our current calculations.

Strong anharmonicity appears in many other elements where the bcc phase appears at high temperatures as well as in the low-temperature hcp phase of Zr and alpha phase of U. The inclusion of strong anharmonicity effects is thus a challenge we are working to overcome as we strive to make DFT more reliable in the construction of equations of state.

For more information contact Sven Rudin at srudin@lanl.gov.

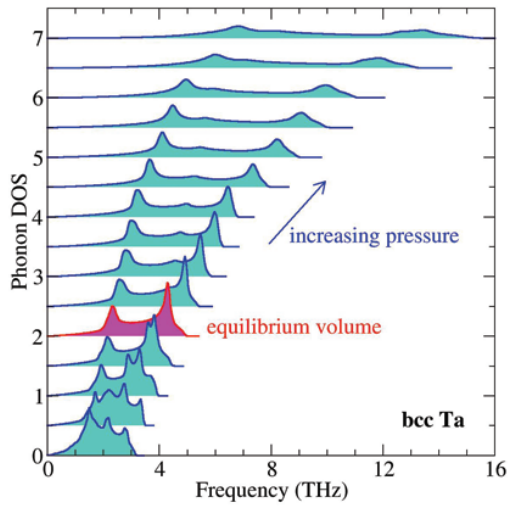

Fig. 2.
Calculated phonon density of states for tantalum in the body-centered cubic structure at a sequence of volumes.

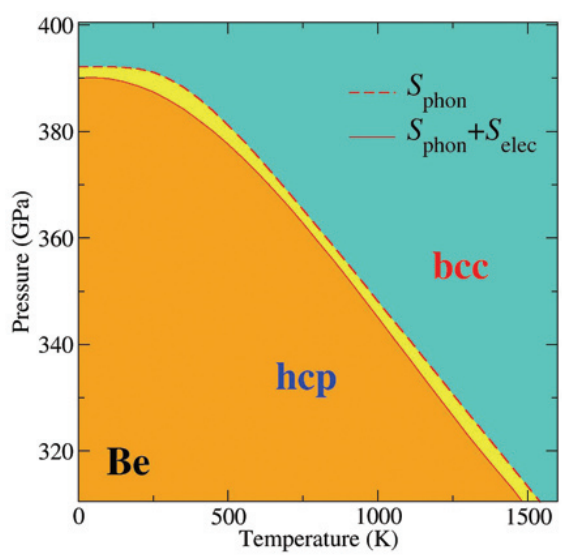

Fig. 3.
Calculated hcp-to-bcc phase transition line for beryllium. The phonons make up the largest contribution to the temperature dependence of the phase transition; the electronic contribution lowers the transition pressure only slightly.

Vibration-Transit Theory for Time Correlation Functions in Liquids: A Model for Transits

Giulia De Lorenzi-Venneri and Duane Wallace, T-1

Great progress has been done in the last two decades on the understanding of liquids, both experimentally [1] and theoretically [2]. The theory developed in T-1, recently given the name of "Vibration-Transit" theory, contributes to this field by providing a Hamiltonian formulation of the dynamics in liquids, so that properties can be readily calculated from first principles, within controllable levels of approximations. After a number of successful results from the theory, we have now applied it to time correlation functions and in particular to the evaluation of the dynamic structure factor $S(q,\omega)$.

Vibration-Transit theory is based on the idea that a liquid system moves on its potential energy surface by performing almost instantaneous jumps, or transits, between valleys. The theory postulates that the dominant majority of visited valleys are all random in structure (see Fig. 1) and that they are all equivalent in energy and vibrational properties. Vibrations and transits are the building blocks of liquid dynamics. The zeroth order approximation to the Hamiltonian expresses the liquid motion in terms of normal mode vibrations in a single infinitely extended harmonic random valley and can be explicitly calculated from first principles for actual systems. On the other hand, the nature and microscopic details of transits are still an open problem.

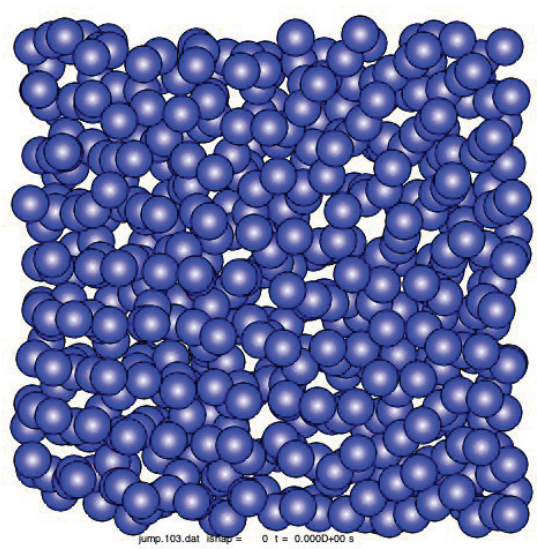

Fig. 1. ***Typical random atomic structure in a liquid.***

The vibrational motion gives a very good account of the equilibrium thermodynamics of monatomic elemental liquids at melt [3]. This was obtained by V-T theory without adjustable parameters, a result that no other tractable theory has yet achieved.

When extended to nonequilibrium properties, namely to time correlation functions [4], V-T theory implies that both contributions, vibrations and transits, must be explicitly taken into account. Again without adjustable parameters, the vibrational contribution to any time correlation function [e.g., $F_{vib}(q,t)$, the density-density autocorrelation function] can be calculated from the zeroth order Hamiltonian. In particular for the dynamic structure factor $S(q,\omega)$—the Fourier transform of $F(q,t)$—the vibrational contribution is the sum of independent scattering cross sections from the normal modes. $S(q,\omega)$ is particularly interesting because it is measured in inelastic scattering experiments. For the case of liquid sodium it was found that it is this vibrational contribution that determines not only a natural width for the Brillouin peak [5], but also it locates the position of its maximum, as shown in Fig. 2. The figure proves that this dispersion curve for the liquid (which is in agreement also with experiments) can be completely evaluated from only the independent

vibrational modes in a single valley, without the need to invoke coupling between the modes and relaxation times, a notion in contrast with previous interpretations.

The major effect of transits, for which an explicit evaluation is not yet available, is to disrupt correlations within the normal mode vibrational motion and provide an additional source of inelastic scattering. We developed a model for the contribution of transits to inelastic scattering [6]. The model was developed for F(q,t). It was built in the spirit of Zwanzig's model for the velocity autocorrelation function, but we kept in mind the specific role played by transits in the decay of time correlation functions. It has three parameters and gives F(q,t) as:

$$F_{liq}(q,t) = F_{Rayleigh} + F_{Brillouin}$$

$$= C(q)\, F_{vib}(q,\infty) \exp(-\alpha_1(q)t) + [F_{vib}(q,t) - F_{vib}(q,\infty)] \exp(-\alpha_2(q)t),$$

where $F_{vib}(q,t)$ is determined by the vibrational contribution and $F_{vib}(q,\infty)$ expresses purely elastic scattering and gives rise to the elastic peak $F(q,\infty)\,\delta(\omega)$ in $S(q,\omega)$. Of the three parameters of the model, C(q) models the additional inelastic scattering due to transits, while $\alpha_1(q)$ and $\alpha_2(q)$ model the decorrelation due to transits, and are close to the mean single-atom transit rate. In $S(q,\omega)$ the effect of transits is to broaden the elastic Rayleigh peak and to broaden but not shift the Brillouin peak. We have shown that this model is capable of accurately reproducing the molecular dynamics (MD) results for $S(q,\omega)$ for liquid sodium (see Fig.3), thus providing a new interpretation of the scattering process in terms of independent scattering events due to the normal vibrational modes and transits.

Work to study the role of transits and how to incorporate them in explicit evaluations within V-T theory is presently underway.

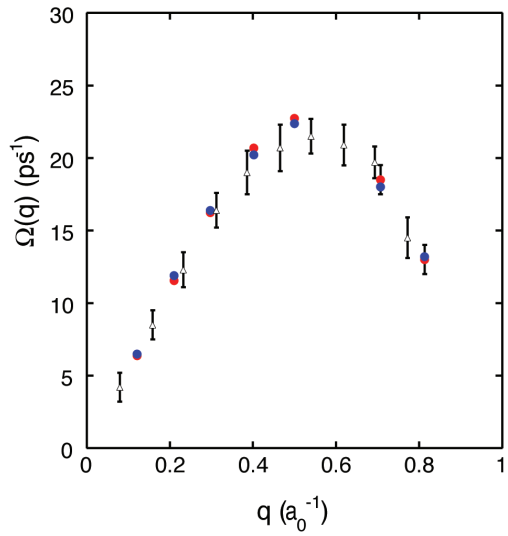

Fig. 2.
Dispersion curve for the Brillouin peak of inelastic scattering in liquid sodium at 395K. The position of the Brillouin peak maximum as a function of q is reported. V-T theory (blue circles) and MD simulation (red circles) almost coincide and also agree with x-ray experiments by Scopigno et al. [1] (triangles with error bars).

For more information contact Giulia De Lorenzi-Venneri at gvenneri@lanl.gov.

[1] T. Scopigno, et al., *Rev. Mod. Phys.* **77**, 881 (2005).
[2] F. Sciortino, *J. Stat. Mech.: Theory and Experiment* 2, P05015 (2005); D.R. Reichman and P. Charbonneau, *J. Stat. Mech.: Theory and Experiment* **2**, P05013 (2005).
[3] D.C. Wallace, *Phys. Rev. E* **56**, 4179 (1997), E.D. Chisolm and D.C. Wallace, *J. Phys.: Conden. Matter* **13**, R739 (2001), D.C. Wallace, *Statistical Physics of Crystals and Liquids* (World Scientific, New Jersey, 2002).
[4] J.P. Hansen and I.R. McDonald, *Theory of Simple Liquids* (Academic, New York, 1986).
[5] D.C. Wallace, et al., arXiv: cond-mat /0506369.
[6] G. De Lorenzi-Venneri and D.C. Wallace, *J. Chem. Phys.* **123**, 244513 (2005).

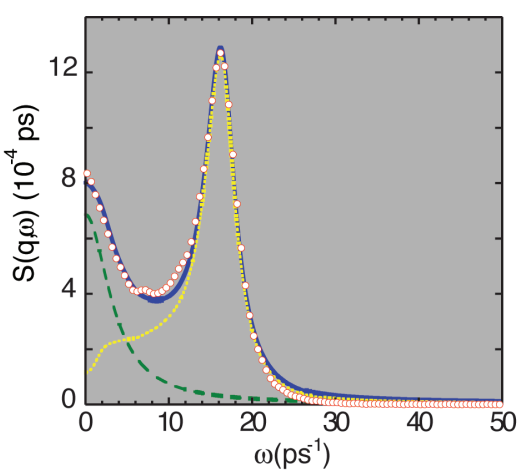

Fig. 3.
Dynamic structure factor for liquid sodium at 395K from V-T theory (blue solid line) and MD simulation (red circles). The V-T theory result is composed of two parts: the Brillouin peak (yellow dotted line), whose exact location and natural width are determined by vibrations, and whose width has a small contribution from transits, and the Rayleigh peak (green broken line), which is instead determined by transits. The vibrational contribution is evaluated within V-T theory, from a first principles Hamiltonian, while the transit contribution, for which an exact evaluation is not yet available, is modeled with a three-parameter relaxation function fitted to the MD results.

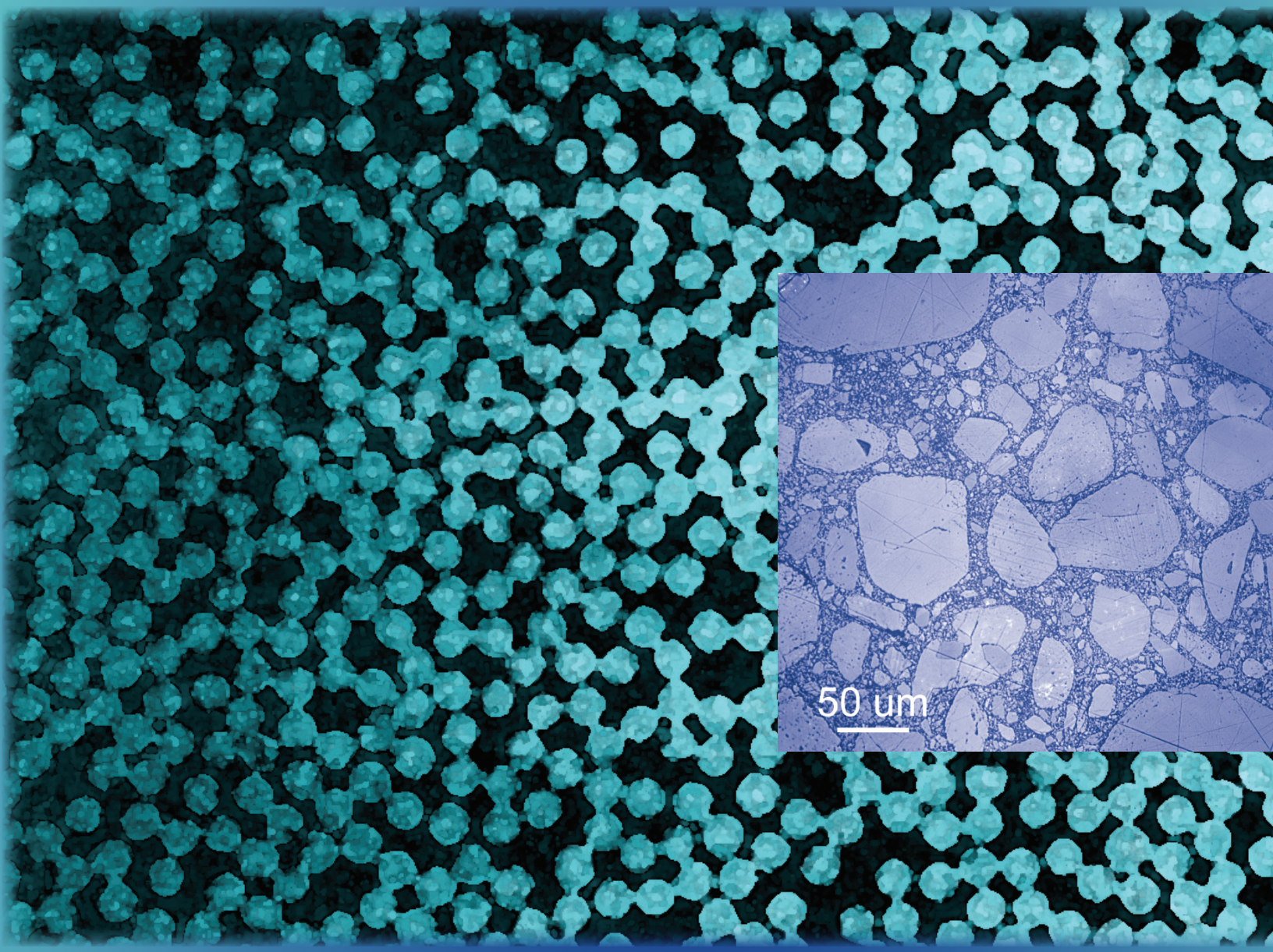
50 um

Fluid Dynamics

T-3

Group Leader: Mark Schraad
505.665.3946; schraad@lanl.gov

T-3 Fluid Dynamics is involved in modern hydrodynamic theory, modeling, and computational simulations. There is an emphasis on coupling advanced numerical methods for fluid dynamics at all flow velocities with models for other processes, including chemical reactions, phase change, heat and mass transfer, plasma behavior, constitutive properties of structural materials, and combustion.

Local Deformation Behavior of Metallic Polycrystals

Curt A. Bronkhorst and B. L. Hansen, T-3

Unless special processing is used, most metallic materials are aggregate composites composed of single crystals. Each of these crystals is generally anisotropic in how it deforms both elastically and plastically. We are developing both the theoretical and numerical tools to allow us to probe the detailed local response of a variety of metallic polycrystals. The single crystal is represented by a model, which accounts for large deformation kinematics, anisotropic elasticity and thermal expansion, temperature and deformation rate sensitive plastic flow. This flow rule is based on mathematics used to represent thermally activated slip processes. The plastic hardening relationship used is based upon first order dislocation generation and annihilation processes. The rate of hardening is also a function of temperature and deformation rate. Plastic flow is restricted to occur only on prescribed slip systems. A polycrystal microstructural model has been developed which is based on a Voronoi tessellation growth process using statistical models for the spatial distribution of seed points. A particular microstructure composed of 48 individual crystals is given in Fig. 1, shown without intragranular subdivision.

The single-crystal model parameters were evaluated for tantalum and the model was applied to the microstructure given in Fig. 1. Each of the 48 crystals were assigned an initial crystallographic orientation chosen by random and given the ability to plastically deform on the twelve {110}⟨111⟩ and twelve {112}⟨111⟩ slip systems. The 2-D model was then deformed (quasi-static and isothermal at 23C) in plane-strain compression up to a true strain of 1.0. The top and bottom surfaces were frictionless with the bottom surface stationary. The left edge is prevented from displacing horizontally while the right surface is stress-free. Response of the model is given in Figs. 2 and 3. Although experiments have not yet been conducted to verify the accuracy of our representation of the local polycrystal deformation field, the vonMises stress results given in Fig. 2 suggest that this metal deforms in a highly heterogeneous manner. For the example shown, the vonMises stress values range between approximately 500 and 1100 MPa. The free surface on the right side of the sample also demonstrates significant inhomogeneity at this length scale. Surface roughening like this is observed experimentally. Interaction between grains also causes nonuniform deformation to occur within each crystal. All of these phenomena are due to the inherent anisotropic nature of metallic crystal deformation. These capabilities are being used to study the physics and statistics of the ductile deformation and damage process for a number of metallic materials.

For more information contact Curt Bronkhorst at cabronk@lanl.gov.

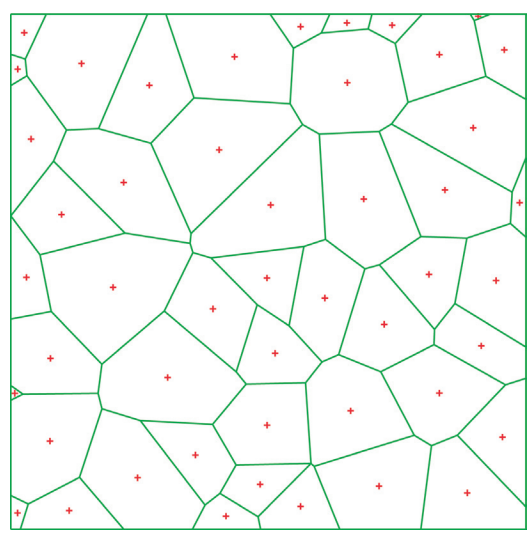

Fig. 1. ***Voronoi tessellated microstructure (2-D) used for the plane-strain compression simulation. There are 48 grains in the aggregate polycrystal.***

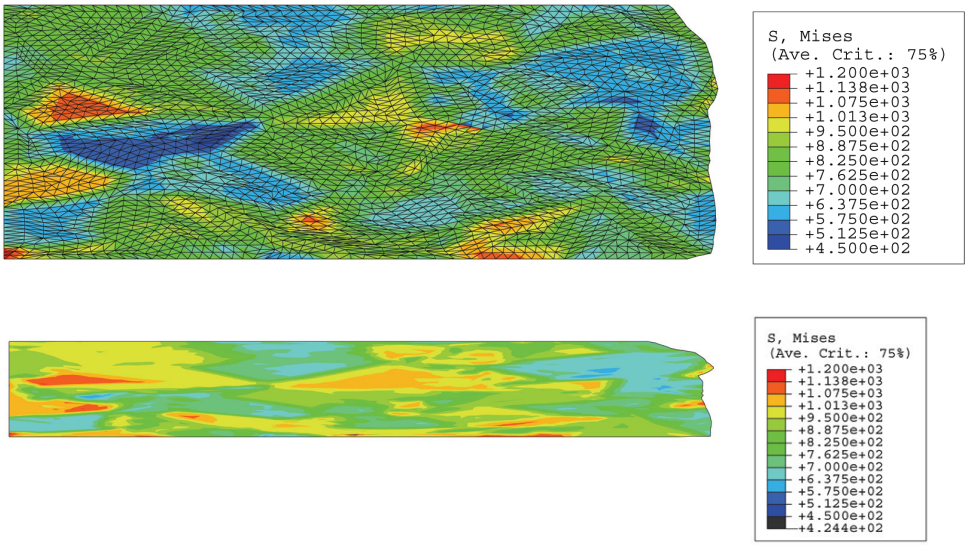

Fig. 2. *vonMises stress distribution within the tantalum polycrystal at a macroscopic compressive strain of (a) 0.52, with mesh shown; (b) 1.0, without mesh shown. The undeformed model is initially square.*

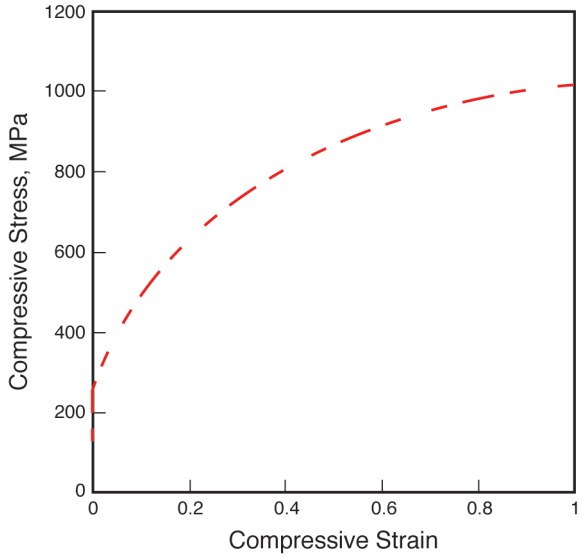

Fig. 3. *Macroscopic plane-strain compression stress-strain response for the 48-grain tantalum simulation.*

A Strength Model for Materials with Phase Transformations

Eric N. Harstad, Francis L. Addessio, and Q. Ken Zuo, T-3; and Carl W. Greeff, T-1

A material model has been developed for the deviatoric components of the stress, which includes the effects of phase transformations. The model accounts for the different material properties of each phase and evolves separate yield surfaces. Relying on a free energy approach, the strength model is coupled to the equation of state, which is applicable to high-pressure applications. The material model has been implemented into a three-dimensional, Lagrangian, finite-element computer code. Results for a simulation demonstrate the importance of including phase transformations for an explosively loaded zirconium (Zr) plate.

Experimental results for the behavior of metals in the titanium group indicate that phase transformations can be an important mechanism in their response to deformation. For example, in Zr plate impact experiments, the phase change is apparent from the VISAR record of the back surface velocity [1]. Plate impact experiments represent a pressure dominated material response, which for purposes of matching the back surface velocity, may be accurately modeled without a sophisticated material strength model. For more general loadings, however, the effects of phase-change on the deviatoric response of the material are important. In order to improve computer simulations that involve solid-solid phase transformations, an isotropic strength model for multiple solid phases has been developed. The model allows each phase to have unique material properties such as the elastic moduli. It also includes a separately evolving yield stress for each phase.

For a material that undergoes a solid-solid phase change, the Helmholtz free energy (Ψ) for the mixture is written as a mass-weighted sum over the phases of the Helmholtz free energies of the individual phases $[\psi_k(\bar{\bar{\varepsilon}}_k^e, T_k)$, where $\bar{\bar{\varepsilon}}_k^e$ is the elastic strain tensor, T_k is the temperature of the kth phase] plus a term representing the mixing between the phases (Ψ^{mix}) [2–6]. For this development, we assume that the energy due to mixing is negligible ($\Psi^{mix} = 0$). The stress for a phase is decomposed into its volumetric and deviatoric components, which are related to the free energy

$$\bar{\bar{\sigma}}_k = \bar{\bar{s}}_k - P_k \bar{\bar{\delta}} = \frac{1}{v_k}\frac{\partial \psi_k}{\partial \bar{\bar{e}}_k^e} + \frac{\partial \psi_k}{\partial v_k}\bar{\bar{\delta}} \quad . (1)$$

In Eq. 1, $\bar{\bar{s}}_k(\bar{\bar{e}}_k^e, T_k)$ is the deviatoric stress, $P_k(v_k, T_k)$ is the pressure, v_k is the specific volume, $\bar{\bar{e}}_k^e$, is the deviatoric elastic strain, and $\bar{\bar{\delta}}$ is the Kronecker delta. The free energy is assumed to be separable into its volumetric (Ψ_k^{eos}) and deviatoric (Ψ_k^{dev}) components. The volumetric component of the free energy provides the equation of state for the material under consideration. For Zr, this component of the free energy was determined by Greeff. It is written as the sum of static lattice energy, an ion motion free energy, and an electron excitation free energy contribution [7]. The deviatoric stress in each phase is related to the elastic part of the deviatoric strain of that phase

$$\bar{\bar{s}}_k = 2\mu_k \bar{\bar{e}}_k^e = 2\mu_k(\bar{\bar{e}}_k - \bar{\bar{e}}_k^p) \quad (2)$$

where $\bar{\bar{e}}_k^p$, is the plastic strain of kth phase. It is assumed that all of the phases are in temperature and stress equilibrium (i.e., the Reuss limit). A mixture equation for the deviatoric components of the stress and strain may be obtained [8], which we present in incremental form

$$d\bar{\bar{s}} = 2\mu\, d\bar{\bar{e}}^e = 2\mu(d\bar{\bar{e}} - d\bar{\bar{e}}^p) \quad . \quad (3)$$

In Eq. 3, the shear modulus (μ) and the strains ($d\bar{\bar{e}}, d\bar{\bar{e}}^e$, *and* $d\bar{\bar{e}}^p$) are volume averaged quantities. It is observed that for this development the increment of the total strain ($d\bar{\bar{e}}$) is split into the elastic ($d\bar{\bar{e}}^e$) and inelastic or plastic ($d\bar{\bar{e}}^p$) contributions. The increment of total

strain is obtained from the velocity gradients, which are computed from the global conservation of momentum.

To complete the formulation for the deviatoric component of stress, it is necessary to provide a constitutive equation for the plastic strain. Assuming associative flow plasticity, the plastic strain increment may be written as

$$d\varepsilon_k^p = d\bar{\bar{e}}_k^p = \frac{\partial f_k}{\partial \bar{\bar{s}}} d\lambda_k = 3\bar{\bar{s}}\, d\lambda_k; \qquad (4)$$

In Eq. 4, f_k is the yield function and $d\lambda_k$ is the plastic multiplier for the kth phase. For this development, separate von-Mises yield functions are used for each of the phases

$$f_k = \tau^2 - \sigma_k^2 \cdot \qquad (5)$$

In Eq. 5, τ is the second invariant of the deviatoric stress or the von Mises stress, σ_k is the flow stress, and $f_k = 0$ represents the yield surface. The proposed model may utilize any general flow stress model, which includes, for example, the effects of strain and strain-rate hardening as well as thermal softening.

For the conditions of equilibrium, the existing phase is determined by the phase with the minimum Gibbs free energy ($G_k = \Psi_k + P\nu_k$). Singh [9] observed that the transformation rate is an exponential function of the pressure, which is reflected in the phenomenological model proposed by Greeff [1]

$$\dot{\xi}_j = (1-\xi_j)\sum_{i \neq j} \nu_{ij} \frac{G_i - G_j}{B_{ij}} \exp\left(\frac{G_i - G_j}{B_{ij}},\right)^2 \qquad (6)$$

where ν_{ij} and B_{ij} are constants that describe the rate at which the material transitions to phase j from phase i.

The model has been implemented into a Lagrangian finite element code [10] and verified through several simple loading cases. For complex deformations, the accurate modeling of the phase change in the material is important. For example, we simulate an explosively loaded plate. A cylindrical case is filled with high explosive and has a Zr plate on one end (see Fig. 1). The high explosive is set off using a point detonation along the axis of the cylinder at the opposite end from the Zr plate. The detonation punches the plate into a parabolic shell. Three material points on the underside of the plate are selected as tracer particles: one in the center, one at the middle radius, and one on the edge. At the tracer particles, the state variables are output as a function of time. The figure depicts the pressure-temperature phase diagram of Zr with the three tracer particles trajectories overlaid. All three particles translate in pressure-temperature space across all three of the phases of Zr. The center and edge particles end in the β phase as a final state, and the midradius particle ends in the α phase. Most of the material within the plate returns to the α phase, with the exception of the center and outer ring, which are in the β phase. A very small amount of material is in the ω phase for the final deformation (not shown).

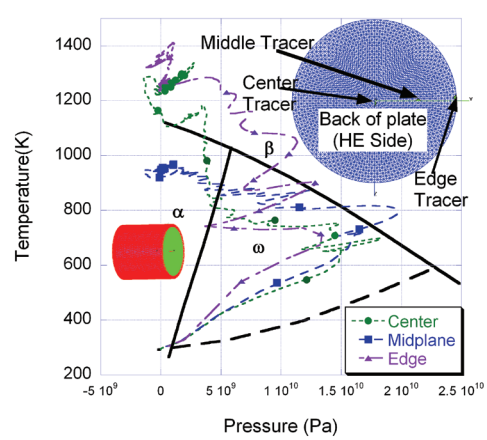

Fig. 1. ***Trajectories in pressure/temperature for three material points of an explosively loaded plate. Solid black lines are the boundaries between the phases and the black dashed line is the Hugoniot.***

For more information contact Eric Harstad at enh@lanl.gov.

[1] C.W. Greeff, et al., *AIP* **CP706**, 209–212, (2003).
[2] D.J.Andrews, *J. Comput. Phys.* **7**, 310 (1971).
[3] D.J. Andrews, *J. Phys. Chem. Solids* **34**, 825 (1973).
[4] J. Lemaitre and J.-L. Chaboche, *Mechanics of Solid Materials* (Cambridge University Press, New York, NY, 1985).
[5] J.G. Boyd and D.C. Lagoudas, *Int. J. Plast.* **12** (6), 805 (1996).
[6] D.A. Porter and K.E. Easterling, *Phase Transformations in Metals and Alloys* (Chapman and Hall, New York, NY, 1985).
[7] C.W. Greeff, submitted to *Modeling and Simulation in Materials Science and Engineering*, 2005.
[8] D.C. Wallace, *Thermodynamics of Crystals* (Dover Publications, Inc., Mineola, NY, 1972).
[9] A.K. Singh, et al., *J. Appl. Phys.* **53**, 1221 (1982).
[10] G.R. Johnson, et al., Wright Laboratory, Armament Directorate, Eglin Air Force Base report, WL-TR-1997-7037 (1997).

Permeating Fluid Effects in Cellular Material Systems under Dynamic Loading

Mark W. Schraad and
Francis H. Harlow, T-3

Cellular materials come in myriad forms and serve an ever-increasing variety of engineering functions. Unfortunately, the basic research devoted to modeling the mechanical response of these materials largely has overlooked some of the most fundamental physical processes involved in the problems and applications of interest. Previous modeling efforts have focused almost exclusively on the mechanical response of the cellular solids, while essentially ignoring the evolving pressure and flow behavior of the gases and liquids permeating the intricate networks of cells that comprise such systems.

The primary objective of this work is to develop a new approach to modeling the dynamic response of cellular materials. The coupled physical response of both the cellular solids and the permeating fluids are considered, and the influence of the permeating fluid on the response of the cellular solid is investigated as the material deforms under dynamic loading [1].

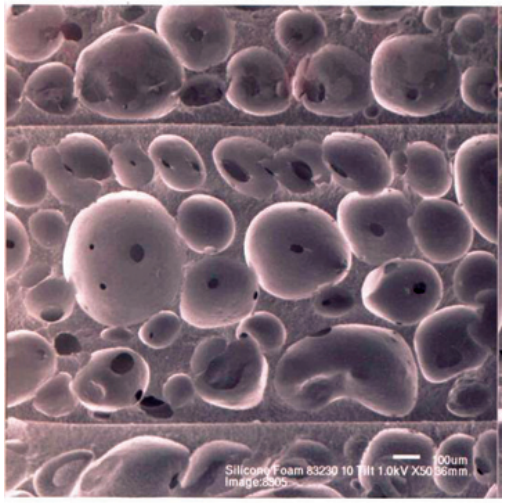

Fig. 1.
A scanning electron micrograph of a highly disordered, open-cell, silicone foam. Note the intricate structure at the cellular scale, the disordered nature of this structure, and the small apertures between cells. Micrograph provided courtesy of David J. Alexander, MST-6.

The new modeling approach couples the mechanical response of cellular solids with the physical behavior of the fluids permeating these materials through a multi-field description of the governing equations of motion. Multifield theory is applicable when the average motion of one material in a multimaterial system is distinctly different from that of the other materials. The response of each material, therefore, is characterized by its own distinct velocity field, while the response of the overall cellular material system is governed by a set of coupled conservation equations.

Equations governing the conservation of mass, momentum, and energy are derived in multifield form using a traditional ensemble-averaging technique. Governing equations derived in this manner necessarily include additional momentum and energy source terms that arise through the averaging process. This set of coupled multifield equations is closed through the development of appropriate constitutive models for the resulting source terms [2].

The multifield approach has been used to simulate the response of highly disordered, open-cell, silicone foams to dynamic loading conditions using a conventional finite-volume computational algorithm, in which the multifield conservation equations are solved in the Lagrangian frame of the solid. The material of interest represents a relatively dense structural foam used primarily in the manufacture of stress cushions for use between much stiffer metallic parts in multicomponent engineering systems.

Simulations represent the first time that advanced constitutive models for cellular solids have been coupled with a physical representation of the associated permeating fluid behavior in a comprehensive continuum-scale response description for the overall

cellular material systems. Results demonstrate that the permeating fluid can play a major role in the general response of cellular material systems, contributing to the overall load-carrying capacity of the materials and affecting rate dependence and signal propagation speeds.

Future research will focus on generalizing the multifield approach to include a more complete description of all relevant physical mechanisms occurring in both the fluid and solid fields. A more general description of the fluid field will be achieved through models that include terms for flow separation, viscosity induced shear stress, and turbulence induced Reynold's stress. Additionally, more general models for the cellular solid will be considered as well. Problems of interest include elastic wave propagation, low-frequency vibrations, sound wave attenuation, and strongly dynamic, shock-inducing phenomena.

For more information contact Mark Schraad at schraad@lanl.gov.

[1] M.W. Schraad and F.H. Harlow, "A Multi-field Approach to Modeling the Dynamic Response of Cellular Materials," *Intl. J. Mech. Sci.* **48**, 85–106 (2006).
[2] M.W. Schraad and F.H. Harlow, "A Stochastic Constitutive Model for Disordered Cellular Materials: Finite-strain Uni-axial Compression," *Intl. J. Solids Structures*, in press (2005).

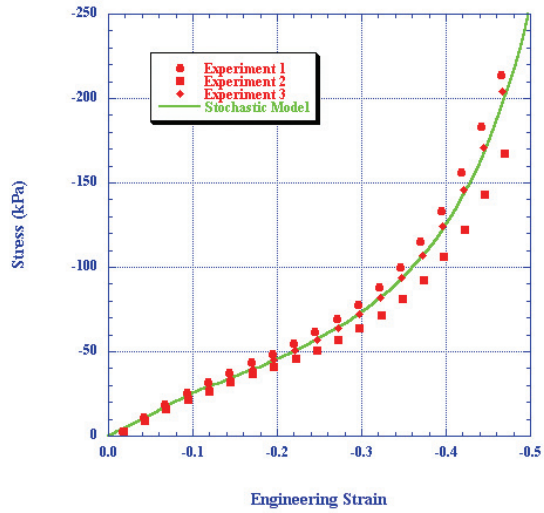

Fig. 2.
The continuum-scale stress-strain response of a silicone foam sample subjected to quasi-static uniaxial compression. Experimental results are plotted using solid data points and are shown for three different foam samples, each nominally possessing the same average material properties. Results obtained using the stochastic constitutive model are plotted using a solid line. Experimental data provided courtesy of Matthew W. Lewis, ESA-WR.

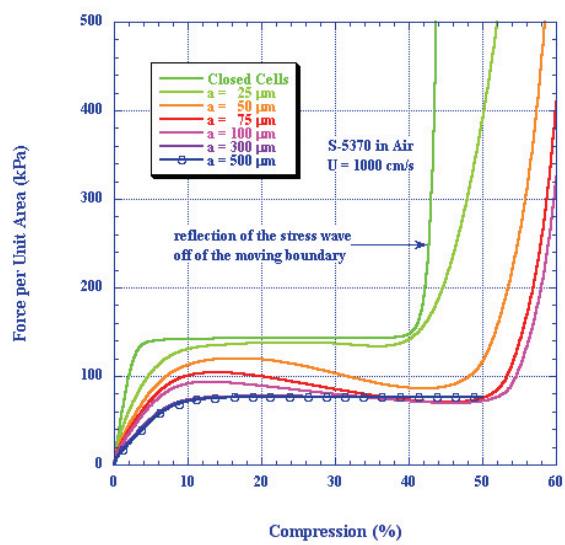

Fig. 3.
The total force per unit area plotted as a function of compression, illustrating the effect of average aperture size on the force required to deform the material. In general, as size increases, the force decreases, because the smallest apertures significantly restrict the flow of the permeating fluid, resulting in higher fluid pressures.

Instabilities in Cellular Solids and the Role of Dispersity in Geometric Structure

Mark W. Schraad, T-3

Failure and the often-associated instabilities in materials with microstructure are manifested in many different ways. The occurrence of an instability can be the precursor to shear band formation, pore and crack nucleation, and ultimately material failure, so an understanding of the relationships among microstructure, continuum-scale mechanical response, and stability is essential in material and engineering component design.

Geometric structures in cellular solids span the spectrum from highly ordered to strictly random. If the degree of dispersity in the underlying cellular geometry is low, failure in these materials typically manifests itself as localized deformation; for example, the collapse of cells. For materials with a high degree of dispersity, however, the stress can become a monotonically increasing function of strain, and thus, no critical point is reached, and the mechanical response remains stable through all regimes of compressive deformation. The primary objective of this investigation is to study the behavior of cellular materials ranging over the spectrum of geometric structures from highly ordered to highly disordered, and to explore the corresponding transition from unstable to stable mechanical response.

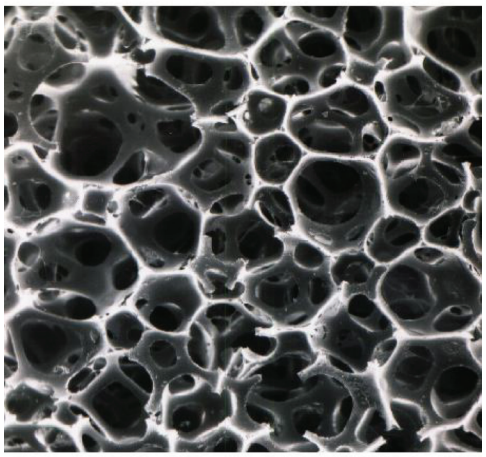

Fig. 1. *A scanning electron micrograph of a low-density, open-cell, polyurethane foam showing the intricate, disordered, geometric structure at the cellular scale. Material provided courtesy of the Dow Chemical Company, and micrograph provided courtesy of David J. Alexander, MST-6.*

An advanced constitutive model is developed and used to investigate the stability of cellular solids [1]. Stochastic variation in cellular-scale geometric structure and material properties is considered through the use of probability density functions for the associated model parameters. Using this approach, ordered cellular structures are represented using monodisperse distributions, while disordered cellular structures with varying degrees of dispersity are represented using other appropriate distribution functions.

Results demonstrate a general stabilizing effect of dispersity in geometric structure on the continuum-scale mechanical response of cellular materials. Consistent with previous investigations, dispersity in geometric structure is shown to have no effect on the initial elastic properties of the cellular materials under investigation. For deformations occurring prior to any instability, however, increasing dispersity is accompanied by decreasing stiffness.

No additional information might lead one to believe that dispersity in geometric structure has an overall detrimental effect on the mechanical response of cellular materials. The results of the present investigation, however, show that as the dispersity increases, the critical strains increase, the extent of localized deformation diminishes, and the materials stiffen for deformations occurring after the critical load. Most notably, the mechanical response of the materials with the highest degrees of dispersity in their cellular structures remains stable for all compressive deformations through full densification.

The results are consistent with trends shown in a wide range of analytical, numerical, and experimental studies of various cellular solids, suggesting that the stochastic constitutive model can be used to quantify the influence of cellular-scale geometric and material variability on the mechanical response, the stability, and the onset of failure in cellular materials. The constitutive model also provides useful information regarding the initial cellular-scale structural configurations in these materials, and the potential for these configurations to admit unstable behavior and eventually succumb to failure. Such information could prove valuable in tailoring these materials at the cellular scale for increased load-carrying capacity and reduced susceptibility to failure, possibly shifting the processing and manufacturing paradigm for this class of materials from properties by trial and error to properties by design.

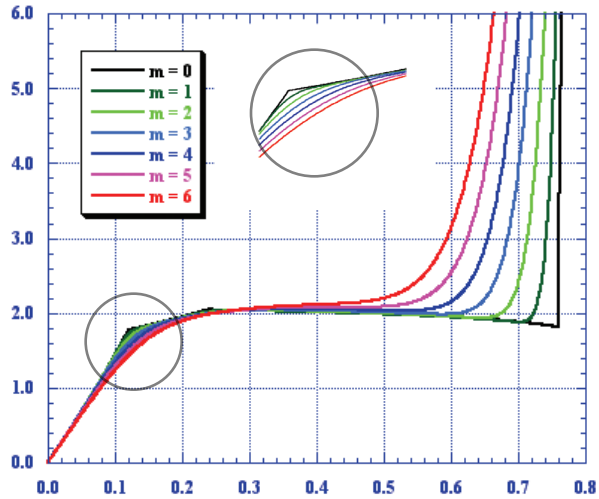

Fig. 2.
The influence of dispersity in geometric structure on the simulated continuum-scale mechanical response of a low-density, open-cell, polyurethane foam. Results for mono-disperse distributions are plotted using a black line, while the results obtained for values of the geometric dispersion parameter ranging from 1–6 are plotted using various colored lines as indicated.

For more information contact Mark Schraad at schraad@lanl.gov.

[1] M.W. Schraad, "The Influence of Dispersity in Geometric Structure on the Stability of Cellular Solids," *Mech. Mater.*, submitted (2006).

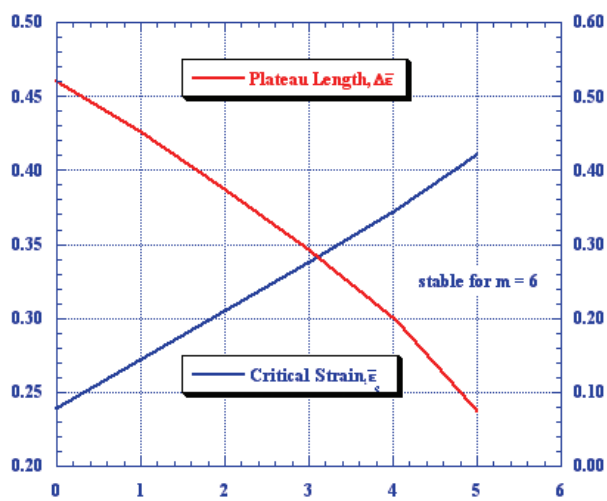

Fig. 3.
The influence of dispersity in geometric structure on the critical strain and load-plateau length. Notice that for m > 5, the load plateau diminishes altogether, as the stress becomes a monotonically increasing function of strain. For m = 6, the mechanical response remains stable for all uniaxial compressive deformations.

Stochastic Multiscale Material Modeling

Todd O. Williams, T-3

All materials are heterogeneous at the microstructural length scale. Furthermore, the vast majority of these materials have random microstructures. High explosives (HEs) and continuous fiber composites, shown in Fig. 1, are both examples of such materials that are of interest to Los Alamos National Laboratory (LANL) as well as to U.S. Department of Energy (DOE) and civil applications.

The extremes in the statistical variations of the material microstructures drive important phenomena such as inelastic behavior and failure. The inelastic behavior and failure of such materials has many obvious implications for many types of analysis (for example, safety analyses). The only hope for correctly capturing the effects of these extremes on the local and bulk material behavior is through the use of stochastic analyses.

A new stochastic, multiscale model has been developed for modeling the constitutive behavior of HEs as well as other types of heterogeneous materials [1]. The formulation utilizes localization relations of the form

$$\varepsilon'(a) = A'(a)\bar{\varepsilon} + \int_{b_-}^{b_+} d'(a,b)(\bar{\mu} + \mu'(b))P(b)db$$

where $\varepsilon'(a)$ is the fluctuating strain, $A'(a)$ is the mechanical concentration tensor that describes how the applied bulk (average) strain $\bar{\varepsilon}$ maps into localization effects, $d'(a,b)$ is the transformation concentration tensor that determines how the distribution of transformation strains (eigenstrains) $\mu(b)$ maps into the fluctuating strain field, a and b are both the set of independent variables that describe the configurational possibilities for the material microstructure, b_+ and b_- are the range of b, and $P(b)$ is the probability distribution function (PDF) for the configurational variable.

Using a hierarchical decomposition the concentration tensors in the different phases in the bulk material are separated into components associated with a phase average fluctuating response (PAFF) and the associated phase zero mean fluctuating response (PZMFF), i.e.

$$A' = \sum_r A'_r X_r = \sum_r (\hat{A}_r + A''_r) X_r =$$

$$\sum_r \left[c_r^{-1} \int_{a_-}^{a_+} A'(a) X_r(a) P(a) da + A''_r \right] X_r$$

where c_r is the volume fraction of the rth phase and $X_{r(a)}$ is the characteristic function which has a value of 1 in the rth phase and zero otherwise. For a two-phase material, the hierarchical decomposition allows the transformation field concentration tensor $d'(a,b)$ to be completely described in terms of the mechanical concentration tensor $A'(a)$. In this case the statistics required to correctly describe the material behavior are substantially reduced.

Currently the input for the theory is the PDFs for the concentration tensors. The distributions for the concentration tensors can be obtained using direct numerical simulations (DNS), various types of analytical micromechanical models (AMM), or any combination of these techniques. Ongoing collaborations with T-1 (DNS) and T-14 (DNS) at LANL as well as the University of South Carolina (AMM) are being pursued with regard to using different techniques to generate the PDFs for the concentration tensors. Sample distributions for a continuous fiber composite are given in Fig. 2.

Given the distributions for the concentration tensors the proposed theory can be used to predict the range of local and bulk responses of a material, as shown in Fig. 3.

For more information contact Todd Williams at oakhill@lanl.gov.

[1] T.O. Williams, "A General, Stochastic Transformation Field Theory," submitted to *J. Eng. Mech.* (2006) in press.

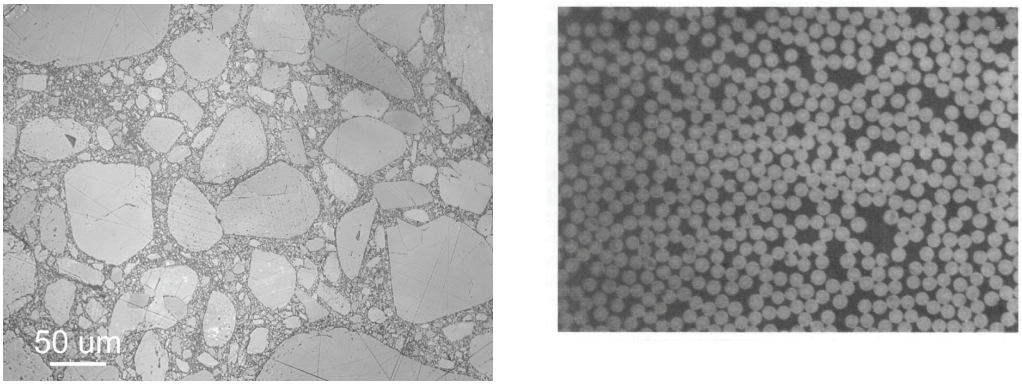

Fig. 1. *Micrographs of a high explosive (left) and a continuous fiber composite (right).*

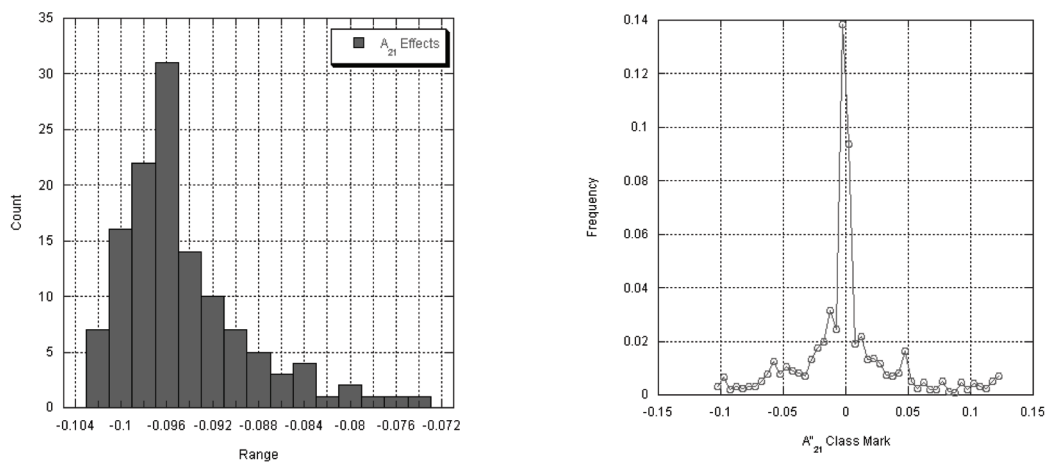

Fig. 2. *The phase average fluctuating response (PAFF) (left) and phase zero mean fluctuating response (PZMFF) (right) distributions for a continuous fiber composite.*

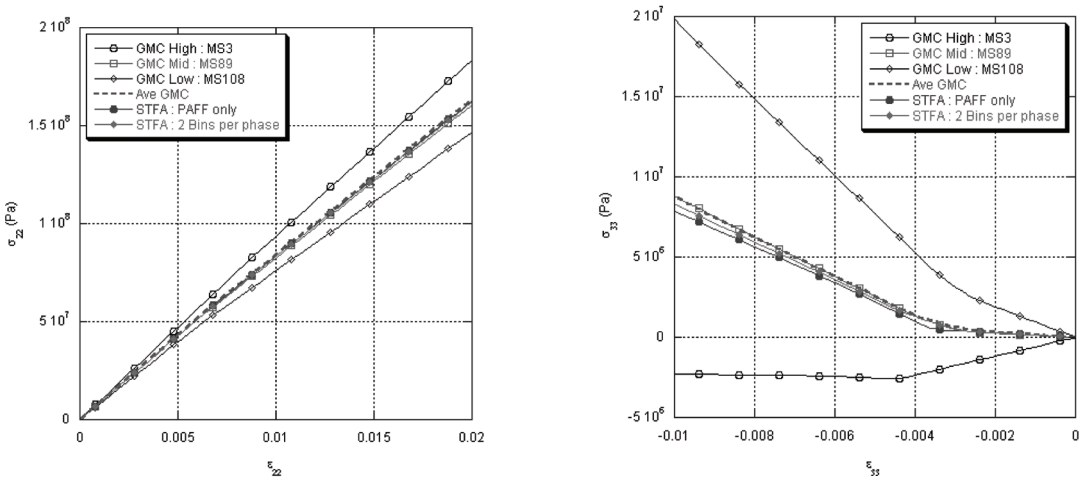

Fig. 3. *The predicted bulk response of a continuous fiber composite subjected to a tri-axial loading state.*

Properties of Metals at Extreme Loading Rates

Aleksander Zubelewicz, T-3

Traditional thermodynamics tells us that all systems exhibit a tendency to maximize entropy. So it is a struggle to understand why so many thermodynamically open systems are able to survive with their organizational and functional integrity intact. Progogine, who won the Nobel Prize in Chemistry in 1977, concluded that the secret to survivability is in an exchange of energy. A stable complex system receives low-entropy energy from the environment while giving away energy that is entropy rich. A sustained exchange of the energies is in fact the condition for survivability. Since these phenomena are rarely observed in solids, mean-field theories of nonlinear continuum dynamics often provide sufficient representation of the solid behavior. These theories describe the deformation and damage processes with the use of constitutive models. In addition, an equation of state (EOS) that couples high hydrostatic pressure with changes in mass density and temperature is formulated. Difficulties arise when a metal is subjected to extreme loading rates and becomes a thermodynamically open system characterized by an exchange of energy caused by dislocations traveling long distances with a nearly sonic velocity.

Our dynamic defect structure (DDS) model described in [1, 2] predicts that various metals (alloys) subjected to extreme loading rates experience a strong mesoscale excitation leading to an entrapment of kinetic energy. While a significant portion of the energy is converted into heat, the remaining part supports a rearrangement of the material's internal structure and causes fluctuations in the field of velocity, strains, and stresses. The DDS model explains the remarkable increase in the plastic hardening rate [3, 4] observed in copper, iron, and nickel at strain rates greater than 10^3 s^{-1}. Also, the model suggests that at these conditions a heterogeneous phase transformation and melting are possible. In our numerical simulations, we were able to reproduce conditions at which two copper plates shown in Fig. 1, when impacted with each other, experience a noticeable excitation.

Our objective is to identify a dilatational deformation in ductile metals, which may impede the formation of the DDS structures. The material's dilatancy is allowed to exist. However, instead of imposing a predetermined relation for void nucleation a different approach is pursued here. We assumed [5] that the rate of void nucleation together

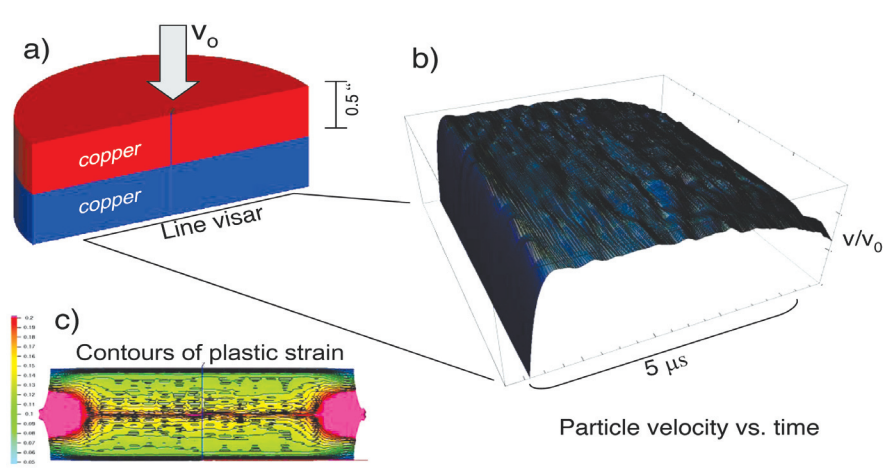

Fig. 1.
Dynamic behavior of a copper plate subjected to impact loading: a) Cu/Cu plate impact; b) particle velocity as a function of time; and c) contours of plastic strain.

with the rate of dissipation due to volumetric change and shear are nonnegative quantities at any point of the material. The missing constitutive equation for void nucleation is replaced by a criterion of minimum rate of energy dissipation. In this manner, the volumetric deformation brings the material as close to its thermodynamic equilibrium as possible. As shown in Fig. 2, three distinct mechanisms of void nucleation are possible near the ductile surroundings of the mode I crack tip. In this plot, values of the minimum energy triaxiality ratio X (vertical axis) are plotted as a function of the stress singularity factor λ (horizontal axis); where the stresses near the crack $\sigma_{ij} = R^{\lambda}\hat{\sigma}_{ij}(\theta)$ are defined in the polar coordinate system {R, θ} attached to the crack tip. The first mechanism (red line) describes the well-known Gurson's (stress triaxiality, σ_{kk}/σ_{eq}) criterion, where voids are uniformly distributed near the crack tip. At a more advanced stage of deformation (brown line) voids nucleate predominantly along a narrow process zone extending ahead of the crack. This mechanism is governed by the maximum tensile stress. There is also a third cavitation mechanism (blue line), in which voids are distributed along two branches at 50 degrees with respect to the crack direction.

Our findings are twofold: 1) Some metals, when subjected to extreme loading rates, exhibit the behavior that is characteristic of a thermodynamically open system. This phenomenon is linked to the high mobility of dislocations that travel long-distances and exchange energy and information between distant material points. 2) It is possible to bring the material close to its thermodynamics equilibrium at the length scale at which the mesoscale dynamic excitation occurs. The first analysis suggests that the void nucleation is such a mechanism. If voids do not nucleate, then the development of the orderly dislocation structures is the most favorable mechanism.

For more information contact Aleksander Zubelewicz at alek@lanl.gov.

[1] A. Zubelewicz, et al., *Phys. Rev. B* **71**, 104107 (1–5) (2005).
[2] A. Zubelewicz, *Mech. Mater.*, submitted (2005).
[3] J.R. Klepaczko, *Trends in Mechanics of Materials*, Ch. 6 (Institute of Fundamental Technological Research of Polish Academy of Science, Warsaw, Poland, 2001).
[4] P.S. Follansbee and U.F. Kocks, *Acta Metall.* **36**, 81 (1988).
[5] A. Zubelewicz, Int. *J. Solids Struct.* **42,** 2755 (2005).

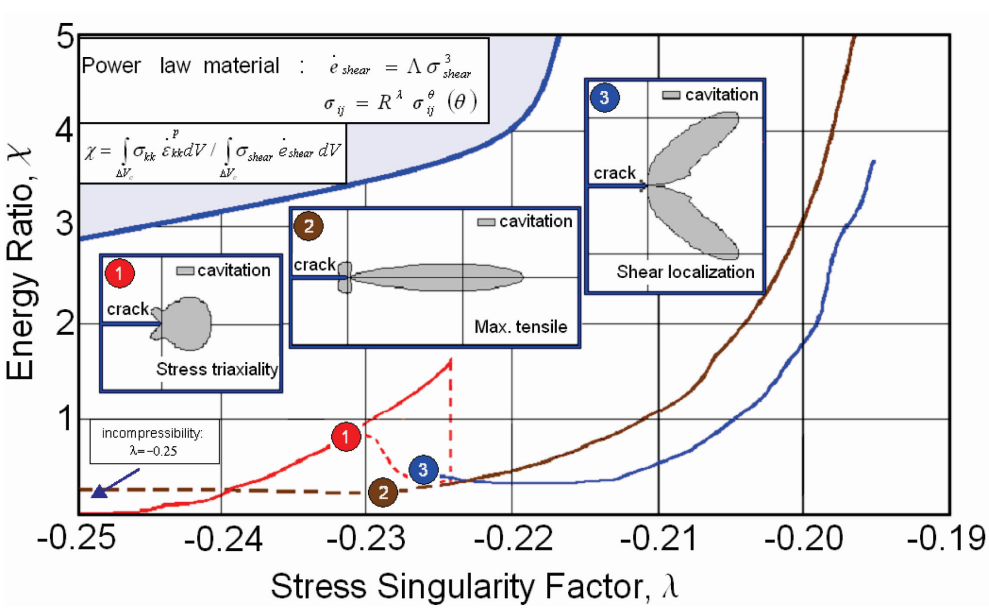

Fig. 2. ***Three mechanisms of void nucleation in ductile surroundings of mode I crack tip.***

A Two-Component Element for Modeling Strain Localization in Materials

Q. Ken Zuo and Paul J. Maudlin, T-3

Many ductile materials are prone to strain localization (shear banding), particularly when they are under high-rate, dynamic loading conditions (such as impact and explosive-loading). Strain localization refers to the formation of highly localized deformation in the form of narrow planar bands of large plastic strains from an initially smooth deformation field. Although these planar bands of localized deformation are often called shear bands, the mode of deformation (i.e., the strain tensor) inside the bands can have both normal and shear components. A tensile normal strain can cause void growth and even form open cracks inside the band. The cause for strain localization is material instability, which can be caused by a variety of physical mechanisms: thermal softening, damage due to nucleation and growth of microcracks and voids, sudden strain-rate drop in the material after a shock passage, effects of texture in anisotropic materials, nonassociative flow behavior, or changes in microstructures such as phase transition due to shock loading. In a recent study of uranium alloyed with 6% niobium (U6), we have found that the alloy can become plastically unstable at modest strain levels in the post-shocked condition [1]. The post-shock condition refers to the material properties after processing by a large amplitude shock wave.

Once a localization band forms in a smooth, uniformly deforming specimen, the deformation field becomes highly nonuniform, with the materials inside the band accounting for almost all the specimen deformation while the bulk material outside the band experiences little further straining (often the outside material unloads elastically to accommodate softening inside the band). One important consequence of this highly nonuniform deformation is that the material inside the bands can have a plastic strain very close to its ductility (the value of plastic strain where failure occurs) while the overall deformation is still fairly modest. Clearly, it is important to understand and properly model shear bands in order to properly model failure of such materials.

Computational modeling of strain localization has previously used the approach of direct numerical simulation, where refined meshes are used to resolve the band features. While it is within the reach of today's computational power to conduct such direct simulations for simple, laboratory-scale structures, it is impractical for a designer to perform routine simulations with such high resolution to address the much more complex three-dimensional (3-D) weapon system. To resolve the band structure would require a mesh size less than the thickness of the bands that are initially of the order of 100s of microns. Constraint of reasonable aspect ratios of computational elements would require millions of elements for even a simple geometry. In an explicit analysis code, tiny elements also require very small time steps due to the stability requirement. The objectives of the current work are to develop a computational model to incorporate localization bands within an element, and to implement the model in a finite-element analysis (FEA) code. The main advantage will be that larger elements (orders of magnitude larger than the shear band thickness), longer time steps, and subsequently less computational time can be used to render a more accurate engineering analysis.

Figure 1 shows schematically the new element containing a thin planar band of localized deformation (shear band). The band centers at the centroid of the element and extends across the element. For an imposed strain there are two sets of strains in the element: that inside the shear band, and the "matrix" strain.

To determine these strains, three conditions are used: 1) the difference in the strain rates inside and outside satisfies the Maxwell compatibility condition, 2) the sum of deformations in the band and matrix matches with the imposed element deformation, and 3) the traction vector is continuous across the band.

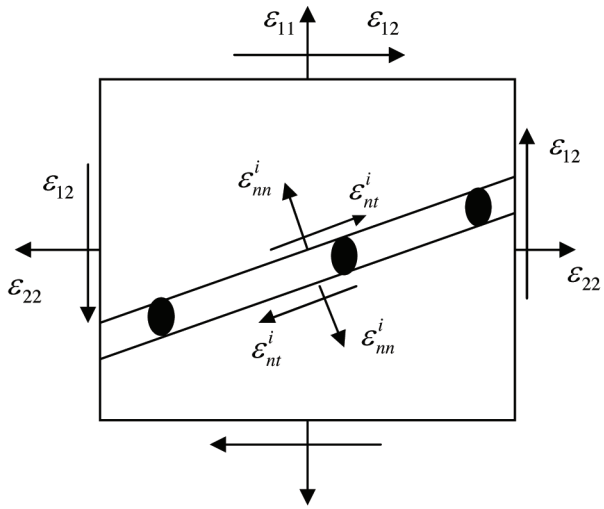

Fig. 1.
The figure shows schematically the new element containing a thin planar band of localized deformation (shear band). The band centers at the centroid of the element and extends across the element.

The new element has been implemented into EPIC, a 3-D, explicit, FEA code for large strain, high strain rate dynamic applications. Figure 2 is a snapshot of the strain distribution in a thin U6 plate under tension. (The strain shown is the normal component along the direction of loading.) The plate is 1 inch square with a thickness of 1/12 inch and is pulled at the top and bottom edges. The material properties used in the calculation simulate U6 under post-shocked condition. Figure 2 shows that, at the background strain of about 0.25, the deformation has localized into two thin bands and one of which (starting from the lower left corner) dominates where the strain reaches 0.4. This numerical result is consistent with our earlier study of a U6 hemi loaded with explosives [1], in which we demonstrated that processing of a large-amplitude shock can have a significant effect on material instability and strain localization.

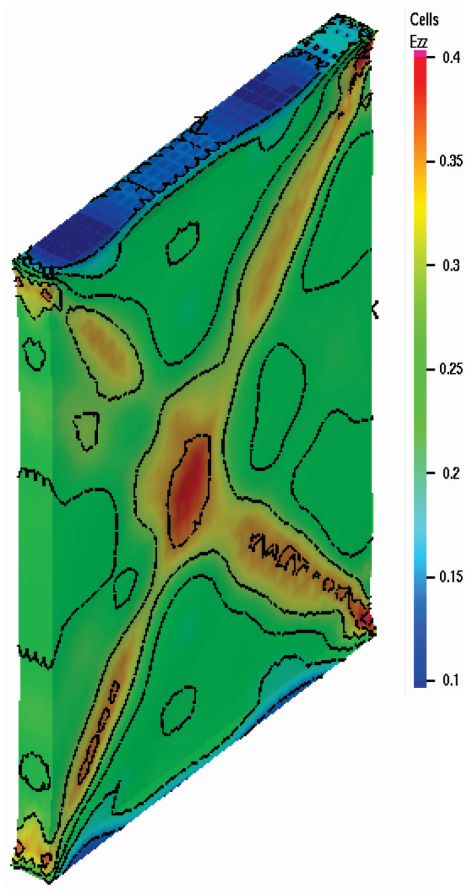

Fig. 2.
A snapshot of the strain distribution in a thin U6 plate under tension. (The strain shown is the normal component along the direction of loading.)

For more information contact Ken Zuo at zuo@lanl.gov.

[1] G.T. Gray, et al., "Predictive Capability for Deformation and Damage in Metals: The Synergy Between Experiments and Modeling," *Los Alamos Science* **29**, 80–93 (2005); also *ASM Int. J. Failure Analysis and Prevention* **5**, 7–17.

A Rate-Dependent Damage Model for Brittle Materials under Dynamic Loading

Q. Ken Zuo and Francis L. Addessio, T-3; and John K. Dienes, T-14

We have recently developed a rate-dependent continuum damage model (Dominant Crack Algorithm, or, DCA) for brittle materials under dynamic loading [1]. The model is derived from the responses of an ensemble of penny-shaped microcracks which are assumed to be randomly distributed within a statistically homogenous volume of a brittle material. It is assumed in the current model that the distribution of microcracks remains isotropic during loading. The main features of the model are: a) the damage tensor is derived from opening and shear of an ensemble of penny-shaped cracks with various orientations and sizes; b) the evolution of damage (through crack growth) is based on the energy-release rate for the dominant crack (having the most unstable orientation); and c) the damage surface, outside which material accumulates additional damage, is found by applying the generalized Griffith instability criterion to the dominant crack. The use of the energy-release rate for damage evolution provides a physical means to introduce rate effects in our damage model. See [1] for details of the model.

To illustrate the features of the model, several standard load paths (isotropic, uniaxial strain, uniaxial stress, and pure-shear) have been simulated with the stand-alone driver program, which provides the model with a strain history. Figure 1 shows: a) the stress response, and b) the evolution of the average crack radius (damage), to an isotropic ($\varepsilon = \varepsilon_{11}\mathbf{i}$, $\sigma = -P\mathbf{i}$), cyclic loading, with a strain rate $\dot{\varepsilon}_{11} = 10^5/\mathrm{s}$. The model material is a SiC ceramic [1]. The material is initially stress-free (point **A**) and is first loaded up to a tensile strain of 0.01 (**C**), then unloaded back to zero strain (**A**) and reverse loaded (compression) to a strain of $\dot{\varepsilon}_{11} = -0.0005$ (**D**), and finally reloaded to a tensile strain of 0.0195 (**E**). The initial loading path (**A-A′-B-C**) begins with an elastic response **A-A′**, with the slightly damaged modulus corresponding to the initial crack size $\bar{c}_0 = 14\mu m$. When the stress reaches the initial damage surface (**A′**), initiating crack growth, this causes the damage surface to contract with further straining. Though the size of the damage surface starts to decrease immediately due to crack growth, the stress level in the material still increases with strain until a peak value (**B**) is reached. This is because the rate of damage accumulation, which is proportional to the square of the crack size, is small when the crack size is small, and the inelastic strain rate due to the crack growth is too small to influence the total strain rate significantly. Consequently, the response remains "strain-hardening" (**A′-B**). Because $\dot{\varepsilon}_c^{gr}$ (the inelastic strain rate due to crack growth) increases with crack size and distance from the stress state to the damage surface, for a given total strain rate $\dot{\varepsilon}$, the inelastic strain rate $\dot{\varepsilon}_c^{gr}$ eventually approaches the total strain rate and the material response changes from hardening to softening (**B-C**).

The unloading path (**C-C′-A**) begins at **C** and, because the stress state is outside the damage surface, crack growth continues until the stress unloads enough to reach the surface (point **C′**). From **C′**, the material unloads elastically (with the damaged modulus) back to the origin (**A**), where both the matrix strain and crack strain are zero, and all the cracks are completely closed. The segment **A-D** corresponds to reverse loading (hydrostatic compression) of the damaged material with the crack size attained at **C′**($\bar{c}_1 = \bar{c}' \approx 10\bar{c}_0$). Because the cracks remain closed under compression, damage accumulated in the material is deactivated (cracks of size $\bar{c}_1$ are still present). Consequently, the material assumes the original (undamaged)

stiffness. The reloading path (**D-A-C′-E**) starts from **D** and continues elastically with the undamaged stiffness back to the origin (**A**). On further loading, the cracks (with the increased size c_1) open under tension and the damage, which has been accumulated at **C′**, becomes active again. Consequently, the reloading path follows the segment **A-C′**. The path intersects the damage surface at point **C′**, and the crack size again increases along the path (**C′-E**). The stress state is outside the damage surface due to rate effects.

It is shown in Fig. 1(b) that the cracks are initially stable when the stress level is low (**A-A′**), become unstable at **A′**, and grow rapidly at first due to the high values of energy release rate, then slowly as the stress level drops. On unloading, the cracks continue to grow slightly (**C-C′**), and then arrest and remain stable (the stress state is inside the damage surface). During reloading, the cracks remain stable (**D-C′**) until the stress reaches the damage surface again at point **C′**. During the rest of the reloading path (**C′- E′**), cracks continue to grow.

For more information contact Ken Zuo at zuo@lanl.gov.

[1] Q.H. Zuo, et al., "A Rate-Dependent Damage Model for Brittle Materials Based on the Dominant Crack," *Int. J. Solids Struct.*, in press, pp. **1–31** (2005) (available online at the journal's website.)

Fig. 1. ***The predicted response under isotropic, cyclic loading: a) The pressure-strain response; and b) Evolution of the crack size as a function of the strain.***

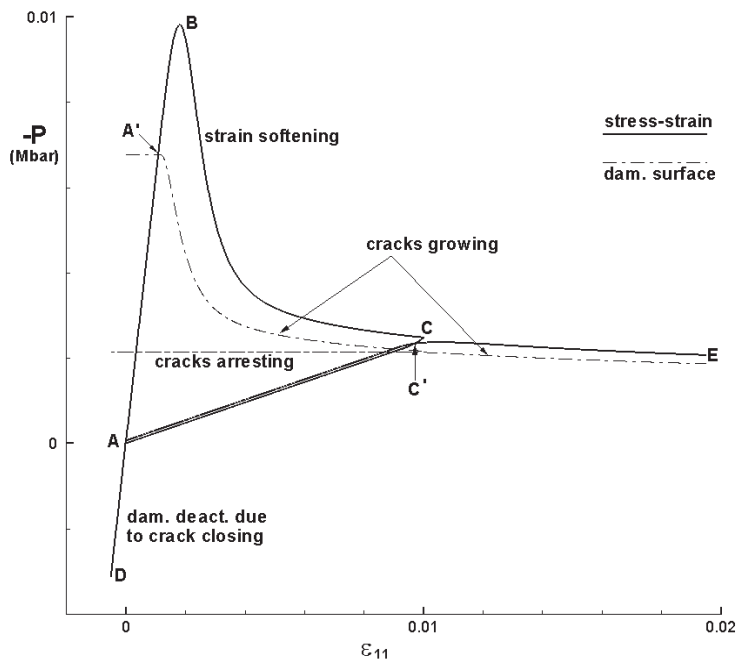

Fig. 1(a)

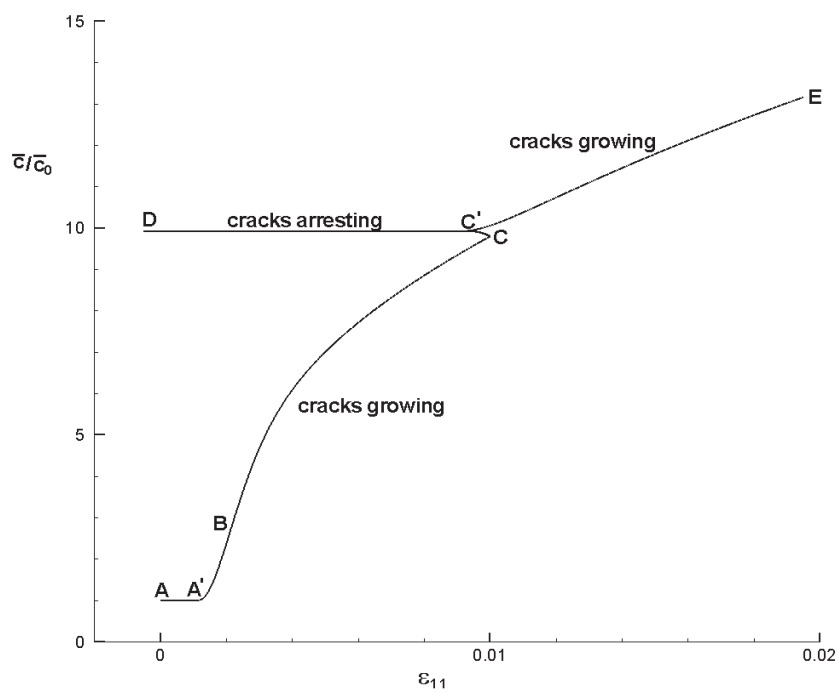

Fig. 1(b)

An Implicit Algorithm for a Rate-Dependent Brittle Damage Model

Q. Ken Zuo, T-3

In another paper in this volume [1], we presented a rate-dependent continuum damage model for brittle materials under dynamic loading. In this paper, we will discuss the numerical algorithm for the model. In an analysis code, the total strain rate $\dot{\varepsilon}$ is obtained from the momentum equation and one needs to find the stress rate $\dot{\sigma}$. For the current model, the evolution equations for the stress and average crack size (damage) can be written as [1]

$$\dot{\sigma} = \left(\mathbf{C}_m + \mathbf{D}(\bar{c})\right)^{-1}\left(\dot{\varepsilon} - 3\left(\dot{\bar{c}}/\bar{c}\right)\mathbf{D}(\bar{c})\sigma\right), \quad (1a)$$

$$\dot{\bar{c}} = \dot{c}_{\max}\left(1 - \frac{1}{1+\left\langle F(\sigma,\bar{c})\right\rangle}\right), \quad (1b)$$

where $\mathbf{C}_m$ is the compliance (4th-order tensor) of the matrix (undamaged) material, $\mathbf{D}(\bar{c})$ is the damage tensor given below; $\bar{c} = \bar{c}(t)$ is the average crack radius, which evolves with the time. The terminal speed $\dot{c}_{max}$ for crack growth is either the shear wave speed of the matrix for closed cracks, or the Rayleigh wave speed for open cracks. The angled bracket in Eq. (1b) is the Macaulay bracket, which takes the value of the argument when positive and is zero otherwise. Crack growth ($\dot{\bar{c}} > 0$) occurs when the stress state is outside the damage surface (i.e., $F(\sigma,c) > 0$). The expression of the damage surface is given in [1].

For an isotropic, linear elastic matrix material, the compliance tensor is $\mathbf{C}_m = 1/(3K)\mathbf{P}^{sp} + 1/(2G)\mathbf{P}^d$, where K and G are the bulk and shear moduli; $\mathbf{P}^{sp}$ and $\mathbf{P}^d$ denote the spherical and deviatoric projection operators, respectively [1]. The damage tensor is related to the average crack radius ($\bar{c}$) by $\mathbf{D}(\bar{c}) = \beta^e N_0 \bar{c}^3 \mathbf{P}(\sigma)$ where $\beta^e = 64\pi(1-\nu)/(15G)$ is a material constant depending on the elastic properties of the undamaged material (ν is the Poisson's ratio); N_0 is the crack number density (number of cracks per unit material volume) and $N_0\bar{c}^3$ is a scalar measure of damage. $\mathbf{P}(\sigma)$ is a 4th-order, dimensionless tensor determined by the signs and directions of the principal stresses [2]. The damage is isotropic when the principal stresses are all tensile or all compressive. When the principal stresses have mixed signs, however, the current model predicts anisotropic damage with the directions of tensile principal stresses accumulating more damage than other directions.

Consider a time step $\Delta t = t^{n+1} - t^n$ with the total strain increment given by $\Delta\varepsilon = \dot{\varepsilon}\Delta t$. Suppose the stress and crack size (radius) at the beginning of the time step are given by $(\sigma^n, \bar{c}^n)$. An implicit algorithm will be used for updating the material state $(\sigma^{n+1}, \bar{c}^{n+1})$. An implicit integration algorithm offers the advantage of placing no additional stability constraint on the size of the time step, which could be an issue for the explicit algorithm (as we will see in Fig. 1). The final crack size $\bar{c}^{n+1}$ is solved with the following procedure. First, define the trial state by assuming the step is elastic, i.e., there is no crack growth during the step,
$c^{tr} = c^n : \sigma^{tr} = \sigma^n + (\mathbf{C}_m + \mathbf{D}(c^n))^{-1}\Delta\varepsilon$.
If both the stress state at the beginning of the time step and the trial stress state are inside or on the damage surface, i.e., $F(\sigma^n, \bar{c}^n) \le 0$ and $F(\sigma^{tr}, \bar{c}^n) \le 0$, then the step is indeed purely elastic. In this case, the trial state is the final solution, $\bar{c}^{n+1} = \bar{c}^{tr}$, $\sigma^{n+1} = \sigma^{tr}$. Otherwise, the step involves crack growth and a correction to the trial state is needed. Suppose $F(\sigma^{tr}, \bar{c}^n) > 0$, that is, the trial state is outside the damage surface. Applying the backward Euler integration scheme to that evolution equation gives the final stress as

$$\sigma^{n+1}(\bar{c}^{n+1}) = \left(\mathbf{I} + 3\left(1 - \frac{\bar{c}^n}{\bar{c}^{n+1}}\right)\left(\mathbf{C}_m + \mathbf{D}\right)^{-1}\mathbf{D}\right)^{-1} \left(\sigma^n + \left(\mathbf{C}_m + \mathbf{D}\right)^{-1}\Delta\varepsilon\right), \quad (2)$$

where the relationship $\dot{\bar{c}}\Delta t = \bar{c}^{n+1} - \bar{c}^n > 0$ has been used, and the dependency of $\mathbf{D}(c^{n+1})$ on c^{n+1} has been dropped for compactness. With the material state

at the beginning of the step (σ^n,c^n) and the strain increment ($\Delta\varepsilon$) given and fixed, the final stress σ^{n+1} is a function of the final crack size $\bar{c}^{n+1}$ only. Applying the central difference scheme (the trapezoidal rule) to the evolution equations for the crack size [Eq. (1b)] yields

$$\frac{\bar{c}^{n+1}-\bar{c}^{n}}{\dot{c}_{\max}\Delta t}-\left(1-\frac{1}{1+\frac{1}{2}\left(F(\sigma^{n+1},\bar{c}^{n+1})+\left\langle F(\sigma^{n},\bar{c}^{n})\right\rangle\right)}\right)=0. \quad (3)$$

With σ^{n+1} given by Eq. (2) as a function of $\bar{c}^{n+1}$ only, Eq. (3) is a nonlinear equation for $\bar{c}^{n+1}$, which can be solved by an iterative method, using the trail state (σ^{tr},$\bar{c}^{n}$) as the starting state for the iteration.

Figure 1 compares the model predictions using the implicit and explicit algorithms with four different time steps (from 0.01ns to 10 ns). The loading is uniaxial strain with a strain rate of $\varepsilon_{11} = 10^5/s$, and the model material is silicon carbide ceramic [1]. As the time step is reduced, both the implicit and explicit algorithms converge to the same result (the curve in the middle with $\Delta t \leq 0.1$ns). It is also shown that the implicit algorithm gives a more accurate result for large time steps. For Δt =10 ns (corresponding to a strain increment of $\Delta\varepsilon_{11} = 10^{-3}$), the explicit algorithm produces severe oscillations.

For more information contact Ken Zuo at zuo@lanl.gov.

[1] Q. Ken Zuo, et al., "A Rate-Dependent Damage Model for Brittle Materials under Dynamic Loading," in this volume on p. 53.
[2] Q.H. Zuo, et al., "A Rate-Dependent Damage Model for Brittle Materials Based on the Dominant Crack," *Int. J. Solids Struct.*, in press, pp. 1–31 (2005) (available online at the journal's website.)

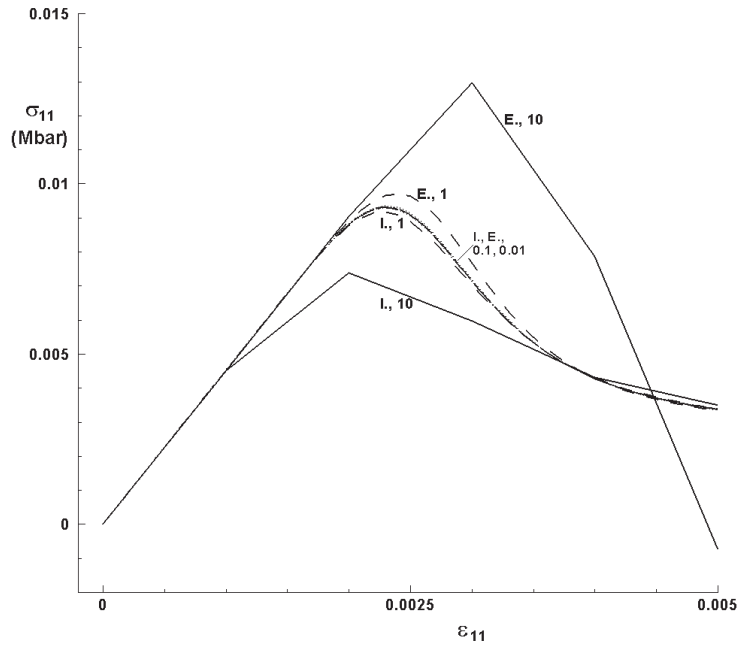

Fig. 1. ***Comparison of the predicted stress-strain responses using implicit (I.) and explicit (E.) algorithms with four time-step sizes: 10 ns, 1 ns, 0.1 ns, and 0.01 ns.***

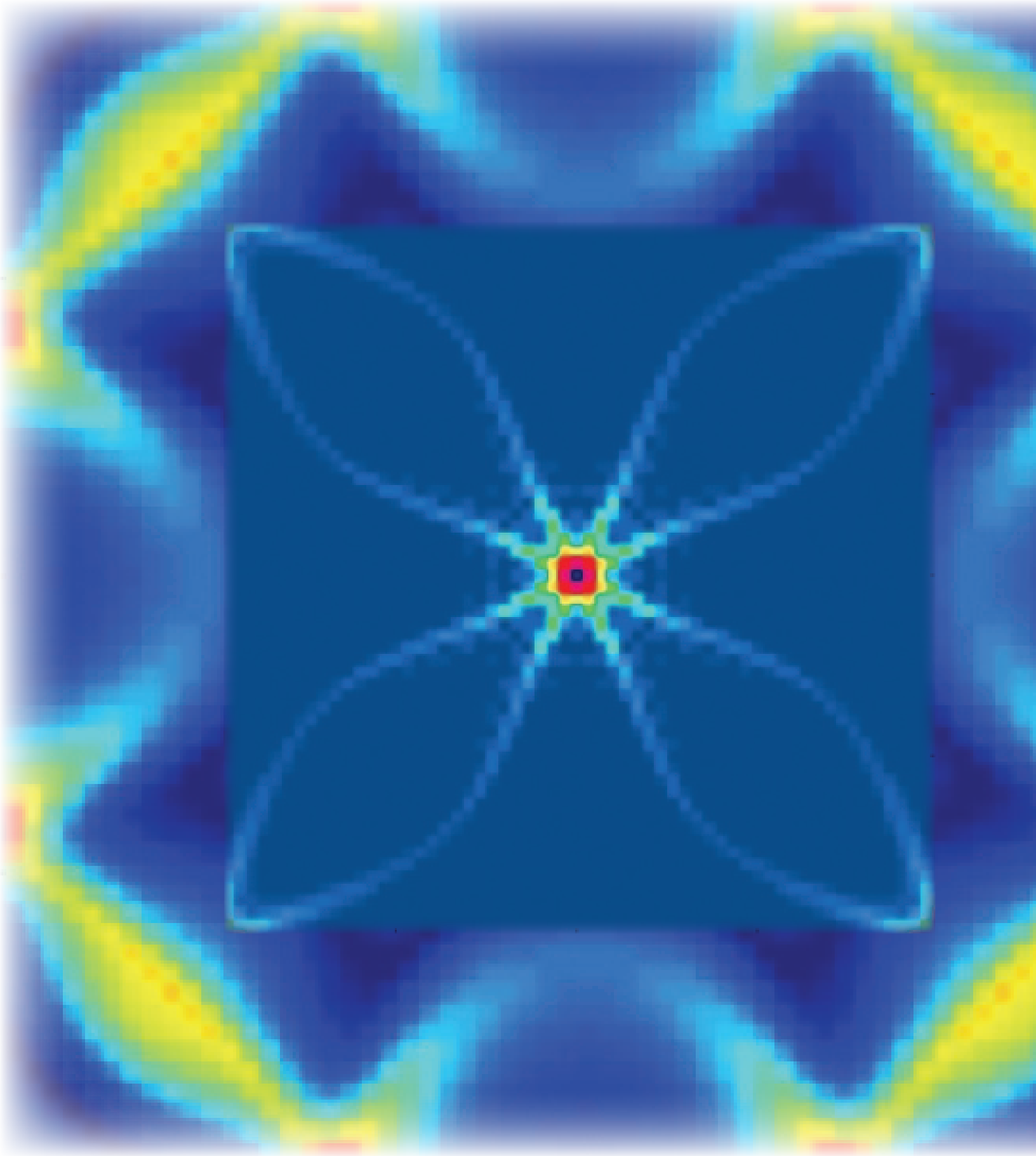

T-11

Condensed Matter and Statistical Physics

Group Leader: Bob Albers
505.665.0417, rca@lanl.gov

T-11 Condensed Matter and Statistical Physics is active in many aspects of condensed matter theory including electronic and structural properties of metals, semiconductors, compounds and alloys, polymers, microscopic modeling of materials properties and textures, fundamental studies of nonlinear and nonequilibrium systems, and investigations of the properties of heavy fermions, high-temperature superconductors, organic charge-transfer salts, and other strongly correlated electronic systems. Ongoing work involves the development of advanced algorithms for scientific computing, e.g., quantum Monte Carlo, molecular and Langevin dynamics involving multiple time and length scales, and the development of visualization tools for large data sets.

Fourier Transform Inelastic Electron Tunneling Spectroscopy and STM

Alexander V. Balatsky and Jian-Xin Zhu, T-11

Recent advances in scanning probes, such as Scanning Tunneling Spectroscopy (STM) have made it possible to investigate the properties of correlated electron systems at extreme spatial resolution. One of the spectroscopies that is used to investigate electronic properties is Inelastic Tunneling Spectroscopy (IETS), which allows us to measure the characteristic energies of local and extended modes that scatter electrons in a sample.

It is known that the inelastic scattering processes produce a feature in tunneling characteristics, dI/dV. These features point to the characteristic excitation energies that are involved in inelastic scattering. Thus, by observing these features in IETS one can perform spectroscopy of the degrees of freedom that are responsible for inelastic scattering of the electrons.

By combining IETS with STM one can investigate the properties of the inelastic scattering at extreme spatial resolution. The IETS scanning tunneling microscopy (IETS-STM) for example, allows us to measure the local vibrational modes of atoms or molecules on a surface.

We propose to extend the use of Fourier Transform STM to address the inelastic processes and detect characteristic energy and momenta of the scattering modes that would produce IETS features. We call the proposed technique Inelastic Electron Tunneling Spectroscopy Fourier Transform STM (IETS FT STM).

First, we outline the conventional FT STM approach, where one deals with static elastic scattering. Consider, for example, simple metal. Any defect on the metal surface is known to produce standing electronic waves. These waves are called Friedel oscillations and are well known in the literature. Encoded in these oscillations is information about the Fermi wave vector of electrons kF. Fourier transform of the standing wave would produce, in a simplest case, a circle in the k-space with the radius 2kF. Straight Fourier transform would reveal the Fermi surface momentum of a metal, as shown in Fig.1.

The standing wave seen in these experiments is a result of elastic scattering, with no energy transferred between defects and incidental electrons. One can ask a question on how the "Friedel oscillations" will look when the scattering will be inelastic.

We took the next step and combined the IETS with FT STM. The proposal is to start with measuring the inelastic tunneling features at each point of a pixelized field of view seen in STM. Central quantity for this would be d2I/dV2 measured in the IETS experiment, at each point r. Then one performs the Fourier transform on r. The resulting quantity is d2I/dV2 as a function of k and energy. This quantity has encoded in it the energy and momentum information of the inelastic scatterers. We suggest that we might extract those from FT d2I/dV2, as seen in Fig. 2

Without going into technical details, we have done some model calculations that show the feasibility of this approach. The ultimate validation of this approach would only be possible using real experimental data. We are collaborating with the STM group at Cornell University to apply FT IETS STM approach to the high temperature superconductors.

For more information contact Alexander Balatsky at avb@lanl.gov.

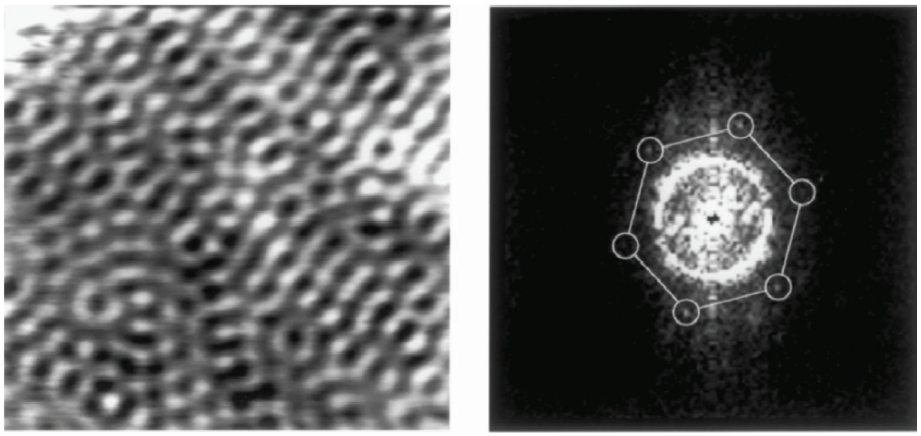

Fig. 1.
Example of FT-STM: a) Be (001) surface, as seen by STM, with the standing waves (Friedel oscillations) produced by defects, b) Fourier transform of (a) reveals a cut through the Fermi surface corresponding to the surface states.

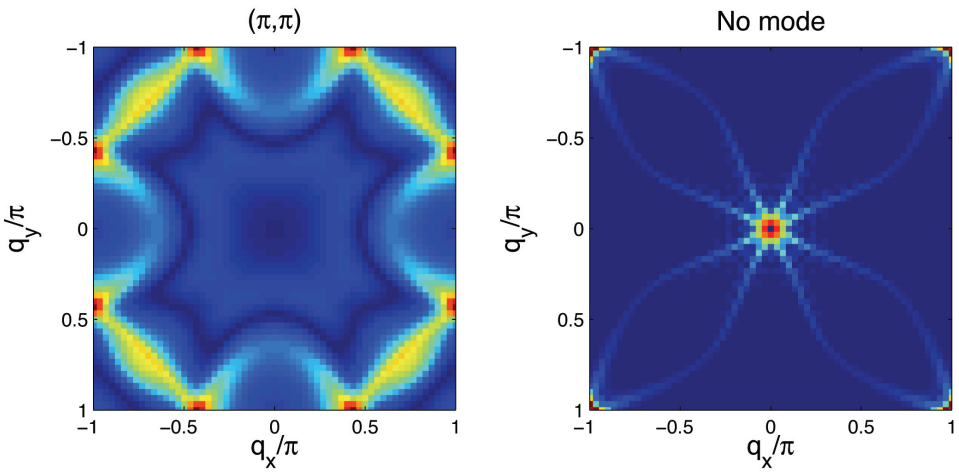

Fig. 2.
The Fourier spectral weight of the energy derivative of the LDOS at E taken at the superconducting gap plus the energy of the mode for a d-wave superconductor with the electronic coupling to the spin resonance modes. For comparison, the quantity is also shown for the case of no mode coupling (g = 0).

Oscillating Elastic Defects: Competition and Frustration

Julien Barré, University of Nice, France; Alan R. Bishop, T-DO; and Turab Lookman and Avadh Saxena, T-11

In his seminal 1957 paper, Eshelby derived the strain fields created by an inhomogeneous ellipsoidal inclusion in an isotropic elastic medium. This result is a cornerstone of the theory of inhomogeneous elastic media, now routinely used in the physical and engineering sciences. The result is a statement of how a distortion is accommodated in the host material and implies that a local perturbation induces long-range strain fields, slowly decaying as $1/r^d$ in d dimensions ($d \geq 2$). Eshelby's work considers static inhomogeneities or strain "defects" only. However, for many applications in physics and materials science, we are interested in the cooperative behavior of inhomogeneities in which the strain is varying or oscillating in time with a given frequency. We find that this situation is, as a function of the defect density and oscillation frequency, inherently frustrated, resulting in self-organization of the patterns, competing ground states, and sensitivity to internal and external perturbations. Such "dynamic" defects arise as small polarons in directionally-bonded transition metal oxides, including high-temperature superconductors, colossal magnetoresistance materials and ferroelectrics. The collective behavior of these polarons in a crystal undergoing distortions, with their coupling to charge, spin or polarization, is believed to determine the overall macroscopic response. Our work also has ramifications for the nondestructive evaluation of elastic media. Methods in this field are typically based on the vibrational response from a defect-free crystal. Here we characterize the behavior of oscillating defects (external oscillatory fields inducing specific defect patterns and responses) extending the conventional analysis to describe the response of elastic media in the presence of such defects [1].

The dynamical generalization of the Eshelby problem has been previously investigated in the context of engineering sciences for spherical inclusions, and very recently for inclusions of various shapes. However, such studies have focused on evaluating displacement fields as solutions to numerical boundary value problems. Our objective here is to understand the effect of dynamics on the nature of the elastic interaction itself and its influence on the collective behavior of assemblies of defects, using our recently developed elasticity formalism, which allows for tractable analytic calculations. We consider the dynamical Eshelby problem for localized oscillating defects in two dimensions for simplicity, and show that, although the strain fields still decay as $1/r^2$ far from the defect, the frequency fundamentally affects the nature of deformation. As expected, the higher the frequency, the more localized is the deformation. This renders the interaction between two defects strongly frequency (and direction) dependent, but the very nature of the interaction changes from "ferromagnetic" to "antiferromagnetic" like behavior as a function of separation and frequency. We subsequently generalize our results to a finite density of defects. This allows us to demonstrate the implications for frequency-driven patterning transitions and phase locking in assemblies of defects by mapping the elastic interaction energy between defects into XY spin-like models with competing interactions.

We use a strain only representation. The state of strain is defined by three fields e_i related to the displacements along the x-axis (u) and the y-axis (v) as follows: $e_1 = (u_x + v_y)/\sqrt{2}$, $e_2 = (u_y + v_x)/\sqrt{2}$, $e_3 = (u_x - v_y)/\sqrt{2}$ (the subscripts x and y indicate differentiation). We write an elastic energy which also includes strain gradient terms and the elastic compatibility constraint through a Lagrange multiplier. We assume for specificity that the oscillation is in e_3. We consider three different cases: one defect, two defects, and an assembly of oscillating defects with oscillation frequency ω_0 and phase ϕ_i. We use periodic boundary conditions in space and study overdamped as well as underdamped dynamics. In general, the larger ω_0, the more localized is the deformation created by the defect. This observation is of primary importance for the interactions between defects.

The main results are illustrated in Figs. 1 and 2, showing strain profiles for different ω_0. A comment on the underdamped case is in order: an underdamped dynamics would not remove the discontinuity at the wave vector $\bar{k} = 0$ created by the compatibility equation;

thus, the $1/r^2$ decay is also valid in this case. The qualitative effect of increasing ω_0 would not be modified either, although there would be some quantitative differences from the overdamped case. Figure 1 depicts the profile of the strain field e_3 for frequencies $\omega_0 = 1$ (diamonds), 10 (circles), and 100 (dots). The smaller ω_0, the wider the profile. The inset shows the surface plot of e_3: notice the anisotropy of the field. Figure 2 shows the Log-Log plot of the strain field e_3 along the diagonal for $\omega_0 = 1$, 10, and 100. We have also added $1/r^2$ fits as guides to the eye.

We have focused here on defects created by a locally oscillating e_3 strain; the solutions for locally oscillating e_1, e_2 strains, or combinations of the three strain components, can also be obtained, and are qualitatively similar. There is one exception to this statement: the solutions corresponding to area strain (e_1) are continuous around $\vec{k} = 0$ and even infinitely differentiable. Their tail in real space is thus *exponential* instead of *power law*. This implies that the e_1 strain field created by a local e_1 defect in an isotropic elastic medium decays exponentially away from the defect with rate $\rho(\omega_0)$; if the defect is oscillating, the exponential decay rate ω_0 grows with ω_0 as $\omega_0^{1/2}$. To our knowledge, this particular case has not been emphasized in the literature; it would be interesting to realize its experimental signatures.

We do not depict the results for two oscillating defects here. However, we note that for this case we find a more dramatic effect: varying the frequency, or the distance, can result in a qualitative change in the interaction, from "ferromagnetic" (phase-locking) to "antiferromagnetic" (anti-phase-locking). For N defects Fig. 3 shows the numerically determined boundary between "antiferromagnetic" ground states (when nearest neighbor interactions dominate) and more complicated ones, as expected from the two-defect calculations. The boundary between ferromagnetic and antiferromagnetic nearest neighbor interactions is also sketched. We have performed our calculations here for special arrangements of defects, but these results demonstrate the existence of collective behavior, controlled by the frequency or interparticle distance. The next natural step is to study phase-locking among defects by adding specific phase dynamics controlling the relaxation pathways. Finally, due to competing ground states we also expect multiscale "glassy" dynamics of oscillating defects.

For more information contact Avadh Saxena at avadh@lanl.gov.

[1] J. Barré, et al., "Oscillating Elastic Defects," Los Alamos National Laboratory report LA-UR-05-4078 (May 2005); cond-mat/0508761.

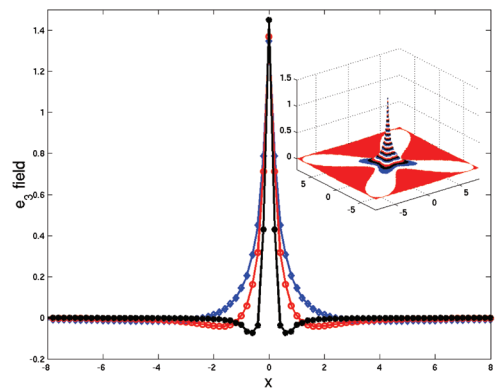

Fig. 1. *The profile of the strain field e_3 for frequencies $\omega_0 = 1$ (diamonds), 10 (circles), and 100 (dots). The smaller ω_0, the wider the profile. The inset shows the surface plot of e_3: notice the anisotropy of the field.*

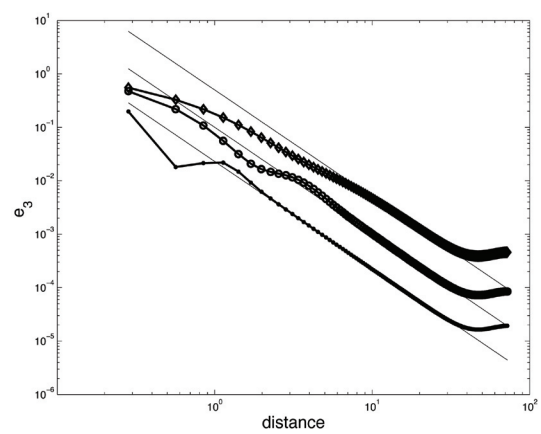

Fig. 2. *The Log-Log plot of the strain field e_3 along the diagonal for $\omega_0 = 1$, 10, and 100. We have also added $1/r^2$ fits as guides to the eye.*

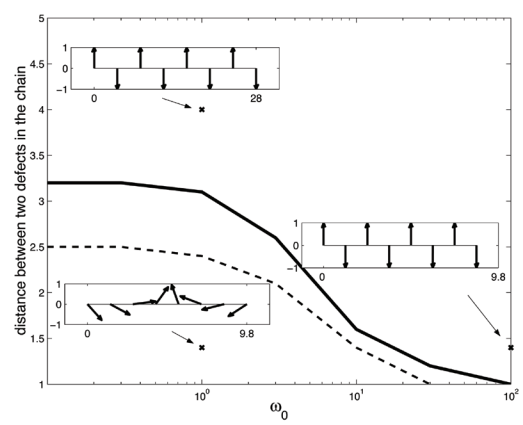

Fig. 3. *The numerically determined boundary between "antiferromagnetic" ground states (when nearest neighbor interactions dominate) and more complicated ones, as expected from the two-defect calculations. The boundary between ferromagnetic and antiferromagnetic nearest neighbor interactions is also sketched.*

Coexistence of Ferroelectricity and Ferromagnetism

Cristian D. Batista and James E. Gubernatis, T-11; and Wei-Guo Yin, Brookhaven National Laboratory

The interplay between order parameters of different natures opens the door for designing new multifunctional devices whose properties can be manipulated with more than one physical field. For instance, the spin and orbital electronic degrees of freedom can order individually or simultaneously in a crystalline environment, producing abundant phases. In particular, orbital ordering can produce different symmetry-breaking states like orbital magnetism, ferroelectricity (FE), quadrupolar electric or magnetic ordering, and other multipolar orderings. The magnetoelectric multiferroics, such as $R(Fe,Mn)O_3$ and RMn_2O_5, are real examples of the multifunctional materials that combine distinct useful properties within a single system. Recent experimental studies on these multiferroic materials have revived interest in the magnetoelectric effect, i.e., the induction of polarization with an applied magnetic field and magnetization with an applied electric field. To date, materials that exhibit both ferromagnetism (FM) and FE are rare because the transition metal ion of typical perovskite ferroelectrics is in a nonmagnetic d_0 electronic configuration. Therefore, it is essential to explore alternative routes to the coexistence of the FM and FE.

Different mechanisms for FE involving electronic degrees of freedom have been proposed. There are those in which FE results from bond ordered states induced either by electron-phonon coupling (Peierls instability) or by pure electron-electron Coulomb interactions. In these cases, the ferroelectric state is clearly nonmagnetic due to the singlet nature of the covalent bonds. In contrast, considering a system of interacting *spinless* fermions with two atomic orbitals of *opposite* inversion symmetry (say the *d* and *f* orbitals), Portengen, et al. [1] predicted that permanent electric dipoles are induced by spontaneous *d-f* hybridization when particle-hole pairs (excitons) undergo a Bose-Einstein condensation. This result was confirmed in the strong coupling limit of an extended Falicov-Kimball spinless fermion model where both bands are dispersive [2]. It was also confirmed numerically in the intermediate coupling regime by using a constrained path Monte Carlo approach [3].

The critical question that naturally emerges is, "How do FE and magnetism interplay when real electrons, instead of spinless fermions, are considered?" We answered this question by proving that the mechanism proposed by Portengen,

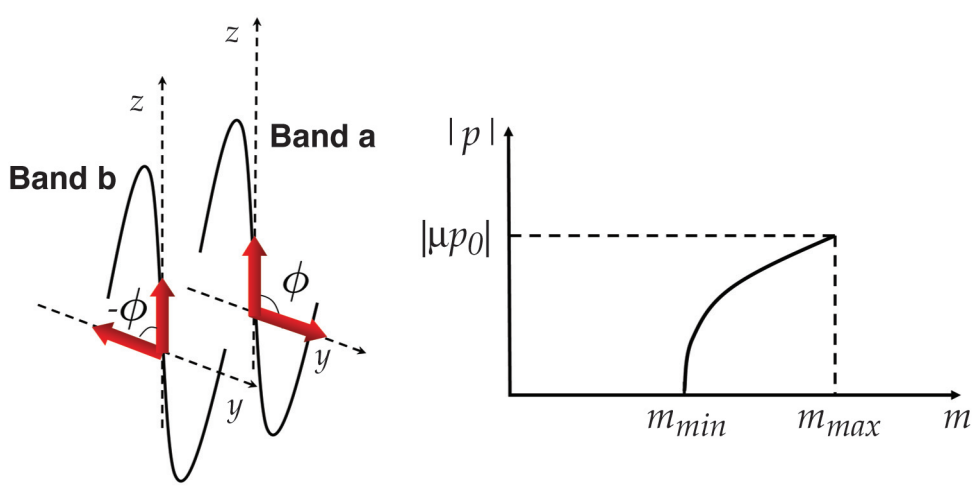

Fig. 1.
Evolution of the magnetization (arrows) on each band under the SO(4) transformation U_ϕ. The P vs M plot shows the change of the electric dipole moment P when the total magnetization M evolves from the minimum value, obtained for $\phi=\pi/2$, to the maximum value M(=0)= N/2, where N is the number of lattice sites.

et al. can coexist with magnetically ordered states. In this case, the single electron occupying the effective (say *d-f* hybridized) orbital simultaneously provides an electric and a magnetic–dipole moment, and the Coulomb repulsion is sufficient to generate a strong effective coupling between the electric and the magnetic dipoles.

We started from a two-band Hubbard Hamiltonian that included an interorbital on-site repulsive interaction U_{ab}. Like in the spinless fermion case, this interaction provided the "glue" for the formation of excitons. At quarter filling and in the strong coupling limit, we mapped the low energy spectrum of the two-band Hubbard model into an effective spin-pseudospin Hamiltonian. We proved that in the limit of large intraorbital repulsive interactions $U_{aa}, U_{bb} \rightarrow \infty$, the effective Hamiltonian has a ferromagnetic ground state that can be partially or fully saturated. By combining this result with the previous analysis for spinless fermions [2, 3, 4], we showed that FM and FE coexisted in that region of parameters, and a divergent magnetoelectric was demonstrated by using the SO(4) symmetry of the original Hamiltonian (see Fig. 1). Our conclusions were reinforced by a semiclassical and a numerical computation of the zero temperature ($T = 0$) phase diagram of original Hamiltonian that went beyond the limiting case $U_{aa}, U_{bb} \rightarrow \infty$. These computations allowed us to sketch the $T = 0$ phase diagram for the effective Hamiltonian (Fig. 2). We note the abundance of phases.

For more information contact Cristian D. Batista at cdb@lanl.gov.

[1] T. Portengen, et al., Phys. Rev. Lett. 76, 3384 (1996); *Phys. Rev.* **54**, 17452 (1996).
[2] C.D. Batista, *Phys. Rev. Lett.* **89**, 166403 (2002).
[3] C.D. Batista, et al., *Phys. Rev. Lett.* **92**, 187601 (2004).
[4] W.G. Yin et al., *Phys. Rev. B* **8**, 075111 (2003).

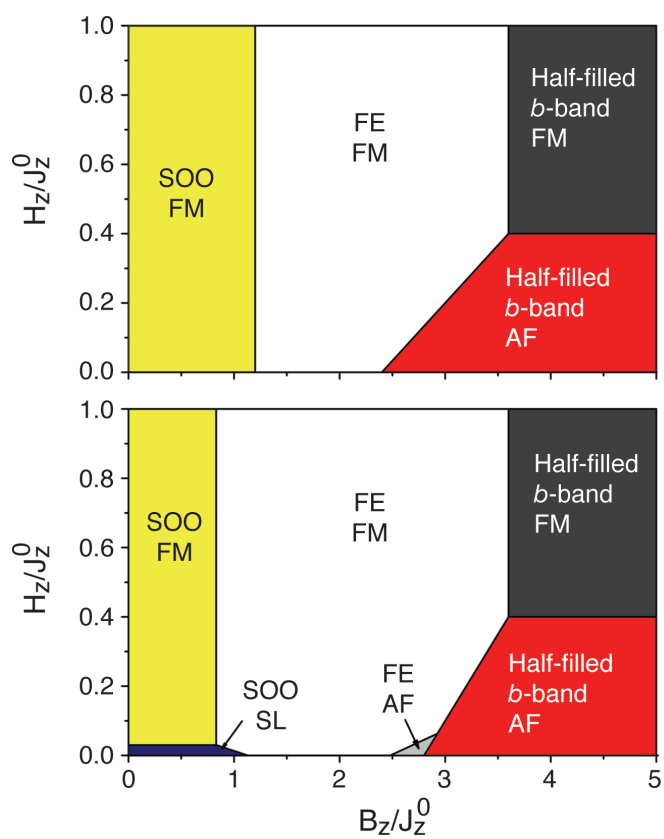

Fig. 2. ***Zero temperature phase diagram of the two-dimensional version of the effective Hamiltonian plus a Zeeman term computed in the spin-wave approximation (top) and by exact diagonalization of a 4 × 4 cluster (bottom).***

Universal Properties of Modulated Antiferromagnetic Systems

Cristian D. Batista, Gerardo Ortiz, and Alexander V. Balatsky, T-11

Magnetism and superconductivity/superfluidity are physical phenomena whose foundations are rooted in quantum mechanics and whose technological applications do not cease to surprise mankind. A fundamental open question in systems where these phenomena may co-exist is the relation between (confined) magnetic and (deconfined) superfluid/superconducting orders. For example, spin fluctuations are thought to be one of the possible mechanisms of the high temperature superconductivity in the cuprates. In this regard, neutron-scattering experimentalists have argued that their techniques could definitely shed some light on the competition and conjectured superconducting *glue*. Recently, we argued that recent inelastic neutron-scattering measurements performed in cuprate superconductors simply indicate that they are prominent representatives of a class of magnetic materials, we christened *modulated antiferromagnetic systems* (MAS). The class, however, is not exclusive to these superconductors. Indeed, we have predicted many materials that should belong to this class, several of them being insulators.

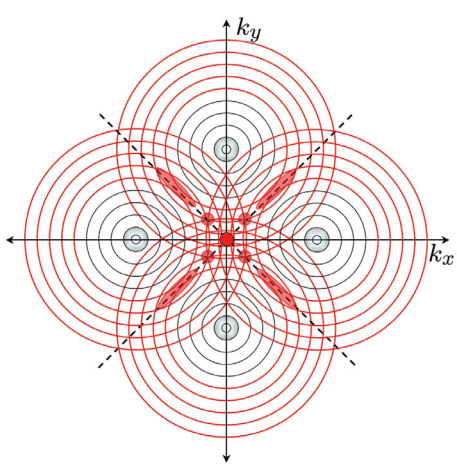

Fig. 1. *Illustration of the emergence of universal properties in MAS. The plane (k_x, k_y) represents momentum space, while the axis perpendicular to it represents the energy of excitations. The figure schematically shows how cones (whose increasing radius relates to increasing energy) centered at the Goldstone modes, or incommensurate points, etc.(indicated by dark circles), give rise to maxima in intensity because of a simple constructive interference as we move along the direction of increasing energy. The resonance peak, that lies at the center, and the twist in intensity after the resonance energy (depicted as blurred circles along the diagonals) represent some of these universal properties. Therefore, these universal signatures are simply the result of a topological characteristic of the spectrum and, thus, are independent of the microscopic details of the MAS.*

Five years ago [1], we claimed that the *resonance* peak observed in several high-T_c superconductors has a magnetic origin and that it is a natural and universal consequence of the low energy incommensurate magnetic fluctuations which appear close to the two-dimensional $\mathbf{Q} = (\pi, \pi)$ antiferromagnetic wavevector. Moreover, we stated that any system with a magnetic dispersion relation exhibiting minima at wavevectors $\mathbf{q}^{\pm} = \mathbf{Q} \pm \delta\pi\hat{\mathbf{k}}$, where $\hat{\mathbf{k}}$ is a unit vector and $\delta \ll 1$, should exhibit a peak in the magnetic structure factor $S(\mathbf{q}, \omega)$ at $\mathbf{q} = \mathbf{Q}$ and $\omega = E_r$. The peak results from the superposition of the two low-energy magnetic branches that emerge from $\mathbf{q}^{\pm}$ and converge at the saddle point at $\mathbf{q} = \mathbf{Q}$ (see Fig. 1). The actual value of the energy E_r depends on the slope of the low-energy branches (spin velocity). Based on this observation, we predicted [1] that a similar peak should be observed in insulating systems that exhibit modulated antiferromagnetic order like $La_{1.69}Sr_{0.31}NiO_4$. This prediction was later confirmed by Bourges, et al. [2]. Succesive measurements of different high-T_c compounds are confirming the idea that a universal magnetic spectrum plus a spin gap can explain various observations in the cuprates [1, 3].

Despite our theory being repeatedly confirmed by neutron scattering experiments, last findings were interpreted as evidence against our predictions [5]. Two independent groups [5, 6] observed that highest intensity high-energy magnetic excitations (above the resonance energy) are rotated 45° from the incommensurate wavevectors. This behaviour was observed in two different compounds $La_{1.875}Ba_{0.125}CuO_4$ [5] and $Yba_2Cu_3O_{6.6}$ [6]. While the first compound exhibits long-range charge and spin ordering [4], the latter only exhibits short range dynamical correlations. We have recently shown that our theory not only

contains the observed twist in the high-energy excitations but also predicts many other insulating systems depicting the same *saddle-point* effect. Since this feature is universal, its observation is not sufficient to discriminate between competing theories that include the incommensurate magnetic correlations (such as 2-leg ladder, etc.). Apart from explaining the twist, we also predicted additional universal signatures that should be observable both in the cuprates as well as in the magnetic insulators that exhibit incommensurate magnetic ordering.

The universal behaviors of MAS are a simple consequence of a few qualitative aspects of the magnetic dispersion relation. This is illustrated by Fig. 1 which shows the qualitative aspects that emerge from the intersection of four cones centered on each incommensurate wavevector (the four low-energy modes result from averaging over the horizontal and vertical orientations). It is important to note that an isotropic conical shape of the low-energy dispersion is only expected for the insulating materials. This is no longer true for metals in which the magnetic branches that move away from the commensurate point **Q** can be overdamped by the particle-hole continuum of excitations. This effect, as well as the presence of a spin gap or a possible anisotropy of the conical shape, *do not* change the following qualitative properties: a) The four cones converge at a saddle point at **q = Q** and the corresponding increase in the spectral weight leads to the observed *resonance* peak [1]; b) For higher energies, the intersections between pairs of adjacent cones leads to four points with higher intensity that are rotated 45° relative to the incommensurate wavevectors; c) A similar twist should be observed for energies $0.7E_r \leq hw \leq 0.9\ E_r$. While a) and b) are experimental facts, c) is a new prediction that requires experimental confirmation. All these universal signatures are merely consequences of the topological characteristics of the spectrum of magnetic excitations (see Fig. 2).

For more information contact Cristian D. Batista at cdb@lanl.gov.

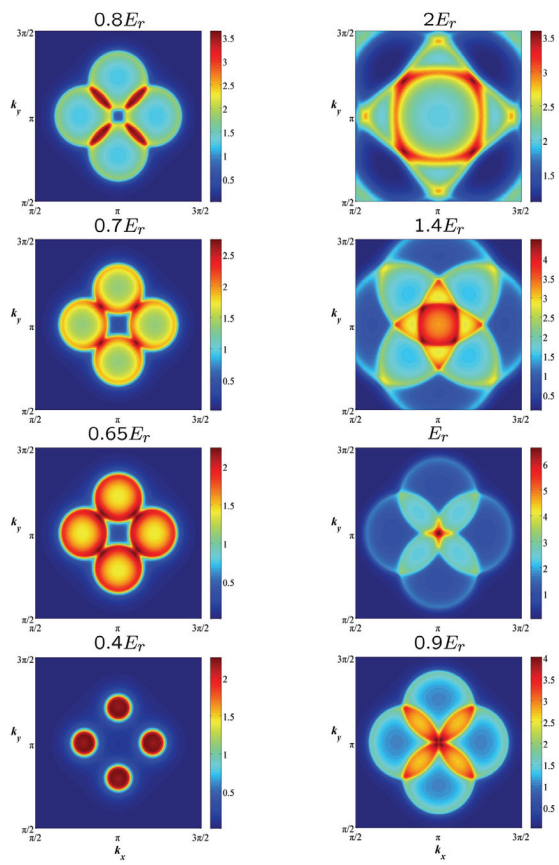

Fig. 2. ***Constant energy contour plots of the magnetic structure factor S(k, ω) (intensity) centered around k = Q = (π, π). For this particular example, we have used the Schwinger-boson mean-field result of Ref. [1]. Notice the way the maxima in intensity evolves as ω increases. Indeed, some of these universal features have been experimentally observed in the cuprates, while others represent our predictions. For example, there ought to be a twist in the location of the maxima for energies close but smaller than the resonance energy, which should be observable if higher experimental resolution were available.***

[1] C.D. Batista, et al., Int. J. Mod. Phys. B 14, 3334 (2000); *Phys. Rev. B* **64**, 172508 (2001).
[2] P. Bourges, et al., *Phys. Rev. Lett.*, **90**, 147202 (2003).
[3] J.M. Tranquada, cond-mat/0508272.
[4] M. Fujita, et al., *Phys. Rev. B* **70**, 104517 (2004).
[5] J.M. Tranquada, et al., *Nature* **429**, 534 (2004).
[6] S.M. Hayden, et al., *Nature* **429**, 531 (2004).

Strong Electron-Phonon Coupling in δ-phase Stabilized Plutonium

Matthias J. Graf and Turab Lookman, T-11; John M. Wills and Duane C. Wallace, T-1; and Jason C. Lashley, MST-NHMFL

Heat capacity measurements of the δ-phase stabilized alloy $Pu_{0.95}Al_{0.05}$ suggest that strong electron-phonon coupling is required to explain the moderate renormalization of the electronic density of states near the Fermi energy. We calculated the contributions of the heat capacity from the lattice and electronic degrees of freedom, as well as from the electron-lattice coupling term, and found good overall agreement between experiment and theory assuming a dimensionless electron-phonon coupling parameter of order unity, $\lambda \sim 0.8$. This large electron-phonon coupling parameter is comparable to reported values in superconducting metals with face-centered cubic crystal structure, for example, Pd ($\lambda \sim 0.7$) and Pb ($\lambda \sim 1.5$). In addition, our analysis showed evidence of a sizable residual low-temperature entropy contribution, $S_{res} \sim 0.4\ k_B$ (per atom), which could be fit by a two-level system. Therefore, we speculated that the observed residual entropy originates from crystal-electric field effects of the Pu atoms or from self-irradiation induced defects frozen in at low temperatures.

The actinide metal plutonium (Pu) exhibits six unique crystal structures (phases) in the solid state at ambient pressure between absolute zero and its melting temperature. The phases range in symmetry from simple monoclinic (sm) to body-centered cubic (bcc). The easily worked face-centered cubic (fcc) phase, denoted by δ, is thermodynamically stable in pure plutonium from 592 K to 736 K, and can be stabilized down to room temperature by small additions of trivalent elements such as gallium or aluminum. The effects of alloying have a profound impact on the electronic structure. Specifically, the low-temperature α phase (sm) of pure Pu has an enhanced Sommerfeld coefficient of $\gamma_S = 17$ mJ/(mol K^2) compared to a simple metal with typically $\gamma_S \sim 1$ mJ/(mol K^2), while the stabilized δ phase exhibits a moderately heavy electron mass with an enhanced Sommerfeld coefficient $\gamma_S = 50$–70 mJ/(mol K^2). It is believed that the high-volume δ phase has localized, nonbinding electrons, while in the low-volume α phase the electrons are itinerant and binding. This behavior resembles the Mott transition in correlated electron systems. In a recent calorimetry study, Lashley and coworkers [1] pointed out that the low-temperature data of the heat capacity of $Pu_{0.95}Al_{0.05}$ exhibit a moderately enhanced Sommerfeld coefficient, $\gamma_S = 64$ mJ/(mol K^2), and a λ-shaped anomaly around 60 K in C/T. These observations were suggestive to those authors to describe $Pu_{0.95}Al_{0.05}$ as an incipient heavy-fermion system.

The purpose of this study [2] was to give a quantitative description of the electron-phonon interaction on the conduction electrons in a plutonium alloy, and whether the observed low-temperature λ-shaped anomaly in C/T is associated with a martensitic phase transformation. From this study we concluded that the observed anomaly was unlikely due to a full or partial martensitic phase transformation from the high-temperature δ phase into the low-temperature α′ phase (note the substitutional binary alloy α′ and α have the same crystal structure). Because on cooling this transformation finishes around 130–180 K and is completely reversed on heating around 380 K. Instead of a structural transformation, we speculated that crystal-electric field effects or self-irradiation induced defects and vacancies, for example, Frenkel pairs, are responsible for the reported excess entropy.

A direct consequence of our analysis is that the relatively strong electron-phonon

coupling of order unity, necessary for describing the measured specific heat data, would suggest that the alloy PuAl should become superconducting below a few Kelvin. So far no evidence of superconductivity has been observed down to roughly 3 K.

We followed the standard approach and divided the calculation of the total heat capacity of a metal into a vibrational, electronic, electron-phonon coupling, and residual (everything else) term, $C = C_{ph}+C_e+C_{ep}+C_{res}$. One by one, we calculated their contributions and importance. Furthermore, we assumed that the thermodynamic properties are dominated by the fcc δ-Pu crystal structure and any possible admixture of α′ is negligible.

In Fig. 1 we are comparing the combined total theoretical heat capacity with experiment. The agreement is excellent. Here we combined the individual contributions to the heat capacity, assuming an electron-phonon coupling parameter $\lambda \sim 0.8$ with Eliashberg's $\alpha^2F(\omega)$ function that has an Einstein mode at 2.8 THz, a two-level system (TLS) with an occupation factor $n \approx 0.5$ and level splitting $T_{TLS} \approx 120$ K, as well as an electron density of states peaked at the Fermi level.

In conclusion, we studied heat capacity measurements of δ-phase stabilized PuAl alloy and calculated the vibrational, electronic, electron-phonon, anharmonic, crystal-electric field, and structural transformation contributions. Thereby, we found several important aspects: 1) electron-phonon coupling is strong and cannot be neglected at low temperatures; 2) an electronic density of states peaked at the Fermi energy with an electron-phonon coupling parameter of order unity, $\lambda \sim 0.8$, is necessary to account for most of the electronic heat capacity; 3) a residual excess entropy of order $S_{res} \sim 0.4\ k_B$ (per atom) can be understood in terms of an additional internal degree of freedom, for example, crystal-electric field effects or self-irradiation induced defects at plutonium sites; 4) a structural transformation from δ→α′ occurs at temperatures too high, and is too small in magnitude, to account for the low-temperature excess entropy; and 5) finally, the excess entropy and the λ-shaped anomaly in *C/T* are not indicative of any significant lattice anharmonicity.

For more information contact Matthias J. Graf at graf@lanl.gov.

[1] J.C. Lashley et al., *Phys. Rev. Lett.* **91**, 205901 (2003).
[2] M.J. Graf et al., *Phys. Rev. B* **72**, 045135 (2005).

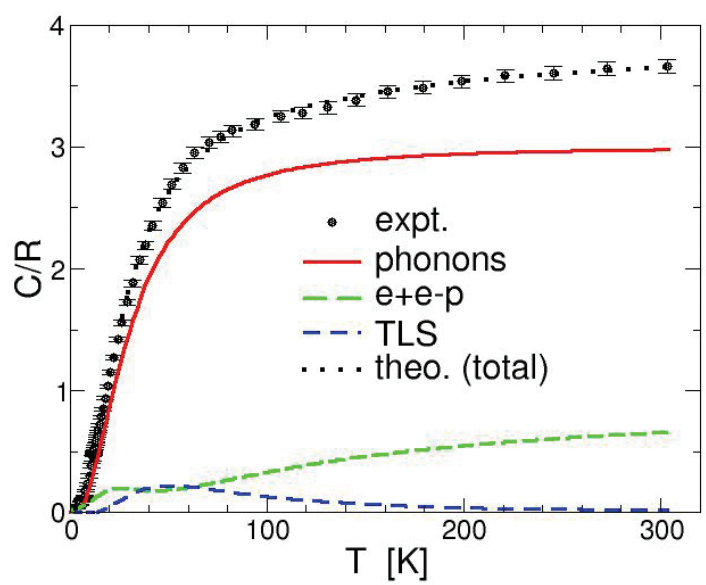

Fig. 1. ***Comparison between experimental heat capacity and theory, which has been decomposed into phonon, electron-phonon renormalized electronic and two-level system contributions.***

The Quantum Dynamics of Polaron Formation

Li-Chung Ku, University of Texas, and Stuart Trugman, T-11

When degrees of freedom interact, they can form composite objects called quasiparticles. An example is the coupling of an electron with phonons, forming a polaron quasiparticle. A polaron is an electron traveling with a cloud of lattice distortions, which can have a mass slightly greater or orders of magnitude greater than a bare electron, depending on the strength of the coupling. By efficiently organizing the many-body Hilbert space, we have calculated the energy, mass, and correlation functions of the polaron many orders of magnitude more accurately than was previously possible. Other types of quasiparticles arise in different contexts, including interactions of electrons with magnetism, with other electrons, etc.

We investigate how a bare electron, injected by fast optical processes or by a tunneling event, dynamically becomes a polaron quasiparticle (plus unbound phonons). The phonons and electrons are treated quantum mechanically. (Treating the phonons classically, a common approximation, fails to capture some of the physics.) The method used is to numerically integrate the time-dependent Schrödinger equation in a many-body Hilbert space of over a million basis states. Various time and position-dependent correlation functions have been calculated and displayed as a movie, frames from which are shown in the figure. Depending on the parameters (the electron-phonon coupling, the optical phonon frequency, and the electron hopping), the polaron can form in a time as short as a phonon period, or arbitrarily longer. The spectral function and other time-dependent correlation functions have also been calculated, and compared to fast optical and two-photon photoemission experiments [1].

The figure shows four snapshots from a movie of a polaron quasiparticle forming from a bare electron. In panel (a), a bare electron is injected moving to the right, with the electron density shown in black. The electron velocity (green) is positive. The phonon displacement $<X_j>$ (red) is initially zero. (For clarity, the red and green curves have been shifted upwards by 0.1.) At time 0.5, panel (b), the phonons are displaced where the initial electron was injected. At time 1.0, panel (c), the electron density (black) has developed two peaks. The peak on the right is a bare electron, moving quickly. The peak on the left is a slower and more massive electron dressed with phonon excitations, the polaron quasiparticle. The phonon displacement (red) is oscillating and is now negative where the electron was initially injected, but it is positive to the right where the electron arrived later. Also shown are the electron density that would have been present if there were no coupling to the phonons (dashed black line), and the phonon number density (blue). The magenta curve plots the phonon number density on the electron site j, $<c_j^\dagger a_j^\dagger a_j>$. The green curve shows that some electron density has been backscattered, and is moving to the left, at the left side of the frame. Panel (d), at time 1.5, shows the bare electron peak getting smaller with time (black arrow), while the polaron peak grows as time goes on (red arrow). Most of the phonons were radiated near where the electron was initially injected (blue). (Note that the phonons are dispersionless optical phonons in this simulation, so they do not move unless the electron is nearby.) The displacement of the oscillating phonons has reversed yet again (red curve). The simulation is for a 30-site system with periodic boundary conditions.

For more information contact Stuart Trugman at sat@lanl.gov.

[1] Li-Chung Ku and S.A. Trugman, "Quantum Dynamics of Polaron Formation," submitted to *Phys. Rev. Lett.*, 2005.

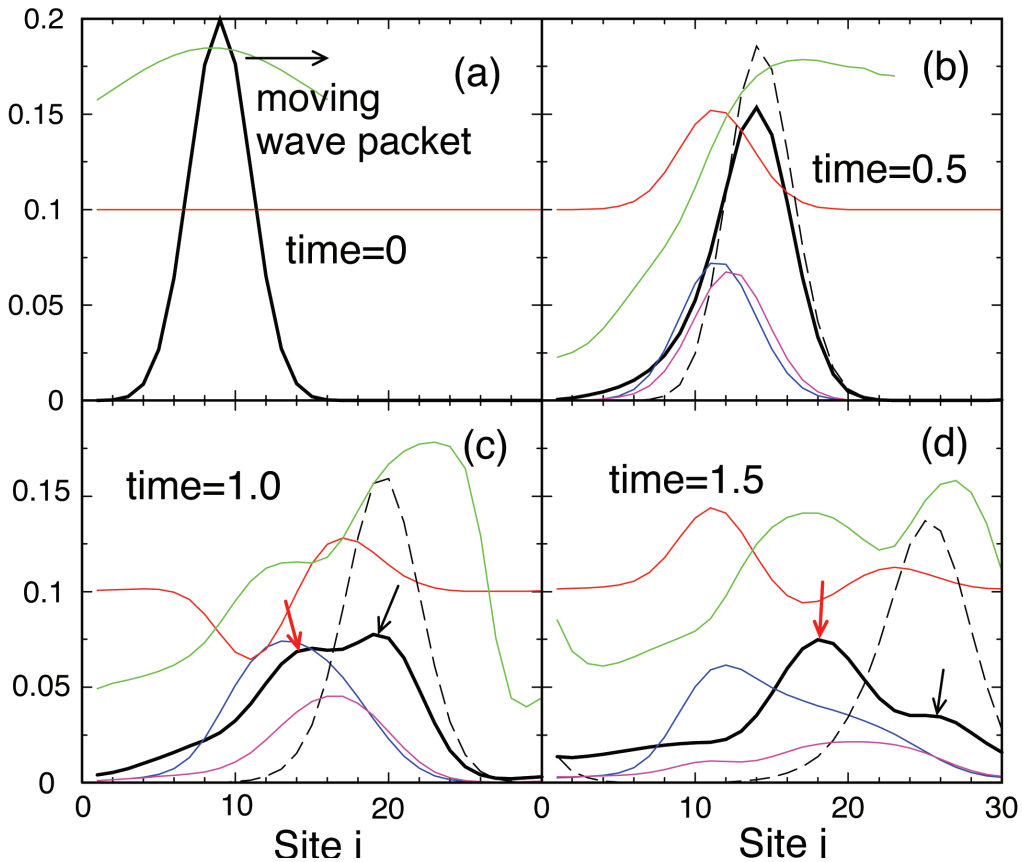

Fig. 1. *Four snapshots from a movie of a polaron quasiparticle forming from a bare electron. The electron and phonons are all treated quantum mechanically. Time is measured in units of the phonon vibrational period.*

Defect-Induced Nucleation in Cubic to Tetragonal Martensites

Turab Lookman and Avadh Saxena, T-11; and Rajeev Ahluwalia, Institute for Materials Research & Engineering, Singapore

Shape memory alloys such as NiTi exhibit interesting mechanical properties due to a diffusionless structural phase transformation from a high temperature (Austenite), in general a cubic, phase to a low temperature (Martensite) tetragonal, orthorhombic or monoclinic phase. This transition is usually first order and is accompanied by a spontaneous strain. The martensitic transition is also responsible for the shape memory effect that refers to the recovery by heating of an apparently permanent deformation undergone below a critical temperature. This property makes shape memory materials suitable for a large number of technological applications. Another important property of shape memory materials is the so-called pseudoelastic behavior that arises due to a reversible stress/strain induced martensitic transformation at a temperature that is higher than the austenite finish temperature of the material. In pseudoelastic deformation, a high temperature cubic austenite phase typically transforms to the martensite under deformation so that there is a plateau in the stress-strain curves. On removing the deformation, the material transforms back to the cubic austenite and the deformation is recovered upon unloading. In fact, some shape memory materials can recover strains of up to 10% under tension, making these materials suitable for actuator applications.

The martensitic transformation results in the formation of a complex microstructure consisting of twin boundaries between the crystallographic variants of the transformation. This microstructure influences the effective mechanical properties of these materials. For example, if a stress is applied to a material in the martensitic phase, there is motion of the twin boundaries as the favored variants grow at the expense of the unfavored variants. Even during pseudoelastic deformation, the strain induced transformation involves nucleation and growth of the martensitic variants. The motion of the domain walls can influence the strain rate dependence of the mechanical response and thus it is important to incorporate this aspect in a theoretical framework. We have theoretically studied the role of microstructural evolution on the mechanical response of shape memory materials, in particular the effects of defect induced heterogeneous nucleation and motion of twin boundaries during cubic to tetragonal deformation of martensite [1].

A number of approaches have been used to model shape memory materials. These include energy minimization techniques that are subject to certain constraints that ensure the integrity of the lattice and micromechanical models that require prior knowledge of the habit planes and their volume fractions. Such techniques have been successful in estimating the recoverable strains for many martensitic transformations. Over the past few years, continuum models based on the Ginzburg-Landau approach have also been used to study the mechanical response of shape memory alloys. The effect of microstructure on the effective stress-strain response has also been simulated using the time-dependent Ginzburg-Landau approach. However, these studies do not consider the strain rate dependence of the stress-strain behavior. We have used a displacement field based dynamical model to study the effect of defects and microstructure on the stress-strain properties of shape memory materials. We have also investigated how microstructural evolution influences the strain rate dependence of the mechanical response [1].

We present 3-D simulations of the microstructure and mechanical response of shape memory alloys undergoing cubic to tetragonal transitions, using FePd as an example. The simulations are based on a nonlinear elastic free-energy in terms of the appropriate strain fields. The dynamics is simulated by force balance equations for the displacement fields with a damping term derived from a dissipation function. Stress-strain properties are investigated using strain loading. Specifically, we have probed the influence of the microstructure on the mechanical response and investigated how the stress-strain behavior changes as a function of strain rate. To illustrate this we obtained through a Ginzburg-Landau

simulation the stress-strain curves in the presence of defects. We expected that the defects will nucleate the transformation even before the system is in the unstable region, thereby reducing the stress required to cause the transition. To study defect induced transformation, we simulated the loading process with an initial "quenched" seed of the transformed phase that is embedded in the initial austenite matrix. The total uniaxial strain field in this direction is given by

$$\epsilon_{xx} = \partial u_x / \partial x + \epsilon_{xx}^{applied} + \epsilon_{xx}^{seed}$$

where ϵ_{xx}^{seed} is the strain due to the defect.

This represents an inclusion of a cube of the martensite phase of length L_0 in the austenite matrix. A loading process for this system with strain rate $\gamma = 2.23 \times 10^6/\mathrm{s}$ (L_0 ~24 nm) is shown in the figure. It shows the stress-strain curve and the spatial distribution of ε_{xx} at points **A, B, C, D**, and **E** on the stress-strain curve. To clearly show the evolution of the microstructure around the defect region, we have displayed two mutually intersecting perpendicular planes that pass through the defect. There is a point on the stress-strain curve where austenite and martensite have the same energy. For strains higher than this critical strain, the nucleation of martensite can take place as martensite has lower energy than the austenite. This nucleation process can be observed by comparing the microstructure at points **B** and **C**. One can see the growth of the martensite domains (regions shaded red) from a seed defect that is embedded in the austenite matrix (regions shaded blue). On further loading, the favored variant grows, as can be observed in the snapshot corresponding to **D**. Eventually, a single variant state of the variant stretched along the x direction is established as can be observed in the snapshot **E**. Notice that the strains in the defect regions are higher (4%) than the bulk value (3%). Even during this loading process, the unfavored variants are also formed. We can also obtain the full microstructures for the three strains ε_{xx}, ε_{yy}, and ε_{zz} corresponding to the point **C**. We found that the magnitude of the distortions along the *y* and *z* directions are smaller than those along the favored *x* direction.

These simulations describe processes at relatively small length (submicron) and time (nanoseconds) scales. Refinement of our scheme to a more coarse grained model in terms of volume fractions of the transformed phase is a possible approach to describing larger length scales.

For more information contact Turab Lookman at txl@lanl.gov.

[1] R. Ahluwalia, et al., *Acta Mater*. **54** (2006).

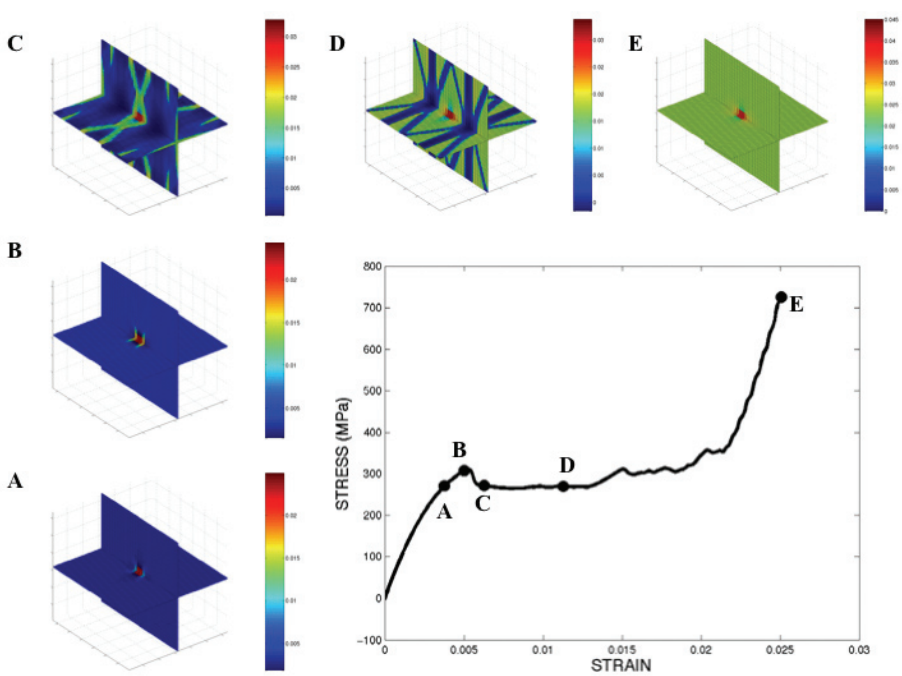

Fig. 1. ***The stress-strain curve and the spatial distribution of ε_{xx} at points A, B, C, D, and E on the stress-strain curve.***

Molecular Bridging in Asymmetric Triblock Copolymers

Kim Rasmussen, T-11; Edward M. Kober, T-14; and R.J. Spontak, North Carolina State University

Unlike immiscible homopolymers that generally phase-separate at macroscopic length scales, incompatible AB diblock copolymers are capable of spontaneous molecular self-organization into a variety of ordered morphologies at nanoscale dimensions. Classical block copolymer morphologies include A(B) spheres arranged on a cubic lattice in a B(A) matrix, A(B) cylinders arranged on a hexagonal lattice in a B(A) matrix and alternating lamellae. Equilibrium or metastable complex morphologies such as the gyroid or perforated lamellae, respectively, consist of bicontinuous channels exhibiting long-range order and spatial symmetry.

The ability to tune the morphologies of microphase-ordered block copolymers is critical to a broad range of emerging nanotechnologies and depends sensitively on the conformational entropy associated with interfacial chain packing. Molecular factors governing interfacial chain packing include copolymer composition, repeat unit asymmetry and (liquid) crystallinity. The dependence of morphological development on interfacial chain packing is further amplified if a third block is added to a diblock copolymer, thereby forming a triblock copolymer. Incorporation of a dissimilar block results in the formation of an ABC triblock copolymer, which can greatly extend the assortment of experimentally accessible, and often hybrid, morphologies.

In this work, we focus on bicomponent ABA triblock copolymers wherein the third block is chemically identical to the first. Although these copolymers have been experimentally found and theoretically predicted to exhibit the same morphologies as their AB diblock counterparts, they can possess markedly different mechanical and flow properties due to the placement of the third block. If it resides in the same microdomain as the first, the B midblock forms a loop. If, on the other hand, the third block locates in a different microdomain, the midblock is forced to span two neighboring microdomains by forming a bridge. Experimental and theoretical studies have long sought to elucidate the conditions favoring, as well as the consequences of, molecular bridging in ABA triblock copolymer systems with limited success. These previous efforts have focused almost exclusively on molecularly (though not necessarily

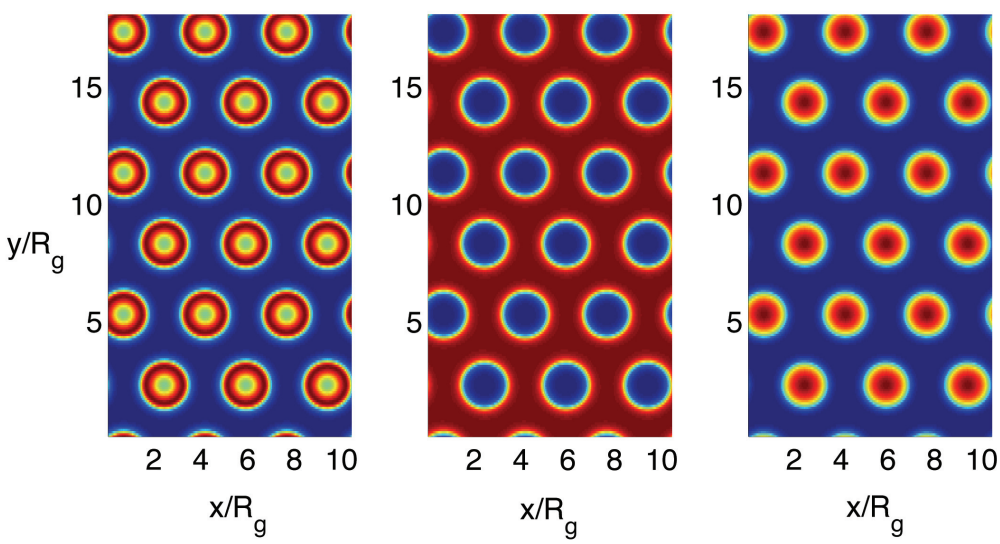

Fig. 1. *Two-dimensional cross section of A rich cylindrical regions in a B rich matrix showing monomer density A_1 (left), B (center), and A_2 (right) for the case of a 16 kDa A_2 block. It is seen that the shorter A block (A_1 in this case) occupies the outer region of the A rich cylinders. Red color indicates high density and blue color indicates low density.*

compositionally) symmetric copolymers wherein the endblocks are of identical length due to commercial interest in such materials as thermoplastic elastomers. Since midblock bridging clearly distinguishes an ordered ABA copolymer from its AB analog, a systematic study of the morphological and property development in molecularly asymmetric A_1BA_2 triblock copolymers progressively grown from a single A_1B diblock copolymer may be able to signal the onset of bridging.

The objective of this work is to discern the conditions signaling the origin of molecular bridging/looping in a series of isomorphic A_1BA_2 triblock copolymers from integrated experimental and self-consistent field theory analyses of morphological and property development as the A_2 block is chemically grown. A parent poly(styrene-*b*-isoprene) A_1B diblock copolymer, along with a series of molecularly asymmetric A_1BA_2 triblock copolymers, was synthesized. The block masses of the parent diblock were 9.4 kDa (styrene, A_1) and 46 kDa (isoprene, B), in which case the copolymer series is designated 9-46-A_2, where the mass of the A_2 block was varied from 0kDa to 20kDa. This entire series was found, experimentally as well as theoretically, to form A-rich cylinders arranged on a hexagonal lattice. A two-dimensional cross section of this morphology is illustrated by Fig. 1. The spacing D of the cylinders were found to change nonmonotonically as the mass of the A_2 block is increased. As seen in Fig. 2 experiment and theory agree almost quantitatively on dependence of the spacing on the molecular weight of the A_2 block. The elastic modulus of these materials has been experimentally determined to also depend nonmonotonously on the molecular weight of the A_2 block, with a dramatic increase as the A_2 block becomes large. The dramatic increase is believed to result from the chain's increased ability to bridge domains and form physical cross links between domains as the A_2 block is increased. We are currently working towards verifying this scenario by calculating the actual fraction of chains forming bridges between domains.

For more information contact Kim Rasmussen at kor@lanl.gov.

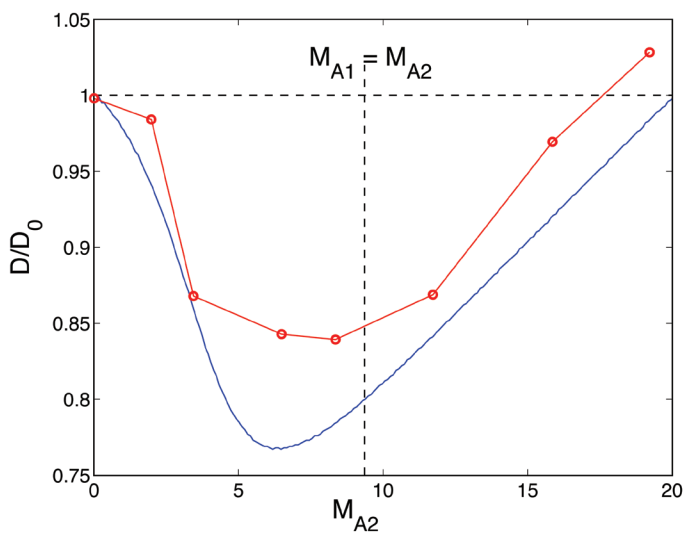

Fig. 2. *Spacing D of cylinders normalized to the spacing D_0 of the diblock system vs molecular weight of the A_2 block. Experimental result is shown in red color and Self-Consistent Field Theory (SCFT) prediction is in blue.*

Theory of Forced DNA Unzipping

Kim Ø. Rasmussen, T-11; Nikolaos Voulgarakis, CNLS; and Alan R. Bishop, T-DO

Genetic information in cells is stored in double-helical double-stranded DNA molecules. The hydrogen bonded and stacked bases are well protected in the interior of the double-stranded molecule. However, separation of the two strands is a key part of both the "reading" of DNA sequences (transcription) and DNA replication. During transcription, a transient "bubble" of single-stranded DNA is formed, to allow the enzyme that makes an RNA copy of the DNA sequence to access the DNA bases. During replication, the two DNA strands are permanently separated, to serve as templates for the synthesis of new strands.

In biochemistry experiments, DNA double-strands are routinely converted to separated single-strands by "melting" at elevated temperature (~80 °C). This approach uses thermal fluctuations to simply overwhelm the base pairing and base stacking interactions that stabilize the double helix at room temperature. In a cell, at physiological temperatures, these thermal fluctuations may still locally melt the double strand to produce small (< 30 base pairs) single-stranded regions, and it has been argued that such thermally induced bubbles play a role in at least the initiation of transcription. However, another possibility, within a cell, is that DNA strands are separated by the application of force, or in chemical terms, by enzymes whose interactions with DNA make strand separation thermodynamically favorable at ambient temperature. Therefore, it is of basic biophysical interest to analyze the separation of DNA strands by force, and recent micromanipulation experiments are beginning to accomplish precisely this feat.

It has been shown that the two strands of double-stranded DNA can be separated (unzipped) by the application of ~15 pN force applied at room temperature. Fluctuations of this unzipping force about this mean have been thought to provide a means to perhaps determine the DNA sequence: slightly higher forces were shown to correspond to DNA regions with higher *GC* densities. This result was in accord with the fact that *GC*-rich sequences have stronger base-pairing interactions than *AT*-rich sequences, causing them to thermally melt at higher temperatures, and provides further strong motivation for the experiment.

Figure 1 provides a simple illustration of a typical setup for unzipping experiments: one of the terminal base-pairs of the double-stranded

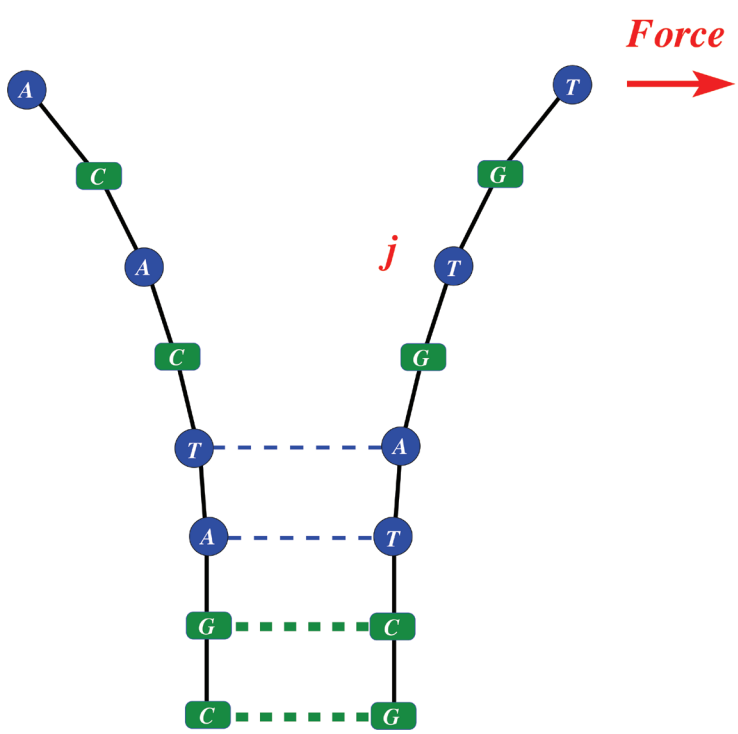

Fig. 1. ***Schematic illustration of forced unzipping of a DNA double-strand.***

molecule is tethered to a surface (left) while the force is applied to the complementary base pair (right) by an atomic force microscope cantilever or by means of optical tweezers. The molecule is then sequentially unzipped into two single-stranded molecules, as shown. The experimental results acquired in this fashion, although impressive, are highly nontrivial to interpret and require some confrontation with modeling. Our model of choice is the Peyrard-Bishop-Dauxois (PBD) model, which is a phenomenological model originally constructed to model the thermal melting of double-stranded DNA. Lately we have been using this model also to investigate sequence dependence of the double-strand's ability to form thermally induced bubbles. We have found that certain subsequences of viral and human DNA are significantly more prone to allowing large bubbles to form. These subsequences have been experimentally confirmed to reside at transcription initiation sites. Since the PBD model has proven so effective for correctly describing double-stranded DNA bubbles, and since such bubbles are thought to play a role in the interpretation of the data acquired through unzipping experiments, we are investigating its predictions regarding forced unzipping. The main result we have obtained from this investigation is given in Fig. 2, which shows the phase diagram determining the force required to unzip the molecule at a given temperature. It is worth noticing that at room temperature the model reproduces the 15 pN, which is the experimentally required force. Recent experimental attempts have been made to determine this phase diagram, and our results are in qualitative agreement with those experiments. Most importantly we have confirmed that the PBD model is accurately describing the unzipping experiments as well as thermal denaturation.

For more information contact Kim Rasmussen at kor@lanl.gov.

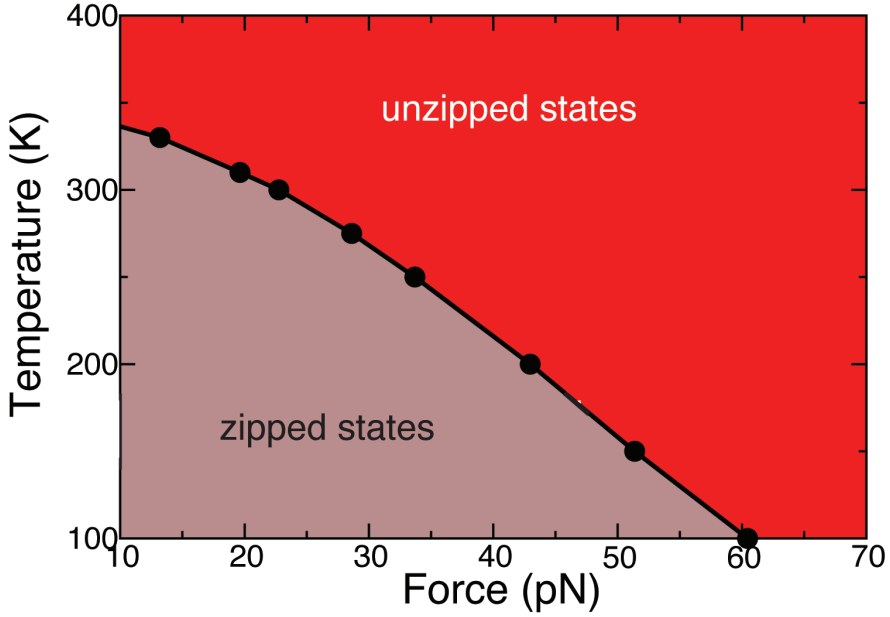

Fig. 2. ***Phase diagram showing the force required to unzip the double-stranded molecule vs temperature.***

Piezoelectric Response of Domains in Ferroelectrics

Avadh Saxena and Turab Lookman, T-11; and Rajeev Ahluwalia, Institute for Materials Research & Engineering, Singapore; and W. Cao, Pennsylvania State University

Ferroelectrics are the best piezoelectric materials that can convert electrical energy into mechanical energy and vice versa. This electromechanical property arises due to the coupling of the spontaneous polarization with lattice strain. Many devices such as ultrasonic transducers and piezoelectric actuators make use of this property. Recently, there has been considerable interest in this field due to the observation of a giant piezoelectric response when the applied field is along a nonpolar direction. It is believed that this "superpiezoelectric" response is due to the symmetry change caused by a rotation of the polarization towards the direction of the applied field. Domain configurations produced by the nonpolar direction field are termed *engineered domains.* It is important to understand to what extent the large response is influenced by the presence of domain walls in the engineered configuration. Recent studies have shown that the low field piezoelectric response of the engineered domain configuration of $0.67Pb(Mg_{1/3}Nb_{2/3})O_3 - 0.33PbTiO_3$ is very close to that of single domain data. However, for large fields, the presence of domain walls may influence the piezoelectric response. We have theoretically studied the effect of domain walls on the piezoelectric properties of engineered domains as a function of the applied field over a range of electric field values.

In previous studies, the electromechanical response of ferroelectrics poled along nonpolar directions has been studied theoretically using first-principle calculations. A continuum Landau theory describing a single domain or homogeneous state has also been used to study electromechanical properties of $BaTiO_3$ as a function of temperature and electric field direction. Although such calculations provide valuable insights into the physics of the polarization-strain coupling, they do not describe inhomogeneities due to domains and domain walls. We have used a continuum time-dependent Ginzburg-Landau framework that incorporates long-range elastic and electrostatic interactions that are crucial to describe multidomain states and domain walls. To illustrate the underlying principles, we restrict ourselves to a 2-D ferroelectric system. However, we choose free energy parameters relevant for $BaTiO_3$. We have also studied the behavior of domain patterns under applied electric field and investigated how the microstructural evolution influences the average electromechanical response of ferroelectric materials.

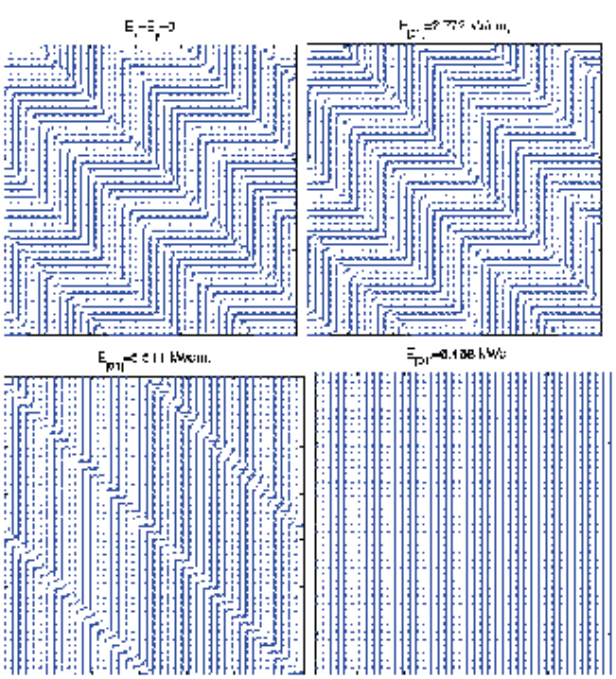

Fig. 1. ***The top left panel of the figure shows the prepared zero-field multidomain state. To simulate the effect of an external electric field, the evolution equations are solved with a varying field for two cases: (i) the field applied along the polar [01] direction, and (ii) the field is applied along the nonpolar [11] direction. The figure depicts the evolution of domains for the field along the polar direction.***

In the top left panel of Fig. 1 we show the prepared zero-field multidomain state. To simulate the effect of an external electric field, the evolution

equations are solved with a varying field for two cases: (i) the field applied along the polar [01] direction, and (ii) the field is applied along the nonpolar [11] direction. The evolution of domains for the field along the polar direction is depicted in Fig. 1. The corresponding (longitudinal) piezoelectric constant d_{33}, derived from the relevant polarization and strain, is shown in Fig. 2 for three different domain sizes (4.5 nm, 11.3 nm, 22.6 nm from left to right, respectively). The inset shows the low-field behavior. We find that the electromechanical response is highly orientation- and microstructure-dependent. When the field is applied along one of the polar directions, domain switching results in higher strains compared to the single domain state. We have also studied the domain evolution, polarization, strain, and the associated piezoelectric constant for electric fields applied along a nonpolar direction. In this case the domain walls serve as nucleation sites for a field-induced structural phase transition.

To summarize, we have used a Ginzburg-Landau formalism to study the electromechanical properties of domain-engineered ferroelectrics. The model calculation incorporates nonlocal elastic and electrostatic effects. The simulations demonstrate that domain walls do not significantly influence the piezoelectric response at small fields. However, at high fields, domain walls act as nuclei for field-induced structural phase transitions and consequently the transition occurs at lower field values for the engineered state compared to the corresponding single domain states. The high-field piezoelectric response is also enhanced due to the nucleating action of the domain walls near the field-induced transition. The low field behavior is consistent with the reported results on $0.67Pb(Mg_{1/3}Nb_{2/3})O_3$ – 0.33PbTiO3. Further experiments would test the large field predictions of our calculations. We also demonstrated the effect of the underlying domain microstructure on electromechanical properties of multidomain ferroelectrics. To account for nonlocal elastic and electrostatic effects, two additional parameters that measure the strength of the long-range interactions were introduced. Our calculations show that these long-range parameters are essential to describe multidomain states. In this work, we have made simple choices for these parameters. In principle, these parameters should be measured for a given experimental multidomain state for a complete characterization of the material.

For more information contact Avadh Saxena at avadh@lanl.gov.

[1] R. Ahluwalia, et al., *Appl. Phys. Lett.* **84**, 3450 (2004).
[2] R. Ahluwalia, et al., *Phys. Rev. B* **72**, 014112 (2005).

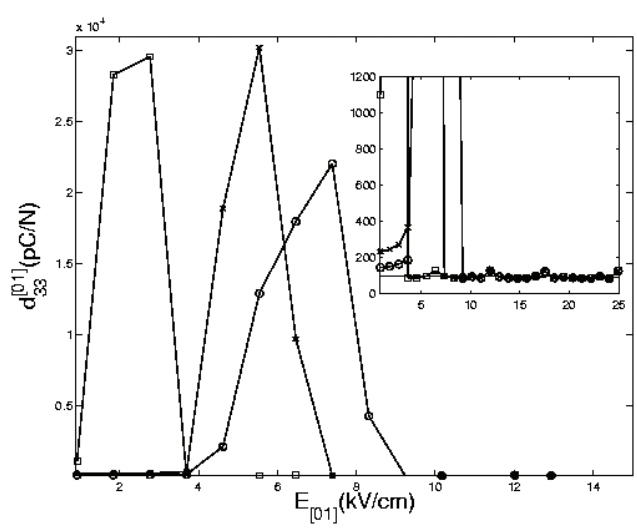

Fig. 2. *The longitudinal piezoelectric constant d_{33}, derived from the relevant polarization and strain for three different domain sizes (4.5 nm, 11.3 nm, 22.6 nm from left to right, respectively). The inset shows the low-field behavior.*

Electron Spin Flow and Transport in Semiconductor Epilayers

Darryl L. Smith, T-11; M. Hruška, Lawrence Livermore National Laboratory; Š. Kos, Cambridge University; Avadh Saxena, T-11; and S.A. Crooker, MST-NHMFL

A new generation of electronic devices, with the potential to outperform conventional electronic circuits in speed, integration density, and power consumption, has been proposed based on the ability to manipulate electron spin in semiconductors. To design semiconductor structures whose function is based on electron spin, it is necessary to understand spin dynamics and spin-polarized transport, and in particular, how they are affected by electric, magnetic, and strain fields. Spin dynamics and spin transport in semiconductors have been studied experimentally using time- and/or spatially-resolved spin-sensitive optical spectroscopies based on the magneto-optical Faraday and Kerr effects [1, 2]. We have microscopically derived an equation of motion for the electron Green's function that gives a full quantum-mechanical description of electron spin dynamics and transport in the presence of electric, magnetic, and strain fields. From this equation of motion we constructed a semiclassical kinetic theory of electron spin dynamics and transport in the presence of these fields [3, 4]. From the semiclassical kinetic theory, we derived a set of spin-drift-diffusion equations for the components of the spin density matrix for the case of spatially uniform fields and electron density. We solved the spin-drift-diffusion equations numerically and found good agreement with scanning Kerr microscopy images of spin-polarized conduction electrons flowing laterally in bulk epilayers of n-type GaAs. We contrast the effects of magnetic and strain fields on electron spin transport.

Figure 1 shows schematics of the two experimental geometries. A [001]-oriented n:GaAs epilayer sample, whose surface normal is along the z-axis, is subject to in-plane electric and magnetic fields, as well as strain fields. As illustrated in Fig. 1a, the sample may be optically excited by a circularly polarized laser beam propagating along the surface normal so that electrons, spin polarized along the z-axis, are optically injected. Alternatively, spin polarized electrons may be electrically injected into the semiconductor from ferromagnetic contacts as illustrated in Fig. 1b. For electrical injection, the injected electron spin polarization follows the magnetization **M** of the ferromagnetic contact, and is, therefore, typically in the x-y plane of the sample surface (for certain special ferromagnetic contacts both **M** and the injected electron spin polarization may be directed along the surface normal). The spin polarized electrons subsequently drift and diffuse in the x-y sample plane. The epilayer, in which the electrons are confined, is thin compared to a spin diffusion length so that the spin density is essentially uniform in the z-direction. The resulting steady state spin polarization is imaged via scanning Kerr microscopy, which is sensitive to the z-component of electron spin polarization, n_z. In the experiments, ohmic side contacts allow for a lateral electrical bias (E_x) in the x-y plane, Helmholtz coils provide an in-plane magnetic field (B_y),

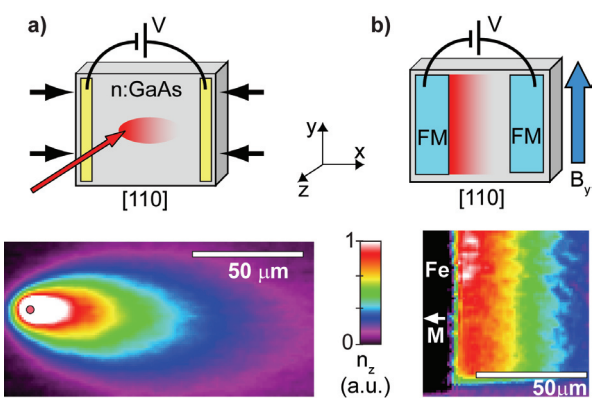

Fig. 1.
Schematics of the two experimental geometries.

and uniform off-diagonal strain (ε_{xy}) is provided by a controlled uniaxial stress applied to the sample along a [110] crystal axis. The experimental data in the lower panels of Fig. 1 show false color 2-D images of the measured z-component of electron spin polarization, showing the flow of spin polarized electrons. In the lower left panel, spin-polarized electrons are optically injected using a laser focused to a 4 μm spot (illustrated by the circular red dot) and these spins subsequently diffuse and drift to the right in an applied electric field (E_x = 10 V/cm). In the lower right panel spin-polarized electrons are electrically injected from an iron tunnel-barrier contact that is magnetized along -x. The injected spin polarization is in the x-direction, and a small magnetic field in the y-direction (B_y = 3.6 G) rotates the spins so that there is a z-component of spin polarization that can be detected by Kerr microscopy.

In Fig. 2 we compare our calculations with experimental results for the case of optical spin injection with the data obtained via scanning Kerr microscopy. In these measurements, a linearly polarized narrowband Ti: sapphire laser, tuned just below the GaAs band-edge and focused to a 4 μm spot on the sample surface, was raster-scanned in the x-y sample plane to construct a 2-D image of n_z. The sample was a Si-doped n-type GaAs epilayer (electron density = 1 x 10^{16} cm^{-3}) grown on a [001] oriented semi-insulating GaAs substrate. Spin polarized electrons were optically injected into the sample by a separate, circularly-polarized 1.58 eV diode laser that was also focused to a 4 μm spot on the sample. Measurements were performed at a temperature of 4 K. Figures (a), (c), and (e) compare calculated and measured results for spin flowing to the right in the presence of uniform off-diagonal strain (ε_{xy} = 4 x 10^{-4}; E_x = 12 V/cm), while Figs. (b), (d), and (f) compare calculated and measured results for spins flowing to the right in the presence of an applied magnetic field (B_y = 16 G; E_x = 7 V/cm). There is very good agreement between theory and experiment. The material parameters used in the calculation were: mobility μ = 3000 cm2/Vs, spin relaxation time τ_s = 125 ns, and diffusion constant D = 10 cm^2/s. We used a value of C_3 = 4.0 eVÅ for the spin-strain coupling coefficient based on previous experiments. Both strain and magnetic field lead to precession of the electron spins. However, the spatial damping of the precession is more pronounced when magnetic rather than strain fields are applied (at the same precession length).

For more information contact Darryl Smith at dsmith@lanl.gov.

[1] S.A. Crooker and D.L. Smith, *Phys. Rev. Lett.* **94**, 236601 (2005).
[2] S.A. Crooker, et al., *Science* **309**, 2191 (2005).
[3] M. Hruška, et al., *Phys. Rev. B* **73**, 075306 (2006)
[4] F.X. Bronold, et al., *Solid State Physics* **58**, 73 (2004); Phys. Rev. B 70, 245210 (2004).

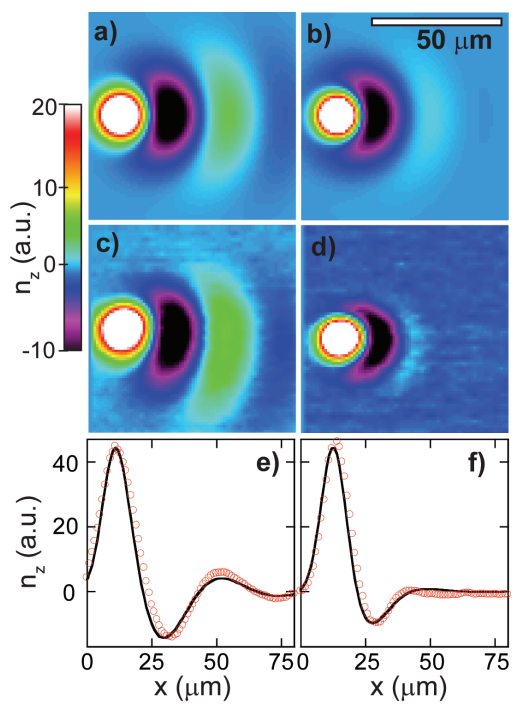

Fig. 2. ***Our calculations compared with experimental results for the case of optical spin injection with data obtained via scanning Kerr microscopy.***

Phase Diagram and Spectroscopy of Fulde-Ferrell-Larkin-Ovchinnikov States of Two-Dimensional d-wave Superconductors

Anton B. Vorontsov, Louisiana State University; James A. Sauls, Northwestern University; and Matthias J. Graf, T-11

Experimental evidence is growing that the Fulde-Ferrell-Larkin-Ovchinnikov (FFLO) state may be realized in the unconventional, heavy-fermion superconductor $CeCoIn_5$ [1, 2]. If confirmed, this would be the first identified system undergoing a phase transition from the uniform Meissner state of the Bardeen-Cooper-Schrieffer (BCS) theory of superconductivity to the spatially nonuniform FFLO state. To provide further tests for its identification we calculated the magnetic field versus temperature phase diagram. This involves a self-consistent calculation of the superconducting order parameter structures for the FFLO states of quasi-two-dimensional d-wave superconductors. Our results predict that the lower critical magnetic field transition between the spatially uniform Meissner and nonuniform FFLO state is of second order, signaled by the appearance of a single domain wall. Thus the signatures of the nonuniform FFLO state should be clearly observable in the I-V characteristics of scanning tunneling spectroscopy measurements.

The FFLO state is predicted for clean spin-singlet superconductors as a result of the competition between pairing correlations favoring anti-parallel spin alignment and the Zeeman effect favoring parallel spin alignment along the field. The compromise is a spatially inhomogeneous state of "normal" and "superconducting" regions. The "normal" regions are defined by a spectrum of spin-polarized quasiparticles. The high-field FFLO phase was originally suggested for superconductors with ferromagnetically aligned impurities, but it was soon realized that a FFLO state should develop in superconductors in an external field if the Zeeman coupling dominates over the orbital coupling.

We performed a comprehensive stability analysis of the nonuniform FFLO phases for two-dimensional (2-D) d-wave superconductors [3]. Our analysis is for applied fields parallel to the superconducting layers over the field range from the lower critical field, B_{c1}, to the upper critical field, B_{c2}. In this geometry the effect of the magnetic field on the superconducting condensate enters only through the Zeeman coupling of the quasiparticle spin to the field. For simplicity we assumed a cylindrical Fermi surface, which is also supported by de Haas-van Alphen measurements on $CeCoIn_5$.

By solving the Eilenberger equation in a magnetic field **B** for the quasiclassical Green's functions, we obtained information about the local density of states and the free energy density [3]. From the latter one we constructed the phase diagram shown in Fig. 1. The Larkin-Ovchinnikov (LO) state is stabilized in the high-**B**, low-T region of the phase diagram. The solid lines in Fig. 1 are second-order phase transition lines that determine the upper critical field, B_{c2}, and separate the normal and FFLO states below the critical point $T_{FFLO} = 0.56\ T_c$. Below $T \sim 0.06\ T_c$ a first-order transition (long-dashed line) occurs between order parameter modulations along [110] and [100] directions. At the lower critical field, B_{c1} a second-order transition (circles-solid) occurs between the uniform and nonuniform [110] oriented LO phase. The unphysical transition line from the uniform state into the [100] oriented nonuniform state is shown for comparison (short-dashed). The Chandrasekhar-Clogston phase transition line between the uniform superconducting and normal state would

be of first order below T_{FFLO} (dot-dashed), but is unphysical. However, it is of second order and physical above T_{FFLO} (thick dot-dashed).

The spin-polarized local quasiparticle density of states (LDOS) is very sensitive to domain walls, where the superconducting order parameter changes sign. In Fig. 2 we show the evolution of the LDOS for spin-up and spin-down excitations for $T/T_c = 0.15$ and $b = \mu B/2\pi T_c = 0.175$ at the domain wall [position (a)] and far away from it [position (b)]. The spin-down (spin-up) LDOS are shown as solid (dashed) lines. Two distinct Andreev bound states, split by $\Delta\varepsilon/2\pi T_c = 2b$, are seen in the middle panel. Once one moves far away from the domain wall [position (b)], see bottom panel, the Andreev bound states have decayed substantially.

In conclusion, the calculated phase diagram does not resemble the experimental one. However, the LDOS calculations suggest that the Andreev resonance spectrum may be used to identify experimentally the intrinsic structure of the FFLO phases. In particular, the topological Andreev bound state is shifted from zero energy by an applied magnetic field. Also their spatial distribution depends on the wavelength of the nonuniform modulations, which are controlled by the strength of the magnetic field. Besides the characteristic energy dependence of the resonances, their spatial periodicity in the FFLO state enables us to tell them apart from random impurities in scanning tunneling spectroscopy measurements.

For more information contact Matthias J. Graf at graf@lanl.gov.

[1] A. Bianchi, et al., *Phys. Rev. Lett.* **91**, 187004 (2003).
[2] H. Radovan, et al., *Nature* **425**, 51 (2003).
[3] A. B. Vorontsov, et al., *Phys. Rev. B* **72**, 184501 (2005).

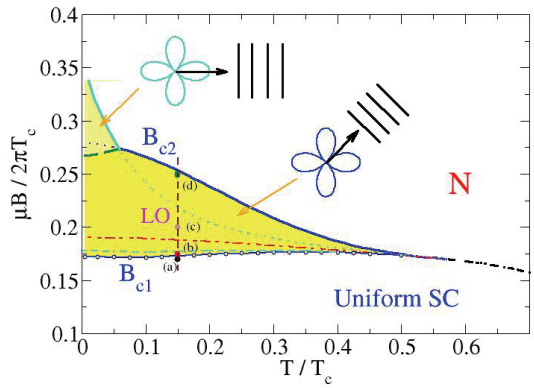

Fig. 1. *Phase diagram of FFLO phases of a 2-D d-wave superconductor (see text for description).*

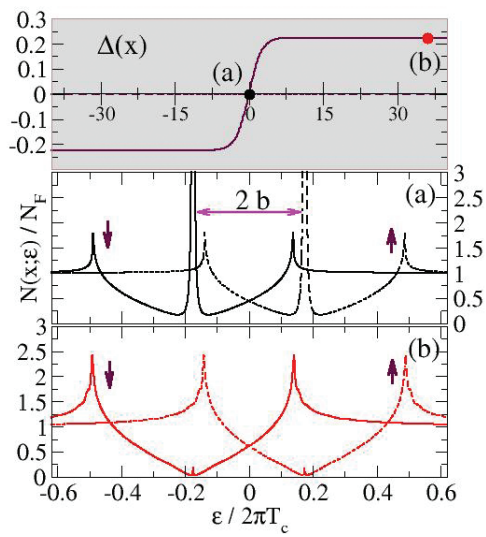

Fig. 2. *LDOS of spin-up (spin-down) excitations near a single domain wall at positions (a) and (b).*

Single Molecule DNA Sequencing with Inelastic Tunneling Spectroscopy STM

Jian-Xin Zhu, Kim Ø. Rasmussen, and Stuart A. Trugman, T-11; Alan R. Bishop, T-DO; and Alexander V. Balatsky, T-11

There is heightened interest in sequencing a genome, which is essential to personalized medicine. The inelastic electron tunneling spectroscopy is a well-established and powerful tool that allows the measurement of the characteristic energies of local and extended modes. The inelastic tunneling spectroscopy scanning tunneling microscopy (IETS-STM) serves to measure the local electronic properties coupled to local vibrational modes of atoms or molecules on a surface. Here we propose the use of STM to sequence a single DNA molecule.

The setup we propose, as shown in Fig. 1, is to use STM in a two-step process. First, we propose to locally excite the vibrational modes by injecting energetic electrons through the molecule into the substrate. The energy of the injected electrons is transferred to excite the vibration of individual base pairs. Second, to measure the local density of states (LDOS) in the vicinity of the injection point. The LDOS at a finite bias but with much smaller drive currents will allow measurement of the inelastic processes revealing the existence of the local vibrational modes. The features in LDOS once the local modes are excited are of main interest.

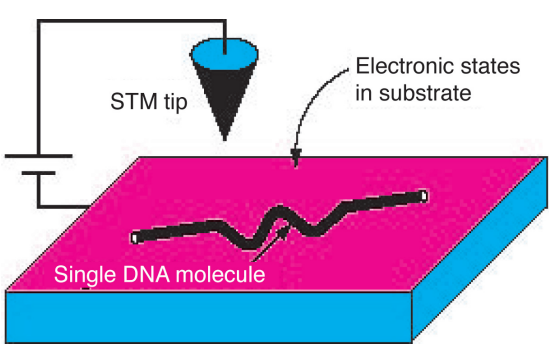

Fig. 1. ***Proposed experimental realizations: A single DNA molecule is placed on the metallic surface. An STM is used to inject/extract electrons from the substrate. Electron-vibration mode coupling can excite the local modes on the molecule.***

To illustrate how this technique works, we use the Peyrard-Bishop-Holstein model to describe the surface conduction electrons coupled to the lattice dynamics degrees of freedom in the single DNA molecule. Within the Peyrard-Bishop (PB) model for the displacement field, the most relevant degrees of freedom, namely the *transverse* stretching of the hydrogen bonds connecting complementary bases in the opposite strands of the double helix, are captured. The PB with fitted model parameters has been successfully compared with the denaturation experiments on short homogeneous sequence. A key observation here is that the adenine-thymine (A-T) base pair has two hydrogen bonds, while the guanine-cytosine (C-G) base pair has three hydrogen bonds. This difference leads to very different energy of low-lying vibrational excitations, which will be reflected in the lost tunneling electron energy to excite these modes, as will be shown below.

We have used the Green's function technique to calculate the change in the LDOS of electrons on the substrate. The correlation function for the displacement field of the base pair, which is involved in the electron self-energy is solved fully quantum mechanically via exact diagonalization. The derivative of the LDOS correction at the individual base pair, which corresponds to d^2I/dV^2 measured in the IETS experiment, is displayed in Fig. 2. The peaks in the figure identify the first excitation energy of the quantum oscillator corresponding to the A-T and C-G base pairs. They are E = 4.703 meV and E = 9.259 meV for A-T and C-G base pairs, respectively. The second group of peaks with much weaker intensity, which corresponds to the second low-lying excitations, comes uniquely from the anharmonicity of the base-pair potential. This feature is absent for the case of a harmonic potential.

Once the different characteristic energies of the vibrational modes associated with A-T and C-G bases are known, one is able to map out the spatial dependence of the energy-derivative LDOS. The quantity is mapped out through the imaging measurement of d^2I/dV^2 in an STM experiment. To be specific, we consider the following sequence as an example:

```
ACTCCAA
|||||||
TGAGGTT
```

Figure 3 shows the spatial variation of the energy derivative of the LDOS correction. The strongest intensity registers the location of individual A-T and C-G base pairs. The ripples away from the brightest spots simply manifest the Friedel oscillation. Our calculations suggest using a metallic substrate with high Fermi wave vector to achieve a high spatial resolution.

For more information contact Jian-Xin Zhu at jxzhu@lanl.gov.

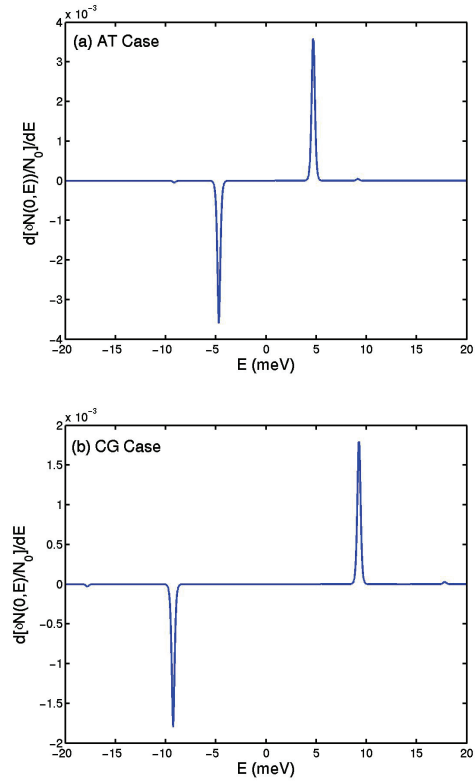

Fig. 2.
The derivative of the correction to the local density of states calculated at the location of an individual base pairs as a function of energy at low temperatures.

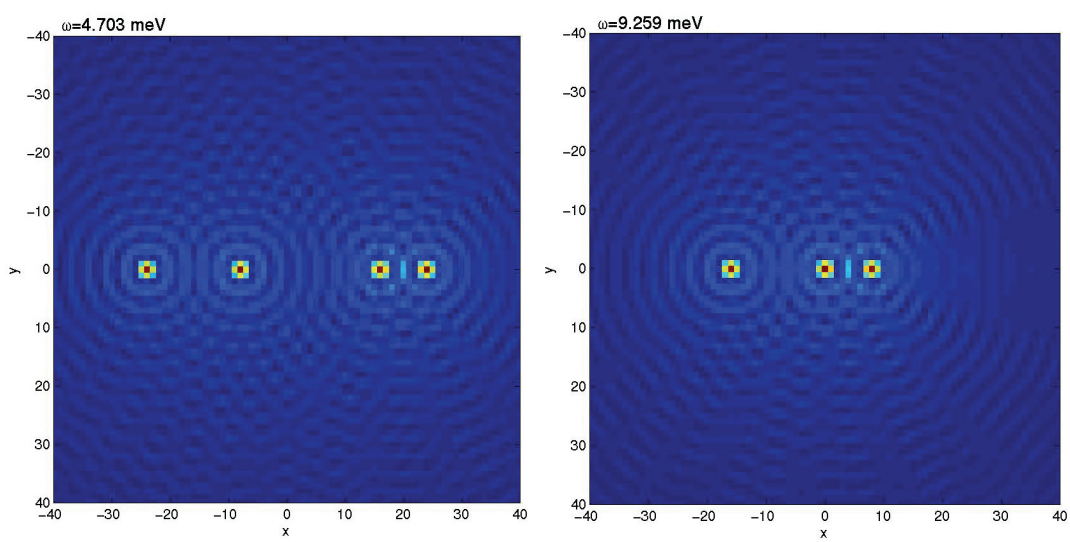

Fig. 3.
The spatial image of the derivative of the LDOS correction at energy ω = 4.703 meV and 9.259 meV at low temperatures.

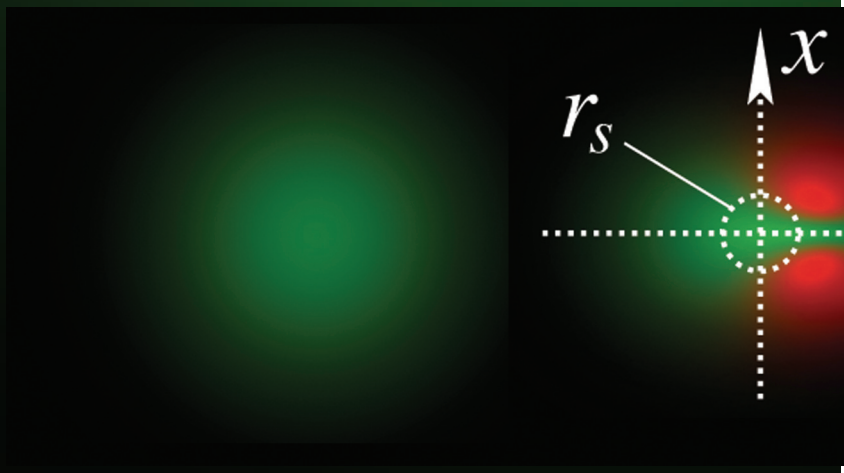
x
r_s

T-12 Theoretical Chemistry and Molecular Physics

Acting Group Leader: Joel Kress
505.667.8906, jdk@lanl.gov

T-12 Theoretical Chemistry and Molecular Physics is staffed by theoretical chemists and physicists who work on projects aimed toward an improved understanding of the behavior of materials. Projects in the group seek to describe how basic forces operating at the atomic and molecular level manifest themselves in the properties of matter at more macroscopic levels. Current activities in T-12 include research both in gas phase and condensed phase phenomena, and we apply state-of-the-art computational approaches in fundamental and applied studies of the physics and chemistry of molecules and materials.

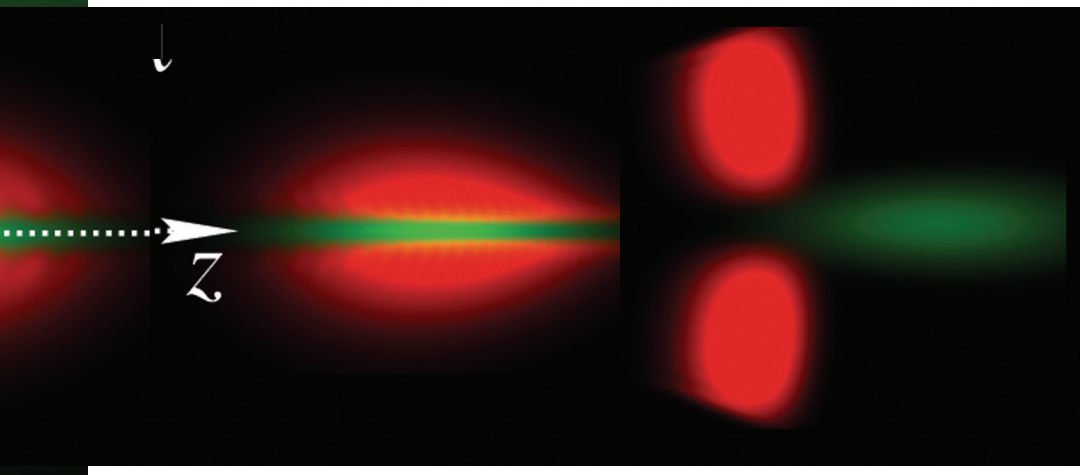

Increasing the Length Scale in Temperature Accelerated Dynamics Simulations

Jacques Amar and Yunsic Shim, University of Toledo; Blas Uberuaga, MST-8; and Arthur F. Voter, T-12

Molecular dynamics (MD) simulation is a powerful tool for probing systems in full atomistic detail. A general limitation, however, has been that the time scale is limited to nanoseconds, while many of the processes we wish to study take place over much longer times. Examples include film growth, bulk diffusion, and radiation damage annealing. Over the last few years, we have been developing *accelerated molecular dynamics* methods [1]. These methods extend the accessible simulation times for infrequent-event systems such as those mentioned above. Built on statistical mechanics principles, they give faster dynamical evolution from state to state without any prior assumptions about the atomistic mechanisms. The most powerful of these methods is temperature accelerated dynamics (TAD) [2], in which an elevated temperature is employed to speed the rate of transitions at the desired, lower temperature. Although direct high temperature dynamics would lead to an incorrect evolution from state to state, in the TAD method, the incorrect transitions are prevented, so that only the transitions that should occur at the lower temperature are accepted. When activation barriers are high relative to the temperature, TAD can give very large computational boost factors. For example, simulating vapor deposition of a metal film (e.g., Cu/Cu(100) at T = 77K [1]), gives a computational boost in the millions, allowing contact with the experimental deposition rate of monolayers per minute. These simulations exhibit surprisingly complicated mechanisms involving concerted motion of many atoms.

A serious limitation of TAD, however, is that only relatively small systems (e.g., ~10^3 atoms) can be treated. The computational scaling with the number of atoms, N, is roughly $N^{1.5}$ - N^3, depending on the ratio of the temperatures and the details of the implementation. This prevents TAD from being applicable to many important systems that have a natural length scale of thousands of atoms or more. In an effort to solve this problem, we are developing a way to spatially parallelize TAD by building on the synchronous sublattice algorithm (SSA) recently proposed by Shim and Amar [3] for parallelizing kinetic Monte Carlo simulations. In SSA, each processor is responsible for a spatial patch of the system, and each patch is further divided into subpatches, as shown in Fig. 1. Dynamical evolution is performed on one subpatch at a time, on all processors simultaneously. Cycling through the subpatch lattices gives very accurate evolution of the system provided the time slice for each subpatch is shorter than or comparable to the shortest event time. In the TAD implementation, each processor performs dynamics on a region larger than the subpatch, but only events centered within the subpatch are allowed to be accepted. Provided the subpatches are large enough to allow complex concerted events, the accuracy of the TAD method is retained.

In our first tests, we are studying the scaling behavior for the simple surface diffusion system shown in Fig. 2, in which the basic cell displayed in aqua is replicated to create a system of a desired size. Figure 3 shows preliminary timing results for both serial (nonparallel) TAD and the new SSA-TAD. The SSA-TAD has more overhead, but dramatically improved scaling is evident, allowing simulation of much larger systems than we have been able to do previously.

Moreover, for systems such as this that are free of long-range elastic relaxation, this scaling may flatten completely at larger sizes, so the accessible length scale would be limited only by the number of available processors. This would represent a significant breakthrough.

For more information contact Art Voter at afv@lanl.gov.

[1] A.F. Voter, et al., *Annu. Rev. Mater. Res.* **32**, 321 (2002).
[2] M.R. Sorensen and A.F. Voter, *J. Chem. Phys.* **112**, 9599 (2000).
[3] Y. Shim and J.G. Amar, *Phys. Rev. B* **71**, 125432 (2005).

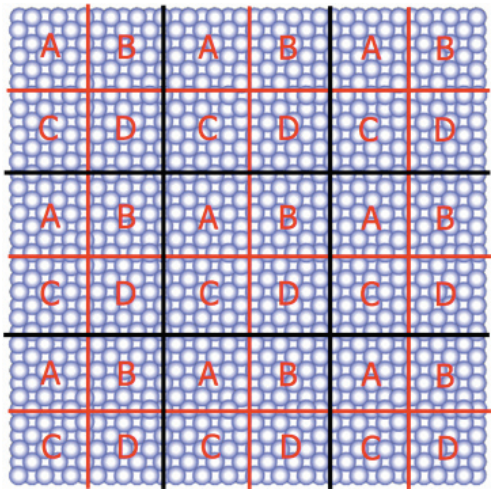

Fig. 1.
Schematic illustration of the synchronous sublattice algorithm (SSA) for spatially parallelizing kinetic Monte Carlo or temperature accelerated dynamics (TAD). A 9-processor case is shown.

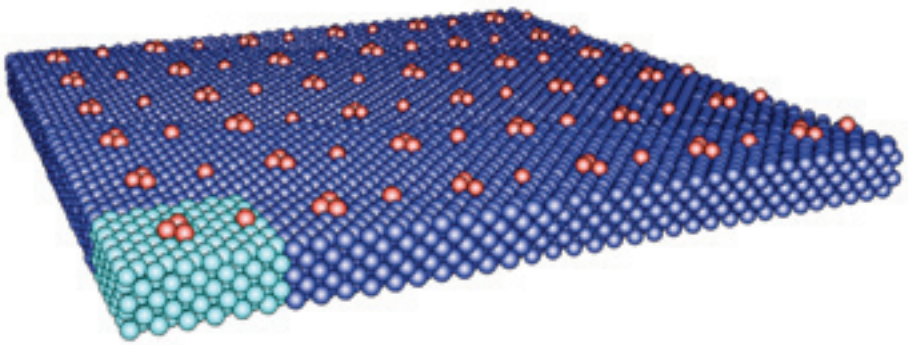

Fig. 2.
Cu/Cu(100) surface diffusion test system for SSA-TAD scaling tests. A 6x6 case for 36 processors is shown, while the unit cell (1x1) is indicated by aqua coloring.

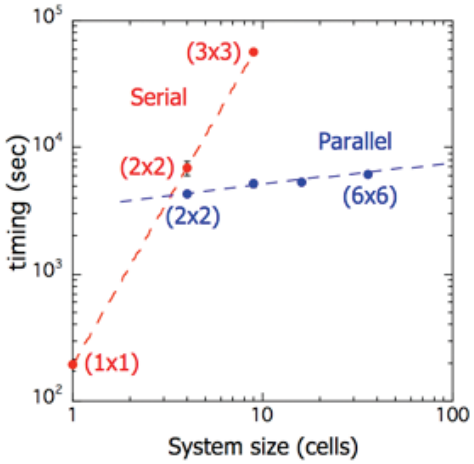

Fig. 3.
Timing results for TAD (red) and parallel SSA-TAD (blue) for propagation of the Cu/Cu(100) system at T = 100K for 0.01 s, using a high temperature of T = 600 K.

Role of Fluctuations in a Snug-fit Mechanism of KcsA Channel Selectivity

D. Asthagiri and Lawrence R. Pratt, T-12; and Michael E. Paulaitis, Ohio State University

A tetrameric constellation of four TTVGYG amino acid sequences comprises the selectivity filter of the KcsA channel shown in Fig. 1. This signature sequence is strongly conserved across a variety of K^+ channels [1]. In each binding site, e.g., the S_2 site defined by $(VG)_4$, the ion is coordinated by four carbonyl oxygens from above and four from below. One mechanism for selectivity based on the atomic structure of the KcsA channel invokes the size difference between K^+ and Na^+, and the molecular complementarity of the selectivity filter with the larger K^+ ion [1]. An alternative view holds that size-based selectivity is precluded because atomic structural fluctuations are greater than the size difference between these two ions [2]. This view is based on extensive free energy calculations that show local interactions leading to structural flexibility of the binding site provides selectivity for K^+. Turning off the electrostatic repulsions between the carbonyl oxygens, while retaining ion-carbonyl oxygen electrostatic attractions shifts the selectivity in favor of Na^+.

We note that these two views are not mutually exclusive. For example, artificially turning off electrostatic repulsions between the carbonyl oxygens while maintaining the ion-carbonyl oxygen attractions collapses the filter around either ion, and the extent of this collapse will depend on the size of the ion. The combination of size differences and fluctuations is also seen in the bulk hydration properties of these two ions. Notably, the partial molar volume of K^+ in water is positive, while the partial molar volume of Na^+ in water is negative [3].

Here we follow [2] in studying a simplified model of the S_2 site of selectivity filter to examine the role of fluctuations in KcsA channel selectivity. The equilibrium selectivity of the filter can be characterized by the difference in the interaction free energy for transferring Na^+ from water into the selectivity filter compared to K^+. Thus, we study

$$\begin{aligned}\Delta\mu^{ex} &= [\mu^{ex}_{Na^+}(filter) - \mu^{ex}_{K^+}(filter)] \\ &\quad -[\mu^{ex}_{Na^+}(aq) - \mu^{ex}_{K^+}(aq)] \\ &\equiv \Delta\mu^{ex}(filter) - \Delta\mu^{ex}(aq), \qquad (1)\end{aligned}$$

where $\mu_x^{ex}(aq)$ ($X = K^+, Na^+$) is the hydration free energy of the ion, and μ_x^{ex} (*filter*) is the analogous quantity in the selectivity filter. The excess chemical potential, μ_x^{ex}, is that part of the chemical potential that would vanish if intermolecular interactions were to be neglected. μ_x^{ex} to the ideal gas result at the same density and temperature. A standard state could be adopted in which $\Delta\mu^{ex}$ would vanish, but that would not change any physical consideration.

The potential distribution theorem [4, 5] tells us how μ_x^{ex} may be calculated from the probability density distribution of the binding energy, ε, of the X ion to the medium. This function is generated with the ion and the medium fully coupled at temperature $T = 1/k_B\beta$ where k_B is Boltzmann's constant. In the present approach, ion positions contributing to the sample are those corresponding to its natural motion in water or in the ion-protein system. If the probability density function is described by a Gaussian of mean $\langle\varepsilon\rangle$ and variance $\sigma^2 = \langle(\varepsilon-\langle\varepsilon\rangle)^2\rangle$, then

$$\mu_X^{ex} = \langle\varepsilon\rangle + \beta\sigma^2/2. \qquad (2)$$

Note that in sampling the fully-coupled system the term $\beta\sigma^2/2$ raises the chemical potential above the mean binding energy $\langle\varepsilon\rangle$. As a check of Eq. 2, we also computed $\Delta\mu^{ex}$ by transforming K^+ to Na^+ on the basis of a coupling-parameter integration through 20 intermediate states. Details of the theory, calculations, and molecular dynamics simulations are given in the supplemental material.

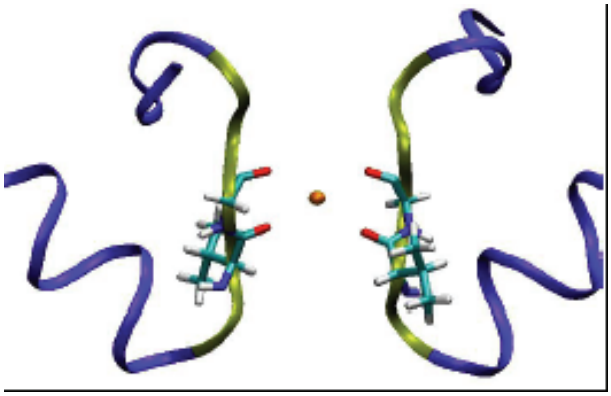

Fig. 1. *Depiction of the channel filter. Only two of the four chains are shown.*

The bulk hydration free energies set the baseline for filter selectivity as is evident in Eq. 1. Coupling-parameter integration yields -20.7 kcal/mol for $\Delta\mu^{ex}(aq)$, in good agreement with [6]. A gaussian model gives -23.0 kcal/mol. It is estimated that $\Delta\mu^{ex}$ is 6 kcal/mol [2], or roughly three times smaller than the difference in bulk hydration free energies. Thus the hydration thermodynamic properties in bulk solution provide the biggest contribution to Na^+/K^+ selectivity.

Figure 2 shows the distribution of ion-carbonyl oxygen binding energies. It is clear that the mean binding energy of Na^+ with the filter is much lower than that for K^+. The distribution of energies for Na^+ is also much broader. The magnitude of the implied difference in fluctuation contributions is comparable to the net selectivity, and this difference is the final contribution discriminating Na^+ from K^+. Analysis of those fluctuation contributions shows that filter configurations conducive to binding Na^+ are constricted and rare occurrences in the ensemble of conformations favorable to binding K^+. We conclude that energetically favorable ion binding in the selectivity filter occurs for both Na^+ and K^+. For Na^+, this is achieved at the expense of enhanced energetic and positional fluctuations compared to K^+, the ion considered to have a better geometrical fit in the selectivity filter. In this sense, the *difference in size* between Na^+ and K^+, and the *molecular complementarity* of the selectivity filter with K^+ play an important role in channel selectivity. Fluctuations induced by the more favorable binding of the smaller Na^+ in the selectivity filter must also be considered, however, and it is this contribution to the binding free energy that discriminates K^+ from Na^+. The key result, that has not been appreciated so far [1, 2], is the *joint* association of strong binding, constriction of the filter, and enhanced fluctuations in the case of the smaller Na^+ ion. The constriction of the filter by the Na^+ ion, relative to the natural fit of K^+ ion, is consistent with the experimental fact that the partial molar volume of K^+(aq) is positive, while the partial molar volume of Na^+(aq) is negative.

For more information contact Lawrence R. Pratt at lrp@lanl.gov.

[1] D.A. Doyle, et al.,*Science* **280**, 69–77 (1998).
[2] S.Y. Noskov, et al., *Nature* **431**, 830–834 (2004).
[3] H.L. Friedman and C.V. Krishnan, "Thermodynamics of Ion Hydration," in F. Franks (Ed.), *Water: A Comprehensive Treatise* (Plenum, New York, 1973), Vol. 3, pp. 1–118.
[4] T.L. Beck, et al., *The Potential Distribution Theorem and Models of Molecular Solutions* (Cambridge University Press, Cambridge, UK, 2006).
[5] M.E. Paulaitis and L.R. Pratt., *Adv. Prot. Chem.* **62,** 283–310 (2002).
[6] D. Beglov and B. Roux, J. *Chem. Phys.* **100,** 9050–9063 (1994).

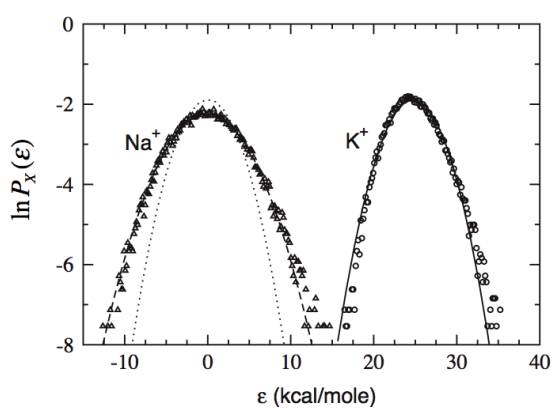

Fig. 2. *Normalized distributions of ion-carbonyl oxygen binding energies, for X = Na+ or K+. The abscissa is the binding energy differences from the mean value for the Na+ case. Solid curves are gaussian fits to the data. The dashed curve is the K+ gaussian model translated leftward to superpose the K+ gaussian model on the Na+ data, showing that that the Na+ distribution is significantly wider.*

Structure and Electronic Excitations in Organometallic Transition Metal Complexes

Enrique R. Batista and Richard L. Martin, T-12

In support of energy programs at the Laboratory, we have been studying the photophysics of Pt-acetylide complexes of interest in the context of the next-generation-lighting initiative, as well as the behavior of molecular systems that mimic Nature's ability to split water into its elemental components. A hydrogen-based economy is feasible only if hydrogen is produced from nonfossil sources. Therefore, molecular systems capable of splitting H_2O using solar energy only have been the focus of our research. To find new, more efficient luminescent materials, we have been studying with researchers within and external to the Laboratory new molecular systems currently being used for organic light-emitting diodes (OLEDs) and for new types of nanowires. The set of materials based on platinum-acetylide π-conjugated oligomers has prompted great interest in recent years for their potential applications in highly efficient organic electroluminescent devices [1]. In these compounds the π-orbitals of the ligands are conjugated with the d orbitals of the Pt allowing for charge migration along the oligomers. Electroluminescence in these materials might also be expected to be reasonably efficient, as the presence of the metal and the consequent spin-orbit coupling would allow both singlet and triplet electron-hole pairs to recombine emissively, an option not available to purely organic polymers due to the strong enforcement of spin selection rules in the light atoms.

In a collaboration with experimentalists in Los Alamos' Bioscience Division and the University of New Mexico we have studied the behavior of electronic excitations in platinum-acetylide complexes. The hybrid density functional theory (DFT) results were analyzed via the computational technique of Natural Transition Orbitals (NTOs) developed at the Laboratory [2]. As shown in Fig. 1, phosphorescence in the platinum monomer comes from a triplet state localized on one side of the molecule, which generally goes by the name of the 2nd order Jahn-Teller effect. This localization stems from a coupling between the electronic state and the vibrational modes of the molecule. After absorption of energy there are two nearly degenerate excited states that can mix with each other upon a geometric deformation of b_{3u} symmetry. Figure 2 shows the energy landscape of the excited states of the molecule which couples the two electronic states. Using linear response theory (commonly referred in the literature as time dependent DFT, TD-DFT) we were able to estimate the barrier for charge migration of the electronic excitation and the phosphorescence emission energy. The latter is in good agreement with experiment [3]. The former led us to predict that the charge

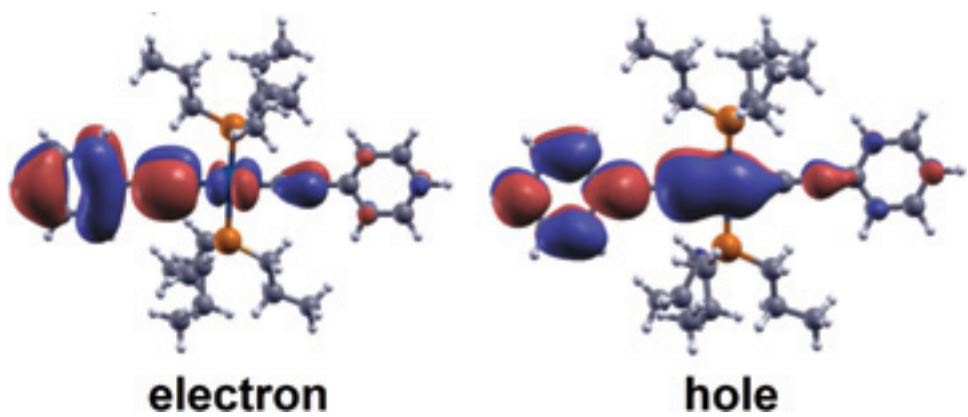

Fig. 1.
The electron and hole pair in the lowest excited state spontaneously localizes on one half of the molecule. This is due to a coupling of the electronic state with a phonon mode that causes the molecule to deform along a b3u mode breaking the symmetry of the molecule. The ethynyl triple bond is weakened in the excited state because of one of the electrons being promoted from the π bonding orbital to a π anti-bonding orbital which leads to a signature in the experimental infrared spectrum.*

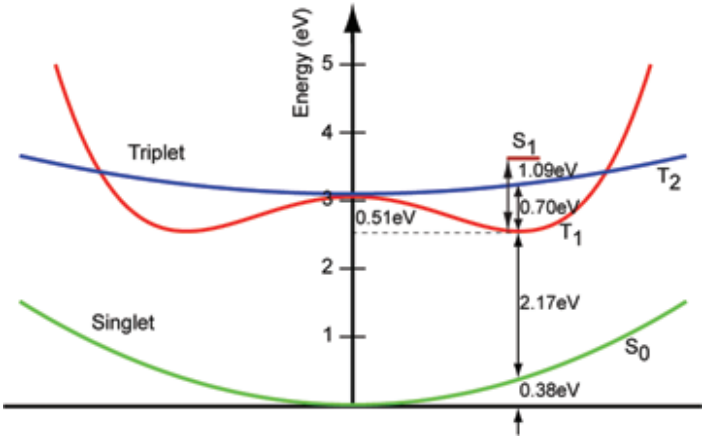

Fig. 2. *Energy landscape for the electronic excitation of $Pt(P(^nBu)_3)_2$(ethynylbenzene)$_2$ calculated via linear response theory (TD-DFT). The calculated energies are in good agreement with the measurements of Liu and coworkers [5].*

migration in these systems will be via an activated hopping mechanism with a barrier of 0.5 eV. This localization persists in longer oligomers. Figure 3 shows the lowest electronic excitation for the platinum-trimer, which also spontaneously localizes on a phenyl ring.

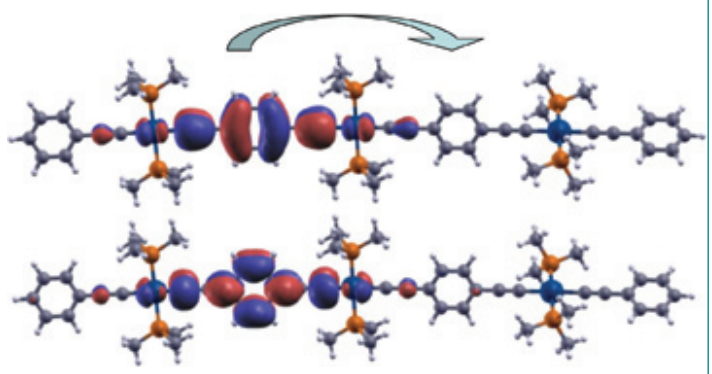

Fig. 3. *In longer oligomers the electron and hole pair in the lowest excited state also localizes spontaneously on one phenyl ring and neighboring ethynyl groups. The conjugation of the excited-state orbital with the d orbital on the platinum facilitates the migration of the excitation. This migration happens via an activated hopping with activation barrier of about 0.60 eV.*

Water oxidation catalysts such as the blue dimmer $[(bpy)_2(H_2O)Ru^{III}ORu^{III}(OH_2)(bpy)_2]^{4+}$ (1) and the recently discovered $[Ru_2^{II}(bpp)(trpy)_2(H_2O)_2]^{3+}$ (2) continue to stir interest in the context of water converting into its constituents for the production of molecular hydrogen using only solar energy. We have studied both these molecules using *ab-initio* techniques. For complex 1 our calculations of vibrational frequencies aided experimental groups in Los Alamos' Materials Science and Technology Division and the University of North Carolina in the interpretation of UV-vis and Raman spectra. In complex 2 we are presently studying the catalytic mechanism. Thus far we have characterized the structure of various steps in the water splitting process. In that vein, it is significant that upon deprotonation of complex 2, we observed that a hydrogen bond network formed in the H_2O solvent next to the ruthenium dimer (see Fig. 4). This explains the lowering in pK_a observed by Sens et al. [4].

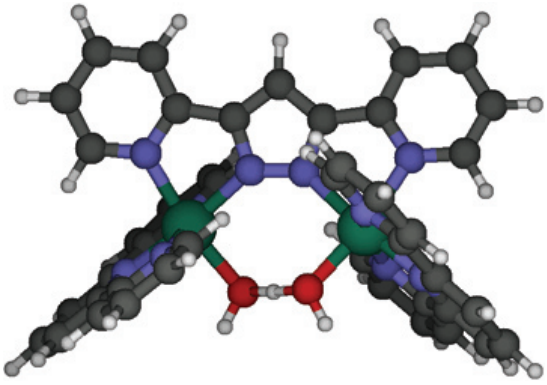

Fig. 4. *Optimal structure of the hydroxo-aqua state of $[Ru^{2II}(bpp)(trpy)_2(OH_2)(OH)]^{3+}$. Upon deprotonation of complex 2, we observed that a hydrogen bond network is formed in the solvent next to the ruthenium dimer. This explains the lowering in pKa observed by Sens et al. [4].*

For more information contact Enrique R. Batista at erb@lanl.gov.

[1] M.A. Baldo, et al., *Nature* **395**, 151 (1998); J.S. Wilson, et al., *Nature* **413**, 828 (2001).
[2] R.L. Martin, *J. Chem. Phys.* **118**, 4775 (2003).
[3] E.R. Batista and R.L. Martin, *J. Phys. Chem. A* **109,** 9856 (2005).
[4] C. Sens, et al., *J. Am. Chem. Soc.* **126**, 7798 (2004).
[5] Y. Liu, et al., *J. Am. Chem. Soc.* **124**, 12412 (2002).

A Mechanism for the Mullins Effect

David E. Hanson, T-12; and Marilyn Hawley and Robert Houlton, MST-8

Under repeated tensile strain, many particle-filled polymers such as silica-filled polydimethylsiloxane (PDMS), exhibit a reduction in stress after the initial extension, the so-called Mullins Effect [1] (see Fig. 1). Understanding the underlying physical mechanism is considered crucial to the development of predictive constitutive and aging models for filled polymers. However, despite more than 50 years of research, the origin of the Mullins Effect is still considered "one of the most important problems in rubber elasticity" [2]. We have developed a theoretical framework that suggests a mechanism to account for this effect [3]. Qualitatively, it accounts for most of the phenomenology associated with the Mullins Effect and makes an additional prediction: stress softening should not occur when the second strain axis is perpendicular to the initial strain axis. This has now been confirmed by experiments at the Laboratory.

Silica-filled PDMS is a material with widespread industrial uses as well as for cushions and mechanical supports in nuclear weapons. It derives its strength by virtue of the continuous, high functionality network that arises due to polymer chains adhering to the surfaces of silica filler particles by Van der Waals' and electrostatic forces. Chain entanglements, created during material preparation, can be permanently removed, under tensile strain, by chains sliding past one another at a connection point on a particle surface, by temporarily breaking (and then reforming) the weak Van der Waals' and electrostatic bonds. Previous estimates of this binding energy and the entanglement density are consistent with the strain energy observed in experiments. We propose that it is this removal of entanglements that produces the initial stress and that the stress observed during the second and subsequent strains can be attributed to elastic chain forces. For subsequent strains, larger than the first, new entanglements will be encountered and similarly removed, causing the stress to recover to the initial strain levels as shown in Fig. 1. This accounts for the material's apparent *memory* of its previous maximum strain state. Clearly, whether two proximate chains are entangled depends on their orientation with respect to the strain axis. It follows that, under tensile strain, only those entanglements associated with the strain axis are removed; entanglements associated with strains along axes perpendicular to the first strain would likely not be affected. From this observation, we can then predict that, if the material is subsequently strained along an axis orthogonal to the first strain axis, strain softening should not be observed. The experimental data shown in Fig. 2 confirms that this is indeed the case.

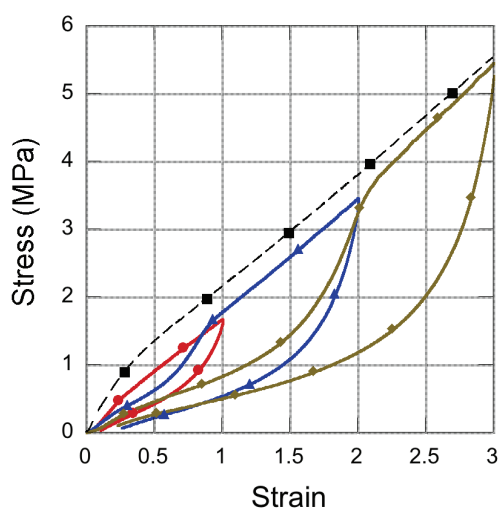

Fig. 1. ***Sequential tensile strain cycles for virgin silica-filled PDMS sample showing stress softening: first pull to 100% (circles), second pull to 200% (triangles), third pull to 300% (diamonds). Also shown is the initial stress/strain for a separate sample pulled to 300% (squares).***

The shape of our stress vs strain curves for the initial extension (Fig. 1), which is typical of other experimental results in the literature, exhibits a steep increase in stress, followed by a more gradual, nearly linear increase with strain up to the point of tensile failure. According to

our proposed mechanism, the stress is due to the rate (with respect to strain) at which chain entanglements are removed. Neglecting for the moment the fact that the chains initially have slack, we conjecture that the chain-crossing rate is proportional to the angular density of chain end-to-end vectors, $s(\lambda) = \alpha H(\lambda)$, where s is the stress, λ is the extension factor, α is a proportionality constant, and H is the angular density of chain end-to-end vectors. By assuming the tensile strain is described by an affine transformation, we can obtain an expression for the average end-to-end angle as a function of λ and use its inverse as an estimate for the angular density:

$$H(\lambda) = \theta_{avg}^{-1} = \left[\frac{2}{\pi} \int_0^{\frac{\pi}{2}} cos^{-1} \left(\frac{\lambda \cos\theta}{\left[\frac{\sin^2\theta}{\lambda} + \lambda^2 \cos^2\theta \right]^{1/2}} \right) d\theta \right]^{-1}$$

As shown in Fig. 3, this function is in qualitative agreement with the experimental initial stress. We feel that our theoretical and experimental work provides a significant step in understanding stress softening in filled polymers.

For more information contact David Hanson at deh@lanl.gov.

[1] L. Mullins, *Rubber Chem. and Tech.* **42**, 339–361 (1969).
[2] M. Mark, et al., *Physical Properties of Polymers* (American Chemical Society: Washington, D.C., 1984).
[3] David E. Hanson, et al., *Polymer 46*, 1089–10995 (2005).

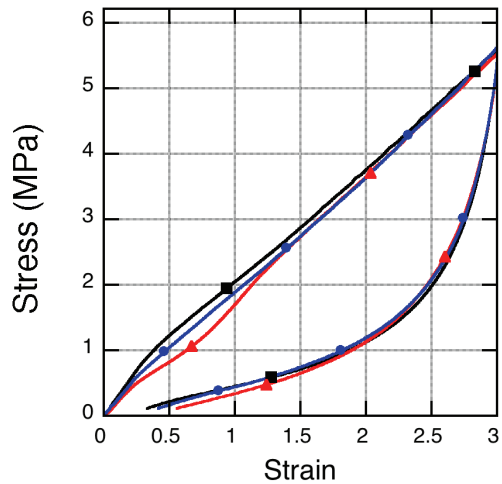

Fig. 2. *Tensile stress/strain for secondary strain for small dog-bone samples cut and strained: perpendicular to initial strain axis (circles), and parallel (triangles). Also shown for comparison is initial stress/strain for a control sample (squares). Note that stress softening is not apparent in the secondary stress curve strained perpendicular to the original strain axis.*

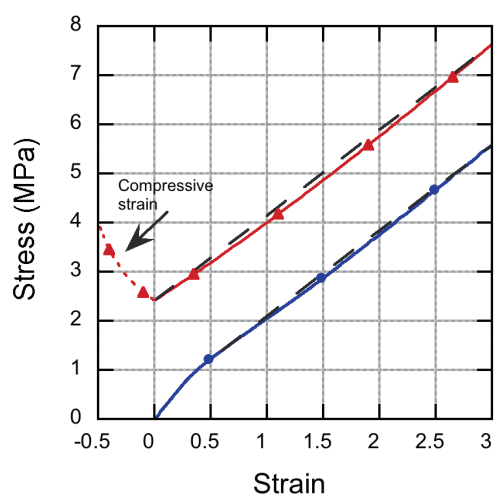

Fig. 3. *Comparison of angular density of chains function, H(λ) (triangles), and experimental data (circles). The experimental data is for the initial tensile strain and the angular density function has been scaled to have the same slope as the experimental data. Also shown adjacent to each curve is a straight line (dashed) for comparison. H(λ) for compressive strains (λ< 0) is also shown.*

Electronic Interactions in Organometallic Actinide Complexes

P. Jeffrey Hay, Richard L. Martin, Enrique R. Batista, T-12; and Aurora E. Clark, Washington State University

We have been examining the electronic interactions in organometallic complexes of the actinide and lanthanide elements using density functional theoretical (DFT) approaches. These interactions determine the chemical bonding in the ground state and define the nature of the excited electronic states as probed spectroscopic and magnetic techniques. One class of molecules synthesized and characterized extensively by our colleagues in the Chemistry Division are the ketimido complexes $(C_5R_5)_2M(N{=}CPh_2)_2$ where M = Th and U and R=CH_3 (Ref. [1]). In each complex there is a metal in the +4 oxidation state, having either a $5f^0$ (Th) or $5f^2$ (U) electronic configuration, surrounded by two Cp* (C_5R_5) and two nitrogen ketimido ligands. The optimized structures of the complexes as calculated using DFT agree well (typically within 0.01 – 0.02 Å) with values from experimental crystal structures. The results exhibit the expected shortening of the M-N bond length as one goes down the actinide series from Th (R = 2.25 Å) to U (R = 2.17 Å). For the electronic excited states we have employed the time-dependent DFT method with the hybrid B3LYP functional to calculate the excited states of the system. As shown schematically in Fig. 1, the low-lying electronic states arise from excitations of the two highest occupied orbitals (HOMO), denoted lone pairs on the nitrogen (N 2p), to the two lowest unoccupied orbitals (LUMO), denoted pi antibonding (CN π*). The theoretical assignments of excitations localized primarily on the ligand with some metal admixture is also borne out by the extensive experimental studies that have been carried out on Zr, Th and U ketimido complexes [2].

A major focus in this project has been the synthesis of assemblies comprised of two or more metal centers having unpaired f electrons and examining the resultant electronic coupling between the metal centers across the intervening organic linkages. Bimetallic ketimido analogs have been made containing two Th or U centers. Our results show the electronic structure mirrors the monometallic species with a similar set of orbitals involved in the excitations (except there are now four occupied and four virtual levels compared to Fig. 1). The calculated spectra for ketimido complexes with one and two Th centers are compared in Fig. 2, where the lowest observed energy absorption peak (~ 2.6 eV) arises from two singlet states (calc. 2.7 – 2.8 eV) in the monomeric species and from four singlet states (calc. 2.4 – 2.5 eV) in the dimeric species.

A second example of unusual bonding in organoactinide species is provided by another unusual bis-imido complex of uranium in the +6 oxidation state (Fig. 3). This represents the first known nitrogen complex with linear (RN)=U=(NR) imido linkages analogous to the well-known uranyl $(O{=}U{=}O)^{2+}$ ion prevalent in solution chemistry

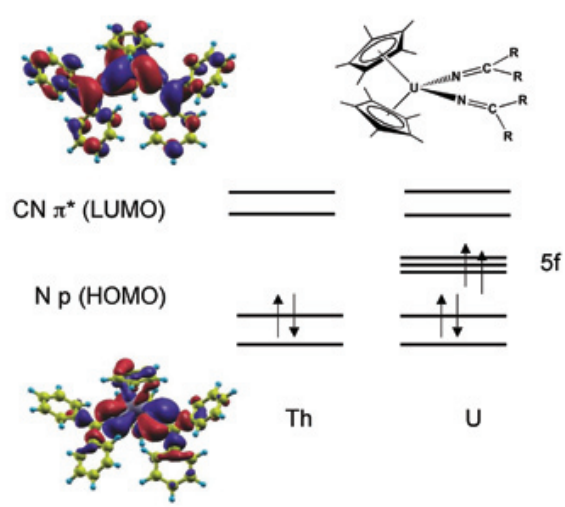

Fig. 1.
Schematic diagram of the electronic structure of the $(C_5R_5)_2M(N{=}CPh_2)_2$ molecule showing the two highest occupied and two lowest unoccupied levels.

[3]. The NR groups can have either alkyl or phenyl substituents. Hybrid DFT calculations were used to understand the role of U 6d and 5f orbitals in the multiple bonds formed to the nitrogens and to compare with the bonding to oxygen in the uranyl species. The calculated U-N bond length (1.85 Å) and N-U-N bond angle (175 deg) for the complex shown in Fig. 3 (R=CH_3) are in close agreement with the experimental structures. We find strong admixture of 6d (up to 24%) and 5f (up to 32%) in the six molecular orbitals comprising the three U-N bonds that is also reminiscent of the metal participation in the uranyl ion. The vibrational frequencies were also computed to help in assignment of the infrared spectrum.

These illustrations demonstrate how current theoretical methods employing DFT can be applied to unravel issues in actinide chemistry using realistic ligands in the calculations.

For more information contact Jeffrey Hay at pjhay@lanl.gov.

[1] A.E. Clark, et al., *J. Phys. Chem. A* **109**, 5481 (2005).
[2] R.E. Da Re, et al., *J. Am Chem. Soc.* **127**, 682 (2005).
[3] T.W. Hayton, et al., *Science* **350,** 1941 (2005)**.**

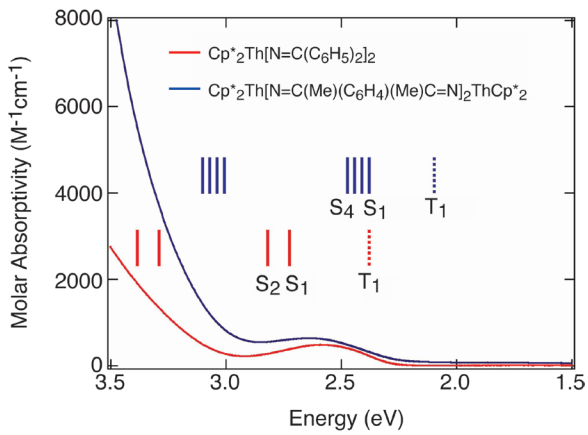

Fig. 2. *Comparison of the predicted excitations for the mono- and bimetallic Th ketimido complexes from time-dependent DFT calculations with the observed experimental spectra. The excitations for these lowest states arise from the levels shown in Fig. 1.*

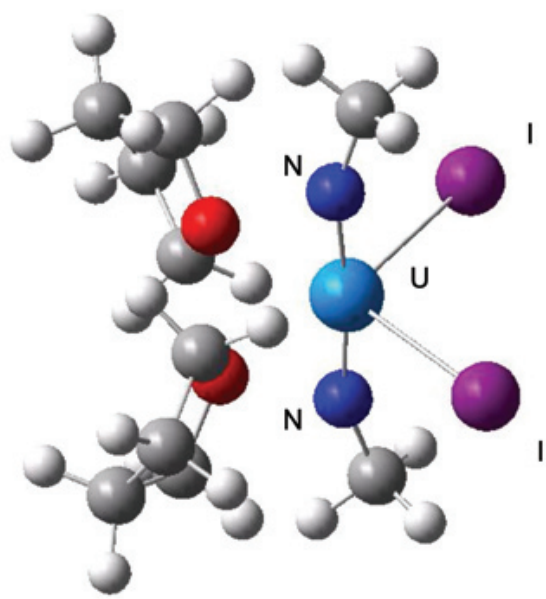

Fig. 3. *Calculated structure of the U complex $U(=NCH_3)_2(I)_2(THF)_2$ that exhibits a linear N=U=N bond as also observed in the crystal structures of several recently synthesized compounds. THF denotes tetrahydrofuran (C_4H_8O) ligand.*

Simulating the Structure and Properties of Magnesium Methoxide

Neil J. Henson, T-12, and Kevin C. Ott, C-SIC

Magnesium methoxide has been intensively studied as a precursor for synthesis of inorganic materials such as perovskite-type mixed oxide phases. Here we are interested in possible uses as a hydrogen storage material. Hydrogen can be routinely generated from reacting methanol with water at high temperature in a process called steam reforming. This process can be represented as:

$$CH_3OH + H_2O \rightarrow 3H_2 + CO_2$$

In an industrial setting, this reaction is catalysed by a Cu/ZnO catalyst. There is evidence that it is the strain on the copper particle caused by the ZnO support that is responsible for the catalyst activity. This study is focused on the study of the elementary chemical processes that occur when magnesium methoxide is heated or calcined.

The crystal structure of magnesium methoxide has been studied using x-ray diffraction by Starikova and coworkers [1] and consists of several structural elements. Unusually for an inorganic solid, the material is a molecular solid built of residues belonging to four types: (i) $[Mg_4\{\mu_3\text{-OMe})_4(OMe)_2(MeOH)_{10}]^{2+}$ cations, (ii) $[(MeO)_2H]^-$ anions, (iii) $[Mg_4\{\mu_3\text{-OMe})_4(OMe)_4(MeOH)_8]$ neutral molecules, and (iv) noncoordinating methanol molecules linked in a 3-D hydrogen-bonding framework. The crystal structure showing the packing of each of the types is shown in Fig. 1. Both the cationic and neutral species are based on the cubane-like structure, which is shown more clearly in Fig. 2.

The eight vertices of the cube are formed from four OMe species and four Mg^{2+} cations. An additional three methoxide or methanol ligands complete the octahedral coordination environment around magnesium; whether these additional ligands are protonated or not determine the overall charge state of the cluster.

We calculated the thermodynamics of the abstraction of a hydrogen atom from various models for magnesium methoxide and also, as a baseline, from a single isolated methanol molecule. We were primarily interested in the breaking of C-H bonds, since this step must occur to ultimately form hydrogen. As a competing reaction, we also considered the breaking of the C-O bond to form a carbon radical species. The calculations were performed using the quantum chemistry software, *Gaussian03* [2]. The PBE density functional was used with a 6-31G* basis set. The results for the isolated methanol molecule are given below:

$$CH_3OH \rightarrow CH_3^{\bullet} + OH^{\bullet} \qquad \Delta E = +432.0\ kJmol^{-1}$$

$$CH_3OH \rightarrow CH_2OH^{\bullet} + H^{\bullet} \qquad \Delta E = +428.0\ kJmol^{-1}$$

This suggests that the C-O bond is the stronger bond in a single methanol molecule.

In the case of magnesium methoxide, we built a cluster model such that the overall charge was neutral [(unit (iii) above)]. In the case of the C-H bond breaking process, there are two possible bonds to consider corresponding to hydrogen abstraction from a methoxy species acting as an additional ligand to magnesium ($MgOCH_2$-H), and also from a methoxy species forming the corner of the cube (OCH_2-H). The results of the calculations on these models are:

$$[\text{Mg-cube}]\text{-}MgOCH_2\text{-}H \rightarrow [\text{Mg-cube}]\text{-}MgOCH_2^{\bullet} + H^{\bullet} \qquad \Delta E = +401.9\ kJmol^{-1}$$

$$[\text{Mg-cube}]\text{-}OCH_2\text{-}H \rightarrow [\text{Mg-cube}]\text{-}OCH_2\bullet + H\bullet$$
$$\Delta E = +429.7\ \text{kJmol}^{-1}$$

We predict a slightly stronger bond in the case of the corner methoxide, although the difference is undoubtedly within the error of the calculation.

Starikova and coworkers further report that upon calcination an amorphous product is formed and speculate that the structure of this material may be related to that observed for the calcium ethoxide crystal structure determined by Turova and co-workers [3]. In this case, the dominant structural unit is a double cube with metal-oxo bridges on the shared faces as in Fig. 3.

Since the calcined structure is the dominant phase in the industrial environment, we are currently performing further calculations to assess the impact of this new structural model on our calculated energies.

For more information contact Neil Henson at neil.henson@lanl.gov.

[1] Z.A. Starikova, et al., *Polyhedron* **16**, 967–974 (1997).
[2] M.J. Frisch, et al., *Gaussian 03*, Revision C.02 (Gaussian, Inc., Wallingford, CT, 2004).
[3] N.Y. Turova, et al., *J. Chem. Soc. Chem. Comm.*, **21–23** (1993).

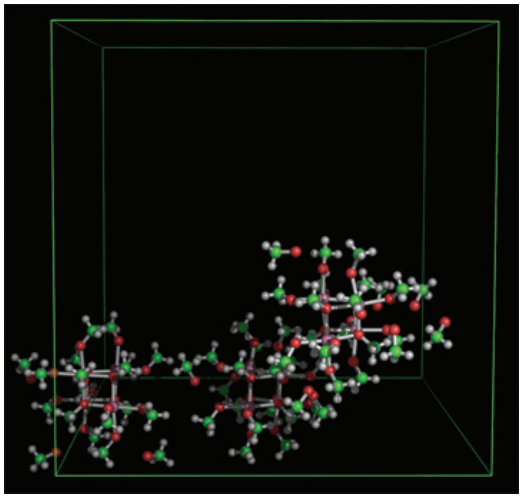

Fig. 1. *Crystal structure of magnesium methoxide after Starikova and co-workers [1] (carbon: green, oxygen: red, hydrogen: white, magnesium: purple).*

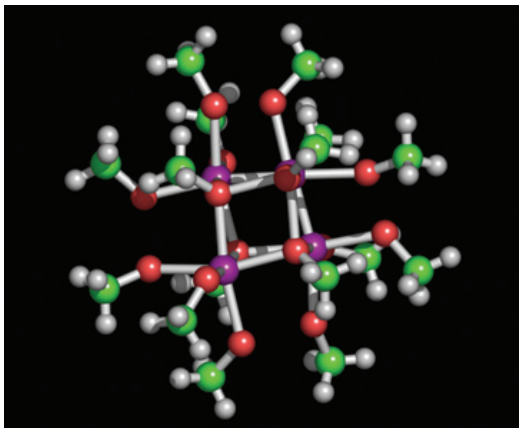

Fig. 2. *The cubane-like structural unit in magnesium methoxide.*

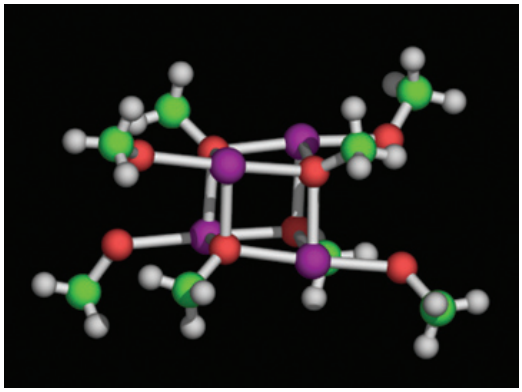

Fig. 3. *Double cube model for calcined structure.*

Update on the Aging of PBX 9501 via Free-Radical Oxidation

Joel D. Kress, T-12

The plastic-bonded explosive PBX 9501, used in weapons, is 94.9% by weight HMX explosive, 2.5% nitroplasticizer (NP), 2.5% Estane® 5703, and 0.1% Irganox 1010 stabilizer (anti-oxidant). Estane® 5703, made by Noveon, is a poly(ester urethane) random copolymer (Fig. 1), which serves as a glue that binds the HMX crystals together to allow for machining of high-precision high-explosive parts. The urethane units segregate (phase separate) into "hard" domains that act as physical crosslinks between the "soft" polyester domains. The NP softens the Estane, and together this markedly decreases the mechanical sensitivity of the PBX. However, the Estane slowly degrades in time, and the corresponding effect on the mechanical properties of the PBX raises safety and reliability concerns. Hence, the study of polymer aging is an integral part of the Enhanced Surveillance Campaign.

We are studying the chemical mechanisms of degradation processes in PBX 9501 and developing kinetics models. We are working very closely with a large number of experimentalists at the Laboratory and Pantex to determine the chemical and mechanical properties of the PBX and how the two are related. For degradation of PBX in weapons storage, free-radical oxidation of the urethane segments may be as important as the hydrolysis of the polyester segments, especially as the PBX dries out, since the storage environment has both low moisture and oxygen content. Nitroplasticizer (NP) is composed of a mixture of two molecules, bis (2,2-dinitropropyl) acetal (BDNPA) and bis (2,2-dinitropropyl) formal (BDNPF). Various research efforts at the Laboratory are showing that upon heating NP loses nitro (NO_2) groups and produces oxidizing species that can degrade Estane.

Exciting results on the oxidative degradation of Estane continue to come out of the Constituent Aging Study (CAS, conducted at Pantex). The goals of the CAS are to artificially age the PBX 9501 constituents (HMX, Estane, NP, stabilizer) in 25 different combinations at accelerated rates, detect chemical reactions, identify reaction products and possible degradation mechanisms, and provide data for lifetime prediction modeling. The samples are aged at different temperatures (ranging from 40° to 64° C) in a dry, oxygen-free environment. Over 1000 samples were aged for a period of three years, with typical samples analyzed at half-year intervals. One of the most striking findings is that combinations containing NP (NP + Estane and NP + Estane + stabilizer) show a strong correlation between the total amount of gas products generated and significant changes in the molecular weight (MW) of the Estane.

Based on the rate of evolution of NO_x (N_2O and NO) gasses at various temperatures, the Arrhenius parameters (prefactor A and energy of activation E_a) for the rate (= A exp($-E_a$/RT), R = gas constant) of NP decomposition were determined for eight different CAS constituent combinations. A likely mechanism is that NO_2 groups dissociate from the NP molecules and subsequently oxidize the carbon atoms in the backbone of the NP molecules as well as oxidize the urethane linkages in Estane. The oxidation of the Estane polymer can cause chain scission (decreased MW) and crosslinking (increased MW and gel formation), while small molecule remnants of the reactions are presumably being detected in the gas analysis. Such large changes in MW can have drastic effects on the mechanical properties of the elastomer. The energy of activation (E_a = 28 kcal/mol) for the rate of evolution of NO_x gasses compares favorably with values determined from an earlier (Wewerka et al., 1976) aging study on PBX 9501.

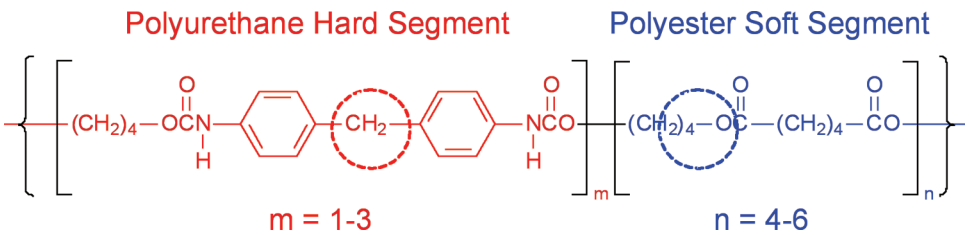

Fig. 1. Chemical structure of Estane®.

During the course of the CAS, the Estane MW was determined using Gel Permeation Chromatography (GPC) with Light Scattering (MALS) detection. In Fig. 3, the change in Estane MW as a function of time (blue open circles) for sample #19 (Estane + NP + Irganox stabilizer) is presented. The MW increases as a function of time at 64ºC indicating that crosslinking is dominating over chain scissioning. The data out to about 70 weeks is well described using the random polymerization theory of Flory and Stockmayer (solid black line) fit with one free parameter (the rate of extent of reaction or crosslinking rate). The data beyond 70 weeks is inaccurate since polymer chains of large MW become insoluble in the GPC solvent (as confirmed with polymer gel recovery measurements). For the three CAS samples analyzed at 64ºC, the rate of evolution of NO_x gasses is about 2–16 times faster than the crosslinking rate.

In another set of experiments (D. Wrobleski and coworkers, in the Los Alamos Materials Science Division, J. M. Lightfoot and coworkers, at Pantex), isotopically labeled model materials were used to understand degradation mechanisms in the binder (Estane + NP) under simulated aging conditions. Isotopic enrichment has been utilized to improve the sensitivity of spectroscopic techniques for observing small quantities of degradation products. Isotopically enriched segmented poly(ester urethane) (PESU) with the nitrogen of the MDI-unit enriched with ^{15}N were prepared. Samples containing ^{15}N PESU and NP have been aged at three different temperatures (50, 70, and 85ºC). Detection of degradation product(s), one of which is the result of oxidation of the bridging methylene carbon of the MDI unit (blue circle in Fig. 1), was accomplished by 1-D and 2-D NMR techniques. A representative 2-D NMR spectra is shown in Fig. 3. By quantifying the amounts of the oxidized product(s) relative to the starting material at different aging times and temperatures, the kinetics of the degradation process was determined. The rate of oxidation of Estane rate for the degradation of PESU is about the same and two times faster (for 70ºC and 85ºC, respectively) than the NO_x gas evolution rate in the decomposition of NP. Furthermore, the energy of activation (29 kcal/mol) derived from the NMR study agrees with that (28 kcal/mol) determined from the rate of evolution of NO_x gasses.

In conclusion, the correlation of the rate of evolution of NO_x gasses with both: 1) the crosslinking rate from the GPC-MALS MW analysis and 2) the methylene bridge oxidation rate from the NMR analysis suggests a correlation between the decomposition of NP and oxidation of Estane. Future work will include correlating changes in chemical properties of PBX (such as Estane MW) with changes in mechanical properties. (See D. E. Hanson's contribution in this volume on page 93.)

For more information contact Joel Kress at jdk@lanl.gov.

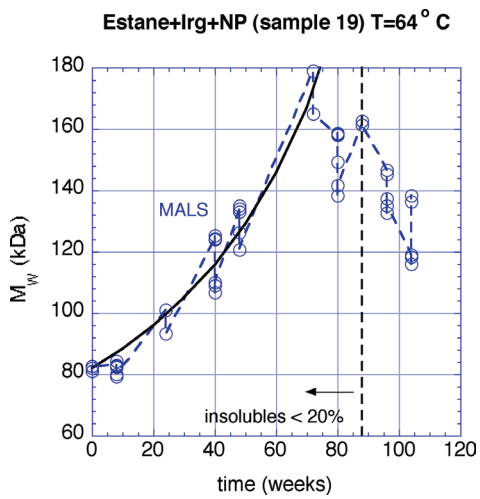

Fig. 2. ***Estane molecular MW as a function of aging time at 64ºC.***

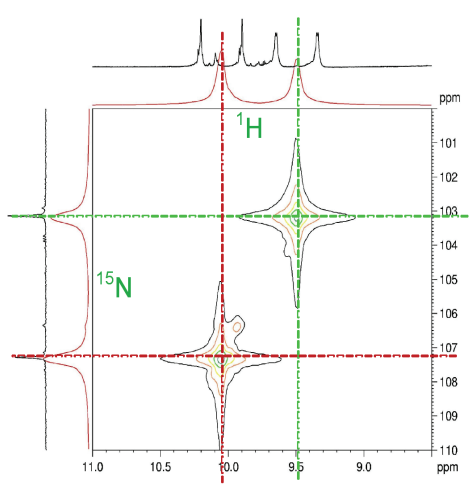

Fig. 3. ***^1H-^{15}N 2-D NMR spectra for PESU/NP aged at 85ºC for 370 days.***

Avalanches and Scaling in Plastic Deformation

Richard LeSar, T-12; Marisol Koslowski, Purdue University; and Robb Thomson, T-12

The common perception is that materials deform by a smooth process, much like pulling taffy. Experiments and simulations have shown, however, that on a microscopic scale deformation is anything but smooth, occurring through intermittent avalanches of dislocations [1, 2]. Here we report results of recent simulations that show that the dislocations form what is called a self-organized critical system, changing the way we think about, and model, deformation.

Bak and coworkers [3] introduced the notion of self-organized criticality (SOC) to explain systems that organize themselves into a (stationary) critical state in which a minor event can start a chain reaction, leading to an effect over a large scale. The critical state is characterized by correlation functions that follow power laws. The importance of SOC theory arises from its ability to explain a wide set of diverse, and seemingly unrelated phenomena, such as earthquakes, fracture, dynamics of magnetic domains, etc. There is no rigorous definition or mathematical formalism of self-organized critical behavior; SOC is a phenomenological definition. If dislocations are self-organized critical systems, however, then we can bring to bear on deformation another important class of scaling and analysis.

We employed a two-dimensional (2-D) phase-field description of deformation to examine the deformation and avalanche behavior in a model of copper [4-5]. In the phase-field formulation, dislocations are not modeled directly; the displacement field in the slip plane serves as the order parameter in the phase field and the dislocation density is found from gradients of the displacement field. While a 2-D model, 3-D effects are included through the inclusion of obstacles to dislocation motion representing forest dislocations crossing the slip plane.

Dislocations move by bowing through the open spaces between obstacles leading to the formation of loops (see Fig. 1); under load the dislocations move and new ones form. In our simulations, as in experiment [1], we see that in each loading step, material deformation occurs in jumps separated by periods where no displacement occurs, corresponding to the release of groups, or avalanches, of dislocations. The energy released by the system is proportional to the area slipped by the dislocations, A, which reflects the size of the avalanche. Figure 2 shows the calculated loop size probability distribution at two different applied stresses. The distribution exhibits a power-law decay over a large range of sizes of the form $N(A) \sim A^{-\sigma}$, with a power law exponent $\sigma = 1.8 \pm 0.1$, in close agreement with the experimental value of about 1.6 [1]. Based on the phenomenological definition

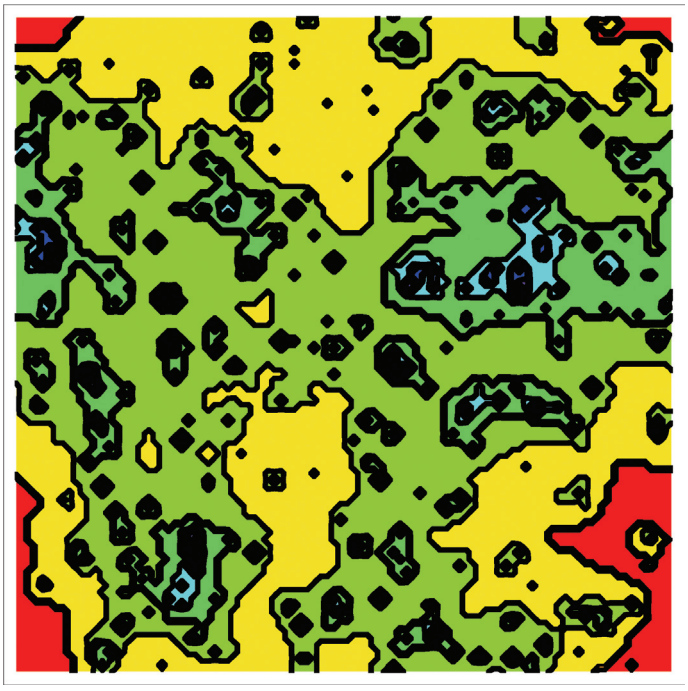

Fig. 1. ***Dislocation pattern in response to an applied stress of $\tau = 0.24 \times 10^{-4}\mu$, where μ is the shear modulus. Lines indicate contours of equal dislocation density.***

given by Bak [3], dislocations form a self-organized critical system. Dislocations thus belong to the class of nonconservative slow-driven systems characterized by scaling laws, in particular the ones used for earthquakes, fluid invasion in porous media, magnetic systems, and fracture.

In Fig. 3, we show experimental data on Ni under quasistatic load showing the shear stress and displacement as a function of time. Analysis of the displacement data yields power-law behavior with an exponent $\sigma = 1.60 \pm 0.02$, in reasonable agreement with our predicted value.

Knowing that dislocations form self-organized critical systems does nothing to help us predict the motion of individual dislocations, in the same way that knowing that earthquakes are SOC systems does not help predict when earthquakes will occur. However, knowing that dislocations form a SOC system changes our way of thinking about the problem and brings dislocations into the arena of other problems that have received a great deal of theoretical attention, suggesting that applying the framework of nonequilibrium statistical mechanics to dislocation systems is likely to be fruitful.

For more information contact Richard LeSar at ral@lanl.gov.

[1] D.M. Dimiduk, et al., "Direct Measurement of Scale-Free Intermittent Flow in Crystal Plasticity," submitted to *Science*.
[2] P. Simmonds, *Nature Mater.* **4**, 425–426 (2005).
[3] P. Bak, et al., *Phys. Rev. Lett.* **59**, 381–384 (1987).
[4] M. Koslowski, et al., *Phys. Rev. Lett.* **93**, 125502 (2004).
[5] M. Koslowski, et al., *Phys. Rev. Lett.* **93**, 265503 (2004).

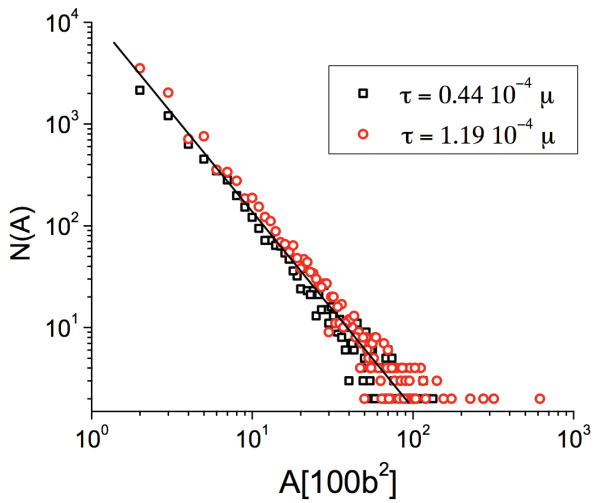

Fig. 2.
Avalanche size distribution N(A) at two applied stresses.

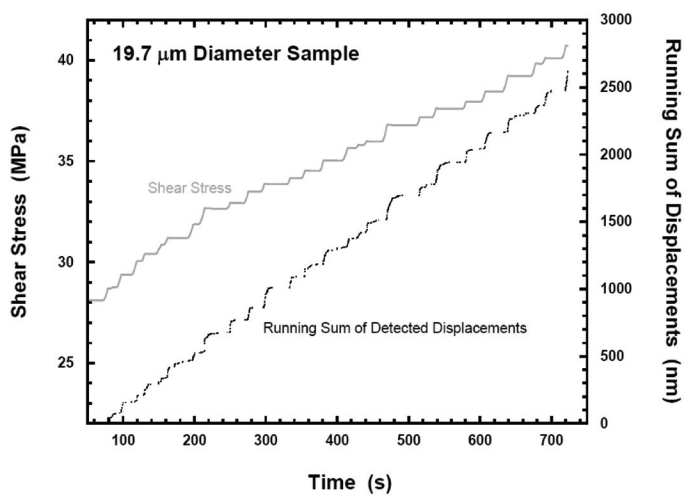

Fig. 3.
Plot of experimental shear stress and cumulative displacements as a function of time for Ni under load showing bursts of dislocations.

Investigations of Hybrid Density Functional Theory in Condensed Matter

Richard L. Martin, Cristian V. Diaconu, Enrique R. Batista, and P. Jeffrey Hay, T-12

In a collaboration with Gustavo Scuseria at Rice University, we have extended his linear scaling periodic boundary condition capability to heavy elements by incorporating the relativistic effective core potential (RECP) capabilities developed earlier at the Laboratory. Both components were implemented in the Gaussian suite of electronic structure codes, and the combination allows the hybrid density functionals developed in the molecular quantum chemistry community to be applied to solids containing transition metal and f elements [1]. Over the past few years we have applied this new tool to a number of problems problematic for conventional functionals.

Recent developments allow us to study metals with these approximations and our results for the metal-insulator transition in MnO are in good agreement with experiment [2]. This work is in collaboration with groups at UC Davis, UC Santa Barbara, and Oak Ridge National Laboratory, who have studied the same problem using different many-body approaches. The collaboration is part of the DOE computational materials science network entitled "Predictive capabilities for strongly correlated electronic systems." More recently, we have applied these techniques to the long-standing problem of the underestimation of the band gap in semiconductors [3] and to predictions of defect energies in silicon [4]. The hybrid functionals are a distinct improvement and should be of interest to the semiconductor modeling community as well as to our colleagues in MST Division.

For more information contact Richard L. Martin at rlmartin@lanl.gov

[1] K.N. Kudin, et al., *Phys. Rev. Lett.* **89**, 266402 (2002).
[2] C.V. Diaconu, et al., "Hybrid DFT Studies of the Metal-Insulator Transition in MnO," in preparation.
[3] J.J. Heyd, et al., *J. Chem. Phys.* **123**, 1 (2005).
[4] E.R. Batista, et al., "Defect Energies in Silicon Studied with Hybrid Density Functional Theory," in preparation.

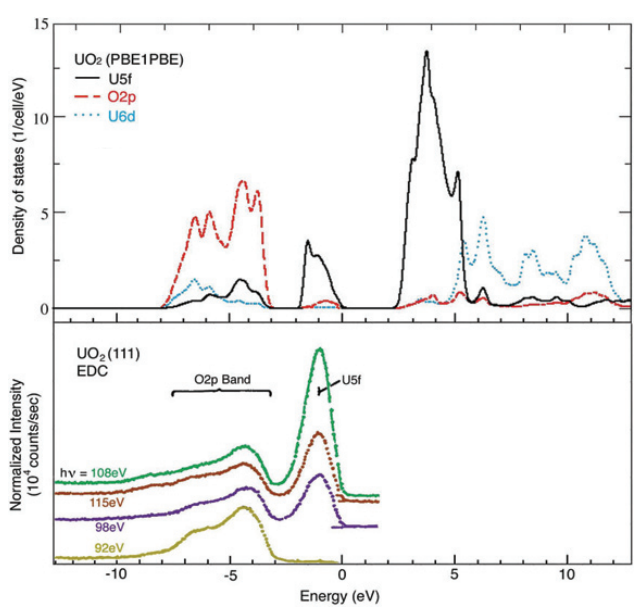

Fig. 1. *The top panel displays the hybrid DFT partial density of states for UO_2. The peak near Ef is primarily U5f with a very small O2p contribution. The bottom panel reproduces the photoemission energy distribution curves taken by Cox, et al. demonstrating the predominantly U5f character of the feature near Ef. The incident photon energies correspond to the resonance (98 and 108 eV) and antiresonance (92eV) in the U5f cross section [1].*

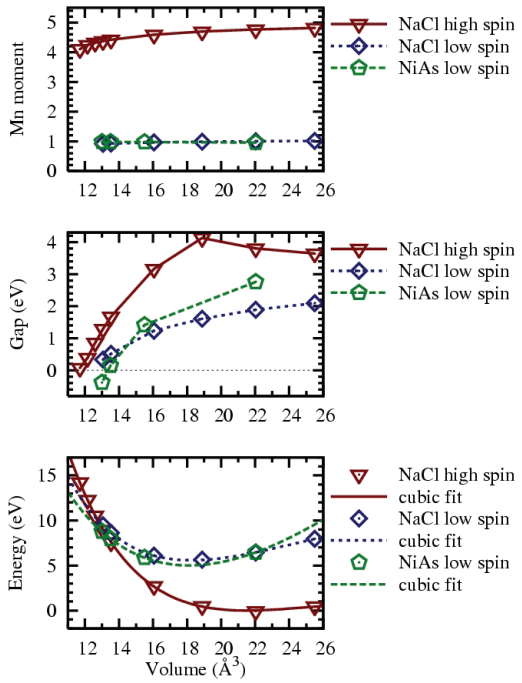

Fig. 2.
Hybrid DFT predictions of the Mott transition in MnO. The magnetic moment, band gap, and energy for MnO are plotted as a function of the volume. Our computations find that a structural phase transition to the NiAs structure preempts this transition and is responsible for the moment collapse. This is in agreement with the experimental observation [2].

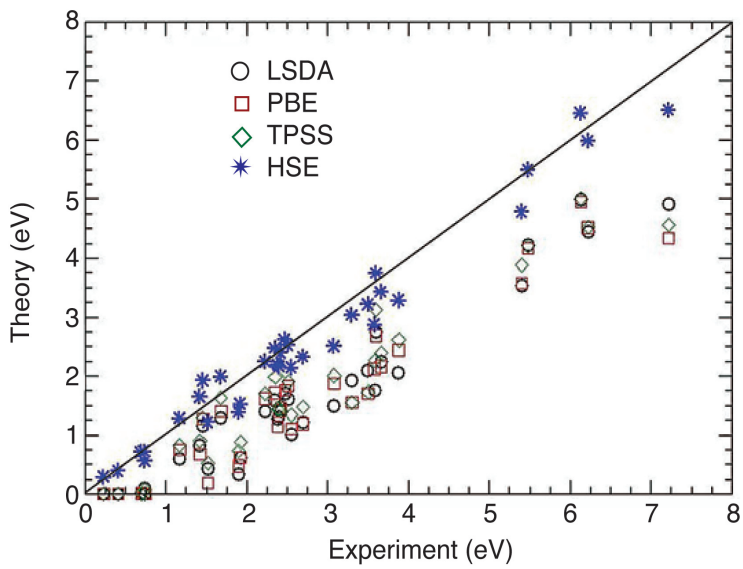

Fig. 3.
A comparison of experimental band-gaps for a collection of 40 semiconductors with values computed with four different generations of DFT: the local spin-density approximation (LSDA), a generalized-gradient approximation (PBE), a meta-GGA (TPSS), and the hybrid functional HSE. The hybrid functional is a distinct improvement, yielding a mean absolute error of 0.26eV, vs 1.14eV (LSDA), 1.13eV (PBE), and 0.98eV (TPSS) for the conventional approaches [3].

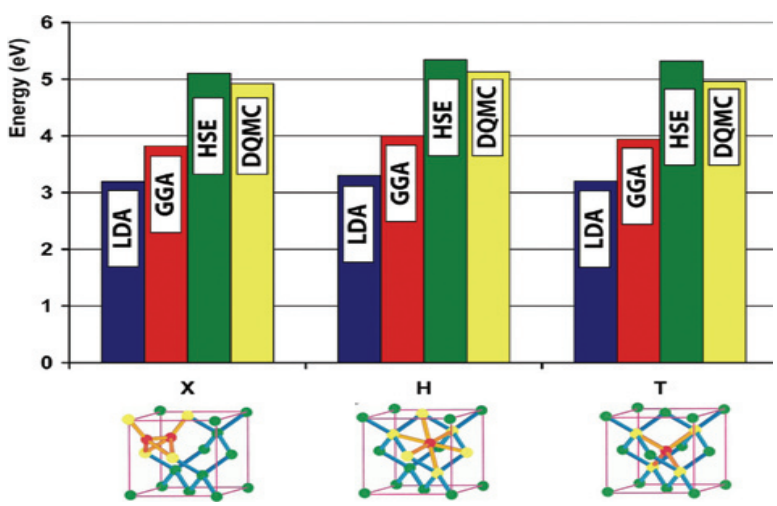

Fig. 4.
Formation energies of three typical defects in silicon. The hybrid functional HSE is in very good agreement with the benchmark values from diffusion quantum Monte Carlo calculations.

Photoexcited Vibrational Dynamics in Vicinity of Conical Intersections

Andrei Piryatinski and Sergei Tretiak, T-12; Misha Stepanov, T-13; and Vladimir Chernyak, Wayne State University

Noninteracting electronic and vibrational dynamics in (bio)molecules and solids is characterized by well separated timescales associated with the energies of electronic and vibrational transitions. Switching on interaction between these degrees of freedom leads to renormalization of their energies and, consequently, dynamics timescales. Provided the electronic surfaces in a molecule are still sufficiently separated, photophysical and spectroscopic processes can be well described within *adiabatic*, i.e., the Born-Oppenheimer approximation. In such a case, separation into slaving and slaved degrees of freedom significantly simplifies analyses of the problem[1]. For instance, molecular dynamics (MD) simulations reduce to propagation of classical nuclei trajectories on the excited electronic state potential surface (Fig. 1), while the forces can be computed separately using first principle quantum chemical methods or model approaches.

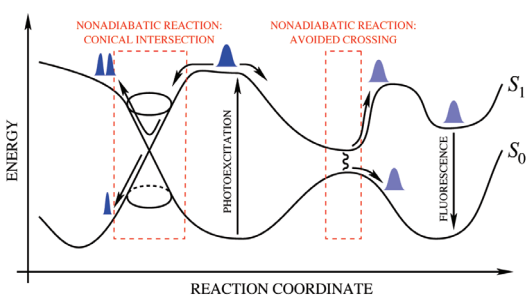

Fig. 1. *Examples of surface crossing and photo-excited dynamics.*

The Born-Oppenheimer approximation breaks down in the vicinity of surface crossings resulting in the need for *nonadiabatic* quantum mechanical MD, which is computationally expensive and often intractable. A variety of ultrafast photoreactions in biological molecules occur in the vicinity of the surface crossings. Among them rhodopsin photoisomerization, radiativeless excited state energy relaxation in fluorescent proteins and DNA base pairs. Importance of these processes for extending our fundamental knowledge in photochemistry of biological objects, as well as rich potential for developing biological and chemical sensor suitable for medical applications, motivates extensive study of nonadiabatic dynamics in macromolecules [2].

There are two important cases of the electronic energy crossings illustrated in Fig. 1. Provided the electronic states coupled to N vibrational degrees of freedom have identical symmetry, and intersect. If the dimensionality of the intersections manifold is $N–1$ then any small interaction lifts the degeneracy corresponding to the so-called avoided crossing[1, 2]. Tunneling through the avoided crossing gap is well described by the celebrated Landau-Zener formula valid in the semiclassical regime.

The other, much more complicated case of true surface crossing occurs when the dimensionality of the crossing manifold becomes $N–2$. As illustrated in Fig. 2, it is possible to expand the electronic energy in the vicinity of the surface crossing up to the linear terms in two-dimensional transverse coordinate space. As a result, the electronic surface becomes a double cone giving rise to the

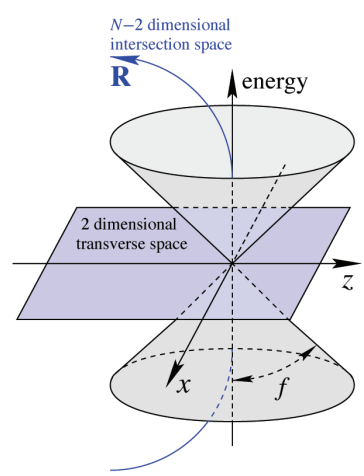

Fig. 2. *The potential energy surface in the vicinity of the CI as a function of transverse vibrational coordinates.*

name of conical intersection (CI) for a true crossing case. The point where the cones touch each other represent N–2 degeneracy space. Provided the interaction region between the surfaces is small, the CI approximation becomes universal [2, 3]. However, no small interaction can lift the degeneracy at the crossing space, and as a result, cannot remove singularity which significantly complicates MD.

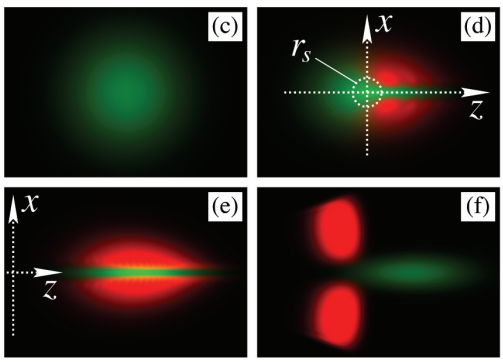

To address the problem of MD in the vicinity of CI, we have developed a wavepacket scattering matrix approach [3]. The theory is based on the scattering matrix expansion controlled by unique dimensionless parameter g_s. The scaling of $g_s \sim \hbar^{1/2}$ suggests that the scattering takes place in the semiclassical regime when $g_s << 1$. We have also found that the scattering radius r_s, also scales as $\hbar^{1/2}$, and that the wavepacket passes through this small vicinity of CI with negligible changes in its velocity, i.e., in the ballistic regime. Calculated zero order scattering amplitude has simple analytical expressions resembling celebrated Landau-Zener result. To verify our analytical results, obtained scattering amplitude was compared with the results of direct numerical simulations (Fig. 3), and demonstrated good agreement for the realistic set of parameters.

Obtained analytical expressions could have several practical implications for large-scale MD simulations as we illustrate in Fig. 4. In the adiabatic regions, a classical treatment of the vibrational degrees of freedom is satisfactory. Therefore, photoexcited dynamics away from CIs can be modeled by running an ensemble of classical trajectories. If some trajectories approach the explicitly defined scattering region r_s around a CI, the dynamics becomes nonadiabatic and should be treated quantum mechanically. According to our theory, instead of numerically demanding quantum calculations, we propose propagating an ensemble of classical trajectories through r_s using our analytical expressions with input parameters from classical MD data. This approach is widely adopted for the case of fast passages through an avoided crossing where the Landau-Zener theory works. Since our results are similar in spirit to the latter theory, their generalization to far more complicated cases of CIs should be efficient and universal.

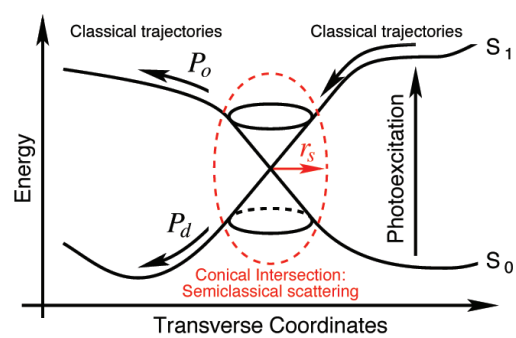

For more information contact Sergei Tretiak at serg@lanl.gov.

[1] L.D. Landau and E.M. Lifshitz, *Quantum Mechanics: Non-relativistic Theory* (Pergamon Press, New York, 1977).
[2] *Conical Intersections: Electronic Structure, Dynamics and Spectroscopy*, W. Domcke, D.R. Yarkony, and H. Koppel, Eds. (World Scientific, New Jersey, 2004).
[3] A. Piryatinski, et al., "Semiclassical Scattering on Conical Intersections," *Phys. Rev. Lett.* **95**, 223001 (2005).

Fig. 3. *Numerical simulations of the semiclassical wavepacket scattering on the CI. The wavepacket is propagating in the z-direction (identical in all panels). The origin of the coordinate system indicates the position of the CI. (c) initial wavepacket, (d)–(e) scattering event characterized by the scattering radus r_S; quantum interference fringes are well resolved, (f) scattered to the other surface (green) wavepacket, and two (red) transmitted ones.*

Fig. 4. *Proposed scheme for large-scale quantum mechanicanics/molecular mechanics photoexcited molecular dynamics incorporating analytical expressions for the CI transition P_O and scattering P_d probabilities entering the semiclassical scattering matrix.*

Noise at the Crossover from Wigner Liquid to Wigner Glass

Charles Reichhardt, T-13, and
Cynthia J. Olson Reichhardt, T-12

Three-dimensional metals have long been known to exist, but when two-dimensional (2-D) electronic systems were first studied in the early 1980s, it was believed on theoretical grounds that a 2-D metallic state could never occur. As the quality of the experimental samples improved over the following decade, more and more evidence emerged of a transition from insulating to metallic behavior for systems in which the electron density exceeds some sample-dependent critical value. Single-electron theories were developed to explain the transition, but these theories were unable to capture the noise behavior observed in recent experiments.

To address the microscopic mechanism of the 2-D metal-insulator transition, we propose a simple model for a classical 2-D electron system consisting of interacting electrons with random disorder and temperature. We monitor the fluctuations and noise characteristics of the current as a function of electron density or temperature. The advantage of our model is that a large number of interacting electrons can be conveniently simulated, while a full quantum mechanical model of similar size would be computationally prohibitive. Despite the limitations of this model, we find that this approach captures many of the key experimental observations [1].

In the left panel of Fig. 1, we show the velocity response of our simulated sample for fixed disorder and different electron densities as the temperature is decreased toward zero. At high electron density (top curve), the sample remains conducting down to zero temperature, as illustrated by the nonzero intercept of the curve. This is a metallic-like behavior. As the electron density is decreased, we find a transition to a regime where the velocity drops to zero within our resolution at a finite temperature. This behavior is consistent with an insulating state.

We next perform a series of simulations in which we measure the relative velocity fluctuations as a function of time for different points on the temperature-electron density phase diagram. When the system is in the metallic regime, as shown by the top curve in the right panel of Fig. 1, the magnitude of the velocity fluctuations is small. In contrast, as the electron density is decreased toward the metal-insulator transition, the size of the relative velocity fluctuations increases by several orders of magnitude (bottom curve). This dramatic behavior is in good agreement with the recent experimental measurements. We find that the velocity noise power appears to diverge both as the electron density is lowered and as the temperature is lowered. Single electron models would predict a *decrease* in velocity noise with decreasing

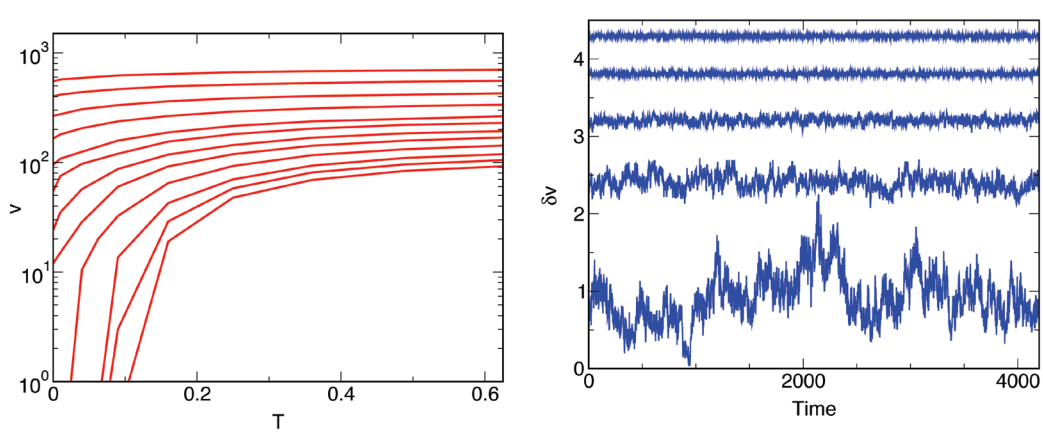

Fig. 1.
Left: The average electron velocity v versus temperature for increasing electron density, from bottom to top. Right: The relative velocity fluctuations δv versus time at fixed temperature for increasing electron density, from bottom to top.

temperature, in contrast to both the experiments and to our simulations, where electron-electron interactions are important.

We find that the large noise just above the insulating transition is due to correlated regions of stringlike electron flow, and that within these regions the electrons move in 1-D or quasi-1-D channels. Because of the reduced dimensionality, the electron motion is more correlated. In Fig. 2 we show the trajectories of the electrons for a fixed period of time for systems held at the same temperature but with a decreasing density of electrons. In Fig. 2(a), the system is in the metallic-like state, and the electrons can flow freely throughout the sample. In Fig. 2(b), larger pinned regions appear and the electron motion consists of a mixture of 2-D and 1-D regions. In Fig. 2(c), where the noise power is at its maximum just above the insulating transition, the electron motion occurs mostly in the form of 1-D channels that percolate through the sample. The channel structures change very slowly with time, with a channel occasionally shutting off while another emerges elsewhere. It is the intermittent opening of the 1-D channels which gives rise to the large noise fluctuations in this regime. When a percolating 1-D channel opens, all the electrons in that channel move in a correlated fashion leading to a large increase in the conduction. Conversely, if a percolating channel closes, all the electrons in that channel cease to move. Our simple model for the glassy freezing of interacting electrons in 2-D with random disorder agrees well with experimental measurements of the 2-D metal-insulator transition, and suggests that correlated electron motion plays an important role in the transition region.

For more information contact Charles Reichhardt at reichhardt@lanl.gov.

[1] C. Reichhardt and C.J. Olson Reichhardt, *Phys. Rev. Lett.* **93**, 176405 (2004).

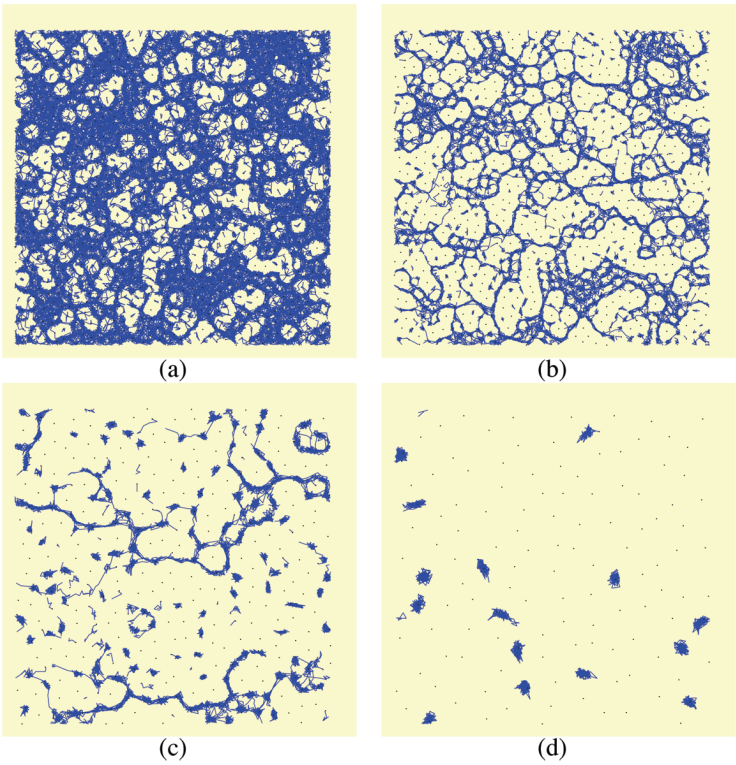

Fig. 2. *Classical electron trajectories for a fixed period of time for fixed temperature and decreasing electron density. (a) An electron liquid in the metallic-like regime. (b) Inhomogeneous electron flow at lower densities. (c) Filamentary, effectively 1-D electron flow at densities just above the insulating transition. (d) The insulating state where no electron transport occurs.*

Do Vortices Entangle?

Cynthia J. Olson Reichhardt, T-12, and Matthew B. Hastings, T-13

The high superconducting transition temperatures of compounds such as $YBa_2Cu_3O_{7-\delta}$ (YBCO) lead to a very rich set of behaviors of the magnetic vortex lines that form inside the superconducting material in the presence of an applied magnetic field. In particular, thermal fluctuations of the vortex lines can produce a vortex melting transition. The nature of the molten vortex state has been a subject of intense debate for nearly two decades. Since there can be significant thermally induced wiggling along the length of the vortex in the liquid state, D. Nelson proposed that neighboring vortex lines may become entangled with each other, much like polymers in a melt. Similarly to the entangled polymer state, the effective viscosity of the entangled vortex state is expected to increase significantly. This could explain the striking experimentally observed increase in critical current upon increasing temperature.

In order for the vortices to entangle, it is crucial that neighboring flux lines cannot cut through each other easily and reconnect into a disentangled state. Theoretical estimates of the cutting barrier range over two orders of magnitude in energy, and span both the regime where cutting is impossible as well as the regime where cutting occurs easily. Numerical simulations have proven similarly ambiguous, with some simulations interpreted as providing evidence for entanglement and others interpreted as showing that the lines cut and do not entangle. It is therefore natural to turn to experiments to resolve the issue. Unfortunately, experimental evidence for or against entanglement based on bulk measurements has also proven ambiguous. Thus, despite more than a decade of theoretical, numerical, and experimental studies, the question of whether vortices can form an entangled state has not yet been convincingly answered.

We propose a direct experimental test of vortex entanglement by means of a local magnetic force microscope (MFM) probe, which can unambiguously determine whether it is possible for two vortices to wind around each other without cutting. We consider a high-temperature superconductor containing two closely spaced magnetic dots at the bottom of sample, shown in Fig. 1(a). A mobile magnetic dot is introduced to the top of the sample in the form of a magnetic MFM tip (open circle). The magnetic dots attract the vortices, so that the top and bottom positions of the vortices are fixed at the dot locations. As the MFM is moved along the surface of the sample, it drags the top of one vortex with a directly measurable force. When the MFM tip moves in a circular path, the two vortices wind together, producing the entangled state illustrated in Fig. 1(b). As the winding angle increases, the force required to drag the vortex further around increases according to a form that we derive theoretically. If the vortices cut, this force will abruptly drop. Thus, using such an experiment, it is possible to directly probe whether vortex entanglement can occur.

The magnitude of the angular force is large enough to be detected experimentally. For two vortices in a YBCO sample, we estimate that the maximum force should be approximately 28 pN; forces as small as 0.4 pN have been measured previously with MFM techniques. In more highly anisotropic materials such as $BiSr_2Ca_2CuO_8$, the elastic line model for vortices assumed in D. Nelson's work is expected to break down and vortex cutting should occur immediately. In this case, the force required to move the top portion of one vortex around the second vortex is two orders of magnitude smaller than the entanglement force in YBCO, placing it below the threshold of detection by MFM.

The local experimental probe that we propose can also be used to explore numerous other properties of the vortex system besides vortex entanglement. For example, in a geometry containing only one magnetic pin and one vortex line, the MFM tip can be used to measure the vortex line tension directly. If the line tension is known, the tip could be used to tear a vortex away from an individual pinning site, such as a grain boundary, and the pinning force could be measured. Local rheology measurements are also possible in the vortex lattice state; for example, the local elastic constants can be probed by moving a single vortex back and forth around its lattice equilibrium position. The temperature dependence of both the elastic constants and the pinning energy could also be probed.

We have proposed an experimental setup for constructing and probing entangled states of superconducting vortices, and shown that the forces associated with vortex entanglement are experimentally measurable. This kind of experimental setup can be generalized to other types of vortices, as in fluid turbulence. Within the elastic string model, we find that the entangled state is stable only up to a maximum pitch or minimum vortex spacing. The instabilities we have found raise the question of whether the entangled state can exist with a high density of vortices [1]. To answer this question and to compare pancake and elastic string models, an experimental test of our proposal is desirable.

For more information contact Cynthia J. Olson Reichhardt at cjrx@lanl.gov.

[1] C.J. Olson Reichhardt and M.B. Hastings, *Phys. Rev. Lett.* **92**, 157002 (2004).

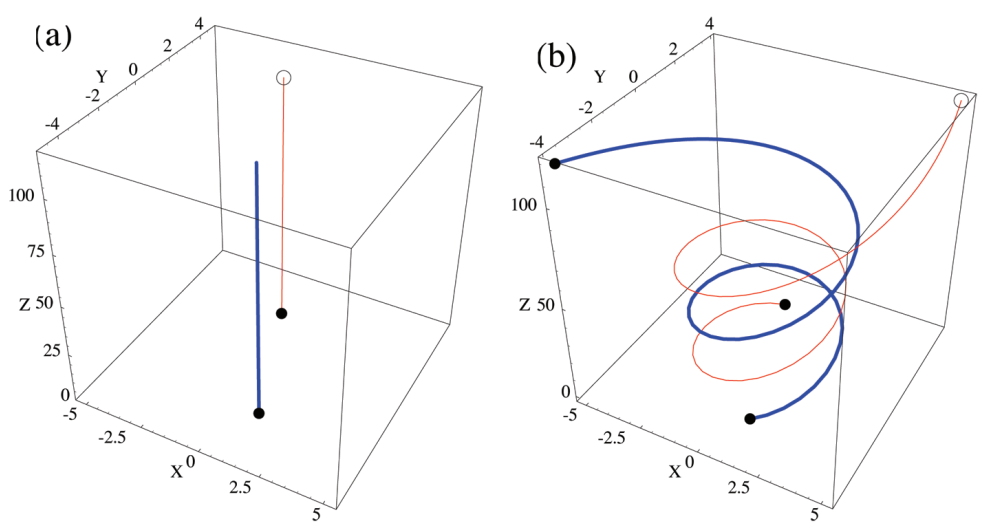

Fig. 1. *Artificial creation of an entangled vortex state. (a) Schematic of the starting state showing fixed pins (black dots) and the magnetic force microscope tip (open circle). (b) The entangled configuration produced by winding the top of one vortex around the other.*

Coulomb Explosion Mechanisms for Ion Damage

Cynthia J. Olson Reichhardt, T-12

It has been known for many years that ion irradiation produces etchable damage tracks, which can be microns in length, in only some materials. The fact that most track-forming materials are insulators, while most metals do not form damage tracks, suggests that electronic processes play an important role in the ion-target interaction. This picture is too simple, however, since not all insulators form tracks equally well. The basic physics of the system was never fully unraveled even as demand for track-forming materials spurred a rapid empirical identification of materials that respond strongly to ion damage.

Numerous models have been developed over the years to explain track formation and sputtering processes, but each has suffered from limitations. One simple picture is to consider a collision cascade initiated when the impinging ion directly strikes a target atom, resulting in a series of collisions that progress through the lattice. Such direct atomic collisions would be expected to occur equally in metals and insulators. Thermal spike models, in which the energy deposited by the impinging ion is converted to lattice phonons that then locally melt the lattice over longer time scales, are also problematic since no correlations have been found between track formation and the thermal properties of the material.

The Coulomb explosion or ion explosion model has proven less popular than other models in spite of the fact that it could potentially reproduce the difference in damage between metals and insulators. In this model, the energy of the ion beam is assumed to lie in the electronic stopping regime. Here, the ion carries an effective charge because it loses those electrons with orbital velocity smaller than the velocity of the ion in the medium. As it passes through the target, the projectile ionizes atoms along its trajectory. These target ions then recoil under their mutual Coulomb repulsion. For example, the potential energy of two electron charges spaced at one interatomic distance is 3.5 eV, and a cluster of five ions has a Coulomb energy of about 30 eV. These amounts of repulsive energy are substantial compared to the binding energy per atom of the solid.

A Coulomb explosion process could be highly effective in destroying local lattice order along the track. The main barrier to the motion of target atoms out of their lattice registry positions is the presence of neighboring target atoms that are simply in the way. Target atoms undergo a decrease in their effective Pauling radius while ionized, due to the loss of electrons in their outer shells. This provides a significant amount of free volume in which the ionized target atoms can move, and permits much more extensive disordering of the lattice than is possible in typical vacancy production models. Furthermore, once the ionized target atoms deionize, they may be permanently trapped out of lattice registry, since thermal excitation is not sufficient to restore order to the lattice, in contrast to the possible recombination of interstitial and vacancy atoms that can occur in damage processes in the nuclear stopping regime.

A major concern with the Coulomb explosion model is the fact that the charge induced along the trajectory must persist long enough to allow significant motion of the target atoms to occur. It has normally been assumed that the time scale for target ion motion to occur is on the order of the inverse phonon frequency, 10^{-12}s. Even in insulating materials, it is likely that electrons from the material outside the strongly charged track region will be able to neutralize the charge in a time shorter than this. I have performed a theoretical estimation

of the radius and charge of the ionized track that would be produced by an ion in the electronic stopping regime. It is important to note that the track develops an intense charge due to the large amount of energy that is deposited on a very local scale by the impinging ion. Figure 1 shows an illustration of local energy deposition by a moving charge in a simulated charged system. Due to the strongly localized charge, a relatively narrow region of charged ions inside the track experience an intense accelerating force from the resulting electric field. This is sufficient to induce significant motion of the target ions on time scales of 10^{-15}s or shorter, long before thermal motion due to phonons can occur. It may be possible for the charge of the track to persist for times of this order, especially in insulating materials. This suggests that Coulomb explosion processes may be more effective than previously believed at producing damage tracks, and underscores the importance of considering direct Coulomb interactions between the target ions and the charged track region, rather than waiting for the energy deposited into the electronic degrees of freedom to thermalize.

For more information contact Cynthia J. Olson Reichhardt at cjrx@lanl.gov.

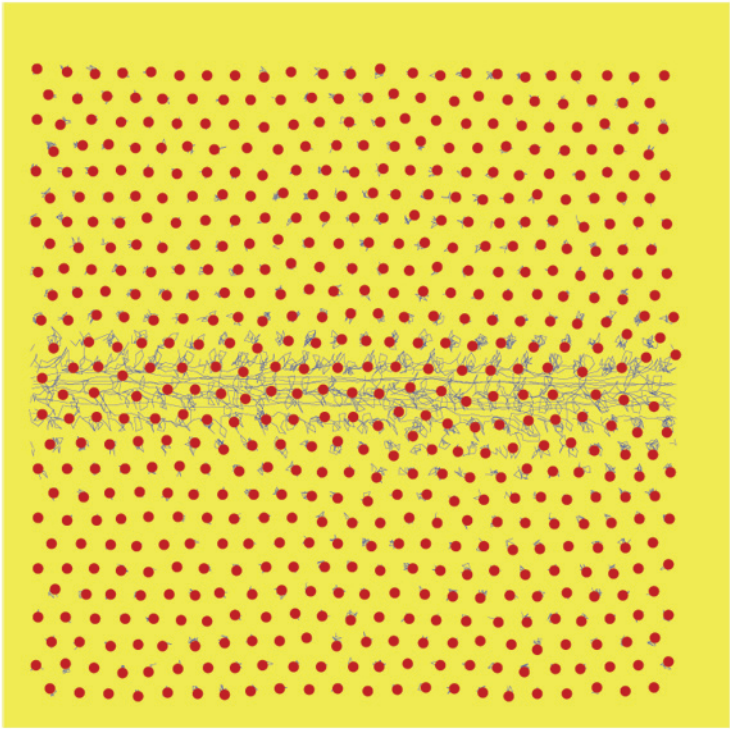

Fig. 1. ***Highly localized deposition of energy by moving charge in a strongly Coulomb interacting system of charges.***

Time-Dependent Density Functional Theory for Frequency-Dependent Nonlinear Optical Response

Sergei Tretiak, T-12

Optical materials with enhanced nonlinear optical (NLO) responses have important technological implications [1] such as optical switching and wave-guiding, compact three-dimensional (3-D) data storage and microfabrication, chemical and biological sensing, optical power limiting, up-conversion lasing, bio-imaging, etc. (e.g., Fig. 1). Even though perfecting synthetic techniques has led to materials with exceptional hyperpolarizabilities, further progress is still hindered by the cost of both synthetic and characterization methods.

Computational design of nonlinear optical materials is a fundamentally difficult problem. Careful and comprehensive analysis is necessary for understanding the key electronic phenomena contributing to NLO properties and their related connections with chemical composition. This is a cornerstone for the rational design of new NLO materials. First-principles calculations of molecular electronic spectra require extensive numerical effort and, therefore, exact treatment becomes impractical even for fairly small molecules. Correct description of excited states involved in NLO responses requires inclusion of the higher order electronic correlations. This makes their computing a much more complicated procedure compared to analogous ground state calculations. Time-dependent density functional theory (TDDFT) in the Kohn-Sham form has recently emerged as an accurate and efficient method for studying the optical response of molecules [3].

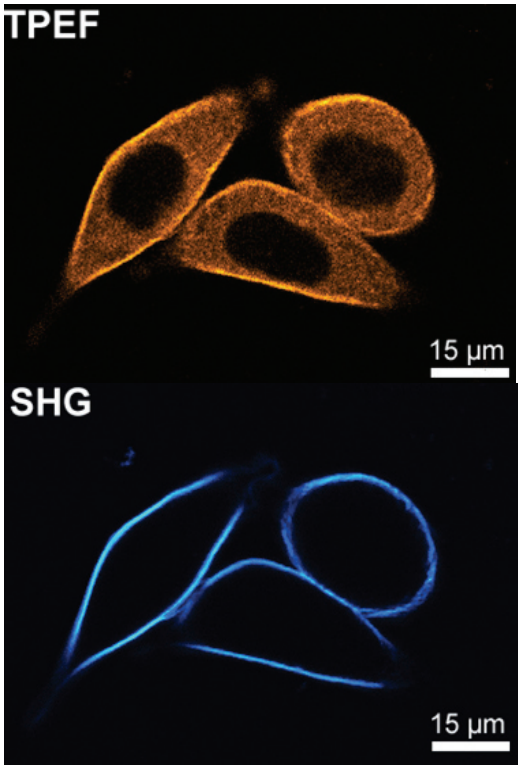

Fig. 1. Application example: noninvasive bioimaging by simultaneous two-photon excited fluorescence and second harmonic generation of isolated Ncad1 cells labeled with a push-pull polyenic chromophore [2].

Recently we have studied the response of the density matrix to an external field in the adiabatic TDDFT theory by mapping the equation of motion for the driven single-electron density matrix into the dynamics of coupled harmonic oscillators. The resulting nonlinear response functions and the closed expressions for arbitrary second- and third-order frequency-dependent nonlinear polarizabilities have been derived [4]. A working code prototype has been developed at Los Alamos as well which computes first-, second- and third-order responses in various regimes using output from the commercial quantum-chemical packages (e.g., Gaussian).

Subsequently, in a benchmark study, calculated excitation energies corresponding to one- and two-photon absorption maxima are found to be in excellent agreement with experiment for all excitation frequencies across the entire set of donor-acceptor substituted molecules (Fig. 2) [5]. Usually this is not the case for other computational methods. In a joint experimental-

theoretical study of large 3-D substituted organic chromophores (up to 250 atoms in size) we found that the TDDFT gives very good agreement with the experiment predicting correctly complex spectroscopic lineshapes of two-photon absorption related to the third-order optical response (Fig. 3) [6]. The theoretical analysis also led to understanding of the dominant structural factors affecting the linear and nonlinear responses in these large molecular systems featuring strong through-space electronic delocalization [7].

In conclusion, we have developed an efficient formalism for computing frequency-dependent nonlinear optical polarizabilities based on the time-dependent DFT [4–7]. The new approach allows quantitative modeling of NLO responses in complex molecules, enveloping all scales from small molecules to large molecular clusters (200 atoms and more), and to the bulk limit.

For more information contact Sergei Tretiak at serg@lanl.gov.

[1] T.C. Lin, et al., *Polymers for Photonics Applications II* **161**, 157 (2003).
[2] L. Moreaux, et al., *Biophys. J.* **80**, 1568 (2001).
[3] M. E. Casida, et al., *J. Chem. Phys.* **108**, 4439 (1998).
[4] S. Tretiak and V. Chernyak, *J. Chem. Phys.* **119**, 8809 (2003).
[5] A. Masunov and S. Tretiak, *J. Phys. Chem. B* **108**, 899 (2004), N. Kobko, et al., Chem. Phys. Lett. 392, 444 (2004).
[6] G.P. Bartholomew, et al., *J. Am. Chem. Soc.* **126**, 11529 (2004).
[7] C. Katan, et al., *J. Phys. Chem. A* **109**, 3024 (2005), E.A. Badaeva, et al., J. Phys. Chem. A 109, 7276 (2005).

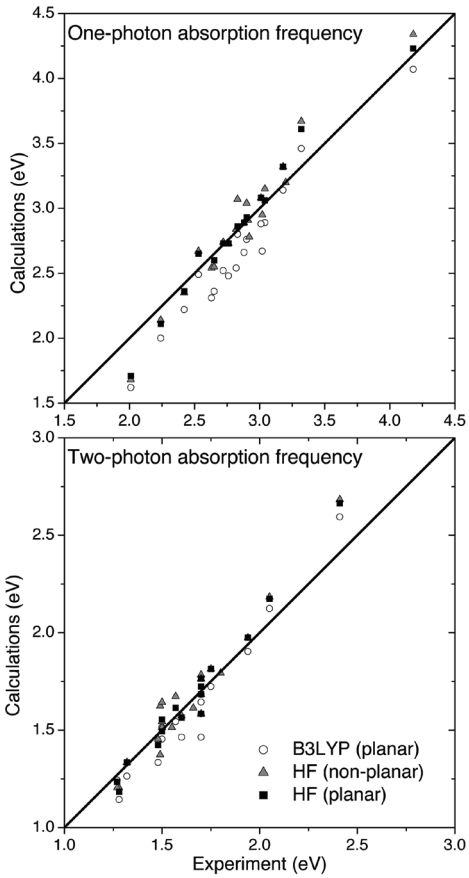

Fig. 2.
We obtained ~ 5% (40 nm) average deviation of one-photon and two-photon frequencies of absorption maxima (theory vs experiment) for series of 20 chromophores (chemical structures are not shown) [5]. For comparison, all calculations reported previously have > 20% (200 nm) errors.

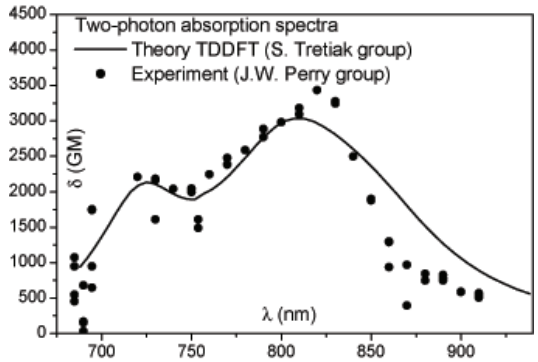

Fig. 3.
Comparison of theoretical and experimental two-photon absorption spectra (third-order response) for a large donor substituted chromophore [6]. Without any adjustable parameters, our TDDFT extension reproduces accurately both magnitudes and positions of bands even in complex multipeaked spectra.

Real Time Observation of Nonlinear Coherent Phonon Dynamics in Single-Wall Carbon Nanotubes

Sergei Tretiak and Andrei Piryatinski, T-12; Avadh Saxena, T-11; Richard L. Martin, T-12; Alan R. Bishop, T-DO; A. Gambetta, C. Manzoni, E. Menna, M. Meneghetti, G. Cerullo, and G. Lanzani, Politecnico di Milano

Single-walled carbon nanotubes (SWNTs) are π-electron, rod-shaped nanostructures with a distinct one-dimensional (1-D) character. The electronic structure, according to geometrical criteria, gives rise to metallic and semiconducting SWNTs. In semiconductors, medium-sized excitons (3–5 nm) are regarded as the fundamental excitation. As a consequence of exciton wavefunction localization and the 1-D character, electron-phonon coupling is expected to be substantial in SWNTs. The time domain observation of phonon dynamics allows direct measurement of excited state dynamics, vibrational dephasing and mode coupling.

Resonant sub-10-fs visible pulses were used to generate and detect coherent phonons in SWNT ensembles. We observed vibrational wavepacket dynamics for the radial breathing mode (RBM) and the longitudinal carbon-stretching mode (G), and in particular their anharmonic coupling. As shown in Fig. 1a, there is a clear oscillation in ΔT/T amplitude. The Fourier transform (FT) of the oscillatory component (Fig. 2a) shows a strong peak at 254 cm^{-1} (131 fs period), recognized as the RBM, associated with expansion and contraction of the tube cross section. Our observation corresponds to an ensemble of semiconducting SWNTs, with diameters of about 0.95 nm, all vibrating in phase.

We further used Los Alamos National Laboratory- (LANL)-developed quantum-chemical computational tool (a semiempirical Excited State Molecular Dynamics, ESMD) approach to understand the underlying dynamics. Calculations based on ESMD confirm that both the RBM and G modes have substantial coupling with the electronic transitions. The RBM and G-mode are both Raman-active Frank-Condon vibrations, i.e., their equilibrium positions change upon electronic excitation. Calculated dimensionless displacements from the ground state to the lowest optically active exciton state are 0.2 for the RBM and 0.4 for the G mode for the chiral (7,6) tube. However, tube-diameter modification in going from the ground to the first exciton state is not as simple as expected. In Fig. 3a, we display the change in tube radius *dr* with atom coordinate along tube Z axis calculated for the (7,6) tube shown

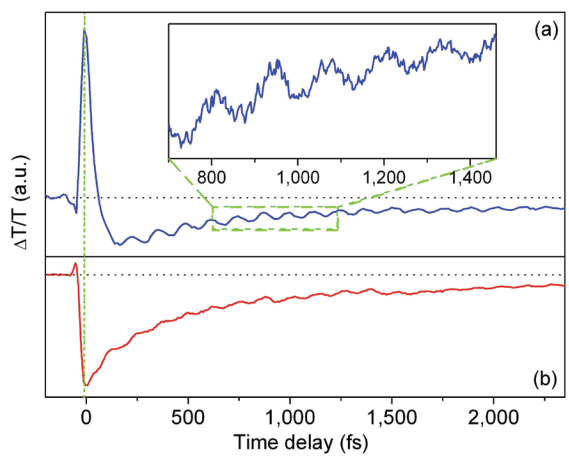

Fig. 1.
Fig. 1. Differential transmission (ΔT/T) dynamics of SWNTs excited and probed by a sub-10-fs visible pulse. Inset shows the high frequency modulation.

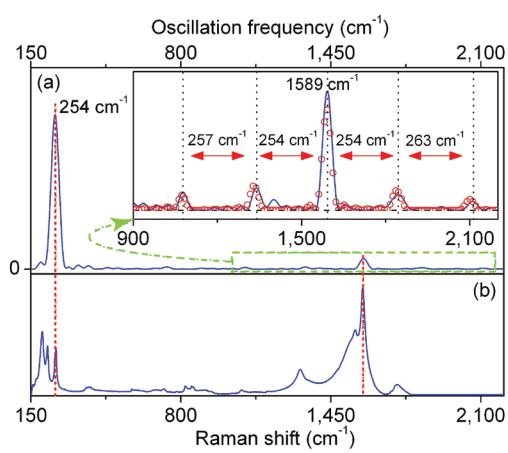

Fig. 2.
(a) FT power spectrum of time trace shown in the top. Inset: Solid line is the zoom of the FT power spectrum, showing side bands in the high frequency region. Regular spacing between the modes is shown by labels and double arrows. (b) CW Raman spectrum.

in the inset. Overall, relaxation of the photoexcitation results in an increase of the average diameter in the middle of the tube. Surprisingly, there is also a corrugation of the tube surface in the excited state, which clearly leads to coupling of radial and longitudinal modes.

Finally, to explore the anharmonic coupling between RBM and G-mode in the excited state, we ran molecular dynamics (MD) simulations. In the ground state, the trajectories (not shown) are perfectly harmonic. The situation is very different in the excited state. Fig. 3b shows the FT of a 1-ps trajectory. In addition to the fundamental RBM frequency, we observe a weak satellites component of the excited state G-mode frequency appearing due to linear mixing of the G and RBM in the excited state. This provides computational confirmation of anharmonic coupling between radial and longitudinal modes induced in the excited state.

In summary, this study shows that ultrashort light pulses can drive coherent atomic motion in SWNTs, in spite of the large inhomogeneous broadening. We have demonstrated the high selectivity of the mechanism. With such a technique, nonlinear MD can be observed. The exciton state modulates the phonon field introducing the nonlinearity, which manifests itself as vibrational coupling. Quantum-chemical dynamic computations show that upon excitation, the surface of the nanotubes corrugates, inducing a coupling between the radial and longitudinal modes, manifesting itself in the frequency modulation experimentally observed in the time domain.

For more information contact Sergei Tretiak at serg@lanl.gov.

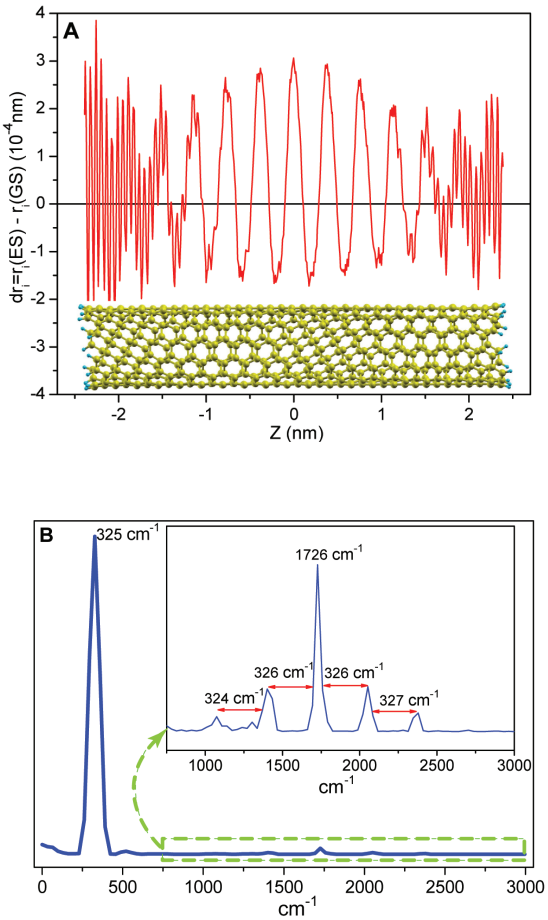

Fig. 3.
(a): Comparison of calculated excited and ground state optimal geometries. Modification of radius dr with carbon coordinate along the tube Z axis for the (7,6) SWNT shown in the inset; (b): FT power spectrum of the trajectory of RBM dimension-less displacement calculated using ESMD approach. Inset: Zoom-out of the FT power spectrum, showing side bands in the high frequency region, which proves experimentally observed vibrational coupling on the excited state.

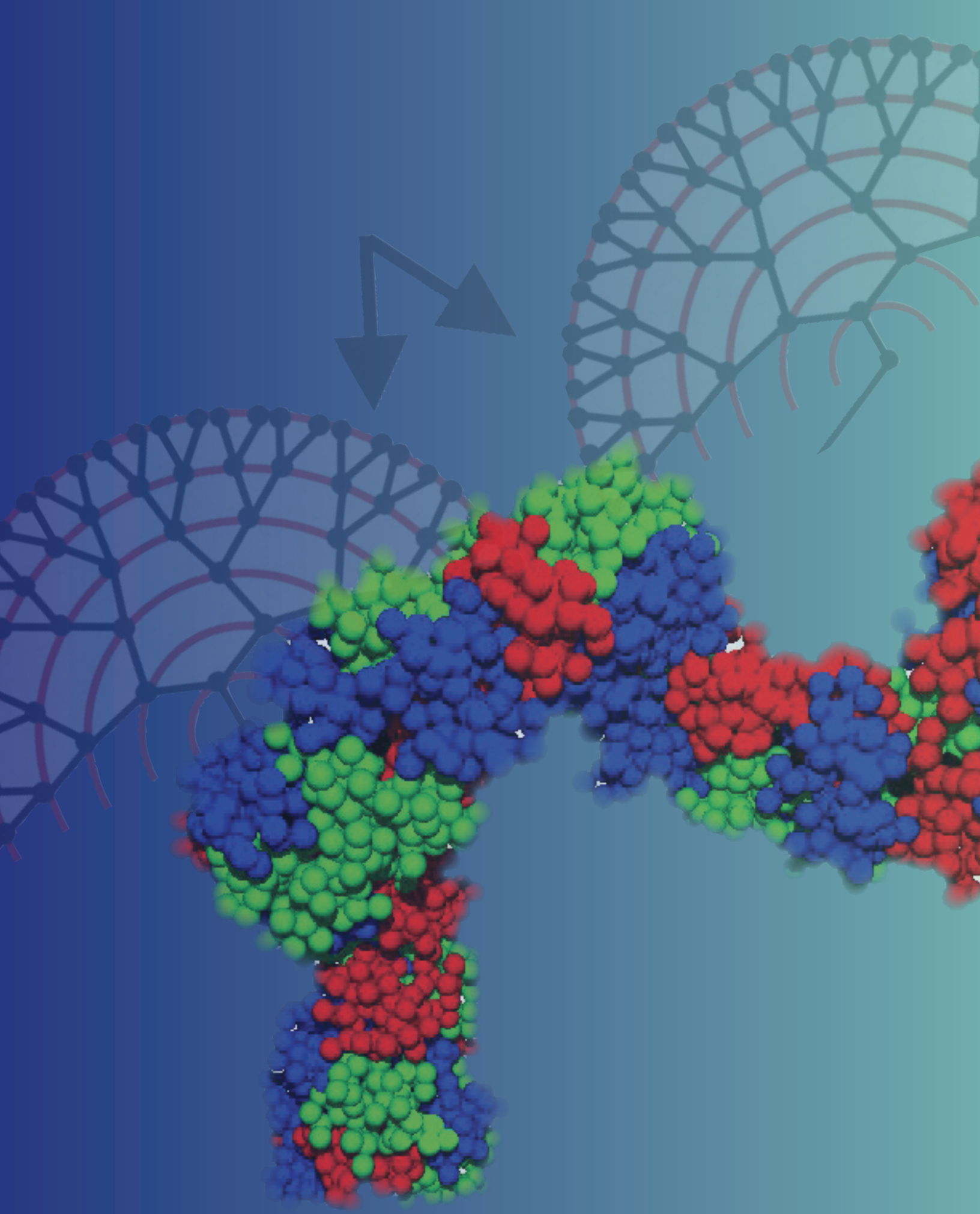

T-14

Explosives and Organic Materials

Group Leader: Ed Kober
505.667.5140, emk@lanl.gov

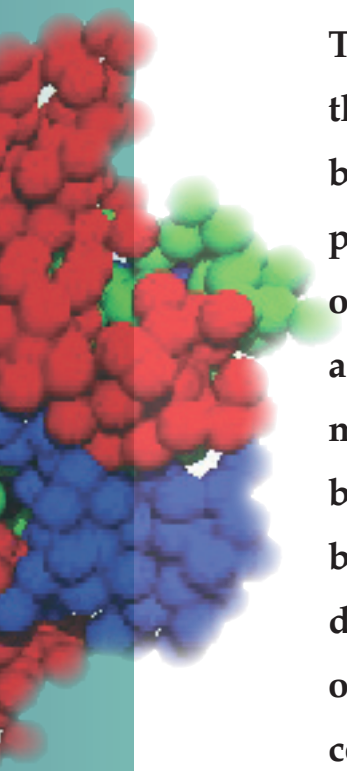

T-14 Explosives and Organic Materials is involved in theoretical modeling of explosives including mechanical behavior, ignition and detonation characteristics, and predicting how these are affected by composition and other factors. This includes expertise in hydrodynamics and shock interactions, reactive flow, equations of state, molecular modeling, and micromechanics and material behavior. Current projects include studies of initiation and burn processes in damaged and intact explosive materials, damaged material behavior, advanced energetic equations of state, *ab initio* molecular modeling, parallel processor computer algorithms, and proliferation issues. These efforts support advanced defense applications and interact strongly with the Laboratory experimental explosives program.

The Rayleigh-Taylor Instability via Direct Simulation Monte Carlo

John L. Barber and Kai Kadau, T-14; Timothy C. Germann, X-1; Peter S. Lomdahl, T-14; Brad L. Holian, X-1; and Berni Alder, and Ed Alley, Lawrence Livermore National Laboratory

The Rayleigh-Taylor (RT) instability occurs whenever a high-density fluid rests on top of a low-density fluid in the presence of a gravitational field g. This arrangement is an unstable equilibrium, and the two fluids will subsequently mix in a process that is a classic example of turbulent mixing. For this reason, the RT instability has been widely investigated over the years, both experimentally and theoretically, starting with Rayleigh in 1883. It has many applications in the study of supernovae, geophysical phenomena such as salt domes or volcanic islands, inertial confinement fusion, and in many other areas.

In recent years the RT instability has been studied via computer simulation. While most simulations have been done using continuum methods, there have also been efforts to perform atomistically based RT simulations that take into account the effects of small-scale thermal fluctuations. This avoids the symmetry or artificiality present in the initial conditions of most continuum RT schemes. Previous work along these lines has involved the use of molecular dynamics (MD) to model the RT instability using on the order of 100,000,000 particles [1]. Due to the computationally intensive nature of MD, systems studied by this method are necessarily restricted to very small length and time scales, which has prompted use of the term "nanohydrodynamics" to refer to these types of calculations. Furthermore, in order to see significant mixing on accessible time scales, it becomes necessary to use a very large value of the gravitational acceleration g, i.e., approximately 10 billion multiples of Earth's gravity in real units.

In the present work, an alternative particle-based scheme known as Direct Simulation Monte Carlo (DSMC) has been applied to the RT instability. Invented by Bird in the late 1960s, DSMC is a Monte Carlo method in which particle collisions are simulated stochastically rather than being calculated explicitly [2]. In addition, DSMC allows the use of a much larger time step. These, and other, factors result in a significant computational speedup when compared to traditional MD. For example, whereas the previous MD work required approximately 250 hours on 1600 CPUs of the ASC Q computer system at Los Alamos, a preliminary DSMC run of about 60,000,000 particles required only 256 processors and less than 12 hours to reach a more advanced point in the development of the flow. In terms of CPU-seconds per particle, this amounts to an increase in speed by a factor of at least 50, even when variations in simulation parameters are taken into account.

Fig. 1.
The local number fraction of heavy particles in the well-developed flow. This is given by n_h/n, where nh is the number density of heavy particles, and n is the total number density. Red corresponds to $n_h/n=1$, and blue corresponds to $n_h/n=0$.

The DSMC run described above was performed using the Scalable Parallel Short-range MD (SPaSM) code [3], and involved the use of 14,370,860 heavy particles of mass m_h=5 and 43,214,549

light particles of mass m_l=1 in the presence of a gravitational field g=0.00025. The system was run in thin slab geometry with periodic boundary conditions in the horizontal directions and specular boundary conditions at the top and bottom. A typical image from the well-developed stage of the flow is shown in Fig. 1. We see that the light fluid moves upward into the heavy fluid in large extrusions known as "bubbles." At the same time, the heavy fluid penetrates the lighter fluid in longer, thinner features known as "spikes."

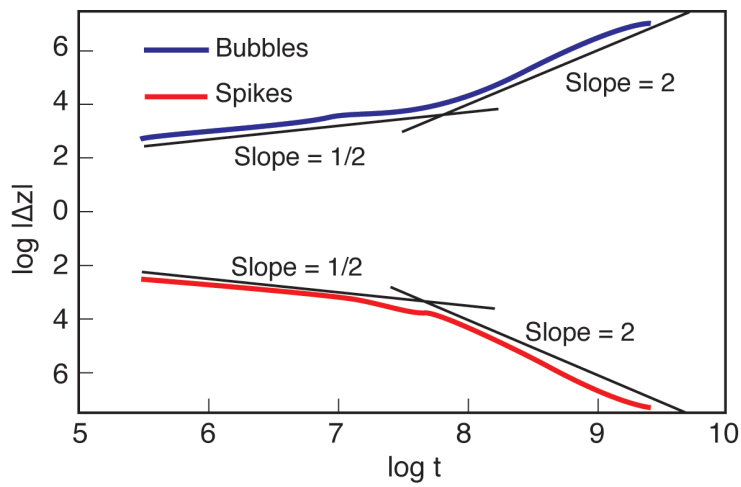

Fig. 2.
A log-log plot of the penetration depth Δz as a function of time for both bubbles and spikes.

It has been found in experiment and predicted by Young that in the turbulent regime the penetration depth of the bubbles and spikes will grow as $\alpha A g t^2$, where $A=(m_h-m_l)/(m_h+m_l)$ is the Atwood number at the interface. The growth of the bubbles and spikes is shown in Fig. 2. As predicted, the penetration depth grows approximately quadratically in t, with α values of about 0.05 and 0.06 for bubbles and spikes, respectively. These values are consistent with the values obtained in experiment, as well as in previous continuum and MD simulations.

Another feature visible in Fig. 2 is the fact that the penetration depth scales as the square root of t for short times. This is a reflection of the fact that, for small t, the dynamics of the interface are dominated by thermal fluctuations due to the random initial atomic coordinates. It is a diffusive effect, which results from the random walks of individual particles. It should be noted that this physical behavior is not accessible in most standard continuum schemes.

Much of the utility of applying DSMC, rather than MD, to the RT instability comes from the fact that the greater speed of DSMC means that larger systems may be considered for longer periods of time, and using a smaller value of g. This allows the simulation of systems that transcend the nanohydrodynamic regime. For example, if we assume that the preliminary run described above has argon as the lighter species, then its width corresponds to about 3 microns in real units. This makes a DSMC simulation of the RT instability better suited for comparison with more traditional continuum schemes, and also with experiments.

For more information contact John L. Barber at jlbarber@lanl.gov.

[1] K. Kadau, et al., PNAS 101, 5851 (2004).
[2] G.A. Bird, *Molecular Gas Dynamics and the Direct Simulation of Gas Flows* (Oxford University Press, Oxford, England, 1994).
[3] P.S. Lomdahl, et al., *Proceedings of Supercomputing 93*, G.S. Ansell, Ed., (IEEE Computer Society Press, Los Alamitos, CA, 1993), p. 520.

Coupling Grain Scale and Bulk Mechanical Response of PBXs via Numerical Simulation

Scott Bardenhagen and Andrew Brydon, T-14

The mechanical response of Plastic-Bonded Explosives (PBXs) is of interest in a variety of munitions and industrial applications. PBXs are composed of energetic grains embedded in a polymeric binder. The heterogeneity at this material scale localizes energy during deformation, resulting in damage nucleation sites and hot spots. Continuum models have been developed to estimate bulk material response, but because there is little connection to the grain scale physics, these models cannot be applied far from their calibrated regime with confidence. To develop predictive models, it is imperative to develop a sound physical understanding of grain scale material response and incorporate the appropriate physics in PBX continuum constitutive models. The Stochastic Transformation Field Analysis (STFA) is a continuum constitutive model that incorporates detailed grain scale information. The STFA develops governing equations applicable to a variety of heterogeneous materials, but requires (grain scale) strain heterogeneity statistics for calibration. This calibration is supplied using numerical simulations of PBXs.

Numerical simulation has been used to extract bulk material properties in a manner analogous to traditional "physical" experiments. In order for the simulations to give repeatable results, they must include a sufficient quantity of material, denoted a "Representative Volume Element" (RVE). For bulk properties, such as moduli, it has been found that good estimates may be obtained with surprisingly small RVEs. Here numerical simulations are used to determine the RVE size for both bulk properties and strain state statistics. The study is performed for detailed geometries and material properties appropriate to PBX-9501, a specific composition of interest at the Laboratory.

A particle method is chosen for performing simulations because of its compatibility with discretization of complex geometries determined experimentally. Samples are extracted from an x-ray microtomography data set and subjected to uniaxial compression. Figure 1 depicts representative grain configurations for the three sample sizes considered; a binder fills the interstitial regions. Bulk composite elastic properties are determined by measuring confining forces during compression. It was found that moduli were accurately estimated (within 1%) using the smallest sample size.

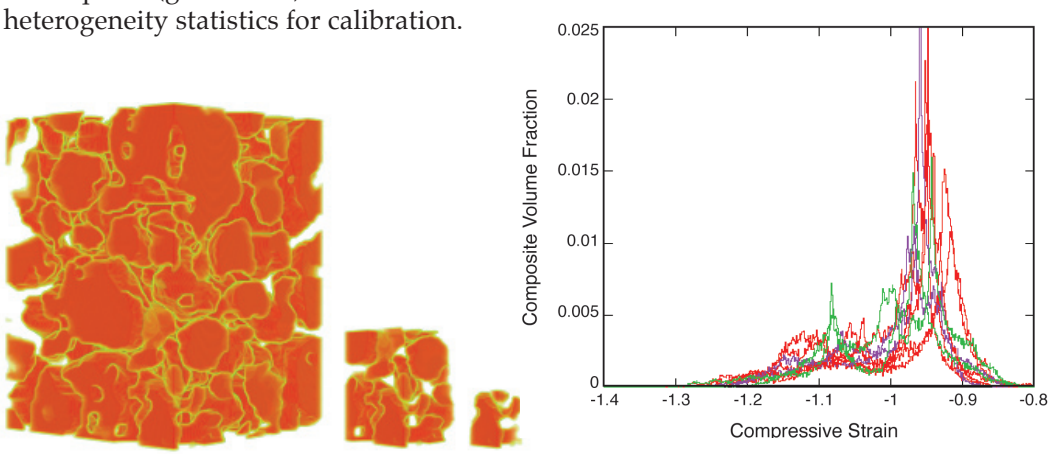

Fig. 1. ***Three material sample sizes used in RVE study (left) and small sample size compressive strain state distributions (nine realizations).***

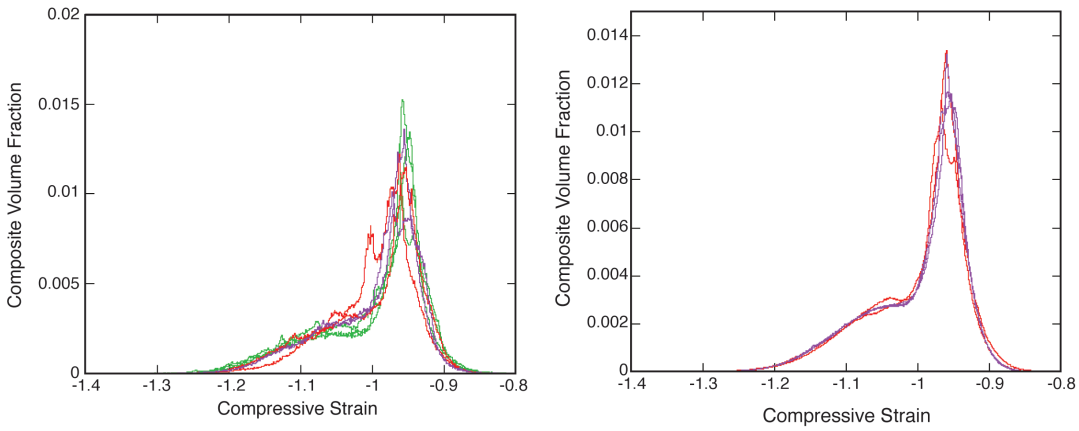

Fig. 2. ***Compressive strain state distributions for the medium (left) and large sample sizes (seven and five realizations, respectively).***

Figure 1 also depicts histograms of the normalized compressive strain for computations on nine small sample size realizations of grain scale structure. Substantial variation in strain distribution is evident. Results for the medium sample size are depicted in Fig. 2. The general similarity of most of the histograms suggests convergence. However, outliers remain, and the definition of the peak is unsatisfactory. Results for the large sample size are also depicted in Fig. 2. While some variation between samples near the peak remains, the general convergence of the histograms suggests that the large sample sizes are statistically representative of PBX-9501. The strain state statistic RVE has physical dimensions 0.39 x 0.39 x 0.53 mm^3, and is approximately one hundred times larger than a bulk property RVE.

The combination of detailed grain scale morphology determined using x-ray microtomography, statistics generated by computations, and a constitutive modeling approach calibrated using these statistics, provides a methodology to include more detailed information in continuum constitutive models of PBX-9501.

For more information contact Scott Bardenhagen at bard@lanl.gov.

Simulation and Analysis of Real Foam Microstructures

Scott Bardenhagen, Andrew Brydon, and Lucas Wharton, T-14

Cellular solids are ubiquitous in nature (e.g., wood, bone), and have been found increasingly valuable in meeting the material demands of an expanding suite of specialized engineering applications (e.g., honeycombs, foams). These materials have unique characteristics relative to more common structural materials, including complex, irregular structure at the cellular scale, i.e., the microstructure. Recent research on polymeric foams is advancing modeling, simulation, and analysis capabilities applicable to Laboratory system components in particular, and cellular solids more generally.

Polymeric foams are light-weight structural components with unique mechanical properties and applications. They are used in packaging to isolate components and absorb energy. They routinely operate over a large range of compressions in service. Well-established "rules of thumb" exist for estimating foam bulk mechanical response from parent material properties and a few basic characteristics of the cellular microstructure. However, the range of mechanical response measured for nominally identical foams clearly indicates that additional characteristics are important.

While this would seem to be a promising scenario for contributions via computation, the simulation of foams is a well-established computational challenge for several reasons: 1) The deformations of interest are large, both bulk and on the cellular scale, 2) extensive "self contact" must be simulated as the microstructure collapses upon itself, and 3) realistic foam microstructures are irregular and difficult to discretize for computations using a body-fit mesh. This combination of challenges has limited many modeling efforts to small deformations and idealized foam microstructures.

Recent developments in particle-in-cell (PIC) methods indicate that these numerical techniques are suitable for precisely this class of problem. Using experimentally determined foam structures (Fig. 1), quasi-static compression was simulated with results in agreement with experimental data in the literature. It was predicted that the full foam sample is an auxetic material at modest compressions, and that it becomes progressively more difficult to remove porosity, resulting in residual porosity even in "fully densified" foam [1].

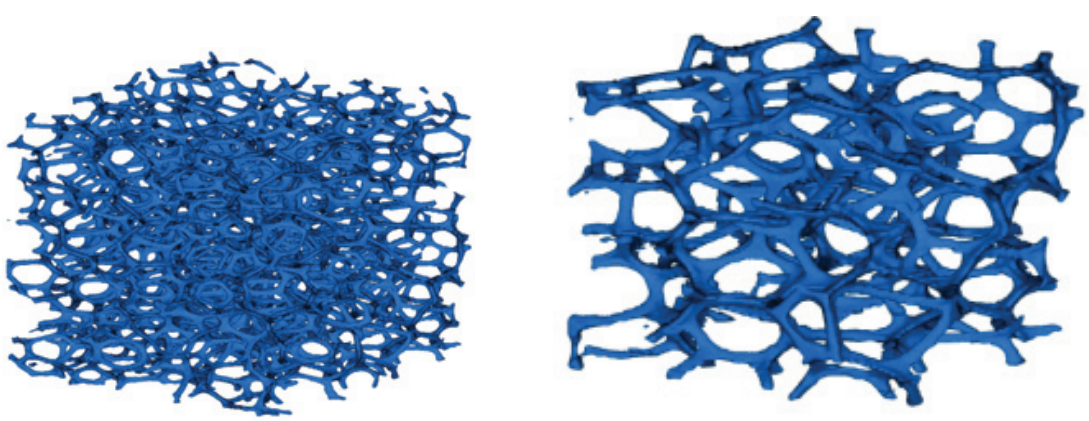

Fig. 1. ***Full sample of a foam microstructure (3.4 x 3.4 x 2.7 mm^3) and an 1/8 sample obtained from the bottom right corner.***

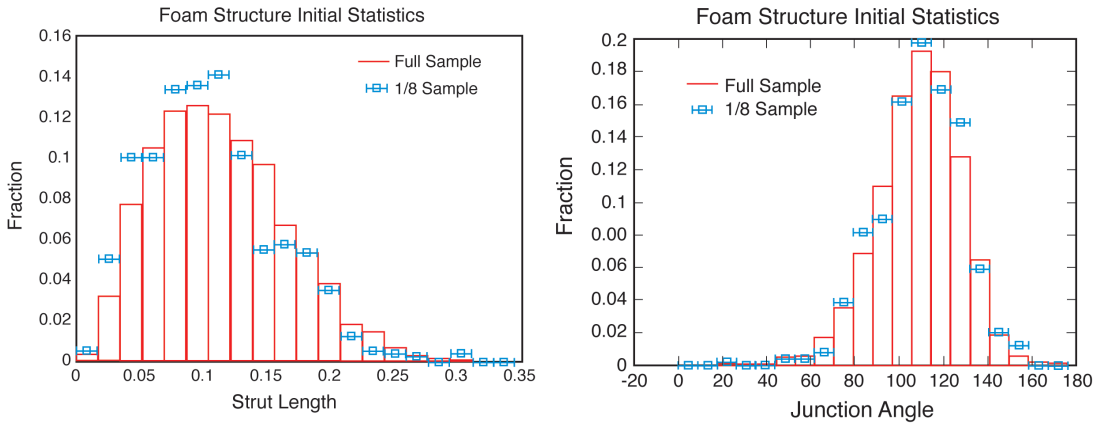

Fig. 2. ***Strut length (left) and strut junction angle distributions.***

More recently, image analysis has been used to identify microstructural features. Figure 2 highlights the differences in strut lengths and strut junction angles (determined pair-wise) between the full foam sample and the subsection, both depicted in Fig. 1. Variations in both microstructural features and average compressive response are being compared in order to 1) characterize foam deformation in detail and identify the features which affect bulk response, and 2) determine the quantity of material required to produce mechanical response representative of bulk foam.

Experimental techniques are being used to measure deformed foam microstructures, providing detailed validation data. An approach to developing bulk foam constitutive models is under development in which bulk response is obtained from unit cell mechanics models, foam structure statistics, and variations in average response. The simulations and analysis described here will be used to calibrate this theory, connecting material scales and providing an additional validation path.

For more information contact Scott Bardenhagen at bard@lanl.gov.

[1] A.D. Brydon, et al., *J. Mech. Phys. Solids* **53** (12), 2638–2660 (2005).

Influence of Supercoiling on the Disruption of dsDNA

Shirish M. Chitanvis and Paul Welch, T-14

Unzipping of double-stranded DNA (dsDNA) as a prelude to transcription is a basic process of life. There are presently two mechanisms that are considered for modeling this phenomenon. One is the Peyrard-Bishop model, in which localization of energy via a Fermi-Pasta-Ulam scenario of coupled nonlinear oscillators causes thermal bubbles to form spontaneously at specific locations along a dsDNA chain. The other mechanism is modeled by representing proteins, which cause unzipping, as an external force. This latter class of models envisions dsDNA as composed of coupled flexible Gaussian chains. It may be a reasonable approximation to treat a long semiflexible chain as an effective Gaussian chain with the monomer length substituted by the persistence length in order to investigate global characteristics. But a realistic attempt to treat the unzipping process through the application of an external force to a small region of the dsDNA must necessarily take into account the semiflexible nature of the system.

There is an additional outstanding issue that complicates our understanding of the unzipping of dsDNA. It arises through the observation that one can estimate the base-pair force as ~ O(100 pN), while the experimentally observed minimum (external) disruptive force is only of the order of ~ O(10 pN). Thus there would appear to be an intrinsic source of energy that allows the dsDNA to overcome this mismatch. What subtle mechanism comes into play during base-pair separation to explain this mismatch?

Supercoiling is an ubiquitous feature of semiflexible rods. One might conjecture that supercoiling plays a role in the packing of dsDNA. We can make the case that supercoiling energy can have an appreciable effect on this phenomenon, by providing extra energy to overcome the free energy barrier to disruption.

Benham was the first to suggest a phenomenological model to describe the influence of supercoiling on base-pair disruption. Benham's seminal model is an effective single-strand helical representation of DNA. He obtained the parameters for his (nonlinear) Ising-like model by calibrating it to one set of DNA data, then verified that the same choice of parameters worked for another experiment.

The model developed in this paper provides a deeper and more detailed, analytical insight into the mechanism of base pair disruption in dsDNA. Marko and Siggia described the supercoiling of DNA by appealing to an evocative image of an over-twisted shoelace. The analogy that best describes the results of our model is that dsDNA is like a ladder made out of bamboo. If the ladder is twisted beyond its normal, equilibrium planar state, one can imagine that it would be easier to break the rungs.

We assert that this is precisely what happens in dsDNA. Supercoiling, or over-twisting, energizes the dsDNA, making it more likely that thermal fluctuations will cause a given base-pair to be disrupted. Our theory provides qualitative insight into the experimental observations that superhelicity can make pBR322 DNA and *E. coli* duplex unwinding elements susceptible to strand separation even if the over-twisting spans only a few base-pairs. This phenomenon is called stress induced duplex destabilization.

We have attached two figures that show how supercoiling can lead to localized distension of a modelized dsDNA. The first figure shows a putative segment of

dsDNA undistorted and in equilibrium. The second displays how supercoiling can lead to localized distension of bonds.

A paper on this subject was recently published [1]. It was also selected to appear in the *Virtual Journal of Biology* as reflective of papers at a research frontier.

For more information contact Shirish Chitanvis at shirish@lanl.gov.

[1] S.M. Chitanvis and P.M. Welch, *J. Chem. Phys.* **123**, 124901 (2005).

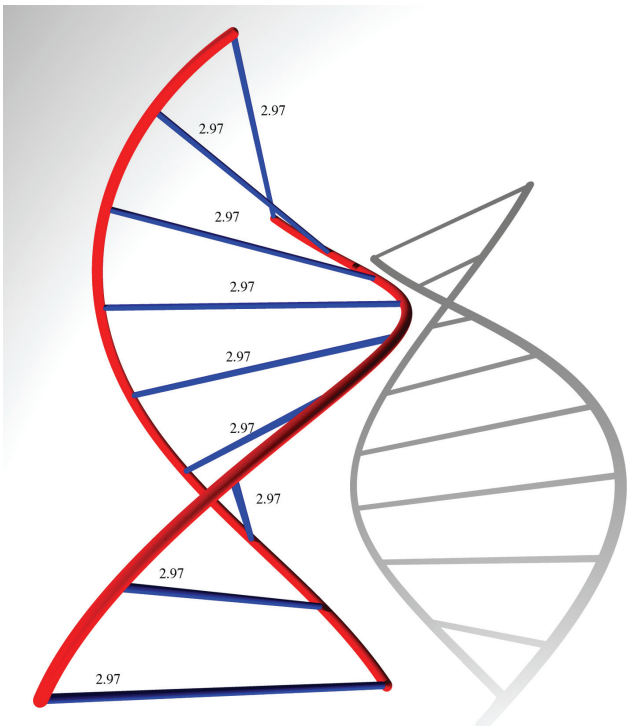

Fig. 1. ***A putative segment of dsDNA undistorted and in equilibrium.***

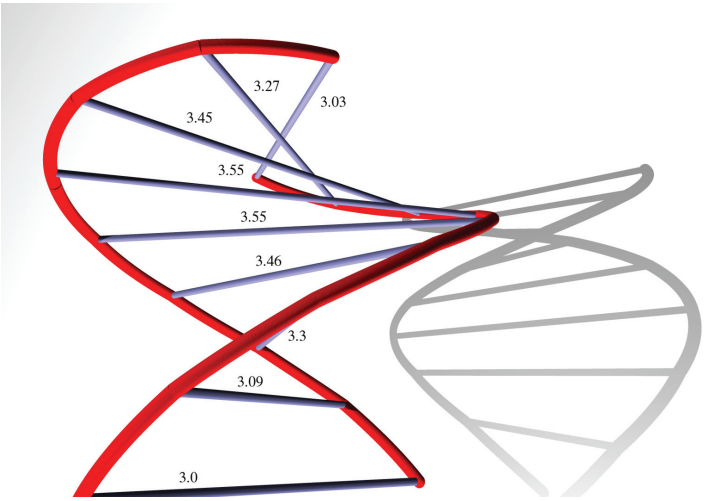

Fig. 2. ***How supercoiling can lead to localized distension of bonds.***

Can Low-Power Electromagnetic Radiation Disrupt Hydrogen Bonds in dsDNA?

Shirish M. Chitanvis, T-14

Experimental studies abound concerning electromagnetic (EM) effects on the cleavage of DNA. Many of these studies focus on the effect of low-power, low-frequency radiation. These investigations fall into two categories. One is epidemiological, where statistical methods appear to be unable to either rule out, or establish the genotoxic effects of low power, low frequency ambient radiation. The other is laboratory studies of DNA samples subjected to various types of EM radiation. Given the proliferation of technology, the questions raised by these studies cannot be ignored.

The experimental papers referred to above study the cleaving effects of EM radiation, which must involve the breakage of covalent bonds. However, hydrogen bonds couple base-pairs along a dsDNA with energies comparable to normal room temperature. As such, they are more likely to be disrupted by external perturbations than covalent bonds. For this reason, we will focus on coupling EM fields to the phonon modes of dsDNA via bound charges on the strands.

The phonon modes refer to oscillations of the backbone of the DNA molecule. In turn, they couple to the hydrogen bond fluctuations between base-pairs. The bound charges are either native to the dsDNA or are counter-ions adsorbed from the surrounding ionic, aqueous solvent. Adair has provided one of the few theoretical treatments of the coupling of environmental EM radiation on biosystems. He made estimates of the damaging effects of EM radiation on macroscopic, static properties of biological systems and found them to be negligible. His approach is based on the assumption of the linearity of the response of a system to infinitesimal perturbations. Ambient conditions are generally accepted to fall into this category.

However, it is possible that dynamic resonant conditions may amplify the disruptive effects of small perturbations via an instability. The rate of growth of this instability is highly dependent on the power level and frequency of the incident EM radiation. It is greatly limited by dissipation to the ubiquitous aqueous solvent. We have been able to show that EM radiation at frequencies resonant with those of the phonon modes of dsDNA will cause disruption *if* the power level of the EM fields exceeds a critical value, and *if* the coupling to the environment is sufficiently weak.

The two figures show what happens when, first, EM radiation in the microwave region is *not* resonant with the fundamental modes of the dsDNA. The second one shows what happens if the radiation is indeed on resonance, and coupling to the environment is weak.

A paper on this subject has been invited for submission to *Polymer Physics Journal B*, for an issue dedicated, among other topics, to biophysics.

For more information contact Shirish Chitanvis at shirish@lanl.gov.

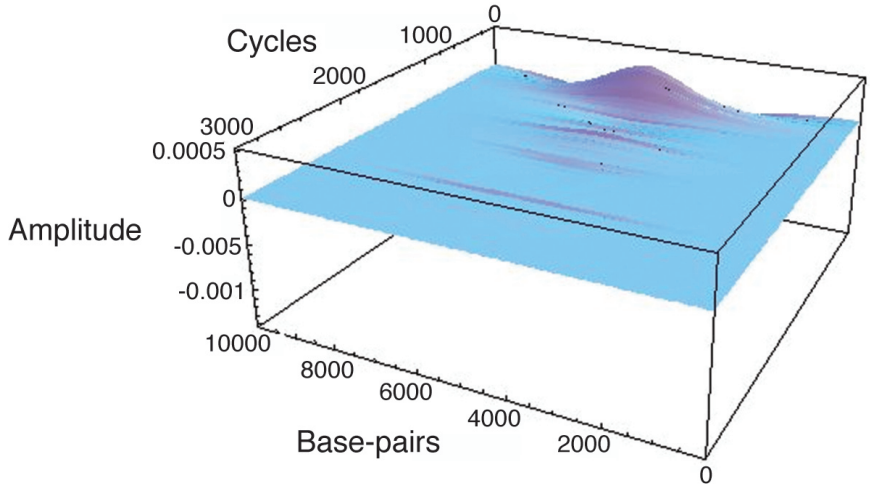

Fig. 1.
What happens when, first, EM radiation in the microwave region is not resonant with the fundamental modes of the dsDNA.

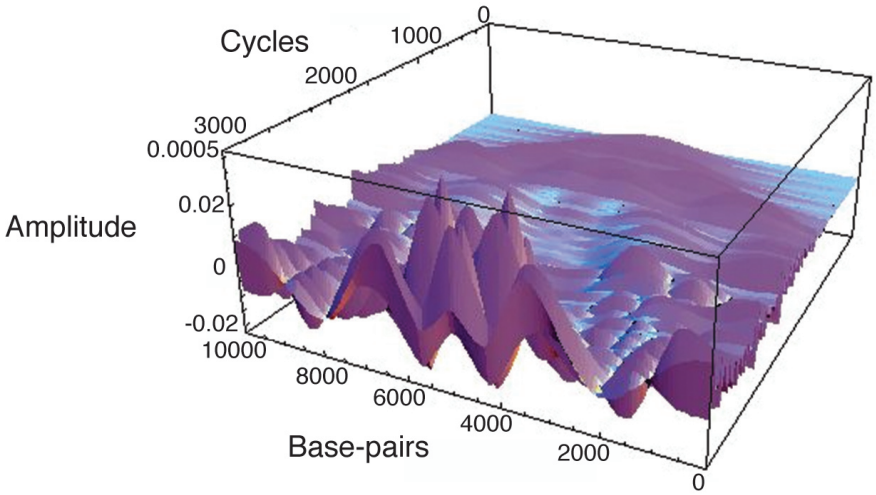

Fig. 2.
What happens if radiation is on resonance, and coupling to the environment is weak.

Probing the Physics of Mix

Shirish M. Chitanvis, T-14

In 2002 Scannapieco and Cheng developed a multifluid theory (SC model) exhibiting direct interpenetration via a difference in the partial pressures of species. They adopted a Prandtl mixing hypothesis that was used successfully to obtain agreement with inertial confinement fusion experiments. Of course, other models have been developed as well to explain mix on an empirical basis. The diversity of ideas brought to bear on this problem serves to emphasize that experiments on mix can be explained in an empirical fashion from various perspectives.

The SC theory derives a set of multifluid hydrodynamic conservation equations, in which mass, momentum, and energy may be transferred between species. It employs a minimalist approach through its use of a single-fitting parameter to characterize momentum and energy transfer. In this sense it is appealing, though daunting, to inquire into the microscopic basis of the SC model.

We have begun to develop an *ab initio* theory to replace the Prandtl hypothesis of the original SC model. We show that the SC mixing length can be expressed in terms of the screening length of a plasma. On one hand, this parameter, which is difficult to obtain from first principles, may be obtained by fitting to experiments involving mix.

Alternatively, we have begun a program to calculate the screening length from first principles. Initial calculations using classical field theory suggest that lowest-order corrections can be significant when the temperature and number density is sufficiently low. This situation is likely to occur in the vicinity of the edge of the distribution of a heavy specie that has penetrated into a light specie. Our method provides an accurate estimate of the mixing length due to atomic scale phenomena. If this turns out to be insufficient to explain experimental results, it will aid in the future development of a more fundamental *stirring* (turbulence) model applicable on a longer scale.

For more information contact Shirish Chitanvis at shirish@lanl.gov.

Atomistic Studies of Quasi-Static Compression in α-HMX

Eugenio Jaramillo and Thomas D. Sewell, T-14; and Alejandro Strachan, Purdue University

We have performed molecular dynamics simulations of uniaxial compression for the α conformer of octahydro-1,3,5,7-tetranitro-1,3,5,7-tetrazocine (α HMX) along different crystallographic directions. The system studied contained 24576 molecules (688128 atoms) in a box with dimensions 180.8 x 192.7 x 194.7 Å. Periodic boundary conditions were employed in all directions. The force field used was taken from Smith and Bharadwaj [1] and includes all degrees of freedom with the exception of C-H bond stretching vibrations, which were fixed at their equilibrium values using the SHAKE algorithm. We performed the simulations using a modified version of the LAMMPS Molecular Dynamics code [2, 3] from Sandia National Laboratories. The system was thermalized for 10 ps at 300 K in the NVT ensemble before starting the compression cycles. Each compression cycle consisted of a uniaxial decrease in volume of 0.1% relative to the original volume V_0 followed by 0.4 ps of NVE equilibration. A total of 250 cycles were performed, producing a final system with a volume that was $0.75V_0$. After compression, the system was expanded to its original volume at the same rate and with the same equilibration as followed during the compression. Compression/expansion cycles were performed for the (100), (010), and (001) directions.

A large degree of directional anisotropy in response to compression was observed. Figure 1 shows pressure vs relative volume for the compression and expansion cycles in all three directions. For compression in the (100) direction, the system begins to exhibit plastic deformation while maintaining the α crystal structure at a pressure of about 2.0 GPa, with planes slipping in the ½(101) direction (Fig. 2a). For compression in the (010) direction a phase transition is observed at a pressure of about 0.5 GPa (not shown), while during compression in the (001) direction a different phase transition is observed at about 1.0 GPa (Fig. 2b) with a further rearrangement at a pressure just below 2.0 GPa. The two phase transitions observed during compression in the (010) and (001) directions persisted even after the system was expanded back to its original volume.

In all cases compression increases the number of first near-neighbors (defined as those with molecular center-of-mass distances less than 9.5 Å) from 14 to 16. Up to 8% of the molecules change ring conformation during compression; most of those that do are localized to the neighborhood of the slip planes, grain boundaries, or "twin" planes [(001, (010), and (001) compressions, respectively].

There are no experimental data to confirm or refute the results reported here, but the robustness of the force field for thermophysical and elastic mechanical properties where data do exist gives us some confidence that the directional anisotropy, plastic deformation and phase transitions are qualitatively representative of what would be observed in the real material during uniaxial quasi-static compression. The results shown here serve a basis for the large-scale molecular dynamics shock compression computations described in another paper by Jaramillo and Sewell in this volume on p. 133.

For more information contact Eugenio Jaramillo at eugenio@lanl.gov.

[1] G.D. Smith and R.K. Bharadwaj, *J. Phys. Chem. B* **103**, 3570 (1999).
[2] S.J. Plimpton, *J. Comp. Phys.* **117**, 1 (1995).
[3] S.J. Plimpton, et al., *in Proc. of the Eighth SIAM Conference on Parallel Processing for Scientific Computing*, (Minneapolis, MN, March 1997).

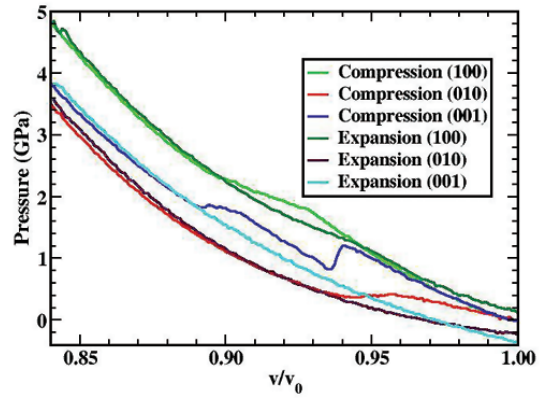

Fig. 1. *Pressure response of α HMX during quasi-static uniaxial compression and expansion.*

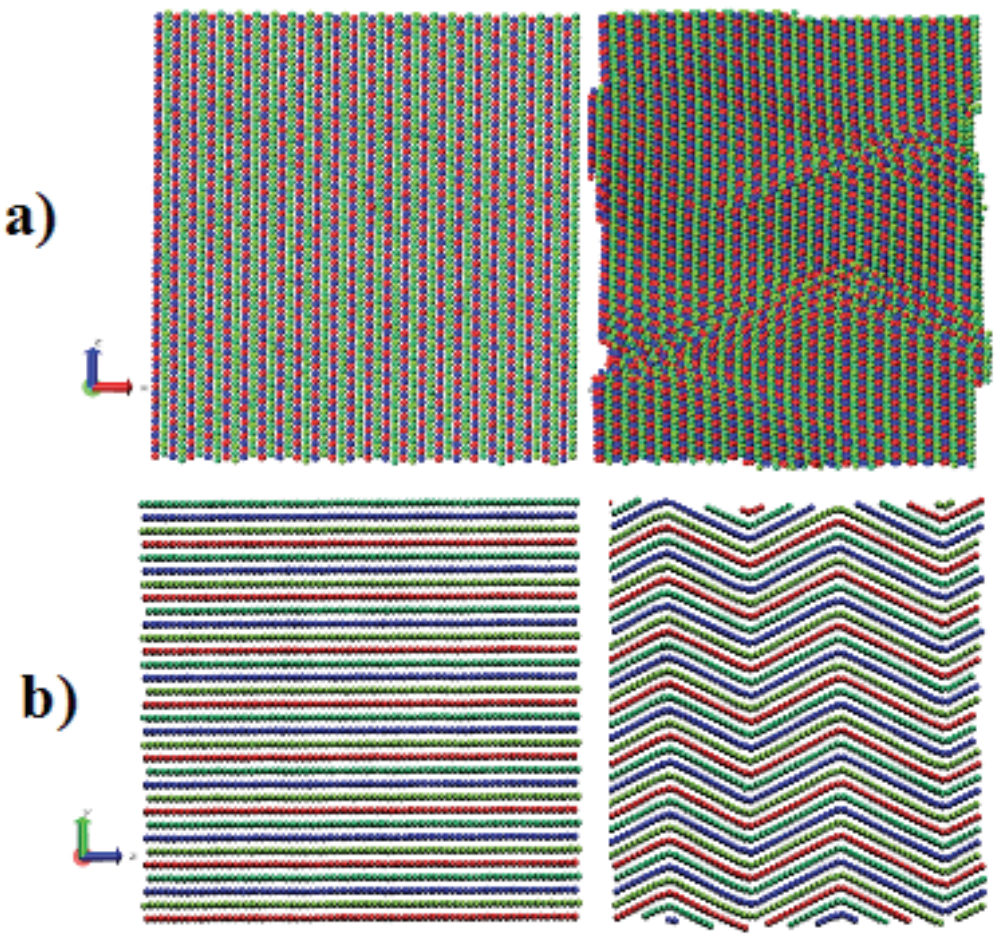

Fig. 2. *Snapshots of the α HMX system before (right) and after (left) compression in the (100) direction (a) and (001) direction (b). For simplicity, the snapshots show only the center of mass of the molecules, although fully atomistic simulations were performed. Molecules were colored only to facilitate the observation of the features created by compression.*

Inelastic Deformation in Shock Loaded HMX

Eugenio Jaramillo and Thomas D. Sewell, T-14; and Alejandro Strachan, Purdue University

In previous editions of T-Division Highlights we summarized calculations of equilibrium thermophysical and elastic mechanical properties of liquid and crystalline HMX. (As with the present report, we described work in progress; full details can be found in the literature.) These results, obtained using atomistic molecular dynamics (MD) and Monte Carlo methods in conjunction with a validated, flexible force field, have found a significant audience within T-Division as well as in other organizations at the Laboratory and elsewhere.

We have extended these equilibrium studies to large-scale MD calculations of the inelastic mechanical response of HMX crystal subjected to shock loading. The purpose of these nonequilibrium studies is to obtain a fundamental description of the mechanisms by which dissipation and inelastic deformation (plasticity) occurs in complicated, anisotropic polyatomic molecular crystals. The practical focus is on weak shocks, relevant for instance to accidental initiation phenomena. Indeed, the long-term goal of these studies is the development of constitutive models for plastic-bonded explosive constituent materials, for use within mesoscale simulation studies of energetic materials formulations.

We impose three major requirements on the present effort: 1) that the simulations treat a piece of material sufficiently large to capture the underlying physics without fear of severe contamination by finite-size effects; 2) that the simulations are sufficiently long to allow that physics to be revealed; and 3) that the simulations are performed for loading scenarios of direct relevance to theorists and simulators working at larger spatial scales. We have determined that three-dimensionally periodic systems containing >250,000 molecules (~7 million atoms, simulated for times of 30–100 ps are required to satisfy the first two requirements for the dynamic loading conditions of interest, namely shocks of up to only a few GPa in strength. Such calculations are only now becoming possible and, even then, only with access to substantial parallel computing resources and efficient parallel computer code. The simulations described here were performed using 128, 256, or 384 processors on the FLASH opteron cluster in conjunction with a version of the LAMMPS computer code modified to treat shockwave boundary conditions.

We focus here on a shock with $U_p = 0.5$ km/s directed along the (100) direction in the orthotropic material α-HMX. Snapshots of the material at time = 32 ps are shown in Fig. 1.

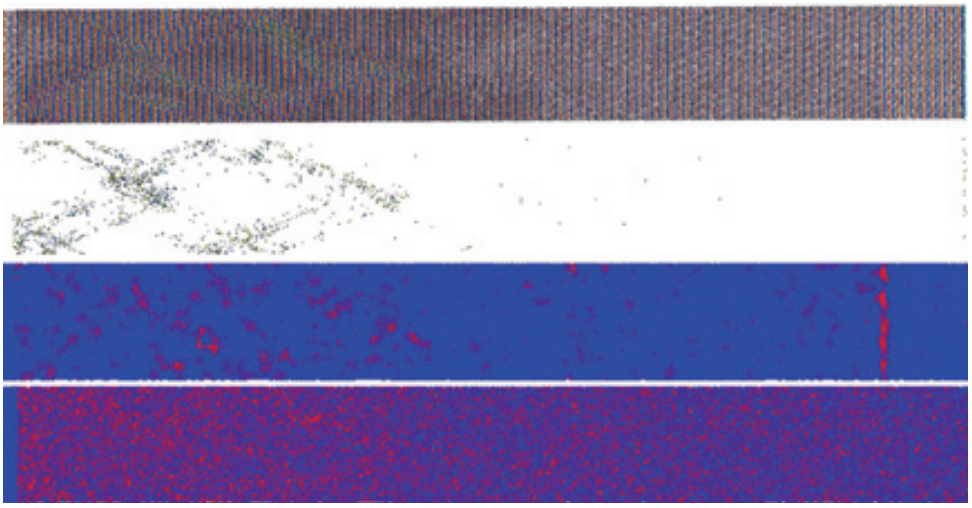

Fig. 1. ***Snapshots taken during a shock in α HMX with particle velocity 0.50 km/s at time t = 32 ps. The top panel shows the position of the center of mass of the molecules, the second panel shows the molecules that have changed conformation during the simulation, and the last two panels show temperature maps for internal and local temperatures (see text for explanations).***

This is a time close to breakout for the shockwave, which is propagating from left to right in the figure. Although all atoms were included in the simulation, only the molecular centers of mass are shown here for ease of presentation (thus, the twenty eight atom HMX molecule is rendered as a spherical chicken!); likewise, the coloring scheme was chosen to highlight the crystal structure present in the material at the beginning of the simulation. It is clear from the upper panel of Fig. 1 that the material has undergone localized plastic deformation, and that the mechanism by which it has done so is slip along well-defined planes in the material; dislocations in which molecular displacements by several lattice spacings are evident. It is also important to note the existence of a two-wave structure: the elastic wave associated with elastic compression at the shock front is well ahead of the plastic wave associated with inelastic deformation — dislocations and slip — in the material.

HMX contains an eight-member ring that can exist in several distinct energy minima separated by small barriers. We show in the second panel of Fig. 1 only those molecules whose conformation is different from those at t = 0, that is, those that have undergone a conformational transition. At this instant, only 0.4% of the molecules have undergone a transition, and those that have are highly correlated with the slip planes in the material. (A transient population is also observed at the shock front, but almost all of those molecules recover the starting conformation once the initial shock has passed by. We show in the bottom two panels of Fig. 1 temperature maps in the material for the "local" and "internal" temperatures, respectively. The local temperature is a measure of the relative center-of-mass velocities in a given neighborhood, whereas the internal temperature is a measure of the molecular vibrational kinetic energy.

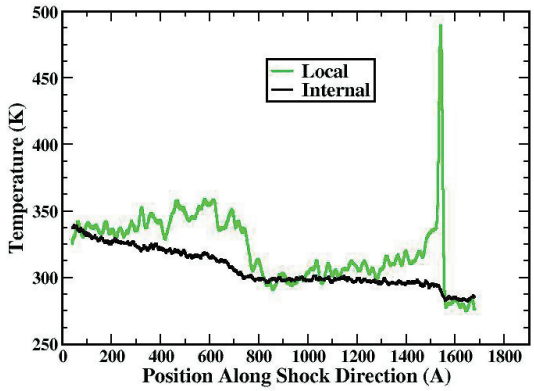

Fig. 2. *Average local and internal temperatures as a function of position for a shock in α HMX with particle velocity 0.50 km/s at time t = 32 ps.*

The local temperature clearly reveals the shock front, due to the large center-of-mass acceleration as the shock passes through the material. Immediately behind the shock, the local temperature in the elastically compressed material remains relatively low. The onset of plastic deformation is clearly correlated with localization of local temperature. By contrast, the shock front is not obvious in the internal temperature map and significant molecular vibrational heating is not readily apparent until after plastic deformation has begun. This is quantified in Fig. 2, which shows the average local and internal temperatures as a function of position in the material, where the differences in magnitudes and spatial scales required for local and internal heating in the elastic and plastic waves is clearly evident.

Studies presently underway will consider the effects of varying shock strength and direction, initial temperature, material phase, and a variety of defect structures such as vacancies, voids, and grain boundaries. In addition, the distribution of local stresses in the material will be quantified to further elucidate the mechanisms of and thresholds for the onset of plastic deformation.

For more information contact Eugenio Jaramillo at eugenio@lanl.gov.

Direct Observation of the alpha-epsilon Transition in Shock-Compressed Iron via Nanosecond X-ray Diffraction

Kai Kadau, T-14; Timothy C. Germann, X-1; Peter S. Lomdahl, T-14; Brad L. Holian, X-1; D.H. Kalantar and J. Hawreliak, Lawrence Livermore National Laboratory; K. Rosolankova, University of Oxford; and J.S. Wark, University of Oxford

One of the most fundamental properties of a solid is its crystallographic structure. Many crystals undergo structural phase transitions under the influence of static pressure or shock compression. One of the most studied systems at high pressure is iron because of its technological importance in society and its geophysical role within the earth's core.

This joint effort of small-scale experiments and large-scale atomistic simulations shows the first direct measurement of a structural transformation in shocked iron, in situ, and with nanosecond resolution [1]. These results are in remarkable agreement with the theoretical predictions on the transformation mechanisms of the alpha → epsilon (bcc → hcp) phase transformation in solid iron single crystals given by K. Kadau, et al. [2]. This work provides an excellent example of how theoretical methods can guide experiments and shows the convergence of large-scale theoretical techniques such as atomistic simulations and small-scale experiments on the other side. Further experiments to compare shocks to atomistic predictions [3] for shocks along [011] and [111] are underway.

For more information contact Kai Kadau at kkadau@lanl.gov.

[1] D.H. Kalantar, et al., *Phys. Rev. Lett.* **95**, 075502 (2005).
[2] K. Kadau, et al., *Science* **296**, 1681 (2002).
[3] K. Kadau, et al., *Physical Review B* **72**, 064120 (2005).

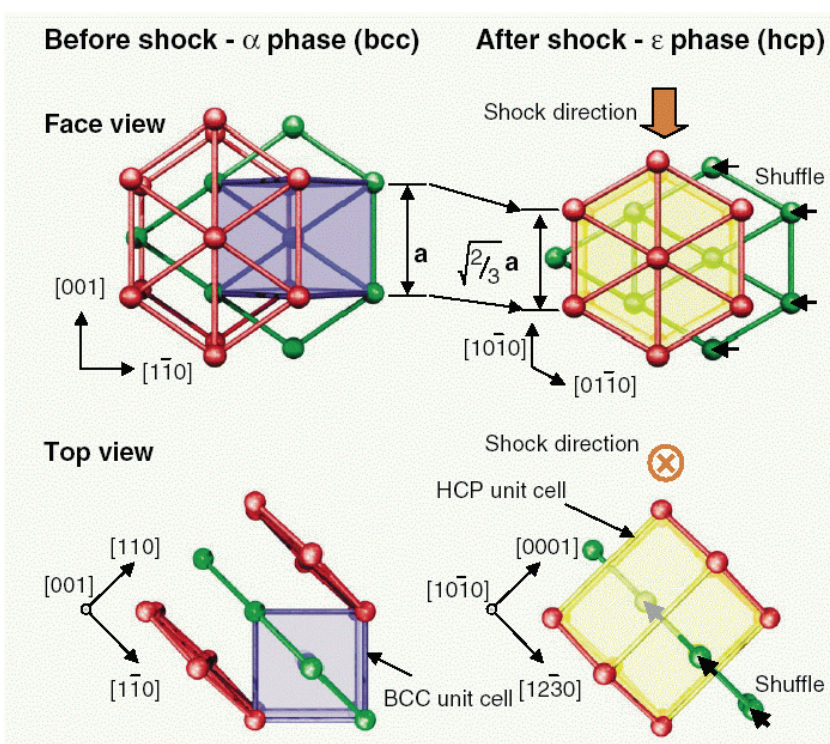

Fig. 1. Schematic showing the lattice structure of the bcc and hcp phase for iron. A pseudohexagonal structure results from the 18.4% compression of a bcc lattice along [001]. Shuffling of alternate (110) planes creates the close-packed structure.

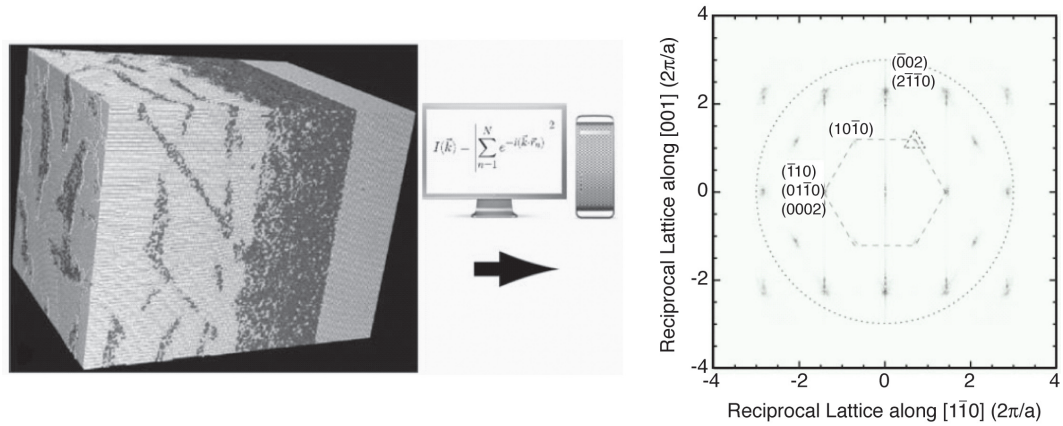

Fig. 2.
This figure shows schematically the method of post processing the molecular dynamics data in order to compare to experimental diffraction data. The atomic positions from the atomistic simulation are Fourier transformed into reciprocal lattice space, so the high intensity peaks represent diffraction planes in the crystal structure. The units are based on the inverse of the original cubic bcc cell. Three points are labeled with the plane labels on the figure. One point contains three labels, to show that there is a bcc component and two hcp components, due to the two degenerate hcp states. A dashed hexagon shows the reciprocal lattice points are approaching a hexagon. The dotted circle gives the limits that can be probed using K-shell radiation from an iron backlighter.

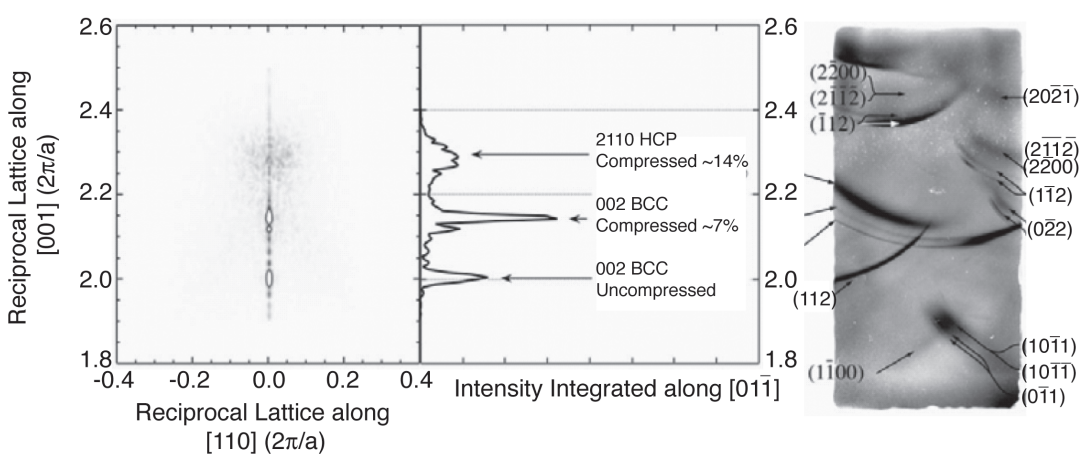

Fig. 3.
A high-resolution image of the bcc (002) and hcp (2-1-10) peaks. It also shows the integration over the [1-10] direction to give an idea of the widths of the representative peaks. Arrows show the location on experimental film the measurement of each of these peaks. Other diffraction planes are labeled with their plane labels, in both bcc and hcp.

Multibillion-Atom Molecular Dynamics Simulations of Shockwave Phenomena on BlueGene/L

Timothy C. Germann and Brad L. Holian, X-1; Kai Kadau and Peter S. Lomdahl, T-14

The IBM BlueGene/L (BG/L) supercomputer at Lawrence Livermore National Laboratory consists of 65,536 nodes, each with two IBM PowerPC 440 processors (at 700 MHz clock speeds) and 512 MB of memory [1, 2] with a theoretical peak performance of 360 Tflop/s. With its three independent internal networks on BG/L, message passing times are excellent compared to most other machines.

We have ported our large-scale molecular dynamics (MD) code SPaSM [3] to the BG/L architecture and run up to 320 billion atoms to test the linear scaling of our algorithm for an enormous number of particles [4] that have never been simulated before [5]. In addition we developed a parallel graphics capability that allows for the rendering of spheres, bonds, and cells [5]. This was necessary since efficient parallel on-the-fly rendering for millions to billions of objects is not available. Here, we report on how these large-scale atomistic simulations can be applied to material science of shock wave phenomena. This work has been accepted together with two other finalists for the Gordon Bell prize performance award at the Supercomputing 2005 conference in Seattle [4].

For large-scale simulations, one would thus like to focus on fast processes, ideally with predictable simulation time requirements. Examples can be found in a variety of high strain-rate processes, including fracture (tensile and/or shear loading), sliding friction (shear loading, often along with compression), and the propagation of shock compression waves. In recent years, we have shown that nonequilibrium MD simulations can provide unprecedented insight into shock-induced plasticity 0 and solid-solid phase transitions 0. A typical simulation geometry used to study both the shock compression as well as release processes is shown in Fig. 1, which can be used to reliably estimate the required simulation time. One such simulation, involving a perfect crystal flyer plate and target with "only" 205 million atoms, is shown in Figs. 2 and 3, illustrating the spall process as well as the visualization capability. In this case, using a "centrosymmetry" order parameter 0 to distinguish fcc from non-fcc atoms provides a clear view of the plastic deformation and spall failure that occurs.

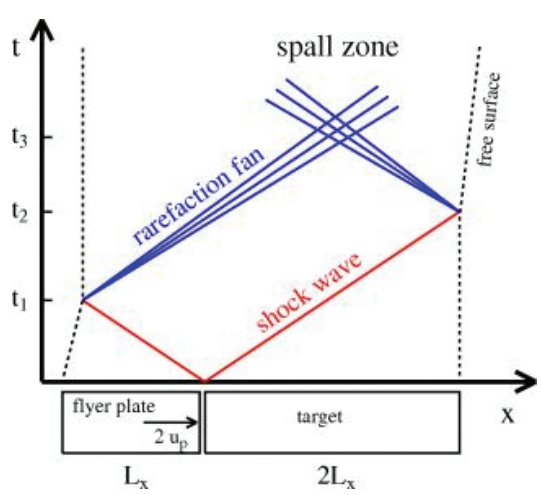

Fig. 1. ***Schematic x-t diagram showing the loading (red shock fronts) and unloading (blue expanding rarefaction fans) geometry, and relationship to required simulation times: $t1 = L_x/u_s$ is the shock transit time through the flyer plate, $t_2 = 2t_1$ the transit time through the target, and $t_3 \approx 3t_1$ the time at which the expanding rarefaction fans collide and induce a tensile region.***

For more information contact Kai Kadau at kkadau@lanl.gov.

[1] N.R. Adiga, et al., "An Overview of the BlueGene/L Supercomputer," *in SC2002 – High Performance Networking and Computing*, Baltimore, MD, November 2002.
[2] G. Almasi, et al., "Unlocking the Performance of the BlueGene/L Supercomputer," *in SC2004 – High Performance Computing, Networking and Storage Conference*, Pittsburgh, PA, November 2004.
[3] D.M. Beazley and P.S. Lomdahl, *Parallel Computing* **20**, 173–195 (1994).

[4] T.C. Germann, et al., "25 Tflop/s Multibillion-Atom Molecular Dynamics Simulations and Visualization/Analysis on BlueGene/L," to appear in *Supercomputing 2005.*
[5] K. Kadau, et al., *Int. J. Modern Phys. C* **15,** 193–201 (2004).
[6] B.L. Holian and P.S. Lomdahl, *Science* **280**, 2085–2088 (1998).
[7] K. Kadau, et al., *Science* **296**, 1681–1684 (2002).
[8] C.L. Kelchner, et al., *Phys. Rev. B* **58**, 11085–11088 (1998).

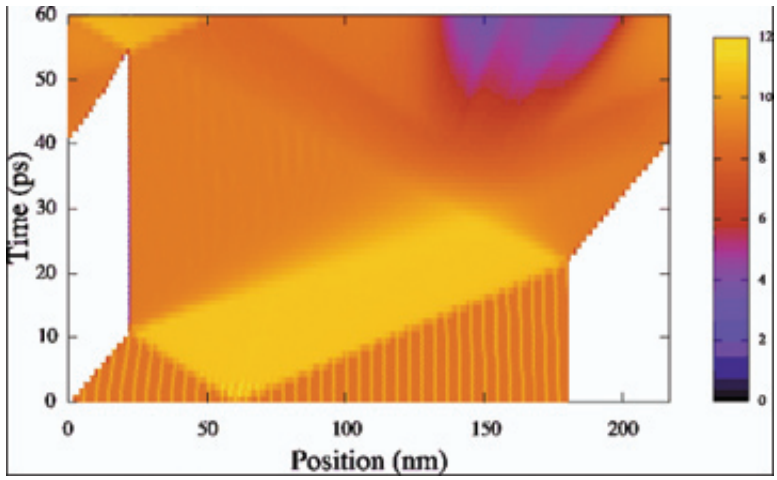

Fig. 2.
Density (in g/cc) evolution for a single crystal of copper shock -compressed in the ⟨100⟩ direction (both flyer plate and target), to particle velocity u_p = 1.0 km/s, resulting in the onset of spall-ation around 50 ps. The initial striations result from an incommensura-bility between the perfect crys-tal lattice and the computa-tional bin width used to calculate densities. The target crosses the periodic boundary around 40 ps, resulting in a subsequent re-shock which is not of interest here.

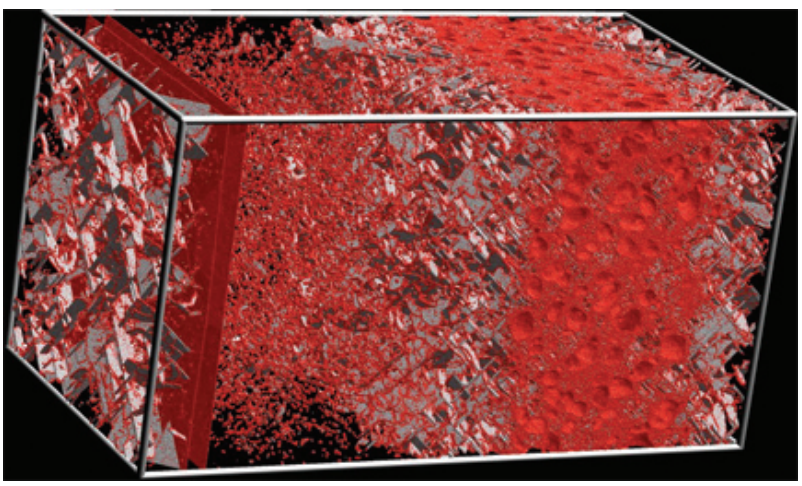

Fig. 3.
Non-fcc atoms, for the simulation shown in Fig. 2 at 50 ps. Hcp stacking fault atoms are grey, and all others red. From left to right, one can see the following features: a) stacking faults intersecting the free surface of the target, which is just about to impact the flyer plate free surface; b) residual damage (primarily in the form of point defects such as Frenkel pairs) due to shock loading and unloading in the flyer plate; and c) the nucleation of a number of voids, which will grow and coalesce to form a spall plane at later times.

Modeling Strategies for Containing Pandemic Influenza in the U.S.

Kai Kadau, T-14; Timothy C. Germann, X-1; Peter S. Lomdahl, T-14; Norman L. Johnson, CHS; Tim McPherson, D-4; Ira M. Longini, Jr., Emory University; and Catherine A. Macken, T-10

The avian influenza H5N1 strain has recently spread among poultry from Southeast Asia and Russia to Europe, probably by migrating birds. So far humans can only be infected by poultry, which makes it a slow spreading disease in humans. However death rates of about 50% are extremely high so far for the about 100 infected humans. By mutation or reassortment with a human strain of influenza, H5N1 influenza could become human-to-human transmissible and cause a worldwide pandemic like the 1918 Spanish flu, or the 1957 and 1968 pandemics which killed tens of millions of people worldwide.

What can be done if such a pandemic hits the world? The current flu shots distributed each year will not protect people from this aggressive strain, never before seen by human immune systems. A variety of mitigation strategies and their combinations have to be imposed by the government. In addition to vaccines and therapeutics, these include the reduction of travel, school closure, nonessential work closure, and other social distancing measures, up to a mandatory quarantine. There are medical opportunities like antiviral drugs that can help prevent transmission of the virus, however this medication (known as the product name Tamiflu) is expensive and in short supply, and thus should be carefully distributed to get the most efficiency per dose. Another opportunity is the fast development of a vaccine, possibly with a low efficacy due to fast production.

In order to test these mitigation strategies and to optimize their combinations, we have developed an agent-based model for the U.S. that captures the transmission of the virus in different mixing groups like community, workplaces, household clusters, schools, and households. In this large-scale model the 280 million agents are distributed among five age groups according to demographic data. This underlying community structure is similar to previous small-scale models [1–3]. The geographic distribution is represented by about 60,000 tracts (each containing about 5000 people) and movement of people between the tracts, whereby the movement is given by data from the transportation bureau and can be split into daily commuter travel to work and longer distance travel (business trips, vacation, etc.). By fitting the model parameters to different aggressive strains — as represented by the basic reproductive number R_0 (basically the number of persons a sick individual infects directly) — of the hypothetical virus, several mitigation scenarios for different virus strengths could be investigated. Preliminary results suggest that for reproductive numbers R_0 less than 2.0, targeted administration of antiviral drugs helps control the spread until vaccine is developed. For more aggressive viruses a more sophisticated combination of measures is necessary to control the spread.

It is noteworthy that the simulations were run on large multiprocessor machines and that we used our large-scale MD platform SPaSM [4] as a base for the multimillion agent simulations necessary for this work. For example, a typical run for one flu season takes about 12 hours on 256 CPUs of the Pink system at Los Alamos. This work was featured in a recent Scientific American article [5].

For more information contact Kai Kadau at kkadau@lanl.gov.

[1] M.E. Halloran, et al., *Science* **298**, 1428 (2002).
[2] I.M. Longini, *Am. J. Epidemiol.* **159**, 623 (2004).
[3] I.M. Longini et al., *Science* **309**, 1083 (2005).
[4] D.M. Beazley and P. S. Lomdahl, *Parallel Comput.* **20**, 173 (1994).
[5] W.W. Gibbs and C. Soares, *Scientific American* **293** (5), 44 (2005).

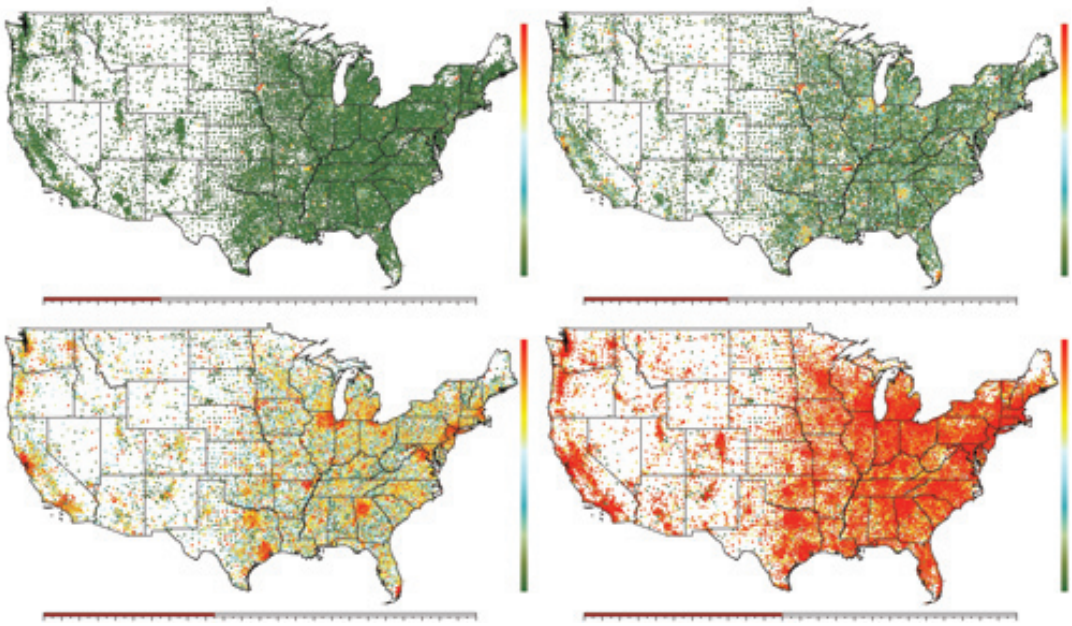

Fig. 1. ***Baseline simulation realization of a pandemic flu outbreak with $R_0 = 1.6$, introduced by the daily entry of a number of infected individuals through 14 major international airports in the continental U.S. (beginning on day 0). The spatiotemporal dynamics of the prevalence (number of symptomatic cases at any point in time) is indicated on a logarithmic color scale at the right edge of each figure, from 0.3–30 cases per 1,000 residents. Snapshots are shown at (left to right, top to bottom) day 65, 80, 95, 110. Each dot on the map represents a tract containing on average of 5000 people; therefore the density of the dots indicates the population density.***

Detonation Wave Profile in PBX-9501

Ralph Menikoff, T-14

A plastic-bonded explosive (PBX) is composed of explosive grains held together by a polymer binder. When compressed by a shock wave, the heterogeneities give rise to energy concentrations or local regions of high temperature known as hot spots. Hot spots are essential for initiation of a detonation wave in a PBX.

One explosive used in Lab applications is PBX-9501. Its main ingredient is the high-melting explosive (HMX). A pure crystal of HMX is very insensitive, i.e., hard to detonate. This property along with other detonation phenomenon, such as "shock desensitization," led to the conjecture that hot spots also are needed to propagate a detonation wave. In fact, burn models used in hydro simulations — such as "Forest fire" or "ignition and growth" — are motivated by the hot spot concept.

With the temporal resolution of the VISAR (Velocity Interferometer System for Any Reflector) technique now on the order of 1 nanosecond (billionth of a second), experiments have been able to measure the velocity profile in the reaction zone of a propagating detonation wave. For PBX-9501, the experimental profile, shown in Fig. 1, has the form of a classical ZND (Zeldovich-von Neumann-Doering) detonation wave; lead shock followed by rapid decrease from the unreacted von Neumann spike state to the fully reacted Chapmann-Jouguet detonation state. Moreover, the reaction zone width is a fraction of the grain size. In addition, related HMX-based explosives, PBX-9404 and EDC-37, have very similar reaction zone profiles, despite having different binders and different sensitivities to initiation. This is contrary to the behavior expected for a propagating detonation wave when reaction is dominated by hot spots.

The experimental reaction zone profiles are in good agreement with 1-D simulations using realistic constitutive properties for PBX-9501 (equations of state of reactants and products) and a global Arrhenius reaction rate fit to time to ignition data over a wide range of temperatures. The experiments used two window materials; PMMA (better known as plexiglas) and LiF, which bracket the acoustic impedance of PBX-9501. The resolution of the VISAR is somewhat lower with the LiF window resulting in the peak or von Neumann spike being clipped. Other experiments with a 1-ns resolution do obtain peak value of particle velocity in agreement with the value expected from the impedance match of the lead shock in PBX-9501 into the window material; see Fig. 2 for the graphical solution in the (particle velocity, pressure) plane. Thus we can conclude that a steady detonation wave in PBX-9501 is propagated by the bulk chemical reaction from shock heating [1].

The experiments measured the profile for a planar detonation wave. In a rate stick, the detonation front is curved with the lead shock being weaker at the boundary. Due to the temperature sensitivity of the Arrhenius rate, the reaction zone width greatly increases as the lead shock strength decreases. As a consequence, near the boundary, reaction is dominated by hot spots. This change of reaction mechanism reconciles the sensitivity of failure diameter to the formulation of a PBX (binder and grain size) with the insensitivity of the planar reaction zone profile.

For more information contact Ralph Menikoff at rtm@lanl.gov.

[1] R. Menikoff, "Detonation Wave Profile in PBX-9501," Los Alamos National Laboratory report LA-UR-05-1633 (March 2005).

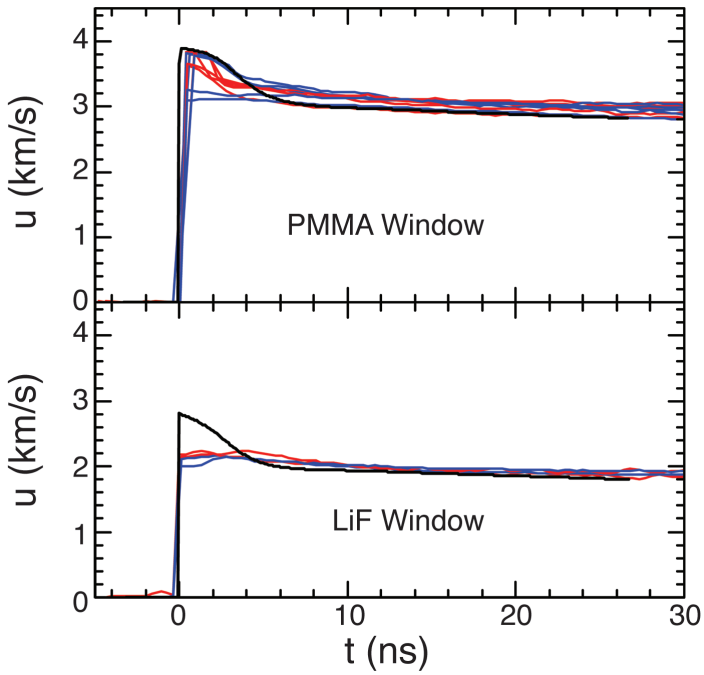

Fig. 1. *Comparison with VISAR data from Gustavsen, Sheffield, and Alcon. Top figure is for PMMA window and bottom is for LiF window. Red and blue curves are experiments and black is simulations. VISAR used two laser beams with different fringe constants per experiment. Experiments varied drive pressure for initiation and the length of PBX sample.*

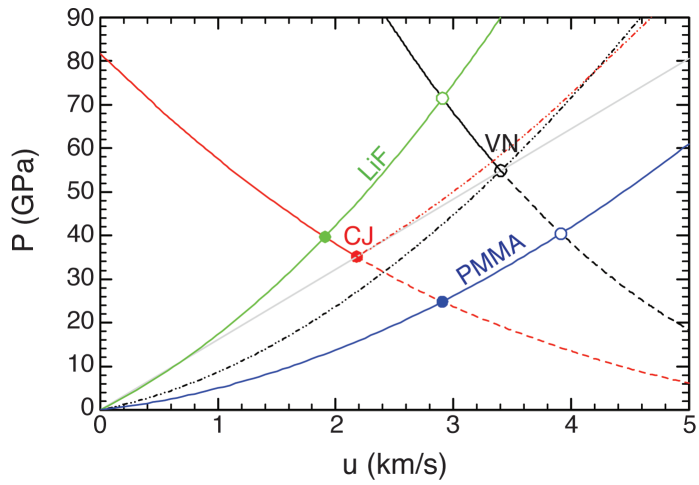

Fig. 2. *Impedance match for detonation wave in PBX-9501 with window. Green and blue curves are Hugoniot loci for LiF and PMMA, respectively. Black and red curves are for reactants and products, respectively. Gray is Rayleigh line corresponding to CJ detonation velocity. Labels VN and CJ denote von Neumann spike and Chapman-Jouguet state, respectively. Open circles are match from VN spike and solid circles are match from CJ state.*

The Effects of Crowding in Dendronized Polymers

Paul M. Welch, T-14, and Cynthia F. Welch, LANSCE-12

Many exponents of nanotechnology tout supramolecular assemblies as potential structural and functional building blocks in a host of devices. The envisioned constructions require materials with several physical characteristics, including a well-defined shape, tunable dimensions, slow relaxation dynamics, the possibility of possessing a large number of chemically active sites, a propensity for self-assembly, and stimuli-responsive local conformations. Dendronized polymers, linear chains with grafted dendrons as schematically pictured in Fig. 1, have recently garnered much attention in the synthetic chemistry literature because they offer many of these traits. Experimental studies indicate that for low degrees of polymerization, the polymer adopts a spherical conformation. However, as the chain's contour length increases, the steric crowding of the side-chain dendrons forces the polymer backbone into an extended or possibly helical conformation, giving the molecule an overall cylindrical or rod-like shape. The length and radial extent of these polymers may be controlled by the number of repeats along the backbone and the generation of growth of the attached dendrons. As recently demonstrated by Das and coworkers, these assemblies behave like single-molecule glasses with relaxation dynamics characterized by stretched exponentials; thus, once assembled into a device, they may be expected to stay in place rather than hopping about as would be expected for more common synthetic polymers. Because their girth derives from the basic building blocks of dendrimers, dendronized polymers may offer many of the same benefits as dendrimers, including a large number of functional moieties at the dendron termini and a tunable density profile. Applications envisioned for these molecules include roles in nanoelectronics, catalysis, biotechnology, and molecular device fabrication.

The large size and often-poor solubility of dendronized polymers makes their characterization challenging, however, and many basic questions regarding their conformational statistics stand open. Though some single-chain studies have been performed, our understanding of the effect that the topological parameters have on the physical properties of these materials remains incomplete. We lack a clear picture of how properties such as the size-mass scaling, the cross-sectional size, the terminal group accessibility, the extent of dendron interpenetration, and the polymer conformation are affected by dendron generation *(G)*, degree of polymerization *(DP)* and the spacing between dendrons along the backbone *(S)*. A better understanding of these trends will improve our ability to tune the polymer's physical properties through chemical design. Thus motivated, we report here the results from computer simulations performed to investigate in a controlled manner the effects of *G*, *DP*, and *S* on both the local and global conformation of locally flexible dendronized polymers. Our results verify some speculation and conjecture found in the literature as well as offer new insight into the importance of steric crowding in these materials. Significantly, we find that the dendrons become extended away from the main chain backbone as *S* decreases, accompanied by a compression of the dendrons and a higher occupancy of the terminal groups near the surface of the molecule.

Dendrimers do not interpenetrate, thus their Newtonian rheological behavior. This exclusiveness should carry

over to the dendronized polymers and is speculated to be the central conformational feature responsible for many of their physical properties. This trait also holds significance for device fabrication; if the dendrons do not interpenetrate, then each dendronized polymer can be viewed as an independent building block. Figure 1B contains an image of a typical conformation from the simulations of a $DP = 100$, $G = 5$, $S = 2$ molecule. All of the dendrons are identical, but are colored to more easily illustrate dendron segregation. Indeed, the dendrons do not appear to interpenetrate. As shown below, the generation G and spacing S of the dendrons dictate the dimensions and physical layout of these molecules as a result of this segregation.

This segregation results in the relegation of the dendrons further away from the chain backbone and affects the accessibility of any chemical functionality present. Plotting the spherical distribution of terminal groups of a dendron about its attachment point along the backbone, $\rho(r)$, for $G = 5$ and $DP \approx 50$ for a range of S values illustrates this, as shown in Fig. 2. For large values of S, the terminal groups distribute themselves in a roughly Gaussian fashion in the effective tube. However, as S decreases and steric crowding begins to force the dendrons further away from the tube axis, the distribution of terminal groups changes dramatically; they segregate preferentially toward the tube surface. This surface segregation of the terminal groups has been proposed to exist in dendrimers, though most experimental and theoretical studies seem to negate this possibility without the introduction of dendron stiffness. Here, however, we observe this sought-after trait in fully flexible molecules. Moreover, while the molecular weight, and thus the number of terminal groups, that can be synthetically achieved in their dendritic precursors is limited, dendronized polymers can continue to add terminal groups by merely increasing DP while holding S constant.

We will report further details on the properties of these curious molecules in a future publication, including evidence for the linear growth of the "tube" diameter with G, the compression of the dendrons, and the glob-to-coil transition. This work was supported under LDRD/ER Computational Schemes for Multiscale Modeling of Polymers, T. D. Sewell, P. I.

For more information contact Paul Welch at pwelch@lanl.gov.

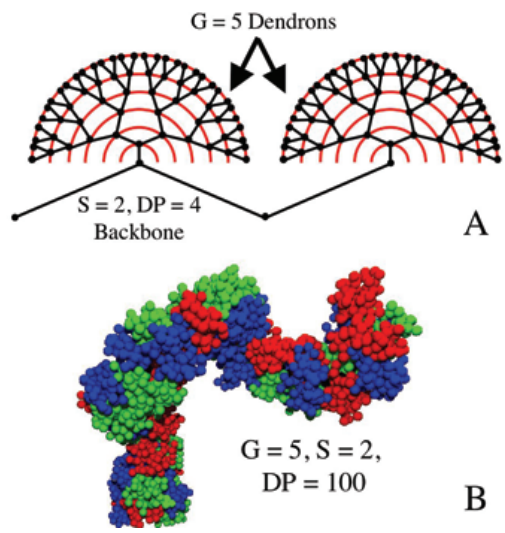

Fig. 1. *A) The topology studied and nomenclature applied here, as exemplified by a $G = 5$, $S = 2$, $DP = 4$ dendronized polymer. B) A representative configuration observed in simulations of $G = 5$, $S = 2$, $DP = 100$ dendronized polymers. Dendrons are colored to highlight segregation.*

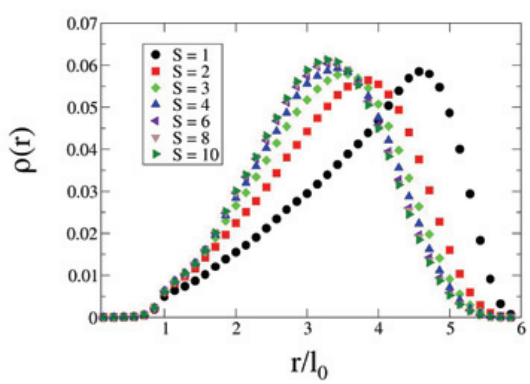

Fig. 2. *The radial density $\rho(r)$ of terminal groups about their respective attachment points along the main chain backbone versus the radial distance r normalized by the equilibrium bond length $l0$.*

Parameterizing Dynamic Field Simulations from Image Analysis

Paul M. Welch and Thomas D. Sewell, T-14; Kim Ø. Rasmussen, T-11; Shirish M. Chitanvis, T-14; and Turab Lookman, T-11

The goal of predicting the dynamic and equilibrium phase behavior of complex materials has driven much of the research in condensed matter physics for the past century. The importance of phase transitions in phenomena as diverse as superfluidity, magnetization, blend miscibility, and the creation of rich morphologies observed in block copolymers motivates these intense efforts. Broadly speaking, statistical mechanics models describing phase behavior can be classified as either "field" or "particle" descriptions. The former consists of defining the system's free energy in terms of lattice or continuum fields representing composite quantities such as local magnetic spin or chemical composition. These models are interrogated with analytical and numerical techniques to extract the universal characteristics of different classes of materials. In principle, explicit chemical details can also be included in these field-theoretical models. However, in practice the complexity required to capture the microscopic information and the mathematical stipulations attached to building these models necessitate that the chemistry be embodied in only a few parameters. Specifying those parameters for a real material often requires retreat to empiricism.

Particle-based simulation techniques such as molecular dynamics (MD) or Monte Carlo (MC), on the other hand, rely upon "force-field" models that are thoroughly parameterized to represent specific chemistries. The increasing sophistication of these methods provides the ability to predict the physical behavior of real materials with a high degree of fidelity. Unfortunately, the computational expense that accompanies explicit particle descriptions severely limits the size and time scales accessible relative to those attained with field theoretical models, especially in the case of polymers.

Circumventing the limitations of both methods by mapping from particle-based to field-based representations would not only provide new insight into the relationship between molecular structure and the free energy, but would also revolutionize our capability to model real chemistries and intelligently design new materials. Thus motivated, many investigators are pursuing research to stitch together the patchwork of particle and continuum descriptions into a cohesive framework. Linking a prominent field-based description, the Ginzburg-Landau [1] free energy functional, to explicit particle models would constitute a major advance in these efforts since it serves as a cornerstone for many numerical and analytical theories.

Moreover, the rise of sophisticated experimental techniques that capture actual images of phase separated materials at the nanometer length scale offers new avenues for exploring the relationship between specific chemistries and field-theoretical descriptions. Methods such as atomic force and transmission electron microscopy have taught us much about equilibrium phase separated morphologies and about the accuracy of our theoretical tools, like self-consistent mean field theory. Now, we are poised to extract dynamic information from these characterization tools to parameterize and refine dynamic field theoretical methods.

We are developing an analysis toolset that permits the parameterization of the Ginzburg-Landau free energy functional from a time series of sufficiently resolved images of phase separation obtained from either experiment or simulation. From these images, an estimate of the local composition and the local time derivatives of the composition can be extracted. Given this information, we numerically fit the evolution of the field to the equation of motion derived from the free energy functional and the continuity equation, commonly referred to as the "time-dependent Ginzburg-Landau" equation (TDGL). We therefore denote our analysis tool as the "inverse time-dependent Ginzburg-Landau" method, or iTDGL.

Here, we demonstrate the iTDGL method by applying it to two different sets of simulated two-dimensional images. First, we modeled phase separation in a binary blend by simply choosing a parameterization for the Ginzburg-Landau free energy functional and propagating the TDGL equation of motion forward in time. Hence, we know what solution we should obtain upon applying the iTDGL method because those parameters

were the input for the TDGL simulations. Next, we performed a set of MC simulations on a simple lattice model of a binary blend of polymers below the critical miscibility temperature. Here, we do not know what the correct solutions for the parameters are, but we show below that the results are in excellent agreement with mean field predictions. In both types of simulations, we followed the phase separation dynamics from an initially homogenous mixture.

The TDGL simulations were performed on a 1024^2 grid with a three-parameter free energy functional $f = A\Psi^2+B\Psi^4+k|\nabla\Psi|^2$, where Ψ is the local composition order parameter. The parameters, denoted *A*, *B*, and *k*, capture the extent of chemical mismatch between the two species in the blend and the interfacial penalty associated with having a region rich in one species in close contact with one rich in the other. With the images in hand, we could investigate the affect of image resolution on the accuracy of the iTDGL method by locally averaging over field elements. Figure 1 shows the fitted values of the parameters as a function of the number of grids used per box-side

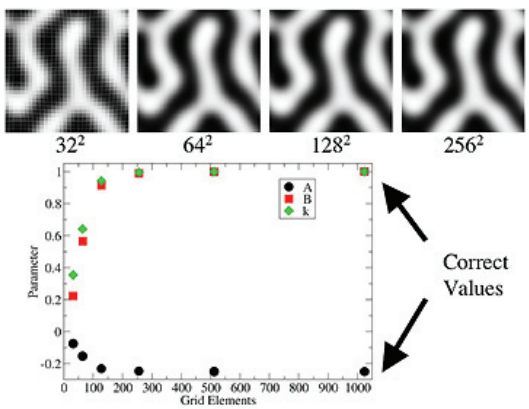

to represent the data. The data points at 1024 exactly match the parameters chosen in the TDGL simulations, thus validating the iTDGL method. In principle, the values of the parameters are dependent upon the length scale chosen to resolve the field. However, as seen in Fig. 1, the values are stable across a number of coarsening steps so long as the interfacial regions between the phases are well resolved.

We employed the original particle model for polymer phase separation due to Baumgärtner and Heermann [2] for the polymer simulations. The simulations are of a symmetric binary blend of two polymer species at 95% density on a 336^2 lattice. The composition fields were estimated by calculating the local concentrations of a given polymer type in an area defined by 16 lattice elements. Various quantities whose scaling behaviors can be theoretically predicted can be estimated from the iTDGL fit. Figure 2 contains a plot of one such quantity, the correlation length ζ, as estimated from two of the fitted parameters, as a function of the quench depth below the critical temperature T_c. As expected from mean field theory, we observe the correlation length to diverge as the temperature approaches its critical value with the inverse square root of the quench depth.

In summary, we have developed a method to parameterize the Ginzburg-Landau free energy functional from a series of images of the evolution of a phase separating material. Though illustrated here with images produced from computer simulations, the data could just as easily be obtained from experimental methods. We are currently pursuing this possibility with outside collaborators at North Carolina State University.

For more information contact Paul Welch at pwelch@lanl.gov.

[1] P.M. Chaikin and T.C. Lubensky, *Principles of Condensed Matter Physics* (Cambridge University Press, Cambridge, England, 1995).
[2] A. Baumgärtner and D.W. Heermann, *Polymer* **27**, 1777 (1986).

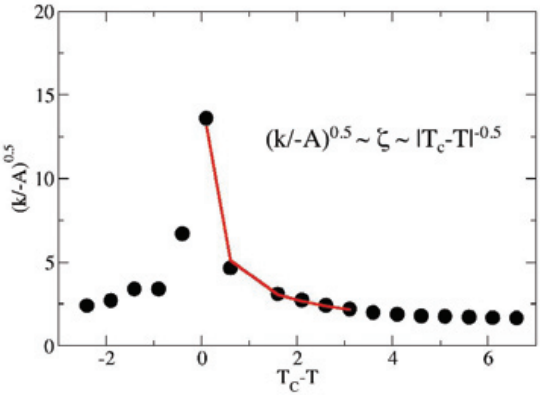

Fig. 1. *The top images show the same field obtained from the TDGL simulation at a given instant in time, but coarsened to different resolutions. The plot represents the iTDGL fit for the three parameters as a function of this coarsening.*

Fig. 2. *The circles represent the estimate of the correlation length ζ from the parameters obtained from the iTDGL method. The red line is the best fit to the data close to the critical point T_c.*

A Tunable Dendritic Molecular Actuator

Paul M. Welch

Molecular devices for applying strains or forces on demand play a central role in many envisioned nanomachines. Thus, there are a number of such actuators proposed in the literature [1]. Many rely upon local conformational changes in their chemical constituents that translate into relatively small but rapidly applied strains or are best described as two-state rotors. Typical polymeric actuators display percent strains in the 3–30% range. If we are to mimic biological processes, however, large strains will also be of interest. For example, the actomyosin complex produces displacements in the range of 5–10 nm [2]. Global conformational changes in linear polymers offer one route to achieve such large-scale motions. Electrostatic attraction seems an obvious choice to effect these conformational changes since the force generated can be quite high and the presence of charges permits coupling of the device to an external electric field. Here, I present a construction designed to mimic a spring-loaded reel, with a linear chain serving as the molecular analog of a string that is pulled onto a dendritic molecular spool. Electrostatic attraction serves as the spring while an applied electric field allows the compliance to be tuned.

Through Brownian dynamics simulations, I studied a model rendition of the proposed device based on a sixth generation monocentric dendrimer, such as monocentric dendritic-poly(propylenimine), with charges at every branch point and terminal group. A noncharged, short tether chain is grown from one of the dendrimer's terminal groups and is immobilized at the chain end on a hard-wall surface. From another terminal group, topologically opposed to the growth point of the tether, another linear chain is attached. This chain is oppositely charged to the dendrimer and has the same number of charged groups as the dendrimer so that the overall system is charge-neutral. An electric field E was applied normal to the surface and acts to pull the chain away from the surface and the dendrimer toward it, except in the one instance noted below in which the field polarity was reversed. This contributes an additional force of magnitude $|Eq|$ to each of the charges of magnitude q along the axis normal to the surface. See Fig. 1.

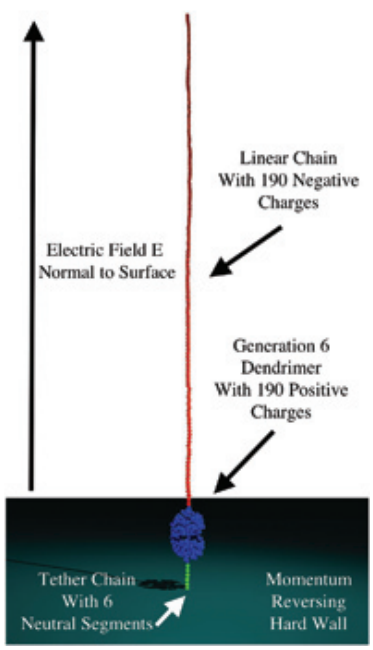

Fig. 1. ***The model molecular actuator.***

The equilibrium free energy as a function of the distance from the chain end to the center of the dendrimer was determined via the Jarzynski [3] identity. To accomplish this, a phantom spring was attached to the free chain end and retracted at a constant rate normal to the surface. Information (instantaneous retractive force, etc.) from numerous simulations was combined after the method of Hummer and Szabo [4] to reconstruct the free energy profiles.

Figure 2 illustrates the location of the minima of the free energy as a function of applied field strength for the case of a high solution salt concentration. The equilibrium displacement X_e remains constant until a critical field strength E^*

is applied, after which there is a rapid rise in the value of X_e. Qualitatively, this indicates that the device undergoes a phase transition similar to that of an Ising magnet in an applied field since the susceptibility dX_e/dE appears to diverge at the critical field strength E^*. The displacement Xe serves as the order parameter analogous to the magnetization in the Ising magnet, and there is a one-to-one correspondence between the applied fields in both models. The critical field strength E^* is expected to shift to higher values with decreasing solution salt concentration; the less salt in the system, the more tightly bound is the chain to the dendrimer and, thus, more energy is required to separate them. This was observed to hold for the model studied here.

Finally, the retractive force F exerted on an attached object may be tuned by cycling the electric field, as shown in Fig. 3. A typical conformation was chosen from an ensemble of equilibrated actuator in a high salt solution and an electric field strength well above the critical value. An immobile phantom spring was attached to the chain end. The first plateau represents the time during which the field was on. The slight positive force exerted by the device results because a configuration with displacement slightly less than X_e was chosen. When the field is turned off, the actuator quickly retracts, exerting a force on the phantom spring. The field is then cycled on again returning the retractive force to its original value. Thus, the actuator displays a lack of hysteresis as expected since no entanglement is observed between the linear and branched segments in this model. This is consistent with rheological studies of blends of hyperbranched and linear chains. The final plateau with a stronger retraction on the phantom spring results when the field polarity is reversed, effectively driving the dendritic and linear portions

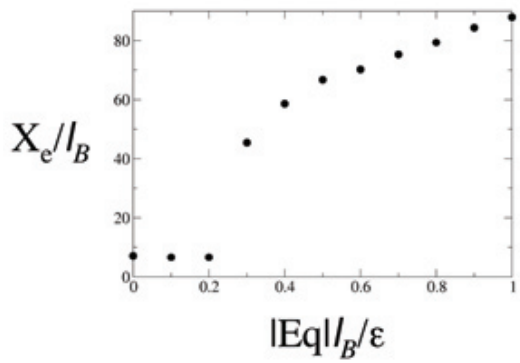

Fig. 2. *The equilibrium distance X_e between the center of the dendrimer and the end of the charged chain as a function of the applied field E. Dimensions of length and energy are given in units of the Bjerrum length l_B and the Lennard-Jones prefactor ε, respectively.*

of the construct together. More details of this study may be found in Ref. [5].

For more information contact Paul Welch at pwelch@lanl.gov.

[1] A.P. Davis, *Nature* **401**, 120, 1999. J.D.W. Madden, et al., *Proc. SPIE on Smart Structures and Materials: Electroactive Polymer Actuators and Devices (EAPAD)* **4695**, 176, 2002. E. Smela, Adv. Mater. 15, 481, 2003. C. Mavroidis, *Annu. Rev. Biomed. Eng.* **6**, 363, 2004.
[2] R. Cooke, *Physiol. Rev.* **77**, 671, 1997.
[3] C. Jarzynski, *Phys. Rev. Letts.* **78**, 2690, 1997. C. Jarzynski, *Phys. Rev. E* **56**, 5018, 1997.
[4] G. Hummer and A. Szabo, *Proc. Nat. Acad. Sci.* **98**, 3658, 2001.
[5] P.M. Welch, *Nano. Lett.* **5**, 1279, 2005.

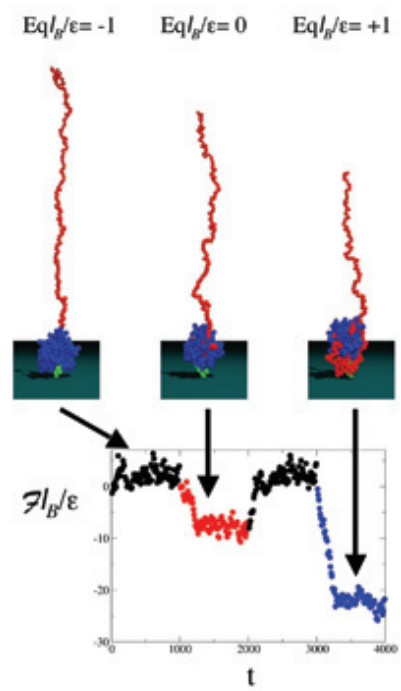

Fig. 3. *The retractive force $\mathcal{F}$ of the extended actuator as a function of time t and typical snapshots for each condition are shown.*

Atomistic Simulations of Chemical Reaction in Nanolaminates under Shock Loading

Shijin Zhao, T-14; Timothy C. Germann, X-1; and Alejandro Strachan, Purdue University

Nanostructured metastable intermolecular composites (MICs) are mixtures of nanosized particles of reactants that undergo exothermic (e.g., thermitic) reactions triggered by an external stimulus. This relatively new class of energetic materials exhibits extraordinary properties [1]: extremely fast burn rates, high temperatures and power, accompanied by lower volume expansion than in traditional energetic materials due to the lack of gaseous products. Furthermore, by modifying the nanostructure, such as the particle size, porosity, and passivation layer, one can control the rate of energy release. These unique properties make MIC formulations promising candidates for a wide range of defense and commercial applications, including localized heat sources for chem/bio neutralization and disease treatment, environmentally clean primers and detonators, ultra-fast fuses, and smart thermal barriers. Despite their technological importance, the fundamental molecular-level mechanisms that govern the extraordinary properties of MICs are unknown; as stated recently [2]: "a lack of understanding of the fundamental mechanisms has hindered the development of nanoenergetic materials."

In this work, we employ molecular dynamics (MD) simulations to uncover these mechanisms at the atomistic level. We characterize the chemical and mechanical response of nanostructured Ni/Al multilayers induced by shock loading, using a novel technique that captures both the initial shock transit as well as the subsequent longer-timescale chemical processes. In our simulation, two Ni/Al multilayers, originally separated by a 1-nm gap, collide with a relative velocity of $2u_p$ (see Fig. 1). The unequal Ni and Al layer thicknesses are set up such that the final stoichiometry is Ni_3Al, and the interfaces are perfectly planar (111) surfaces. The interatomic interactions are described by an embedded atom method (EAM) potential developed by Mishin et al. [3].

Periodic boundary conditions are imposed in all three dimensions, with a shrinking boundary condition (the left boundary moving at $+u_p$, and the right boundary at $-u_p$) imposed in the ⟨111⟩ shock direction to maintain that periodicity. (Both the periodic boundary and the central impact plane are located at the midpoint of an Al layer.) Upon collision of the two multilayers, two shock waves (with particle velocity u_p relative to the uncompressed material) propagate outwards in opposite

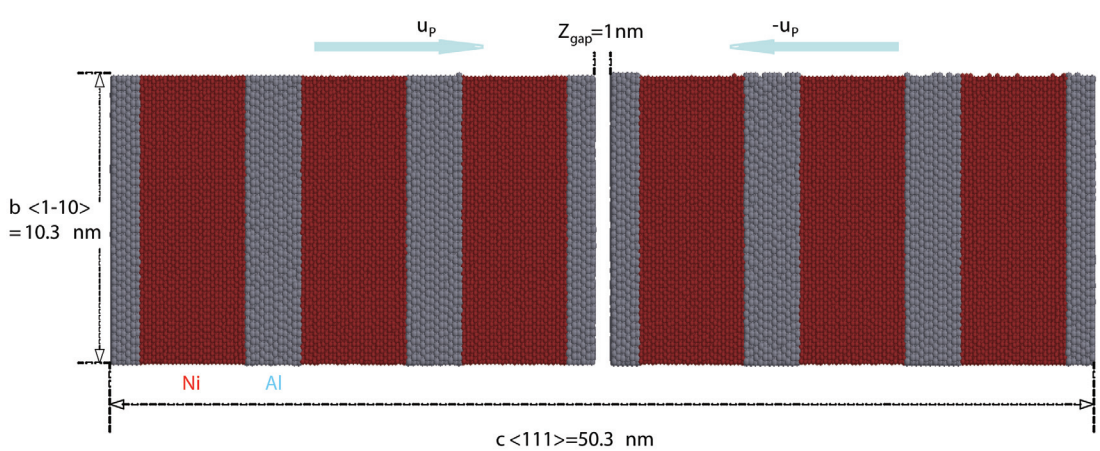

Fig. 1. Schematic of the simulation geometry. The length in a ⟨11-2⟩ (the direction perpendicular to the paper) is 8.9 nm. The sample includes $N_{Ni} + N_{Al}$ = 379,080 atoms with $N_{Ni} \sim 3N_{Al}$.

directions, leaving behind a longitudinal particle velocity, which is locally zero in the simulation reference frame.[1] Just at the point when these two shock waves meet at the ⟨111⟩ periodic boundary, we stop the shrinking boundary condition and begin a constant-volume (NVE) MD run to follow the longer-timescale chemistry initiation and propagation.

Due to the impedance mismatch between the (harder) Ni and (softer) Al layers, the initial shock compression is followed by a complex series of reshocks and rarefaction fans. As these waves move back and forth in the Al and Ni layers, they gradually decay, with characteristic damping rates for each medium [5]. This wave reflection and damping contributes to an additional temperature rise beyond the original shock heating, particularly in the softer Al layers which are increasingly shock-compressed and are heated to a higher temperature than the harder Ni layers (see Fig. 2). The central Al layer (where the initial impact occurred) reaches the highest local temperature because this layer has been subjected to the greatest number and intensity of wave reflections.

Figure 3 shows profiles of the fraction of Al atoms across the nanolayer at various times. We see that chemical reaction begin at the interfaces surrounding the central Al layer, causing a significant degrease in the fraction of Al atoms as Ni diffuses towards the center of the system. The heat generated by these exothermic reactions, as well as further heating due to internal wave reflection, subsequently leads to the initiation of chemistry at interfaces further from the center. In this manner, a reactive wave propagates outwards, with a velocity of approximately 0.1 to 0.2 nm/ps. The highly exothermic alloying reactions propagate in a self-sustained manner by mass and temperature transport, and energy release from chemical reaction at the interfaces [5].

[1]Note that in the standard shrinking periodic boundary condition technique [4], the sample is initially at rest and a pair of inward-moving shock waves are generated from the periodic boundary.

For more information contact Shijin Zhao at shijin@lanl.gov.

[1] R.W. Armstrong, et al., *Nano. Lett.* **3**, 253–255 (2003).
[2] Y. Yang, et al., *J. Phys. Chem. B* **107**, 4485–4493 (2003).
[3] Y. Mishin, et al., *Phys. Rev. B* **65**, 224114 (2002).
[4] B.L. Holian, *Phys. Rev. A* **37**, 2562–2568 (1988).
[5] Zhao, S. J., Germann, T. C., and Strachan, A., to be published.

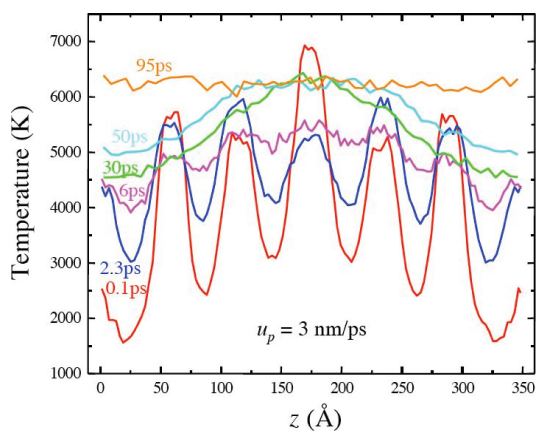

Fig. 2. *Temperature distribution along the shock direction (z) at various times, for u_p = 3 nm/ps.*

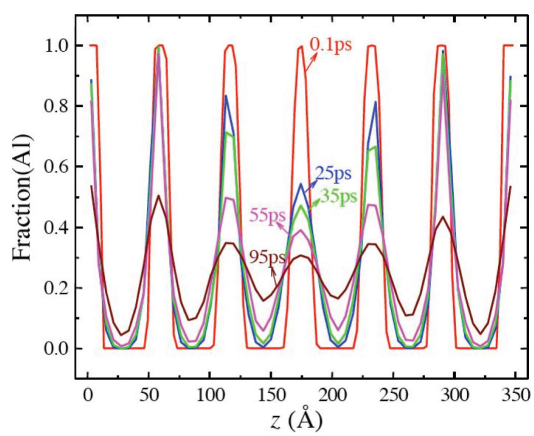

Fig. 3. *Al number fraction at various times, indicating chemistry initiation and propagation. The final Al fraction in the central bin has approached a value close to 1/4, the overall Ni_3Al stoichiometry.*

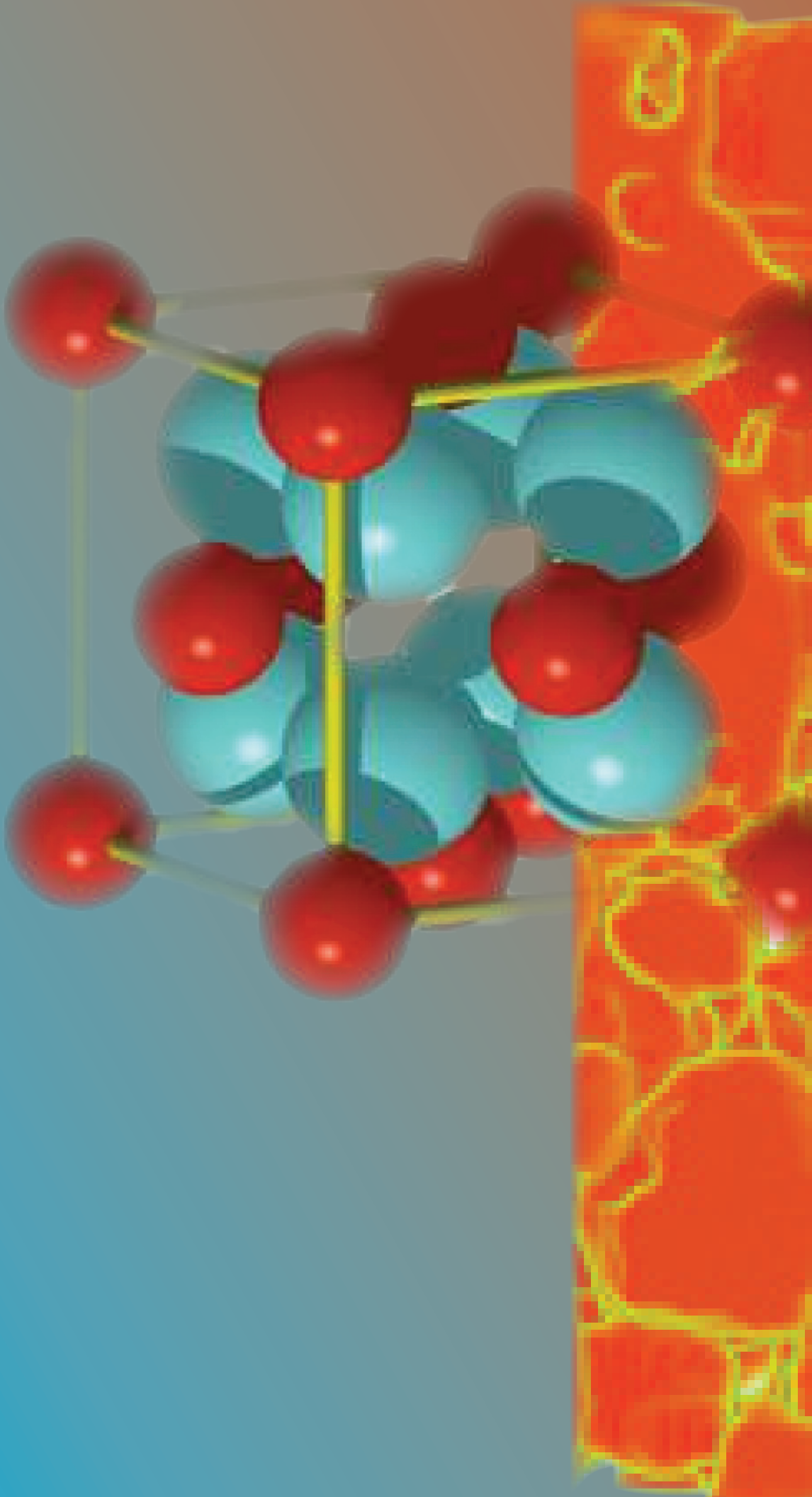

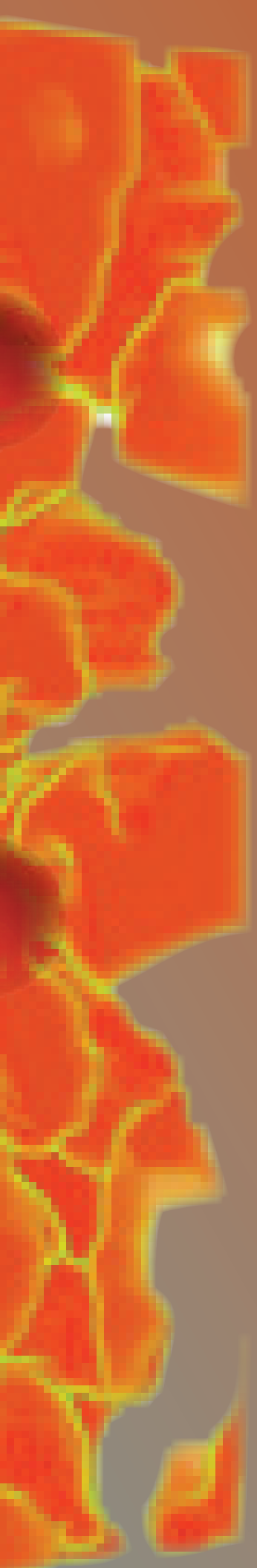

Part 2:

Other T-Division Groups
T-3 NonMaterials, T-4, T-6, T-7, T-8, T-10, T-13, T-15, T-16, T-QC

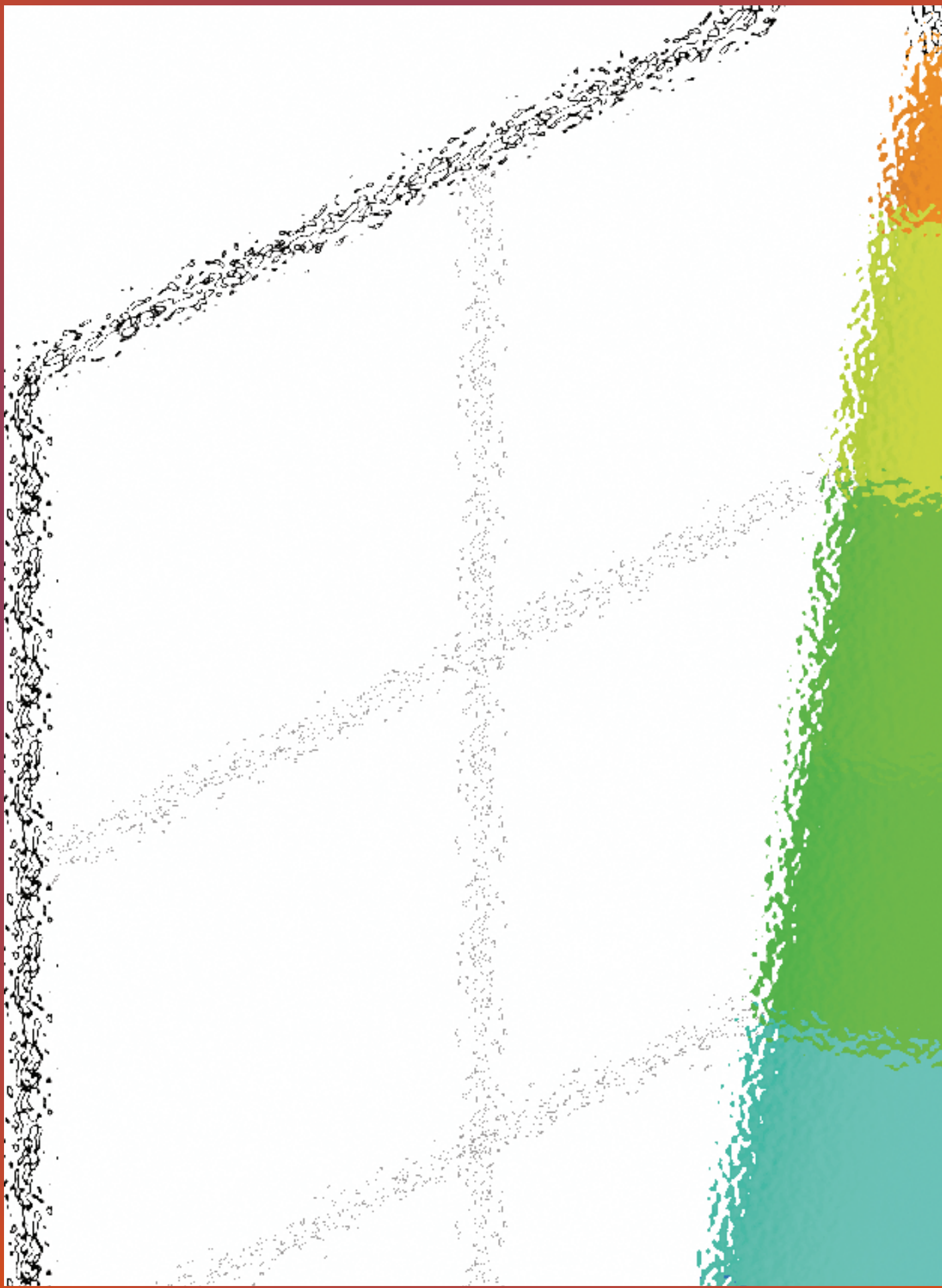

T-3

Fluid Dynamics Nonmaterials

Group Leader: Mark Schraad
505.665.3946; schraad@lanl.gov

T-3 Fluid Dynamics is involved in modern hydrodynamic theory, modeling, and computational simulations. There is an emphasis on coupling advanced numerical methods for fluid dynamics at all flow velocities with models for other processes, including chemical reactions, phase change, heat and mass transfer, plasma behavior, constitutive properties of structural materials, and combustion.

Multiphysics Time Integration and Long Time Integration Error

Dana A. Knoll, Vincent A. Mousseau, Rick M. Rauenzahn, Katherine J. Evans, T-3; and Luis Chacón, T-15

Predictive computer simulation of multiphysics systems is one of the Laboratory's core missions. This endeavor is at the heart of such DOE programs as the Advanced Simulation and Computing (ASC) program and the Scientific Discovery through Advanced Computing (SciDAC) program. There are many factors that affect the accuracy of a simulation, including proper physics models, accurate spatial discretization, and adequate spatial grid resolution. Perhaps the least appreciated, understood, and studied factor is the issue of multiphysics time integration methods and long time integration error.

Modern multiphysics time integration methods are comprised of basic time integration methods, and nonlinear and linear solver techniques that can be abstracted and generally applied to accurately, robustly and efficiently solve multiphysics systems. These systems are characterized by a myriad of complex interacting physical mechanisms. These mechanisms often nearly balance to evolve a solution on a dynamical time scale that is long relative to the component time scales. Solution methods for such systems require the use of significant coupling in the nonlinear and linear solution techniques and a significant implicit character to the time integration methods.

The number of time steps required for a multiphysics computer simulation is typically proportional to the ratio of the slowest time scale to one of the faster time scales. Because of this ratio, multiphysics simulations often require many (10^6) time steps. The resulting accuracy after a large number of time steps depends more on a temporal integration schemes ability to track the solution than on the size of the error on a single time step. A temporal integration scheme that drifts away from the solution may end up with a global error that is very large even if it has a small error per time step.

This solution drift error is particularly dangerous because the solution is qualitatively correct and thus there are no obvious symptoms that the error even exists. Because this error currently goes unmeasured in large-scale multiphysics simulations, we must develop a deeper understanding of this weak link in predictive simulation to further quantify this uncertainty.

Within the overall field, we have been working on developing new solution algorithms which are second-order accurate in time, using numerical analysis to understand errors in existing first-order in time methods, and gaining a deeper understanding of how the time integration errors may accumulate within a multiphysics computer simulation. In algorithm development we have focused on Jacobian-Free Newton-Krylov methods with physics-based preconditioners [1] along with second-order in time operator splitting methods [2, 3]. We have concentrated on using modified equation analysis [4] and asymptotic analysis as numerical analysis tools for studying the errors and behaviors of splitting methods.

All of our multiphysics problems of interest have fluid dynamics as the core of the problem, with additional physics contributing to the overall problem. In addition to working with prototype systems, we have been applying our research to multiphysics systems such as radiation hydrodynamics, extended magnetohydrodynamics [5], multiphase flow hurricane systems [6], solidifying flows [7], and nuclear power reactor thermal hydraulics [8].

As a simple example of accumulation of time integration error consider Fig. 1, which displays a solution at two different times (t = 5 and 10) for a one dimensional (1-D) reaction diffusion problem. This is a thermal wave moving left to right in time. The exact solution is EX, BE is a first-order in time solution, and CN is a second-order in time solution. For a given time step we see the first-order method drifting in time from the EX solution, while the second-order in time method tracks the EX solution. Figure 2 shows that even when the two methods have

the same local truncation error (LTE) per time step (x-axis), and we integrate to the same time (t = 15), the global error (y-axis) is different. The BE methods drifts from the solution at a faster rate than the CN method and this gap increases as we increase the allowable LTE per time step. This is directly related to our premise that these two different LTE's integrate differently in time since in BE the truncation error is dissipative and in CN the truncation error is dispersive.

As a second example we look at nonequilibrium radiation diffusion. In the asymptotic limit, where the coupling between radiation and material is tight, the two fields should have the same temperature (equilibrium). We have used asymptotic analysis to show that a "standard" split/linearized method for this problem does not enforce this asymptotic balance. In the problem shown in Figs. 3 and 4, a radiation front is moving from left to right heating the material. Solutions are plotted for t = 0.1 and 0.5. There is no physical mechanism for the material temperature, Tm, to be hotter than the radiation temperature, Tr. As shown in Fig. 3, the results coming from an unsplit (implicitly balanced) method show a physically credible solution with the temperatures close, but Tr > Tm. The result in Fig. 4, coming from a split/linearized method, was predicted by our analysis and is not physically correct since Tm > Tr. This analysis has helped to explain a "frequently observed" inaccuracy in such simulations.

For more information contact Dana Knoll at nol@lanl.gov.

[1] D.A. Knoll and D.E. Keyes, *J. Comput. Phys.* **193**, 357–397 (2004).
[2] R.M. Rauenzahn, et al., *Comput. Phys. Comm.*, 2005, in press.
[3] V.A. Mousseau and D.A. Knoll, *Nuc. Sci. Eng.*, 2005, accepted.
[4] D.A. Knoll, et al., *J. Comput. Phys.* **185**, 583–611 (2003).
[5] L. Chacón and D.A. Knoll, *J. Comput. Phys.* **188**, 573–592 (2003).
[6] J. Reisner, et al., *Mon. Weather Rev.* **133**, 1003–1022 (2004).
[7] D.A. Knoll, et al., SIAM *J. Sci. Comput.* **23**, 381–397 (2002).
[8] V.A. Mousseau, *J. Comput. Phys.* **200**, 104–132 (2004).

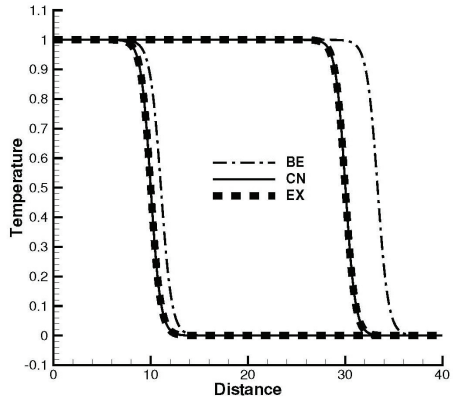

Fig. 1. *Various solutions of the reaction diffusion problem at t = 5 and 10.*

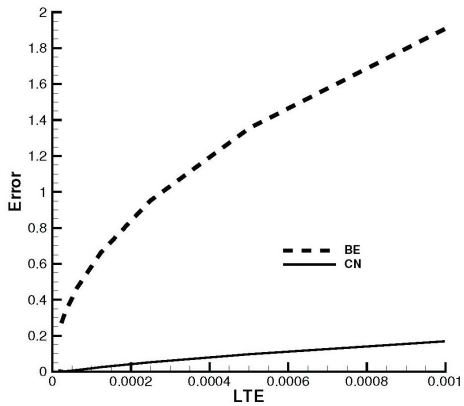

Fig. 2. *Global solution error as a function of LTE per time step.*

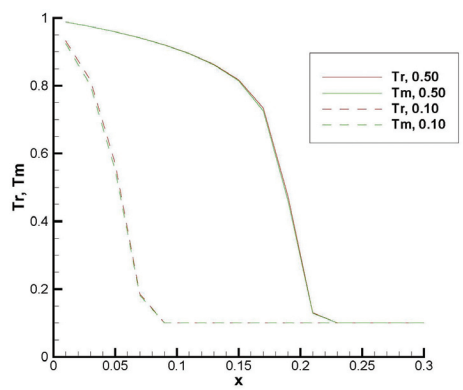

Fig. 3. *Implicitly balanced solution.*

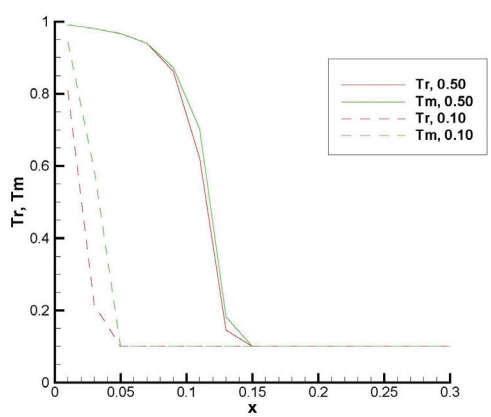

Fig. 4. *Split/linearized solution.*

Nuclear Reactor Safety

Vince A. Mousseau, T-3

There has been renewed interest in nuclear reactor power due to a variety of reasons. From a security standpoint it makes our nation less dependent on foreign countries. From an environmental point of view it mitigates the amount of greenhouse gasses being introduced into the atmosphere. Finally, from an economic point of view, the demand for energy is increasing worldwide and therefore the cost is growing steadily. Because of the increased regulation and cost of experimentation, development of modern nuclear reactors will rely more heavily on simulation and less on experimentation. This shift of emphasis to simulation will require an increase in the accuracy of nuclear reactor simulation codes. Because of this increased accuracy and decreased dependence on experimentation there is a natural transfer of technology that was developed for the Advanced Simulation and Computing (ASC) program to increase the efficiency and accuracy of these codes.

The current reactor simulators used in the U.S. were developed in the late 1970s to early 1980s. Because of the compute power available at that time many sacrifices had to be made to the accuracy of the simulation so that it would run in a reasonable amount of time. However, since there were large amounts of experimental data for these older reactors, the simulation codes mainly had to provide an answer that was close to the experimental data. In addition, older nuclear reactor designs depended heavily on large pumps to quickly cool the reactor in case of an incident.

Modern reactor designs have passive cooling systems that do not rely on pumps for safety. This however leads to safety transients that are much longer than their older reactor counterparts. This increase in transient simulation time requires a higher level of accuracy since the accumulation of small errors over a large number of time steps can lead to severe degradation of accuracy. However, because of the rapid growth in computer hardware, nonlinear equation solution algorithms, and software engineering, new simulation codes can be improved to meet the modern requirements of speed and accuracy.

Work has been progressing on development of numerical algorithms to obtain the accuracy [1] required for modern reactor safety applications. This approach obtains the accuracy through solving all of the nonlinear equations in a single implicitly balanced approach [2]. The efficiency of this algorithm comes from a hybrid approach based on combining the older algorithms, which are fast but inaccurate, with modern algorithms, that are accurate but computationally intensive [3]. This approach of using an older solution algorithm to accelerate a newer solution algorithm is called physics-based preconditioning. This preconditioner employed for these reactor safety simulations was originally developed on simplified equations in 2002 [4].

The difficulty in solving reactor safety transients is the spread in time scales of the different physics involved. When the reactor has not been SCRAM'ed (control rods inserted to stop the fission reaction), there is a very fast time scale associated with the neutron transport. The next fastest time scale deals with the mass, momentum, and energy exchange between the liquid and vapor phases of the cooling water, the next fastest time scale deals with the motion of the fluid, and the final slowest time scale deals with the conduction heat transfer in the metal of the reactor. These physical time scales can be different by many orders of magnitude.

The results presented are for a transient where the reactor is running at full power and then the heat addition due to nuclear fission is turned off (SCRAM). The transient then tracks the rate that the wall is cooled due to convection and phase change of the water. As the wall temperature cools, after the fission heat source has been turned off, the amount of steam produced goes down as an increase in the liquid volume fraction.

For the old solution algorithms, the physics of the heat conduction in the wall is operator split from the physics of the boiling water. In addition, the physics of heat conduction is additionally operator split into separate conduction solves in the "X" and "Y" directions. The physics of the boiling water is separated into a component from the speed of sound in the fluid and a component that corresponds to the velocity of the fluid. This breaking of the problem into smaller

pieces was required to improve the speed of the simulation and to make the linear algebra solutions small enough to fit into the memory of a 1970s computer.

This splitting of the physics comes at a cost of accuracy and stability. Although these algorithms are fast and only require a small amount of computer memory, they must be run at time steps that are small. The modern algorithms, that solve the nonlinear system of equations in a single nonlinear solve, do not have the same problems with stability. Therefore, the only constraint on the time step is due to accuracy. However, since the implicitly balanced solution does not introduce any unphysical time scales due to splitting the physics, its accuracy constraints are determined by the physics of the simulation only.

Figure 1 shows these effects on a time step convergence study to examine the accuracy of the different algorithms. In this study the different algorithms are run for multiple time steps (on the X-axis) and their error (on the Y-axis) is plotted. The error is computed by taking the difference between an exact solution and the computed solution. The results from the old solution algorithms are shown with circles and the results from the modern algorithms are shown with squares. Three different transients are run for both the old and new algorithms. In the different transients the time scale of heat conduction was slowed down (by making the wall bigger) to lengthen the simulation time and spread the heat conduction time scale from the fluid time scales. The thicker lines (larger symbols) are for a larger spread in time scales and long transients; the thinner lines (smaller symbols) are for a smaller spread in time scales and shorter transients. A few observations can be made from this plot. First the old algorithm (circles) has a stability constraint at CFL = 1.0, therefore that is the largest time step that can be run. The new algorithm (squares) is always more accurate than the old algorithm and in addition, it can obtain high levels of accuracy at time steps much larger than the old algorithm's stability limit. The thick lines (and large symbols) represent the longer transients that will occur in the modern passive cooling systems.

The most difficult transients to analyze for nuclear reactor safety are incidents that occur when the reactor does not SCRAM (shut down). To analyze these transients the time scales are spread even farther by the inclusion of the fast neutron transport time scale. However, since the fission reaction rate is a function of both the wall temperature and the liquid volume fraction, the nonlinear coupling between all of the physics is actually increased. A fast and accurate solution method for this larger system will require improvements in the efficiency of the current algorithm as well as a more accurate algorithm for calculating the largest accurate time step for the simulation. In addition, since the transients for modern passive cooling systems are longer, additional work needs to be done to assess the long time accuracy of the different methods. This will ensure that the new reactor simulators will not accumulate error in these long transients.

For more information contact Vincent Mousseau at vmss@lanl.gov.

[1] V.A. Mousseau, "Accurate Solution of the Nonlinear PDE's from Thermal Hydraulics," *Nucl. Technol. J.*, accepted, (2005).
[2] V.A. Mousseau, *J. Comput. Phys.* **200**, 104–132 (2004).
[3] V.A. Mousseau, *J. Heat Transfer* **127**, 531–539, (2005).
[4] V.A. Mousseau, et al., *Mon. Weather Rev.* **130**, 2611–2625, (2002).

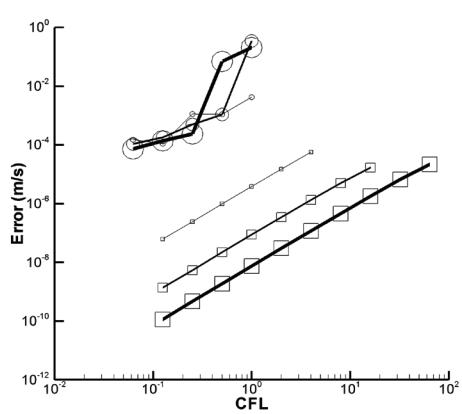

Fig. 1.
Accuracy comparisons between the old (circle) and new (square) methods.

Multiphase Flow Approach toward Fluid-Structure Interactions

Xia Ma, Qisu Zou, Duan Z. Zhang, W. Brian VanderHeyden, and Nely Padial-Collins, T-3

Fluid-structure interactions with possible large deformations pose a great challenge to numerical simulations. These types of problems include interactions of solid high explosives (HE) and product gas generated from chemical reactions at the initiation of explosions, projectile-target interactions, etc. In these cases one needs to consider the stress states in both the solid phase and the fluid phase. An Eulerian mesh-based method encounters significant difficulties associated with numerical diffusion. A Lagrangian mesh-based method encounters the mesh-tangling problem. Expensive re-meshing procedures need to be done frequently. To meet these challenges, we represent different materials by different phases and treat the problem as a multiphase flow problem. To take the advantages of both Lagrangian and Eulerian methods, while avoiding their disadvantages, a particle-in-cell (PIC) method is employed to represent the solid phase.

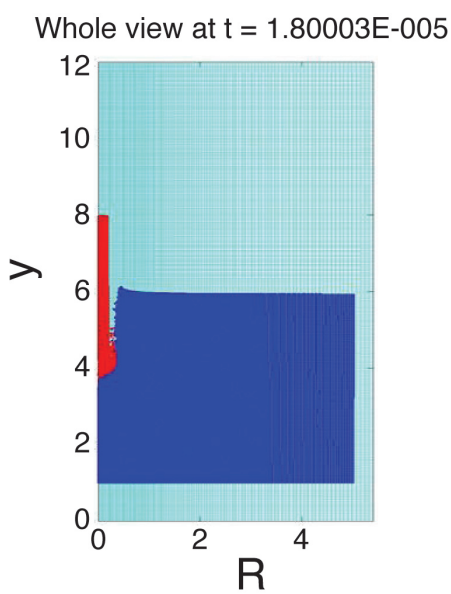

Fig. 1.
The tungsten problem.

In the method the fluid phases are computed on an Eulerian grid only and the solid phase is represented by particles and also represented on the same Eulerian grid. The solid particles are Lagrangian material points. Information like deformation, stress, damage, etc. is carried on the particles. Certain information of the solid phase is interpolated back and forth between particle and the Eulerian grid to account for the interaction with fluids. These ideas are implemented in an award-winning (R&D 100, 2005) computer package called CartaBlanca using the object-oriented language Java. The features of the Java language enable us to easily implement many practical engineering material models and to perform parallel calculations easily.

We also extended the multiphase flow theory by studying a multipressure model. In many calculations of multiphase flows, a single pressure called the equilibrium pressure is used for all phases. However, in some of the continuous multiphase flows, the notion of the equilibrium pressure encounters conceptual difficulties. For instance, the single pressure model cannot be used to study the tension break of a sponge with interconnected pores filled with air because the air can never go into tension. We found that the equilibrium pressure model corresponds to a particular assumption in deriving the multiphase flow equations. Other assumptions are also possible, and one of the assumptions that we propose leads to a multipressure model. This model is also implemented in CartaBlanca.

To validate our implementation of the PIC method, a simulation of tungsten penetrating a steel plate was performed. It is a case with cylindrical symmetry. Figure 1 shows the problem in the middle of penetration, and Fig. 2 is a comparison of the simulation and the experiment for the tungsten tail position and the lowest penetration point. The

agreement with experiment is quite good. To demonstrate the capability of the two-pressure model, we consider a spalling damage case for a porous plate. At time t = 0, a plate of thickness h impacts a thicker plate of the same material of thickness 2h with velocity V. Both plates have a small air volume fraction and are surrounded by air. At the impact time, a compression stress wave with strength σ is generated, travels in both directions, and reflects at the boundaries to become two tensile stress waves. At a certain time, the two waves meet at the middle of the thicker plate to generate a tensile stress of 2σ. If the material strength is between σ and 2σ, the thicker plate breaks at this point. Figure 3 is a sketch of the problem, and Fig. 4 shows the simulation result. The blue part represents both plates together with a black dashed line indicating the interface of the plates; the red color indicates the damaged part. Thus, the breakage indeed occurs at the middle of the thicker plate. The damage time and the impact stress are compared with elastic theory and found to agree with the theory with errors of 5% and 11% respectively. Finally, we apply the code to an HE problem using the multipressure model. Figure 5 shows the case of a drop-skid problem: an HE charge of hemisphere shape is swung into a plate. Ignition depends on the drop height and the property of the plate. Figure. 6 is a plot of the 2-D simulation result when ignition occurs. Simulations for different drop heights and different plates are in agreement with experiments in terms of "go" or "no go," that is, whether or not an explosion occurs.

For more information contact Qisu Zou at qisu@lanl.gov.

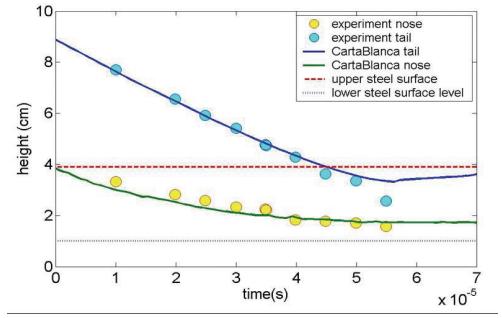

Fig. 2.
Comparison with experiment of the tungsten problem.

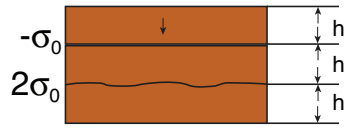

Fig. 3.
The spalling problem.

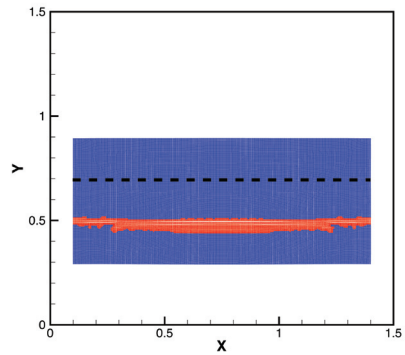

Fig. 4.
Simulation result of the spalling problem.

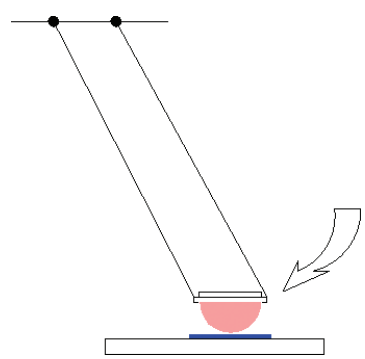

Fig. 5.
The drop-skid problem.

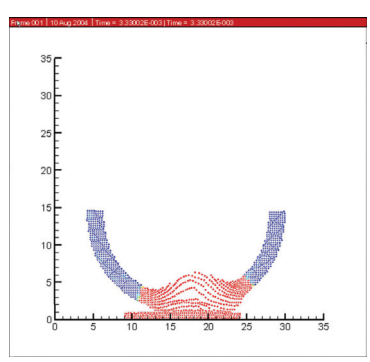

Fig. 6.
A snapshot of the drop-skid simulation.

Acoustic Wave Propagation in a Particle-Laden Gas

Peter J. O'Rourke, Michael C. Cline, and Manjit S. Sahota, T-3

In work supported by the Advanced Simulation and Computing (ASC) Turbulent Mix Project, we are continuing the development of a compressible particle/spray model for ejecta calculations [1], using the CHAD code as a test bed [2, 3].

This research uses the propagation of an acoustic wave to test the ability of the particle/spray model to compute the sound speed in a particle-laden gas. This sound speed is reduced below the sound speed of the un-laden gas. Here, a gas of uniform density ρ_g and sound speed c_g is contained in a one-dimensional tube of length L. The ends of the tube, at x = 0 and x = L, are rigid walls. The gas is laden with a uniform dispersion of small particles that exchange momentum with the gas through drag forces but do not exchange heat with the gas. The (uniform) volume fraction of the particles θ_p is small compared to unity, but, because the particle material density ρ_p is much larger than the density of the gas, the particle-phase macroscopic density $\rho_p\theta_p$ is comparable to ρ_g. The lowest sound speed of this two-phase mixture, the equilibrium sound speed c_{eq}, is attained in the limit of infinite drag between the particles and gas. Under these circumstances the sound speed c_{eq} is given by [4]

$$c_{eq}^2 = c_g^2 \frac{\rho_g}{\rho_g + \theta_p \rho_p} \qquad (1)$$

Equation (1) displays the well-known lowering of the sound speed in two-phase flows. For this calculation, we used $\theta_p = 0.001$ and $\rho_p = 1000.0\rho_g$, so that for the equilibrium sound speed $c_{eq} = \frac{c_g}{\sqrt{2}}$.

Upon this uniform mixture we initially superimpose the fundamental mode velocity perturbation $u(x,0) = u_m \sin(\pi x/L)$, where u_m is the initial velocity at the center of the tube and L is the perturbation wavelength. There is no pressure perturbation, so that $u_t(x,0) = 0$. This is an acoustic perturbation, so that $u_m << c_{eq}$. The analytic solution to this problem is

$$u(x,t) = u_m \cos\left(\frac{\pi c}{L} t\right) \sin\left(\frac{\pi x}{L}\right), \qquad (2)$$

where c is the mixture sound speed.

Because of numerical errors, there is numerical damping and dispersion of sound waves, and these errors are reduced by reducing both the Courant number $C = \frac{c_s \delta t}{\delta x}$, where δt is the computational time step and δx is the computational cell size, and the dimensionless wave number $k = \frac{\delta x}{L}$.

As seen in Fig. 1, for C = 0.015 and k = 0.01, the computed accuracy of the sound waves is quite acceptable. Thus, these values for the numerical parameters are used for the following results.

We performed a series of calculations in which a linear drag law was used:

$$\frac{du_p}{dt} = \frac{1}{t_{drag}}\left(u - u_p\right), \qquad (3)$$

where u_p is the particle velocity and t_{drag} is a drag time that is varied from calculation to calculation. Figure 2 gives the computed mixture sound speed versus the drag time t_{drag}. The dimensional period of oscillation of the acoustic wave, based on c_g, is $P = 8.65*10^{-4}$s. It is seen from Fig. 2 that the mixture sound speed is near

$$c_{eq} \text{ for } \frac{t_{drag}}{P} > 0.1$$

and near the equilibrium sound speed

$$c_{eq} \text{ for } \frac{t_{drag}}{P} < 10^{-6},$$

and drops in a monotone fashion between these values.

For more information contact Peter J. O'Rourke at pjor@lanl.gov.

[1] P.J. O'Rourke, et al., "Status of CHAD's Particle/Spray Model – September 30, 2005," Los Alamos National Laboratory report LA-UR-05-7412 (Sept. 2005).
[2] P.J. O'Rourke and M.S. Sahota, *J. Comput. Phys.* **143**, 312–345 (1998).
[3] P.J. O'Rourke and M. S. Sahota, "NO-UTOPIA: The Flow Solver for the CHAD Computer Program," Los Alamos National Laboratory report (in preparation).
[4] G.B. Wallace, *One-Dimensional Two-Phase Flow* (McGraw-Hill, New York, 1969).

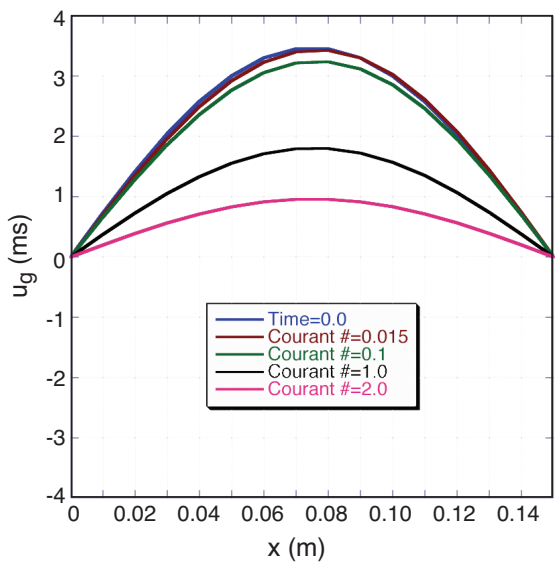

Fig. 1. *Effect of varying the Courant number on the computed solution. These are plots of gas velocity versus distance after one period of oscillation of the acoustic wave, along with the initial (time = 0.0) gas velocity profile.*

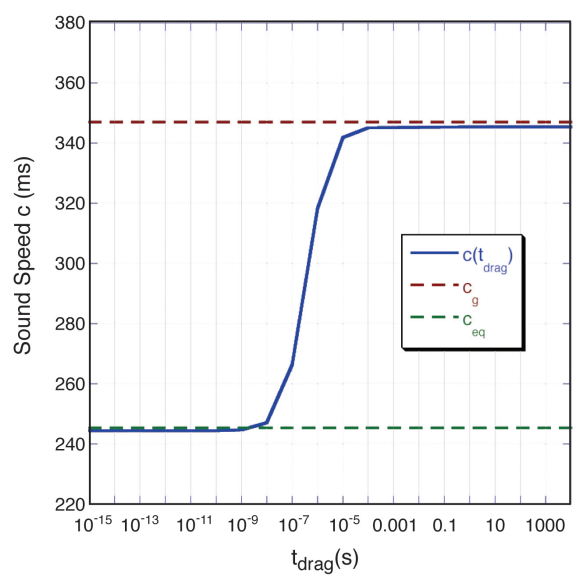

Fig. 2. *Computed mixture sound speed vs the drag time t_{drag}.*

KIVA-4: An Unstructured Version of KIVA-3V

David J. Torres, T-3

KIVA is a name given to a series of multidimensional codes designed at Los Alamos National Laboratory to simulate internal combustion engines. KIVA was capable of computing transient compressible flow dynamics with fuel sprays and combustion in relatively simple two- and three-dimensional (2- and 3-D) geometries [1, 2]. KIVA-II [3] made much of the temporal differencing in KIVA implicit. While advection remained explicit with a subcycled time step, advection was made more accurate with an improved upwinding scheme. A k - ε turbulence model was also incorporated. KIVA-3 [4] added the capability of using a block-structured mesh where multiple blocks of cells could be patched together to construct a mesh. Software to generate block-structured meshes and post-processing visualization tools were included with the KIVA-3 package. The code was enhanced by a procedure (snapping) used to remove or add layers of cells during piston movement. KIVA-3V [5] added vertical or canted valves and a particle-based liquid wall film model.

KIVA-4 is the next generation of KIVA codes [6, 7] produced under the sponsorship of the DOE's Office of Freedom Car and Vehicle Technologies. While KIVA-4 maintains the full generality of KIVA-3V, it adds the capability of computing with unstructured grids. Unstructured grids, which include structured grids, are a more general class of grids. The unstructured grids can be composed of a variety of elements including hexahedra, prisms, pyramids, and tetrahedra. Unstructured grids can be generated more easily than structured grids for complex engine geometries. KIVA-4 also features a multicomponent fuel evaporation algorithm [8], where an injected liquid fuel can be composed of many types of fuels. In designing KIVA-4, an emphasis was placed on keeping the code comparable in computational efficiency to KIVA-3V. This entailed foregoing more expensive advection schemes. Current efforts are focused on completing the parallelization of KIVA-4 so it can run on multiple processors simultaneously.

Figure 1 (a) and (b) are a comparison of a 3-D engine computation with valves and injected fuel spray. The figures show color contours of fuel concentrations performed on a

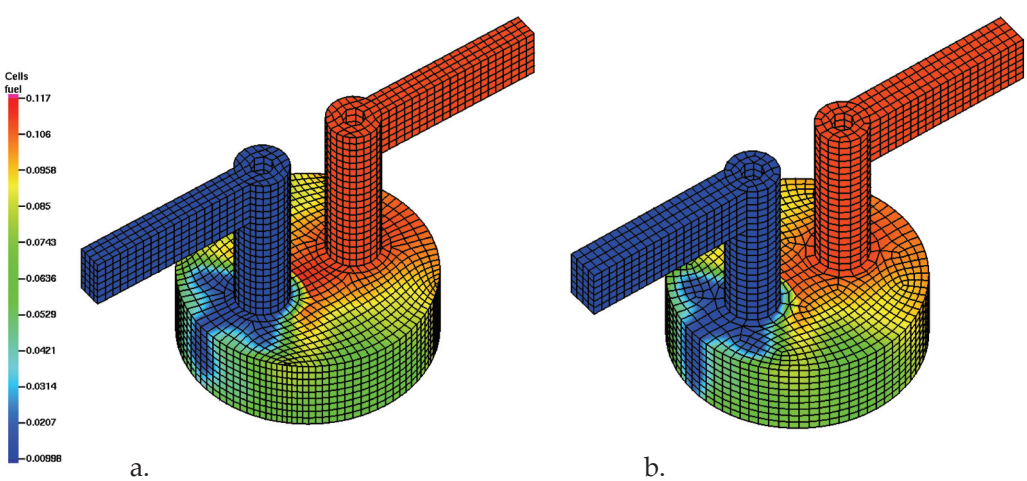

Fig. 1.
The figures show a comparison of a 3-D engine computation with valves and injected fuel spray. They show color contours of fuel concentrations performed on a structured grid with KIVA-3V (a) and an equivalent unstructured grid with KIVA-4 (b). Despite differences in the grid and numerical schemes, both plots show similar distributions of fuel.

structured grid with KIVA-3V (a) and an equivalent unstructured grid with KIVA-4 (b). Despite differences in the grid and numerical schemes, both plots show similar distributions of fuel.

Figure 2 shows the performance of a parallel version of KIVA-4 in a cylinder with 53,760 cells. The horizontal axis plots the number of processors. The red line shows the time required to complete 100 cycles. The green line shows the computational speed-up. The computational speed-up is the time required to complete the simulation with one processor divided by the time required to complete the simulation with multiple processors. One notices a puzzling trend in Fig. 2 when the number of processors exceeds 16. At this point, the amount of time spent communicating information between processors starts to offset the benefits of distributing the computational work to processors. In a larger grid, one would continue to realize improving efficiency gains with larger number of processors before encountering this communication penalty.

Our eventual goal is to have KIVA-4 adopted by industry and academia and used as a modeling tool to improve fuel efficiency and reduce fuel emissions in engines. A beta-version of KIVA-4 has been distributed to universities and industries to initiate collaborations and improve KIVA-4 with feedback we receive.

For more information contact David Torres at dtorres@lanl.gov.

[1] A.A. Amsden, et al., "KIVA: A Computer Program for Two- and Three-Dimensional Fluid Flows with Chemical Reactions and Fuel Sprays," Los Alamos National Laboratory report LA-10245-MS (Aug. 1985).
[2] A.A. Amsden, et al., "Improvements and Extensions to the KIVA Computer Program," Los Alamos National Laboratory report LA-10534-MS (Aug. 1985).
[3] A.A. Amsden, et al., "KIVA-II: A Computer Program for Chemically Reactive Flows with Sprays," Los Alamos National Laboratory report LA-11560-MS (Feb. 1989).
[4] A.A. Amsden, "KIVA-3: A KIVA Program with Block-Structured Mesh for Complex Geometries," Los Alamos National Laboratory report LA-12503-MS (Dec. 1992).
[5] A.A. Amsden, "KIVA-3V: A Block-Structured KIVA Program for Engines with Vertical or Canted Valves," Los Alamos National Laboratory report LA-13313-MS (May 1997).
[6] D.J. Torres, "KIVA-4: Validation, Rezoning, and Remapping," in *15th International Multidimensional Engine Modeling User's Group Meeting*, Detroit, April 2005.
[7] D.J. Torres and P.J. O'Rourke, "KIVA-4," in *14th International Multidimensional Engine Modeling User's Group Meeting*, Detroit, March 2004.
[8] D.J. Torres, et al., "Efficient Multicomponent Fuel Algorithm," *Combustion Theory and Modeling* **7**, 67–86 (2003).

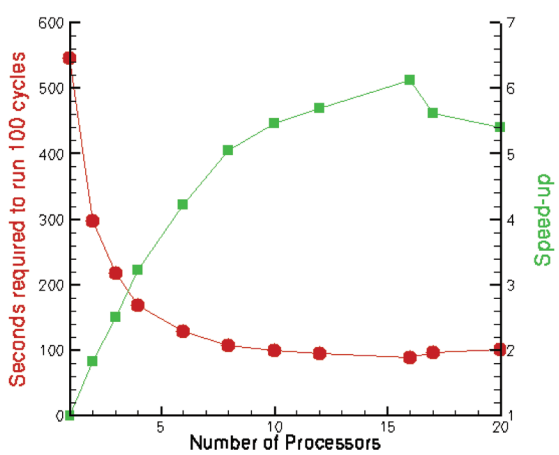

Fig. 2.
The performance of a parallel version of KIVA-4 in a cylinder with 53,760 cells. The horizontal axis plots the number of processors. The red line shows the time required to complete 100 cycles. The green line shows the computational speed-up.

Coupled Chemical Climate Modeling

Mathew E. Maltrud, T-3; Scott Elliott, CCS-2; Shaoping Chu, EES-2; P. Jones, T-3; and J. Drake, Oak Ridge National Laboratory

Over the past year, climate researchers in T-3 and their collaborators produced a fully coupled climate simulation with extensive interactive chemistry and biogeochemistry. This was the first attempt to include full carbon and sulfur cycles within a coupled climate simulation. In previous climate simulations, only physical quantities were predicted and a few important chemical species, like carbon dioxide and sulfate aerosols, were specified based on observed concentrations or estimated future concentrations. Such models allowed the climate community to predict the impacts of these concentrations on the climate but were not adequate for determining how changes to the climate system might impact the ability of the land and oceans to take up or release additional carbon or sulfur. The current simulation is a first step toward a climate system model in which only the emissions themselves are specified so that the physics and associated feedbacks in the climate system will determine the actual atmospheric concentrations of greenhouse gases and aerosols and their impacts on such important fields as temperature and precipitation.

The model being used is a version of the Community Climate System Model (CCSM) containing atmosphere, ocean, sea ice and land surface components. In addition to the physical fluxes of momentum, heat and water, carbon dioxide and dimethyl sulfide were allowed to be exchanged between these four components. These two specific chemical compounds were chosen for initial study for their important, but distinct, effects on climate. Carbon dioxide is a leading greenhouse gas responsible for recent climate change. Dimethyl sulfide is an important natural source of atmospheric aerosols, which act as additional condensation nuclei for the formation of clouds. In order to compute these fluxes across the interfaces between models, a full atmospheric chemistry model with 90–100 species and over 200 reactions were required. Since dimethyl sulfide is produced by microscopic organisms in the ocean, a full marine ecosystem and trace gas model consisting of 26 plant, animal, and chemical species were implemented within the ocean model. The land surface also included a large number of carbon pools from various plant and soil properties.

Los Alamos National Laboratory (LANL) researchers, as part of the Climate, Ocean and Sea Ice Modeling (COSIM) project, provided the Parallel Ocean Program (POP) and CICE models as the ocean and sea ice components for the coupled model. In addition, COSIM researchers implemented an ocean ecosystem model of Moore et al. [1] within the ocean model and added an additional trace gas module that includes the production of dimethyl sulfide, as well as a number of other trace gases (such as carbon monoxide and nitrous oxide) that will soon be added to these simulations.

This work was funded by the Scientific Discovery through Advanced Computing (SciDAC) program through the Office of Biological and Environmental Research within the DOE Office of Science. The project is a collaboration between researchers at LANL and collaborators at Lawrence Livermore National Laboratory (P. Cameron-Smith), National Center for Atmospheric Research (J.-F. Lemarque), Oak Ridge National Laboratory (F. Hoffman, D. Erickson, J. Drake), and Argonne National Laboratory (R. Jacob).

For more information contact Mathew Maltrud at maltrud@lanl.gov.

[1] J.K. Moore, et al., "Upper Ocean Ecosystem Dynamics and Iron Cycling in a Global Model," *Global Biogeochem. Cycles* **18**, doi 10.1029/2004 GB002220 (2004).

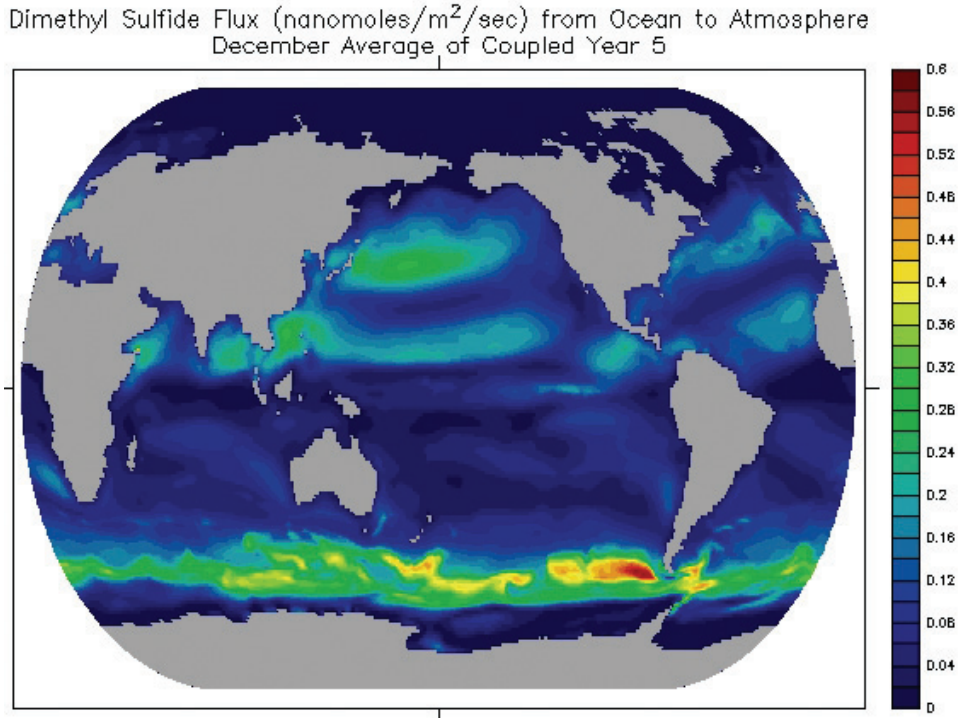

Fig. 1. *Average of dimethlyl sulfide flux (nanomoles/m²/s) from the ocean to the atmosphere in December of year 5 in the fully coupled simulation.*

Temporal Accuracy of the Solution of Radiation Hydrodynamics Equations

Rick M. Rauenzahn, Vincent A. Mousseau, and Dana A. Knoll, T-3

Traditional methods for time integration of the nonequilibrium radiation diffusion equations are first-order accurate in time, i.e., errors scale linearly with computational time step [1]. These methods rely on linearizations and operator splitting to simplify the linear algebra so small systems can be solved easily on the computer. A second more modern approach is to solve the nonlinear system in a single matrix that is large and complicated [2]. When employing this approach, it is fairly straightforward to make the time integration second-order (quadratic scaling of errors with time step) accurate in time but with increased computational cost. The purpose of this work is to investigate the middle ground between the first-order in time split and linearized methods and the second-order in time implicitly balanced methods. Recent works by the authors [3] and others have presented second-order in time split and linearized methods for nonequilibrium radiation diffusion.

The mathematical model for nonequilibrium radiation diffusion consists of two equations, one for conservation of energy in the radiation field and one for conservation of energy in the material field. If one couples the solution of the nonequilibrium radiation diffusion equations to a solution of the fluid motion in the material, the resulting system is a large, tightly coupled, system of nonlinear equations. Since we are only now beginning to have the computer capacity and the algorithmic efficiency to solve this as a single nonlinear system, traditional solution methods have had to rely on linearizations and operator splitting to make the solution tractable on existing computers with mainstream algorithms. It is important to analyze the trade-off between computational speed and accuracy when these simplifications (linearizing and operator splitting) are made.

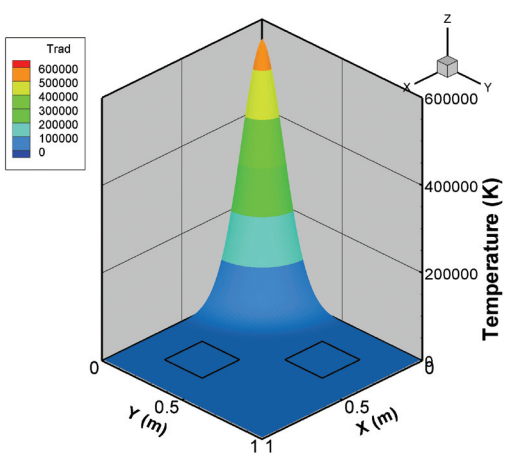

Fig. 1.
Initial conditions for the 2-D Blast problem.

Our benchmark, most accurate method for solving these equations is a popular modern scheme called the second-order Newton-Krylov method. This method is second-order in time, and contains no operator splitting and no linearizations. This nonlinear system of nonequilibrium radiation diffusion and material energy coupling equations is solved using Newton's method and the resulting linear equations of the Newton iterations are solved with a Krylov linear solver. This method is second-order accurate and robust but the solution of the large nonlinear system can be computationally expensive. Because of the potential complexity of the matrix equations to be solved, the efficiency of this method is heavily impacted by the preconditioning strategy.

This traditional workhorse algorithm [1] for solving the nonequilibrium radiation diffusion equations is first-order in time, operator split, and linearized. The basic idea of this approach is to recognize that if the material conduction effects are separated and solved on their own in an operator split step, then the material energy and the radiation energy can be combined, without introducing another split step, into a single matrix after the equations have been appropriately linearized. The solution of this matrix provides the new time radiation energy. The material conduction is then solved as a separate system, which yields the new time material temperature.

Our new contribution to second-order algorithms is motivated not only by previous studies of the behavior of the two algorithms

just outlined, but also other attempts at developing linearized, and thus cheaper, second-order methods. During investigations of previously proposed second-order split and linearized algorithms, it was discovered that, for certain test problems, the separation of the diffusion and the reaction (coupling) terms into two distinct steps resulted in large and often fatal errors [4] which could cause the method to abort. These types of errors did not occur in the Newton-Krylov solution where there are no linearizations or operator splitting. However, the traditional solution method, although it had a large first-order in time error, ran these problems without difficulty. We have constructed a method that is second-order accurate in time that maintains the tight coupling between the radiation diffusion and the source coupling to the material energy. This new solution method uses what is known as Strang splitting to separate the material conduction from the material reaction and the radiation diffusion and reaction. We then replaced the first-order linearizations in the traditional linearized method of Olson with second-order linearizations.

An example of the test problems that we have used to assess these methods is presented below. An initial pulse of radiation energy is placed in the lower-left corner of the box with reflective walls over a radial extent of about 0.1 m. The two square obstacles have an atomic number of 10, giving those regions opacities 1000 times higher than that of the background material, which has an atomic number of one. The initial conditions are shown in Fig. 1. A contour plot of the resulting final radiation temperature at a time of 5 ns is shown in Fig. 2.

Most recently, we have added the hydrodynamic equations to our studies to model more realistic problems that include fluid flow, like radiation-driven shocks and blast waves in real fluids. Our results with the fully coupled Newton-Krylov methods, which solve the Euler equations of hydrodynamics with the radiation diffusion equations in a fully coupled manner, verify that we can generate second-order results, while an operator-split method very similar to that used in large production codes is only first-order in time. Our immediate goals are

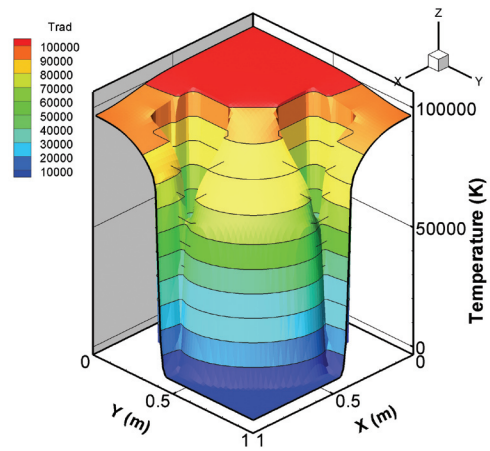

Fig. 2. ***Radiation temperature contours for the 2-D Blast problem.***

to (1) improve our prototyping to mimic a production code algorithms more closely, (2) confirm that we can generate both first- and second-order results when expected, and then (3) propose, if feasible, methods that display improved accuracy without incurring the cost of second-order Newton-Krylov.

For more information contact Rick Rauenzahn at rick@lanl.gov.

[1] G.L. Olson and J.E. Morel, "Solution of the Radiation Diffusion Equations on an AMR Eulerian Mesh with Material Interfaces," Los Alamos National Laboratory report LA-UR-99-2949 (June 1999).
[2] V.A. Mousseau, et al., *J. Comput. Phys.* **160**, 743–765 (2000).
[3] V.A. Mousseau and D.A. Knoll, "Temporal Accuracy of the Nonequilibrium Radiation Diffusion Equations Applied to Two-Dimensional Multimaterial Simulations," *Nucl. Sci. Eng.*, submitted, (2005).
[4] D.L. Ropp and J.N. Shadid, *J. Comput. Phys.* **203**, 449–466, (2005

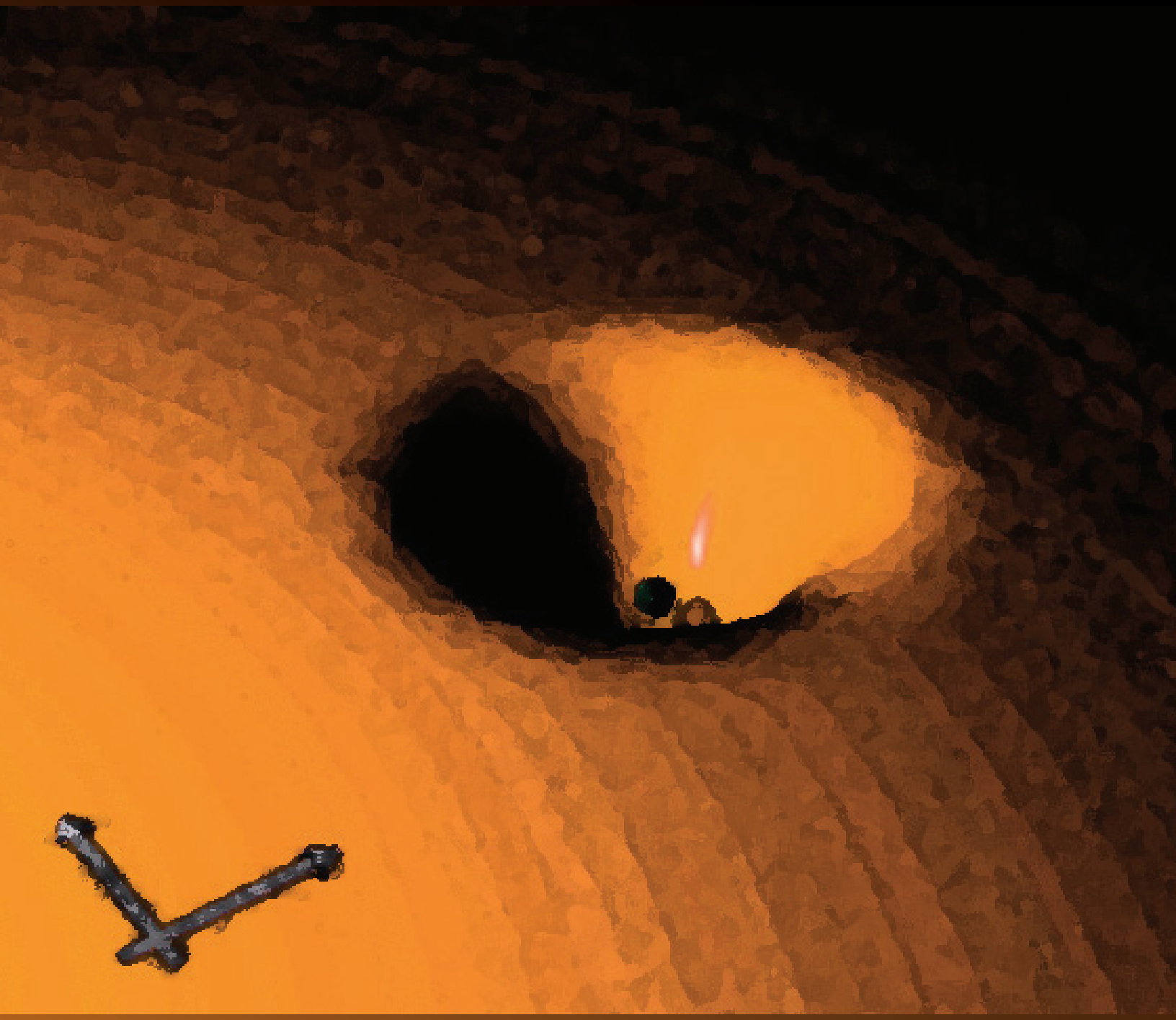

T-4

Atomic and Optical Theory

Group Leader: James Cohen
505.667.5982; cohen@lanl.gov

T-4 Atomic and Optical Theory develops methods for and performs calculations of atomic structure, scattering cross sections, opacities, exotic atoms, and quantum and nonlinear optics, including effects of high energy density environments and interaction with external electromagnetic fields.

Small Polarons in a Dilute Bose-Einstein Condensate

Fernando M. Cucchietti and Eddy Timmermans, T-4

Since the 1995 realization of dilute gas Bose-Einstein condensation [1], the area and technology of cold atom physics grew at an astonishing pace. Following Bose's derivation of the spectral density of thermal light from the statistics of indistinguishable "Bose" particles, Einstein predicted in 1924 that a significant fraction of such particles, if their number is conserved, occupy (or "condense" into) the same single particle state at sufficiently low temperatures. The current cold atom technology provides an impressive ability to study and manipulate this laser-like state of matter. This system, the Bose-Einstein condensate (BEC) has served as a paradigm of superfluidity.

The observation of a superfluid's response after the insertion of "foreign" — distinguishable — particles has been a successful method to study their microscopic structure. In cold atom physics, this strategy led to the demonstration of dissipationless flow in dilute BECs [2]. In these experiments, a number of impurities were created in the BEC with controllable momentum. The sudden suppression of incoherent scattering of sufficiently slow impurities by the BEC illustrated the superfluid ability of sustaining dissipationless flow.

Quantum mechanically, however, the probe necessarily affects the measured system. Recently, we found [3] that even when the change in the condensate due to the presence of the impurity is almost negligible, it can be enough to "back-react" on the impurity and modify its nature drastically. In particular, we show that there exists a regime where the impurities in the condensate can self-localize.

The process is similar to the formation of a small polaron in a solid. When an impurity interacts with the particles of a homogeneous condensate, it pulls (or repels, depending on the sign of the interaction) some bosons so that a small bump in the condensate density appears. The variation of the BEC-density provides a local minimum of the effective potential experienced by the impurity. If the impurity-boson interaction is sufficiently strong, the potential minimum is deep enough to pay for the kinetic energy cost of localizing the impurity atom, thereby trapping it near the density variation originated by the impurity's localization.

Fueled by a host of scientific and technological prospects, the localization of particles within a BEC has been pursued for the past several years. Our proposal — inducing self-localization

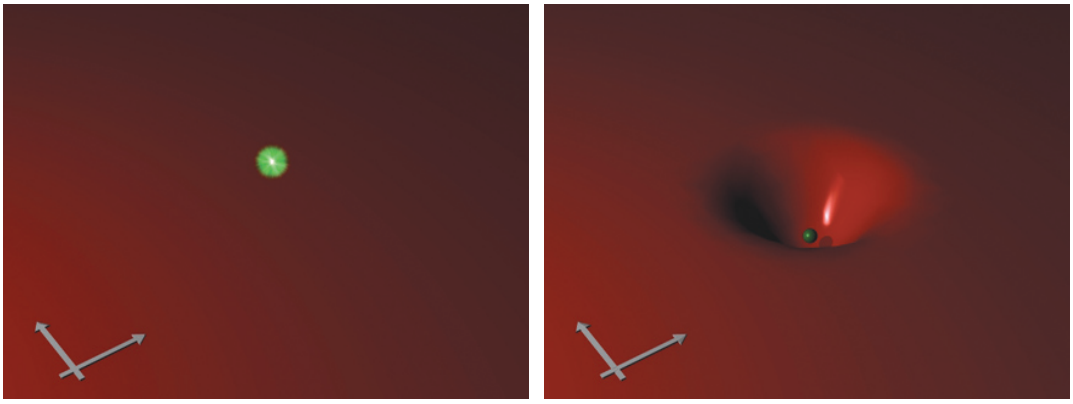

Fig. 1. *Informal representation of the formation of the polaron. On the left, an extended wavefunction for the impurity (green) interacts with the condensate particles (red). On the right, the interaction with the impurity distorts the condensate density creating a local minimum for the impurity's effective potential. If the interaction is strong enough, the impurity will self-localize.*

by increasing the impurity-boson interaction — can achieve this elusive goal and provide the flexibility and versatility necessary to create quantum-dot like single-particle devices, test the Unruh effect, provide a mean to isolate and transport quantum bits in cold atom quantum information experiments and realize other fascinating applications.

Summing up, our work opens up an avenue of research inside the field of cold atom gases. The regime of formation of the polarons is well within state-of-the-art experimental technology. We expect that the intriguing prospects will entice experimental groups to test our prediction, thereby posing new theoretical and experimental challenges. The small BEC-polaron would then join the cold atom toolbox, both as a technique and as an object for fundamental physics studies.

For more information contact Fernando M. Cucchietti at fercook@lanl.gov.

[1] M.H. Anderson, et al., Science 269, 198 (1995); K.B. Davis, *Phys. Rev. Lett.* **75**, 3969 (1995).
[2] A.P. Chikkatur, et al., *Phys. Rev. Lett.* **85**, 483 (2000)
[3] F.M. Cucchietti and E. Timmermans, "Small polarons from neutral impurity atoms in a dilute Bose-Einstein condensate," cond-mat/061228.

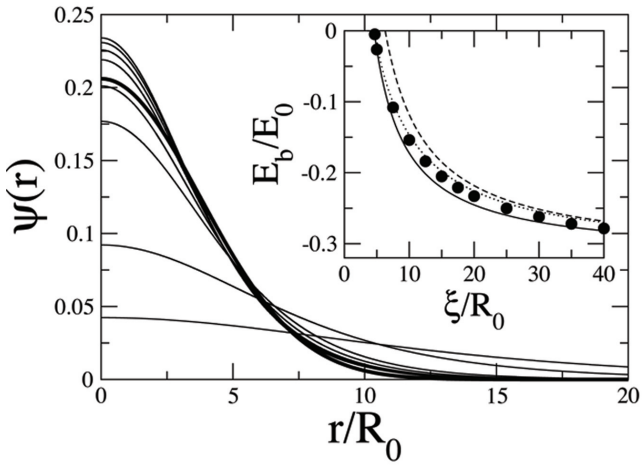

Fig. 2. ***Radial wavefunction of the impurity obtained numerically for increasing values of the healing length of the condensate ξ (from bottom to top). In bold line, the initial Gaussian ansatz. In the inset, the energy of the ground wavefunction vs ξ (dots). In dotted line, a variational calculation. The analytical expansion for large ξ is in dashed line, and the best fit to the data $E_b/E_0 \approx -1/\pi + 1.5\, R_0/\xi$ in solid line. [All lengths and energies are in units of the Bohr radius R_0 and Rydberg energy E_0 (respectively) of the effective Coulomb potential suffered by the impurity at infinite healing length.]***

Spectroscopic Characterization of an Ultrashort Laser Driven Ar Cluster Target

Manolo Sherrill, Joseph Abdallah, Jr., George Csanak, T-4; Evan Dodd, X-5; Yuji Fukuda, JAERI, Kyoto, Japan; and Anatoly Faenov, VNIIFTRI Moscow, Russia

Intense ultrashort laser irradiated rare-gas cluster targets are of considerable interest due to their extensive x-ray emission in the keV energy range and their production of highly energetic electrons and ions. Such qualities have led applied scientists to consider these targets as debris-free x-ray sources for nanolithography and biological imaging as well as ion and neutron sources.

Spectroscopic modeling of intense ultrashort laser irradiated targets have predominately relied on steady state models with electron energy distribution functions (EEDF) composed of a low-temperature Maxwellian containing the bulk of the free electrons with a high temperature component constituting a small fraction of the total population. Though this type of model has been successful at describing the effects of hot electrons on the x-ray spectra, it relies on the unrealistic assumption that the EEDF is in steady state.

In this work, a coupled electron kinetic and collisional-radiative model [1] has been used to describe the time evolution of the EEDF, level populations, and x-ray spectra beginning immediately after the end of the main laser pulse and ending at an estimated time when the density of the expanding cluster is expected to fail to produce, to any spectroscopically significant amount, He- and Li-like transitions in the He_α spectrum. This period of time will be referred to as the after glow phase (AGP).

Experimental spectra were obtained in a collaborative experiment performed at the Advanced Photon Research Center, JAERI in Kyoto, Japan under the direction of Yuji Fukuda and Anatoly Faenov. A Ti:sapphire laser with an intensity of 1 x 10^{19} W/cm^2, a main temporal pulse width of 30 fs, and a 10-ns, 1 x 10^{14} W/cm^2 prepulse was focused on a Ar cluster gas jet. He-like spectra of Ar, including the associated satellites were recorded [2].

The time history of the irradiated cluster has been considered to evolve in three phases (Fig. 1). Beginning with a cold target, a 10-ns prepulse transforms the cluster into a moderately dense plasma: we assume the system is left in a Ne-like plasma state with a free-electron temperature of ~140 eV. Doubly-excited states in the Li-like spectral features suggest that the high energy electrons produced by the main pulse, and not the low energy electrons produced by the prepulse, are responsible for ionizing

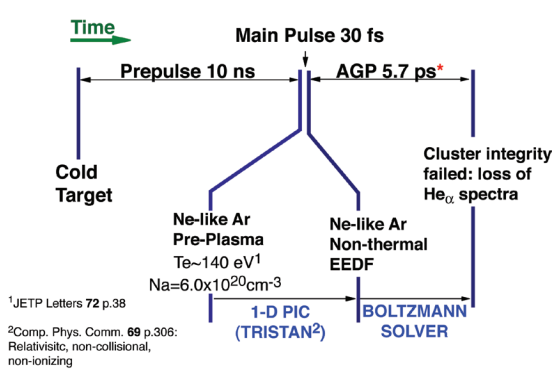

Fig. 1. *This diagram describes the evolution of the ultrashort laser driven Ar cluster target and the techniques used to model the different temporal stages.*

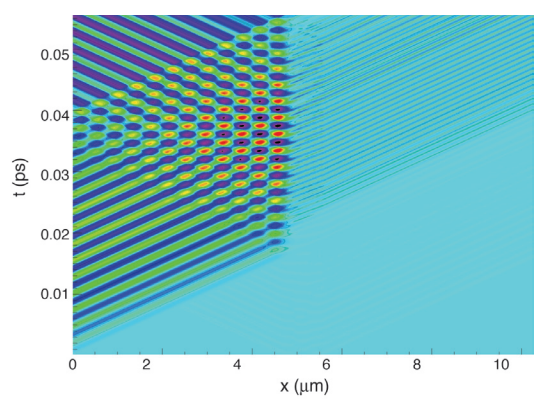

Fig. 2. *TRISTAN PIC simulation of the electric field due to the main laser pulse interacting with a cluster target placed between 4.5 and 5.5 microns. Laser pulse (approaching the target from the left) is predominantly reflected. Only a small component is transmitted (right half of image).*

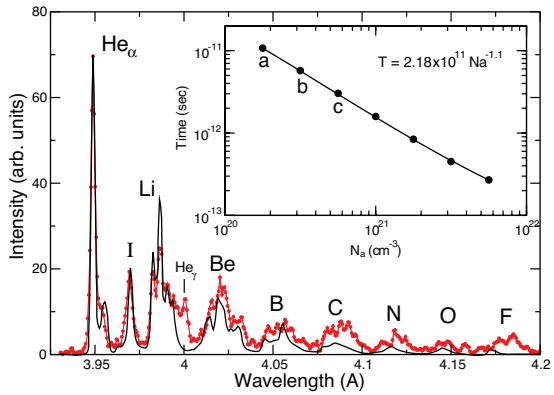

Fig. 3. ***Synthetic (black line) and experimental (red points) time integrated He$_\alpha$ and satellite spectra for Case b: Na = 3.162 x 10^{20} cm^{-3}, T = 5.7 ps is shown. Insert contains least squares best fit for different Na and their corresponding AGP termination times.***

the plasma through the L-shell series of ions.

During the interaction of the main laser pulse with the cluster target, the EEDF was shown, by one-dimensional particle-in-cell (PIC) simulations with the TRISTAN code [3], to be driven far from a Maxwellian distribution as seen in the solid red line of Fig. 4. However, the PIC simulation with a reported core cluster electric field of E = 1 x 10^{10} V/cm, Fig. 2, was too small for tunneling ionization [4] to drive the ionization balance from the initial Ne-like Ar state.

A coupled electron kinetic and collisional-radiative model (Boltzmann Solver) was used to model the AGP phase of the irradiated cluster. The model included 3000 fine-structure levels spanning the Ne-like to He-like ionization stages with atomic configurations up to principle quantum number n = 3, and all x-ray transitions from n = 2 to n = 1 within the n = 3 manifold.

With the initial AGP EEDF taken from the TRISTAN code, the Boltzmann solver was run for a large number of cases, where the ion number densities and cluster integrity times were allowed to vary. This set of calculations resulted in the production of synthetic x-ray spectra such as the one seen in Fig. 3. A least squares fitting procedure of the synthetic to experimental spectra was performed as a coarse survey to limit the number of acceptable ion density, integrity time pair candidates. Further analysis comparing the ratio of the line intensities between the He$_\alpha$ and intercombination line (I), Fig. 3, revealed the proper ion density and integrity time to be Na = 3.162 x 10^{20} cm^{-3} and T = 5.7 ps respectively for this experiment.

The evolution of the EEDF during the AGP is shown in Fig. 4. Interestingly, by the end of the predicted AGP (cluste integrity time of 5.7 ps), the EEDF is still very far from the steady state result and the pseudothermalization of the free electrons is predicted to occur much later (after T = 27.0 ps). Through the use of the above time-dependent kinetic model we have obtained a realistic description of the evolution of an ultrashort laser irradiated cluster. This technique will allow exploration into the possibility of producing table-top x-ray sources with temporal pulses widths in the 100s of femtosecond time scale critical for studying ultrafast processes.

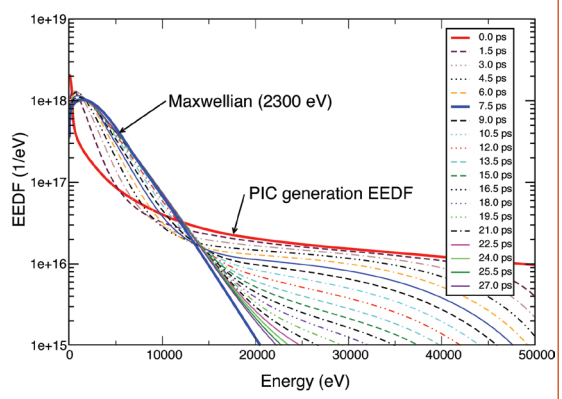

Fig. 4. ***The time history of the EEDF for time after the end of the main laser pulse (AGP), computed for Na = 3.162 x 10^{20} cm^{-3}.***

For more information contact Manolo Sherrill at manolo@lanl.gov.

[1] M.E. Sherrill, et al., *J. Quant. Spectrosc. Radiat. Transfer*, accepted (2005).
[2] Y. Fukuda, et al., *Laser Part. Beams* **22**, 215 (2004).
[3] E.S. Dodd, et al., *Phys. Rev. E* **70**, 56410 (2004).
[4] M.V. Ammosov, et al., *Sov. Phys. JETP* **64**, 1191 (1985)

Ab-initio Simulations of the Nonequilibrium Properties of Warm Dense Gold

Stephane Mazevet, T-4; and J. Clérouin, P.M. Anglade, V. Recoules, and G. Zerah, CEA/DAM Île-de-France

Recent experiments on gold thin films suggested that electrical and optical properties of metals in the warm dense matter regime can be measured by performing time-resolved measurements after the illumination of a metallic thin film by a short-pulse laser [1]. In this experimental configuration, the laser energy is uniformly deposited on a gold thin film with intensity ranging from 0.5×10^6 to 2×10^7 J/Kg. As the laser energy is directly absorbed by the conduction band electrons, the system is out of equilibrium with different electron and ion temperatures immediately after illumination. Optical properties are subsequently measured while the ions and electrons relax to their new equilibrium temperatures.

Molecular dynamics (MD) simulations based on density functional have been rather successful at describing the physical properties of equilibrium states reached in shock experiments. However, the nonequilibrium situation created in this experimental setup poses new challenges as the simulation method needs to accurately describe the time evolution of the sample after illumination by the short-pulse laser. The subsequent transfer of energy between the electrons and ions is a nonadiabatic effect, and its formal treatment is beyond the current *ab-initio* capabilities. We follow previous work by Ivanov et al. [1] and introduce the electron-phonon coupling by using a thermostat in the *ab-initio* method to produce time resolved optical conductivities for this nonequilibrium simulation.

As *ab-initio* simulations are limited by the size of the simulation cell that can be used, we further used a hybrid MD method, as proposed by Ivanov et al., to characterize the time evolution of the lattice structure as a function of laser energy. As illustrated in Fig. 1, the hybrid MD approach couples a continuum model, the two temperature model, with a classical MD method to follow the evolution of both the electron and ion temperatures as a function of time. Using this method, we were able to calculate the time needed for the fcc lattice to melt as a function of laser energies and to identify a quasi-steady state observed in the experimental optical conductivities as the duration of a superheated fcc state.

Using this result, we performed *ab-initio* calculations of the optical properties assuming that the underlying ion lattice preserves its initial fcc structure along

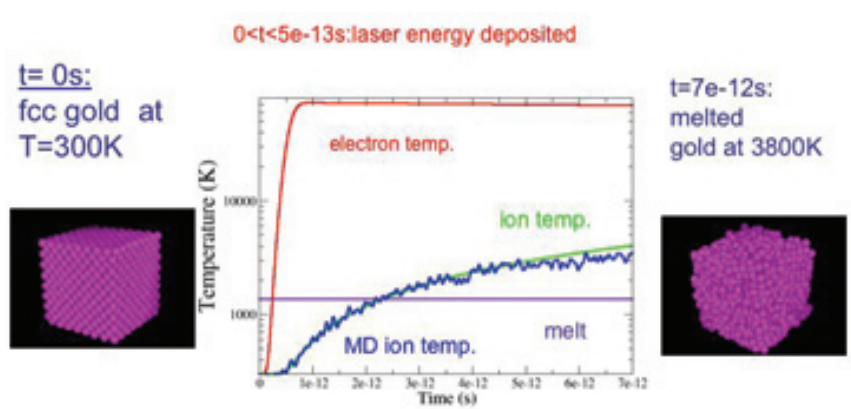

Fig. 1.
Variation of the electronic and ionic temperatures as given by the TTM.

the quasi-steady state during which experimental optical properties are averaged. In Fig. 2, we compare the variation of the real and imaginary parts of the optical conductivity as a function of laser energy and at the frequency measured experimentally. We find a remarkable agreement with the experimental data, especially for the real part of the conductivity. Overall, the calculations reproduce both the magnitude and the trend as a function of laser energy observed experimentally. This clearly shows that the experimental measurements are compatible with the existence of a metastable fcc state lasting for the duration of the quasi-steady state. Finally, we further tested this assumption by calculating conductivities of a liquid state equilibrated at 2000 K. In this situation, the dependence on the laser energy was obtained by calculating conductivities using electron temperatures given by the TTM model. We see, in Fig. 2, that for both the real and imaginary parts, the transition to a liquid state should be clearly visible in measuring the optical properties and at all the laser energies studied here.

In conclusion, we find, using a combination of classical and *ab-initio* simulations, that for the conditions created experimentally, the ions mostly preserved their initial fcc structure for several picoseconds before evolving into a liquid state. The near perfect agreement with the experimental measurements on gold thin films first showed that the quasi-steady state observed experimentally corresponds to a metastable fcc state where the lattice has not yet reacted to the elevation of the electron temperature. This study also demonstrates that *ab-initio* simulations combined with linear response theory provide a powerful tool to calculate the physical properties of nonequilibrium states generated by laser-matter interactions or short-pulse high energy-density physics experiments [3].

For more information contact Stephane Mazevet at smazevet@lanl.gov.

[1] D.S. Ivanov and L.V. Zhigilei, *Phys. Rev. B* **68**, 064114 (2003).
[2] K. Widmann, et al., *Phys. Rev. Lett.* **92**, 125002 (2004).
[3] S. Mazevet, et al., *Phys. Rev. Lett.* **95**, 085002 (2005).

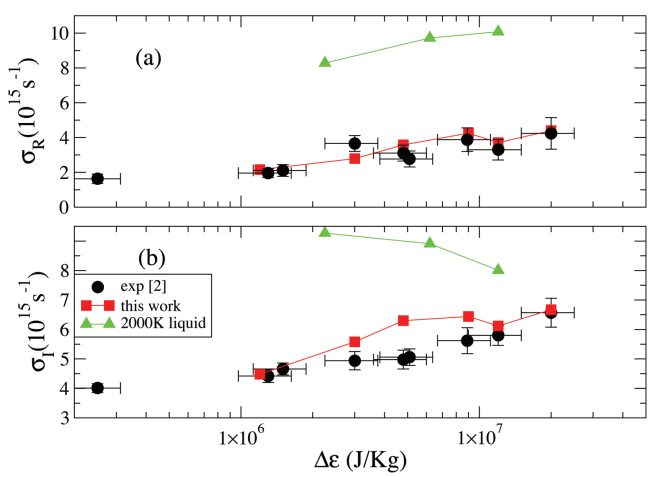

Fig. 2. ***Comparison of the variation of the real and imaginary parts of the optical conductivity as a function of laser energy and at the frequency measured experimentally.***

Improvements to the Finite-Temperature Average-Atom Model

James Colgan, George Csanak, and Lee A. Collins, T-4; Christopher J. Fontes, X-5

Radiative properties of hot, dense plasmas remain a subject of current interest. In many plasma environments, the effects of the free electrons on the bound electrons cannot be neglected. The principal approach used previously for the inclusion of such effects is termed the average-atom (AA) model. In this approach, the Kohn-Sham equation is solved for the bound electrons in several possible approximations to model the response of these electrons to the plasma environment.

Recently a program of work has been underway to describe the response properties of atoms (or ions) in hot, dense plasmas, using what is known as the Finite-Temperature Random-Phase-Approximation (FTRPA) in the calculation of spectral properties of the plasma. This was first introduced by des Cloizeaux [1]. This approach produces the appropriate potential for the calculation of the wavefunctions of the excited electrons. This work was greatly extended and developed by Csanak and Kilcrease [2], who derived expressions from which the linear response function can be calculated, which allows a straightforward calculation of spectral quantities such as the photoabsorption cross section and the oscillator strength. More recently, this approach has been further developed by Csanak and Meneses [3] to formulate the FTRPA approach into a tractable system of coupled integro-differential equations. These equations were then solved by Csanak and Meneses [3], and Csanak and Daughton [4] in the uncoupled "single-channel" approximation for hot helium and lithium plasmas at a variety of densities.

The current work on this subject has focused on solving the full set of coupled FTRPA integro-differential equations. The solution of these equations is based on the Linear Algebra method [5], which is a well-known, robust, numerical technique for the efficient solution of coupled equations. This technique has previously been used with considerable success in electron-molecule scattering [6]. We chose to focus on the spectroscopic properties of neon-like ions in finite-temperature systems, in which coupling effects should be more pronounced than in helium-like or lithium-like systems.

As a check on our method, we first solved the FTRPA coupled-channel equations at zero temperature and density in order to compare with previous results from atomic physics calculations. At finite temperature and density, there are no previous results with which to compare. Figure 1 shows the oscillator strength for a selection of neon-like ions calculated in various approximations. In (a) we show the oscillator strength calculated in the single-channel approximation formulated previously [3, 4] and we compare with configuration-average calculations from the well-established atomic structure code, CATS, developed at Los Alamos by Cowan and coworkers [7]. It is clear that the two methods are in excellent agreement. In (b) we present the oscillator strength calculated using our current coupled-channel approach. Again, we compare with calculations from the CATS code, which in this case is run in the fine-structure approximation, which includes configuration-interaction effects in a manner that is similar, but not identical, to the coupled-channel approach of the FTRPA equations. In this case we see good agreement between the two sets of calculations over a wide range of ion charges. The coupling between the channels has increased the oscillator strength by well over 20%, even for high Z.

We are currently applying the solution of the coupled-channel FTRPA equations for neon-like systems at finite temperatures and densities. In this case, we use the average-atom model developed by Daughton and Snell [8], which includes a "pseudo-atom" approach for the interaction of the "average-atom" with the rest of the plasma. This allows the energy of the system to be clearly defined, so that the resulting equation-of-state is unambiguous. We hope to report these new results in the near future.

For more information contact James Colgan at jcolgan@lanl.gov.

[1] J. des Cloizeaux, in: *Many-body Physics*, C. de Witt and R. Balian, Eds. (Gordon and Breach, New York, 1968).
[2] G. Csanak and D. Kilcrease, *J. Quant. Spect. & Rad. Transfer* **58**, 537 (1997).
[3] G. Csanak and G.D. Meneses, *J. Quant. Spect. & Rad. Transfer* **71**, 281 (2001).
[4] G. Csanak and W. Daughton, *J. Quant. Spect. & Rad. Transfer* **83**, 83 (2004).
[5] B.I. Schneider and L.A. Collins, *Comput. Rep.* **10**, 49 (1989).
[6] L.A. Collins and B.I. Schneider, *Phys. Rev. A* **24**, 2387 (1981).
[7] R.D. Cowan, *Theory of Atomic Structure and Spectra* (University of California Press, Berkeley and Los Angeles, California, 1981); J. Abdallah, Jr., et al., Theoretical Atomic Physics Code Development I. CATS: Cowan Atomic Structure Code, Los Alamos National Laboratory report LA-11436-M, Vol. I (December 1988).
[8] W. Daughton and C. Snell, "TN Burn Project: New Model for the EOS of Dense High-Z Plasmas," Los Alamos National Laboratory memorandum X-1-RN (U)03-60 (November 17, 2003).

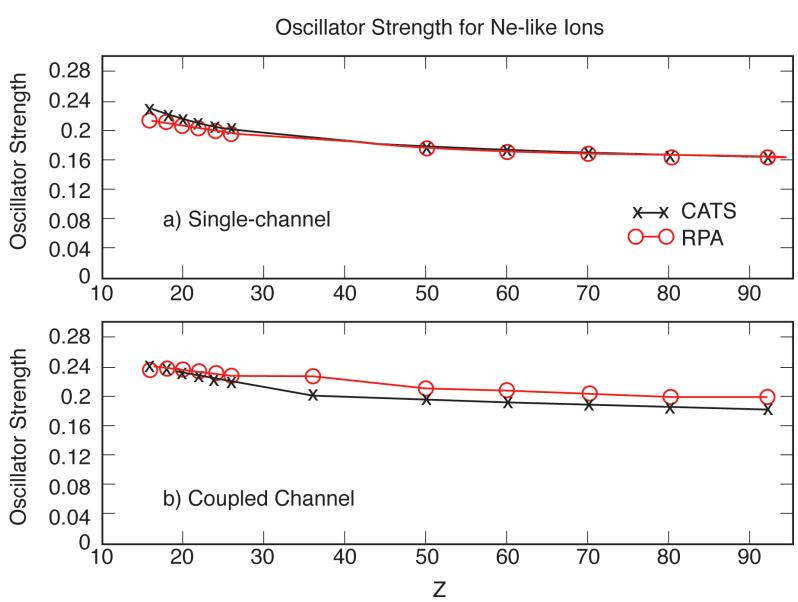

Fig. 1. ***Oscillator strength for a selection of neon-like ions calculated in various approximations. (a) Oscillator strength calculated in the single-channel approximation formulated previously [3, 4] compared with configuration-average calculations from CATS; and (b) the oscillator strength calculated using our current coupled-channel approach compared with calculations from the CATS code, which in this case is run in the fine-structure approximation, which includes configuration-interaction effects in a manner that is similar, but not identical, to the coupled-channel approach of the FTRPA equations.***

Triple Photoionization of Li and Be

James Colgan, T-4

Recent intensive efforts to accurately describe the double photoionization of helium, the simplest two-electron atom, have now reached the point where almost all measurable quantities now show good agreement between experiment and several leading theoretical techniques. This process, in which the impact of one photon on the atom leads to the ionization of both electrons, is one of the cleanest systems in which electron-electron correlation plays a dominant role. Agreement between experiment and theory has been demonstrated for the total double photoionization cross section, and the differential cross sections with respect to the energy sharing and outgoing angles of both electrons.

Extensions of this work include examining the interaction between three outgoing electrons. This is most simply found in the triple photoionization of the lithium atom, in which one incoming photon results in the ionization of all three electrons of the atom. This ionization cross section was recently measured for lithium [1]. In the last few years, the time-dependent close-coupling method (TDCC) has been extended to examine this process, by treating equally the motion of all three outgoing electrons [2]. This method solves the time-dependent Schrödinger equation for all three electrons without approximation, and all electron-electron correlations are taken into account in an accurate manner. The 9-dimensional time-dependent wavefunction for the three electrons is reduced to three radial dimensions by a coupled-channel expansion over the angular momenta of the electrons. The resulting set of coupled radial differential equations is solved on a numerical lattice and propagated in time until the interaction is complete. For three electrons, the number of coupled channels which must be employed to ensure convergence can quickly become large, unlike a two-electron calculation, where perhaps 10 or 12 channels are sufficient for convergence. After this propagation, the time-dependent wavefunction for the three electrons contains *all* the scattering information about the process, including single, double, and triple photoionization probabilities. By projection onto appropriate antisymmetric spatial and spin functions, one can obtain the cross section for any of these processes. Double photoionization cross sections (where two electrons are ionized, and one electron may be left in a ground or excited state of Li^{2+}) were calculated and compared to experiment. The agreement between experiment and theory was excellent. Triple photoionization cross sections for lithium were then extracted and compared with the recent synchrotron experiments of Wehlitz et al. [1]. The cross sections are shown in Fig. 1(a); the agreement between experiment and theory is in general very good.

One can also consider similar processes in the beryllium atom. In this case, however, there are very few experiments with which to compare, as beryllium is much more toxic to work with than lithium. However, previous model calculations for the triple photoionization of beryllium indicated a much larger cross section than for lithium [3]. The time-dependent close-coupling method was therefore applied to the photoionization of beryllium, and double and triple photoionization cross sections were calculated [4]. The resulting TDCC triple photoionization cross sections, which are presented in Figure 1(b), show a much lower cross section than the previous model calculations [3]. The large difference between the two sets of calculations may be due to the neglect of the interaction between one of the outgoing electrons and the other

two electrons in the model calculations [3]. This interaction is treated fully in the time-dependent close-coupling method. It would, however, be desirable to compare these sets of calculations with experimental measurements. Such experiments, although difficult, are currently under consideration.

The time-dependent calculations discussed here make intensive use of massively parallel computing resources. Computing time at high-performance computer centers at Los Alamos, Lawrence Berkeley, and Oak Ridge national laboratories were all utilized in these calculations. We look forward to exploiting further these invaluable resources in future calculations, which include the exploration of energy sharing between all three electrons during the ionization process.

For more information contact James Colgan at jcolgan@lanl.gov.

[1] R. Wehlitz, et al., *Phys. Rev. Lett.* **81**, 1813 (1998).
[2] J. Colgan, et al., *Phys. Rev. Lett.* **93**, 053201 (2004).
[3] A.S. Kheifets and I. Bray, *J. Phys B* **36**, L211 (2003).
[4] J. Colgan, et al., *Phys. Rev. A* **72**, 022727 (2005).

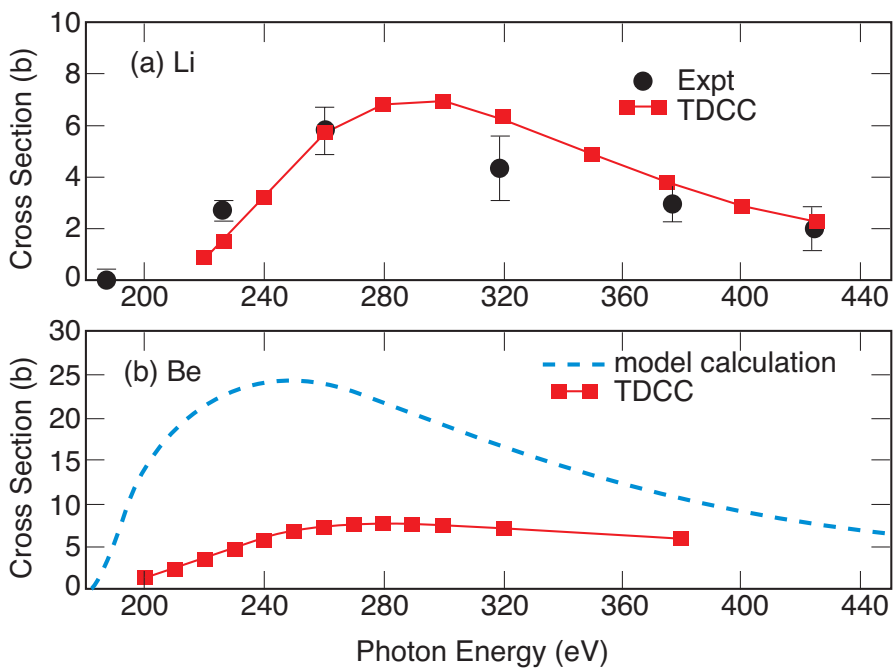

Fig. 1.
(a) Triple photoionization cross sections for lithium. (b) Triple photoionization cross sections for beryllium.

Mean-Field Statistical Theory of Finite Quantum Systems with Applications to Hot Dense Plasmas

Sergey A. Ponomarenko, George Csanak, David P. Kilcrease, and Manolo Sherrill, T-4

Recently, there has been a growing interest in statistical properties of the mesoscopic quantum systems, containing a large but finite number of interacting particles. There exist examples galore of such finite many-body systems in nature as well as in laboratory experiments, including ultracold Bose and Fermi gases confined in atomic traps, multinucleon nuclei and multielectron neutral atoms, nanoscale atomic clusters, and multielectron ions in hot dense plasmas. The number of coupled particles in such mesoscopic systems can vary from a few, as is the case with the bound electrons in low-Z atoms or ions, to hundreds of thousands for the case of trapped neutral alkali atoms. The range of relevant thermodynamic conditions is also very broad: from ultralow, cryogenic temperatures and low densities in the case of trapped Bose and Fermi gases to very high temperatures and densities in the case of some plasmas. Hence the development of a unified statistical theory of such systems, capable of taking into account finite size effects, is quite timely, and it can have a broad spectrum of potential applications. Since the number of particles is finite and fixed, we have to work with the canonical ensemble, which usually presents formidable difficulties.

Some progress along these lines has however been made to date [1–11]. Unfortunately, all these approaches suffer from significant drawbacks. In particular, some authors only consider either the systems with large numbers of particles [1–6, 9], or those at low temperatures [1–6], or they neglect the particle-particle interactions [1–5, 10, 11]. Other researchers treat the interactions phenomenologically, using a rather simplified statistical model [9]. Some alternative versions of the theory require an extensive amount of numerical work to obtain results for realistic systems [7, 8]. The other class of theories is only concerned with particles obeying classical statistics [12, 13]. Thus a problem of formulating a self-consistent statistical theory of finite systems, free of the just mentioned flaws, remains open.

The purpose of this report is to outline the highlights of such a theory. We follow the path integral approach to the generation of the statistical mean-field theory of Kerman and Levit, previously formulated for very large nuclear systems whose statistical behavior is specified by the grand canonical ensemble [14, 15]. We generalize this method to treat finite-size systems described by the canonical ensemble. We first develop the simplest possible variant of the mean-field theory that does not take into account the exchange effects, and we provide an exact closed form expression for the occupation number distribution of particles in finite quantum systems within the framework of the independent particle approximation. The derived occupation distribution function has simple analytical expressions in the important limiting cases of large and small numbers of particles in the system. The first case is relevant for trapped Bose and Fermi gases as well as nanoscale clusters, whereas the second one is of interest for low-Z atomic or plasma systems, having ions with a few bound electrons. We also show how our results can be straightforwardly generalized to include the exchange effects using the approach of Ref. [15]. Not only does our theory enable us to derive the canonical occupation number distribution in a self-consistent manner, but it treats Bose and Fermi systems within the same general framework as well.

For more information contact Sergey Ponomarenko at sergeyp@lanl.gov.

[1] S. Grossman and M. Holthaus, Z. Naturforsch, A: *Phys. Sci.* **50**, 921 (1995).
[2] W. Ketterle and N.J. van Druten, *Phys. Rev. A*. **54**, 656 (1996).
[3] K. Kirsten and D.J. Tom, *Phys. Rev. A*. **54**, 4188 (1996).
[4] H. Haugerud, et al., *Phys. Lett. A* **225**, 18 (1997).
[5] M.O. Scully, *Phys. Rev. Lett.* **82**, 3927 (1999).
[6] S. Giorgini, et al., *Phys. Rev. Lett.* **80**, 5048 (1998).
[7] R. Rossignoli and Plastino, *Phys. Rev. C* **40**,1798 (1989).
[8] R. Rossignoli, et al., *Phys. Rev. C* **42,** 2065 (1990), ibid. 43, 1599 (1991).
[9] F. Gilleron and J.C. Pain, *Phys. Rev. E* **69**, 056117 (2004).
[10] H. J. Schmidt and J. Schnack, *Physica A* **260**, 479 (1998).
[11] P. Borrmann and G. Franke, *J. Chem. Phys.* **98**, 2484 (1993).
[12] J.A. White, et al., *Phys. Rev. Lett.* **84,** 1220 (2000).
[13] J.A. White and S. Velasco, *Phys. Rev. E* **62**, 4427 (2000).
[14] A.K. Kerman and S. Levit, *Phys. Rev. C* **24**, 1029 (1981).
[15] A.K. Kerman, et al., Ann. *Phys.* **148**, 436 (1983).

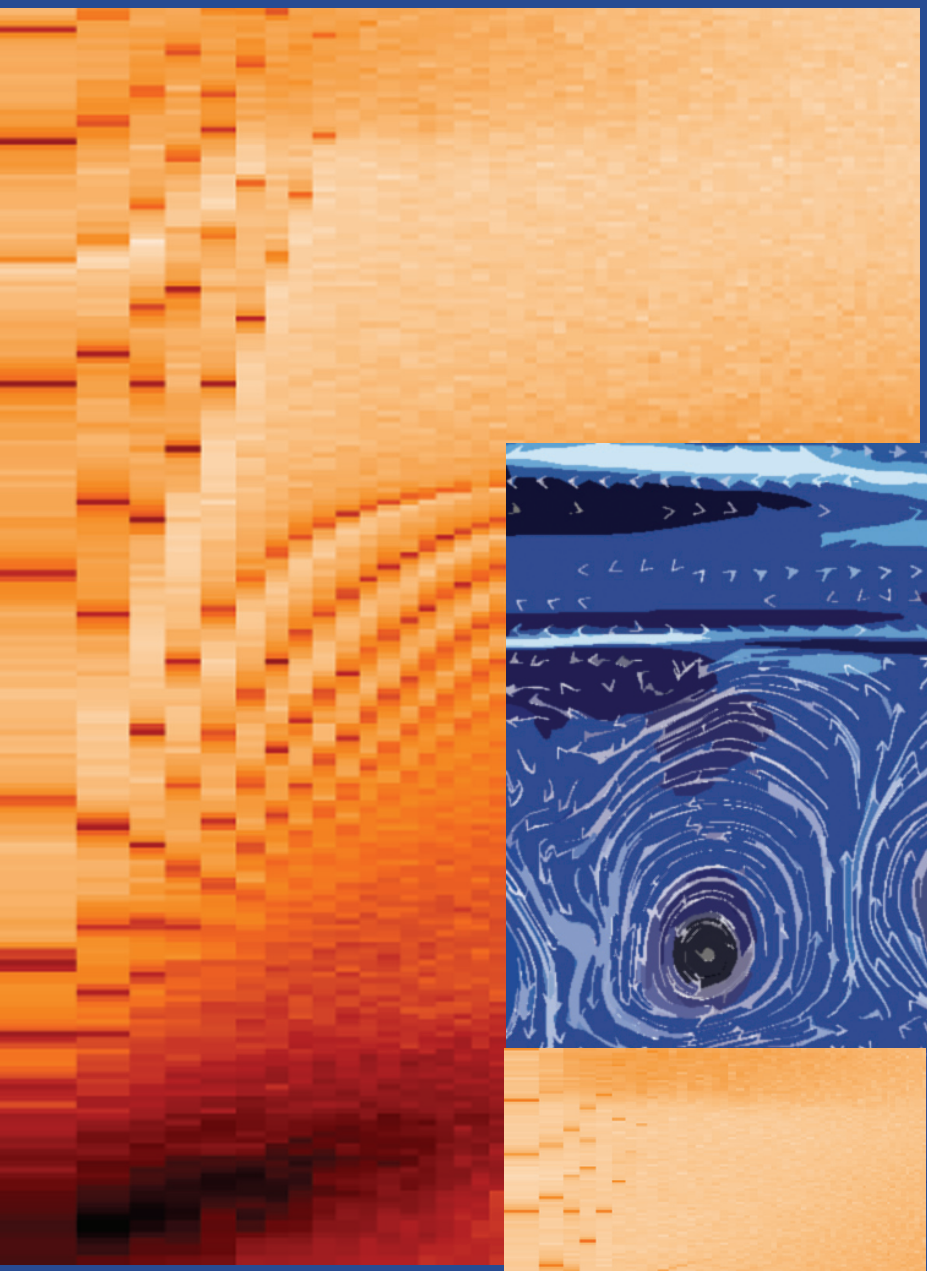

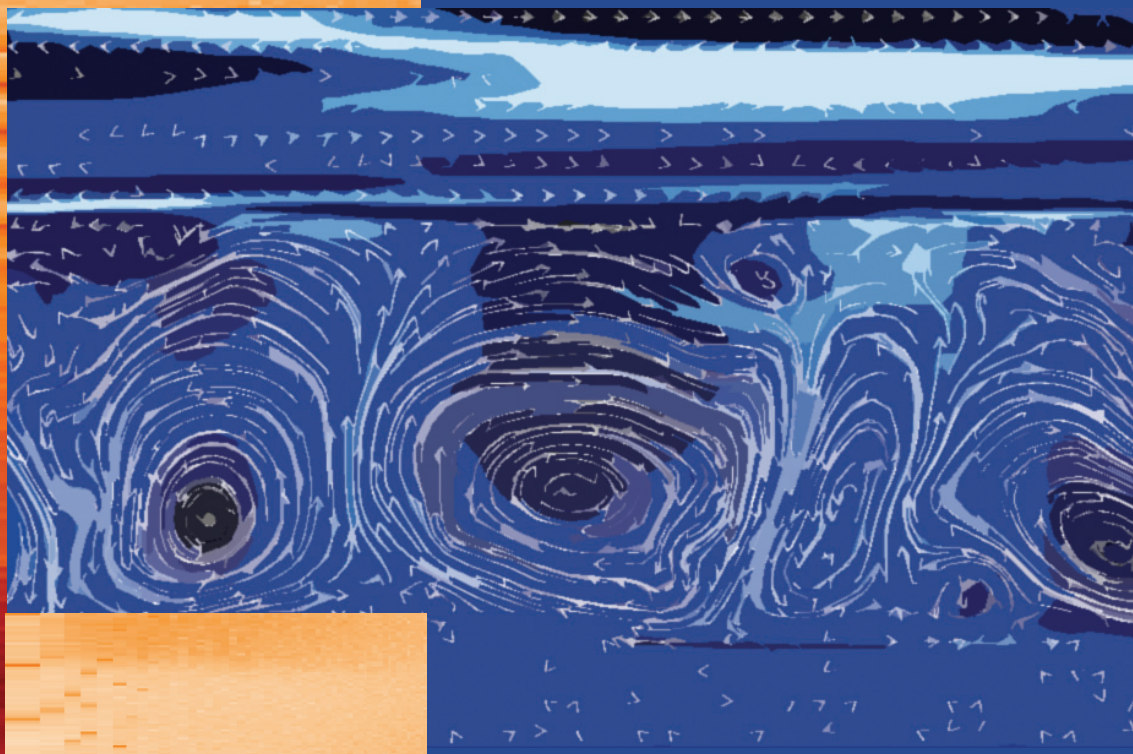

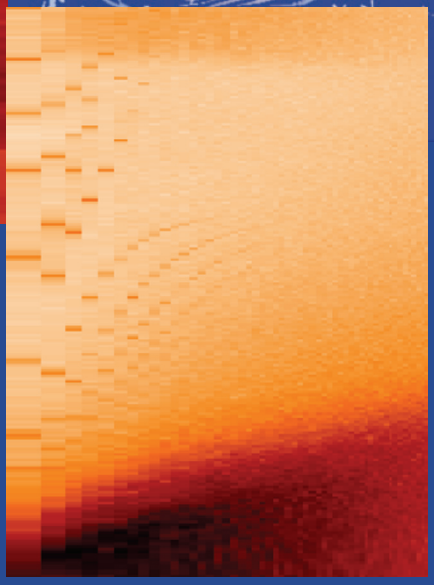

T-6

Theoretical Astrophysics

Acting Group Leader: Mike Warren
505.665.5023; mswarren@lanl.gov

T-6 Theoretical Astrophysics staff are involved in a broad range of issues in astrophysics. These include (1) stars from cradle-to-grave star formation, stellar evolution, stellar oscillations, supernovae, nucleosynthesis, and chemical evolution; (2) relativistic astrophysics involving white dwarfs, neutron stars, and black holes; and (3) large-scale structure in the universe, cosmic magnetic fields, and cosmology. There is some ongoing research on planet formation, impacts by comets and asteroids in the solar system, and high energy density plasmas.

Oscillating Burning on Accreting Neutron Stars

Alexander Heger, T-6; Andrew Cumming, McGill University; and Stan Woosley, University of California, Santa Cruz

Low mass x-ray binaries, in which a neutron star or black hole accretes from a low mass companion star, exhibit a range of periodic and quasiperiodic phenomena, ranging from very low frequency (mHz) noise to kHz quasiperiodic oscillations (QPOs). This variability has mostly been associated with material orbiting in the accretion flow close to the compact object. In the case of a neutron star accretor, an important question is whether any of these phenomena originate from, or are associated with, the neutron star surface. This could allow us to identify the compact object as a neutron star or a black hole, as well as offering a probe of the neutron star surface layers. Unstable nuclear burning on neutron star surfaces has been known for a long time, and is observed as Type I x-ray bursts. Not all accreting neutron stars, however, show Type I x-ray bursts.

Revnivtsev et al. [1] discovered a new class of mHz QPOs in three Atoll sources, 4U 1608-52, 4U 1636-54, and Aql X-1, which they proposed were due to a special mode of nuclear burning on the neutron star surface. These mHz QPOs have frequencies in the range 7–9 mHz (timescales of ~ 2 min). The centroid frequency of the mHz QPO was stable on year timescales in a given source, and the same to within tens of per cent in all three sources in which it was detected. In 4U 1608-52, a transient source whose luminosity is observed to change by orders of magnitude, the mHz QPO was only present within a narrow range of luminosity, $L_X \approx 0.5$–1.5 times 10^{37} rm erg s^{-1}. This luminosity marks a transition from frequent Type I x-ray bursting at low accretion rates to the disappearance of Type I x-ray bursts at high accretion rates, a transition that is common to many x-ray bursters.

We model this transition of behavior from Type I x-ray bursting to stable burning and find the occurrence of MHz QPOs at the transition accretion rate ([2], Fig. 1). The calculations are done using an implicit one-dimensional hydro code that includes the energy release from nuclear burning and follow the nuclear reactions on some 1000 isotopes. Figure 2 shows the band of nuclear energy generation (blue) below the surface (black), the oscillations in nuclear energy release and the corresponding variations of the emitted radiation. In Fig. 3 we show in more detail the structure of the burning surface layer of the neutron stars at four different phases during an oscillation. This is the same model as shown in Fig. 2, Panel C. The white and gray stripes correspond to one cycle of oscillation each, with the interfaces corresponding to the time of a

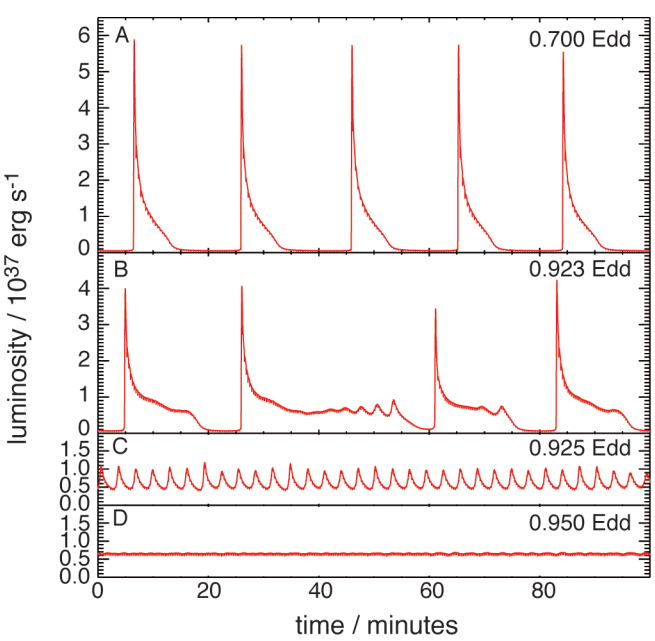

Fig. 1. *Light curves for different accretion rates (upper right corner gives accretion rate in units of Eddington accretion rate). Panel A shows regular bursting with stable recurrence times. Panel B shows weaker bursts with a partial oscillatory behavior in the tail of the burst light curves. Panel C shows oscillatory rather behavior and no bursts. Panel D shows very small oscillations, essentially stable behavior.*

maximum in the light curve at the time of the accretion of that layer. The small inserts at the upper right corners indicate the position in the light curve (red) cycle of the snapshot (black dot; intensionally aligned with a layer interface). Note that the decreases of some of the radioactive isotopes in the right-hand side of the figure are due to their radioactive decay.

For more information contact Alexander Heger at aheger@lanl.gov.

[1] M. Revnivtsev, et al., *A&A* **372**, 138 (2001).
[2] A. Heger, et al., "Millihertz Quasi-Periodic Oscillations from Marginally Stable Nuclear Burning on an Accreting Neutron Star," Los Alamos National Laboratory report LA-UR-05-8083 (2006); *Astrophys. J.*, accepted, 2006; arXiv:astro-ph/0511292.

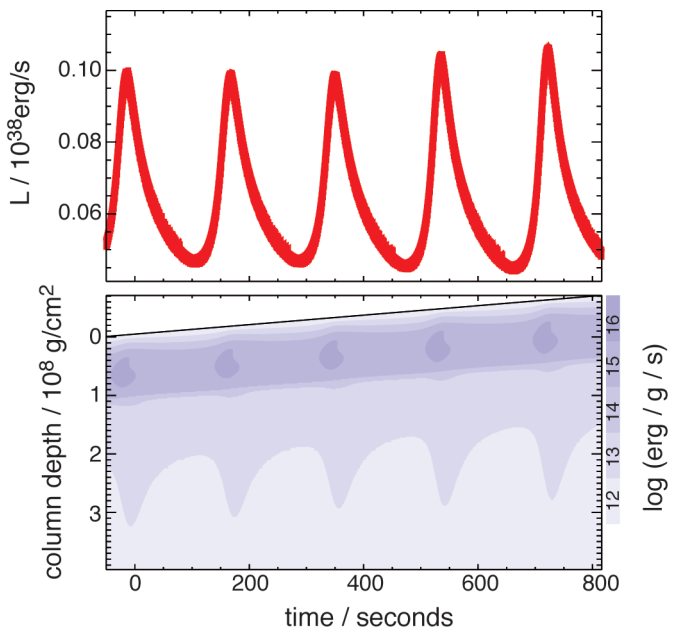

Fig. 2. *Detailed light curve (upper panel) and specific nuclear energy generation as a function of time and column depth (lower panel). Each darker shading of blue corresponds to a value one order of magnitude higher (see scale on right-hand side of the figure). The tilted black line is the surface of the neutron star and the rise of the line shows the accretion onto the surface of the neutron star (the slope of the line corresponds to the accretion rate).*

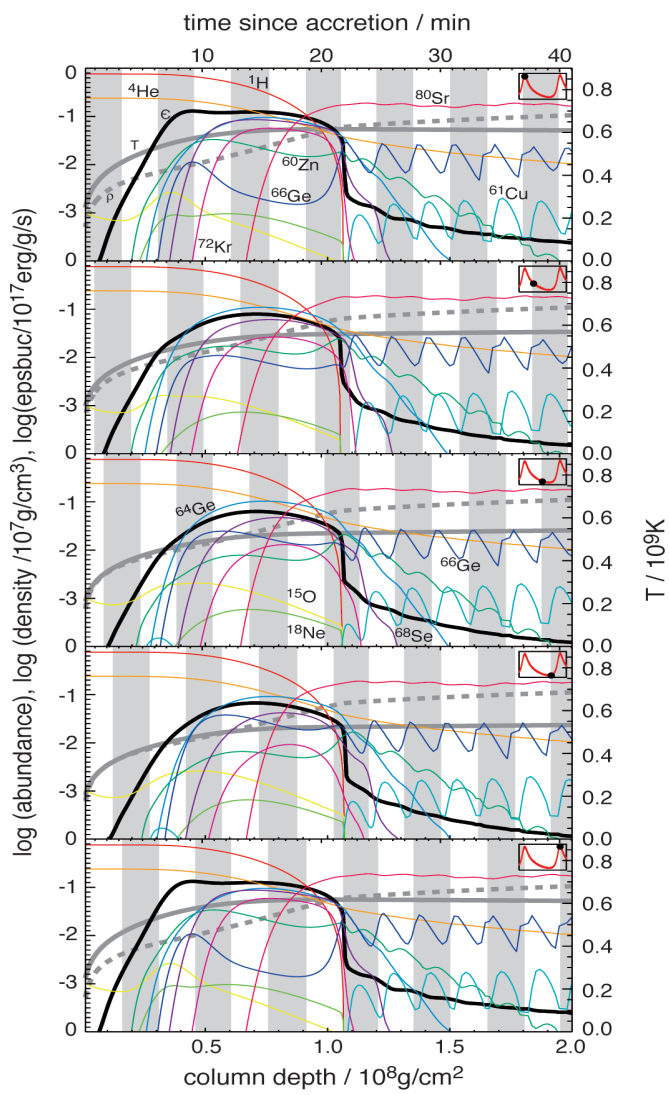

Fig. 3. *Snapshots of structure (temperature: thick gray line; density: thick gray dashed line; specific nuclear energy generation: black line) and composition (select isotopes, colored lines) during one oscillation cycle; each panel is advanced in time by a quarter of the oscillation period relative to the panel above it; the bottom panel is advanced by one full cycle relative to the top panel. The bottom axis for each figure gives column depth, the top axis the corresponding time since accretion.*

Hydrodynamic Simulations of He-shell Flash Convection

Falk Herwig, T-6; Bernd Freytag, T-6/ Michigan State University/Uppsala University; Robert M. Hueckstaedt and Francis X. Timmes, X-2

We have performed the first hydrodynamic, multidimensional simulations of He-shell flash convection [1]. This is an important nuclear production site in stars of low and intermediate mass. In particular the slow neutron capture process, which generates half of all trans-iron elements, is associated with this hot and turbulent He-burning environments. Current models of this stellar interior region exist only in one-dimensional (1-D) simulations that make averaging assumptions about the properties of convection. Here, we study this important nuclear astrophysics environment for the first time in multidimensional simulations. Our simulations are based on the hydrodynamics code RAGE.

We investigated the properties of shell convection at a time immediately before the He-luminosity peak during a He-shell flash of a stellar evolution track with initially two solar masses and half the solar metal content. We constructed the initial vertical stratification with a set of polytropes to resemble the stellar evolution structure. Convection is driven by a constant volume heating in a thin layer at the bottom of the unstable layer. We calculated a grid of 2-D simulations with different resolutions and heating rates. Our set of simulations includes one low-resolution 3-D run. The computational domain includes 11.4 pressure scale heights.

He-shell flash convection is dominated by large convective cells that are centered in the lower half of the convection zone (Fig. 1). Convective rolls have an almost circular appearance because focusing mechanisms exist in the form of the density stratification for downdrafts and the heating of localized eddies that generate upflows. Nevertheless, downdrafts appear to be somewhat more focused.

The He-shell flash convection generates a rich spectrum of gravity waves in both stable layers above and beneath the convective shell. An analysis of the oscillation modes shows that both g-modes and convective motions cross the formal convective boundaries, which leads to mixing across the boundaries (Fig. 2). Our resolution study shows consistent flow structures among the higher resolution runs, and we see indications for convergence of the vertical velocity profile inside the convection zone for the highest resolution simulations.

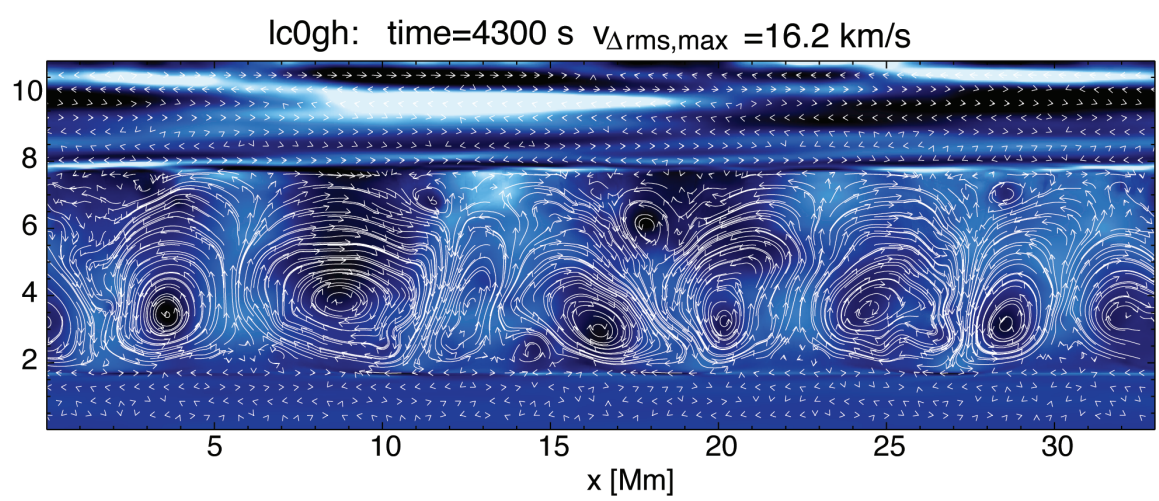

Fig. 1. *Snapshot of pressure fluctuations with pseudo-streamlines of fully developed convection in a high-resolution 2-D run. Darker areas have low pressure. The boundaries of the unstable at y = 1.7 Mm and y = 7.7 Mm are clearly marked in the flow field and the pressure inhomogeneities.*

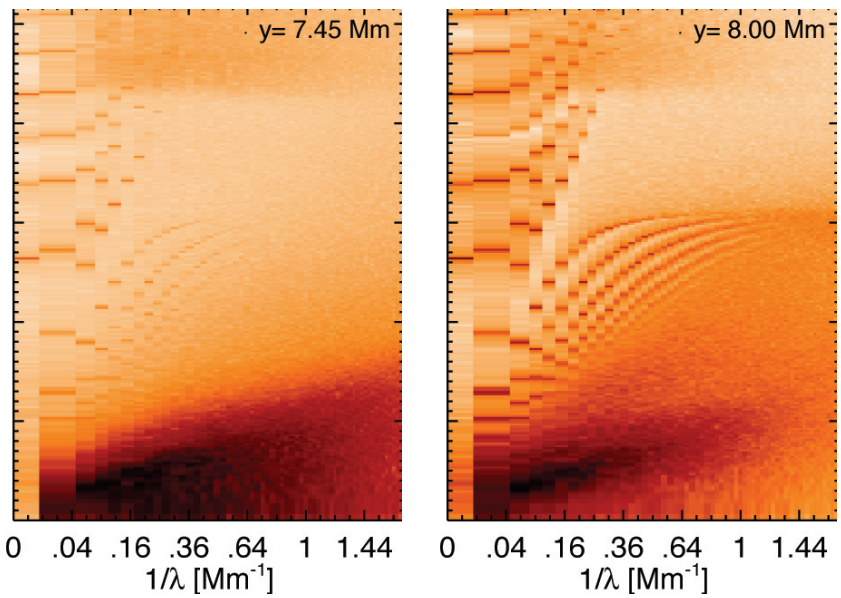

Fig.2.
k-ω diagrams for a vertical position just below and above the top convection boundary. This diagram reveals the properties of the oscillations that are excited in the simulation. The dark blob in the lower left area represents the convective motions. Ridge systems of signals above correspond to gravity and pressure modes. The comparison of these two diagrams allows a quantitiative analysis of how effectively convective motions, which induce mixing, can cross the convective boundary.

The magnitude of the convective velocities from our 1-D stellar evolution theory model and the rms-averaged vertical velocities from the hydrodynamic model are consistent within a factor of a few (Fig. 3). However, the velocity profile in the hydrodynamic simulation is more asymmetric, and decays exponentially inside the convection zone.

For more information contact Falk Herwig at fherwig@lanl.gov.

[1] F. Herwig, et al., Los Alamos National Laboratory report LA-UR-05-8084 (2005); astro-ph/0601164; *Astrophys. J.* 2006, in press.

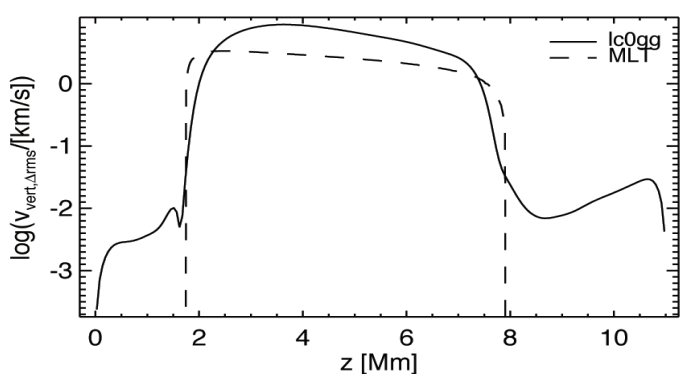

Fig. 3.
Comparison of vertical velocities derived from a hydrodynamics model (continuous line) and 1-D stellar evolution model (dashed line).

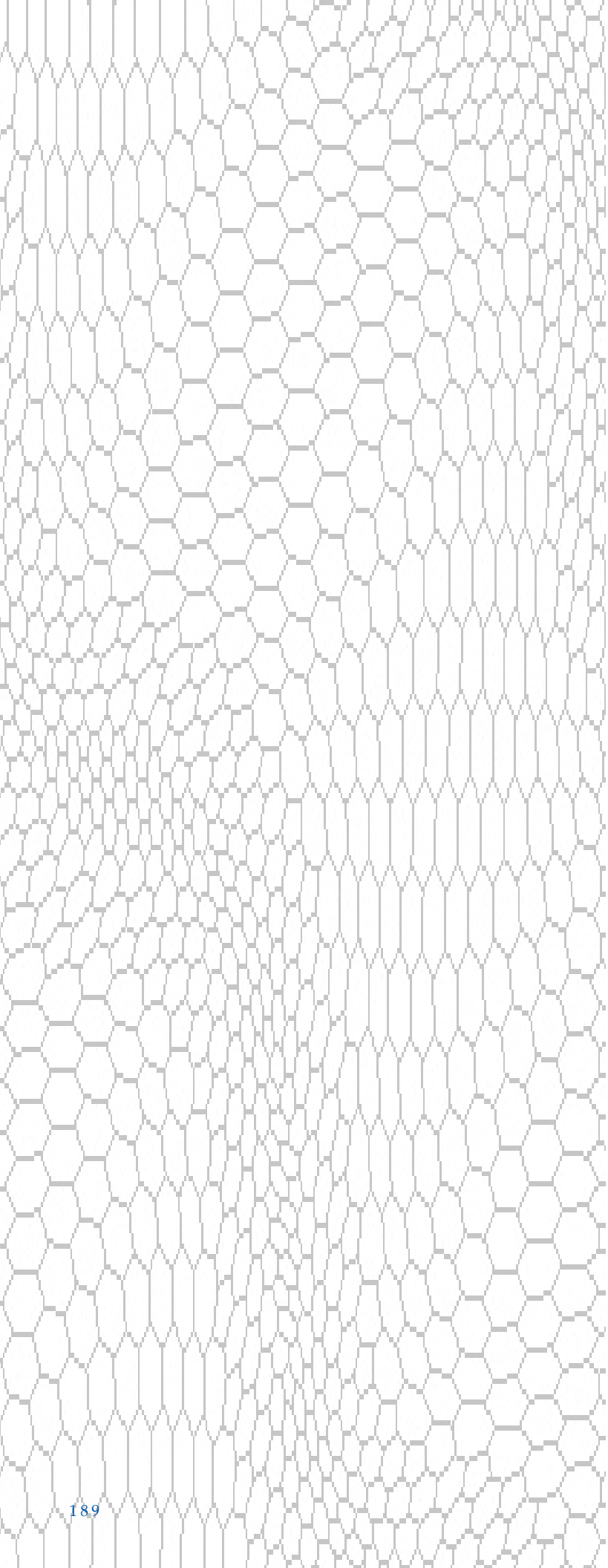

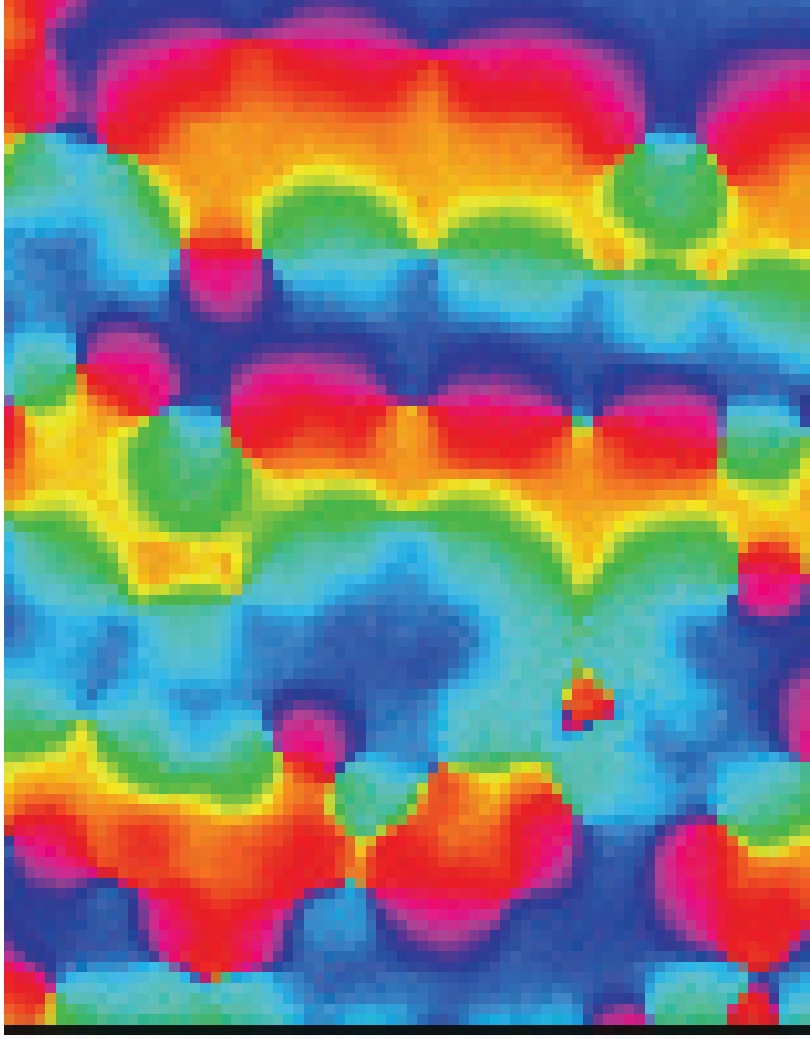

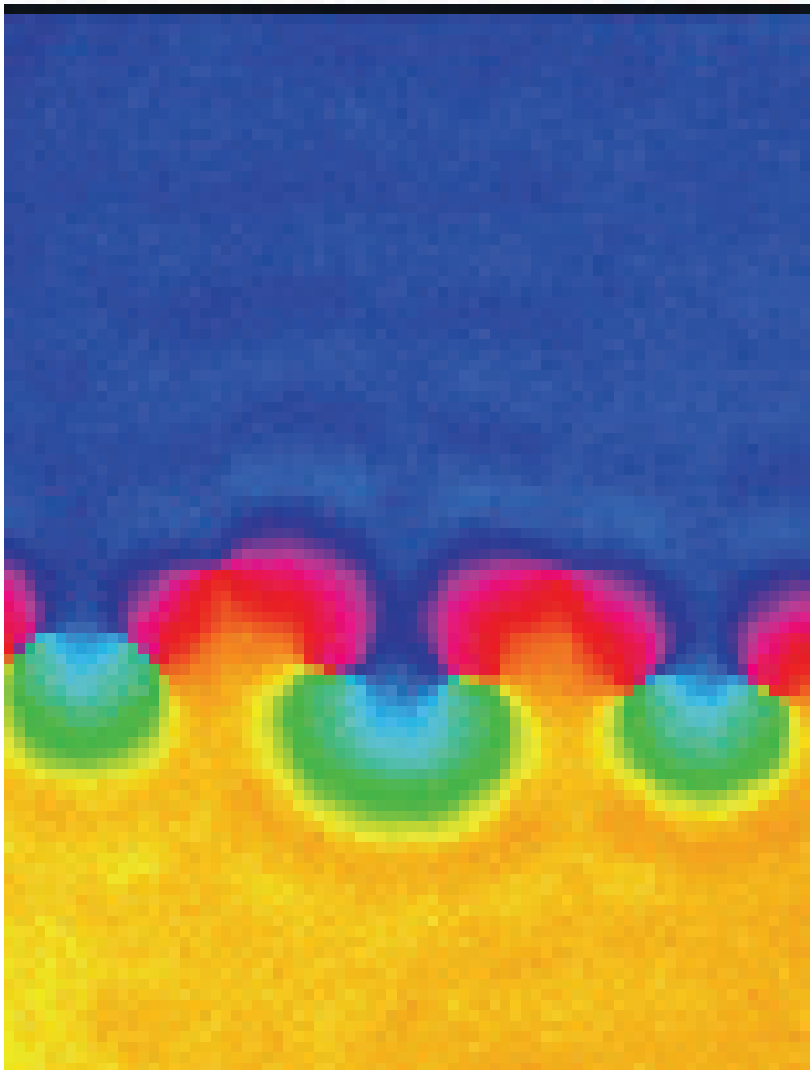

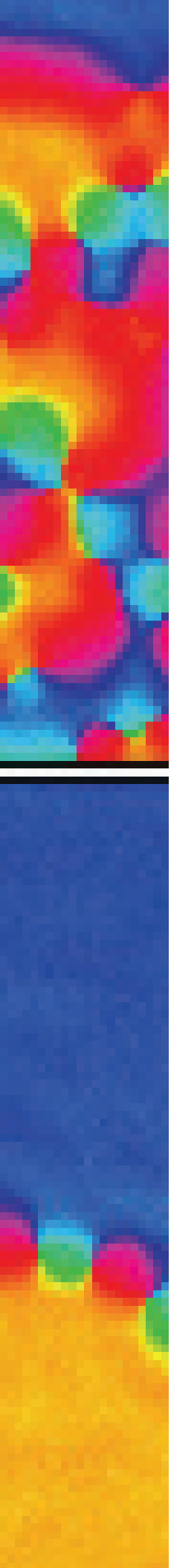

T-7

Mathematical Modeling and Analysis

Group Leader: Mac Hyman
505.667.6294; jh@lanl.gov

T-7 Mathematical Modeling and Analysis combines the strengths of applied mathematicians, mathematical physicists, and numerical analysts to derive, analyze, and solve mathematical models of complex problems. Its mission is to conduct forefront basic and applied research in mathematical modeling and analysis, provide theoretical leadership and support for the Los Alamos National Laboratory and other programs of national interest, and to furnish an effective interface with academic science.

A Family of Mimetic Finite Difference Methods on Polygonal and Polyhedral Meshes

Franco Brezzi, University of Pavia;
Konstantin Lipnikov and
Valeria Simoncini, T-7

In many applications, the mathematical model is formulated initially as a system of first-order partial differential equations, with each equation having a natural connection to physical aspects of the problem. For the diffusion problem these equations are

$$div\ F = b, \quad F = -K\ \ grad\ p,$$

which describe the mass conservation and the Darcy law, respectively. The unknown variables are pressure p and flux F. The material properties are described by a full symmetric tensor K.

There are many discretization schemes with equivalent properties which can be used to solve the diffusion problem. The mimetic finite difference (MFD) method [1] is well suited for solving the first-order system, since it preserves essential properties (symmetry and mass conservation) of the continuum equations. The MFD method has been successfully employed for solving the diffusion problem on simplicial, quadrilateral, hexahedral, and unstructured polygonal and polyhedral meshes in both Cartesian and cylindrical coordinate systems.

In Ref. [2], we employed an innovative technique to give the first rigorous mathematical description of a rich family of MFD methods with equivalent properties. This family will allow us to tackle other computational problems such as enforcement of the discrete maximum principle.

We also developed a novel computationally inexpensive algorithm for deriving particular members of

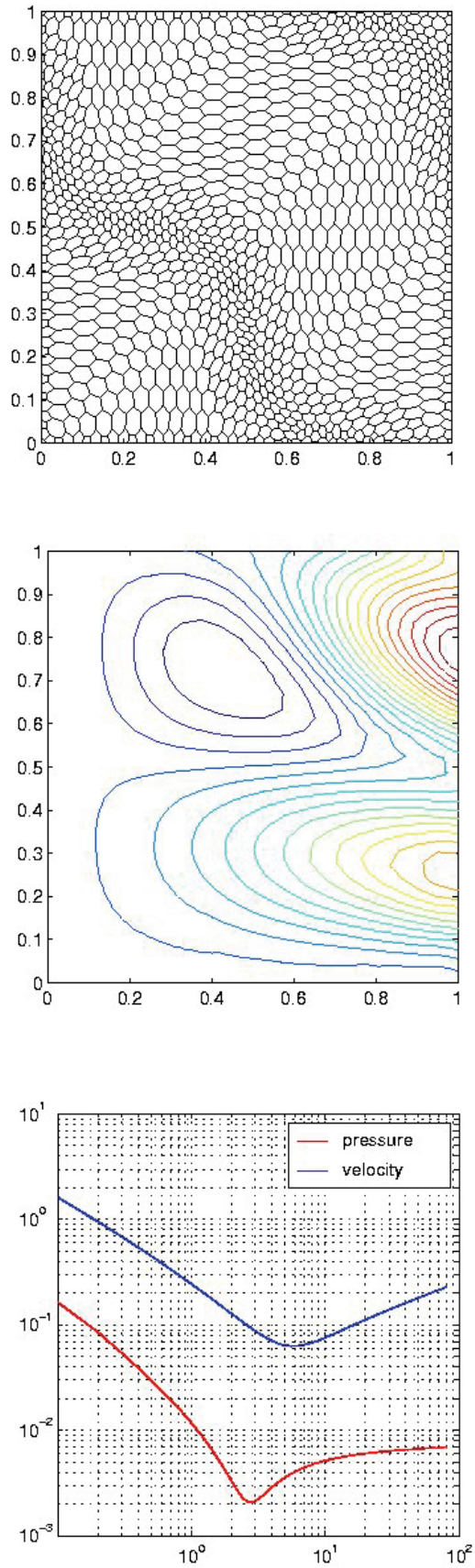

Fig. 1-3.
The top picture shows polygonal mesh used in the convergence study. The middle picture shows the solution isolines. The bottom picture shows the mesh dependent L_2-norm of errors for pressure p and flux F (vertical axis) as functions of parameter u (horizontal axis).

the family of MFD methods. These members are described by a single parameter. With this algorithm, solving the diffusion problems on a polyhedral mesh is as simple as on a tetrahedral mesh.

The illustrative example shows that there is a big interval for the parameter u where the discretization errors vary only 3 times. What is remarkable here is that for all values of u we observed second order convergence rate for the pressure and 1.5 convergence rate for the flux.

For more information contact Konstantin Lipnikov at lipkinov@lanl.gov.

[1] J. Hyman, et al., *Comput. Geosciences* **6**, 333–352 (2002).
[2] F. Brezzi, et al., *Math. Model. Methods Appl. Sci.* **15**, 10, 1533–1552 (2005).

New Discretization Methodology on Generalized Polyhedral Meshes

Franco Brezzi, University of Pavia;
Konstantin Lipnikov and
Mikhail Shashkov, T-7

Tetrahedral and structured hexahedral meshes have been used for decades in a majority of engineering simulations; they are relatively easy to generate and there exists an enormous repository of numerical methods designed for these meshes. Nowadays, a growing number of complex simulations show advantage of using polyhedral meshes. For example, in the simulation of flow through a water jacket of an engine [1], the results obtained on a polyhedral mesh are more accurate than the results obtained on a tetrahedral mesh with a comparable number of cells. In oil reservoir simulations, the polyhedral mesh topology offers unlimited possibilities: cells can be automatically joined, split, or modified by introducing additional points, edges, and faces to model complex geological features. Unfortunately, most of the existing numerical methods cannot be extended to polyhedral meshes, especially to meshes with cells having strongly curved (nonplanar) faces.

In [2], we considered a diffusion problem, which appears in computational fluid dynamics, heat conduction, radiation transport, etc., and developed a new discretization methodology that has no analogs in literature. The methodology follows the general principle of the mimetic finite difference (MFD) method — to mimic the essential underlying properties of the original continuum differential operators such as the conservation laws, solution symmetries, and the fundamental identities and theorems of vector and tensor calculus.

The mixed form of the diffusion problem is

$$F = -K \, grad \; p, \quad div \, F = b$$

where the first equation is the constitutive equation relating the scalar function p (pressure in flow simulations) to the velocity field F and the second one is the mass conservation law. The material properties are described by the full symmetric tensor K, and b is the source function. For this problem, the MFD method mimics the Gauss divergence theorem, the symmetry between the continuous gradient and divergence operators, and the null spaces of these operators. Therefore, it produces the discretization scheme which is symmetric and locally conservative.

Note that the finite volume discretization methodology results in nonsymmetric schemes. The old MFD method [3]

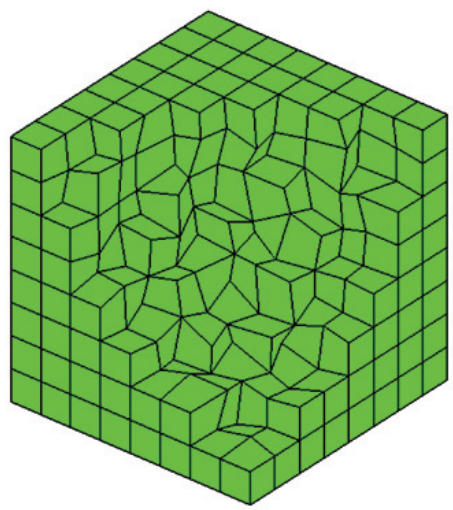

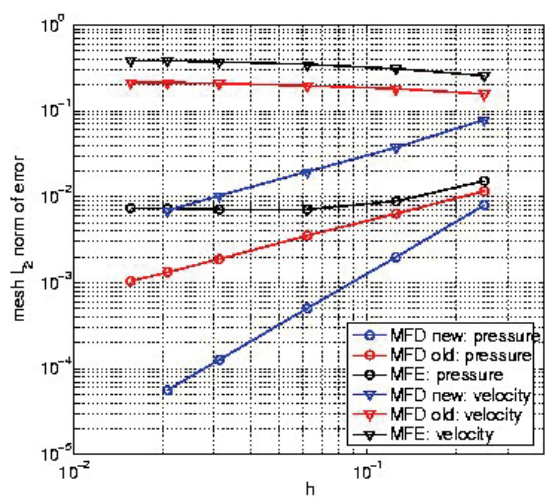

Fig. 1.
The top picture shows the interior of a logically cubic mesh with randomly perturbed points. The bottom picture shows the optimal convergence rates for the new MFD method (blue), and the lack of convergence for the mixed finite element (black) and the old MFD (red) methods.

used one degree of freedom per cell to approximate the pressure and one degree of freedom per mesh face to approximate the average normal component of the velocity. The same degrees of freedom are used in the mixed finite element method on tetrahedral and hexahedral meshes.

The new discretization methodology [2] uses three degrees of freedom, three average velocity components, to approximate velocity on strongly curved faces. It results in the new MFD method that improves drastically the capabilities of the existing methods (see figures). When faces of mesh cells are plane segments, or slightly perturbed plane segments, the new MFD method is reduced to the old one from [3]. When the faces are strongly curved, the extra degrees of freedom allow the new method to succeed and perform much better than other methods. Necessity to use three velocity components on strongly curved faces is possibly the intrinsic difficulty and the reason why nobody succeeded in doing a reasonable job on meshes with such cells. The theoretical analysis of the new method is done in [2].

Another advantage of the developed methodology is that its practical implementation is simple and follows roughly the path described in [4]. In particular, we get a family of discretization schemes with similar properties. This family of schemes may be used to tackle other computational problems.

For more information contact Mikhail Shashkov at shashkov@lanl.gov.

[1] M. Peric, S. Ferguson, *ERCOFTAC Bulletin* **62** (September 2004).
[2] F. Brezzi, et al., "Convergence of Mimetic Finite Difference Method for Diffusion Problems on Polyhedral Meshes with Curved Faces," *Math. Model. Methods Appl. Sci.* **16** (2), 275–297 (2006).
[3] F. Brezzi, et al., "Convergence of Mimetic Finite Difference Method for Diffusion Problems on Polyhedral Meshes," *SIAM J. Numer. Anal.* **43** (5), 1872–1896 (2005).
[4] F. Brezzi, et al., *Math. Model. Methods Appl. Sci.* **15** (10), 1533–1552 (2005).

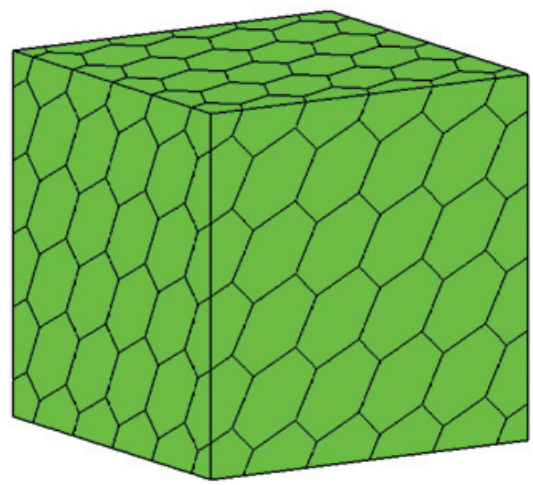

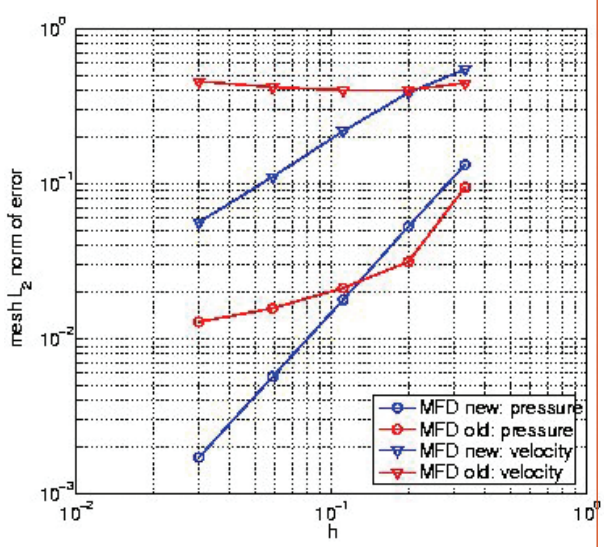

Fig. 2. ***The top picture shows a generalized polyhedral mesh where the mixed finite element method cannot be used. Note that 68% of interior mesh faces are nonplanar. The bottom picture shows optimal convergence rates for the new MFD method (blue) and the lack of convergence for the old MFD method (red).***

Interface Reconstruction in Multifluid Flow Simulations

Rao Garimella, Vadim Dyadechko, Blair Swartz, and Mikhail Shashkov, T-7

We have developed an advanced method for reconstructing piecewise linear approximations of material interfaces in multimaterial flows. Results indicated that our method reconstructs smoother, more continuous and more accurate interfaces than other methods in its class. Hydrodynamic simulation of multimaterial flows is important for understanding many problems such as droplet deposition, sandwich molding, underwater explosions, mold-filling in casting, and the behavior of microjetting devices.

An important feature of such flows is the interface between the materials, and it is often crucial to follow such interfaces during the simulation. Lagrangian simulations (where the mesh nodes move with the flow) automatically maintain interfaces but cannot handle large deformations and topology changes of these interfaces. On the other hand, Eulerian simulations (where the mesh nodes are stationary) must incorporate special procedures to keep track of the interfaces in the flow.

We have developed an advanced method for recovering a piecewise linear approximation of material interfaces in flow simulations given the volume fractions of materials in the cells of an unstructured mesh. The method incorporates several new techniques designed to make the reconstruction method more accurate, rapid, and robust. These include the careful selection and use of interface neighbor cells, and a topological consistency checking and repair algorithm for the interface that is designed to minimize fragmentation of the material regions being reconstructed. The volume of the materials is conserved exactly in the method.

The main steps of the procedure are:

Interface Estimation: A rough estimate of the interface is constructed using the volume fraction data specified on cells. The interface is represented by one line segment per cell.

Interface Smoothing: Interface segments are adjusted taking into account other interface segments in the neighborhood so that the resulting interface is as smooth as possible. Straight-line interfaces are typically recovered by this interface smoothing step.

Interface Topology Repair: The interface segments are adjusted so that they satisfy essential consistency requirements. The result of this is that the reconstructed material regions are continuous and do not have holes or fragments as far as possible.

Constrained Interface Smoothing: Alterations made to the interface in the repair step are smoothed, with the constraint that the topological consistency of vertices cannot be destroyed.

Interface Subdivision and Matching: The interface segment in each cell is subdivided into two. The two segments in the cell are then adjusted so that their slopes match the slopes of the appropriate interface segments in neighboring cells and the material volumes in the cell are conserved.

The procedure recovers complex interfaces more accurately than other interface reconstruction procedures, particularly exhibiting reduced fragmentation in the single vortex test. Additional details of the new interface reconstruction algorithms can be found in [2].

For more information contact Rao Garimella at rao@lanl.gov.

[1] W.J. Rider and D. B. Kothe, *J. Comput. Phys.* **141**, 112–152 (1998).
[2] R.V. Garimella, et al., "Interface Reconstruction in Multi-Fluid, Multi-Phase Flow Simulations," in *Proceedings of the 14th International Meshing Roundtable, San Diego, CA* (Springer-Verlag, Berlin, Germany, 2005) pp. 19–32.

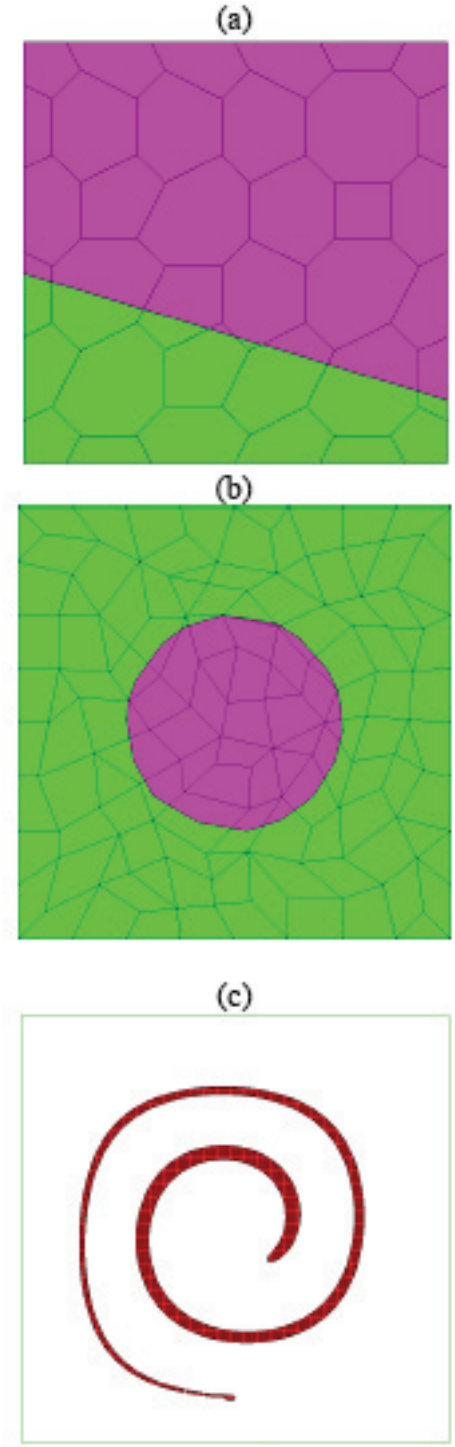

Fig. 1. ***Interface reconstruction on structured and unstructured meshes (a) straight line interface, (b) complex interface, and (c) vortex-in-box test of Rider and Kothe [1].***

Bloch-Front Turbulence in a Periodically Forced Belousov-Zhabotinsky Reaction

Aric Hagberg, T-7

Spatio-temporal disorder in extended systems commonly involves the spontaneous creation and annihilation of localized structures such as defects and vortices. The driving forces for the nucleation of defects and vortices are instabilities of periodic patterns or fronts. Defects in periodic patterns often result from the Benjamin-Feir-Newell instability, while spiral-vortex nucleation in bistable systems has been related to a front instability—the Nonequilibrium Ising-Bloch bifurcation.

We have demonstrated, in a periodically forced oscillatory Belousov-Zhabotinsky reaction and in mathematical models, a mechanism for creating spatio-temporal disorder. The mechanism consists of the creation of spiral vortex pairs through a transverse instability of fronts in the vicinity of a nonequilibrium Ising-Bloch bifurcation. This is the first direct experimental evidence tying front instabilities to vortex nucleation and disorder.

We used an amplitude equation model, the forced complex Ginzburg-Landau equation, to reproduce the experimental observations with numerical solutions, and further described the mechanism for vortex creation with the normal form equations for a curved front line.

The normal form equations reduce the two-dimensional problem to the study of a one-dimensional set of equations for the curvature and velocity of the interface. With these equations we can capture the physics of a spiral-vortex nucleation event.

For more information contact Aric Hagberg at hagberg@lanl.gov.

[1] Bradley Marts, et al., *Phys. Rev. Lett.* **93**, 108305 (2004).

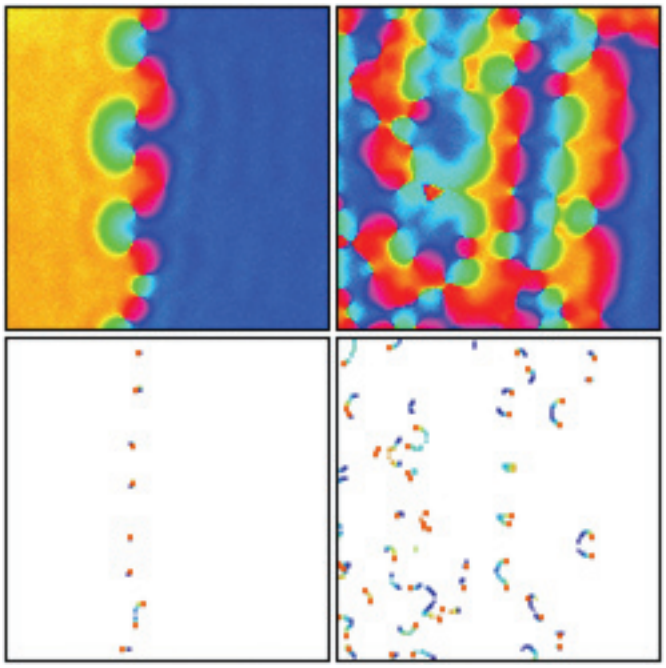

Fig. 1. *Experiments on a periodically forced Belousov-Zhabotinsky chemical reaction show front break-up into a state of spatio-temporal disorder involving continual events of spiral-vortex nucleation and destruction. The initial front of the oscillation phase is unstable to transverse perturbations and vortices form in pairs along the front line. The bottom frames show the position of the vortices, the core location of the spiral wave, as red dots with colored tails indicating the motion and direction of travel.*

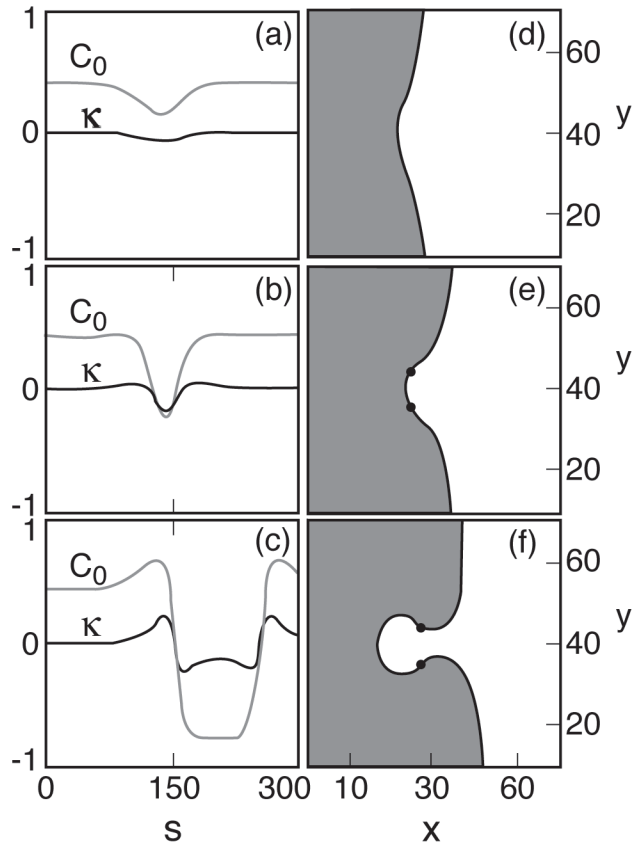

Fig. 2.
Nucleation of a single spiral-vortex pair in the front-line equations. Frames (a)–(c) show the front velocity C_0 and curvature k vs the arclength s. Frames (d)–(f) are the corresponding representation in the laboratory coordinate frame. A small perturbation in the curvature grows and a portion of the domain reverses direction causing spiral-vortex pair to nucleate along the front line.

Rare Events in Turbulence Might not be So Rare

Susan Kurien, T-7

We have shown, using a compilation of data from experiments and direct numerical simulations, that intense, intermittent events are not merely associated with the rare events in the flow but are in fact present in the high frequency events. Thus our results motivate the theoretical study of turbulence statistics in the limit of zeroth order moments, unbiased by so-called rare events which might be flow-dependent. This report is a summary of work published in [1].

In 1941, the Russian mathematician Andrei N. Kolmogorov deduced scaling laws for the velocity statistics of turbulent flows. At the core of the Kolmogorov theory lies the hypothesis that the scales in fully developed turbulence are statistically self-similar. The theory predicts that the n-th order moment of the velocity difference across scales of size r should scale as $r^{n/3}$. Experimental data has shown that for $n > 3$ the scaling exponents are $\zeta_n < n/3$. It is now believed that the turbulent scales are not self-similar but intermittent and the scaling exponents of moments of velocity increments are anomalous, that is, the departures from Kolmogorov's self-similar scaling increase nonlinearly with the increasing order of the moment. Since high-order moments sample the tails of a probability distribution function, it is also believed that the intermittency in turbulence is associated with rare events. We have shown, using a compilation of data from experiments and direct numerical simulations, that intermittency is not merely associated with the rare events in the flow but is in fact present in the high frequency events. Thus our results motivate the theoretical study of anomalous scaling in the limit of zeroth-order moments, unbiased by so-called rare events. The moments of the velocity difference across spatial scales are known as structure functions and are defined by

$$S_n(r) = (|\delta u(r)|^n) = \int_0^\infty |\delta u(r)|^n P(\delta u(r)) d(\delta u(r))$$

where $\delta u(r) = (u(x+r) - u(x))$. $\hat{r}$ is the longitudinal velocity increment across scales of size r. The $(.)$ denotes an ensemble average which in practice is implemented as an average over the space-time domain. $P(\delta u(r))$ is the probability density distribution. In the probabilistic sense, it is clear from the above equation that the large n moments are associated with tail of P, or the low probability events. Structure functions are useful measures of the statistical properties of turbulent flows as a function of scale. In particular, the second-order moment of velocity difference across scales of size r is a measurement of the energy contained in those scales. Kolmogorov derived an exact law from the energy balance equation governing the third-order structure function, yielding $S_3 \sim r$ for homogeneous and isotropic turbulence. The self-similarity assumption then yields for statistically isotropic turbulence $S_n(r) \sim r^{n/3}$. Empirical measurement of self-similar scaling for $n = 2$ and 3 have been consistent with the Kolmogorov theory. However, as higher-order moments began to be reliably measured, it became clear that there is a pronounced departure from the self-similar scaling laws (so-called *anomalous* scaling).

We analyzed three sets of data in this work. Experimental measurements of velocity fluctuations in the atmospheric boundary layer, resolved direct numerical simulations (DNS) of the forced Navier-Stokes equation in a periodic cube of 512 grid-point to a side, and another computed in a cube of 1024 grid points to a side. The figure shows the relative departure from the Kolmogorov prediction, of scaling exponents of moments of order

$-0.8 \leq n \leq 10$. Most current theoretical efforts are focused on the intermittency for integer $n > 3$. The empirical results presented here show that there is significant anomalous scaling for moments of order $n < 3$ provide motivation to seek a theoretical explanation for intermittency in the high frequency events, and correspondingly for anomalous scaling in the low-order moments.

For more information contact Susan Kurien at skurien@lanl.gov.

[1] S. Chen, et al., *J. Fluid Mech.* **533**, 183–192 (2005).
[2] C. Meneveau and K.R. Sreenivasan, *Phys. Rev. Lett.* **59**, 1424–1427 (1987).

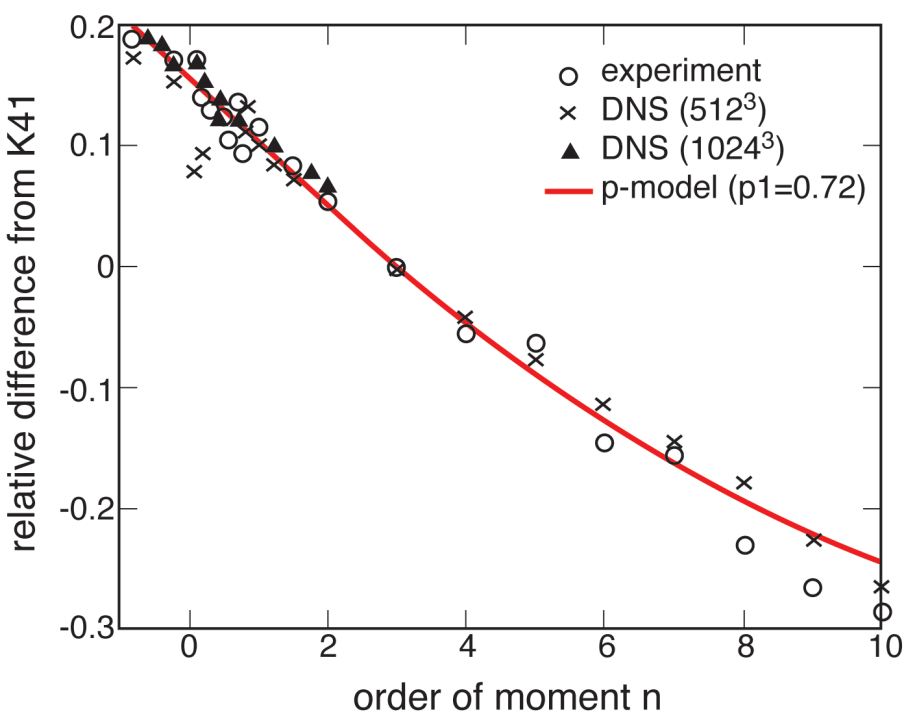

Fig. 1. *The relative departure from the Kolmogorov1941 self-similarity theory for moments ranging from $-0.8 \leq n \leq 10$ as computed from various sources of data. The solid line is the comparison to the so-called p-model [2] derived by assuming multifractality of the scales. The important feature to note is that for $n < 2$ the absolute relative departure from Kolmogorov scaling increases at the same rate as for $n > 2$.*

Differential Equations in Random Domains

Daniel M. Tartakovsky, T-7; and Dongbin Xiu, Purdue University

Physical phenomena in domains with rough boundaries play an important role in a variety of applications ranging from surface imaging to manufacturing of nanodevices. Often the topology of such boundaries cannot be accurately described in all of its relevant details due to either insufficient data, or measurement errors, or both. In such cases, this topological uncertainty can be efficiently handled by treating rough boundaries as random fields, so that an underlying physical phenomenon is described by deterministic or stochastic differential equations in random domains. To deal with this class of problems, we developed a novel computational framework, which is based on stochastic mappings to transform the original deterministic/stochastic problem in a random domain into a stochastic problem in a deterministic domain. The latter problem has been studied more extensively, and existing analytical/numerical techniques can be readily applied.

Given a proper spatial resolution, virtually any natural or manufactured surface becomes rough. Consequently, there is a growing interest in experimental, theoretical, and numerical studies of deterministic and probabilistic descriptions of such surfaces and of solutions of differential equations defined on the resulting domains.

The early attempts to represent surface roughness and to study its effects on the system behavior were based on simplified, easily parameterizable, deterministic surface inhomogeneities, such as symmetrical asperities to represent indentations and semispheres to represent protrusions. Alternatively, one can use random fields to represent rough surfaces whose detailed topology cannot be ascertained due to the lack of sufficient information and/or measurement errors. We adopted random representations of rough surfaces because of their generality. Such an approach allows one, not only to make predictions of the system behavior, but also to quantify the corresponding predictive uncertainties.

The presence of uncertainty in rough boundaries necessitates the development of new approaches for the analysis and numerical solution of differential equations defined on random domains. For example, it has been demonstrated that classical variational formulations might not be suitable for such problems, and finite difference approaches remain accurate only for relatively simple rectangular irregularities.

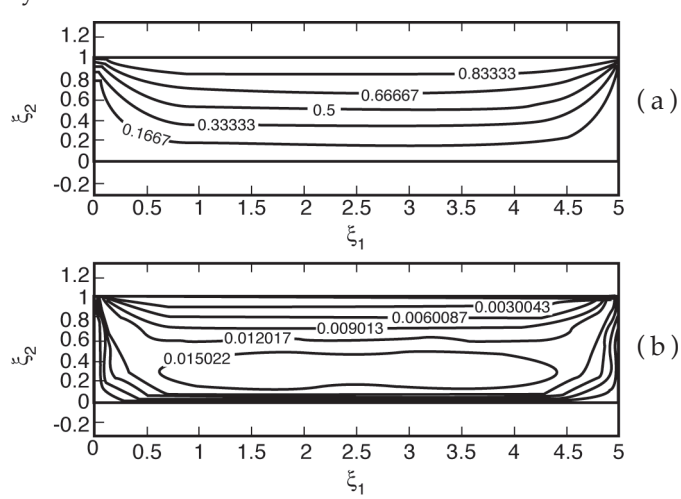

Fig. 1.
(a) Predicted concentration distribution, and (b) the corresponding predictive error bounds.

The adoption of a probabilistic framework to describe rough surfaces makes even an essentially deterministic problem stochastic, e.g., deterministic equations in random domains give rise to stochastic boundary-value problems. This necessitates the search for new stochastic analyses and algorithms. For example, one of the very few existing numerical studies has employed traditional Monte Carlo simulations, which have turned out to be so computationally expensive, as to become impractical.

Recently, we presented a computational framework that is applicable to a wide class of deterministic and stochastic differential equations defined on domains with random (rough) boundaries. A key component of this framework is the use of robust stochastic mappings to transform an original deterministic or stochastic differential equation defined on a random domain into a stochastic differential equation defined on a deterministic domain. This allowed us to employ the well-developed theoretical and numerical techniques for solving stochastic differential equations in deterministic domains.

In [1], we analyzed diffusion in the rectangle with the rough random bottom. The geometric uncertainty translates into the predictive uncertainty. Hence, the best estimate of the concentration of a diffusing substance must be accompanied by a measure of the corresponding predictive uncertainty. This is accomplished by computing the mean and standard deviation of concentration, both of which are shown in Fig. 1.

In [2], we conducted a similar analysis of transport in Stockes flow in a tube with a rough surface (see Fig. 2). We found that for low to moderate roughness (the normalized standard deviation of the surface roughness below 5%), its effects on dispersion of a passive scalar are negligible, so that one can employ standard deterministic models that are much less computationally intensive.

For more information contact Daniel M. Tartakovsky at dmt@lanl.gov.

[1] D. Xiu and D.M. Tartakovsky, "Numerical Methods for Differential Equations in Random Domains," SIAM *J. Sci. Comput.*, (under review) 2005.
[2] D.M. Tartakovsky and D. Xiu, "Stochastic Analysis of Transport in Tubes with Rough Walls," *J. Comp. Phys.*, (under review) 2005.

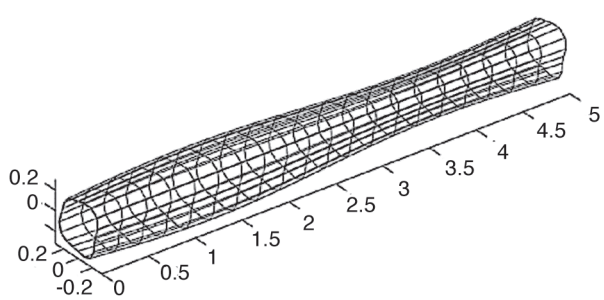

Fig. 2.
A schematic representation of a tube with a rough surface.

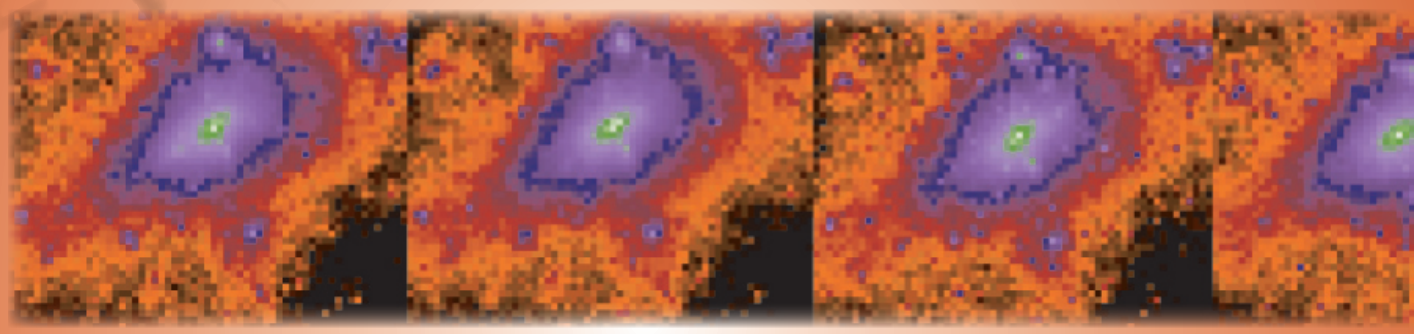

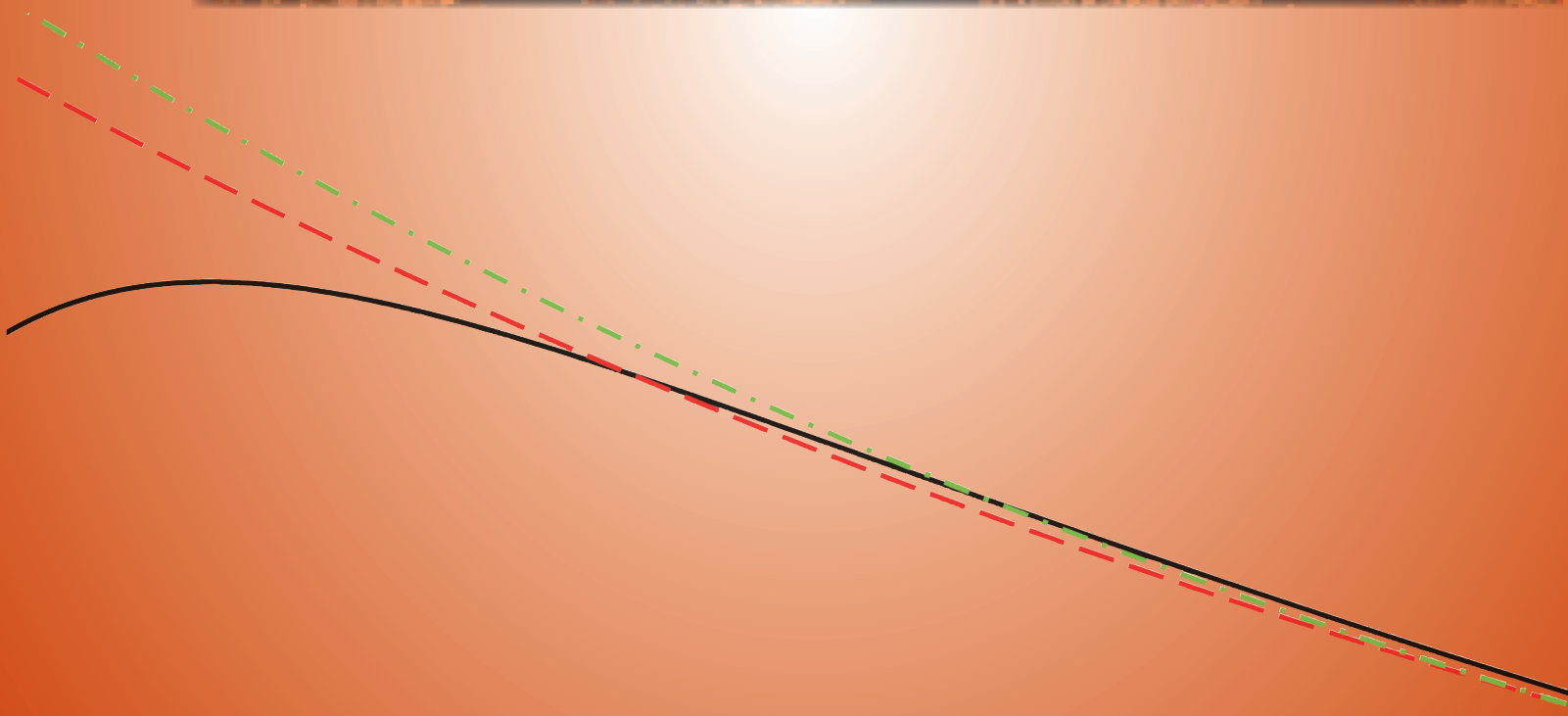

T-8 Elementary Particles and Field Theory

Group Leader: Rajan Gupta
505.667.7664; rg@lanl.gov

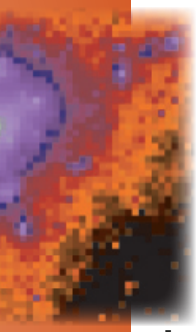

T-8 Elementary Particles and Field Theory conducts research in field theory, particle physics, and gravity, including applications to astrophysics and cosmology. The group's efforts encompass a study of strong interactions of hadrons; properties of neutrinos and their applications to problems in astrophysics and cosmology; gravity and cosmology to explain the cosmic microwave background radiation and large-scale structure of the universe; large-distance tests of gravity; and a significant effort to elucidate the structure of theories beyond the standard model. Another key focus is fundamental issues of quantum field theory, especially in the arena of systems far away from equilibrium, to understand the early universe and the quark gluon plasma created in relativistic heavy ion collisions.

Inverse-Scattering Theory and the Density Perturbations from Inflation

Salman Habib, T-8; Katrin Heitmann, ISR-1; and Gerard Jungman, T-6

A wealth of data drives much of the current activity in cosmology. Amongst these data, perhaps the cleanest signal from the primordial universe is the power spectrum of density fluctuations, which is obtained from observations of fluctuations in the microwave background sky and from observations of the large-scale clustering of matter. Especially in the case of microwave background observations, the observed fluctuations give direct information on the "initial conditions" for the density perturbations that manifest in the gravitational clustering of matter in the universe.

In an inflationary universe, these initial density perturbations arise as a relic of quantum fluctuations from the very earliest times. The inflationary evolution causes these modes to grow in amplitude, with a time-evolution that is determined completely by the evolution of the space-time geometry, encoded in the scale-factor $a(t)$. This evolution imprints a signature of the inflationary evolution on the spectrum of modes. Therefore, structure in the mode spectrum can be directly related to the evolution of $a(t)$ and hence to the nature of the stress-energy which drives inflation. Because the nature of inflation is quite mysterious, information of this sort is very important for cosmology.

Recently, we have developed a completely new method for understanding the primordial density fluctuations in the universe [1]. Our new approach relies on inverse methods, specifically inverse scattering theory, to work backwards from the fluctuations observed today. This is in contrast with previous work in the field, which is based on model calculations. Our method extracts the information in the data that is model-independent and nonparametric and thus provides a completely general framework for understanding the origin of primordial fluctuations in the universe.

Figure 1 illustrates the simplest application of our ideas, showing the asymptotic reconstruction of the "effective potential" for density waves as a function of time in the very early universe, for example, time-evolution.

For more information contact Salman Habib at habib@lanl.gov.

[1] S. Habib, et al., *Phys. Rev. Lett.* **94**, 061303 (2005).

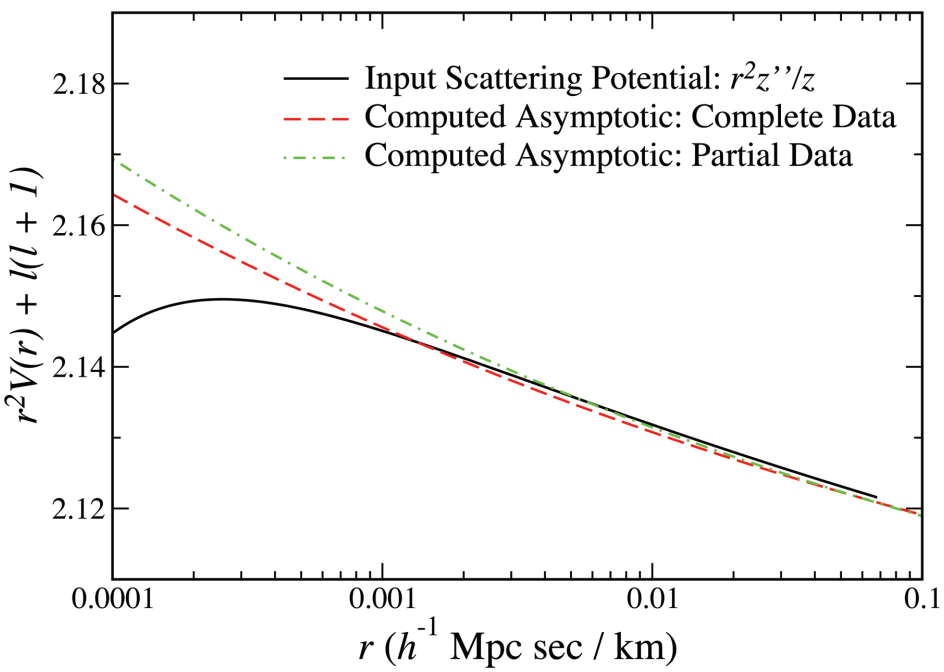

Fig. 1. *Asymptotic comparison of reconstructed scattering potential to the input. The input was tabulated during the initial computation of the power spectrum for the assumed evolution.*

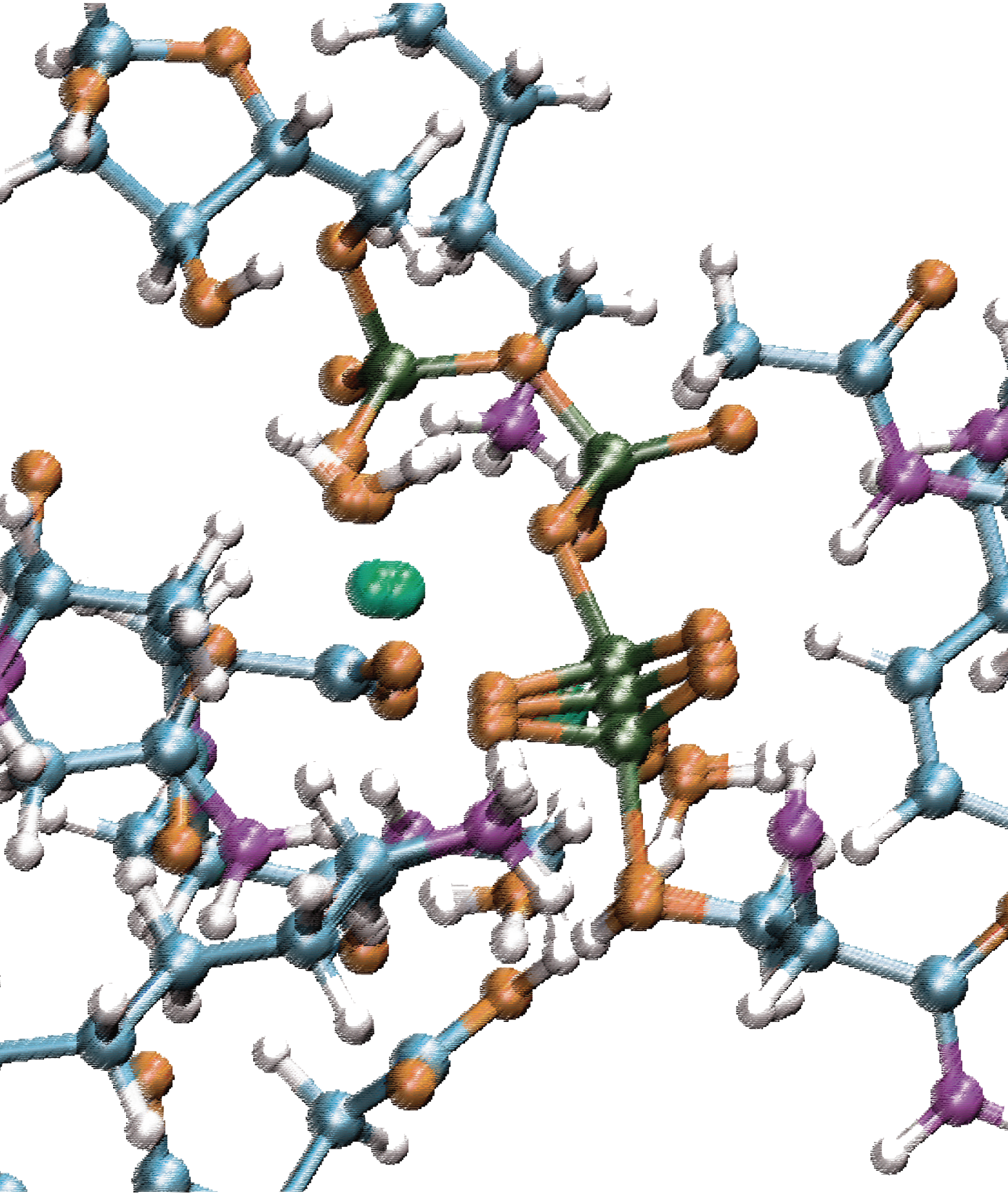

T-10

Theoretical Biology and Biophysics

Group Leader: Antonio Redondo
505.667.9738; redondo@lanl.gov

T-10 Theoretical Biology and Biophysics focuses on the modeling of biological systems and the analysis and informatics of molecular and cellular biological data. T-10 is one of the few research groups in the world devoted to mathematical modeling and computational analysis of problems in cellular and molecular biology. Research efforts include understanding dynamics and treatment of viral diseases such as HIV, influenza, and hepatitis; immune system modeling; receptor-ligand interactions and cell signaling; computational aspects of the human genome initiative; pattern recognition in DNA sequences; characterization and prediction of macromolecular structure; protein function and dynamics; and protein folding. T-10 has created and is also responsible for the maintenance of the HIV and Influenza Sequence Databases as well as the HIV Immunology Database and the HIV Resistance Database.

Conformational Dependence of Enzyme Function

Montiago X. LaBute, Paul W. Fenimore, Chang-Shung Tung, Benjamin H. McMahon, T-10

Proteins are dynamic molecules that must move to function. For proteins that are catalytic (i.e., enzymes) some of these motions regulate their catalytic function. Although plausible models of the allosteric regulation of enzymatic reactions by protein conformation were first proposed 40 years ago to great acclaim [1], the elucidation of the physical basis for this control has taken a steady, decades-long course and is still incomplete. Much has been learned in the intervening decades about the physical basis of allostery, for instance the relationship between conformational heterogeneity and ligand binding [2], and the stereochemical basis of allostery in a prototypical protein [3]. However, answers to a number of questions, such as the quantitative dependence of an enzymatic reaction barrier on structurally characterized protein conformations, have been elusive.

Protein kinases compose an important family of enzymes that site-specifically catalyze the transfer of the terminal phosphoryl group from adenosine triphosphate (ATP) to a protein or peptide substrate. This site-specific catalytic addition of a bulky, charged phosphoryl group, in the form of a phospho-ester, to the side chain of the aminoacids serine, threonine, or tyrosine plays an essential biological function by changing the conformation of the substrate protein and thus allosterically regulating protein function. This regulatory mechanism is widespread in biology, playing both regulatory and signaling roles in all phases of cell growth and regulation. The ability to manipulate this mechanism has become medically useful, the most striking example being the recent cure of many cases of adult mylogenous leukemia. This cure is effected by a single 590 Dalton tyrosine kinase-inhibiting compound, imatinib.

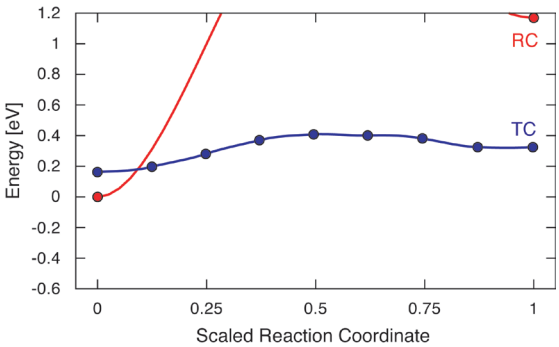

Fig. 1. ***PKA phosphoryl transfer energetics depend on protein conformation. (a) The energy along the reaction pathway for 244 atoms involved in the reaction. The reactant conformation (inactive, RC) and the transition conformation (active, TC) are markedly different. If the protein conformation is RC (inactive), there is a large barrier and more than 1eV of energy must be absorbed to reach the product state.***

The activity of the enzymatic region of protein kinases is related to the conformation of the protein, and is thus also an example of allostery. The structure of many protein kinases is known, many with a peptide substrate and the product ligand adenosine diphosphate (ADP) bound to the enzyme. While this combination of enzyme, ligand-product and an appropriate substrate often allows the crystal structure of a kinase to be determined, the protein conformation of these kinases is uniformly enzymatically inactive. In the last few years the structure of a transition-state analog for a phophoryl transfer reaction was published, revealing an enzymatically active conformation of the kinase PKA. These structural data allowed us to compute the reaction barrier energy for this phosphoryl transfer reaction in the enzyme [4]. Our technique for computing the energetics along the path of the chemical reaction uses density functional theory to calculate electron densities and system energies at a series of points along the reaction path. The reaction path is identified using a nudged-elastic band method.

Using the inactive conformation of the protein (PKA) and the active conformation, we modeled in atoms

missing from the experimentally determined structures. Primarily the atoms modeled in were those in the missing transferred phosphoryl group, either attached to the ATP (to make the reactants state) or to the substrate serine residue (to make the products state). A few missing protein atoms were also added to complete the picture. Having pictures of the protein with reactants or products bound in two different conformations (one active and one inactive) we were able to compute the energy barrier and change in equilibrium energy during transfer of the phosphoryl group in both conformations of the protein. The details of this density functional calculation reveal much of interest about the coupling between (slow) protein conformational motions and (fast) chemical reaction dynamics.

Calculation of the energetics during phosphoryl transfer is computationally intensive; no more than 250 atoms from the protein are included in the density functional calculation of the chemical reaction. By varying the size of the model system included in the density functional calculation, it becomes eminently clear that if too little of the protein is included in the calculation (less than about 200 atoms) two problems arise. First, the electronic state of the computational model system does not accurately mimic the electronic state of the real system. Second, the active and inactive conformations of the protein merge into a single, physically irrelevant conformation during the geometry optimization steps of the calculation.

Of fundamental interest are the results in larger systems (greater than 200 atoms): the chemical reaction in the inactive conformation requires the absorption of 1.2 eV to proceed (thus the barrier must be at least this large), while the reaction in the active protein conformation is nearly isoenergetic and

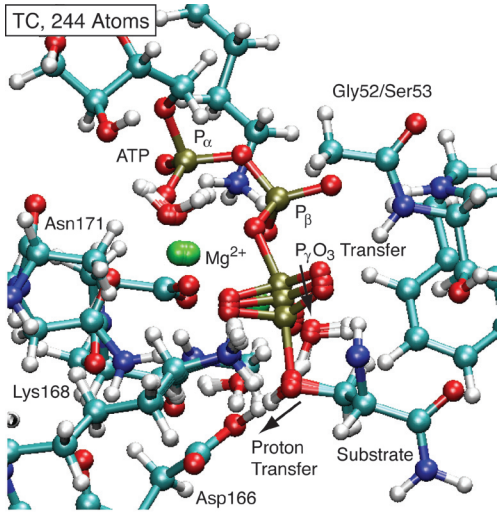

Fig. 2.
A picture of the reaction center in the protein kinase. The gold atom is the phosphorus atom in the transferred phosphoryl group. ATP and the substrate are the reactants, ADP and a phosphorylated substrate the products of the reaction.

the barrier is 0.2 eV. This demonstrates that, at least in some proteins, the conformational, allosteric motions of the protein are a slow modulation of the reaction barrier and that the reaction proceeds not by the vibrational crossing of a comparatively high barrier, but instead by the protein slowly lining up requisite atoms for the chemical reaction to proceed in a semireversible manner. The theoretical underpinnings for this kind of reaction were published by Agmon and Hopfield in 1983 [5].

This work points toward a scheme for analyzing protein catalysis that decouples the explicit protein conformational dynamics responsible for allostery from the chemical reaction, and then screens protein conformations for those that are reactive. Calculations of the barrier between chemical reactants and products can then be done using large-scale, but standard, density functional calculations.

For more information contact Paul Fenimore at paulf@lanl.gov.

[1] J. Monod, et al., *J. Mol. Biol.* **12,** 88 (1965).
[2] R.H. Austin et al., *J. Mol. Biol.* **14**, 5355 (1975).
[3] M. Perutz, *Annu. Rev. Biophys. Biomol. Struct.* **27**, 1 (1998).
[4] G. Henkelman, et al., Proc. *Nat. Acad. Sci. USA* **102**, 15347 (2005).
[5] N. Agmon, J.J. Hopfield, *J. Chem. Phys.* **79**, 2042 (1983); N. Agmon, J.J. Hopfield, *J. Chem. Phys.* **79**, 6947 (1983).

Nanocomputers Inside Our Bodies: Understanding How the Ribosome Decodes Genetic Information

Kevin Y. Sanbonmatsu, T-10

The ribosome is a giant molecular complex central to all living things and ancient in evolutionary terms. Its job is to read genes and synthesize the proteins that the genes code for. It is analogous to a computer's CPU in the sense that it is able to perform a complex 'look-up table' operation, reading sequences based on the 4-letter alphabet used by DNA and RNA, and converting these sequences into new sequences written in a 20-letter alphabet (i.e., the amino acid sequences which constitute proteins). It accomplishes this feat with a suite of adapter molecules called transfer RNAs, which were first predicted to exist by Francis Crick, codiscoverer of the DNA double helix structure. The ribosome is, in fact, a nanoscale computer and is very much analogous to the 'CPU' of the cell. The ribosome is so fundamental to life that many portions of this molecular machine are identical in every organism ever sequenced. These 100% evolutionarily conserved portions are called universal bases.

We have simulated the key step by which the ribosome decodes genes using the Advanced Simulation and Computing Q Machine. Until now, only static snapshot structures of the ribosome have been available. Limitations in time resolution and spatial resolution make it impossible to image the ribosome in motion in atomic detail. However, large-scale supercomputers make it possible to simulate the movement of the ribosome between these experimentally determined snapshots. We have used these supercomputers to determine how the transfer RNA molecule moves inside the ribosome, enabling it to decode genes [1]. We have identified a corridor inside the ribosome that the transfer RNA must pass through for the decoding to occur. This corridor happens to be constructed almost entirely of universal bases, implying that it is evolutionarily ancient. The corridor represents a new region of the ribosome containing a slew of potential new antibiotic targets. We have also shown that the transfer RNA must be flexible in two places for this movement to occur, suggesting that the transfer RNA plays an even more active role in decoding than previously thought. Recent developments are leading researchers to conclude that the transfer RNA played a role equally important to the ribosome in the development of protein synthesis, a key step in the origin of life on Earth.

The simulation method also presents a proof-of-principle for locating potential antibiotic targets on large molecular complexes. Antibiotic drugs are less than 1/1000th the size of the ribosome but have the ability to diffuse into the most critical sites of this huge molecular factory and grind the inner workings to a halt like a 'monkey wrench.' The simulation maps out where, exactly, we expect the transfer RNA to rub against the ribosome, giving us the best places to insert the molecular monkey wrench if we want to take out the ribosomes of harmful bacteria such as anthrax. Because the ribosomes are analogous to the CPU of the bacteria, taking out the ribosomes results in rapid cell death of the bacteria.

For more information contact Kevin Sanbonmatsu at kys@lanl.gov.

[1] K.Y. Sanbonmatsu, et al., *Proc. Nat. Acad. Sci.* **102** (44), 15854 (November 1, 2005).

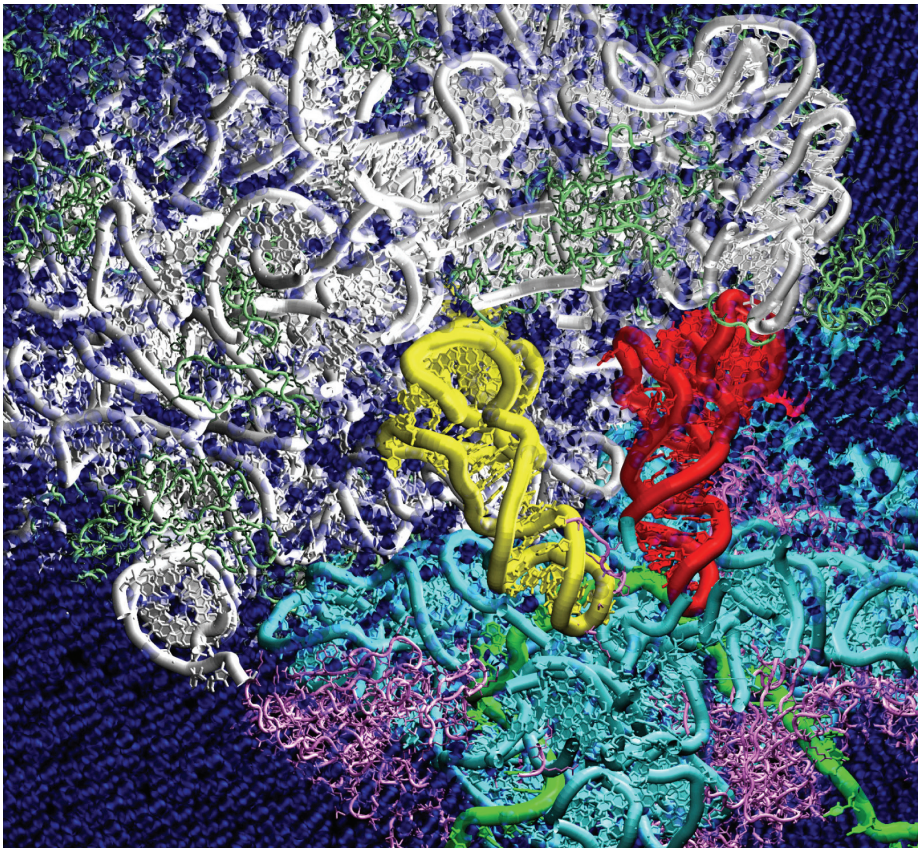

Fig. 1.
The ribosome is a living factory, the essential element within cells that creates proteins by decoding each protein type's specific recipe that is stored within messenger RNA. Ribosomes are a fundamental model for future nanomachines, producing the protein building blocks of all living tissue.

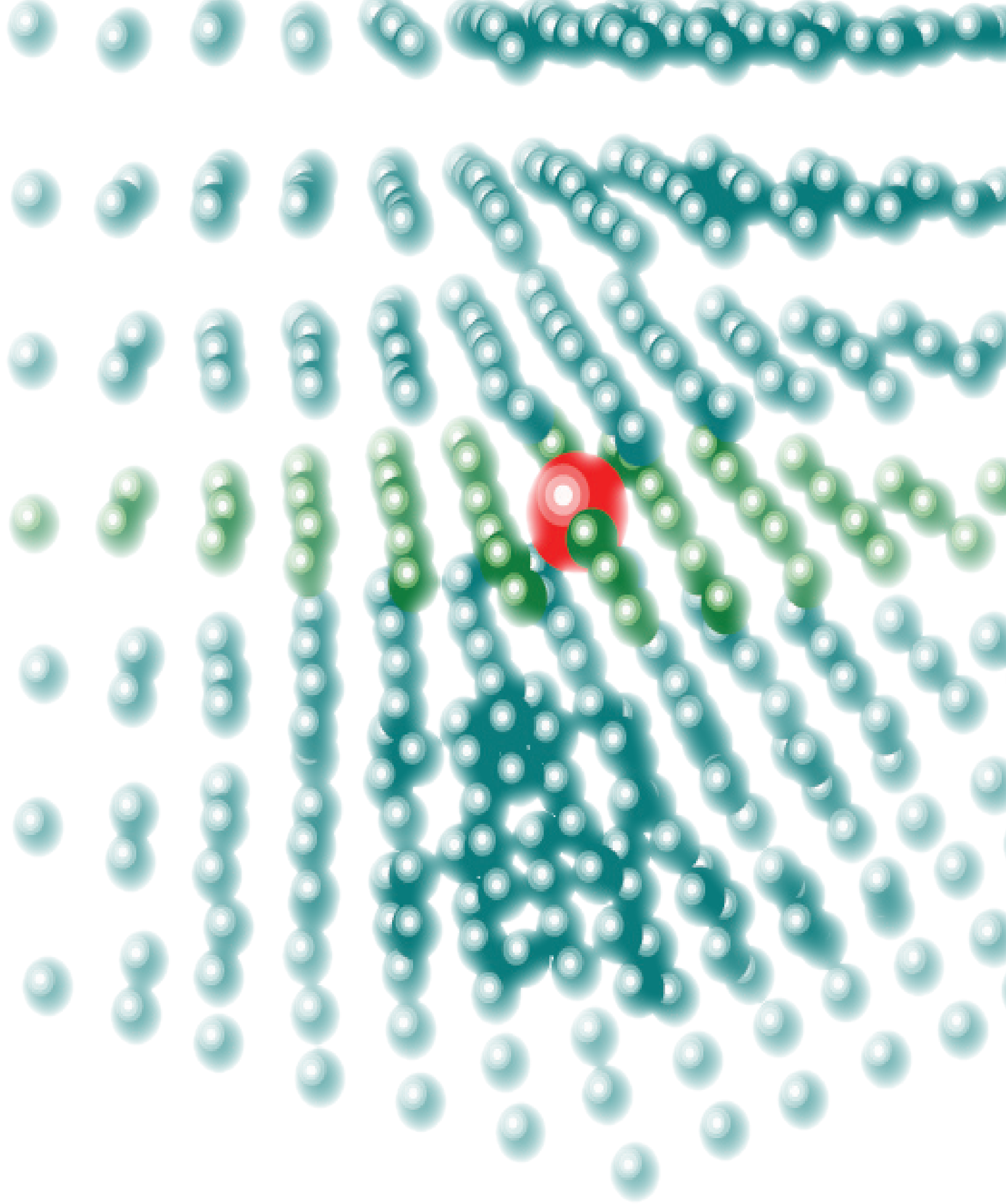

Complex Systems T-13

Group Leader: Eli Ben-Naim
505.667.9471; ebn@lanl.gov

T-13 Complex Systems creates new methods for solving complex problems and applies them to problems at the forefront of technology. Computational fluid modeling, simulations of large quantum computers, design of solid state quantum computers, granular flows, and nanotechnology are of great interest to researchers in this group. Current research includes modeling of the spread of influenza, determining the shapes of functionally equivalent biological molecules, rapid and accurate modeling of enhanced oil recovery processes, fundamental turbulence modeling, designing laser-matter interaction systems for the National Ignition Facility, determining the predictability of large complex systems, and creating new information scanning and gathering systems.

Application of Optically Detected Magnetic Resonance in a Nanoprobe to Measurement of Single Electron and Nuclear Spin States

Gennady P. Berman, T-13; Alan R. Bishop, T-DO; Boris M. Chernobrod, T-13; Marilyn E. Hawley and Geoffrey W. Brown, MST-8; and Vladimir I. Tsifrinovich, Polytechnic University

Progress in nanotechnology, including spintronics and quantum information processing based on a solid-state quantum computer, has brought significant attention to the problem of measurements of single electron and nuclear spin states. Here we suggest a novel approach for measurement of single electron and nuclear spin states. The novel aspects of our approach are: 1) use of a nanoprobe for the optically detected magnetic resonance (OMDR), 2) nondestruction of the spin state being measured, 3) nanoscale spatial resolution, and 4) high sensitivity of ODMR to a single electron or nuclear spin orientation relative to an external magnetic field. Our modified ODMR approach consists of an AFM with a photoluminescent material (nanoparticle) located at the apex of an AFM tip (see Fig. 1), which exhibits ODMR in the vicinity of an unpaired electron or nuclear spin in the sample. This approach transfers the detection of electron magnetic resonance from a microwave frequency domain to an optical domain, which significantly increases measurement sensitivity.

In this method, the nanoparticle is excited from its ground state 1 into the first excited state 2 by absorption from a laser field, and subsequently decays through nonradiative transitions to magnetic sublevel states 3. (See Fig. 2.) An external magnetic field lifts the degeneracy of the triplet states and changes the energy splitting between these magnetic sublevels as well as their populations and lifetimes. Resonance is achieved by scanning the magnetic field from a nearby radio-frequency coil to induce transitions between these magnetic sublevels to change their relative populations, thus increasing or decreasing the intensity of specific peaks in the photoluminescence spectrum resulting from decay back to the ground state. Nanoprobe absorption in an evanescent laser field could be significantly enhanced when placed at the apex of a sharp silicon tip. The potential resolution of this method is related to the size of the photoluminescent probe, typically 1–10 nm. One of the most promising applications is the nondestructive measurement of a qubit single spin state in a quantum computer.

Measurement of a single electron spin state. Our preliminary analysis of the dependence of the sensitivity on geometry shows that at optimal conditions the ODMR of a nanosize probe can sense the magnetic field of a single electron spin [1].

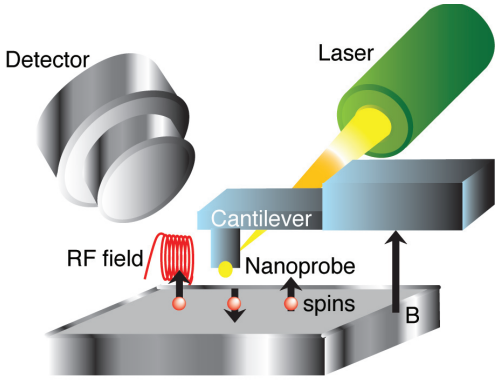

Fig. 1. AFM-ODMR setup.

Measurement of a single nuclear spin state. We consider the two states of a single nuclear spin of an impurity atom with an electron inside the solid-state matrix (Fig. 3). The scheme of energy levels of electron-nuclear spin states in the permanent magnetic field is presented by Fig. 4. The energy levels of an electron spin have a shift due to hyperfine interaction that depends on the state of a nuclear spin. To measure the state of the nuclear spin, we exploit the fact that the electron spin resonance with transition frequency between sublevels of the electron spin depends on the state of the nuclear spin (see Fig. 4). Thus, for example, the RF field will selectively induce transitions only between the states $<S_e = -1/2, I_n = 1/2|$ and $<S_e = 1/2, I_n = 1/2|$ (blue arrow in Fig. 4), and will not interact with the transition $<S_e = -1/2, I_n = -1/2| - <S_e = 1/2, I_n = -1/2$ (red arrow in Fig. 4). Finally, the two electron spin states involved in the transitions correspond to the same nuclear spin "up" state. Therefore, the proposed measurement procedure does not change the state of a nuclear spin, and realizes a nondestructive measurement of a nuclear spin state.

For more information contact Boris M. Chernobrod at boris@lanl.gov.

[1] B.M. Chernobrod and G.P. Berman, *J. Appl. Phys.* **97**, 014903 (2005).

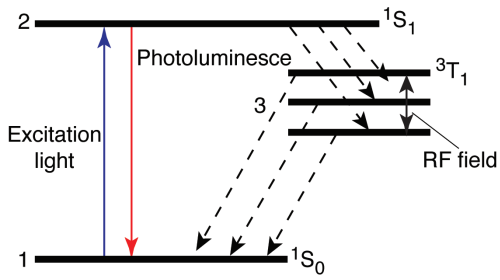

Fig. 2. *Transitions in the nanoparticle.*

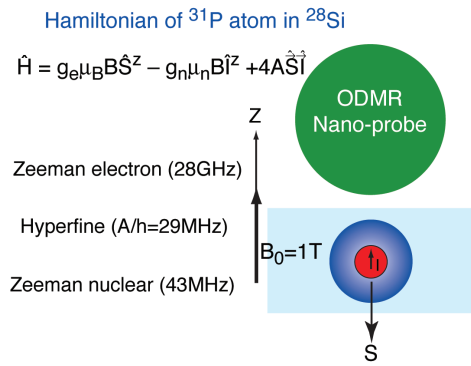

Fig. 3. *Nanoprobe and ^{31}P atom in ^{28}Si matrix. Relevant energies are shown at left.*

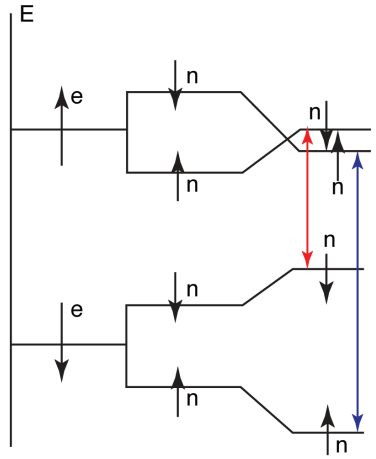

Fig. 4. *Hyperfine structure of electron-nuclear spin energy levels.*

Collective Decoherence of the Superpositional Entangled States in Quantum Shor Algorithm

Gennady P. Berman and Dmitry I. Kamenev, T-13; and Vladimir I. Tsifrinovich, Polytechnic University

The quantum Shor algorithm solves the problem of factorization of large integers. A quantum computer is needed in order to implement this algorithm. The most important problem preventing an experimental realization of the quantum computer is decoherence, i.e., the destructive influence of environment on quantum states in the quantum computer register. We considered the collective decoherence for the quantum Shor algorithm when all spins interact with the same environment [1]. This model describes, for example, the decoherence caused by low-frequency phonons in a solid-state spin quantum computer.

Different approaches to suppress this collective decoherence have been proposed. One approach is based on logical quantum bits (qubits). Each logical qubit is represented by a group of physical qubits in such a way that the states of the logical qubits are free from decoherence (decoherence-free subspaces). It has been shown that universal quantum computation is possible within decoherence-free subspaces. In another (more abstract) approach, the quantum information is represented in terms of conserved quantities of the quantum system, which are not affected by noise (noiseless subsystems). Both decoherence-preventing schemes require additional computational resources and complexity. Our results are important for preserving quantum entanglement without the application of complicated decoherence-preventing strategies.

Each quantum bit in our quantum computer is represented by a particle with spin 1/2. The environment is represented by a system of oscillators with continuously distributed frequencies. We analyzed the interaction between the environment and the z-components of all spins. The process of decoherence in the quantum computer is caused by entanglement between the thermal environment and the quantum computer.

In the system under consideration, different states of the quantum superposition are affected differently by the environment. We have shown that the probability p of very fast decoherence rate (superdecoherence) for the quantum Shor algorithm is extremely small. In particular, $p \sim \exp[-(\Delta I_z)^2]$, where $|\Delta I_z|$ is the sum of the differences $|b_i - c_i|$. Here b_i and c_i are the ith bits ($b_i = 0,1$; $c_i = 0,1$; $I = 1,2,\ldots L$) of the numbers b and c which form a superposition of two states in the quantum register. As Fig.1 demonstrates, the probability P of the appearance of large $|\Delta I_z|$ in the quantum Shor algorithm is small.

In order to estimate the decoherence time, we assumed that the size of the sample is 1 cm, the speed of the elastic waves is 500 m/s, and the temperature is 1 mK. Then, using our results we estimated the decoherence time to be of the order of 0.04 s. This long decoherence time allows one to implement thousands of quantum logic operations before the quantum state is destroyed by the environment.

For more information contact Gennady P. Berman at gpb@lanl.gov.

[1] G.P. Berman, et al., *Phys. Rev. A* **71**, 032346 (2005).

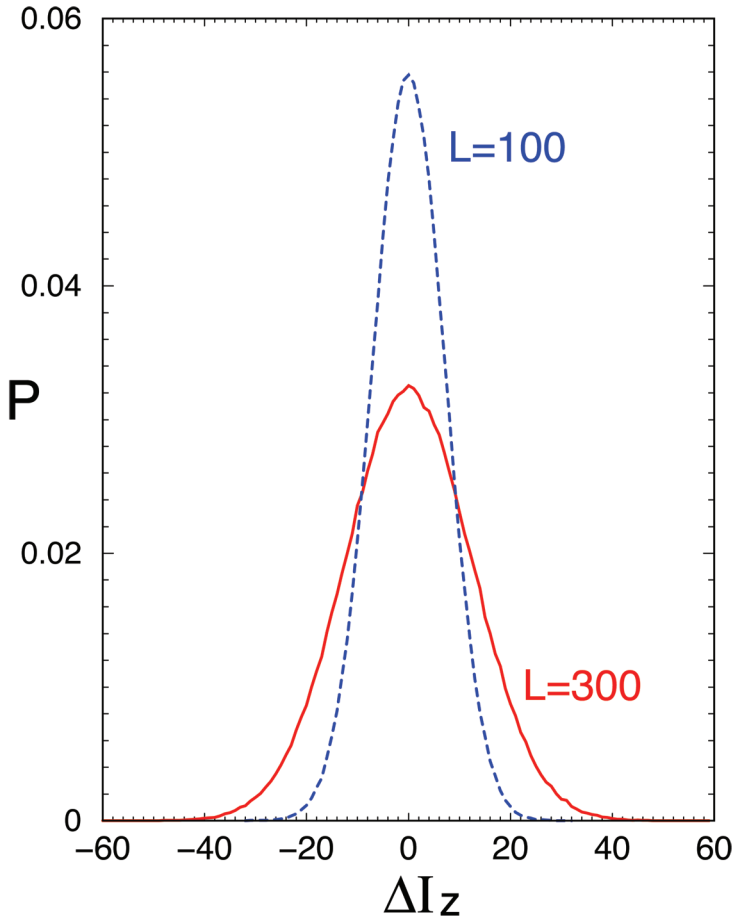

Fig. 1.
The figure shows the probability P of the appearance of large $|\Delta I_z|$ in the quantum Shor algorithm is small.

Iterative Algorithm for Finding Frequent Patterns in Transactional Databases

Gennady P. Berman, Vyacheslav N. Gorshkov, Edward P. MacKerrow, T-13; and Xidi Wang, Citigroup, Sao Paulo, Brazil

Vast amounts of consumer transactional details are being captured daily that describe the trajectories of consumer behaviors, e.g., credit card transactions. It is a well-known observation that past behaviors predict future behaviors. Credit risk models are among the most widely used to rely on this observation to predict the future risk based on the past behaviors. In fact, various kinds of models are commonly used for making daily decisions throughout the credit cycle in the card business, ranging from new customer acquisition, account maintenance, collection queuing, etc. There are situations in which the behaviors of customers are much more sophisticated than a simple model can describe where important information is hidden among the subtle interactions/correlations among the variables. An example of such is a case of the credit card fraud detection model, where the interactions among the transaction variables provide important clues about transactions being made, namely, fraudulent or not. We carried out our joint research effort between the Laboratory and Citigroup to develop and benchmark effective algorithms, such as the frequent patterns (FPs) algorithm, for detecting abnormal behavior in transactional databases. New algorithms were developed using the available global credit card transaction database of Citigroup.

In the future, we propose to leverage the existing experience of Citigroup in credit card fraud detection and prevention for use by the Department of Homeland Security to detect signatures of criminal behavior and terrorist activities. Our existing collaboration with Citigroup allows us to benchmark potential new algorithms against conventional algorithms using the database provided by Citigroup. The partnership with Citigroup will benefit Citigroup by improving their detection algorithms and will also benefit the Laboratory and the U.S. government by increasing our expertise and capability for detecting terrorist activities.

Our iterative algorithm for searching for frequent patterns in transactional databases is presented in [1]. The search for FPs is carried out by using an iterative sieve algorithm by computing the set of enclosed cycles. In each inner cycle of level ***m*** FPs composed of ***m*** elements are generated. The assigned number of enclosed cycles (the parameter of the problem) defines the maximum length of the desired FPs. The efficiency of the algorithm is produced by (1) the extremely simple logical searching scheme, (2) the avoidance of recursive procedures, and (3) the usage of only one-dimensional arrays of integers.

Suppose that we have a set of elements $X = \{x_1, x_2, x_3, ..., x_K\}$ (see Fig. 1). Any subset of these elements, with arbitrary number of elements (or "length"), $x_i, x_j, x_k, ..., x_m$, represents a transaction. A transactional database (DB_0) is a set of N transactions. Usually, a DB_0 can be characterized by, at least, two parameters, K — the maximum length of a transaction, and N — the total number of transactions. Except for these two parameters, another useful characteristic of the DB_0 can be introduced, namely, a "pattern" which is an arbitrary set of the elements. A pattern can have a different length, from 1 to K. The elementary information is represented by the frequencies of the elements x_k, $f(x_k) \equiv f_k$ (patterns of the length one). The number f_k indicates how many times the element x_k appears in all transactions in the DB_0. More detailed information about the

DB_0 is represented by the frequencies of the patterns of the lengths 2,3,…,K. For example, the frequency f_{nm} is the number of patterns $x_n x_m$ in DB_0; the same is true for the pattern $x_n x_m x_l$ and so on.

For many applications, the patterns with the frequencies less than some critical value (or threshold) ξ may not be considered as a characteristic property of the DB_0. The patterns for which the corresponding frequencies satisfy the condition $f \geq \xi$ are called *frequent patterns* (FPs). If the probability, $p(w)$, of the FP $w = x_i, x_j, \ldots x_k x_l, \ldots, x_m$ ($w = u \cup v$, where the FPs $v = x_l, \ldots, x_m$, and $u = x_i x_j \ldots, x_k$), essentially differs from the product $p(u) \cdot p(v)$, then the FP w includes the "interacting" elements of the set X. Such FPs, which are made up of the interacting elements, characterize the principal statistical properties of DB_0 .

Our iterative algorithm for searching for frequent patterns was created for detecting a fraudulent activity in transactional databases. This algorithm was tested in T-13 (on artificial databases) and in Citigroup (on real databases).

Fraud models are widely used for detecting fraudulent and abnormal transactions in large financial institutions. These models use the historical behavior of the customers. By examining both fraudulent and nonfraudulent behaviors, one can construct mathematical models, which predict the fraud probability of both the current and future transactions. These models can yield high degrees of prediction accuracy. For example, in the credit card business, suspicious transactions can be detected with a 30% probability of being a fraudulent one, much higher than the average fraud rate of 0.1%. Various types of fraudulent behavior, including cloned credit cards, Internet fraud, and self-fraud, all of which can be detected automatically by implementing the fraud models in production. The automated fraud detection process greatly reduces the current and the future fraud losses. It is important to develop high-quality fraud models.

In the future, we plan to apply our algorithms for solving problems that are relevant to threat reduction and homeland security needs.

For more information contact Gennady Berman at gpb@lanl.gov.

[1] G.P. Berman, et al. "Iterative Algorithm for Finding Frequent Patterns in Transactional Databases," lanl.arXiv.org e-Print archive, cs.DB/0508120 (2005).

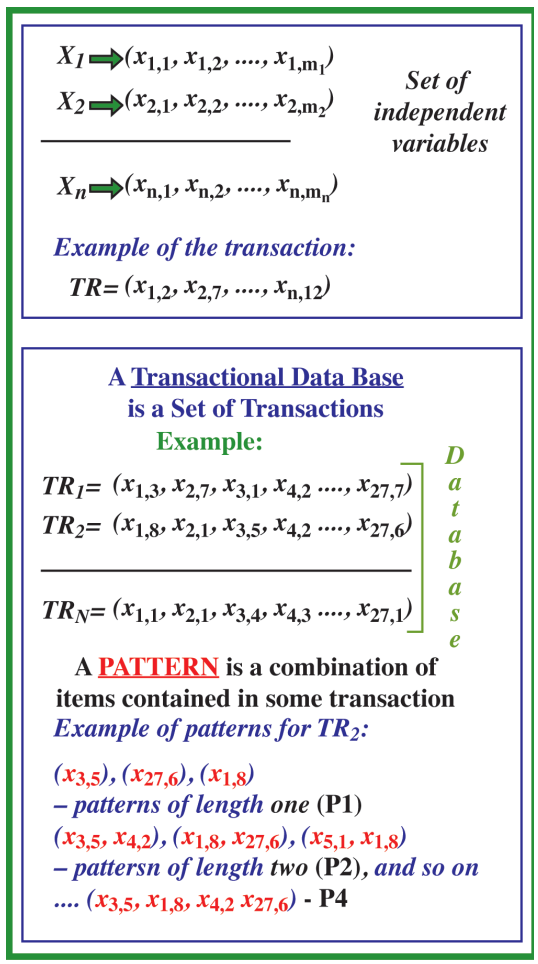

Fig. 1. Examples of a set of independent variables, a transaction, and the elements of a transactional database.

Novel Opto-Nanomechanical Photodetector for Improving the Sensitivity of LIDAR and Local Optical Sensors

Gennady P. Berman, T-13; Alan R. Bishop, T-DO; Boris M. Chernobrod, T-13; and Marilyn E. Hawley and Geoffrey W. Brown, MST-8

Until recently, the most widely used technique for remote sensing was differential absorption LIDAR (DIAL). The basic principle of DIAL is based on using two radiation frequencies: one is tuned to an absorption spectral line of the species of interest, and the other is tuned off this spectral line. The attenuation of the backscattered light at these two frequencies is compared and the absorbance of the species is extracted from the difference. The main limitation of this technique is the difficulty of detecting small changes due to absorption on a large fluctuating background. To avoid this limitation, the frequency modulation (FM) technique has been applied by several research groups, including the Pacific Northwest National Laboratory (http://infrared.pnl.gov/LIDAR.htm), the NASA/Goddard Space Flight Center (www.grss-ieee.org/), and the Sarnoff Research Institute (www.sri.com/rd/Remote_Gas_Leak_Sensor.pdf).

Frequency Modulation spectroscopy has proven to be one of the most sensitive absorption-based spectroscopic techniques. The essential idea is that when a frequency modulated laser beam enters an absorbing medium the emerging, partially absorbed beam is amplitude modulated (AM). If the modulation index of the FM is sufficiently small, the spectrum of the incident FM beam consists primarily of the peak at the carrier frequency ω_c and sidebands at $\omega_c \pm \Omega$, where Ω is the modulation frequency. In addition to the component at the carrier frequency, the intensity of the output beam has a component that oscillates sinusoidally at Ω and with an amplitude proportional to the modulation index and to the difference in the attenuation coefficients of the absorber at the frequencies $\omega_c + \Omega$ and $\omega_c - \Omega$. It is important for the FM method that there be little spectral overlap between the carrier and the sidebands. If the modulation frequency is not high enough, the spectral wings of the sidebands and the carrier will

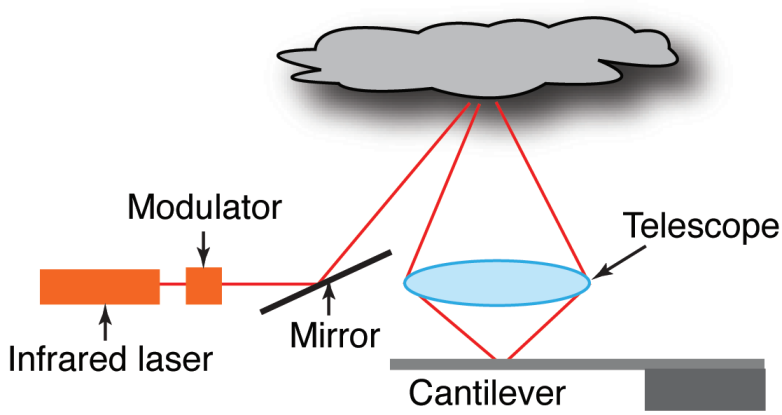

Fig. 1.
The schematic setup of the FM-LIDAR system with opto-nano-mechanical photo-detector.

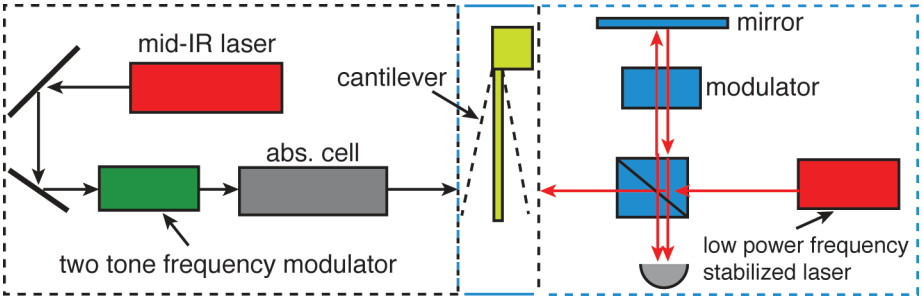

Fig. 2.
Left: FM absorption spectroscopy setup. Right: A setup for optical detection of the cantilever vibrations.

overlap, making the exact amplitude and phase balance required for full FM beat cancellation impossible. Thus, one of the major limiting factors in FM spectroscopy is laser noise, which requires that the modulation frequency be large compared with the laser bandwidth. However, electronic detection systems, consisting of a photodetector and several amplification cascades, produce an additional noise that increases with increasing modulation frequency, so that the shift to higher modulation frequency could be inefficient.

We suggest the use of nanomechanical cantilevers as photodetectors and filters with much higher Q factors than are currently possible by conventional electronic methods. Recent progress in the fabrication of nanomechanical resonators (cantilevers) has resulted in high-frequency cantilevers (up to 100 MHz) with quality factors ($Q = 10^5$), which are at least three orders of magnitude higher than for electronic filters. These ultralow mass devices enable an entirely new paradigm in photonics: sensitive detection of photon momentum rather than conventional detection by photon energy. In this approach the AM signal reflected by the Earth's surface (in the case of airborne sensor) or aerosols and molecular backscattering in the atmosphere actuates a cantilever by resonant light pressure or by optical gradient forces (see Fig. 1). In a variant of the local sensor (see Fig. 2), the light emerges from a multipass absorption cell and actuates the cantilever. Optical actuation of cantilevers by light has been demonstrated [1, 2]. In our case, the cantilever functions both as a high-frequency detector and as a high-Q filter. By choosing the cantilever resonance frequency appropriately, the proposed sensor can be made to operate in the thermal noise limit [3]. The use of cantilevers in FM-LIDAR and local FM-sensors in this way offers the possibility of detecting low absorptions and concentrations with unprecedented sensitivity.

For more information contact Boris M. Chernobrod at boris@lanl.gov.

[1] O. Marti, et al., *Ultramicrosc.* **42–44**, 345 (1992).
[2] J. Yang, et al., *Appl. Phys. Lett.* **77**, 3860 (2000).
[3] B.M. Chernobrod, et al., *Appl. Phys. Lett.* **85**, 3896 (2004).

Quasiclassical Model of Spin Diffusion and Relaxation in a Nonuniform Magnetic Field

Gennady P. Berman, Boris Chernobrod, Vyacheslav N. Gorshkov, T-13; and Vladimir I. Tsifrinovich, Polytechnic University

Operation of any quantum spin device crucially depends on the relaxation rate in the spin system. Spin diffusion is recognized as one of the most important factors in a spin relaxation process. The idea of spin diffusion originated from Bloembergen who explained nuclear spin-lattice relaxation in insulating crystals [1]. He demonstrated that the transport of magnetization from fast relaxing spins (FRS) to slow relaxing spins (SRS) can be described by as a diffusion process. Due to the spin diffusion, a small amount of FRS (e.g., located near the impurities) can greatly accelerate the spin-lattice relaxation in the whole spin system. A number of theoretical approaches have been used to describe the spin diffusion. The general theory of the spin diffusion and relaxation in electron spin resonance has been developed in [2].

Recently Budakian, Mamin, and Rugar [3] demonstrated effective manipulation with the electron spin relaxation of E′ — centers in silica using the high gradient of the magnetic field produced by a ferromagnetic particle in the magnetic resonance force microscopy.

Inspired by this experiment we have considered a quasiclassical computational model [4] that allows us to simulate the process of spin diffusion and relaxation in the presence of a highly nonuniform magnetic field. The energy of the SRS flows to the FRS due to the dipole-dipole interaction between the spins.

Our computations show that in case of the uniform external magnetic B_z field the overall relaxation time τ_r can be described by the relation

$$\tau_r \approx \frac{\tau_0}{1+\beta/(\alpha N)} ,$$

where α is the parameter of relaxation of the SRS, $\beta >> \alpha$ is that for the FRS, $N \approx n_S/n_F >> l$, n_F and n_S are the concentrations of FRS and SRS, τ_0 is the time of relaxation in the absence of the FRS .

The suppression of the relaxation process depends on parameter,

$$K = a\frac{\partial B_z}{\partial z} \Big/ \frac{\mu_0}{4\pi}\frac{\mu_B}{a^3} ,$$

which is the ratio of the Larmor frequency difference to the dipole-dipole constant (a is the average distance between the spins). The significant increase of the relaxation time τ_r appears in the region $4.4 \le K \le 44$, which corresponds to the values $10^3 T/m \le \partial B_z/\partial_z \le 10^4 T/m$ in a good agreement with experiments [3]. (See Fig. 1.) For $K > 44$, the ratio $R(K) = \tau_r(K)/\tau_r(K=0)$ is approaching the value $1 + \beta/(aN)$. It means that the overall relaxation time $\tau_r(K)$ is approaching the expected value τ_0. We have found that in the absence of the magnetic field gradient ($K = 0$) the

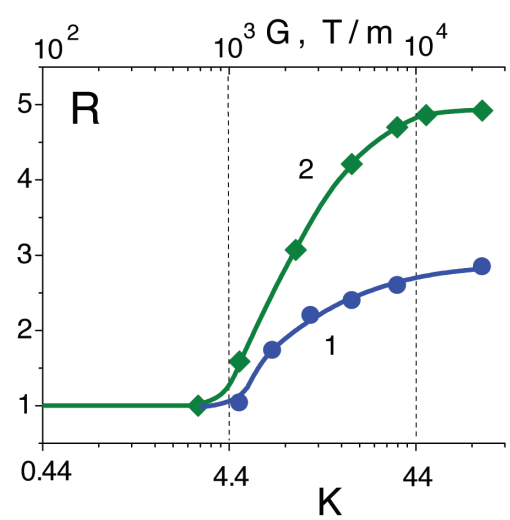

Fig. 1.
Dependence R(K) on K. Curves 1–2: $\beta/(aN) = 4, 2$. $G = \partial B_z/\partial z$.

relaxation process spreads randomly in all directions from FRS to SRS. In the presence of the magnetic field gradient the spin diffusion process becomes anisotropic (See Fig. 2). One can see that the relaxation process first develops in the slice containing FRS ($i = 0$), then it spreads to the slices $i < 0$ below the central slice, then it spreads to the upper slices $i > 0$. The reason of the phenomenon has been thoroughly investigated by us [4].

The processes of spin diffusion and relaxation are studied theoretically and numerically for quantum computation applications in our paper [5]. Two possible realizations of a spin quantum computer (SQC) are analyzed: i) a boundary spin chain in a 2-D spin array, and ii) an isolated spin chain. In both cases, spin diffusion and relaxation are caused by a FRS located outside the SQC. We have shown that in both cases the relaxation can be suppressed by an external nonuniform magnetic field. In the second case, our computer simulations have revealed various types of relaxation processes including the excitation of a random distribution of magnetic moments and the formation of stationary and moving domain walls. The region of optimal parameters for suppression of rapid spin relaxation is discussed.

For more information contact Gennady Berman at gpb@lanl.gov.

[1] N. Bloembergen, *Physica (Utrecht)* **15**, 386 (1949).
[2] B.E. Vugmeister, *Phys. Stat. Sol. (b)* **90**, 711 (1978).
[3] R. Budakian, et al., *Phys. Rev. Lett.* **92**, 037205 (2004).
[4] G.P. Berman, et al., *Phys. Rev. B* **71**, 184409 (2005).
[5] G.P. Berman, et al., Cond-mat: 0503107 (2005).

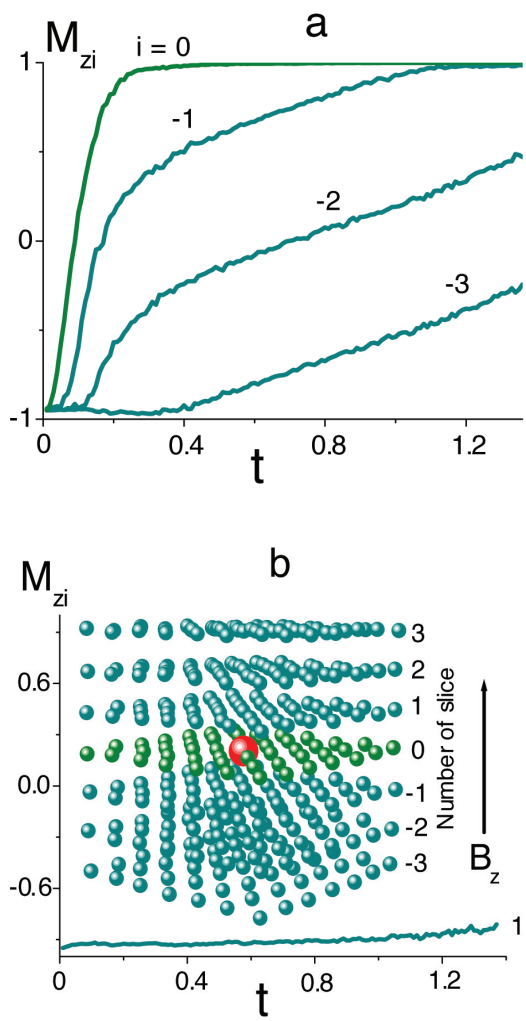

Fig. 2. ***Relaxation of the slice magnetic moments $M_{zi}(\tau)$ (τ is the dimensionless time) in the presence of the magnetic field gradient: a- for the central slice, which contain FRS ($i = 0$, the red sphere), and for the slices below the central slice; b- for the slice 1 above the central slice. $\beta/(aN) = 4$, $K = 10$.***

Sub Shot-Noise Phase Sensitivity with a Bose-Einstein Condensate Mach-Zehnder Interferometer

Gennady P. Berman, T-13; Alan R. Bishop, T-DO; Lee A. Collins, T-4; Luca Pezzé and Augusto Smerzi, T-13

Quantum-enhancement measurement techniques are the subject of lively research in modern technology. Bose Einstein Condensates (BECs), with their coherence properties, have attracted wide interest for their possible application on ultra precise interferometry and ultra weak force sensors. Since BECs, unlike photons, are interacting, they may permit the realization of the specific quantum states needed as input of an interferometer to approach sensitivities surpassing the classical shot noise limit $1/N^{1/2}$ (being N the total number of particles). In particular, several efforts focus on the possibility of interferometrically estimated phases with precision bounded by the Heisenberg limit $1/N$, which is widely believed to be the ultimate limit imposed by quantum mechanics.

We have studied the sensitivity of a matter-wave Mach-Zehnder interferometer to an external weak phase perturbation, see Fig. 1. The inputs are two Bose-Einstein condensates created by splitting a single condensate in two parts [1]. The recent experimental creation of very stable double-well traps [2, 3] bodes well for the future of matter-wave interferometry. The interferometric phase sensitivity depends on the specific quantum state created with the two condensates. This quantum state can be taylored by varying the time scale τ of the splitting process and the tunneling coupling energy $K(t)$ (which is proportional to the overlap of the wavefunctions localized in each well). We have studied the dynamical splitting of the two wells solving the bosonic quantum field equation in two-mode approximation. The MZ phase uncertainty, $\Delta\theta$, as a function of the splitting time and the tunneling coupling were calculated using the error propagation formula

$$(\Delta\theta)^2 \approx \frac{(\Delta \hat{J}_z^{out})^2}{|\partial\langle \hat{J}_z^{out}\rangle/\partial\theta|^2},$$

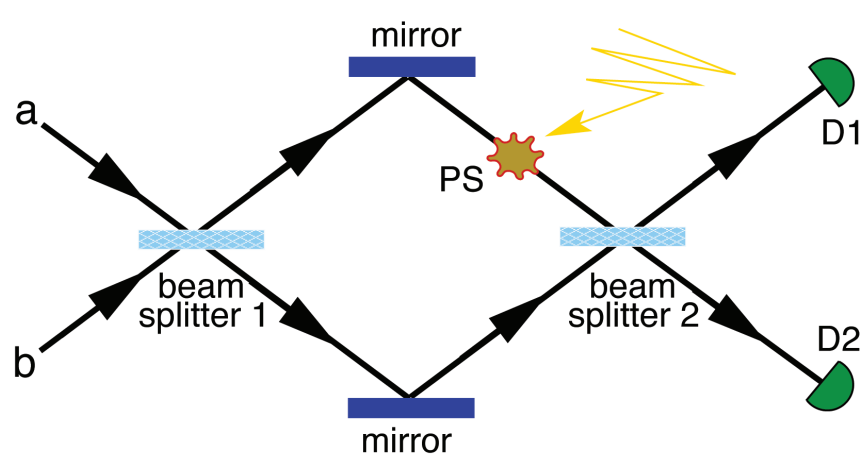

Fig. 1. *Schematic representation of the Mach-Zehnder interferometer. Atoms/photons enter the a and b input ports, mix and recombine in the beam splitters and are finally detected in D1 and D2. The phase shift is inferred from the number of atoms/photons measured in each output port.*

with $\hat{J}^{out}$ the relative number of particles operator whose expectation values are calculated at the output ports.

We found three different regimes, see Fig. 2, which, in analogy to three corresponding regimes existing in the dynamical Josephson effect, we termed Rabi, Josephson, and Fock. These three regimes are characterized by different scalings of the phase sensitivity $\Delta\theta$ with the total number of condensate particles N.

Rabi Regime. This is a semiclassical regime characterized by a strong tunneling coupling K between the two condensates. In this regime the phase sensitivity scales at the standard quantum limit $\Delta\theta \sim /N^{1/2}$.

Josephson Regime. This is the most interesting regime since it can be reached in a realistic experimental setting, see Fig. 3 (ramping time $\Delta t_R \approx 100$ msec and final distance between the wells $d_R \approx 10\ \mu$m) [2, 3]. By creating the states feeding the interferometer in this regime, it is possible to reach a sub shot-noise sensitivity $\Delta\theta \sim 1/N^{3/4}$. We have also found that the $1/N^{3/4}$ scaling is a rigorous upper bound in the limit $N \to \infty$, while keeping constant all different parameters of the bosonic Mach-Zehnder interferometer.

Fock Regime. In this regime, the initial condensate has been fragmented into two independent condensates. Once these feed the input ports of the MZ, it is possible to reach the Heisenberg limit $\Delta\theta \sim 1/N$. However, in a realistic dynamical BEC splitting, the $1/N$ limit requires a very long adiabaticity time-scale, which is hardly achievable experimentally.

For more information contact Augusto Smerzi at smerzi@lanl.gov.

[1] L. Pezzé, et al., *Phys. Rev. A.* **72**, 043612 (2005).
[2] Y. Shin, et al., *Phys. Rev. Lett.* **92**, 050405 (2004).
[3] M. Albiez, *Phys. Rev. Lett.* **95**, 010402 (2005).

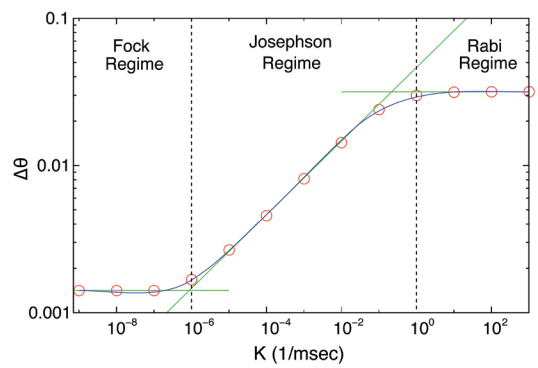

Fig. 2. ***Mach Zehnder phase sensitivity $\Delta\theta$ as given by Eq. 1, as a function of the tunneling coupling energy K. The green lines are the analytical predictions in three regimes: i) Rabi Regime, where $\Delta\theta \approx 1/\sqrt{N}$; ii) Josephson Regime, where $\Delta\theta \approx 1/N^{3/4}$; and iii) Fock Regime, where $\Delta\theta \approx 1/N$. Here N = 1000. The red circles are given by exact numerical solutions, while the blue line is an approximate, variational, calculation.***

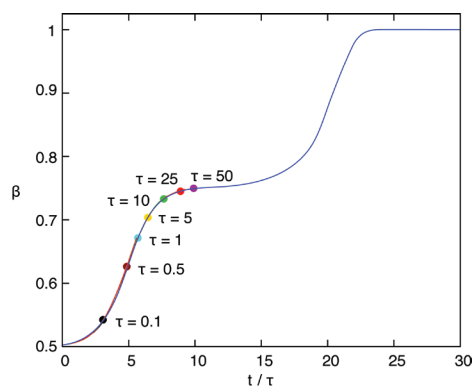

Fig. 3.
Plot of the scaling parameter β defined as $\Delta\theta = \alpha/N^{\beta}$, as a function of time. The calculation has been made with N = 1000 and N = 10000, particles. The blue line represents the adiabatic behavior; the points correspond to the minimum of MZ phase sensitivity occurring for different values of the effective ramping time τ (in msec), $\tau = \dfrac{\Delta t_{ramp}}{d_R\sqrt{V_0 - \mu}}$

with Δt_{ramp} the ramping time, d_R the final distance between the wells, V_0 the height of the potential barrier at the end of the splitting, and μ the chemical potential.

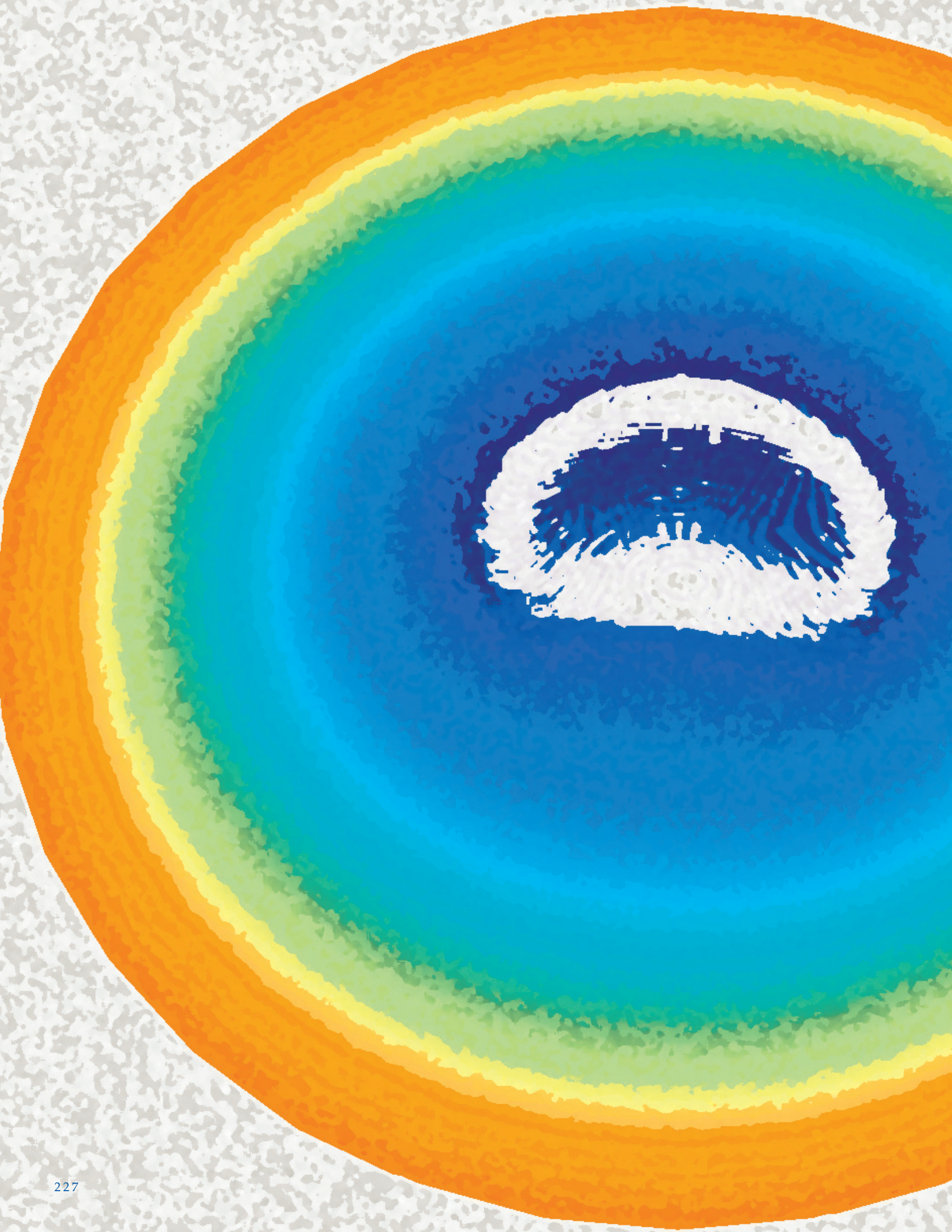

Plasma Theory T-15

Group Leader: Alan Glasser
505.667.7723; ahg@lanl.gov

T-15 Plasma Theory studies the theory of the fourth state of matter, plasma, or ionized gas, after solid, liquid, and gas. A major activity is computer modeling and simulation of plasmas, developing and applying such widely used codes as the NIMROD 3-D, nonlinear time-dependent simulation code for magnetically confined plasmas and the DCON code for rapid determination of the stability of axisymmetric toroidal plasmas. Numerical simulation of magnetized plasmas is particularly challenging because of the high degree of anisotropy and range of length and time scales. T-15 specializes in development of novel numerical methods to deal with this challenge.

A Nonlinear, Fully Coupled Moving Mesh Adaptive Grid Strategy

Luis Chacón and Giovanni Lapenta, T-15

In the numerical simulation of complex physical phenomena, the crucial requirement is predictability, i.e., that the simulation results remain faithful to the actual physical processes. Accordingly, the generation and accumulation of numerical error during the simulation is of special concern, since it introduces distortions that fundamentally alter the fidelity of the simulation. Errors resulting from a lack of spatial resolution are particularly deleterious. However, over-resolving is computationally expensive.

Adaptive grids attempt to provide sufficient resolution where needed while minimizing the computational cost of the simulation. Our emphasis is on moving grid methods (also known as *r*-refinement), where grid points are able to move to follow the solution. The grid positions are determined from a suitable grid evolution equation. While many grid evolution equations have been proposed in the literature [1], here we focus on harmonic maps [2], which are desirable because, under certain conditions, they guarantee the existence and uniqueness of the grid mapping. In two dimensions (2-D), for a scalar error monitor function $w(\vec{x},t)$, harmonic function theory results in Winslow's variable diffusion method grid evolution equation for $\xi(\vec{x})$, $\nabla\cdot(\frac{1}{\omega}\nabla\xi)=0$, with ξ the logical variable and x spanning the configuration space. The inverse of this equation [to determine $\vec{x}(\xi)$] can be readily expressed in terms of the contravariant metric tensor components $g^{ij}=\nabla\xi i\cdot\nabla\xi j$ and the Jacobian of the transformation $\vec{x}(\xi)$, J, as:

$$E(w,\vec{x})=\frac{\partial}{\partial\xi_i}\left(\frac{Jg^{ij}}{w}\right)=0\ ;\ j=1,2 \qquad (1)$$

This is the (nonlinear) grid evolution equation for a given error function w (which generally depends on the solution of a physical model) [3, 4]. For time-stepping problems, it is common to relax the elliptic constraint in Eq. 1 by introducing a time-dependent term. This is advantageous for numerical stability, as perturbations in the solution of Eq. 1 may grow undamped [5] to the point of folding the grid. Here, we employ the following choice:

$$E(\bar{w},\mathbf{x}^{n+1})=e^{-\Delta t/\tau}E^{n}(\bar{w},\mathbf{x}^{n})\ ;$$
$$\bar{w}=0.5(w^{n+1}+w^{n}), \qquad (2)$$

with τ an adjustable parameter, which in general we take proportional to the time step. It can be shown [5] that this choice appropriately damps arising perturbations while asymptotically satisfying Eq. 1 for $t \gg \tau$.

One drawback of harmonic function theory is that the resulting grid evolution equation is generally very nonlinear and stiff.

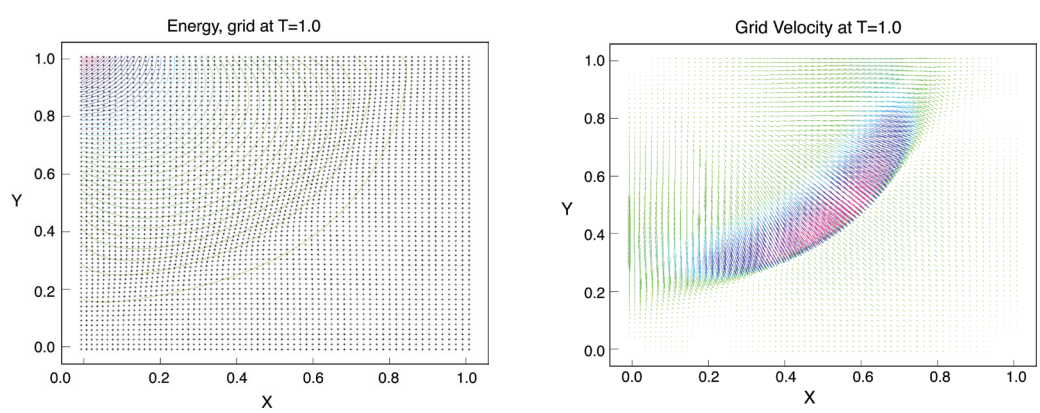

Fig. 1.
Snapshot of implicit moving mesh computation in a 128 x 128 grid.

Table 1. Grid convergence study for $\Delta t = 0.1$, $\tau = 2\Delta t$, reporting nonlinear (NLI), linear (GM) iterations per time step.

Grid	NLI/Δt	GM/Δt	CPU (s)
16x16	6	1	22
32x32	6	1	89
64x64	6	1.3	350
128x128	6	1.5	1396

Furthermore, physics models for which spatial adaptation is necessary are typically very stiff as well. For such systems, implicit temporal schemes are preferred for efficiency, as they allow one to use time steps comparable to the dynamical time scale of interest in the problem at hand. However, when coupled to a grid evolution equation, such large implicit time steps may not be advantageous from an accuracy standpoint unless both grid and physics equations are solved in coupled manner.

The coupled nonlinear solution of such physics-grid systems represents, however, a formidable numerical challenge. It is this challenge that we undertake in this research. At the heart of the matter is to demonstrate that developing a scalable, efficient nonlinear algorithm to solve such systems is indeed possible. We base our strategy on Newton-Krylov methods [6], which are ideally suited for this task owing to their robustness and the possibility of preconditioning. We employ a lagged-grid strategy for preconditioning, where the current grid generation step is based on the physics field at the previous Newton step. This is equivalent to the standard practice in the moving mesh community of splitting the grid generation step from the evolution of the physical system. Because this approach effectively decouples the grid and the physics in the preconditioner, it allows one to straightforwardly transfer successful preconditioning technologies in fixed grids to the moving mesh framework.

Such preconditioning approach requires an effective standalone solver for Eq. 2. This has been recently proposed in Ref. [7]. Here, we report on recent results that demonstrate that a scalable nonlinear solver for the coupled nonlinear physics-grid system in two dimensions is indeed possible. We focus on the equilibrium radiation-diffusion model in the matter-dominated regime as the physical system of interest, which is described by:

$$\partial_t T = \nabla \cdot (D_L \nabla E) \; ;$$

$$D_L^{-1} = \frac{3}{T^3} + \left| \frac{\nabla E}{E} \right| \; ; \; E = T^4,$$

where D_L is a limited nonlinear diffusion coefficient. We use a gradient-based error estimator,

$$w = \sqrt{1 + (\nabla T)^2}$$

as the monitor function in Eq. 2. We initialize the calculation with a bilinear profile in the temperature, with corner values in a 2-D domain given by: $T(0, 1) = 1.0$; $T(1, 1) = T(1, 0) = T(0, 0) = 0.2$.

The nonlinear evolution of this system results in an oblique front propagating from the top-left corner to bottom-right corner. A snapshot is shown in Fig. 1 (left). The corresponding grid velocity is shown in Fig. 1 (right), demonstrating that the nodes are indeed following the front. The grid convergence study in Table 1 demonstrates that the nonlinear solver scales optimally with grid refinement, with CPU proportional to the grid size. Future work will consider multimaterial configurations, the use of more rigorous error estimators, and the cost-effectiveness of this approach vs fixed grids.

For more information contact Luis Chacón at chacon@lanl.gov.

[1] V.D. Liseikin, *Grid Generation Methods* (Springer, Berlin, New York, 1999).
[2] A.S. Dvinsky, *J. Comput. Phys.* **95**, 450 (1991).
[3] G. Lapenta, Int. *J. Numer. Meth. Engng.* **59**, 2065 (2004).
[4] G. Lapenta, *J. Comput. Phys.* **193,** 159 (2004).
[5] W. Huang, et al., *SIAM J. Numer. Anal.* **31,** 709 (1994).
[6] C.T. Kelley, *Iterative Methods for Linear and Nonlinear Equations* (SIAM, Philadelphia, 1995).
[7] L. Chacón and G. Lapenta, *J. Comput. Phys.* **212** (2), 703 (2006).

Single Helicity States in Reversed Field Pinches

Gian Luca Delzanno, Luis Chacón, and John M. Finn, T-15

The Reversed Field Pinch (RFP), like the tokamak and the stellarator, belongs to the family of toroidal devices for fusion energy where a toroidal plasma is magnetically confined. However, the RFP differs from a tokamak in several aspects [1]. First, the toroidal and poloidal magnetic fields are of the same order, mainly generated by currents inside the plasma. Second, the poloidal currents in the plasma are sustained by a dynamo mechanism. Third, the toroidal magnetic field becomes negative at the edge of the plasma such that the safety factor profile q (winding number of field lines) is a decreasing function of radius, starting typically from q(r = 0) ~0.1 and reversing sign at the edge. For this reason, the RFP is subject to several magnetohydrodynamic (MHD) instabilities with poloidal mode number m = 1 and various toroidal mode number n (depending of the aspect ratio R/a of the machine, where *R* and *a* are the major and minor radius of the torus, respectively).

For several decades the RFP has been considered a device with bad plasma confinement properties, characterized by a turbulent state with magnetic field line chaos. This state, characterized by a wide spectrum of modes fluctuating with similar amplitudes, is known as the multiple helicity state. However, recent experimental results (motivated by numerical simulations of the early nineties [2]) have shown a new paradigm for the RFP: under certain conditions, the plasma can achieve the so-called quasi-single helicity state, namely a state where the mode spectrum is dominated by a ($m = 1$, $n = n_0$) mode while the other modes are fluctuating at much smaller amplitude [3]. The quasi-single helicity state has been observed in several experiments (with fairly different characteristics) throughout the world such that this result is now considered very solid. More important, the quasi-single helicity state is characterized by improved flux surfaces and less magnetic chaos and turbulence, which mean better confinement properties.

It is worth mentioning at this point that the RFP with strong improvement of the plasma confinement can be really interesting for fusion applications. In fact, RFPs do not require the toroidal field coils to be superconducting (since the confinement field is produced mainly by the plasma), can reach high β (ratio of internal energy to magnetic field energy), thus reducing the amplitude of the confining field. They are also are very compact and can reach thermonuclear temperatures without additional heating (due to the higher ohmic dissipation and higher currents with respect to the tokamak) [4].

Given the premise above, the work conducted within the T-15 Plasma Theory Group is devoted to understand the reasons leading to the transition from multiple helicity states to quasi-single helicity states. The task is addressed through three-dimensional visco-resistive MHD simulations with the code PIXIE3D [5]. This code has been developed in T-15 by L. Chacón. It is parallel, fully implicit, and written in curvilinear geometry such that it is possible to run it in various geometries (of particular interest for the present study are the helical, cylindrical, and toroidal geometries).

The simulations are conducted by starting from the paramagnetic pinch equilibrium. This is a cylindrical equilibrium where the axial magnetic field at the edge of the plasma is not reversed. The paramagnetic pinch is the typical choice when describing the start-up scenario of the RFP and is subject to several ($m = 1$, n) instabilities (see Fig. 1).

As the mode grows, the cylindrical symmetry is lost and the plasma column becomes helically distorted.

Furthermore, the toroidal magnetic field decreases at the edge and becomes reversed (and so does the safety factor profile q). As a result of toroidal flux conservation, the mean-field q profile grows at r = 0 (see Fig. 2), thus changing the position where the linearly unstable modes are resonant. The helical flux reveals a very interesting nonlinear dynamics property, in which the separatrix characteristic of the resonant mode disappears as the island grows (see Fig. 3). The final aim of the work consists in applying external forcing to the device such to have a stationary single-helicity state in the plasma over a wider range of parameters.

For more information contact Gian Luca Delzanno at delzanno@lanl.gov.

[1] D.D. Biskamp, *Nonlinear Magnetohydrodynamics* (Cambridge, Cambridge University Press, 1993).
[2] J.M. Finn, et al., *Phys. Fluids B* **4**, 5 (1992).
[3] P. Martin et al., *Nucl. Fusion* **43**, 1855 (2003).
[4] D.F. Escande, "Magnetic Self-organization in the Reversed-field Pinch," to be published (2006).
[5] L. Chacón, Comp. *Phys. Comm.* **163**, (3), 143 (2004).

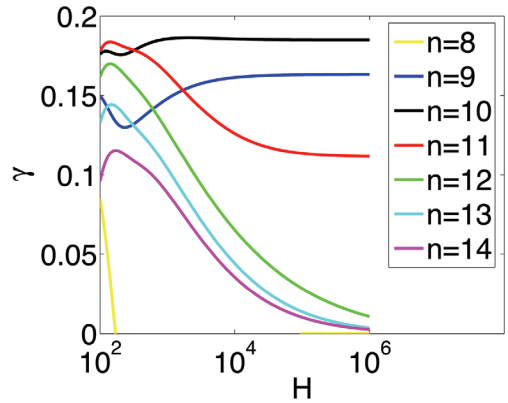

Fig. 1. *Stability analysis of the paramagnetic pinch. Several modes are simultaneously unstable for a wide range of Hartmann number.*

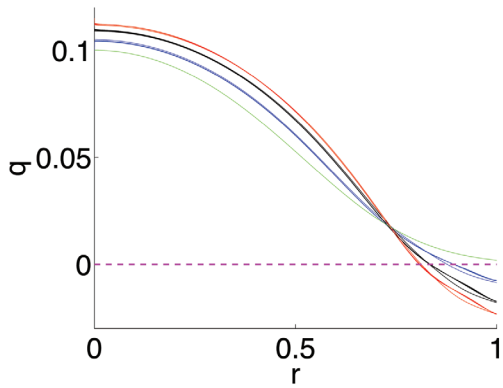

Fig. 2. *Mean-field q profile computed from the saturated state of various runs with PIX-IE3D. Only a single helicity is present: (m = 1, n = 9) blue, (m = 1, n = 10) black and (m = 1, n = 11) red. The green curve is obtained for the paramagnetic pinch equilibrium.*

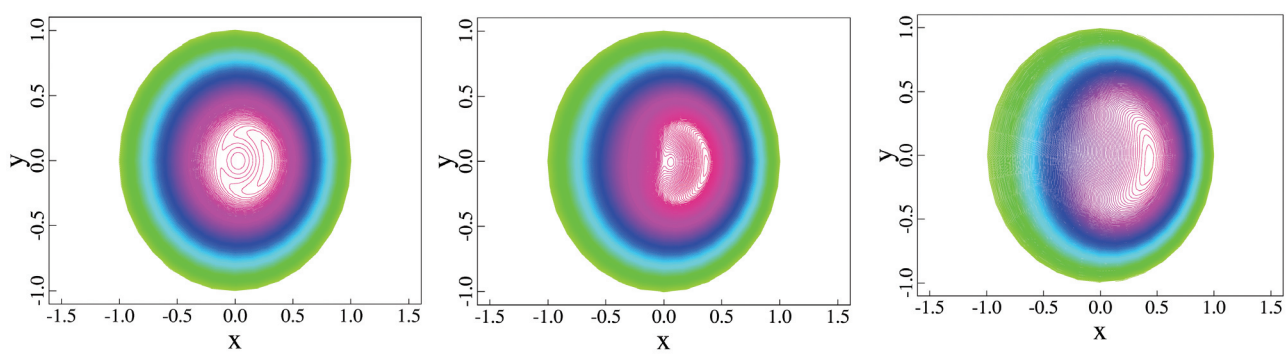

Fig. 3. *Evolution of the helical flux for a single helicity run with (m = 1, n = 11).*

Kink Stability with Line Tying

Evstati G. Evstatiev, Gian Luca Delzanno, and John M. Finn, T-15

An important and still open physical problem is the one of solar flares and coronal mass ejections. A related problem is the formation of astrophysical jets. It is thought that the main reason for the stability of the solar loops is the effective anchoring of their footpoints in the much denser and highly conducting layer of the sun, the photosphere. (See Fig. 1.) The magnetic field lines immersed in the photosphere produce a stabilizing effect, line tying. However, for sufficient footpoint twisting, instability is expected to occur in spite of line tying, and the associated magnetic reconnection is thought to be responsible for flares.

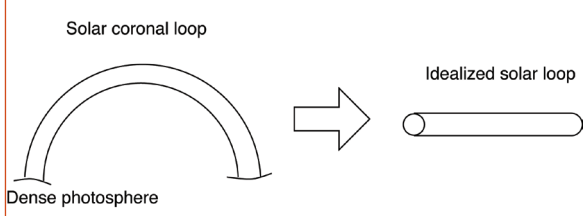

Fig. 1. ***Solar coronal loop and an idealized cylinder model.***

For the study of this problem, experiments as shown in Fig. 2 have been constructed [1, 2]. The curvature of the loop has been neglected because it is of secondary importance for the stability study. The plasma column is created inside the cavity of the device and a strong external axial magnetic field is imposed. Current is run from one end to the other, thus creating poloidal magnetic field. As the current is gradually increased, the poloidal magnetic field increases correspondingly. Past a certain value of the current the plasma column becomes unstable. The main instability is the kink instability—the plasma column bends as in Fig. 3. As the instability develops and becomes nonlinear, the configuration reaches a point where magnetic lines can reconnect and possibly form current sheets, see Fig. 4.

Theoretically the studies to date are either mostly numerical, involve overly simplified models, or only determine sufficient conditions for the instability. We propose a new semianalytical method for linear stability study based on expansion in radial eigenfunctions. Temporarily considering the growth rate γ to be given, the radial eigenfunctions and their corresponding eigenvalues, the axial wavenumbers k, possibly complex, are found. Summing over a small number of eigenfunctions, the value of γ is adjusted until the boundary conditions at the two end conducting plates are satisfied. A strong point of our method is that it allows us to better understand the importance of the individual eigenmodes. It is also computationally more efficient than a two-dimensional code since at each stage only ordinary differential equations are solved.

Linear theory suggests that in an infinitely long cylinder the instability leads to the formation of a current sheet. For a finite length and line-tied boundary conditions, however, it is still an open question whether a current sheet forms or not. Different authors have argued in favor of both. The new method allows a better understanding of how the instability develops and

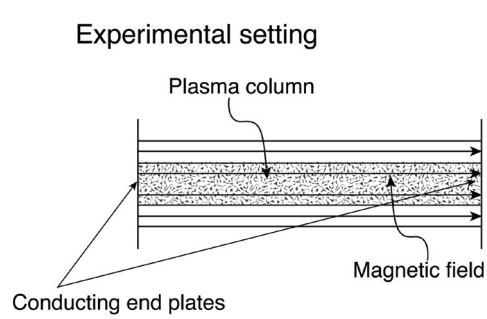

Fig. 2. ***Experiment on stability of a plasma column.***

what are the important regimes that could possibly lead to current sheet formation. The results so far suggest that a long loop will have current sheets where indicated by linear theory, but shorter loops may develop current sheets nonlinearly as the topology of the field changes, see Fig. 4. The issue of development of current sheets in such configurations is generally called the Parker problem.

For more information contact Evstati G. Evstatiev at eevstatiev@lanl.gov.

[1] I. Furno, et al., *Rev. Sci. Instruments* **74,** 2324–2331 (2003).
[2] W.F. Bergerson, et al., *Phys. Rev. Lett.* **96,** 015004/1–4 (2006).

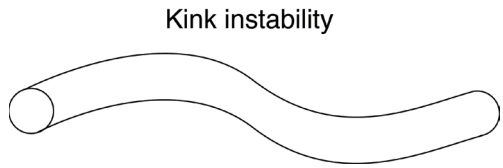

Fig. 3. ***Linear stage of the kink instability.***

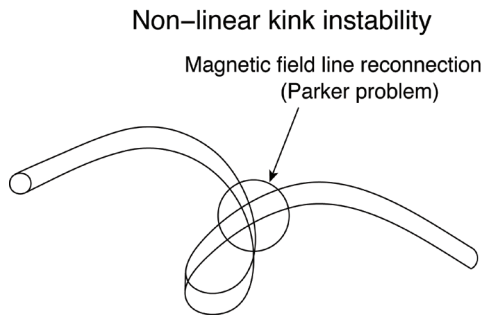

Fig. 4. ***Nonlinear stage of the kink instability.***

Regression in the Presence of Strongly Correlated Data

Christopher S. Jones and John M. Finn, T-15; and Nicolas Hengartner, D-1

In plasma equilibrium reconstruction in plasmas one attempts to find equilibrium parameters that give the best fit to a set of experimental measurements, such as the magnetic field at the boundary or internal pressure measurements. This reconstruction problem is patently nonlinear in its parameters because of the nonlinearity in the magnetohydrodynamic (MHD) equilibrium equation, the Grad-Shafranov equation. We have studied the effect of correlations on the equilibrium reconstruction problem [1]. These correlated errors represent fluctuations in the data due to shorter time scale physical processes in the plasma, and were treated as correlated gaussian noise. We observed that the fit becomes perfect in the limit of large correlations. The quality of the fit was measured by the covariance matrix of the parameters, or in Bayesian language, the *posterior covariance matrix* $\mathbf{C}_p$. The case studied in [1] had noise characterized by a single parameter, the *correlation length* δ. In terms of δ, Cp was, quite surprisingly, found to go to zero in the limit of perfect correlation $\delta \to \infty$. Thus, if the physical processes that are modeled as noise are highly correlated in space, the estimate may be much better than expected.

More recently, we have performed analysis to understand better this result and determine its range of validity. We have found that it occurs as well in linear estimation, i.e., linear regression, and we have studied the linear version because the effect is most transparent there. We have found that if the data can indeed be described in terms of a single parameter δ, the best linear unbiased estimate in the limit $\delta \to \infty$ generically gives $\mathbf{C}_p \to 0$.

The simplest form of this effect occurs when measuring a single variable a with repeated correlated measurements. That is, we have, for $i = 1, \ldots, n$,

$$y_i = a + \eta i;$$

the noise η_i has zero mean and a data covariance matrix $C_{ij} = \sigma_i \sigma_j R_{ij}$, with $R_{ij} = \varepsilon^{|i-j|}$. In terms of the correlation length, the correlation parameter ε equals $\varepsilon^{-\Delta/\delta}$, where Δ is the distance (in space or time) between successive measurements. The parameters σ_i are the standard deviations of the individual errors and R_{ij} is the matrix of correlations.

These data are of the form

$$\mathbf{y} = \mathbf{X}\mathbf{a} + \eta,$$

where $\mathbf{X}$ is the design matrix and $\mathbf{a} = (a_l, \ldots, a_m$ for $m < n$ is the estimate. For (Eq. 1), i.e., $m = 1$, $n = 2$, and $\mathbf{X} = (1, 1)^T$, we recover the familiar weighted least squares result for $\varepsilon = 0$

$$a_e = \frac{y_1/\sigma_1^2 + y_2/\sigma_2^2}{1/\sigma_1^2 + 1/\sigma_2^2}; \quad V_p = \frac{1}{1/\sigma_1^2 + 1/\sigma_2^2},$$

where V_p is the posterior variance. For the generic case $\sigma_1 \neq \sigma_2$ and $\varepsilon \to 1$, we have

$$a_e \to \frac{y_1/\sigma_1 - y_2/\sigma_2}{1/\sigma_1 - 1/\sigma_2}; \quad V_p \to \frac{2(1-\epsilon)}{(1/\sigma_1 - 1/\sigma_2)^2}.$$

Note that $V_p \to 0$ as $\varepsilon \to 1$. Also, if we assume $\sigma_2 > \sigma_1$ without loss of generality, then y_2 has *negative weighting*. That is, the estimate a_e is outside the range of the data (y_1, y_2). The exception to this rule is when $\sigma_1 = \sigma_2$. The posterior variance V_p as a function of the correlation ε is shown in Fig. 1; for all cases except $\sigma_2 = \sigma_1$, V_p increases for small ε and decreases to zero as $\varepsilon \to 1$. For this case, negative weighting occurs for ε to the right of the peak of V_p.

Negative weighting has been observed in the nuclear data community, where it is discussed — but without mention of the result $V_p \rightarrow 0$ — in the context of *Peelle's pertinent puzzle* [2, 3].

The generalization of this result to arbitrary *m, n* is that the *m x m* posterior covariance matrix $\mathbf{C}_p$ goes to zero except for the special cases when the vector of variations ($\sigma_1, \ldots, \sigma_n$) is in the range space of the design matrix **X**. Since this possibility is measure zero, the result $\mathbf{C}_p \rightarrow 0$ holds generically.

For more information contact Christopher S. Jones at csjones@lanl.gov.

[1] C.S. Jones and J.M. Finn, *Nucl. Fusion* **46**, 335–349 (2006).
[2] G. D'Agostini, *Nucl. Instr. Meth. Phys. Res.* **346**, 306 (1994).
[3] K.M. Hanson, et al., "Probabilistic Interpretation of Peelle's Pertinent Puzzle and Its Resolution," *Proc. Int. Conf. Nuc. Data Sci. and Tech.*, R.C. Haight, et al., Eds., *AIP Conf. Proc.* **769**, 304–307 (AIP, Melville, 2005).

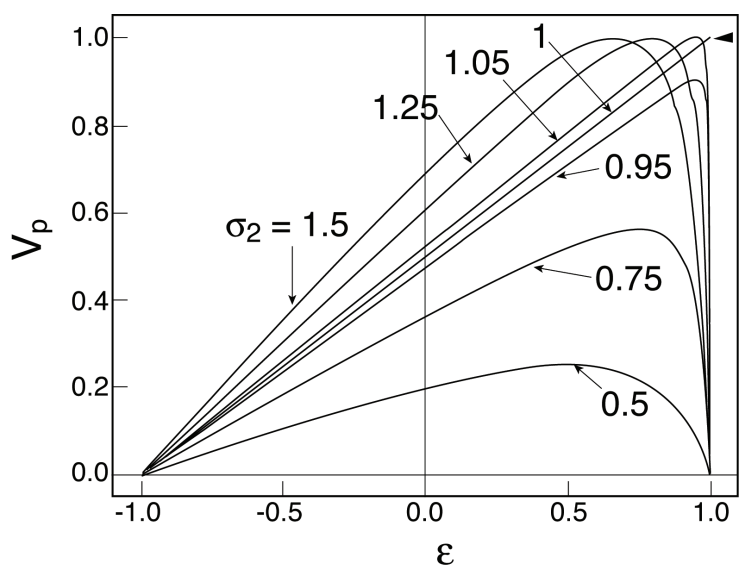

Fig. 1. ***Variance V_p as a function of ε for 7 values of σ_2 (0.5, 0.75, 0.95, 1, 1.05, 1.25, 1.5) and $\sigma_1 = 1$. For $\sigma_2 \neq \sigma_1$, $V_p \rightarrow 0$ as $\varepsilon \rightarrow 1$.***

Electrostatic Fields Mediate Micro/Macro Coupling in Plasmas

Giovanni Lapenta, T-15; William Daughton, X-1; Thomas Intrator, P-24; and Benoit Lavraud, ISR-1

A crucial issue in modern physics is the ability to understand and model the coupling existing between large-scale and small-scale processes in nature and in the laboratory. In plasma physics, the issue can be best understood considering the simple picture of electric conductivity. We all learn in high school that electrical resistivity arises from collisions of electrons with the nuclei of the atoms forming the conducting materials. In very hot materials, the 4th state of matter, called plasma, is reached. Plasmas are nearly perfect superconductors and collisions are often nearly totally absent. Yet observations prove without doubt that plasmas display a behavior that is consistent with the presence of yet mysterious dissipation processes. Such processes are called "anomalous" for their unexplained nature.

Since the realization of the existence of such processes in natural and man-made plasmas, the scientific community has tried to arrive at an explanation of how such anomalous processes can be explained. Their origin is firmly established to come from the coupling of macroscopic processes with small-scale microinstabilities. But how are the microinstabilities affecting large-scale processes?

The dominant paradigm for the last few decades has been that of microscopic turbulence. The idea was that microinstabilities are seen by the plasma particles just like the collisions in the simple high school electrical conductor picture. Small-scale fluctuations in the electric field due to the microinstabilities scatter the electrons in the plasma and act just as collisions would, providing the needed dissipations. The explanation was compelling but the lack of theoretical or experimental confirmation for such a theory has been puzzling. In space and laboratory experiments, the lack of a clear link between fluctuations due to microinstabilities and anomalous effects has been proven in a number of works over the last 30 years.

We have now provided a possible alternative view. In a recent letter published by *Physical Review Letters* [2], we have discovered via simulations a new effect. We have conducted the largest ever kinetic plasma simulation, on the Q machine, and we have used our unique implicit kinetic plasma simulation code CELESTE to test via direct simulation the physics of micro-macro coupling.

The discovery is that the microinstabilities create directly a large-scale electrostatic field. The electrostatic field is macroscopic but is created by microscopic processes. The mechanism for such a remarkable effect is related to the action of the microinstabilities on the particle (specifically on the ion) trajectories. Unlike the effective collisions postulated by the old paradigm, the effect is now coherent and leads directly to a macroscopic alteration.

We report one instance of the creation of the large-scale electrostatic field in the Fig. 1. The small-scale instabilities are seen in the graininess of the data and are due to the so-called lower hybrid drift instability created by the density gradients present in the plasma [3].

Ongoing work is trying to determine whether our new paradigm can really apply in nature. We are conducting a data analysis campaign in collaboration with the Space Science and Applications Group (ISR-1) to identify the signature of our new model in satellite observations. We are also collaborating with the Plasma Physics Group (P-24) to conduct direct laboratory observations to detect the newly discovered electrostatic field.

For more information contact Giovanni Lapenta at lapenta@lanl.gov.

[1] G. Lapenta, *Space Sci. Rev.* **107**, 167 (2003).
[2] W. Daughton, et al., *Phys. Rev. Lett.* **93**, 105004 (2004).
[3] G. Lapenta, et al., *Phys. Plasmas* **10,** 1577 (2003).

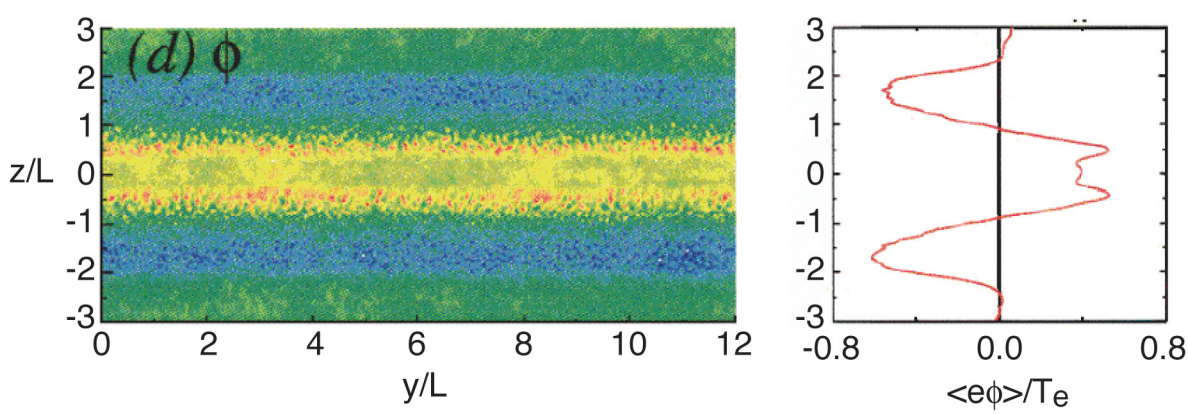

Fig. 1. ***Electrostatic potential formed by the large-scale consequences of microinstabilites. The averaged profile (red) is shown on the right. The crucial point is that the small-scale instabilities (observed in the graininess of the figure) lead directly to a large-scale electrostatic field.***

Virtual Nanoscience Laboratory: A Tool for the Mesoscale Simulation of Nanomaterials

Giovanni Lapenta and Gianluca Zuccaro, T-15

On December 3, 2003, the President signed the 21st Century Nanotechnology Research and Development Act, assigning $3.7 billion dollars for FY 2005–2008 to nanotechnology R&D. This bipartisan legislation, that passed the House and the Senate with overwhelming support, recognizes the need to focus the efforts of the scientific community to make progress in the development and understanding of nanoscience.

The emerging fields of nanoscale science, engineering, and technology — the ability to work at the molecular level, atom by atom, to create large structures with fundamentally new properties and functions — are leading to unprecedented understanding and control over the basic building blocks and properties of all natural and man-made things. The word technological revolution is often used in relation with the current research and development of nanotechnologies.

An enumeration of the areas interested by nanotechnology would resemble the phone book. For the Laboratory and DOE, nanoscience is not only important for its relevance to strategic science but also for the interest towards material science applied to stockpile stewardship. Furthermore, chemical and biological threats can be hidden within new developments in nanotechnologies. It should be emphasized that indeed DOE is one of the five agencies involved in the 21st Century Nanotechnology Research and Development Act.

We have recently initiated an international collaboration with the Polytechnic University of Turin in Italy and with the Sumitomo Company in Japan, to develop a new computer simulation capability for nanoscale processes. We are developing the Virtual Nanoscience Laboratory that can provide the nanoscience community with a tool for the simulation of processes that live in the cross-linked area covered by atomistic, nano, and bulk scales. Nanomaterials are by definition materials where the intrinsic scales link at the lower end the atom scale and at the higher end the macroscopic continuum scale. Neither approach is sufficient: too many atoms are involved to make a pure atomistic model viable and too many structures and processes at the nano and subnano scale are important to simply resort to continuum models. New theories and new numerical approaches have to be devised.

To address the presence of such diverse time and length scales and the multiplicity of physical processes, we have proposed a new approach [1]. We bridge the gap by interlinking three numerical schemes: Molecular Dynamics (MD) for the smallest (atomistic) scales, Particle-In-Cell (PIC) for the intermediate (nano) scales and finite volume (FV) methods for the largest (bulk) scales. The key ingredient of the algorithm is the use of an intermediate scale between the nanoscale object and the atoms that compose it: we called it *cluster* (of atoms). With the use of computational clusters we designed an efficient scheme that allows us to bridge such diverse scales that range over several orders of magnitude.

A crucial innovation of the Virtual Nanoscience Laboratory is the use of a software architecture based on the Java language. This feature provides two advantages. The first is the ability to achieve remarkable parallel performances thanks to the innovations introduced in the object-oriented

Java programming environment [2]. The second is to make the Virtual Nanoscience Laboratory available to anyone over the Web, the strongest feature of the Java language. We remark that our effort in the development of a new high-performance scientific computing paradigm based on the Java language has been awarded the R&D 100 prize in 2005 with the CartaBlanca team.

To illustrate the capability of the Virtual Nanoscience Laboratory, we present results of a recent application of this approach to the simulation of nanoparticles formation in self-propagating high-temperature synthesis process (SHS) reactors [1]. The SHS is a promising method employed for the synthesis of many advanced nanomaterials, such as ceramics, intermetallics, composites, starting from a powders mixture formed by compacting micron-sized pellets. The SHS exploits the ability of certain material mixtures in producing high exothermic and self-sustaining reactions once ignited locally or uniformly. Ignition can be initiated by a laser, by induction, by resistance, by radiant heat, or by a spark source. The exothermal reaction increases the temperature rapidly producing the combustion of the micron-sized particles and the formation of much smaller non-sized particles.

For more information contact Giovanni Lapenta at lapenta@lanl.gov.

[1] G. Zuccaro, et al., *Comput. Phys. Comm.* **162**, 89 (2004).
[2] S. Markidis, et al., *Concurrency and Computation: Practice and Experience* **17**, 821 (2005).

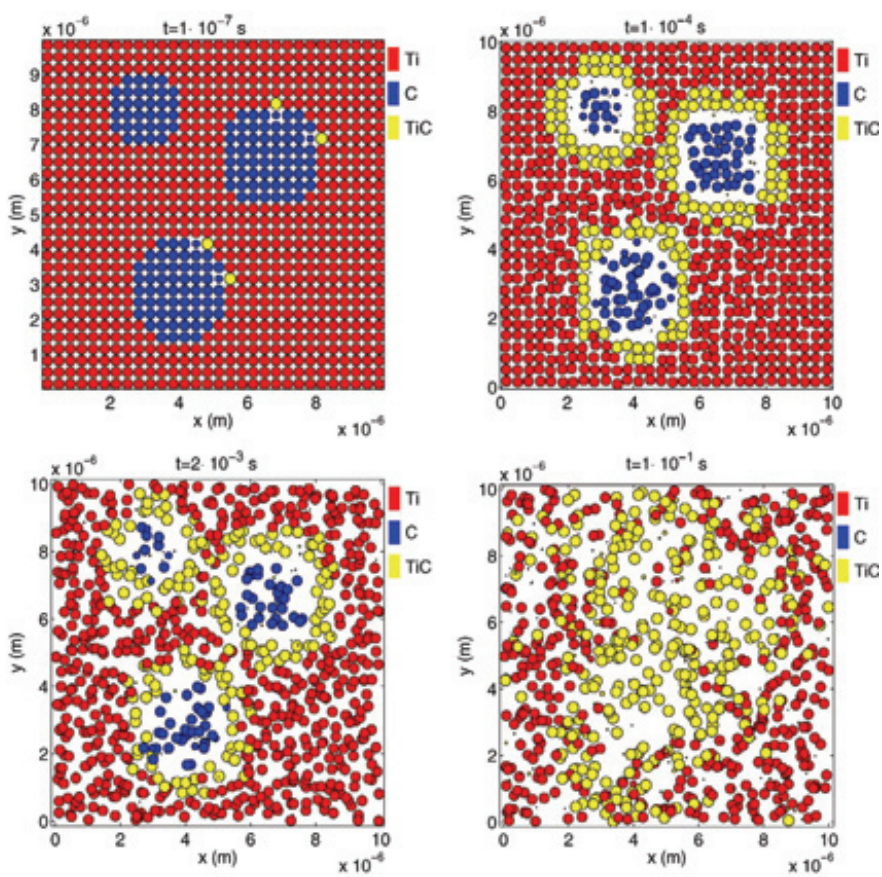

Fig. 1. ***Evolution of the SHS process, showing the disintegration of the carbon microparticles (blue) and the formation of the TiC nanoparticles (yellow). The reacting Ti is in red.***

NUTHELLA: A Simulation Tool for Generation IV Nuclear Reactors

Giovanni Lapenta, T-15

Access to energy is one of the pillars of civilization. How energy is generated contributes to defining a society. There is no doubt that we are at a critical point in the technological history of energy production. Legislation is being considered and passed to address the problem and serious policy decisions are being discussed and made that will shape the future of our society and of the environment. The duty of the scientific and technological community is to provide the public with reliable tools to arrive at an informed decision about energy policy.

A viable and proven source of energy is nuclear fission. Current reactors are basically still based on concepts developed in the early days of nuclear engineering. The U.S. DOE and the energy authorities of the European Union, Japan, and other countries have launched the Generation IV initiative [1] to consider new reactor concepts that hold the promise of solving some or all of the perceived pitfalls of nuclear energy production. Two main issues to address are: availability of fissile material and disposal of radioactive waste. If energy is to be produced in larger fractions from nuclear energy, the available fuel for current reactors would be severely limited, if the current prevailing paradigm remains true. In current reactors, the fuel is used once and it is not reprocessed to avoid the risks involved in the procedure. Furthermore the burned nuclear fuel is highly radioactive and it remains so for geological times.

Among the Generation IV reactors, one category is particularly promising: fluid-fuel recirculated reactors, critical or subcritical driven by particle accelerators. In such reactors, the fuel is treated and fully consumed on site. The most problematic nuclear waste materials, the actinides, are destroyed in the nuclear reactions developing within the reactor. In one stroke, the concept solves the problem of the insufficient use of fresh uranium and of the disposal of long-term radioactive waste. This concept, as all others pursued within the Generation IV initiative, needs to be investigated and analyzed for future development. While many experimental and technological issues are of extreme importance, in particular material and chemistry issues, we focus here on the safety and control of the new concept. The use of fluid-fuels is a largely unexplored concept for nuclear engineering. In the early years of the golden age of nuclear engineering, the concept was considered with the pencil and paper tools of the time. We have taken upon ourselves to contribute to bringing this topic into the 21st century.

In our previous experience within the European fission energy program, we developed a new formulation of the fundamental mathematical model for fluid-fuel reactors [2]. As can be expected, the model mixes complex physical processes including heat transfer, fluid dynamics, and neutron transport. The model is particularly challenging as the scales involved in such diverse processes cover many orders of magnitude.

We addressed such a very challenging multiphysics and multiscale process using some of the most modern simulation techniques. We are developing a new fully implicit coupled thermodynamics-fluid dynamics-neutronics code, NUTHELLA [3]. The key aspect of our approach is the use of the Newton-Krylov method to solve the highly nonlinear coupled equations of the model. Furthermore, we have developed a new predictor-corrector

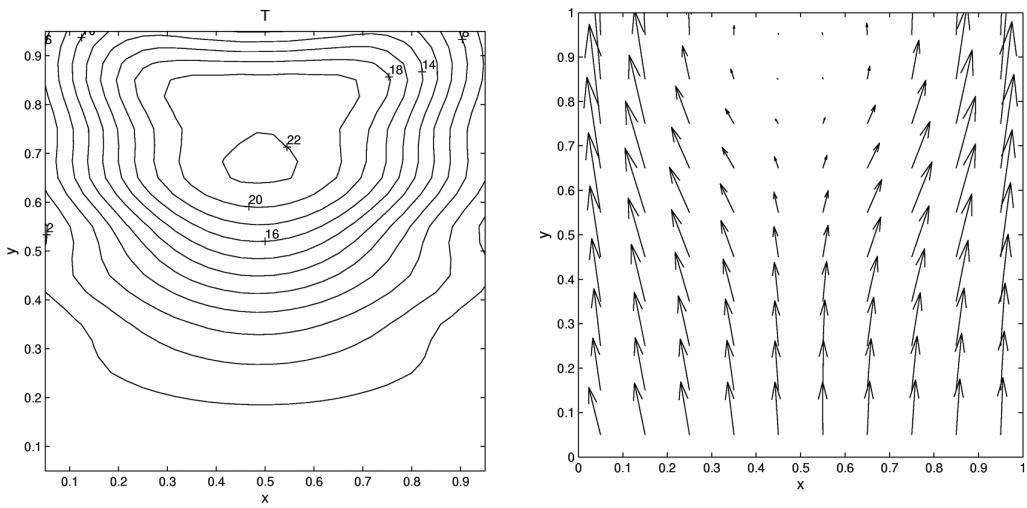

Fig. 1.
Typical result of the new NUT-HELLA code. Flow pattern (right figure) and temperature (left figure) on a vertical section a fluid fuel reactor. The temperature is in Kelvin above average and the flow speed is proportional to the arrow length.

preconditioning technique to increase the efficiency of the method [4].

Below we show a typical reactor state computed with the new code. In the example, an abnormal transient leads to localized temperature intensification. A vicious cycle is created, where the hot region diverts the flow and heats up further. This dangerous possibility is avoided in current designs by the addition of flow guiding walls that prevent the flow from being diverted away from hot spots. This is but an example of the predictive capability of our new code that can be used for the design and operation of fluid-fuel nuclear reactors.

For more information contact Giovanni Lapenta at lapenta@lanl.gov.

[1] http://gen-iv.ne.doe.gov/
[2] G. Lapenta and P. Ravetto, "Neutron Model for the Safety Assessment of Actinide Burners with Circulating Fuel," *9th International Conference on Emerging Nuclear Energy Systems ICENES'98* (1998).
[3] G. Lapenta, "Mathematical Models of the Coupling of Neutronics and Thermal-Hydrodynamics in Circulating Fuel Nuclear Reactors," *M&C 2005: Mathematics and Computation, Supercomputing, Reactor Physics and Nuclear Biological Applications* (2005).
[4] G. Lapenta, J. Jianwei, "Predictor-Corrector Preconditioners for Newton-Krylov Solvers," *J. Comput. Phys.*, submitted.

PARSEK: A New Integrated Package for Plasma Simulation Based on Particles

Giovanni Lapenta and Stephano Markidis, T-15

Plasma physics involves a multiplicity of processes and scales that require a multiplicity of models. We are developing a new tool designed to address such complexity by resorting to a common approach: the use of particle algorithms. The applications of plasma simulation include the new international fusion reactor device ITER [1], laser-plasma interaction, space and astrophysical problems, and industrial applications in the field of material science and processes.

Plasma simulation requires the study of a N-body problem from its most fundamental single particle level, to the kinetic level, and finally to the fluid level. Our aim is to use a single algorithm and software paradigm capable of describing all levels for a given system. We focus our attention to particle algorithms. While other methods might be more popular at some level of description, particle-based methods are commonly and widely in use at all levels of description.

Table 1 reports the crucial features of the different levels of description relevant to the present study. All methods are characterized by four fundamental ingredients: the definition of the particle, of the fields, of the direct interactions (pair interactions or collisions among the particles) and of the interactions mediated by the fields. All methods listed in Table 1 are widely used in the scientific and engineering community and all are available to the proposing team in the form of highly successful and extensively used codes.

Based on this approach we have developed a new software environment, PARSEK [2], that includes modules and tools for particle simulation at all levels described in Table 1. The project is ongoing but a number of published concrete results are already available. The approach is unique in two respects.

First, the methods involved are all available and solidly tested. We are not developing new numerical algorithms but are using previously available tools. Furthermore, the methods used are already available to us from previous computer codes developed at the Laboratory over the years. This is a crucial point, as computer codes are not the simple backbone algorithms published in journals but rather are complex organisms composed of parts whose function might not be immediately recognized. By relying on previous codes we are inheriting a whole expertise and not just method.

Table 1. The different levels of description widely used in the scientific and engineering community.

Method	Particle	Field	Particle-Particle interaction	Particle-Field interaction
Particle-Particle (PP)	Physical particle	NO	collisions	NO
Particle-Particle, Particle-Mesh (P^3M)	Physical particle	E,B	collisions	Lorentz
Particle-Mesh (PM)	Element of phase space (sample)	E,B	NO	Lorentz
Fluid PIC	Element of fluid	E,B,n,v,T,…	SPH	Lorentz, Drift,…

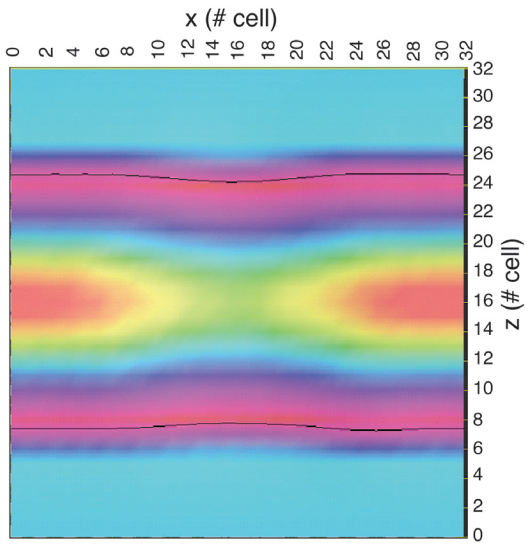

Fig. 1.
GEM Challenge [1]: plot of the electromagnetic vector potential where the formation of a magnetic island in a current sheet is observed as the red area (periodic boundary conditions are used).

An added benefit of our approach is the large previous body of verification and validation efforts involved.

Second, the specific tools we use are based on implicit algorithm. In particular, at the kinetic level we use the CELESTE implicit PM moment algorithm [1]. At the fluid level we use the implicit fluid PIC method, FLIP [2]. Both approaches were developed at the Laboratory and are uniquely available here. Such tools are proven in their ability to handle multiple scales in space and time. In the last decade, the two codes have been used extensively and their properties are tested and proven.

An example of the use of PARSEK is shown. Figure 1 shows the formation of a magnetic island in the classic GEM Challenge benchmark [1]. The electromagnetic vector potential is displayed in a false color scale, and the island is shown by the red area (periodic boundary conditions are used). For the same problem Fig. 2 shows the parallel performance.

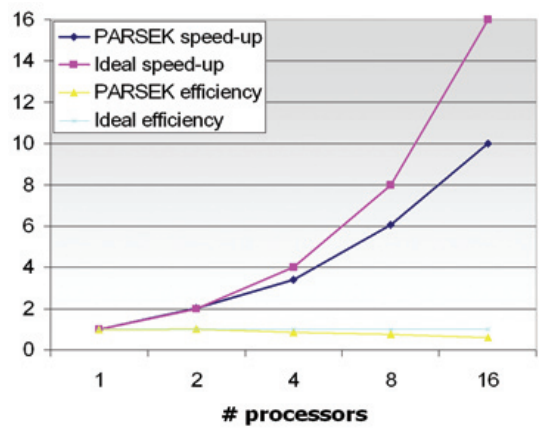

Fig. 2.
PARSEK: parallel performance on the T-15 cluster.

For more information contact Giovanni Lapenta at lapenta@lanl.gov.

[1] G. Lapenta, et al., "Kinetic Approach to Microscopic-macroscopic Coupling in Space and Laboratory Plasmas," *Phys. Plasmas*, submitted 2005.
[2] G. Lapenta, S. Markidis, *Lecture Notes in Comput. Sci.*, **3516**, 88 (2005).

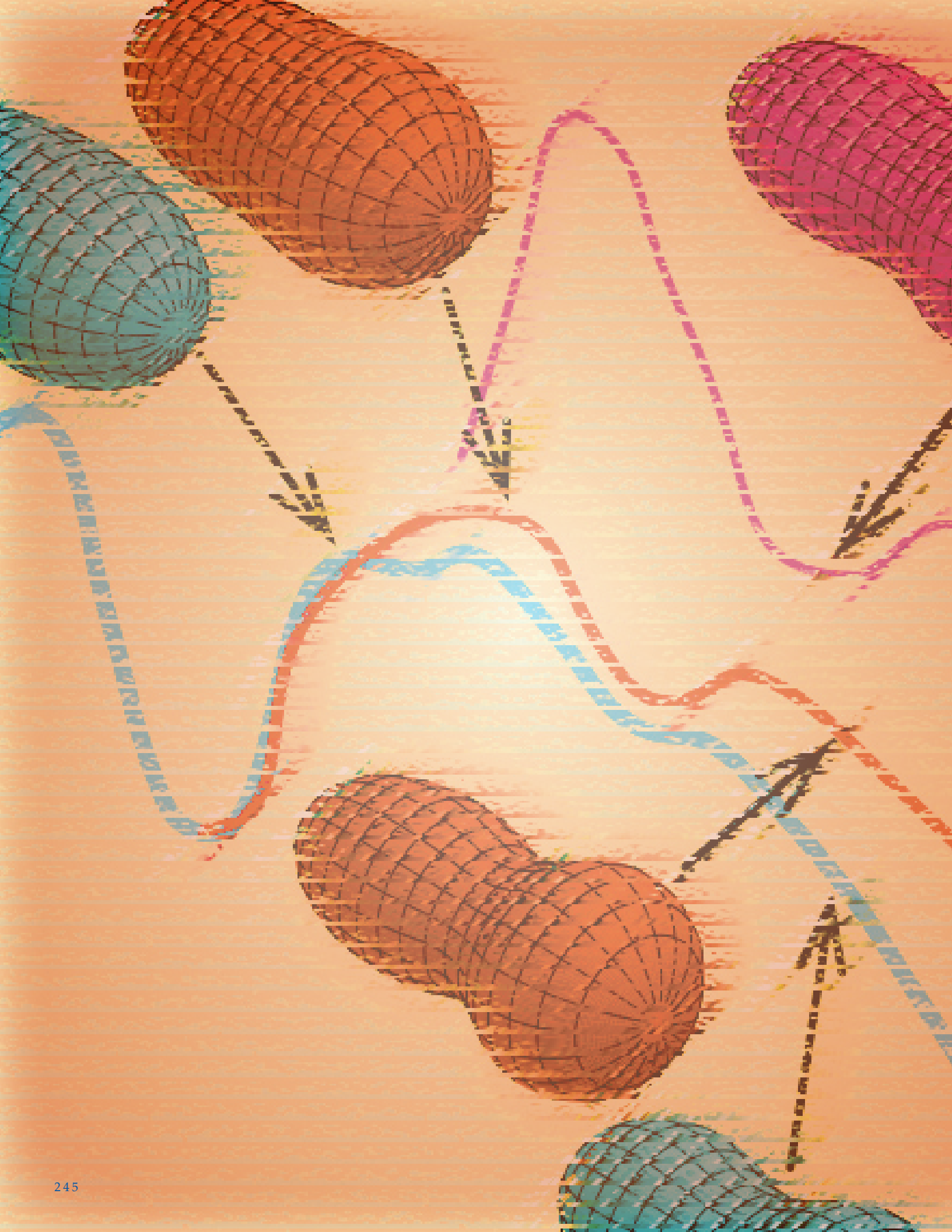

Nuclear Physics T-16

Group Leader: Joe Carlson
505.667.6245; carlson@lanl.gov

The Nuclear Physics Group (T-16) covers a wide range of basic and applied nuclear physics relevant to the Laboratory, NNSA, and the Department of Energy (DOE). Basic nuclear physics research includes few-body to many-body nuclear physics including nuclear structure and reactions; quantum chromodynamics (QCD) at high density in astrophysics and at high energy-density addressing relativistic heavy ion collider physics; nuclear astrophysics; and neutrino physics and fundamental symmetries. The theory effort is closely tied to the Laboratory and DOE experimental nuclear physics programs. Applied nuclear physics encompasses nuclear physics relevant to Threat Reduction and Stockpile Stewardship, including fission theory, reaction theory, and sensitivity studies; and analyzing and testing nuclear data for the Laboratory and the nation. Current efforts include modeling of nuclear cross-sections and spectra; improving fission theories; developing codes and libraries for transmutation and radioactivity calculations, and processing and testing nuclear data for use in radiation transport codes. T-16 maintains close ties with leading university and national laboratory groups in both basic and applied theory.

Symmetry of the Relativistic Quantum Mechanical Harmonic Oscillator and the Antinucleon Spectrum in Nuclei

Joseph N. Ginocchio, T-16

As is well-known, the nonrelativistic spherical harmonic oscillator has degeneracies in addition to those due to rotational invariance. The energy spectrum depends only on the *total* harmonic oscillator quantum number N, $N = 2n + \ell$, where n is the radial quantum number and ℓ is the orbital angular momentum. Hence, the states with $\ell = N, N-2, \ldots 0$ or 1 have the same energy. These degeneracies are produced by an U(3) symmetry which has been influential in connecting the shell model with collective motion. Also the energy does not depend on the orientation of the spin and hence the nonrelativistic harmonic oscillator has a spin symmetry as well.

Since relativistic models of nuclei are now so prevalent [1], we can ask if U(3) symmetry resides in the relativistic harmonic oscillator. Indeed the Dirac Hamiltonian for which the scalar and vector potentials are equal and harmonic has been solved analytically and is invariant under a spin symmetry [2, 3]. Just as for the nonrelativistic harmonic oscillator, the spherically symmetric relativistic harmonic oscillator energy spectrum depends only on the total harmonic oscillator quantum number N, although the energy spectrum for the relativistic harmonic oscillator spectrum in general does not have a linear dependence on N as does the nonrelativistic harmonic oscillator. In Fig. 1 we plot the spherical harmonic oscillator Dirac binding energies E_D, the solid curve, as a function of N. We chose the harmonic oscillator strength to fit the lowest eigenenergies of the spectrum of an antiproton outside of ^{16}O in the relativistic mean field approximation [4]. The dashed curve is E_D in the pertubation approximation for large antiproton mass, which reduces to the nonrelativistic approximation. The short-dashed curve is E_D in the asymptotic limit for small mass and is the highly relativistic limit. Clearly the eigenenergies are in the relativistic asymptotic regime and not the linear regime of the nonrelativistic harmonic oscillator.

The fact that the relativistic spectrum depends only on N does suggest that the relativistic harmonic oscillator has an U(3) symmetry. We have shown that there is indeed a U(3) symmetry and we have derived the generators which commute with the Dirac Hamiltonian [5].

If speculation that an antinucleon can be bound inside a nucleus is valid [4], the antinucleon spectrum will have an approximate spin symmetry, and most likely an approximate U(3) symmetry, because the vector and scalar potentials are approximately equal and are very strong [2].

For more information contact Joseph N. Ginocchio at gino@lanl.gov.

[1] P. Ring, and D. Vretenar, "Extended Density Functionals in Nuclear Structure Physics," G. Lalazissis, Ed., *Lecture Notes in Physics* **641**, 219 (2004).
[2] J. N. Ginocchio, *Physics Reports* **414**, 165 (2005).
[3] J.N. Ginocchio, *Phys. Rev. C* **69**, 034318 (2004).
[4] T. Bürvenich, et al., *Phys. Lett. B* **542**, 261 (2002).
[5] J.N. Ginocchio, *Phys. Rev. Lett.* **95**, 252501 (2005).

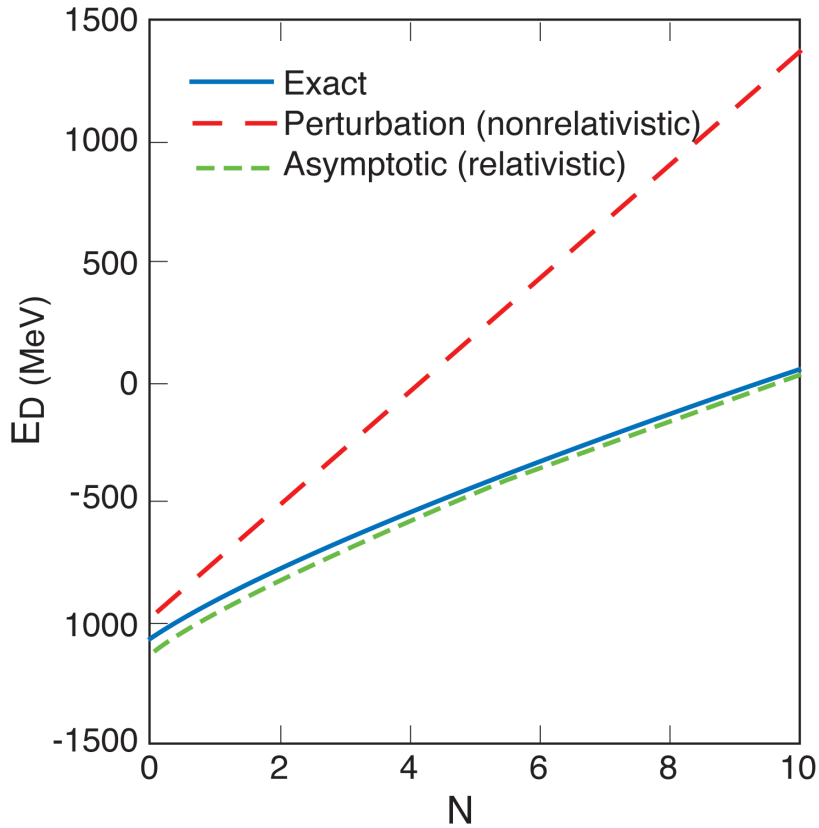

Fig. 1.
The Dirac binding energies, E_D, for the spherical harmonic oscillator as a function of N. The exact energies are the solid line, the perturbation approximation (nonrelativistic) is the dashed line, and the asymptotic approximation (relativistic) is the short dashed line.

Calculation of Neutron Spectra in beta-delayed Neutron-Emission

Toshihiko Kawano, Peter Möller, and William B. Wilson, T-16

Nuclear fission produces both "prompt" and "delayed" neutrons. The fraction of delayed neutrons, which are emitted after β-decay of parent precursors, is small. However, they still contribute to the neutron multiplicity of the nuclear criticality systems.

We have previously discussed β-decay half-life and β-delayed neutron-emission calculations in our microscopic QRPA-FY model [1]. This and other models of ours are able to provide not only calculated values for β-decay half-lives $T_{1/2}$ and β-delayed neutron-emission probabilities P_n for decays from the nuclear ground state but also provide these for decays from spin-isomeric states [2]. In addition they provide single-particle levels and complete β-strength functions for nuclei throughout the nuclear chart.

We have now started a program to calculate β-delayed neutron spectra. The first step is to calculate the relative β-decay intensities from a fission-fragment parent precursor ground-state to all accessible states in the daughter nucleus. As an example we show in Fig. 1 the calculated β-strength function in the decay of ^{147}Cs. The intensities of the decays are obtained by multiplying the strength functions with the phase space factor for electron and neutrino emission. The wide arrows in the figure indicate the one, two, and three-neutron separation energies S_{1n}, S_{2n}, and S_{3n}, whereas the thin arrow is the Q value for the decay: only states below this energy can be populated in the decay. The fraction of the decays that terminate in states above S_{in} (and below Q_β), that is 11.81% of the decays may emit a neutron.

For each state in the daughter nucleus (^{147}Ba, when the precursor is ^{147}Cs) above the neutron separation energy, we calculate the neutron emission probabilities to the ground and excited states of residual nucleus (^{146}Ba), using the Hauser-Feshbach statistical model. Figure 2 shows the calculated β-delayed neutron spectrum for ^{147}Cs, compared with the ENDF delayed neutron data.

We plan to extend these calculations to all fission products. Model issues that remain to be studied are how or if to account for the spins of the parent and daughter states and how or if to account for the influence of first forbidden transitions on the delayed neutron spectra.

For more information contact Toshihiko Kawano at kawano@lanl.gov.

[1] P. Möller and J. Randrup, *Nucl. Phys. A* **514** 1–48 (1990).
[2] Bernd Pfeiffer, et al., *Prog. Nucl. Energy* **41** 49–69 (2002); B. Pfeiffer, et al, "Status of Delayed-Neutron Precursor Data: Half-lives and Neutron Emission Probabilities," Los Alamos National Laboratory report LA-UR-00-5897 (December 2000).

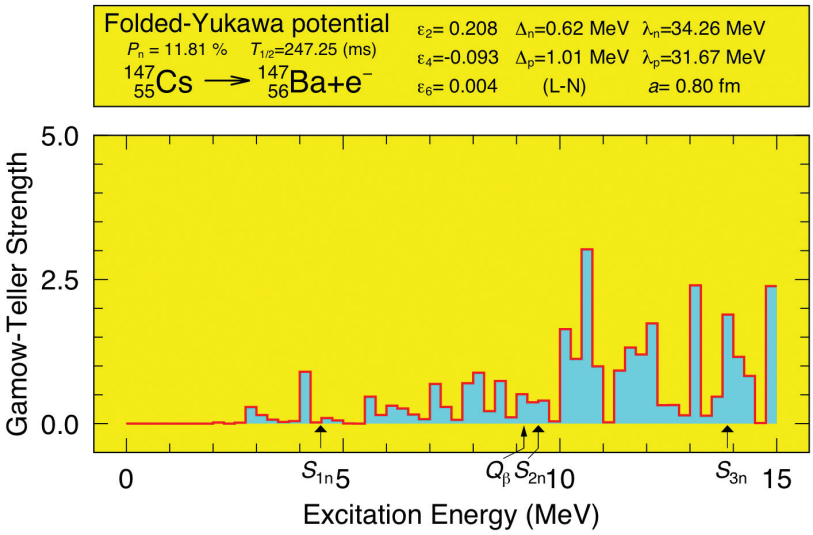

Fig. 1. *Calculated β-strength function for ^{147}Cs β-decay to ^{147}Ba.*

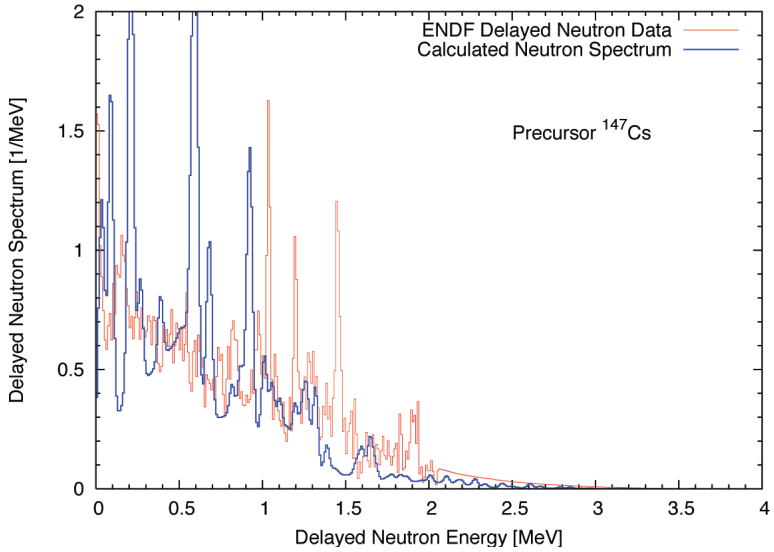

Fig. 2. *Calculated β-delayed neutron spectrum following the β-decay of ^{147}Cs, compared to ENDF data.*

Determination of Am Fission Barriers from Calculated High-Dimensional Potential-Energy Surfaces

Peter Möller, T-16

In previous T-Division *Special Feature* and *Research Highlights* publications we have discussed calculations of fission potential-energy surfaces as functions of up to five different nuclear shape coordinates as the system evolves from a ground-state shape to two separated fission fragments. The five shape coordinates we consider beyond the second minimum in the fission barrier are elongation, neck radius, spheroidal deformations of the emerging left and right fragments, and left-right mass asymmetry. For less deformed shapes between the spherical shape and the second minimum in the barrier we consider three shape coordinates: ε_2 (quadrupole), ε_4 (hexadecapole), and γ (axial asymmetry). It is relatively straightforward (but a few thousand lines of fortran codes and scripts are required) by use of automated scripts to determine the height of the first, inner peak and of the second, outer peak in the fission barrier from the calculated potential-energy surfaces. We showed in the *Special Feature 2004* such results for a long chain of uranium isotopes. It is more complicated to develop completely automated scripts to determine additional features of the barriers. The reason is that it is not clear to what detail barriers need to be known for modeling fission cross sections and other quantities.

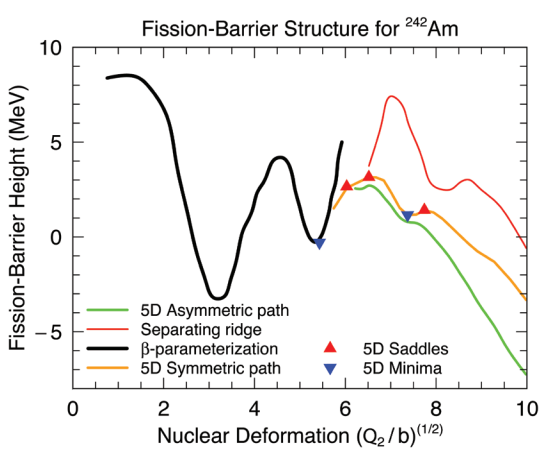

Fig. 1. ***Structures identified in the calculated fission potential-energy for ^{242}Am.***

Actually, the detail needed would depend on the sophistication of the neutron-induced fission cross-section model. Currently many such models describe the fission barrier as a single-peaked parabolic barrier. However, it is anticipated that better accounting for the additional complexity of the fission barrier will result in cross-section models with better predictability. Such work is in progress.

As an example of our work on Am, we show in Fig. 1 some fission-barrier characteristics we have determined, by use of imaginary water-immersion techniques from the full potential-energy surfaces. The green curve in the right part of the figure represents a "valley," corresponding to mass-asymmetric shapes, in the potential energy surface. It is determined in the following way. For each Q_2 value considered in the calculation we locate all minima in the remaining 4-dimensional (4-D) space. Normally there are only 2 to 5 such minima that are deeper than a prescribed tolerance value.

For ^{242}Am we find that for each Q_2 value one of the minima always corresponds to a shape with emerging fragment masses around 140 and 100, which is the usual mean mass asymmetry observed in fission. Moreover, the shape of the large emerging fragment is near spherical, whereas the smaller fragment is well deformed. The green line connects the minima corresponding to this characteristic shape that we have identified for successive Q_2 values.

Another valley representing mass-symmetric shapes is also found and is shown in yellow. The red curve represents the ridge between these two valleys. In the full 5-D space we have furthermore located minima shown by downward-pointing blue triangles and saddles shown by upward-pointing red triangles. The thick black curve represents the potential energy from just beyond the sphere to slightly beyond the second minimum. It is obtained in the β multipole parameterization for successive β_2 values by minimizing the potential energy with respect to higher multipoles (up to β_6). We have earlier emphasized that such a procedure in general *does not* give potential energy curves that include the correct saddle points. In this case this deficiency is very visible: the right part of the thick black curve drastically overshoots the saddle points we have found in another parameterization in a full 5-D space. However, the minimum found in

this *different* shape parameterization at about $\sqrt{Q_2} = 5.5$ coincides very well with the second minimum on the black curve. This is a very important consistency check on our calculations. We have from other nonconstrained calculations verified that to the left of the second minimum the black curve properly represents the results that are obtained from full, higher-dimensional calculations.

Further analyses by water-flow techniques reveal that the saddle at $\sqrt{Q_2} = 6$ represents the saddle between the second minimum and the asymmetric (green curve) valley, whereas the saddle at $\sqrt{Q_2} = 6.5$ represents the saddle between the second minimum and the symmetric (yellow) valley. From the figure we see that a well-established asymmetric valley does not appear until slightly beyond the saddle corresponding to the asymmetric fission mode, whereas the symmetric valley is well manifested across the saddle corresponding to the symmetric fission mode. From Fig. 1 we obtain Fig. 2 in which the ^{242}Am barrier is represented as a *multiple-mode* fission barrier, in this case *bimodal*, asymmetric, and symmetric, in a form that might serve as a starting point for a more sophisticated model for (n,f) cross-section modeling than is a simple parabolic barrier. In this figure we also indicate a few representative nuclear shapes at various stages of the fission process.

In Fig. 3 we compare to experimental data for a sequence of Am isotopes calculated inner and outer barrier heights, which we have determined from an analysis similar to the one above for ^{242}Am. Especially the calculated outer barriers seem to show some systematic deviations from experimental data. However we need to observe that the barrier heights are not measured directly, they are deduced from modeling fission cross sections. Often these models assume a much simpler barrier structure than the one we have determined here and have phenomenological prescriptions for model features such as level densities. It is therefore desirable to model fission cross sections based on more realistic barriers such as the calculated ^{242}Am barrier shown in Figs. 1 and 2, and also to use calculated microscopic levels at the saddle points shown as starting points

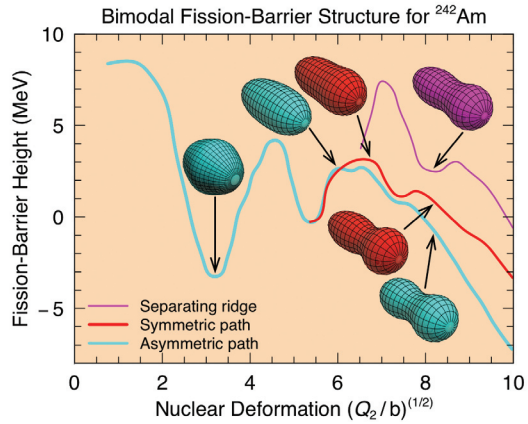

Fig. 2. ***Representation of the potential energy structure of ^{242}Am in terms of a bimodal fission barrier.***

for level density modeling. Such work may lead to less phenomenological models and consequently more predictive models, and to better correspondence between calculated barriers and the "experimental" barriers that are extracted from fission-cross-section modeling.

For more information contact Peter Möller at moller@lanl.gov.

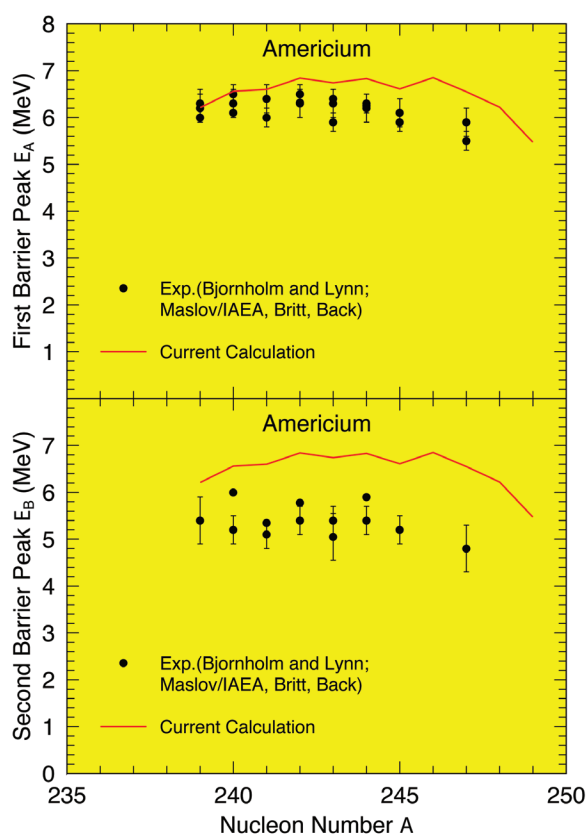

Fig. 2. ***Calculated inner and outer barrier heights for a sequence of Am isotopes compared to barrier heights deduced from experimental fission cross sections.***

The Reactions $^{13}C(p,\gamma)$ ^{14}N and $^{10}B(p,\alpha)$ ^{7}Be

Philip R. Page and Gerald M. Hale, T-16

Explosives containing ^{14}N inside cargo should be inspected for Homeland Security mainly at airports, but also at other ports. In order to perform such an inspection a nuclear resonance absorption technique has been proposed [1] where the ^{14}N is bombarded (interrogated) by a monoenergetic γ-ray beam where the cross section is very high. The way this can be done is by preparing laboratory energy 1.76 MeV protons in a storage ring, which then impinges on a very pure ^{13}C target to form monoenergetic γ-rays because of a very narrow resonance in the ^{14}N nucleus. These γ-rays are emitted at a laboratory angle of 80.7° and an energy of 9.17 MeV, and serve as the beam that is needed to inspect cargo containing ^{14}N. Hence a high flux monoenergetic proton beam produces a monoenergetic γ-beam, suitable for rapid cargo inspection, via the reaction ^{13}C(p, γ_0) ^{14}N. The fact that the recoil nucleus (here ^{14}N) is in its ground state will be indicated by a subscript "0" from now on. The current evaluation focuses on the very narrow resonance and parameterizes the background of various other resonances for proton energies up to 2 MeV.

The result of an R-matrix fit to known resonances is shown in Fig. 1. Since the cross section is plotted logarithmically, the height of the resonance at 1.76 MeV proton energy is underemphasized. An evaluated cross-section file with angular distributions in ENDF format is prepared for the reaction ^{13}C(p, γ_0) in the proton energy range 0.01–2 MeV.

As a separate project, the reaction $^{10}B(p,\alpha)^{7}Be$ is evaluated because it is relevant to thermonuclear explosions. This evaluation comes from the first multichannel R-matrix analysis of the reactions in the ^{11}C system ever performed. An evaluation of the S-factor for ^{10}B(p, α_0) had been done earlier [2], because of its importance in astrophysics.

An R-matrix fit of experimental nuclear data on the elastic scattering reaction $^{10}B(p,p_0)$ ^{10}B and of the exothermic reaction $^{10}B(p,\alpha_0)$ is performed. Data sets from 10 experimental references with 1845 data points are used. The overall χ^2 per degree of freedom for all data entered is 2.2.

The evaluated $^{10}B(p,\alpha_0)$ cross section is presented in Fig. 1. The large renormalizations needed for the modern Angulo 1993 and Youn 1991 data may not be a concern as it is known that these reactions disagree by large factors. It is comforting that the Chiari 2001 data on elastic scattering, which is available above 0.5 MeV, determine the normalizations of the Angulo 1993 and Youn 1991 data, while itself fitting with normalizations within 4% of the experimental value. The normalization of the $^{10}B(p,\alpha_0)$ data is hence strongly constrained by the $^{10}B(p,p_0)^{10}B$ data. The exact normalizations of the $^{10}B(p,\alpha_0)$ data above 1.5 MeV have changed considerably at various stages of the analysis.

An evaluated cross-section file with angular distributions in ENDF format is prepared for the reactions $^{10}B(p,\alpha_0)$ and $p^{10}B$ elastic scattering in the energy range 0.01–3 MeV. Maxwellian averaged cross sections in nuclear data interface (NDI) format are prepared for the reaction $^{10}B(p,\alpha_0)$. These may not be very accurate below a temperature of about 10 keV. Details of the analysis are available in Ref. [3].

For more information contact Philip R. Page at prp@lanl.gov.

[1] R.E. Morgado, et al., "Prototype Explosives-Detection System Based on Nuclear-Resonance Absorption in Nitrogen," Los Alamos National Laboratory report LA-12776-MS (June 1994); D. Vartsky, et al., *Nucl. Phys. A* **505**, 328 (1989); W. Biesot and P.B. Smith, *Phys. Rev. C* **24**, 6 (1981).

[2] C. Angulo, et al., *Nucl. Phys. A* **656**, 3 (1999).
[3] P.R. Page, "^{11}C Nuclear Data Evaluation," Los Alamos National Laboratory report LA-UR-05-6250 (August 2005).

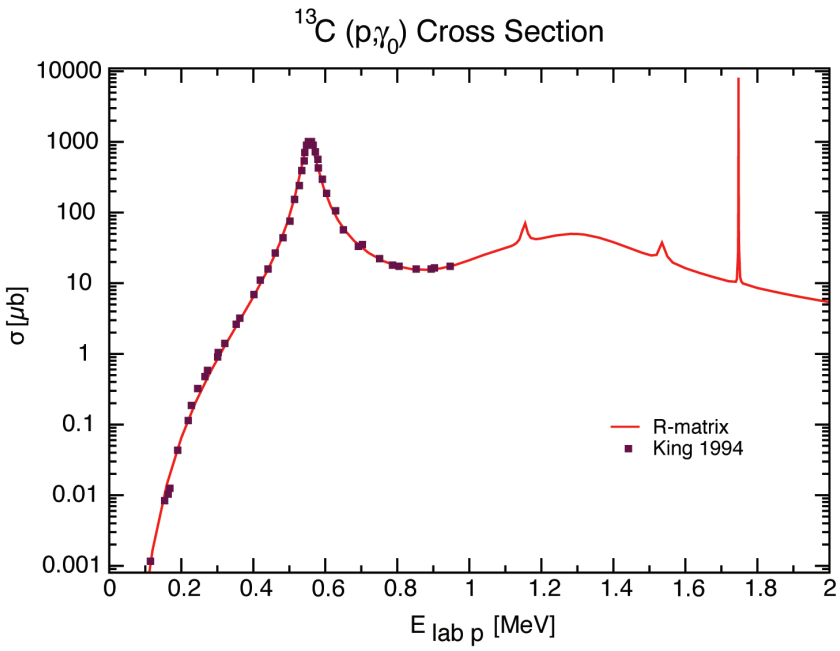

Fig. 1.
The R-matrix analysis cross section (red curve) in microbarns for the $^{13}C(p, \gamma_0)^{14}N$ reaction up to a proton laboratory energy $E_{lab\ p}$ of 2 MeV, with the one set of experimental (integrated) cross-section data entered in the analysis.

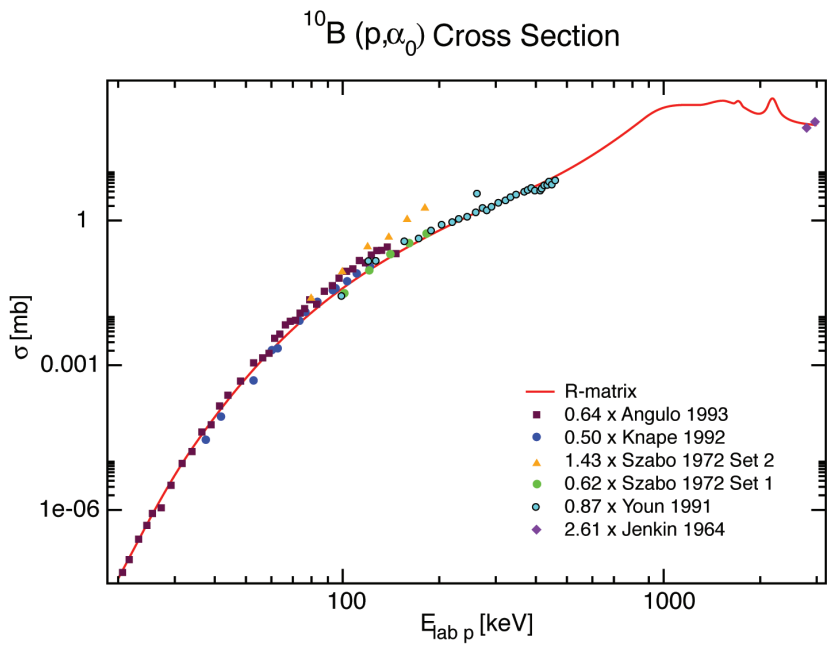

Fig. 2.
The R-matrix analysis cross section (red curve) in millibarns for the $^{10}B(p, \alpha_0)^{7}Be$ reaction up to a proton laboratory energy $E_{lab\ p}$ of 3 MeV, with the six sets of experimental (integrated) cross-section data entered in the analysis. The numerical factors in front of the experimental data labels indicate that the data must be multiplied by those factors to obtain the points plotted.

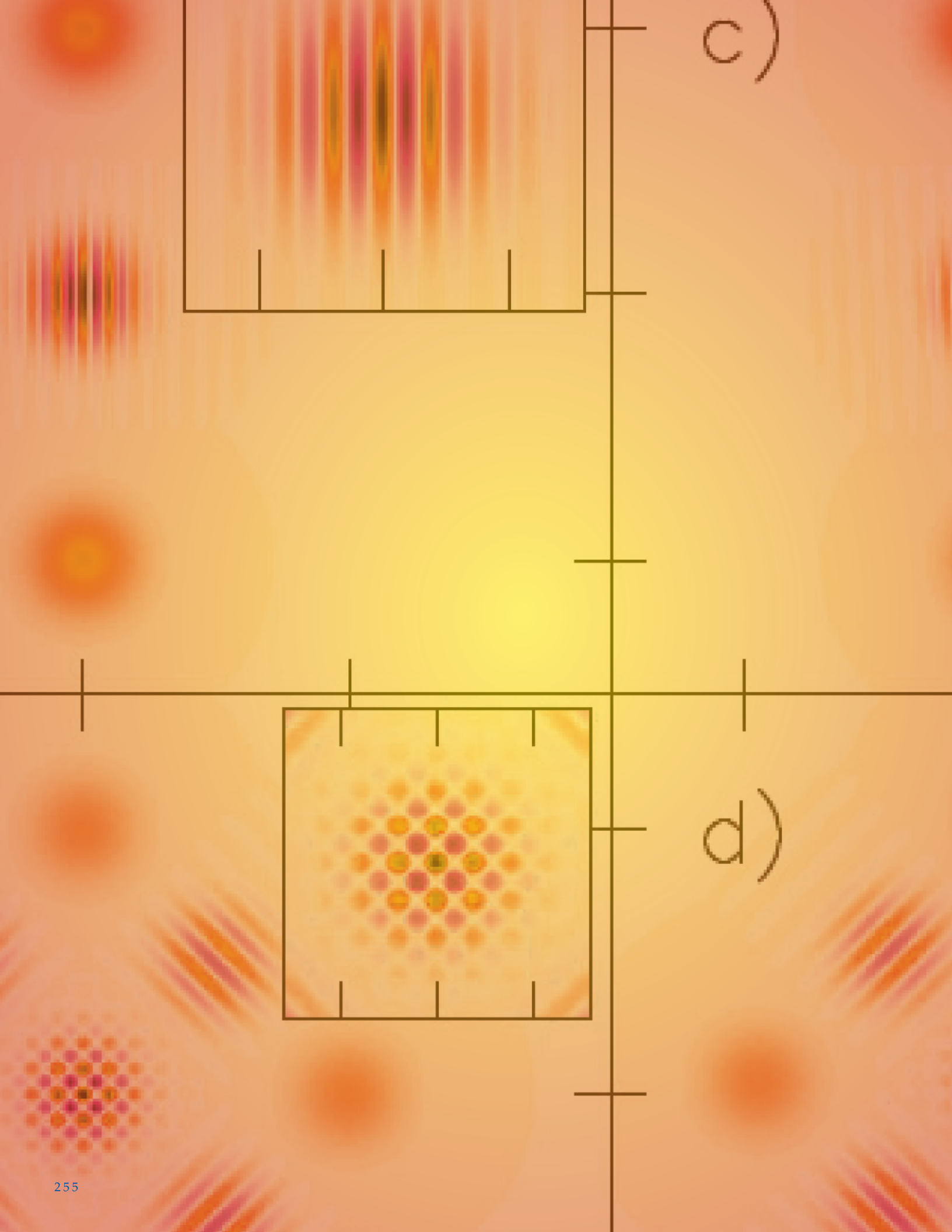
c)
d)

Quantum Computing

T-QC

Project Team Leader: Juan P. Paz
505.664.0441; jpaz@lanl.gov

Quantum Computing (T-QC) holds tremendous promise for efficiently solving some of the most difficult problems in computational science, such as integer factorization, discrete logarithms, and quantum modeling that are intractable on any present or future conventional computer. New concepts for T-QC implementations, alogrithms, and advances in theoretical understanding of the physics requirements for T-QC appear almost weekly in the scientific literature.

Sub-Planck Structures in Phase Space and Heisenberg-Limited Measurements

Diego A. R. Dalvit and Wojciech H. Zurek, T-QC; and Luiz Davidovich and Fabricio Toscano, Rio de Janeiro

Quantum measurement was, for a long time, synonymous with the foundations of quantum theory. Yet, this subject has recently acquired practical, engineering relevance, as it is now known that using probes prepared in judiciously chosen quantum states can increase their sensitivity. As a consequence, quantum metrology became a subject of great practical interest. Typical problems in quantum metrology are high-precision phase measurements (for example, in quantum interferometry), and the detection of weak forces (such as signal in gravitational wave detectors). The precision of the measurement of these small perturbations depends on the resources involved in the measurement process, such as the total number of photons employed, the type of probes used for the detection, the efficiency of the detectors, etc. Using probes prepared in quasiclassical states, such as coherent states of light, the precision is at the standard quantum limit (SQL): the minimal detectable phase shift is inversely proportional to the square root of the number of photons used. By employing highly nonclassical quantum states (such as Schrödinger cat states) it is possible to surpass the SQL limit and reach the ultimate precision allowed by quantum theory: the Heisenberg limit. Here the minimal detectable phase shift scales as the inverse of the number of photons. Achieving such a limit would open exciting possibilities for ultrasensitive detection of weak forces and other quantum technology applications [1].

Every quantum state can be represented in phase space by means of the Wigner distribution, which is the closest analog to the classical phase space representation of a system. The Wigner function of a nonclassical quantum state, such as superpositions of coherent states (Fig. 1), possesses small-scale structures that are surprisingly small [2]: they have phase space areas much smaller than the Planck size one would naively guess for the size of phase space features from the Heisenberg uncertainty principle. These sub-Planck structures represent interference effects. Typical area of such structures can be as small as (but no smaller than) Planck constant *divided* by the classical action associated with the state (which is proportional to the number of photons contained in that state). When a perturbation acts on such a nonlocal state, it will typically rotate or displace it in phase space. The perturbed and unperturbed states can be distinguished from one another (they become quasiorthogonal) when the peaks (valleys) of the sub-Planck structures of one come on top of the valleys (peaks) of the sub-Planck structures of the other (Fig.1). Thus, the size of the sub-Planck structures sets a sensitivity limit on a probe prepared initially in such a state [2]. The typical linear size of the sub-Planck structures is inversely proportional to the square root of the number of photons contained in the nonclassical state. Therefore, states that saturate the limit on the smallest phase space structures can allow one to attain Heisenberg-limited sensitivity.

We have developed [3] two experimental proposals to implement these ideas with cold atomic systems, both in the context of cavity quantum electrodynamics (QED) and trapped ions. In the cavity QED experiment, one would entangle the state of the electromagnetic field inside the cavity with the internal electronic states of an atom that flies through the cavity. By appropriately choosing the interaction time between the two systems it is possible to create a "Schrödinger

cat" state of the electromagnetic field (i.e., a superposition of two coherent states of light) that, when subjected to a perturbation, has Heisenberg-limited sensitivity. The information of the perturbation is encoded in the atomic state, so that by measuring the populations of the atom as it exits the cavity, one can retrieve information of the perturbation. The ion trap experiment has more flexibility, and it is possible to create more complicated correlated states, such as a superposition of four coherent states (a "compass state") of the vibrational motion of the ion in the trap. Such states have sub-Planck structures, and are therefore useful to Heisenberg-limited precision measurements. Compass states can be generated using quantum state engineering by tailoring the interaction between external lasers and the internal and external dynamics of the trapped ion. This provides us with different operations for doing controlled coherent quantum dynamics, such as conditional rotations and translations. These and other operations form a toolbox that is required, not only for doing ultrasensitive detection, but are also employed for quantum information processing and quantum simulation with cold atomic systems.

For more information contact Diego A. R. Dalvit at dalvit@lanl.gov.

[1] V. Giovannetti, et al., *Science* **306**, 1330 (2004).
[2] W.H. Zurek, *Nature* (London) **412**, 712 (2001).
[3] D.A.R. Dalvit and W. Zurek, "Heisenberg-limited Measurement of Displacements and Rotations with Cavity QED and Ion Traps," Los Alamos National Laboratory report LA-UR-05-4229 (June 2005). F. Toscano, et al., quant-ph/0508093.

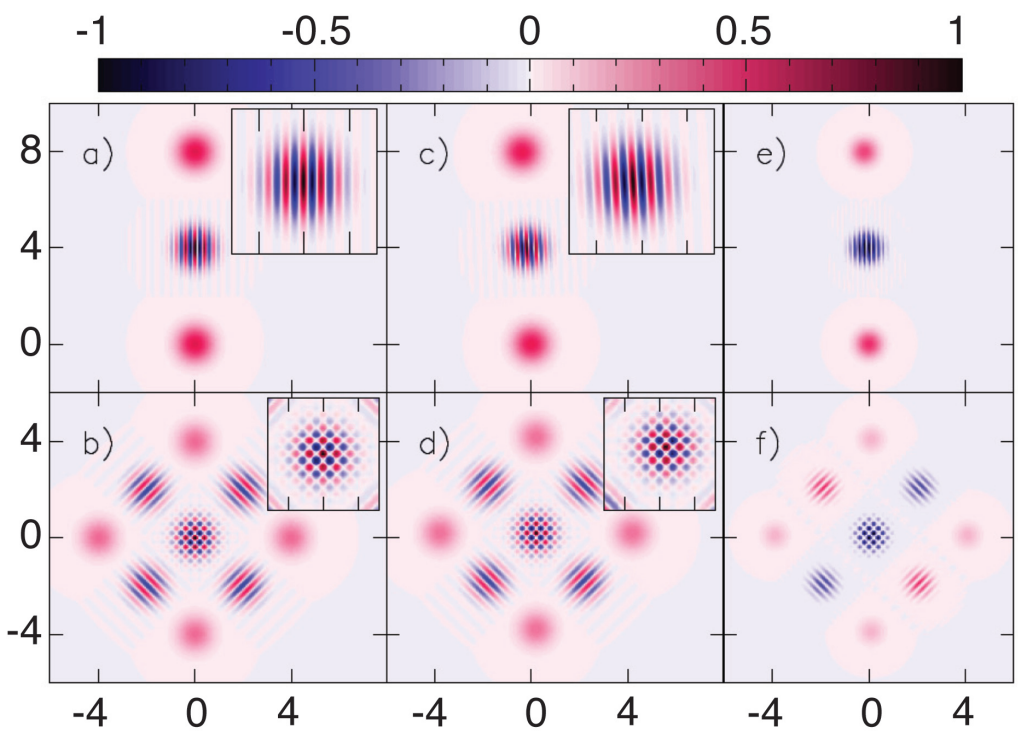

Fig. 1. ***Correlated quantum states have sub-Planck structures in their Wigner function that are closely related to Heisenberg-limited sensitivity. Panels a) and c) show a cat state (i.e., the superposition of two coherent states) before and after a rotation is applied to the system. Panels b) and d) show a compass state (i.e., the superposition of four coherent states) before and after a displacement is applied to the system. In e) and f) we display the respective products of the unperturbed and perturbed Wigner functions. When performing the integration over phase space, the negative contributions (in blue) cancel the positive ones (in red), leading to quasiorthogonality. The minimal detectable rotations and displacements are at the Heisenberg limit.***

Shock Waves in Ultracold Atomic Gases

Bogdan Damski, T-QC

Ultracold atomic gases, e.g., ^{87}Rb below Bose-Einstein condensation temperature or ^{6}Li below Fermi temperature, can be nowadays routinely studied in laboratories. One of the great properties of these gases is that they can be easily manipulated by external magnetic potentials and laser beams. For instance, almost arbitrarily shaped initial density perturbation can be created with the help of a properly detuned laser beam, and then one can switch a laser off and let a perturbation evolve. A typical time evolution (Fig. 1) leads to formation of shock waves, i.e., steep density profiles where density changes occur on the smallest available length scale in the system. Once a shock wave is formed, density oscillations are produced in front of it.

The aim of this research is to theoretically characterize shock formation and propagation in ultracold atomic gases [1, 2, 3]. In particular, I have derived a simple expression that relates the speed of propagation of a broad pulse to its amplitude and sound velocity in the cloud [3]. This expression might be used for a precise determination of sound velocity in a cold atom cloud.

For more information contact Bogdan Damski at bodzio@lanl.gov.

[1] B. Damski, *J. Phys. B* **37**, L85 (2004).
[2] B. Damski, *Phys. Rev. A* **69**, 043610 (2004).
[3] B. Damski, cond-mat/0506210 (to appear in *Phys. Rev. A*).

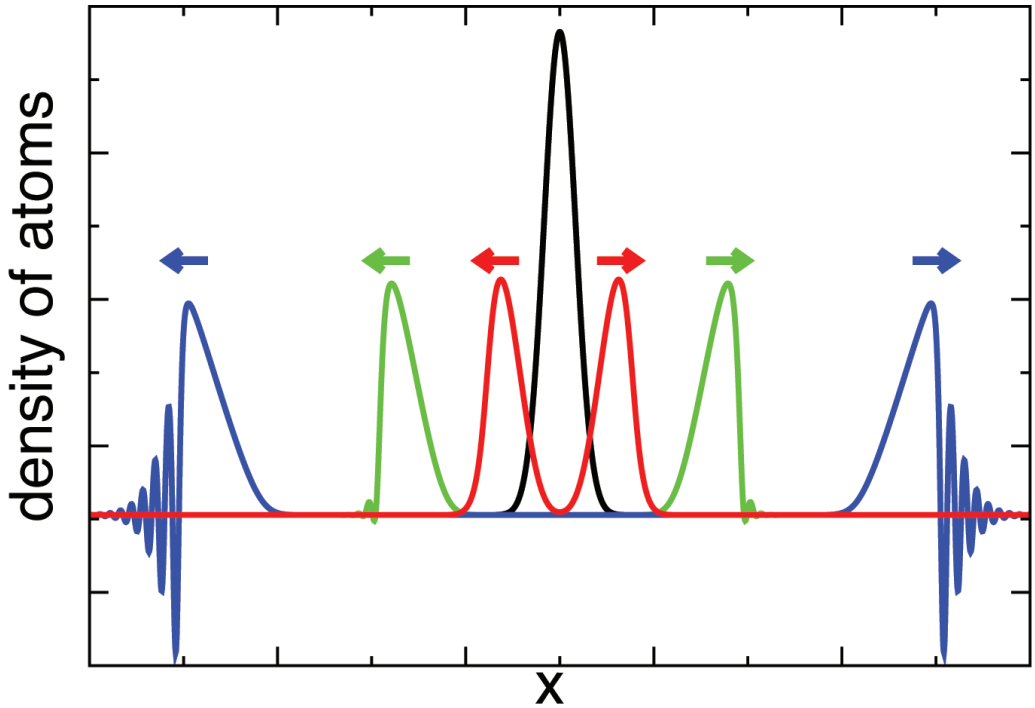

Fig. 1.
Density profiles of a quasi-one-dimensional, homogeneous gas of ultracold atoms at different time instants. The black line is the initial density profile with a bump created by an external laser beam. The red line shows that the bump in the initial density profile splits into two, oppositely moving, pieces after a laser turnoff. The green line presents the self-steepening of impulses during evolution. The blue line shows shocks propagation resulting in creation of density oscillations.

A
Abdallah, Jr., Joseph 173
Addessio, Francis L. 9, 29, 41, 53
Ahluwalia, Rajeev 71, 77
Alder, Berni 119
Alley, Ed 119
Amar, Jacques 87
Anglade, P.M. 175
Asthagiri, D. 89

B
Balatsky, Alexander V. 59, 65, 83
Barber, John L. 119
Bardenhagen, Scott 121, 123
Barré, Julien 61
Batista, Cristian D. 63, 65
Batista, Enrique R. 91, 95, 103
Berman, Gennady P. 215, 217, 219, 221, 223, 225
Bishop, Alan R. iii, 61, 75, 83, 115, 215, 221, 225
Bock, Nicolas 5, 19
Brezzi, Franco 191, 193
Bronkhorst, Curt A. 11, 39
Brown, Geoffrey W. 215, 221
Brydon, Andrew 121, 123
Burakovsky, Leonid 5

C
Cao, W. 77
Cerullo, G. 115
Chacón, Luis 155, 229, 231
Chernobrod, Boris M. 215, 221, 223
Chernyak, Vladimir 105
Chisolm, Eric 5, 7
Chitanvis, Shirish M. 125, 127, 129, 145
Chu, Shaoping 165
Clark, Aurora E. 95
Clements, Bradford E. 9, 11, 13, 21, 27, 29
Clérouin, J. 175
Cline, Michael C. 161
Colarieti-Tosti, Massimiliano 23, 25
Colgan, James 177, 179
Collins, Lee A. 177, 225
Crockett, Scott 5
Crooker, S.A. 79
Csanak, George 173, 177, 181
Cucchietti, Fernando M. 171
Cumming, Andrew 185

D
Dalvit, Diego A.R. 257
Damski, Bogdan 259
Daughton, William 237
Davidovich, Luiz 257
De Lorenzi-Venneri, Giulia 5, 35
Delzanno, Gian Luca 231, 233
Diaconu, Cristian V. 103
Dienes, John K. 53
Dodd, Evan 173
Dotson, Paul J. iii
Drake, J. 165
Dyadechko, Vadim 195

E
Elliott, Scott 165
Eriksson, Olle 23, 25
Evans, Katherine J. 155
Evstatiev, Evstati G. 233

F
Faenov, Anatoly 173
Fenimore, Paul W. 209
Finn, John M. 231, 233, 235
Fontes, Christopher J. 177
Freytag, Bernd 187
Fukuda, Yuji 173

G
Gambetta, A. 115
Gammel, Tinka 5
Garimella, Rao 195
George, Denise 5, 7, 15
Germann, Timothy C. 119, 135, 137, 139, 149
Ginocchio, Joseph N. 247
Gorshkov, Vyacheslav N. 219, 223
Graf, Matthias J. 67, 81
Greeff, Carl 5, 7, 17, 41
Gubernatis, James E. 63

H
Habib, Salman 205
Hagberg, Aric 197
Hale, Gerald M. 253
Hansen, B.L. 39
Hanson, David E. 93
Harlow, Francis H. 43
Harstad, Eric N. 41
Hastings, Matthew B. 109
Hawley, Marilyn 215, 221
Hawreliak, J. 135
Hay, P. Jeffrey 95, 103

Los Alamos NATIONAL LABORATORY EST. 1943

Heger, Alexander 185
Heitmann, Katrin 205
Hengartner, Nicolas 235
Henson, Neil J. 97
Herwig, Falk 187
Holian, Brad L. 119, 135, 137
Holmström, Erik 19
Houlton, Robert 93
Hueckstaedt, Robert M. 187
Hruška, M. 79

I
Ionita, Axinte 9, 21, 27
Intrator, Thomas 237

J
Jaramillo, Eugenio 131, 133
Johnson, J.D. 5, 33
Johnson, Norman L. 139
Jones, Christopher S. 235
Jones, P. 165
Jungman, Gerard 205

K
Kadau, Kai 119, 135, 137, 139
Kalantar, D.H. 135
Kamenev, Dmitry I. 217
Kawano, Toshihiko 249
Kilcrease, David P. 181
Knoll, Dana A. 155, 167
Kober, Edward M. 73
Kos, Š. 79
Koslowski, Marisol 101
Kress, Joel D. 99
Ku, Li-Chung 69
Kurien, Susan 199

L
LaBute, Montiago X. 209
Lanzani, G. 115
Lapenta, Giovanni 229, 237, 239, 241, 243
Lashley, Jason C. 67
Lavraud, Benoit 237
LeSar, Richard 101
Lipnikov, Konstantin 191, 193
Lizárraga, Raquel 23, 25
Lomdahl, Peter S. 119, 135, 137, 139
Longini, Ira M. 139
Lookman, Turab 61, 67, 71, 77, 145

M
Ma, Xia 159
Macken, Catherine A. 139
MacKerrow, Edward P. 219
Maltrud, Mathew E. 165
Manzoni, C. 115
Markidis, Stephano 243
Martin, Richard L. 91, 95, 103, 115
Mas, Eric M. 9, 11, 21, 27
Maudlin, Paul J. 51
Mazevet, Stephane 175
McMahon, Benjamin H. 209
McPherson, Tim 139
Meneghetti, M. 115
Menikoff, Ralph 141
Menna, E. 115
Möller, Peter 249, 251
Mousseau, Vincent A. 155, 157, 167

N
Niklasson, Anders M. N. 19
Nordström, Lars 23, 25

O
O'Rourke, Peter J. 161
Ortiz, Gerardo 65
Ott, Kevin C. 97

P
Padial-Collins, Nely 159
Page, Philip R. 253
Paulaitis, Michael E. 89
Peery, Travis 5
Peterson, Paul D. 27
Pezzé, Luca 225
Piryatinski, Andrei 105, 115
Plohr, JeeYeon N. 9, 29
Ponomarenko, Sergey A. 181
Pratt, Lawrence R. 89

Q

R
Rasmussen, Kim Ø. 73, 75, 83, 145
Rauenzahn, Rick M. 155, 167
Recoules, V. 175
Reichhardt, Charles 107

Los Alamos NATIONAL LABORATORY EST. 1943

Reichhardt, Cynthia J. Olson 107, 109, 111
Rosolankova, K. 135
Rudin, Sven 5, 31, 33

S
Sahota, Manjit S. 161
Sanbonmatsu, Kevin Y. 211
Sauls, James A. 81
Saxena, Avadh 61, 71, 77, 79, 115
Schraad, Mark W. 43, 45
Sewell, Thomas D. 131, 133, 145
Shashkov, Mikhail 193, 195
Sherrill, Manolo 173, 181
Shim, Yunsic 87
Simoncini, Valeria 191
Smerzi, Augusto 225
Smith, Darryl L. 79
Spontak, R.J. 73
Stepanov, Misha 105
Strachan, Alejandro 131, 133, 149
Swartz, Blair 195

T
Tartakovsky, Daniel M. 201
Thomson, Robb 101
Timmermans, Eddy 171
Timmes, Francis X. 187
Torres, David J. 163
Toscano, Fabricio 257
Tretiak, Sergei 105, 113, 115
Trugman, Stuart 69, 83
Tsifrinovich, Vladimir I. 215, 217, 223
Tung, Chang-Shung 209

U
Uberuaga, Blas 87

V
VanderHeyden, W. Brian 159
Vorontsov, Anton B. 81
Voter, Arthur F. 87
Voulgarakis, Nikolaos 75

W
Wallace, Duane 5, 35, 67
Wang, Xidi 219
Wark, J.S. 135
Welch, Cynthia F. 143
Welch, Paul 125, 143, 145, 147
Wharton, Lucas 123
Williams, Todd O. 11, 47
Wills, John 19, 23, 25, 31, 33, 67
Wilson, William B. 249
Woosley, Stan 185

X
Xiu, Dongbin 201

Y
Yin, Wei-Guo 63

Z
Zerah, G. 175
Zhang, Duan Z. 159
Zhao, Shijin 149
Zhu, Jian-Xin 83
Zou, Qisu 159
Zubelewicz, Aleksander 49
Zuccaro, Gianluca 239
Zuo, Q. Ken 41, 51, 53, 55
Zurek, Wojciech H. 257

Los Alamos NATIONAL LABORATORY EST. 1943